Feeding the ocean?

A biological mediation of estuarine silicon

Author:
Holly Jo Welsby

Supervisors:
Doctor Katharine Hendry
Doctor Rupert Perkins
Professor Marian Yallop
Professor Sandra Arndt

A dissertation submitted to the University of Bristol in accordance with the requirements for award of the degree of Degree of Doctor of Philosophy in the Faculty of Science.

School of Earth Sciences

May 2019

Word count: 56,763

Abstract

Riverine dissolved silicon (DSi) and biogenic silica (BSi) are altered along the estuarine gradient by several biological and abiological processes governed by physical forcings. An important area controlling silicon (Si) transport in estuaries, which is often overlooked, is the benthic diatom-dominated biofilm system on intertidal mudflats. Here, the hypertidal Severn Estuary, southwest UK has been used as a case study to improve our understanding of DSi and BSi transport in these benthic-dominated systems. Between 2016 and 2018, ecological surveys were carried out along the River Severn, and its estuary and tributaries (Wye, Usk, Avon, and Cardiff Bay), alongside surveys of the benthic biofilms on the intertidal mudflats.

A combination of high turbidity, lack of stratification, low nutrient concentrations and low residence times restricted phytoplankton development in the Severn and its tributaries. Low phytoplankton DSi uptake, land-use changes and groundwater supply, contributed to the isotopically light river water (denoted by $\delta^{30}Si_{DSi}$: +0.61-1.05‰). River and tidal hydrodynamics drove spatio-temporal changes in dissolved constituents; the longitudinal profiles followed the classical view of dilution with downstream transport, resulting in low concentrations in the Bristol Channel. Despite other estuarine systems retaining DSi (global average of 20%), the hypertidal regime of the Severn Estuary coupled to the low pelagic uptake of DSi, prevented any significant DSi retention.

Several sources of BSi into the estuary water column were identified. Siliceous phytoplankton contributed to a small amount of the estuarine BSi budget, whilst riverine inputs of BSi (e.g. phytoliths), and most importantly, benthic-sourced BSi, influenced the spatio-temporal changes in estuarine BSi. Relatively high BSi concentrations were measured in the upper Severn Estuary (maximum of 14.9 mg/L), and accounted for over 66% of the total bioavailable Si present in the estuary, and were characterised by isotopically heavy waters ($\delta^{30}Si_{DSi}$). It was hypothesised that the BSi originated from the diatom-dominated biofilms on the intertidal mudflats. The biofilms were found to be biomass-rich (173.6±24.7 μg/g *dw. sed.* chl *a* content) with high productivity (relative electron transport rates of 155±13 *rel. units*), driven by their photoprotective adaptions (behavioural and photophysiological down-regulation) to these harsh intertidal environments. The biofilm organisms had a high potential to consume DSi and biomineralize BSi, despite the short emersion periods, and contributed to isotopically heavy mudflat water (+1.19-2.03 ‰), alongside abiological processes when biological activity was suppressed. The shear stress of the fast-flowing tidal currents would have exceeded the erosion thresholds of the biofilms, despite the biofilms exhibiting sediment biostabilization properties (total and colloidal-S carbohydrates). These tidal currents likely eroded and transported the sediment-polymer-diatom matrix, and thus BSi into the water column (maximum of 91.4 mg BSi/L), with SPM and BSi remaining tightly coupled in the near-bed suspension (fluid-mud layer) and the surf zone (bioflocculation). The combination of physical forcings (erosion, deposition, burial, dispersion and advection) reduced the BSi concentration in the surf zone (maximum 15.4 mg BSi/L).

Here, a modified version of the one-dimensional reactive transport Carbon-Generic Estuarine Model has been applied as an alternative tool to disentangle the complex hydro-biogeochemical estuarine processes. Maximum erosion rates of sediment and eroded benthic BSi occurred in the river-estuarine transition zone as a function of estuarine convergence and tidal/fluvial dynamics. The simulations produced the upper

Estuarine Turbidity Maximum (ETM) zone, with the location and turbidity concentrations in-line with previous published ETM values. These model outputs can be used to inform future sampling strategies especially in this zone.

The first time-series datasets of DSi and BSi, as well as Si isotopes in the Severn are presented. These have improved our understanding of the complex processes governing Si transport in hypertidal, benthic-dominated estuaries, and improves our understanding of the importance of estuaries in the terrestrial Si export, which is key to decipher the global Si budget. Regarding the Severn, with the pressures of climate change and the need to find predictable, renewable energy on the rise, the development of tidal power in the Severn Estuary is almost inevitable. The vital role these biofilms play as a food source, in stabilizing sediment and as an essential component of the Severn's Si cycle, must be considered prior to these developments.

Declaration

I declare that the work in this dissertation was carried out in accordance with the requirements of the University's Regulations and Code of Practice for Research Degree Programmes and that it has not been submitted for any other academic award. Except where indicated by specific reference in the text, the work is the candidate's own work. Work done in collaboration with, or with the assistance of, others, is indicated as such. Any views expressed in the dissertation are those of the author.

Signed .....

Date .....

To Dad.

Acknowledgements

First, I would like to express my sincere gratitude to my supervisor Dr Kate Hendry. Since meeting Kate during my first year of my undergraduate at Cardiff University back in 2011, she has supported me on several projects including my integrated Masters dissertation, which led to this PhD at the University of Bristol. None of this would have been possible if it weren't for Kate. She helped secure the Tratman Scholarship that has allowed me to carry out this research, and over the last three years she has been very supporting through every aspect of my work. The past two years have been the most difficult of my life so far, and Kate has done her utmost to support me through these times; she has never given up on me and she is always enthusiastic and positive! Kate has given me many opportunities throughout my PhD, from which I have learnt new skills, and has helped me become a better researcher. She also encouraged networking and attending conferences; some of which have led to some of the best experiences of my life. Kate is without a doubt, one of the best supervisor a PhD student could wish for, and it has been a great privilege working with her.

Secondly, I would like to sincerely thank Dr Rupert Perkins. I have also known Roo since my first year at Cardiff University. Not only has he given me valuable support throughout my undergraduate degree, his advice, guidance and patience throughout my PhD has been most helpful. Without Roo, I would never have been introduced to this field of work! Roo was also very kind to lend a lot of his equipment for this study. Thirdly, I would like to thank Prof. Sandra Arndt, my third supervisor, who introduced us to the reactive transport model applied in this thesis. I would like to thank her for her patience and continued help over the years, and for accommodating me at the University of Brussels. Fourthly, I would like to thank Prof. Marian Yallop for her kind and continued support over the course of the PhD. I have learnt new skills from Marian, and I am extremely grateful for her time measuring the mudflat samples for chlorophyll *a* content and carbohydrate concentrations.

Accompanying these acknowledgements, I would like to thank everyone who assisted me during fieldwork. For those who helped on the research vessels, I'd like to thank Ian Fryett (skipper), Jen Pinnion, Scott Armstrong, Lucy Taylor and Dr Elaine Mawbery. I would also like to express my thanks to all who assisted me sampling the intertidal mudflats and the rivers; Leanne Staddon, Timothy Gregory, Frances Boreham, Edward Bunker, James Chen. A special thanks goes to Jolene Cook for her help sampling the mudflats and for her work in the laboratory. I would also like to thank two Biology undergraduate students, Kate Spence and Aidan Byrne, for their extensive help in the summer of 2017 sampling the intertidal mudflats and measuring samples in the laboratory. I would also like to thank Dr Hong Chin Ng for his help on the research vessel, sampling the mudflats and for helping me measure silicon isotopes. I would also like to

sincerely thank Dr Lucie Cassarino, Jade Hatton and Dr Stephanie Bates, and everyone else at the Bristol Isotope Group for their help in measuring the silicon isotopes. I would also like to express my thanks to Dr Chung Choi, Dr Stuart Bellamy, Dr Tom Davis for their continued help sorting out laboratory protocols and fieldwork risk assessments. I would like to thank Dr Fotis Sgouridis and the team in the School of Geographical Sciences laboratory for helping me measure Total Organic Carbon concentrations. I would also like to thank Dr Christopher Williamson for his help running the light curve data in R. I would also like to thank Dr Paul Halloran (University of Exeter) for measuring our samples using Flow Cytometry, and Malcolm Woodward (Plymouth Marine Laboratory) for measuring nutrient concentrations in all the saline water samples.

I would like to give a very special thank you to George Wallington. This PhD would not have been possible without George's continued support, and the number of days he took off work to help me out on fieldwork! I'd like to thank my parents for their continued encouragement and to my mum for helping me sample a mudflat! A special thank you to my sister for her support throughout the PhD, especially surrounding LaTeX issues. Finally, I would like to thank all my extended family and friends, who have supported me throughout this PhD.

Contents

List of Figures

List of Tables

Chapter 1

Introduction

1.1 Study motivation and purpose

The silicon (Si) cycle through processes such as weathering and biological activity, is strongly intertwined with other elemental biogeochemical cycles. Most importantly, the Si cycle is associated with the carbon cycle, whereby siliceous organisms influence the oceanic carbon biological pump, which results in the drawdown of atmospheric carbon dioxide (Pondaven et al., 2000). Previous Si studies have focused on weathering (West et al., 2005), marine Si cycles, often centred around the polar oceans (Hendry and Brzezinski, 2014; Cassarino et al., 2017; Hawkings et al., 2017), studies on the paleoclimate (Conley et al., 2017; Fontorbe et al., 2017), and on the role coastal ecosystems have on biogeochemically modifying the riverine Si inputs to a marine zone (DeMaster et al., 1983; Conley and Malone, 1992; Ragueneau and Tréguer, 1994; Gamier et al., 1995; Arndt et al., 2007; Arndt and Regnier, 2007; Pastuszak et al., 2008; Carbonnel et al., 2009; Laruelle, 2009; Leynaert et al., 2011; Carbonnel et al., 2013; Raimonet et al., 2013). Particularly, estuarine Si cycling has recently gained momentum with new insight into the importance of estuarine benthic-pelagic coupling as a component of the Si cycle (Raimonet et al., 2013). Estuaries are influential areas and form the dynamic transition zones between the river and the marine environment. The coupled hydrodynamics, geodynamics and biogeochemical processes in estuaries interact on different spatial and temporal scales, induced by a wide range of physical forcings (Dale and Prego, 2002; Arndt and Regnier, 2007). As a result, the land-derived Si inputs are biogeochemically modified along the estuarine gradient (Volta et al., 2014). This modification is likely to have consequences on the estuarine ecosystem and ultimately, on global biogeochemical cycles (Laruelle et al., 2009a; Arndt et al., 2011; Regnier et al., 2013a). Current global Si budget estimates (Treguer et al., 1995; Tréguer and De La Rocha, 2013; Frings et al., 2016) have considered estuarine Si cycling, however they have primarily focused on two processes: the pelagic Si biological production and reverse weathering (Michalopoulos

and Aller, 1995, 2004), neglecting the potential Si supply from the estuarine benthic ecosystem. Therefore, disregarding the potential estuarine benthic Si cycle, combined with the errors identified with the extrapolation of river flow rates to the global budget, and the seasonal variability in river flow rates and benthic-pelagic productivity, estimates of the Si budgets are often accompanied by large uncertainties. Further, to date, estuaries and the coastal environment remain under-sampled (Brewin et al., 2016), leaving changes in the Si budgets to go unnoticed through the filter of land-ocean exchange.

The chemical weathering of silicate minerals forms soils and releases solutes, including orthosilicic acid ($Si(OH)_4$) referred to here as dissolved silicon (hereafter DSi), which enters the biogeochemical cycle (Frings et al., 2016). DSi, an inorganic macronutrient in aquatic environments, is essential to siliceous organisms, for example, photosynthetic diatoms that form their frustules from opal and contribute to approximately half of all surface ocean productivity (Treguer et al., 1995). Terrestrial-sea interactions and transfers by both biological and abiological processes, control the proportion of Si, which is present as DSi, and as precipitated particulates following biological uptake as hydrated amorphous silica, hereafter called 'biogenic silica (BSi)'. The uptake of DSi and biomineralization to BSi, is referred to here as 'biological mediation of Si'. DSi and BSi fractions have previously been used as proxies for Si utilization and diatom productivity in surface marine ecosystems (Conley and Malone, 1992). Further use of these proxies should now be adapted to the coastal zone, which will provide important information on estuarine Si biological uptake by the benthic and pelagic ecosystems. In addition, terrestrial or aquatic processes taking place in estuaries that can influence the production and consumption of Si, and subsequently the Si budget, must be explored.

Despite previous estuarine Si cycling studies, which are centred on the Scheldt Estuary, northwest Europe (Belgium/The Netherlands) (Struyf et al., 2005a,b; Chou and Wollast, 2006; Arndt et al., 2007; Arndt and Regnier, 2007; Carbonnel et al., 2009, 2013), knowledge of the potential Si modifications in an estuary, which is dominated by a biologically productive benthic system, is less well-known. Substantial research has been carried out on the role that saltmarshes and wetlands play in cycling Si in the coastal environment (Struyf et al., 2005b; Jacobs et al., 2008; Struyf and Conley, 2009; Struyf et al., 2010; Carey and Fulweiler, 2014), but few have studied the Si cycle in complex benthic biofilm ecosystems on intertidal mudflats. Laruelle (2009) using a fully transient two-dimensional physical and biological model on the Bay of Brest, which incorporates strong benthic-pelagic coupling, showed the benthic recycling flux of DSi to be an important contributor to the Si budget. However, the growth of intertidal mudflat diatom-dominated biofilms and the subsequent accumulation of BSi in the form of benthic frustules, as a contributor of Si to the coastal Si budget, is often overlooked.

Here, I aim to draw attention to the importance of this neglected benthic system in modifying riverine DSi and BSi export to a marine zone. Correspondingly, the Severn

Estuary, southwest UK, is a suitable case study for this research. The estuary is heterogeneous as a result of complex hydro-geomorphological dynamics (Morris, 1984; Kirby, 2010; Uncles, 2010; Liang et al., 2014) and has the third largest hyper-tidal range in Europe. This large tidal range results in the presence of large intertidal mudflats that are inhabited by diatom-dominated microphytobenthos (MPB) biofilms (Underwood, 2010) at the sediment-water interface (SWI), which are subject to high erosion rates (Manning et al., 2010) associated with the extreme tidal dynamics (Neill and Couch, 2011). Previous research by Welsby et al. (2016) suggests these biofilms have the potential to biologically mediate benthic dissolved silicon (BDSi) and benthic biogenic silica (BBSi). This benthic ecosystem, alongside other Si production and consumption processes, may influence the export of Si from the River Severn to the southwest pelagic zone in the Bristol Channel, and are at the forefront of this study. This assessment covers temporal changes in Si (i.e. sampled different periods in 2016) to account for fluctuations in riverine discharge and benthic-pelagic biological production.

First, the study presents the potential factors influencing pelagic Si cycling, encompassing the hydro-geological dynamics and pelagic productivity, alongside potential external Si inputs into the Severn Estuary from the tributaries, groundwater and rainwater. Secondly, the study investigates whether the MPB biofilms are a source of Si to the water column, with a detailed analysis of the biofilm biomass and productivity, and subsequent the uptake of BDSi and accumulation of BBSi. The potential export of Si from the intertidal mudflats is then discussed, with a study relating sediment stability to Si dynamics on the intertidal mudflats. Fourthly, silicon isotopes, which have benefited from a growing interest but are still poorly studied, notably in estuaries, have been applied as a powerful tool to constrain the various biological and abiological processes affecting Si in the pelagic and benthic environments of the Severn. Lastly, due to the complex estuarine Si system, a modified version of the one-dimensional reactive transport model published by Volta et al. (2014) has been applied to better constrain the estuarine Si transport. The pelagic model has been coupled to a benthic biofilm component to represent the benthic diatom production and consumption of Si.

1.2 The silicon cycle: transport of silicon to the ocean

Estimates of the global DSi riverine supply into the ocean almost spans a century (Clarke, 1924; Livingstone, 1963; Treguer et al., 1995; Beusen et al., 2009; Tréguer and De La Rocha, 2013). However, there are few reports of DSi concentrations in rivers since the first few estimates (Clarke, 1924), with later studies primarily focused on the nitrogen and phosphorus cycles (Livingstone, 1963; Meybeck, 1987, 1988; Turner et al., 2003; Powers et al., 2016; Vilmin et al., 2018). Rivers are estimated to contribute up to 82% of all DSi inputs into the ocean (Treguer et al., 1995). The current estimate of

the total gross riverine DSi input, based on 60% of global rivers, is 6.2 ± 1.8 Tmol/yr (Tréguer and De La Rocha, 2013), with an average concentration of 158 μM (Dürr et al., 2011). This total gross estimate includes a 30% uncertainty, reflecting the lack of coastal Si research, and the errors associated with the extrapolation of data to a global scale.

The particulate Si, lithogenic (LSi) and amorphous (ASi) riverine flux into estuaries, has been estimated to be 147 ± 44 Tmol/yr (Dürr et al., 2011). See Fig. 1.1 for the forms of Si discussed in this study. The lithogenic fraction, which is largely insoluble, is more easily accounted in global mass balance estimates, however the amorphous Si, predominately the biogenic fraction (e.g. diatom frustules, referred to here as BSi) can easily be dissolved on biological timescales, and retained in coastal sediments. The dissolution of BSi would be a noteworthy supply of DSi to the marine zone. In the open ocean, the dissolution of BSi is a crucial export of organic carbon to the deep ocean, forming a key component of the carbon biological pump, which has implications for the global climate system (Dugdale and Wilkerson, 1998). In estuaries, Si sinks, for example reverse weathering, which is particularly active in deltaic systems, could reduce this coastal DSi supply by up to 20-25%, resulting in a sink of 1.5 ± 0.5 Tmol/yr (Michalopoulos and Aller, 1995; Holland, 2005; Tréguer and De La Rocha, 2013). In the most recent review of global Si cycling by Tréguer and De La Rocha (2013), the amorphous Si supply is reported as a small fraction of the total riverine particulate Si supply. Consequently, they adopt Conley (1997) riverine BSi flux estimate of only 1.1 ± 0.2 Tmol/yr, making a total gross Si supply (i.e. DSi + BSi) of 5.8 ± 2.5 Tmol/yr to the ocean. Even though these studies considered the Si mediation by pelagic siliceous blooms, with an estimate of BSi production of 136 Tmol/yr in the coastal zone (Tréguer and De La Rocha, 2013), they don't directly consider the benthic MPB biofilm uptake of DSi and the subsequent productions of BSi in these zones. MPB biofilms, which are often dominated by diatoms, contribute significantly to estuarine ecosystem primary productivity, which, in turbid systems, may exceed that of the phytoplankton in the overlying water column (Underwood, 2010), making MPB biofilms one of the most productive ecosystems in the world (Kromkamp et al., 1998). Therefore, these benthic ecosystems have a high potential to mediate Si supply from estuaries to the ocean, and should theoretically be included in the global Si budget estimates reviewed above.

A substantial quantity of Si is also transported to the marine zone in submarine groundwater discharge (SGD) (Kim et al., 2005; Rahman et al., 2019). For example, Georg et al. (2009) reports groundwater DSi inputs in the Bay of Bengal of 0.093 Tmol/yr, equivalent to 66% of the Ganges-Brahmaputra river DSi flux. Tréguer and De La Rocha (2013) estimate an SGD DSi flux to the ocean of 0.6 ± 0.6 Tmol/yr. However, a recent study by Rahman et al. (2019) that includes new estimates of the SGD DSi supply, along with the dissolution of lithogenic material, concludes there is a 25-30% increased supply of SGD DSi. Further DSi sources include aeolian inputs, with

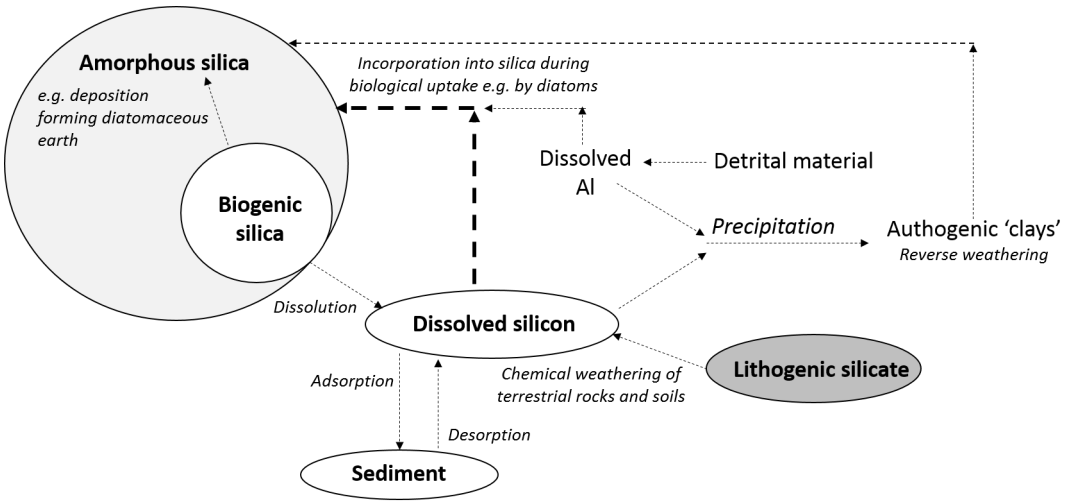

Figure 1.1: Forms of silicon discussed in this study.

estimates of 0.5 ± 0.5 Tmol/yr, which takes into account the uncertainties linked to the deposition and solubility of dust, rainwater (Treguer et al., 1995; Zhang et al., 2005), and hydrothermal inputs (0.6 ± 0.4 Tmol/yr), which act to increase the deep-sea Si reservoir (Tréguer and De La Rocha, 2013). This latter process is beyond the scope of the present study. The combined input of DSi into the ocean via the above processes, has been estimated to be 9.4 ± 4.7 Tmol/yr (Tréguer and De La Rocha, 2013), and is summarised in Fig. 1.2. Considering the new SGD estimates, Rahman et al. (2019) suggest between 14.1 and 14.9 Tmol/yr of DSi is supplied to the ocean, in agreement with the upper range presented by Tréguer and De La Rocha (2013).

1.3 Diatoms and the silicon cycle

1.3.1 Diatom silicon uptake

Diatoms, a diverse group of photosynthetic eukaryotic algae from the class Bacillariophyceae, are one of the largest groups of silicifying organisms, with an obligate growth requirement for Si. The magnitude of taxonomic and phylogenetic diversity of diatoms results in the constant development of their classification, with over 100,000 species documented (Mann and Vanormelingen, 2013). Diatoms are broadly categorised into two orders: Centrales, which have radial symmetrical pore patterns, and Pennales, which have bilaterally symmetrical pore patterns (Fig. 1.3). Both orders have a rigid outershell (frustule) consisting of two overlapping thecae, the epitheca and hypotheca, which are joined by the segmented girdle band.

Siliceous organisms including diatoms, radiolarians, silicoflagellates and sponges, biomineralize this soluble DSi into BSi. DSi uptake in diatoms is dependent on equilibrium factors including, 1) high intracellular and low extracellular concentrations of

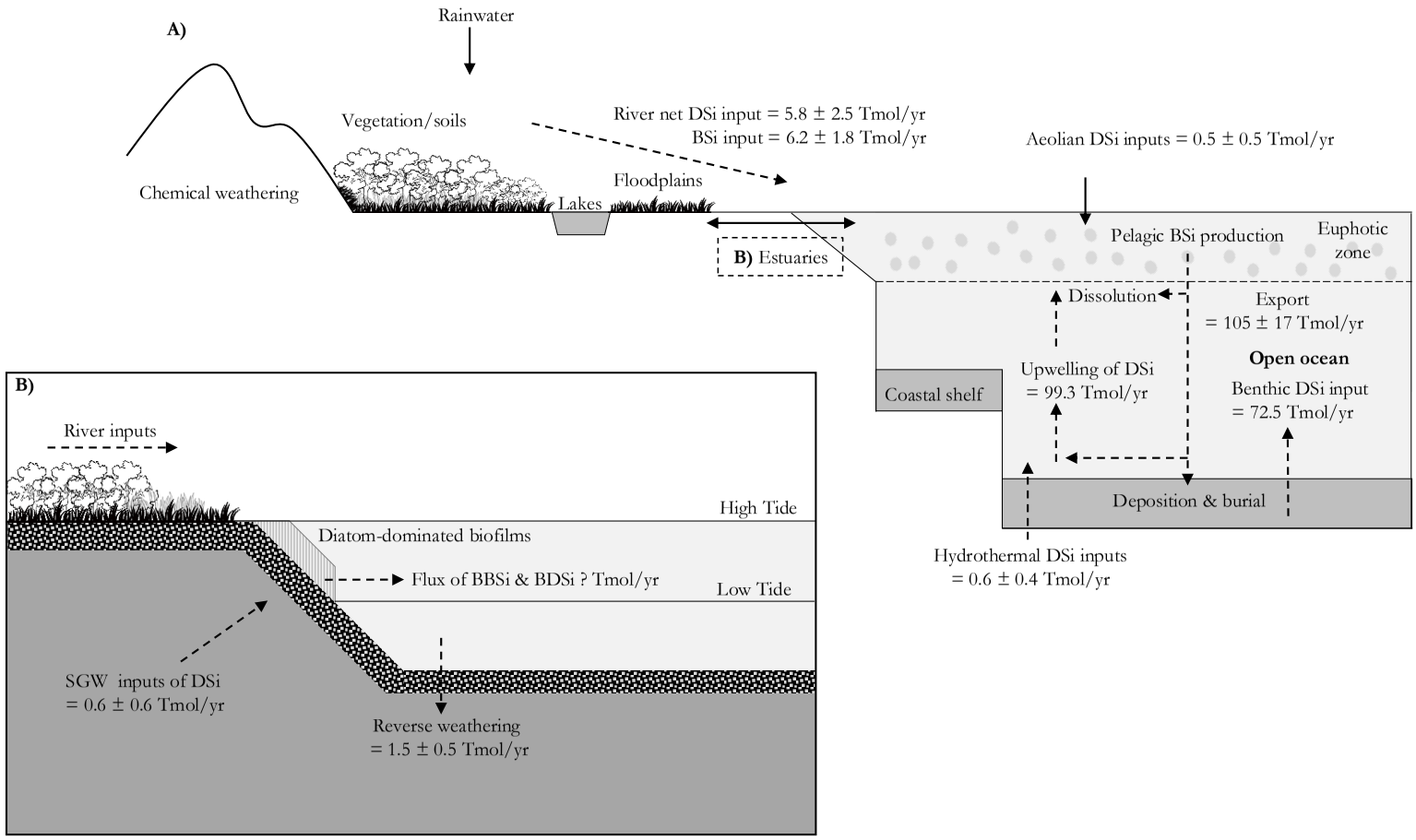

Figure 1.2: Global silicon cycle. **A)** Land-ocean interface. **B)** Simplified estuarine silicon cycle. Estimated budgets from Treguer et al. (1995) and Tréguer and De La Rocha (2013).

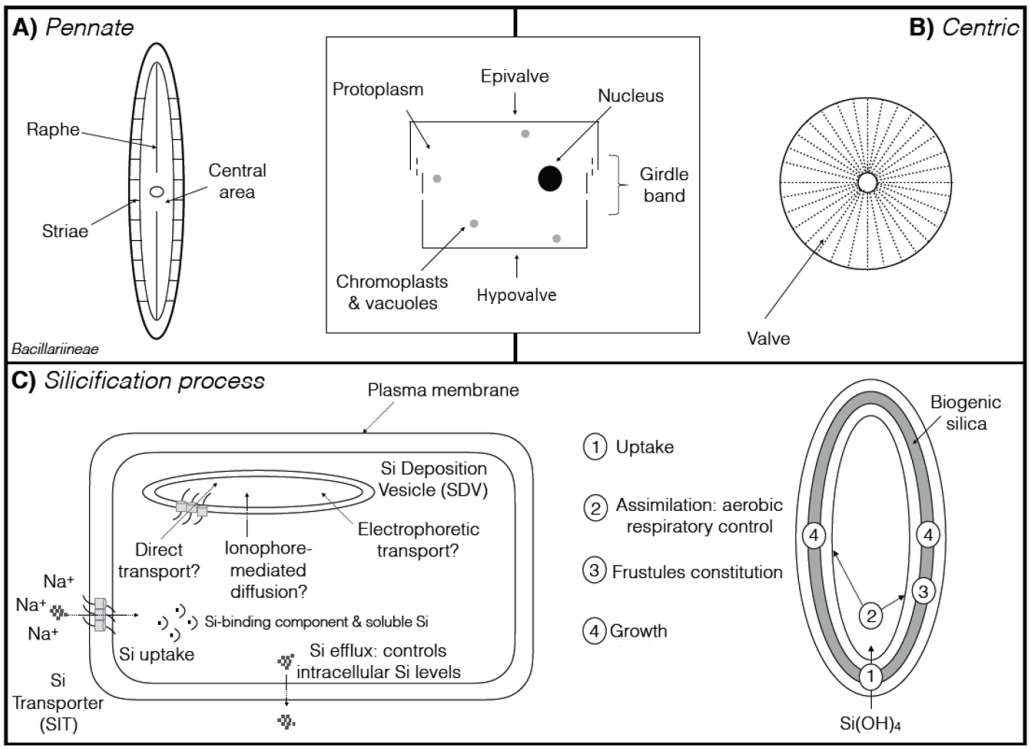

Figure 1.3: Diatom Silicon uptake. **A)** Pennate diatom. **B)** Centric diatom. **C)** Schematic view of a diatom cell with Si metabolism [adapted from Ragueneau et al. (2000)]. Si is co-transported with sodium (Na^+) across the plasma membrane via Si transporters (STIs), and across the cytoplasm to the silica deposition vesicle (SDV) by an unknown mechanism.

DSi, 2) different forms of DSi (extracellular: $Si(OH)_4$ or silicate; intracellular: $Si(OH)_4$ complexed with organics), and 3) the solid form of Si in the cell wall (Thamatrakoln and Hildebrand, 2008) (see Fig. 1.3). The uptake of DSi has typically been described by Michaelis-Menten-type saturation kinetics, however biphasic and non-saturable kinetics have also been recorded (Azam et al., 1974; Nelson et al., 1976). Numerous diatom species have been shown (Grachev et al., 2002; Sherbakova et al., 2005) to use Si transporters (SITs)(Fig. 1.3), which are specific membrane-associated proteins that transport DSi across the lipid bilayer membranes (Thamatrakoln and Hildebrand, 2008). However, recently it has been suggested that the first step of Si acquisition is mediated by (macro)pinocytosis rather than SITs (Vrieling et al., 2007). A new cell wall is formed (i.e. BSi) in a slightly acidic vesicle (silica deposition vesicle, SDV), although the mechanism by which $Si(OH)_4$ enters the SDV is unknown. It has been suggested there is a genetic basis for pattern formation through the precise reproduction of Si frustules from one generation to the next (Thamatrakoln and Kustka, 2009). These detailed silicification processes are out of the scope of the present study but have been reviewed elsewhere (Martin-Jézéquel et al., 2000; Zurzolo and Bowler, 2001).

1.3.2 Microphytobenthos biofilm formation

Diatom-dominated biofilms are adapted to the unstable, transient nature of estuarine intertidal mudflat sediments, where burial and erosion events are frequent (Herlory et al., 2007). There are two groups of benthic diatoms: epipsammic (low motility) and epipelic (highly motile) (Round, 1979). The motile pennate epipelic diatoms are major photoautotrophic organisms that colonizing these dense MPB biofilms at the sediment water interface (SWI) (Underwood, 2010). Four phases can be distinguished during the colonization of the sediment surface (Fig. 1.4). These include: biochemical conditioning, bacterial attachment, unicellular eukaryotes and finally, multicellular eukaryote colonization (Meyer-Reil, 1994). There are several environmental factors which influence the structure and functioning of these diatom-dominated biofilms, including:

- Sediment grain shape and size. Increased particle roundness (sand flats) decreases microbial colonization (Yallop et al., 1994).
- Taxa present (De Deckere et al., 2001; Thornton et al., 2002; Defew et al., 2002; Orvain et al., 2004).
- Light intensity, wavelength and UV radiation (Hopkins, 1963, 1965, 1966; Waring et al., 2006; Mouget et al., 2008).
- Air and water temperature (Round and Palmer, 1966).
- Salinity (Rijstenbil, 2005; Juneau et al., 2015).
- Disturbance by wave action (resuspension/deposition) (Underwood and Paterson, 1993; Ubertini et al., 2015).
- Desiccation and water content (Blanchard et al., 2000; Perkins et al., 2003; Coelho et al., 2009).

These environmental factors may affect the biofilms ability to 'biologically mediate Si'. This 'biologically mediate Si' term is defined as the product of increased biomass and photosynthetic rates that leads to DSi uptake, biomineralization, and subsequently the accumulation of BBSi.

1.3.3 Biostabilization

Biofilms in hypertidal estuaries experience frequent resuspension events, which enhances floc formation and prevents well developed MPB biofilms forming. Diatoms secrete extracellular polymeric substances (EPS), which forms polysaccharide and glycoprotein-rich mucilage's, an organic network around sediment and detrital particles, which together with other excreted carbohydrates during photosynthesis, produces the self-assembled biofilm at the SWI (Smith and Underwood, 1998; Kromkamp et al., 1998).

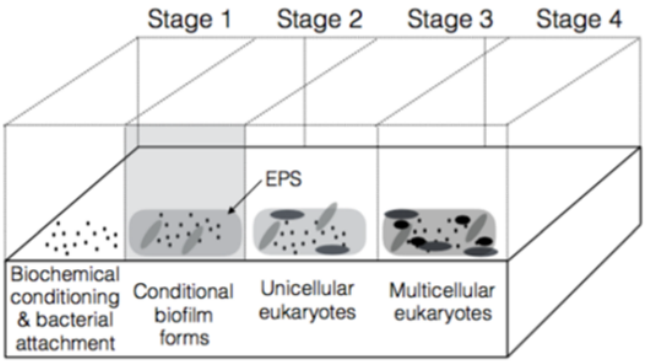

Figure 1.4: Formation of microphytobenthos biofilms. Stage 1. Biofilms consist of organic macromolecules (e.g. polysaccharides, protein, glycoproteins) which allow for bacteria to attach. Stage 2. Conditional biofilms forms. Stage 3. Unicellular (diatoms, yeast, protozoa) colonize. Stage 4. Multicellular eukaryotes (planktonic larvae, algal spores) attach. The biofilms appear golden-brown to the eye due to their fucoxanthin pigments. Adapted from Consalvey et al. (2004).

EPS is a generic term and exists as a continuum from capsular EPS surrounding the cells (hot bicarbonate-extracted carbohydrate fractions), to loose colloidal (water-soluble) carbohydrates which are secreted into the surrounding environment.

Sediment stabilization has been associated with colloidal carbohydrate concentrations by increasing sediment particle cohesion (Yallop et al., 2000; Tolhurst et al., 2002; Consalvey et al., 2004), a process defined as biostabilization, which has been well documented (Paterson, 1989; Underwood and Paterson, 1993; Sutherland et al., 1998; Stal and De Brouwer, 2003; Perkins et al., 2004a). Critical shear stress often increases with greater MPB biomass, and variability in sediment erodibility can be attributed to the loss/accumulation of MPB biofilms, as shown by Yallop et al. (2000). Whilst the relationship between biostabilization and biofilm biomass is complex, and often weakly significant, partly due to the natural variability and complexity of the system, colloidal carbohydrate concentrations have been shown to correlate with MPB biomass in estuarine sediments (Underwood and Paterson, 1993; Underwood et al., 1995; Sutherland et al., 1998; Yallop et al., 2000; Bellinger et al., 2005). As described above, mudflat sediment biostabilization has been well documented, however the effects of biostabilization on the resuspension of BDSi and BBSi, to my knowledge, has not yet been studied.

1.3.4 Diatom primary productivity

Diatoms contain two types of pigments, chlorophylls (chl) and carotenoids, which are involved in light harvesting and photoprotection. Two forms of chl occur in diatoms: chl *a* and chl *c*. Chl *a* is central to the photosynthetic processes, and is the main light harvesting pigment, absorbing spectrum wavelengths peaking around 664 nm and 430

nm (Table 1.1). Chl *c*, used as a proxy for the presence of diatoms, participates in photosynthesis effectively as an antenna accessory pigment, similar to the functional activity to chl *b* in higher plants (used as a proxy for the presence of green algae) (Kuczynska et al., 2015). The most abundant forms of chl *c* are chl c_1 and c_2.

Table 1.1: Chlorophyll pigment absorbing spectrum wavelengths (nm).

Chl pigment	**Wavelength (nm)**
Chl *a*	664
Chl *b*	647
Chl *c*	630

Diatom chloroplasts are the site for photosynthesis, which involves light-driven reactions. Light energy is harnessed to fix carbon from carbon dioxide (CO_2) to form energy-rich organic compounds (e.g. carbohydrates) from low-energy inorganic compounds. This photosynthetic process uses reducing agents from the hydrolysis of water, which releases oxygen (Consalvey et al., 2005) (see Fig. 1.5).

Photosynthesis can be divided into two sets of reactions, 1) the thylakoid membrane-bound light reactions (photo), and 2) the CO_2-fixation and CO_2-reduction reactions in the stroma, also termed the Calvin cycle (synthesis). The antenna complexes situated in the thylakoid membrane are formed of hundreds of pigment molecules grouped into two photosystems: photosystem I (PSI), and photosystem II (PSII). These antenna complexes harvest light, and channels energy towards a reaction centre - the chlorophyll *a*-protein complex. The PSII reaction centre consist of chl *a* molecules called P680, whilst the PSI corresponding chl *a* is termed P700 (Fig. 1.6). The study of the kinetics of chlorophyll fluorescence quenching in diatoms, used as an ecological tool due to the rapid, relatively non-invasive technique is primarily based on the properties of PSII (Perkins et al., 2001).

The Z scheme (see Fig. 1.5) has often been used to characterise light reactions (Beer et al., 2014). The energy acquired from a single photon in the light harvesting antenna complex is used to excite an electron from its low stable orbital to a higher orbital. Energy is converted via three de-excitation, competitive processes (see Klughammer and Schreiber (2008) for details):

- Energy is used to drive photosynthesis through photochemistry (photochemical quenching).
- Excess energy is dissipated as molecular motion (heat) to non-specific neighbouring molecules. This is a regulated form of non-photochemical quenching [Y(NPQ)], dependent on the energisation of the thylakoid membrane through the proton gradient. NPQ is a combination of both regulated [Y(NPQ)] and non-regulated

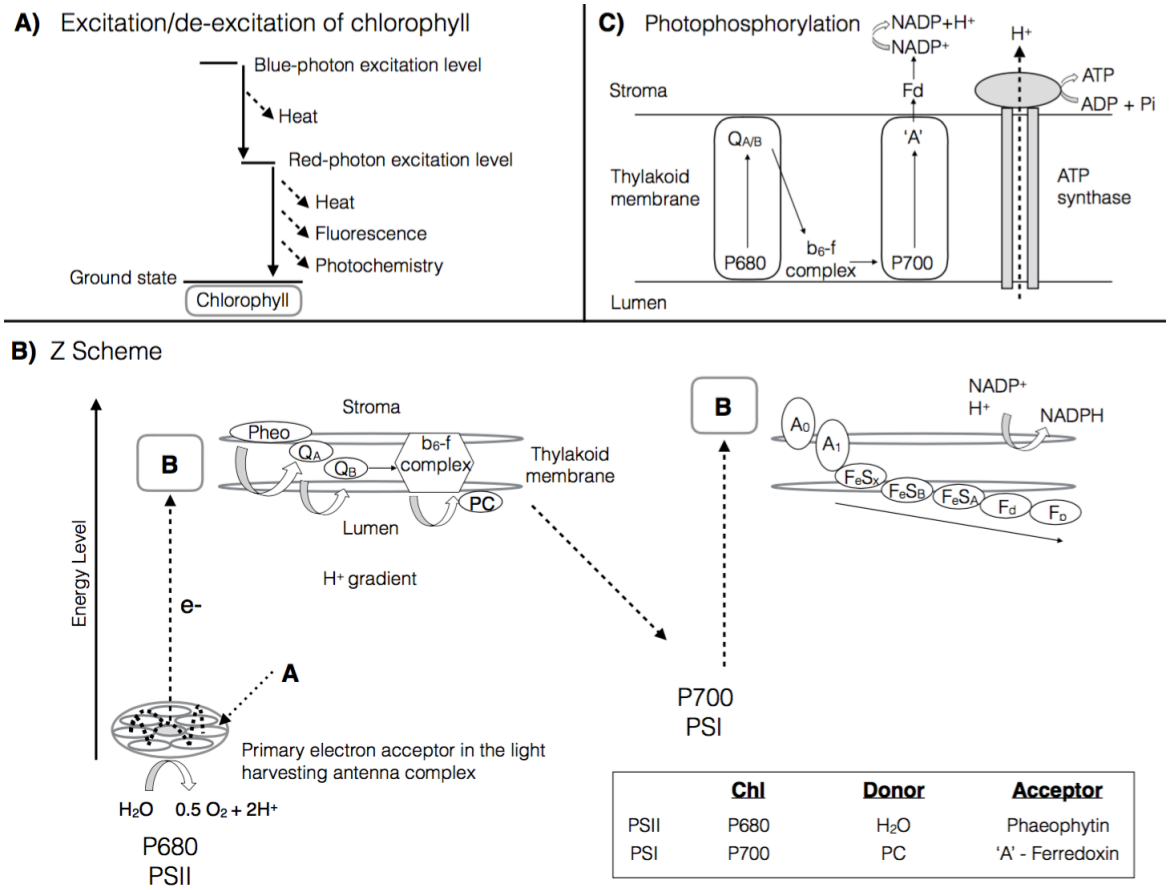

Figure 1.5: **A)** De-excitation pathways. **B)** Photochemical quenching (Z scheme). **C)** Photophosphorylation. Synthesis of ATP through ATP synthetase is powered by the electrochemical gradient formed across the thylakoid membrane by $NADP^+$. Dark reaction: NADPH and ATP are used to fix carbon to form carbohydrates via RUBISCO enzyme. Adapted from Consalvey et al. (2005) and Beer et al. (2014).

[Y(NO)] forms of excitation dissipation (Perkins et al., 2018).

- Energy loss associated with non-regulated heat dissipation [Y(NO)] and energy re-emitted as light-chlorophyll fluorescence. The latter can be used as a proxy for photochemical efficiency and photosynthetic rate due to the inverse relationship between photosynthetic yield and fluorescence yield.

Rapid Light Curves (RLCs) (Fig. 1.6) of the re-emitted light-chlorophyll fluorescence are used to explore the relationship between irradiance and photosynthesis. The Photosynthetically Active Radiation (PAR, μmol photons/m^2/s) represents the irradiance for the wavelength range of 400-700 nm [reviewed in Consalvey et al. (2005)]. The photosynthetic rate, and a proxy for biofilm productivity, has increasingly been investigated through the calculations of Electron Transport Rate (ETR, in μmol/m^2/s) and

the relative photosynthetic rate by the relative ETR (rETR, in *rel. units*). ETR can be derived from the quantum yield (Y) and the absorbed irradiance (E) of the photosystem (E = 0.5, assuming 50% of the absorbed light is distributed between PSI and PSII), whereby, Y * PAR * AF * 0.5 (Perkins et al., 2010b). AF is the absorption factor. If AF is unknown, the rETR is calculated from quantum efficiency of PSII i.e. Y(PSII) (Kromkamp et al., 1998). This latter method is followed in this study (see Chapter Two, Section 2.1.2.2 and Chapter Four, Section 4.3.3). A RLC consists of a linear light-limited increase in photosynthetic rate until a maximum light-saturated rate is reached (P_{max} or ETR_{max}). The maximum light use coefficient for PSII (α) is a measure of the maximum photosynthetic efficiency (or quantum yield). The PAR at which light saturation begins to occur, and the profile starts to curve, is termed the light saturation coefficient (E_K).

To mitigate the high irradiance levels, diatoms have evolved photoprotective mechanisms, including behavioural and photophysiological photoprotection (Kromkamp et al., 1998; Consalvey et al., 2005; Lavaud, 2007; Mouget et al., 2008; Perkins et al., 2010b,a; Cartaxana et al., 2016). Behavioural photoprotection involves the movement of diatoms from the sediment surface into deeper sediment layers to avoid irradiance levels that may lead to photodamage. This photophobic movement of cells to reach optimum irradiance levels, and the subsequent replacement by others at the sediment surface, has been termed microcycling (Kromkamp et al., 1998; Underwood et al., 2005; Cartaxana and Serôdio, 2008; Perkins et al., 2010b,a).

In high irradiance exposure, diatoms may down-regulate their photochemistry through non-photochemical dissipation of excitation energy away from PSII, as either heat energy and/or as a balance of excitation energy in the photosynthetic apparatus (Lavaud and Lepetit, 2013). Non-photochemical quenching (NPQ) is a mechanism to dissipate the energy as heat (Lavaud and Goss, 2014). The regulated build-up of the transthylakoid proton gradient (ΔpH), activates the de-epoxidation of diadinoxanthin (Ddx), a light harvesting pigment, to diatoxanthin (Dtx), a photoprotective pigment (Lavaud and Kroth, 2006; Grouneva et al., 2009, 2013). This process is termed NPQ induction, which with increasing PAR, leads to the reduction in quantum efficiency of PSII [Y(PSII)], and thus the reduction in the electron transport rate (ETR) (Perkins et al., 2018). An important characteristic of NPQ in diatoms, is the high potential to dissipate up to 90% of energy (Lavaud et al., 2002). Further, compared to planktonic species, estuarine MPB biofilms exhibit a faster shift between NPQ induction and reversal (Perkins et al., 2018). NPQ reversal occurs in low light when photochemical quenching causes the loss of this proton gradient, resulting in the epoxidation of Dtx to Ddx.

NPQ is further separated into two components: regulated [Y(NPQ)], which involves the mediated xanthophyll cycle (Bilger and Björkman, 1990), and non-regulated [Y(NO)], i.e. the thermal energy dissipation that occurs even when the maximum pho-

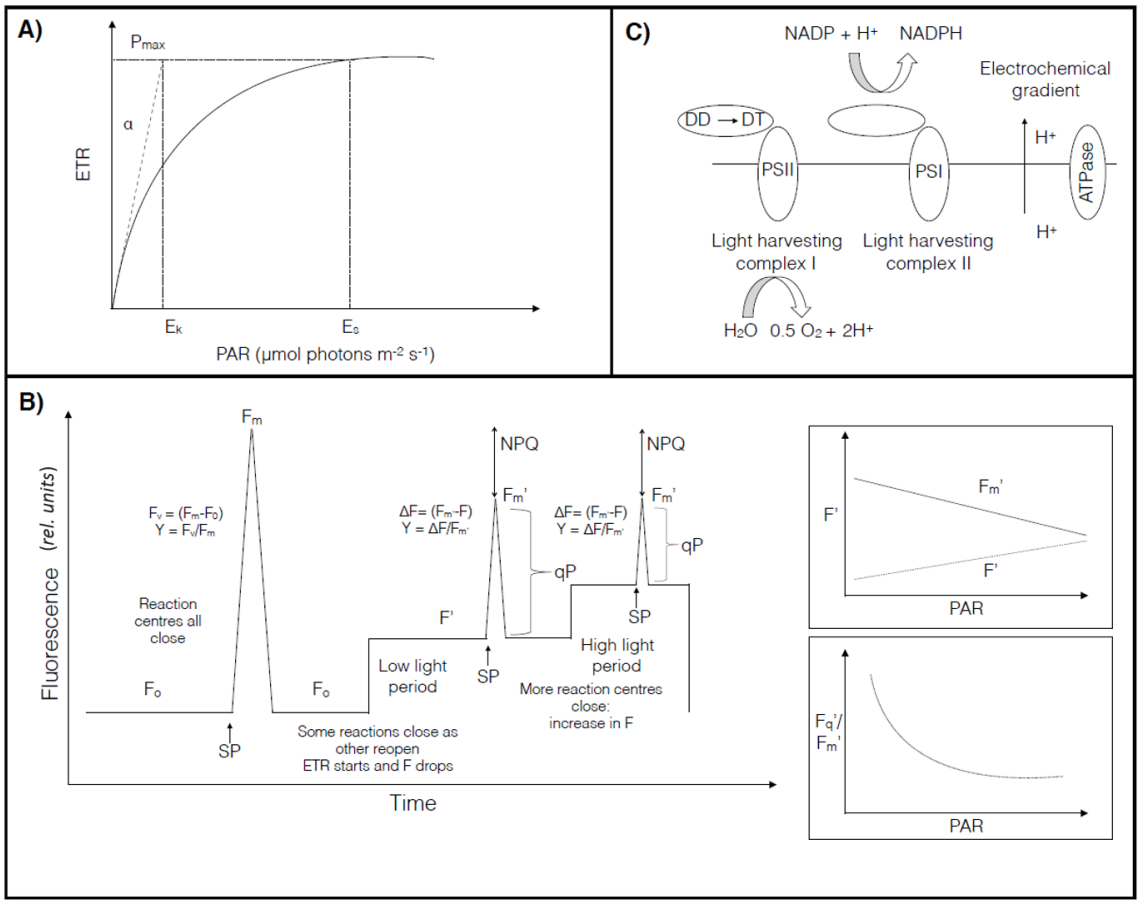

Figure 1.6: **A)** Rapid Light Curve. **B)** Theoretical trace of fluorescence. Dark period: No actinic light and low (<1 μmol photons/m^2/s) measuring light emitted from PAM fluorometer reaches biofilm. Reaction centres in the light-harvesting antenna complex are oxidised. No photons are absorbed. Q_A is oxidised and the fluorescent yield is at a minimum, F_o. Low light period: A saturation pulse is applied by the PAM fluorometer towards the biofilm through its optical fibre for *ca.* 1 s (short time to avoid photodamage), and causes the reaction centres to 'close' (reduced Q_A) and the fluorescence yield (F) will increase. F_v is the difference between F_m and F_o. Photons (actinic light) strike the reaction centres in the light-harvesting antenna complex and almost all reaction centres are reduced. High light period: Fluorescent signal increases to a yield between $F^{'}$ and $F^{'}_m$. Reactions centres are reduced and temporally unavailable to undertake photochemistry. Following darkness, F decreases to original F_o value. Variable fluorescence ($F_v = F_m$-F_o) represent the degree of photochemical quenching, qP (which decreases with increasing irradiance). F_v/F_m is not affected by light and can be used as an indicator for 'stress' affecting PSII components. F increases with increasing irradiance, but $F^{'}_m$ decreases because of down regulation by cell movement or/and NPQ induction. Y(PSII), the proportion of light used in PSII photochemistry, declines with higher irradiance. **C)** Diadinoxanthin (Ddx) - diatoxanthin (Dtx) (Xanthophyll) cycle. Adapted from Consalvey et al. (2005).

tochemical yield is reached (Klughammer and Schreiber, 2008). However, Y(NO) is quenched by Y(NPQ), resulting in the absence of Y(NO) at high irradiance levels. For example, Perkins et al. (2018) using treated and non-treated diatoms with DL-dithiothreitol, which inhibits the xanthophyll cycle leading to a suppressed Y(NPQ) (Bilger and Björkman, 1990), showed a continuous rise in Y(NO) with increasing irradiance levels in treated diatoms, and reduced Y(NO) as Y(NPQ) was induced, in non-treated diatoms. The NPQ mechanism has been described in detail (Serôdio et al., 2005b, 2006; Klughammer and Schreiber, 2008; Perkins et al., 2018).

The combination of photophysiological (NPQ) and behavioural (vertical cell movement) mechanisms aids in the diatoms flexibility and quick response to changing light environments. These adaptions allow diatoms to maintain high photosynthetic rates and limits the presence of photodamage or photoinhibition (Serodio et al., 2008). The diatoms high capacity to induce Y(NPQ) under light stress, with or without vertical cell movement, may be central in explaining their success in variable light environments and often relatively high irradiance levels during emersion. Previously, vertical cell movement and Y(NPQ) were considered complimentary, with Y(NPQ) induction favoured prior to the onset of cell movement, especially under conditions where motility was limited. However, previous work by Perkins et al. (2010a) using chemical inhibitors of cell motility and Y(NPQ), note the energetically more favourable cell movement was preferred over Y(NPQ) induction. Epipelic diatom vertical cell movement is now often considered as the primary photoprotective mechanism when motility is possible (Serôdio, 2004; Serodio et al., 2008; Serôdio et al., 2012; Laviale et al., 2015; Cartaxana et al., 2016).

1.4 Severn Estuary introduction

The Severn Estuary is situated between South Wales and South-West England (Fig. 1.7), and forms the coastal transition zone between the River Severn and the Bristol Channel. The estuary is primarily fed by the River Severn, the longest river in the UK, which is sourced in the Cambrian Mountains of mid-Wales. There are several smaller secondary tributaries, including the rivers Wye, Usk, Avon, Taff and Elly (via Cardiff Bay) which discharge into the Severn Estuary. The estuary discharges into the Bristol Channel, and later into the Irish Sea and the North Atlantic. The lower estuarine boundary lays on a transect between Lavernock Point and Weston-Super-Mare (*ca.* 13 km wide), with a maximum water depth >50 m (Neill and Couch, 2011). The upper estuarine boundary lays past the tidal limit at Elmore, near Maisemore (GOV., 2006).

The estuary's geological history begins during the Devensian epoch (110-112 ka). A large river valley with a deep canyon formed following the erosion of the underlying Triassic mudstone and Carboniferous limestone by the Weichselian ice sheet's seasonal

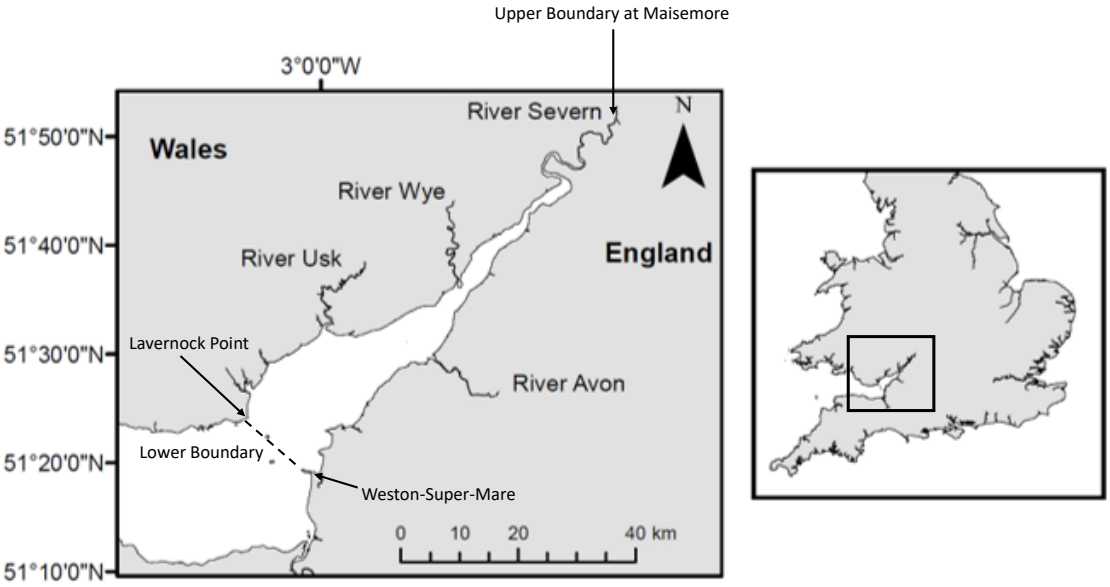

Figure 1.7: Location of the Severn Estuary between South Wales and South-West England. Upper boundary near Maisemore. Lower boundary between Lavernock Point and Weston-Super-Mare. Created in ArcGIS.

meltwater rivers (Allen and Rae, 1987). The fast-flowing rivers deposited eroded material onto a wide plain - the Bristol Channel. With the receding ice sheets, isostatic rebound and *ca.* 30 m eustatic sea level rise in the Holocene (Peltier et al., 2002), the river valley gradually formed the Severn Estuary that we see today. The estuary maintains the cross-sectional profile of this original river valley.

The low-lying land immediately surrounding the estuary was once saltmarshes and alluvial wetlands, much of which has been reclaimed by human activity, including major industrial action over the past 200 years (Langston et al., 2010a). The combination of the coal industry and mining alongside intense agriculture around the estuary, led to polluted waters and mudflats with both organic and inorganic contaminants. However, over recent years, with the end of large-scale industrial activity, and the enforcement of cleaner environmental standards, these habitats have been designated sites of special scientific interest (SSSIs) and Special Areas of Conservation (SACs) (Morris, 1984; Duquesne et al., 2006; Jonas and Millward, 2010).

The hyper-tidal estuary (Dyer, 1973) has the third highest astronomical tide in the world of 14.7 m, with a mean spring range of 12.3 m and a mean neap range of 6.5 m (Kirby, 2010). The estuary is classified more specifically as a Hypertidal-C to Hypertidal-E regime, i.e. 10-16 m tide height (Archer, 2013). The high tidal range results from the combination of:

- The funnelled shape of the estuary, which is typical of a hypersynchronous-type, where the tidal prism is compressed further upstream, forcing the vertical upward shift of the water level at the head of the estuary.
- The strong tidal resonance (Fong and Heaps, 1978), set up primarily by a) the distance of the estuary to the continental slope in the west causing a shelf resonance, and b) within the estuary as a result of the interaction between primary and secondary waves amplifying the tidal wave (Liang et al., 2014). The tidal constituents are discussed in detail in Chapter Severn.

The combination of the funnelled topography and the prevailing west and south-westerly winds (Collins and Williams, 1981), amplifies high and low water heights, and consequently a surge wave forms, called the Severn Bore (Rowbotham, 1983). This exceptional tidal range has interested numerous tidal power generation projects, including various tidal barrage proposals and tidal lagoons (SEP, 2018). These complex hydrodynamic processes and the irregular geometry of the estuary are well studied (Uncles, 1981; Falconer et al., 2009; Kirby, 2010; Manning et al., 2010; Xia et al., 2010a,b; Liang et al., 2014).

Due to the complex hydro-geodynamics of the Severn, the estuary has the highest energy levels of all estuaries in the UK. The intense vertical mixing produces homogenous conditions of salinity, temperature and turbidity (Manning et al., 2010; Uncles, 2010; Underwood, 2010). These high turbidity levels (Manning et al., 2010) limits pelagic productivity, and as a result the Severn Estuary primary productivity is dominated by benthic biofilms on the intertidal mudflats (Underwood, 2010). The estuary has an asymmetrical tidal duration, with the ebb flow lasting *ca.* 2 hrs longer than the flood (Wolf, 1987; Neill and Couch, 2011). As a result, the intertidal mudflats are exposed to long photoperiods (Underwood, 2010), which may aid in the MPB biofilm growth and subsequently in the biological mediation of Si (Welsby et al., 2016). The Severn Estuary has been extensively reviewed in complementary reviews in "The Severn Estuary and Bristol Channel: A 25 year critical review" (Langston et al., 2010b).

1.5 Aims and objectives of the study

This research intends to contribute to a better understanding of how estuaries influence the export of dissolved and particulate forms of Si to a marine zone. Using the Severn Estuary as a case study, the aim of the study is to determine the key forcings, and production and consumption processes influencing Si cycling along the Severn continuum. Within this framework the following specific hypotheses and objectives are embedded:

Hypothesis one: The pelagic productivity in the turbid Severn Estuary is low, reducing the importance of the pelagic biological mediation of Si.

Objective One: To determine the Si concentrations and flux along the Severn from the freshwater end-member to the saline-end member each sampled period in 2016.

Objective Two: Assess the multiple hydrological and biogeochemical controls on Si in the Severn.

Objective Three: To determine the potential external input of Si from the Severn Estuary tributaries (Wye, Avon, Usk and Cardiff Bay), groundwater and rainwater.

Hypothesis Two: The diatom-dominated biofilms on the intertidal mudflats of the Severn Estuary have high rates of primary productivity, resulting in a large biofilm biomass, and subsequently the uptake of BDSi and accumulation of BBSi.

Objective One: Determine the Si budgets of the intertidal mudflats during different periods in 2016.

Objective Two: Assess the benthic diatoms biological mediation of Si, through the analysis of benthic biomass (chlorophyll *a* content) and photosynthetic rate (chlorophyll fluorescence), alongside environmental limiting factors including sediment composition, temperature, water content, irradiance levels and nutrient availability.

Hypothesis Three: The benthic-pelagic coupling influences the Si budget of the Severn and the potential export of Si to the southwest UK coastal-marine zone.

Objective One: To determine the amount of BDSi and BBSi supplied to the water column from the intertidal mudflats, and the effect of biofilm biostabilization on this Si export.

Objective Two: Measure Si isotopes (δ^{30}Si) from the water column and benthic system to further explore the biological and abiological controls on Si, and to help decipher whether the benthic system is a source of Si to the water column.

Objective Three: Use the framework of the pelagic Carbon-Generic Estuarine Model (C-GEM) (Volta et al., 2014) to model Si transport and cycling in the Severn Estuary. This model will be largely modified to represent the Severn's system, and include DSi and BSi, as well as a benthic biofilm component.

1.6 Thesis outline

This thesis is separated into the following chapters:

Chapter Two provides a detailed explanation of the sampling scheme undertaken in the Severn during different periods in 2016. This scheme includes the ecological surveys carried out aboard a research vessel sampling the estuarine water column, sampling of the estuarine tributaries and sampling four intertidal mudflats. This is followed by a detailed account of the laboratory methodologies and procedures used to measure the samples. This chapter also details the statistical analyses applied. A brief account of the sediment stability study carried out in the summer of 2017/18 is given, along with an overview of the Si isotopes method, and the reactive transport model set-up. Detailed descriptions of these methodologies are provided in Chapter Five (Section 5.2), Chapter Six (Section 6.2) and Chapter Severn (Section 7.2), respectively.

Chapter Three investigates the multiple forcings driving Si transport along the Severn during sampled periods in 2016. The concentrations and flux of pelagic DSi (PDSi) and pelagic BSi (PBSi) is provided, followed by subsections on the hydrodynamic forcings (discharge and salinity), sediment transport, and pelagic biological mediation of Si (chl *a* concentrations, Total Organic Carbon and nutrient concentrations). The external supply of Si from the estuarine tributaries, groundwater and rainwater is discussed. Here, the high turbidity in the Severn is shown to limit PBSi production. The study hypothesised that the sediment and BSi, which showed strong coupling in biologically productive periods, originated from the intertidal mudflats and formed bioflocs in the water column.

Chapter Four presents the budgets of BDSi and BBSi on four intertidal mudflats of the Severn Estuary during sampled periods in 2016. The multiple biological and abiological factors which may influence these benthic Si budgets are discussed. This chapter also focuses extensively on the benthic biological mediation of Si, through a detailed analysis of the diatom-dominated biofilm biomass, and their electron transport rates (used as a proxy of primary productivity). The benthic diatoms had the potential to biologically mediate Si, through the formation of large biofilms (chl *a* content) and high electron transport rates. The percentage of BBSi was found to be low, similar to other estuarine systems, and were attributed to the high resuspension rates in the hypertidal estuary. With high photosynthetic rates aiding the formation of large biofilms during emersion periods, fast turnover

rates of BBSi and the subsequent continuous supply of BBSi to the water column, is proposed.

Chapter Five investigates this potential supply of BDSi and BBSi from the intertidal mudflats to the water column. Presented are the erosion thresholds measured using a Cohesive Strength Meter (CSM). The BDSi concentrations and percentage of BBSi (g/g of sediment) were determined, along with depth profiles of DSi, to estimate the diffusive flux of DSi out of the sediment. The amount of eroded BBSi and BDSi was calculated from the resuspended material and compared to the surf zone Si concentrations. The effect of biostabilization was assessed through measurements of MPB biomass (chl *a* content), total carbohydrate and colloidal-S carbohydrate concentrations. The growth of the biofilms was shown to increase sediment stability, leading to an accumulation of BBSi. However, despite some biostabilization, due to the strong tidal currents in the hypertidal Severn Estuary, the erosion threshold of the sampled biofilms was exceeded, leading to the resuspension and flux of BDSi and BBSi to the overlaying water column. The suspended sediment and BBSi again displayed strong linear correlations in the resuspended matrix and surf zone, supporting the theory of bioflocculation.

Chapter Six further investigates the contribution of benthic Si to the water column of the Severn Estuary using the Si isotope signatures in the water column and mudflat water (a mixture of surface and pore fluids) sampled in the summer and autumn periods of 2016. Here, I present the first Si isotope measurements from the benthic and pelagic systems of the Severn Estuary. Isotopically heavy mudflat waters further support the benthic mediation of Si, which could have contributed to the isotopically heavy estuarine waters compared to the isotopically light water from the River Severn. Several estuarine water column and mudflat water analyses exhibited mass-independent fractionation possibly associated with a high matrix organic matter content. The calculated constant isotopic fractionation factor (ϵ) introduced the possibility of clay formation also influencing the benthic Si budgets during less biologically active periods. Both biological and abiological processes were shown to drive the Si isotopes, but due to the limited data set from this preliminary study, the findings are speculative.

Chapter Severn applies a one-dimensional reactive transport model (RTM) to capture and help decipher the complex cycling of Si in the estuary over temporal-spatial scales. Initially, the model setup of the geometry, hydrodynamics, sediment transport and biogeochemistry components are explained, and the modifications are outlined in detail. The model has been useful in deciphering the possible sediment transport in the river-estuary transition zone (40-80 km), which previously remained unknown due to accessibility issues. The estuarine turbidity maximum

zone (ETM) was shown to occur *ca.* 60 km upstream of the outer boundary, in agreement with previous research on turbidity in the Severn. The model output also suggests the benthic biofilm system supplied BBSi to the water column, increasing PBSi concentrations. These findings can be used to influence future sampling strategies in the Severn, with the aim to target this difficult to access area. Several processes facilitating this BBSi export are discussed, including the heterogenous spatial distribution of the biofilms ('patchiness'), nutrient limitation, photosynthetic parameters used in the model setup, benthic organism mortality, and other processes not considered in the current setup, including bioturbation and burial.

Chapter Eight provides a final synthesis of the findings and places them into a wider real-world context, including the possible effects of renewable energy developments (e.g. Tidal Barrage and Tidal Lagoons).

Chapter 2

Methodology

This chapter provides an overview of the studied locations (Severn River, Estuary, tributaries and the intertidal mudflats), followed by a detailed explanation of the fieldwork, the laboratory methods and processing of samples. This is succeeded by a description of the data analysis carried out. This chapter only provides the detailed methodology for the main sampling period (2016). A brief report of the sediment stability study carried out in the summers of 2017 and 2018 is given (Chapter Five), along with an overview of the Si isotope methods (Chapter Six), followed by the reactive transport model setup (Chapter Severn). For a detailed account of these sub-studies, refer to the methodologies in each individual chapter.

2.1 Sampling methodology

Ecological surveys were carried out in the River Severn, Severn Estuary and upper Bristol Channel (Fig. 2.1). For temporal variability, the water column of the Severn and the intertidal mudflats were sampled at different periods in 2016. These sampled periods coincided with the seasons, and for clearness, are referred to here as; winter (January-March), spring (April-June), summer (July-September) and autumn (October-December). However, due to constraints, these sampled days, although span the entire season, do not necessarily reflect the temporal change associated with each season, which would require daily sampling.

2.1.1 Water column

Water column samples were taken along the Severn, approximately every 3 to 4 months, which coincided with neap lunar cycles. A transect aboard Guiding Light, Cardiff University's small research vessel, was taken from the upper estuary at high tide, along the longitudinal axis, to the outer estuary. Sampled stations were: The shoots (51°55´N, 2°71´W), South Middle Grounds (51°45´N, 2°96´W), and Tail Patch (51°37´N, 3°06´W). A station in the Bristol Channel (Culver Sands: 51°29´N, 3°18´W) was sampled for the marine end-member Si concentrations. A separate transect of four stations was sampled at low tide along the River Severn: Epney (51°47´N, 2°21´W), Elmore (51°50´N, 2°18´W), Maisemore (51°53´N, 2°16´W), Tirley (51°56´N, 2°13´W) (Table. 2.1). Each season, a transect of four stations was taken along each of the main tributaries: River Wye, River Usk, and River Avon, along with a sampling station in Cardiff Bay for the Rivers Taff and Ely Si inputs.

Table 2.1: Sampled location in the Severn. *Distance from the lower estuarine boundary (Weston Super-Mare to Lavernock Point, boundary marked between Zone 3c and Zone 4).

Name	Zones	Distance (km)*
Tirley	Zone 1a	112
Maisemore	Zone 1b	103
Elmore	Zone 2a	96
Epney	Zone 2b	83
Upper Estuary	Zone 3a	33
Mid-Estuary	Zone 3b	14
Lower Estuary	Zone 3c	5
Bristol Channel	Zone 4	-10

In the Severn Estuary, water was collected from the surface (<2 m deep) and at depths (>15 m deep) using a 5 L Niskin bottle. From the River Severn, estuary and its tributaries, three replicates (3 x 1 L) of sampled water were used to measure PBSi

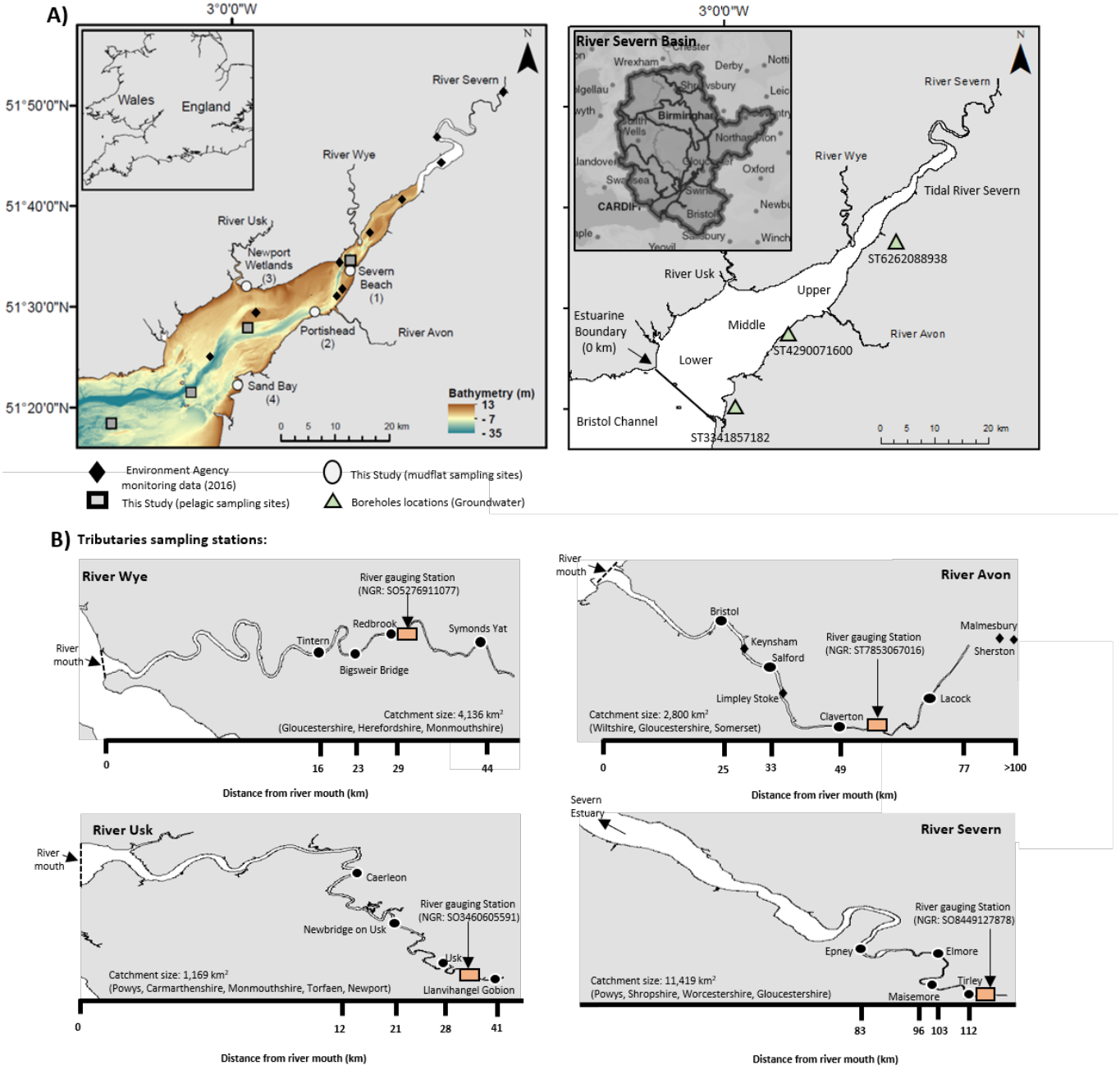

Figure 2.1: **A)** The River Severn, Tidal River Severn, Upper, Middle and Lower Severn Estuary, and Bristol Channel. Severn Estuary bathymetry (depth relative to OSGB 1936 datum) showing the original river valley from the Devensian epoch. Pelagic sampling points (squares) in the upper, middle and lower estuary and Bristol Channel. Environment Agency monitoring sampling stations [diamonds, Agency (2016)]. Mudflat sampling sites (circles): Severn Beach (Site 1), Portishead (Site 2), Newport Wetlands (Site 3) and Sand Bay (Site 4). Boreholes locations [triangles, Agency (2016)]. **B)** River Severn and tributaries (River Wye, River Usk, and River Avon) sampling stations and distance from their river mouths (km). Note, River Severn mouth considered as the estuarine lower boundary. Also note, River Severn basin (A), catchment size (km^2), and river gauging stations in the tributaries (discharge data) [Orange squares, Agency (2016)].

and chlorophyll (chl) *a* concentrations. River and estuarine pelagic water were filtered through pre-weighed polycarbonate filters (Whatman Cyclopore Track Etched Membrane Filter, 47 mm, 0.4 μm pore space) using a vacuum filter, and cut in half for chl *a* and BSi concentrations (see Section 2.2.1 and Section 2.2.2, respectively).

Water samples were collected during the summer, preserved in Lugols iodine and analysed using Flow Cytometry at Exeter University by Dr Paul Halloran for pennate/centric ratios in the surface and bottom estuarine waters. Chlorophyll fluorescence, using the Water Pulse Amplitude Modulation (PAM) fluorometer (Walz, Effeltrich, Germany), was used on water sub-samples (2-3 mL) immediately sampled and placed into the cuvette (WATER-ED Emitter-Detector Unit), however water column productivity was too low for any measurements (F<150 *rel. units*, *pers. comm.* with Dr Rupert Perkins).

Acid cleaned (10% HCl) HDPE bottles were filled with 50 mL filtered water through PALL Acrodisc PF 32 mm syringe filters with 0.8/0.2 μm pore space supor membranes for analysis of PDSi, Total Organic Carbon (TOC), and macronutrient (nitrate, nitrite, ammonium, and phosphate) concentrations, along with Si isotopes (Section 2.6). Further three water sample replicas (3 x 1 L) were collected for suspended particulate matter (SPM) concentrations (g/L) and composition. The samples were filtered through Whatman quantitative filter paper (grade 42), using a vacuum filter. Samples were dried and weighed (g) for estimations of SPM, calculated from known volume (mL) of filtered water. Sediment samples were viewed under a Binocular microscopy to estimate the degree of roundness, and percentage of grain sizes and composition of the SPM.

In the estuary, a CTD was deployed at each station along the transect to record conductivity, temperature, depth, pH, and dissolved oxygen (autumn sampled period only). A Secchi disk was used to determine estuarine turbidity (i.e. estimate depth based on when the disk is no longer visible).

In the rivers, the pH was logged using pH pocket pals calibrated to a pH buffer of 4, 7 and 10. Riverine conductivity was measured using a conductivity probe calibrated using potassium chloride, and converted to salinity (psu). Air and water temperatures (°C) were recorded using a hand-held digital thermometer.

2.1.2 Intertidal mudflats

2.1.2.1 Sample collection

Sampled intertidal mudflat sites (Fig. 2.1) ranged from the upper Severn Estuary at Severn Beach, Site 1 (51°57´N, 2°67´W), to the mid-estuary on the English coast at Portishead, Site 2 (51°49´N, 2°77´W), and on the Welsh coast at Newport Wetlands, Site 3 (51°53´N, 2°95´W), to the outer estuary at Sand Bay, Site 4 (51°38´N, 2°97´W). Due to sampling constraints, only four mudflats could be sampled each season, and

coincided with spring cycles. These mudflats were chosen to encompass the entire estuary (from the upper to lower boundary on the Welsh and English coastline) and were selected based on their accessibility/safety.

Microphytobenthos (MPB) biofilms at the sediment-water interface (SWI) were sampled during daytime low tide periods, between *ca.* 11:00 hrs and 16:00 hrs (note, each mudflat was sampled on different days). At each mudflat, 15 replicates (i.e. stations) were taken, along a *ca.* 100 m transect, at the mid-shore tide height, parallel to the surf zone, using a semi-random sampling scheme targeting areas of extensive biofilms (*ca.* 5 m between each biofilm). Sediment mini-cores of a diameter of 2.54 cm were extracted for the surficial 5 mm biofilm for chlorophyll *a* analysis (Section 2.2.1), and BBSi content (Section 2.2.2). Community structure was assessed by sub-sampling a weighed proportion of the biofilms. Cell counts of pennate and centric diatoms, cyanobacteria and euglenoids were estimated (note, no species identified) using a Sedgewick Rafter Counting Cell under a bright-field microscope (Olympus CH). Weighed sediment samples were diluted with DI water, and due to the rich samples, the abundance of each group was counted per 10 squares. Note, these were simple group counts, and cyanobacteria filaments were considered as 1 cell.

At each station, a well was formed which allowed surface water and pore fluid to drain into and accumulate. A sample (50 mL) of the mixed mudflat water (a mixture of surface and pore fluids) placed into acid (10% HCl) cleaned 50 mL centrifuge tubes, centrifuged at 4000 rpm for 10 minutes (Thermo Scientific Heraeus Megafuge 8), with the supernatant decanted and filtered through PALL Acrodisc PF 32 mm syringe filters with 0.8/0.2 μm pore space supor membranes for the concentrations of BDSi, phosphate, nitrate, nitrite, ammonium and TOC.

Air and mudflat water temperatures (°C) were recorded at each station using a hand-held digital thermometer. The dimensionless sediment porosity (ϕ) (eq. 2.1) was calculated at each station. Porosity represents the relative pore space between the sediment grains and is defined by the wet and dry sediment mass, and the wet bulk density.

$$\phi = \frac{\text{mass of wet sediment (g)} - \text{mass of dry sediment (g)}}{\text{mass of wet sediment (g)}} \times \frac{\rho_s}{\rho_w} \tag{2.1}$$

where, ρ_s is the wet bulk density (assumed to be 1.5 for unconsolidated sediment), and ρ_w is the density of water (assumed to be about that of seawater, 1.02).

From three randomly selected stations at each site, mudflat biofilm sediment compositions were analysed using the grain size mass (g) of each size fractions separated using sampling sieves (<63 μm, 63-150 μm, 150-212 μm, 212-250 μm, 250-300 μm and >300 μm), and presented as a percentage of the total mass.

2.1.2.2 Chlorophyll fluorescence

Variable chlorophyll fluorescence of undisturbed diatom-dominated biofilms was logged at each station using a Water Pulse Amplitude Modulation (PAM) fluorometer (Walz, Effeltrich, Germany), equipped with an EDF/B fluorometer (blue actinic light measuring beam). The Water PAM 0.6 cm Fluid Light Guide fiberoptics probe was applied to the biofilm surface perpendicularly, at a fixed distance (using an iron stand and clamp) of 2 mm and an area of 0.28 cm^2. The light levels were calibrated using the supplied cosine corrected quantum sensor following the mode point 7 internal programme, and auto zeroed. A measuring beam of a low frequency (non-actinic light, i.e. that will not facilitate photosynthesis) and a 0.6 s saturation pulse >8000 μmol photons/m^2/s PAR were used. To ensure fluorescence yields for all measurements were >300 units, the fluorometer photomultiplier signal gain was set at an appropriate level. Data were stored and downloaded using WinControl-3 software.

Ambient irradiance was measured at each station using the Mini Quantum Sensor attached to the Walz PAM fluorometer (2 Pi radians downwelling cosine corrected light meter) and is reported in μmol/m^2/s. The Quantum Sensor is pre-calibrated for the PAM by Walz. Irradiance was measured at the beginning of each RLC at each station on the mudflats (n=15), each sampled period (note, these irradiance levels are snap-shot of the day sampled, and do not represent the highly fluctuating irradiance levels expected over a season).

Rapid Light Curves (RLCs), defined as short light steps of different intensities, were used to show the relationship between nine different actinic irradiance levels of a duration of 20s and the relative Electron Transport Rate (rETR in *rel. units*, a proxy for primary productivity). RLCs were used to determine the rETR (eq. 2.2), the maximum relative ETR ($rETR_{max}$: *rel. units*) (eq. 2.3); the light use coefficient for PSII i.e. the initial slop of the RLC (α) (eq. 2.4), and the light saturation coefficient i.e. the PAR value at which light saturation begins (E_K: μmol photons/m^2/s) (eq. 2.5). These fluorescent parameters were derived from the curve fitting of the model of Eilers and Peeters (1988), using R studio software (RStudio Team, 2015). The model consists of 100 iterations and the significant (p<0.001) coefficients of a (0.00003), b(-0.003) and c(4) (coefficient initial values provided in the R script written by Dr Christopher Williamson, with the coefficient values originally from Dr Rupert Perkins).

$$rETR = \frac{F_q^{'}}{F_m^{'}} * \frac{PAR}{2} \tag{2.2}$$

where, $F_q^{'}/F_m^{'}$ is the maximum quantum efficiency of PSII ($F_m^{'}$ - $F^{'}/F_m^{'}$), hereafter Y(PSII). Y(PSII) gives the efficiency of absorbed light, which is used in PSII, i.e. the operating efficiency of electron transport in the light.

$$\mathrm{rETR_{max}} = \frac{1}{(\mathrm{b}+2) * \sqrt{(\mathrm{a} \times \mathrm{c})}} \tag{2.3}$$

$$\alpha = \frac{1}{\mathrm{c}} \tag{2.4}$$

$$\mathrm{E_K} = \frac{\mathrm{rETR_{max}}}{\alpha} \tag{2.5}$$

The minimum operational PSII chl fluorescence yield in actinic light (F') was recorded as the saturating pulse was applied to the sediment. The maximum PSII chl fluorescence yield in the dark ($\mathrm{F_m}$) is the first step of the RLC, whereas the yield in actinic light, F'_m is obtained in subsequent steps of the RLC. The residual non-photochemical quenching (NPQ) in the dark often causes these fluorescent parameters, $\mathrm{F_m}$ and F'_m when all reaction centres are closed, to be quenched, and hence a true $\mathrm{F_m}$ is not determined (i.e. underestimated). Consequently, the maximum F'_m value ($\mathrm{F}'_{\mathrm{m\ max}}$) measured under actinic light, i.e. the maximum F'_m value in a LC, which takes into account residual NPQ, was used to calculate the associated photophysiological parameters (Ezequiel et al., 2015), including $\mathrm{F_v/F_m}$ i.e. an indicator of photosystem stress (eq. 2.6) (Genty et al., 1989), the regulated Y(NPQ) (eq. 2.7) and the non-regulated energy dissipation Y(NO) (eq. 2.8) (following *pers. com.* with Dr Rupert Perkins). The non-regulated energy release, describes the radiative and non-radiative deexcitation reactions not contributing to photochemical quenching or involving the NPQ-mechanism (Klughammer and Schreiber, 2008). Compared to Serôdio and Lavaud (2011), where NPQ was determined following the fitting of a LC, and is simply an undefined ratio of Y(NPQ) to Y(NO) and is not constrained by the energetics of photochemistry (Dr Rupert Perkins, *pers. comm.*), here, Y(NPQ) and Y(NO) were calculated individually, where the rate constants show that PSII + Y(NPQ) + Y(NO) = 1, i.e. are energetically competitive (see Table. 2.2 for abbreviations).

$$\frac{\mathrm{F_v}}{\mathrm{F_m}} = \frac{\mathrm{F_{m'max}} - \mathrm{F_o}}{\mathrm{F_{m'max}}} \tag{2.6}$$

$$\mathrm{Y(NPQ)} = \frac{\mathrm{F}'}{\mathrm{F_{m'}}} - \frac{\mathrm{F}'}{\mathrm{F_{m'max}}} \tag{2.7}$$

$$\mathrm{Y(NO)} = \frac{\mathrm{F}'}{\mathrm{F_{m'max}}} \tag{2.8}$$

Table 2.2: Definition of parameters measuring microphytobenthos diatom-dominated biofilm photosynthesis and fluorescence.

Parameter	Description
PSII	Photosystem Two
RLC	Rapid Light Curve
PAR	Photosynthetically Active Radiation (μmol photons/m^2/s)
rETR$_{max}$	Maximum relative Electron Transport Rate (*rel. units*)
E_k	Light saturation coefficient (μmol/m^2/s)
α	Light use coefficient for PSII
Y(PSII)	Maximum quantum efficiency of PSII
F'	Minimum operational PSII chlorophyll fluorescence yield in actinic light
F'_m	Maximum operational PSII chlorophyll fluorescence yield in actinic light when all reaction centres are closed
$F'_{m\ max}$	Maximum F'_m
F_v/F_m	Maximum quantum efficiency of PSII photochemistry
Y(NPQ)	Regulated NPQ
Y(NO)	Non-regulated NPQ

2.2 Laboratory analysis

2.2.1 Biomass: chlorophyll pigments

The surface of the sediment core samples were sub-sampled, and mass obtained (g). Wet sediment was used for all chl pigment extractions. Productive biofilm biomass and water column biomass were assessed via chl *a* content (bulk biomass) (eq. 2.9), chl *b* content (a proxy for the presence of green algae) (eq. 2.10), and chl *c* content (a proxy for the presence of diatoms) (eq. 2.11), and were determined following Mackereth et al. (1978), with 4 mL acetone buffered with $MgCO_3$ to prevent degradation of chl *a* to phaeophytin. Samples were refrigerated at 4°C in the dark for 24 hrs. Samples were vortex mixed at 2000 rpm for 15 minutes. Absorbances were measured at 630 nm, 647 nm, 664 nm and 750 nm on a JENWAY 6305 spectrophotometer.

$$Chla = 11.85 * OD664 - 1.54 * OD647 - 0.08 * OD630 \tag{2.9}$$

$$Chlb = 21.03 * OD647 - 5.43 * OD664 - 2.66 * OD630 \tag{2.10}$$

$$Chlc = 24.52 * OD630 - 7.60 * OD647 - 1.67 * OD664 \tag{2.11}$$

where, the corrected optical densities (OD), after subtracting 750 nm, were inserted into the above formulas. Chl content were corrected for water content (loss of weight upon drying at 85°C for 24 hrs), calculated from the BSi samples (Section 2.2.2). Chl content is presented in μg/g of dry sediment. Chl content were also corrected for the extraction in 4 mL of acetone. Water column samples were also corrected for taking half the polycarbonate filter and the amount of water filtered.

2.2.2 Biogenic silica

Biogenic silica (BSi) has been used here as an additional parameter to chl *a*, as a proxy for diatoms. Approximately 25% of the surficial biofilms were removed from the mudflat sediment mini-cores and placed in clean pre-weighed petri-dishes (g) and dried in an oven at 85°C for 24 hrs to determine the percentage loss of weight upon drying. Dried surface algal biofilms were scrapped off, crushed, weighed (∼0.05 g) and placed in clean centrifuge tubes. River and estuarine pelagic water were filtered through pre-weighed polycarbonate filters using a vacuum filter (Section 2.1.1). The filtered SPM was dried, and weighed (g).

BSi was measured using the weak alkaline extraction method of marine sediments, adapted from DeMaster (1981). With growing awareness that this conventional protocol using weak alkali leaches do not necessarily target BSi, but a range of non-crystalline

siliceous phases, the term amorphous silica (ASi) is often used. However, in this study the alkaline extractable silica will be defined as BSi as it is likely that the River Severn and estuarine benthic fractions are predominately biogenic (Cary et al., 2005).

Samples were leached in hydrogen peroxide (5 mL of 10% H_2O_2 solution) for at least 30 minutes to remove the organic matter without altering the mineral phase (Robinson, 1922), followed by acid (5 mL of 1 M HCl solution) to dissolve the calcium carbonate. Samples were sonified and left for another 30 minutes. To each sample, 40 mL of DI H_20 was added, and samples were centrifuged at 4000 rpm for 5 minutes. Supernatant was removed, and samples were left to dry in a fume cupboard overnight. To maximise Si dissolution with minimal impact on more refractory crystalline material, 40 mL of 0.1 M sodium carbonate (Na_2CO_3), a weak base solution, was added to each sample. This commonly used alkaline extraction (using Na_2CO_3) was preferred over using sodium hydroxide (NaOH), predominately as it has previously been found that NaOH extraction technique does not extract all the ASi and thus BSi (Saccone et al., 2007). Whilst the alkaline extraction may underestimate BSi (Frings et al., 2014), it has been found that using NaOH, a stronger alkaline solution, may dissolve more clay minerals, which would decrease the accuracy of the BSi results (Barao et al., 2015). Therefore, Na_2CO_3 is the more conventional technique for BSi extraction. Samples were placed in a constant temperature water bath at 85°C for the duration of the extraction. Analysis at 1, 3 and 5 hrs yielded the BSi concentrations (DeMaster, 1981). At the end of each time slot, 130 μL of the sample was added to 9.85 mL of Milli-Q H_2O, immediately diluted and neutralized with 20 μL of 10% HCl to make up a 10 mL solution. BSi concentrations were measured using the standard Heteropoly Blue method, modified from the original molybosilicate acid spectrophotographic method on a Hach Lange DR3900 spectrophotometer (Strickland and Parsons, 1972). To each sample, molybdate 3 reagents was added to form yellow silicomolybdic acid complexes and phosphomolybdic acid complexes. Citric acid reagent powder pillow (10 mL) was added after 4 minutes to destroy the phosphate complexes, followed by amino acid F reagent pillow (10 mL) to reduce the yellow silicomolybdic acid to a blue colour, which was proportional to the Si concentration. Blanks were processed alongside each sample. The internal error (i.e. precision) of the spectrophotometer was 2%. Three replicas were taken at each station to capture the natural variability of the system. These three aliquots were plotted, and the resulting intercept of the regression indicated the total amount of BSi extracted. BSi was corrected for diluting, sub-sampling (130 μL), extracting in 40 mL Na_2CO_3, and for the weight of the sediment sample (g).

Mudflat BBSi is presented as a percentage of dried Si mass (g/g), averaged for each mudflat site and presented with the 1 standard error (SE) of the number of sampled station (n=15). Water column PBSi (%) was converted to a concentrations (mg/L) using the SPM concentration, and as a flux (eq. 2.12), the latter is presented with

propagated standard error (i.e. error in the concentration (n=3) and error in the flow). For a detailed explanation of the Si flux calculations, see Chapter Three (Section 3.2.3).

$$\mathrm{BSi}(\frac{\mathrm{mg}}{\mathrm{s}}) = \mathrm{BSi}(\frac{\mathrm{mg}}{\mathrm{L}}) \times \mathrm{flow}(\frac{\mathrm{L}}{\mathrm{s}}) \tag{2.12}$$

2.2.3 Dissolved macronutrients

Aliquots of all filtered mudflat and pelagic waters (200 μL) were diluted with Milli-Q H_2O (9.8 mL) for DSi concentrations (mg/L) following the Heteropoly Blue method (see above). Sub-samples of benthic and pelagic waters (2.0 mL) were measured for phosphate concentration (PO_4-P, mg/L) using the Hach Lange DR3900 spectrophotometer, following the LCK 349 method. All phosphate concentrations were below 50 mg/L and did not interfere with the BSi measurements according to manufacture guidelines. Nitrate (NO_3-N) and nitrite (NO_2-N) concentrations (mg/L) were measured from sub-samples (2.0 mL) using the LCK method 339 and 341, respectively. Ammonium concentrations (NH_4-N, mg/L) were measured from sub-samples (5 mL) using the 304 LCK method. The internal error (i.e. precision) of the spectrophotometer was 2%.

Due to interferences of chloride ions on these macronutrients, for example nitrate levels through nitrate reduction (Malhotra and Zanoni, 1970), the above spectrophotometer could not be used on the saline estuarine samples. HDPE bottled estuarine water samples were immediately frozen on return to the laboratory. Samples were analysed for PDSi and other macronutrient concentrations at Plymouth Marine Laboratory by Malcolm Woodward, using the defrosting technique of heating the frozen samples in a warm water bath for 45 min, and then calibrating to room temperature for another 30 min prior to analysis. This method is recommended by GO-SHIP (Hydes et al., 2010). A SEAL analytical AAIII segmented flow colorimetric auto-analyser was used, which had higher levels of detection, appropriate for the likely low concentrations expected in the estuary due to dilution with marine water. Classical analytical techniques were followed: nitrate (Brewer and Riley, 1965); nitrite (Grasshoff, 1976); ammonium (Mantoura and Woodward, 1983); and phosphate and DSi (Kirkwood, 1989). To check the performance of the analyser and to guarantee the quality control of the final data, seawater nutrient reference materials (KANSO Ltd. Japan) were analysed. The typical uncertainty was between 2% and 3%. Nutrient concentrations are presented in mg/L. Due to the possible discrepancies between the River Severn and Severn Estuary associated with the different method to measure DSi, Environment Agency monitoring data (Agency, 2016) has been used to validate the data presented here. However, caution is required because of the spatio-temporal variations associated with Si dynamics in the Severn.

2.2.4 Total Organic Carbon

TOC concentrations were measured using the Non-Purgeable Organic Carbon (NPOC) technique at the School of Geographical Sciences, University of Bristol. Samples were acidified and purged with nitrogen gas to remove inorganic carbon, with the remaining carbon measured as organic carbon. Calibration standards used were: 0 mg/L TOC, 2 mg/L TOC, 4 mg/L TOC, 6 mg/L TOC, 8 mg/L TOC, 10 mg/L TOC, 15 mg/L TOC, 25 mg/L TOC, 25 mg/L TIC/TOC, with a regression (y = mx + c) used to calculate TOC concentrations (mg/L).

2.3 Dissolution experiment

BBSi dissolution in the intertidal mudflat of the Severn Estuary was investigated using sampled sediment from the sampled periods in 2016. Surficial biofilms (5 mm) from each of the four studied sites, from each season, were dried at 85°C, and crushed, with 1 g of sediment placed into 15 mL clean centrifuge tubes, and vortex mixed with DI water. Samples were subject to different environmental conditions which varied by light levels and temperature: 1) samples were left in daylight at room temperature (*ca.* 20°C); 2) samples were left in the dark at room temperature (*ca.* 20°C); and 3) samples were left in the dark at below 4°C. Sub-samples were taken on average every month, filtered, and measured for Si concentrations (mg/L) using the Heteropoly Blue Method (see above). After a year, samples were dried and measured for BSi content (see above).

2.4 Statistical analyses

Data was tested for normal distribution ($p>0.05$) and equal variance ($p>0.05$). Only few data met these assumptions, and were tested using Two-Way ANOVA (spatial and temporal difference). However, when the Two-Way ANOVA showed significant interaction, data was tested using One-Way ANOVA, followed by a *post hoc* test. Data which failed to meet the assumptions of normal distribution were log transformed. Data that failed to meet the assumptions of both normality and equal variance were tested using the non-parametric Kruskal-Wallis test, followed by a *post hoc* Mann-Whitney pairwise test. To test the linear associations between Si and biological, nutrient and environmental factors in the benthic and pelagic systems, Pearson's product momentum correlations were applied. A Principal Component Analysis (PCA) was applied to normalized data to assess the interaction between Si and biological, nutrient and environmental factors in the pelagic and benthic systems. Sigmaplot (Systat Software, San Jose, CA) was used. PC1 and PC2 loadings and scores are presented.

2.5 Sediment stability experiment

To determine the export of Si from the intertidal mudflats, four sites (Fig. 2.1) were sampled in September 2018. The diffusive flux of BDSi from the SWI was calculated following Fick's First Law of diffusion under steady-state conditions (Schulz and Zabel, 2006). Sediment stability was analysed using a Cohesive Strength Meter (CSM), to determine the equivalent horizontal bed shear stress (τ_0 in N/m^2) and the shear velocity (U*). Surface sediment (i.e. biofilms) and sediment depth profiles (up to 20 cm's deep) were measured for BDSi (mg/L) and BBSi (%). To determine the resuspension (i.e. erosion flux) of DSi, BSi and SPM upon emersion, the time (s) elapsed between the start of the CSM measurements and the point at which the critical erosion threshold [$\tau_{0\ \text{critical}}$, Tolhurst et al. (1999)] was reached was used, along with the volume of the bulk resuspended matrix (mL) in the sensor head chamber. This erosion flux is expressed per unit area ($mg/m^2/s$).

To determine the influence of the diatom-dominated biofilms on sediment stability (i.e. biostabilization), chl *a* and carbohydrate (total and colloidal-S) analyses were carried out. Chl *a* content was measured following Staats et al. (2001), and carbohydrate concentrations were measured following the phenol-sulfuric acid assay (Dubois et al., 1956). These analyses were carried out by Prof. Marian Yallop in Bristol University's Life Science Building. For details regarding the pilot study carried out in August 2017, and a detailed field and laboratory methodology for this above sediment stability experiment, see Chapter Five.

2.6 Silicon isotopes

Silicon isotopes have been applied to further explore the transport of Si along the Severn, and the relationship between the benthic and pelagic systems. Filtered pelagic and benthic mudflat water from the summer and autumn sampled periods of 2016 were analysed for their Si isotopic composition. Note, summer and autumn seasons were further investigated due to findings presented in Chapter Three. Saline water samples were prepared following the Magnesium Induced Co-precipitation (MAGIC) method using sodium hydroxide (Karl and Tien, 1992) with Reynolds et al. (2006) modifications, prior to column chromatography, using the cation exchange resin, adapted from Georg et al. (2006). The BioRad resin (DOWEX 50W-X12, 200-400 mesh) was pre-cleaned, and rinsed with acid (3M, 6M and concentrated HCl) and MQ, before the sample and standards were passed through the columns. The determination of Si isotopes was performed on a Thermo ScientificTM Neptune PlusTM High Resolution multicollector inductively coupled plasma mass spectrometry (MC-ICP-MS) at the Bristol Isotope Group laboratories, University of Bristol. For a detailed explanation of the Si isotope

methodology see Chapter Six.

2.7 Reactive Transport Model

A one-dimensional reactive transport model has been applied to further investigate the transport of Si along the Severn over spatio-temporal scales. A modified version of the Carbon-Generic Estuarine Model (C-GEM) (Volta et al., 2014) has been applied. The pelagic biogeochemical component has been modified and coupled to a Si-driven benthic biofilm system. For the model set-up, see Chapter Severn.

Chapter 3

Dissolved silicon and particulate silica transport along the Severn river-estuary-marine continuum

3.1 Introduction

Diatoms have an obligate growth requirement for dissolved silicon (DSi). Diatoms uptake DSi, and through biomineralization, form their particulate silica frustules, referred to here as biogenic silica (BSi). DSi enters the hydrosphere and is transported to the ocean in rivers and groundwater (Frings et al., 2016). Rivers are also a key network in transporting BSi from the terrestrial environment to the marine zone (Treguer et al., 1995). DSi and BSi are biogeochemically modified along the estuarine gradient due to the interaction of hydrological, geochemical and biological processes over difference spatio-temporal scales. However, these coastal modifications to the terrestrial Si inputs are likely to have consequences on the coastal and marine ecosystems, on global biogeochemical cycles (Laruelle et al., 2009a,b; Arndt et al., 2011; Regnier et al., 2013a,b), and ultimately, on the estimates of both global terrestrial and marine Si budgets (e.g. Tréguer and De La Rocha, 2013; Frings et al., 2016).

Here, the Severn Estuary in the southwest UK has been used as a case study to investigate the influence of the coupled hydro-biogeochemical processes on the transport of DSi and BSi along the Severn. The Severn Estuary is heterogeneous because of complex hydro-geomorphological dynamics (Morris, 1984; Kirby, 2010; Manning et al., 2010; Uncles, 2010; Underwood, 2010; Liang et al., 2014), which may influence Si transport to the marine zone. For example, river discharge and tidal dynamics exert a first-order control on sediment transport and biogeochemical processes (Arndt and Regnier, 2007; Volta et al., 2016), and consequently, on the transport of particulates, such as BSi, and dissolved macronutrients, such as DSi. The Severn Estuary has the third largest

hyper-tidal range in Europe, which exposes large intertidal mudflats that are inhabited by diatom-dominated microphytobenthos biofilms (Yallop et al., 1994, 2000; Underwood, 2010). With the potential strong benthic-pelagic coupling between the benthic ecosystem on the intertidal mudflats and the Severn's water column, the biogeochemical forcings, alongside the estuarine hydrodynamics, are expected to significantly influence the transport of Si.

In this first results chapter, the aim is to investigate the effects of these multiple forcings that influenced the transport and transformations of pelagic DSi and BSi, hereafter PDSi and PBSi, from the freshwater riverine zone to the marine limit of the Severn Estuary, each sampled period in 2016. These forcings include: i) river discharge rates; ii) salt and sediment transport (Suspended Particulate Matter, SPM); iii) pelagic biomass (chl *a*); iv) Total Organic Carbon (TOC) concentrations; v) and macronutrient (nitrate, nitrite, ammonium, and phosphate) concentrations; vi) Si input from external sources including the estuarine tributaries and DSi inputs from groundwater and rainwater.

3.2 Methodology

3.2.1 Fieldwork

Ecological surveys were carried out along the Severn, approximately every 3 to 4 months, which coincided with neap lunar cycles in 2016. A transect aboard Guiding Light, Cardiff University's research vessel, was taken from the upper estuary at high tide, along the longitudinal axis, to the outer estuary (see Chapter Two, Section 2.1). The River Severn and estuary were sampled on different days due to accessibility issues in the Severn between 40 and 80 km, with the river sampled at low tide to estimate the Si inputs into the estuary, and the estuary sampled at high tide to reach the upper estuary in the research vessel. Therefore, the longitudinal profiles of Si along the Severn represent variations in both tidal regime and sampling different days. To account for the Si dynamics in this transition zone, Environment Agency monitoring data (Agency, 2016) has been used to validate the data presented here.

Four main tributaries were sampled each season: River Wye, River Usk, and River Avon, along with a sampling station in Cardiff Bay for the Rivers Taff and Ely Si inputs. The River Severn and the estuarine tributaries (Wye, Avon and Usk) were sampled on separate days due to time constraints. A positive consequence of sampling different days meant there was a more integrated seasonal signature. Further, weather conditions hampered the sampling strategy, with a storm causing extensive flooding of the River Usk in February 2016, which prevented sampling the lower riverine station.

In the Severn Estuary, water was collected from the surface (<2 m deep) and at depths (>15 m deep) using a 5 L Niskin bottle. From the River Severn, estuary and its tributaries, three replicas (3 x 1 L) of water were used to measure PBSi, chlorophyll *a* concentrations, and centric vs pennate diatom abundance (Flow Cytometry, summer samples only). Acid cleaned HDPE bottles were filled with 50 mL filtered water through PALL Acrodisc PF 32 mm syringe filters with 08/0.2 μm pore space supor membranes for analysis of PDSi, nitrate, nitrite, ammonium, phosphate and TOC concentrations. Further three water sample replicas (3 x 1 L) were collected for SPM concentrations and composition. In the estuary, a CTD was deployed at each station along the transect to record conductivity, temperature, depth, pH, and dissolved oxygen (autumn sampled periods only). A Secchi disk was used to determine estuarine turbidity. For a detailed field description see Chapter Two (Section 2.1.1).

3.2.2 Laboratory analyses

PBSi in the SPM was measured following the weak alkaline extraction method of marine sediments, adapted from DeMaster (1981), and presented here in mg/L. For a detailed methodology on BSi measurements see Chapter Two (Section 2.2.2). Freshwater PDSi concentrations were measured using the standard Heteropoly Blue method (Strickland

and Parsons, 1972), and presented here in mg/L. Water samples were filtered through Whatman quantitative filter paper (grade 42), using a vacuum filter for SPM concentrations. Samples were dried and weighed (g) for estimations of SPM, calculated from known volumes (mL) of filtered water, and presented here in g/L.

Filtered riverine samples were sub-sampled and measured for nitrate (NO_3-N), nitrite (NO_2-N), phosphate (PO_4-P) and ammonium (NH_4-N) concentrations on a Hach Lange Spectrophotometer using the Hach LCK cuvette tests. The internal error (i.e. precision) of the spectrophotometer was 2%. Three replicas were taken at each station to capture the natural variability of the system. Due to interferences of chloride ions on these macronutrients, the above spectrophotometer could not be used on the saline estuarine samples. Samples were analysed for PDSi and other macronutrient concentrations at Plymouth Marine Laboratory, following the recommended GO-SHIP methodology (Hydes et al., 2010).

TOC concentrations were measured using the Non-Purgeable Organic Carbon technique at the School of Geographical Sciences, University of Bristol. Chl *a* concentrations in the filtered SPM were analysed using acetone extraction following Mackereth et al. (1978). Chlorophyll fluorescence was measured using the water Pulse Amplitude Modulation (PAM) device with a WATER-ED Emitter-Detector Unit. Summer water column sub-samples were preserved in Lugols iodine, and analysed using the Flow Cytometry method to determine the presence of centric and pennate diatoms. For a detailed outline of these procedures see Chapter Two (Section 2.2).

3.2.3 Si flux and retention calculations

To calculate the flux of PDSi and PBSi, daily discharge data in m^3/s (Agency, 2016) was used for the River Severn (see Chapter Two, Fig. 2.1 for gauging station). Because no discharge data was available for the estuary, bathymetric profiles were taken at each sampled point using ArcGIS, and corrected for the tidal height on the day of sampling. Current velocities from the Severn's hydrological charts (m/s), were used with the cross-section area (m^2) to estimate the flux (m^3/s). Here we assume the Si concentration was constant throughout the cross-section profile. This method followed the "cubage technique" (Vandenbruwaene et al., 2013), which only requires bathymetric and flow data. This study assumed the Si concentrations at each distance were constant throughout the cross-section area of the selected body of water, made possible by the well-mixed nature of the estuary (Manning et al., 2010). Note, these fluxes are a simple representation of the flux; directed downstream only and do not consider any lateral flows or tidal dynamics. To calculate the error in these flow calculations, a conservative estimate of 1 m^2 was added to each trapezoid area, and summed for the total cross-sectional area. This error, along with the error in the current velocities, was propagated to calculate the overall error in the flow, and propagated again to work out the error in

the flux of Si.

The percentage (%) of retention (i.e. positive values) or release (i.e. negative values) of PDSi and PBSi between each zone (see Fig. 3.1) was determined following Vollenweider (1968) (eq. 3.1).

$$X = \left(\frac{X_i - X_o}{X_i} \right) * 100 \tag{3.1}$$

where X is the percentage (%) of either PDSi or PBSi, X_i is the input into a zone (kg/s), and X_o is the output from a zone (kg/s) (Fig. 3.1).

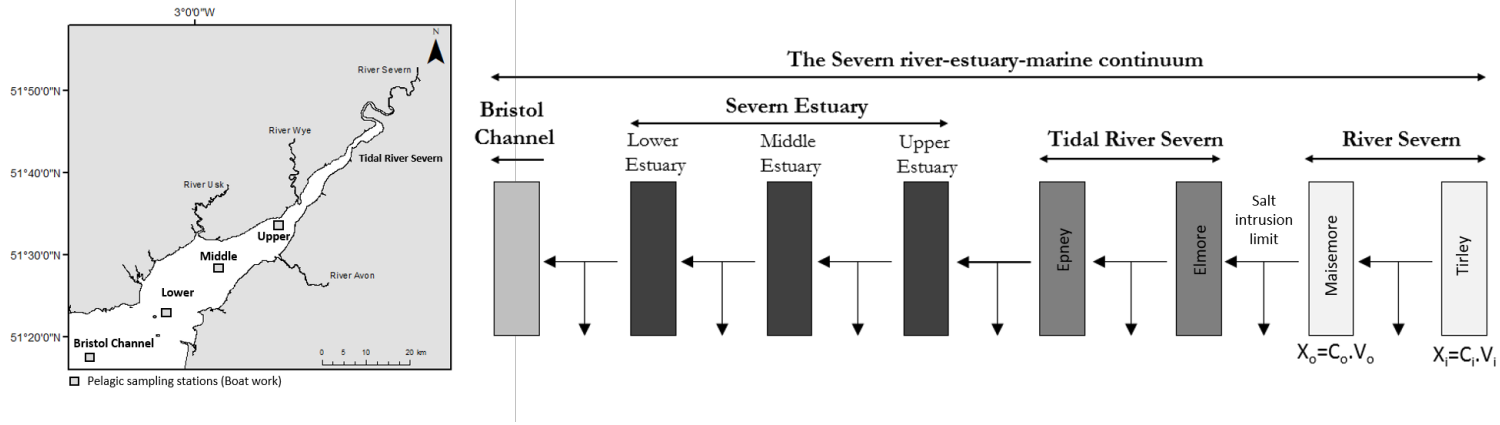

Figure 3.1: Severn river-estuary-marine continuum zones. River Severn, Tidal River Severn, Severn Estuary (upper, middle and lower) and Bristol Channel. Lower estuarine boundary between Bristol Channel and the lower Severn Estuary. Arrow down = retention. Arrow across = release. X is flux (g/s) calculated using the concentration, C (g/m^3) and volume, V (m^3/s). O is the output and i is the input out/into each zone. Note, Si retention/release calculated along the riverine direction of flow. No tidal effects considered (i.e. opposite to the direction of flow).

3.3 Results

3.3.1 Silicon dynamics in the Severn continuum

PDSi concentrations (mg/L) progressively decreased towards the marine zone (*ca.* 15 km downstream of the lower estuarine boundary in the inner Bristol Channel), where salinity levels were >20 psu in each period sampled in 2016 (Fig. 3.2). Relatively higher PDSi concentrations were measured in the freshwater River Severn (salinity: <0.5 psu) compared to the Severn Estuary and marine zone in the Bristol Channel (Table. 3.1). The transition zone between the tidal River Severn and the Severn Estuary lies *ca.* 40-80 km from the lower estuarine boundary. This large transition zone represents an area of poor accessibility, which prevented any sampling. Environment Agency monitoring data has therefore been used to confirm the estuarine dynamics in this transition zone. Despite the temporal difference between the data presented here and the monitoring data, a similar PDSi profile in 2016 is presented (Fig. 3.2), lending confidence in the data presented in the study. PDSi concentrations displayed significant variation between sampled periods (H= 22.79, d.f=3, $p<0.001$). A significant difference in PDSi concentrations was found between the winter and the other sampled periods (*post hoc* analysis $p<0.05$), with peak PDSi concentrations of >1.3 mg/L in the estuary in the winter sampled period (Fig. 3.2).

PBSi concentrations lacked a specific trend along the Severn (Fig. 3.3). Relatively higher PBSi concentrations were measured in the estuary each season compared to the river and marine zone (Table. 3.2). Peak PBSi concentrations were observed in the upper estuary in the summer and autumn sampled periods (max. 14.9 mg/L and 10.0 mg/L, respectively). Alternatively, in the winter and spring sampled periods, PBSi concentrations peaked in the lower boundary of the Severn Estuary (max. 3.1 mg/L and 7.0 mg/L, respectively). PBSi concentrations displayed significant variation between sampled periods (H=20.35, d.f=3, $p<0.001$). A significant difference was found between the winter and the other sampled periods (*post hoc* analysis $p<0.05$), but no difference was found between the spring, summer and autumn sampled periods. Considering the entire data set for each sampled period, no linear correlation was observed between PDSi and PBSi in the Severn.

The River Severn had a low flux of PDSi (Table. 3.1) and PBSi (Table. 3.2) compared to the relatively high Si flux in the Severn Estuary and Bristol Channel in each sampled period (Fig. 3.4). Riverine PDSi and PBSi flux remained below 0.5 kg/s and 0.2 kg/s, respectively. Estuarine PDSi flux was between 109 and 162 kg/s, whilst PBSi flux was between 130 and 394 kg/s in the sampled periods of 2016.

PDSi dominated 76% of the proportion of Si (PDSi + PBSi) in the River Severn in the sampled periods of 2016 (Table. 3.3), and was more dominant in the summer (93%) and autumn (85%) compared to the winter (73%) and spring (52%). Si export in the

Table 3.1: Average River Severn, Severn Estuary and marine Bristol Channel PDSi budgets in each sampled period of 2016.

Season	Location	mg/L	kg/s	μmol/L	Mmol/yr	Tmol/yr
Winter	River Severn	2.6 ± 0.2	0.5	89	610	0.00061
	Estuary	1.5 ± 0.05	162	45	182,449	0.18
	Marine zone	1.2 ± 0.03	370	40	416,282	0.4
Spring	River Severn	1.4 ± 0.1	0.1	52	112	0.00011
	Estuary	0.9 ± 0.02	109	30	122,506	0.12
	Marine zone	0.8 ± 0.03	201	28	225,813	0.3
Summer	River Severn	3.4 ± 0.05	0.2	112	256	0.00026
	Estuary	1.0 ± 0.05	117	30	131,437	0.13
	Marine zone	0.9 ± 0.06	245	32	275,775	0.3
Autumn	River Severn	2.6 ± 0.1	0.1	89	109	0.00011
	Estuary	1.0 ± 0.05	120	31	134,711	0.13
	Marine zone	0.8 ± 0.004	237	27	266,722	0.3
Average	River Severn	2.5 ± 0.1	7.6 x10^{6}	88	272	0.00027
	Estuary	1.1 ± 0.04	4.0 x10^{9}	35	142,776	0.14
	Marine zone	0.9 ± 0.03	8.3 x10^{9}	32	296,148	0.3

Table 3.2: Average River Severn, Severn Estuary and marine Bristol Channel PBSi budgets in each sampled periods of 2016.

Season	Location	mg/L	kg/s	μmol/L	Mmol/yr	Tmol/yr
Winter	River Severn	0.9 ± 0.2	0.2	47	224	0.000224
	Estuary	0.9 ± 0.2 (max. 3.1)	130	53	146,700	0.15
	Marine zone	0.5 ± 0.1	172	19	193,795	0.2
Spring	River Severn	1.3 ± 0.2	0.1	64	105	0.00011
	Estuary	2.4 ± 0.4 (max. 7.0)	286	101	321,903	0.32
	Marine zone	2.2 ± 0.3	533	75	600,314	0.6
Summer	River Severn	0.3 ± 0.1	0.02	14	20	0.00002
	Estuary	3.4 ± 0.9 (max. 14.9)	276	68	311,079	0.31
	Marine zone	1.4 ± 0.1	359	47	404,737	0.4
Autumn	River Severn	0.5 ± 0.1	0.02	26	19	0.00002
	Estuary	3.5 ± 0.6 (max. 10.0)	394	114	444,077	0.44
	Marine zone	1.9 ± 0.2	581	67	653,680	0.7
Average	River Severn	1.5 ± 0.2	2.6 x10^{6}	38	92	0.0001
	Estuary	2.6 ± 0.5	8.6 x10^{9}	84	305,940	0.31
	Marine zone	0.8 ± 0.2	1.3 x10^{10}	52	463,132	0.5

estuary was likely controlled by seasonal variations, with the proportion of Si dominated by BSi (66%) in the sampled periods of 2016, especially in more typically biologically productive periods: spring (72%), summer (77%) and autumn (77%), compared to the winter (38%) (Table. 3.3).

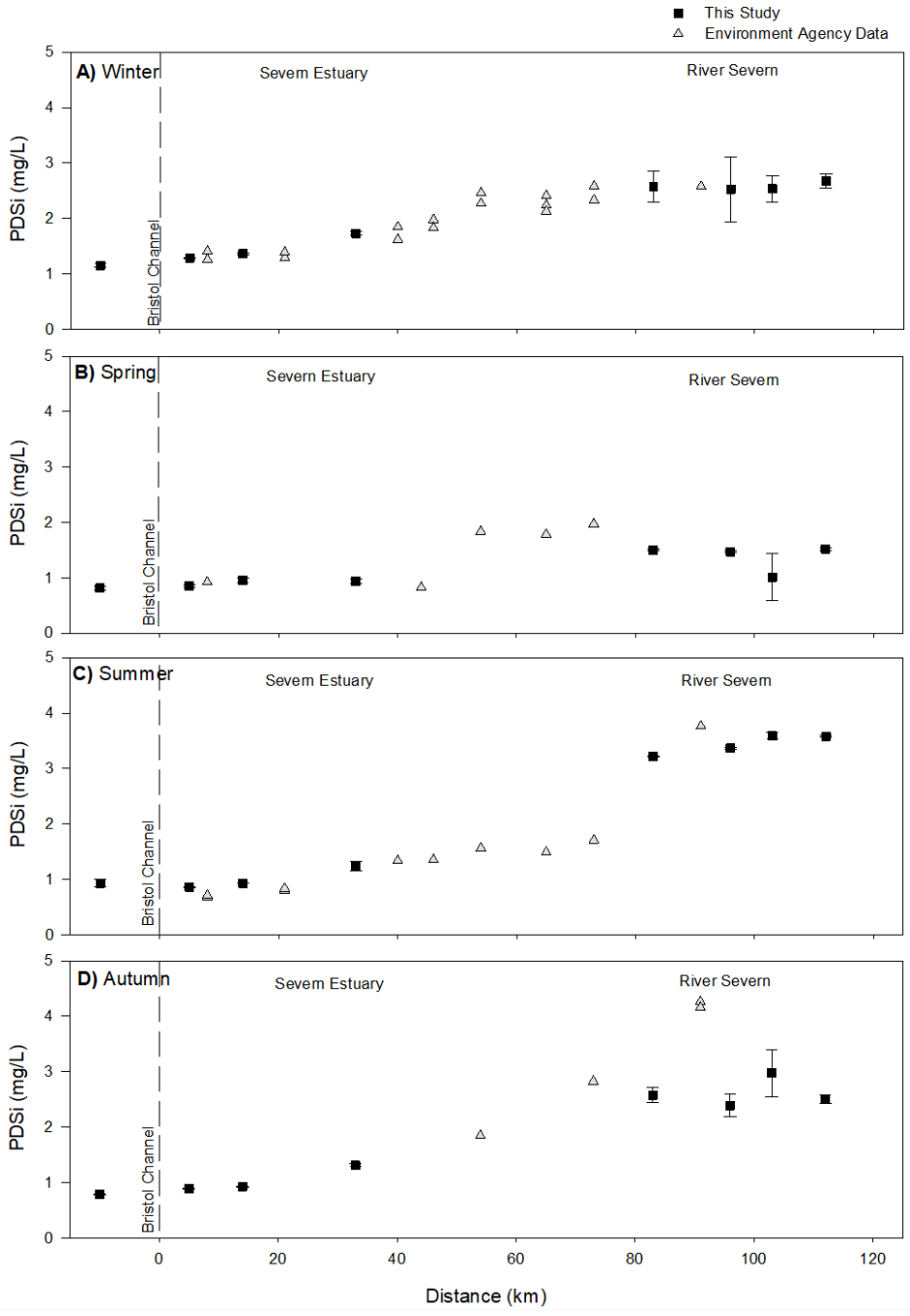

Figure 3.2: Pelagic silicon concentrations along the Severn each season in 2016. This study (black squares). Environment Agency data 2016 (grey triangles), Agency (2016). **A)** Winter. **B)** Spring. **C)** Summer. **D)** Autumn. River Severn: 80-120 km. River-Estuary transition zone: 40-80 km (no data available from this study). Severn Estuary: 0-40 km. Lower estuarine boundary defined as 0 km. Upper Bristol Channel: <0 km. Data reported with 1SE for each station: river (*n=3*), estuary (*n=6*).

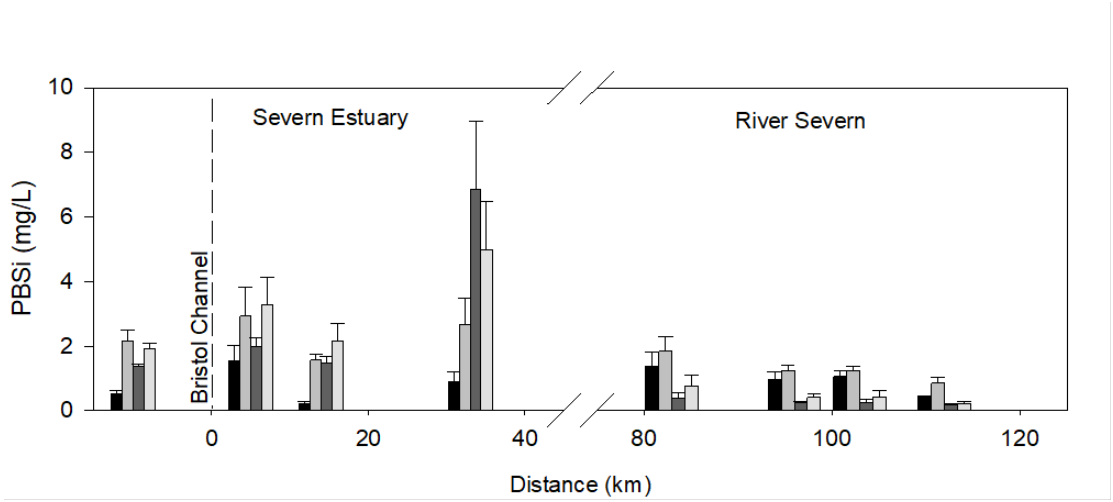

Figure 3.3: Pelagic BSi concentrations along the Severn each season in 2016. River Severn: 80-120 km. River-Estuary transition zone: 40-80 km (no data available). Severn Estuary: 0-40 km. Lower estuarine boundary defined as 0 km. Upper Bristol Channel: <0 km. Data reported with 1SE for each station: river (*n=3*), estuary (*n=6*).

Table 3.3: Proportion of PDSi and PBSi compared to the total amount of bioavailable Si (DSi+BSi) in each sampled period. Note, PBSi dominated the available Si in the typically more biologically productive periods (in bold).

Season	Location	PDSi (%)	PBSi (%)
Winter	River	73	27
Spring	River	52	48
Summer	River	93	7
Autumn	River	85	15
Winter	Estuary	62	38
Spring	Estuary	28	**72**
Summer	Estuary	23	**77**
Autumn	Estuary	23	**77**
2016	River	77	23
2016	Estuary	30	70

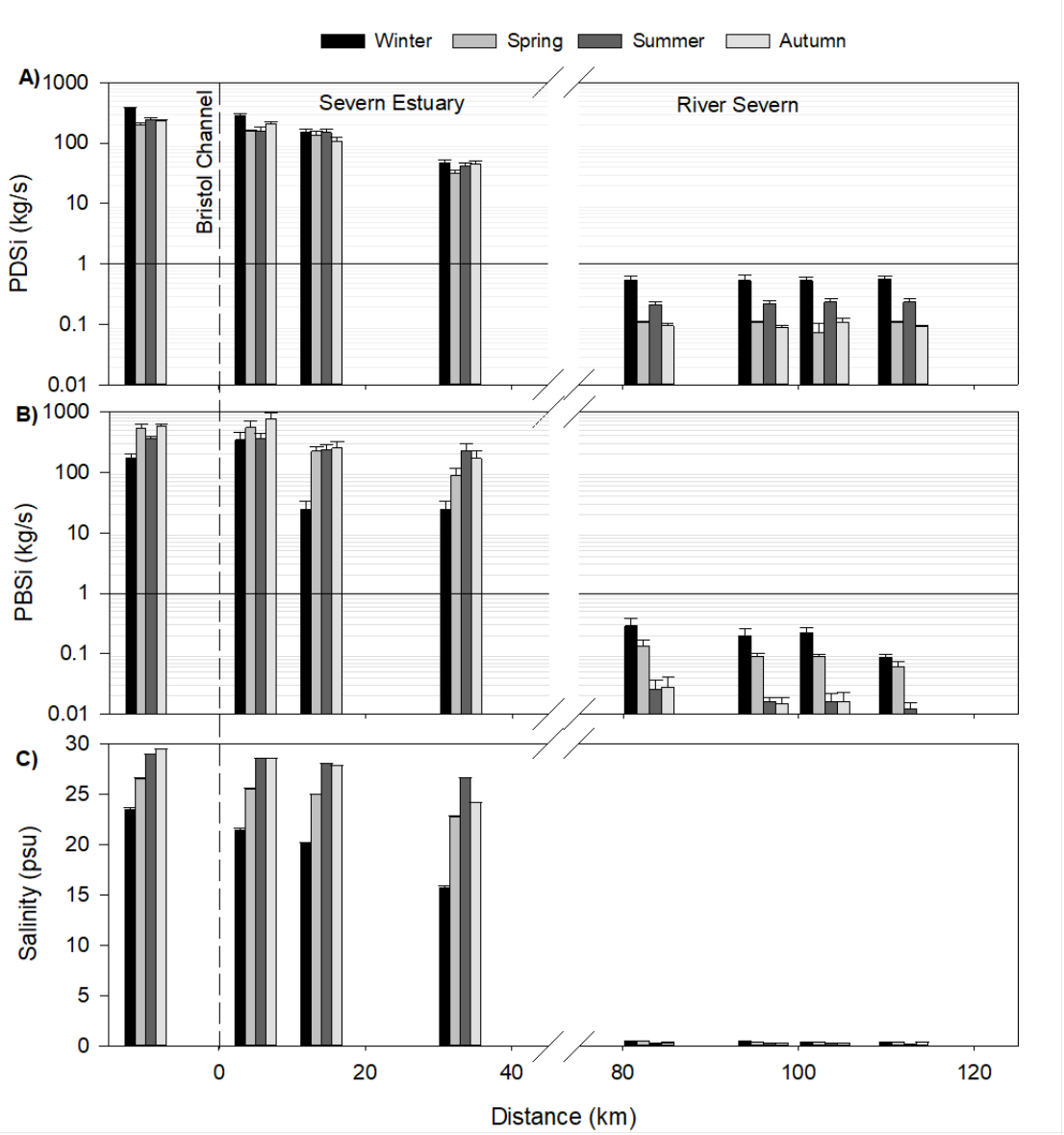

Figure 3.4: Pelagic silicon flux along the Severn each season, with propagated standard error. **A)** Dissolved silicon (PDSi, kg/s). **B)** Biogenic silica (PBSi, kg/s). **C)** Salinity (psu). Si flux plotted on a logarithmic scale. River Severn: 80-120 km. River-Estuary transition zone: 40-80 km (no data available). Severn Estuary: 0-40 km. Lower estuarine boundary defined as 0 km. Upper Bristol Channel: <0 km. Data reported with 1SE for each station: river (n=3), estuary (n=6).

3.3.2 Silicon retention and flux from the River Severn and Severn Estuary

There was no retention of PDSi and PBSi in the River Severn. There was a high flux of Si from the lower River Severn into the upper Severn Estuary (Table. 3.4). The Severn Estuary also acted as a source of PDSi to the marine Bristol Channel in the sampled periods of 2016: winter (-28%), spring (-26%), summer (-53%) and autumn (-14%). PBSi was retained in the Severn Estuary in the sampled periods of 2016: winter (50%), spring (2%), summer (2%) and autumn (24%) (Table. 3.4).

Table 3.4: PDSi and PBSi **retention** (+ive) and flux (-ive) from the River Severn and Severn Estuary.

Location	Season	PDSi(%)	PBSi(%)
River Severn output			
	Winter	-8,598	-8,334
	Spring	-28,744	-66,554
	Summer	-19,243	-880,973
	Autumn	-46,559	-599,478
Severn Estuary output			
	Winter	-28	**50**
	Spring	-26	**2**
	Summer	-53	**2**
	Autumn	-14	**24**

3.3.3 Dissolved silicon transport: simple mixing models

Mixing models are often used to describe the behaviour of elements in estuaries in relation to conservative or non-conservative behaviour (Morris et al., 1985; Statham, 2012). However, this approach follows a theoretical profile which assumes a steady-state system with mixing only between the freshwater and saline end-members, ignoring any hysteresis, transient dynamics and non-linearities that may arise, for instance, as a result of tidal dynamics, varying riverine inputs, and multiple sources of PDSi into the estuarine system (Regnier et al., 1998). These mixing models have been applied here to simply show the presence of complex mixing in the Severn, which requires more advanced, process-based computational models. For example, reaction-transport models presented in Volta et al. (2014) & Volta et al. (2016), to comprehensively depict the transport of dissolved and particulate constituents along the longitudinal axis of the Severn.

Simple conservative mixing models of PDSi in the winter and spring sampled periods followed the theoretical conservative dilution line (TDL), whereby both freshwater and saline end-members appeared to have the same concentrations (Fig. 3.5). Thus, PDSi was unlikely removed or added within the estuarine mixing system and behaved conser-

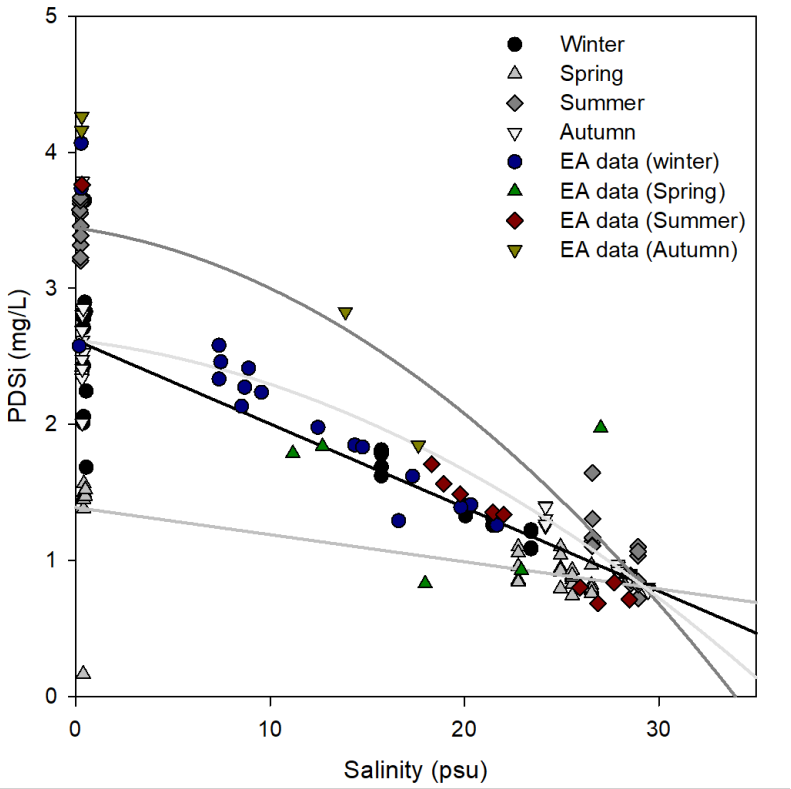

Figure 3.5: PDSi conservative mixing plots in the Severn in sampled periods of 2016. This Study data and Environment Agency data presented Agency (2016).

vatively. Note, the river and estuary were sampled on different days (see this chapter's study caveats, Section 3.4.6). PDSi mixing models in the summer and autumn displayed non-conservative behaviour, with deviations away from the TDL, as PDSi was added near the freshwater end-member.

3.3.4 Hydrodynamics in the Severn

Rainfall and the number of rain days in the Severn's catchment area in 2016 peaked in January (215 mm over 21 days) (MetOffice, 2016). Corresponding to the high and more persistent rainfall and windier conditions, the River Severn discharge rates were significantly greater (H=197.04, d.f=3, $p<0.001$, *post hoc* analysis $p<0.05$) in the winter (307 ± 17 m^3/s), reaching maximum flows of 479 m^3/s, compared to the spring (125 ± 9 m^3/s), summer (53 ± 3 m^3/s) and autumn (77 ± 8 m^3/s) (Fig. 3.6). No clear relationship was observed between Si concentrations in the River Severn and discharge rates in sampled periods of 2016 (Fig. 3.7).

The relatively high winter discharge (Fig. 3.6) shifted the salt intrusion zone towards the marine end-member, reducing salinity levels in the upper estuary (Fig. 3.7). Despite

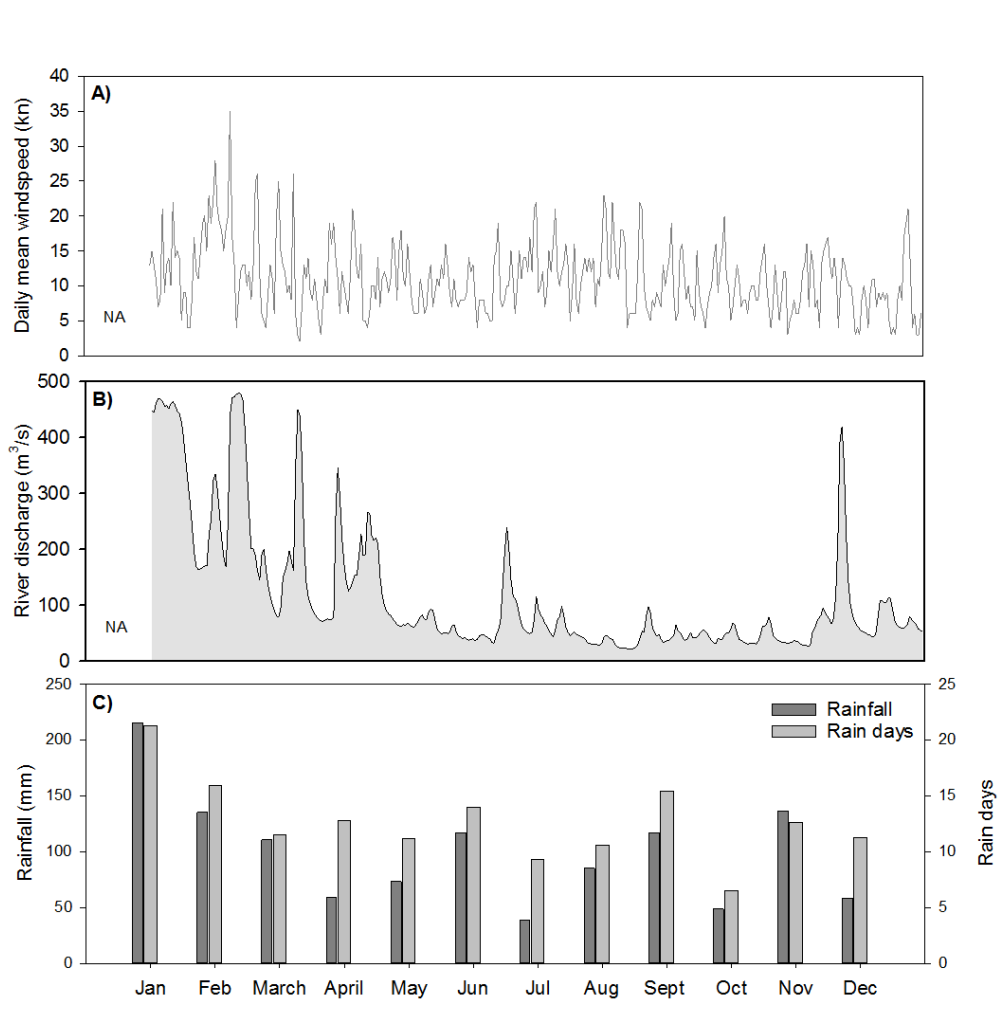

Figure 3.6: Meteorological factors in the Severn. **A)** Daily mean windspeed (kn) at Avonmouth. **B)** River Severn discharge (m^3/s) each month from the gauging station at Tirley (NGR: SO8449127878). River Severn catchment size: 11,419 km^2. **C)** Rainfall (mm) and number of rain days in the River Severn catchment area per month.

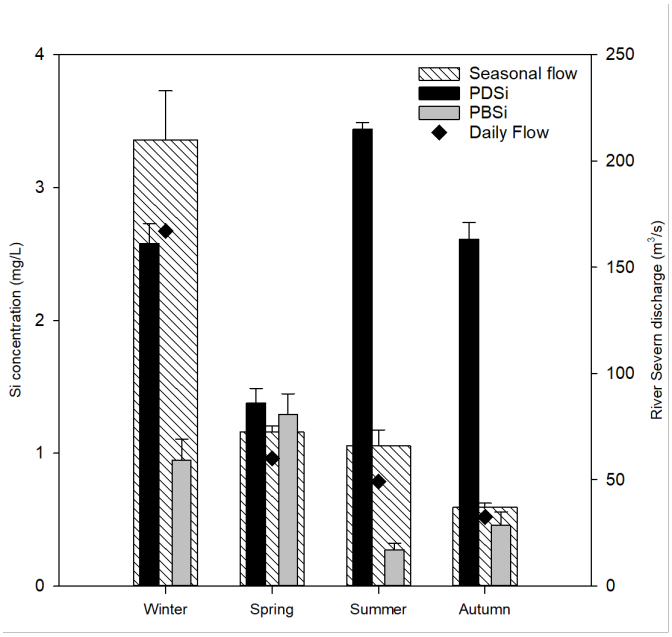

Figure 3.7: Relationship between River Severn discharge and PDSi and PBSi concentrations in sampled periods of 2016. Diamonds: river flow rate on the day of sampling. DSi data reported with 1SE of *n=12* samples from each sampled period. Flow reported with 1SE calculated from the daily flow rates each season (*ca. n=60*).

seasonal variation in the River Severn discharge, salinity in the River Severn and the tidal section of the River Severn on the days of sampling, remained below 0.5 psu, representing the true river signal (Fig. 3.7). Note, the tidal River Severn was sampled at low tide to ensure the true riverine Si signal was sampled. In the estuary, salinity progressively increased towards the Bristol Channel, where salinity levels peaked at 29 psu.

Salinity depth profiles from the upper estuary, near the expected location of the salt intrusion wedge, also displayed variation between sampled periods with saline estuarine bottom waters intruding upstream during the winter, summer and autumn (Fig. 3.8). However, in the spring, salinity decreased with depth (Fig. 3.8).

Water column temperatures in the Severn were relatively lower during the winter (5.4 ± 0.3°C) and autumn (9.3 ± 0.03°C) compared to the spring (13.2 ± 0.1°C) and summer (17.9 ± 0.03°C) sampled periods (Fig. 3.9). In the winter, summer and autumn, water column temperatures increased along the longitudinal axis of the Severn, however in the spring, water column temperature peaked in upper estuary. Further, the water column was not stratified in any sampled period, owing to the turbulent, well-mixed nature of the estuary (see Appendix, Section 3.6.1, Fig. 3.32). In the Severn Estuary, pH fluctuated within the range of 6.9 and 7.9. In the River Severn, pH fluctuated between 6.7 and 8.3 (Table. 3.5).

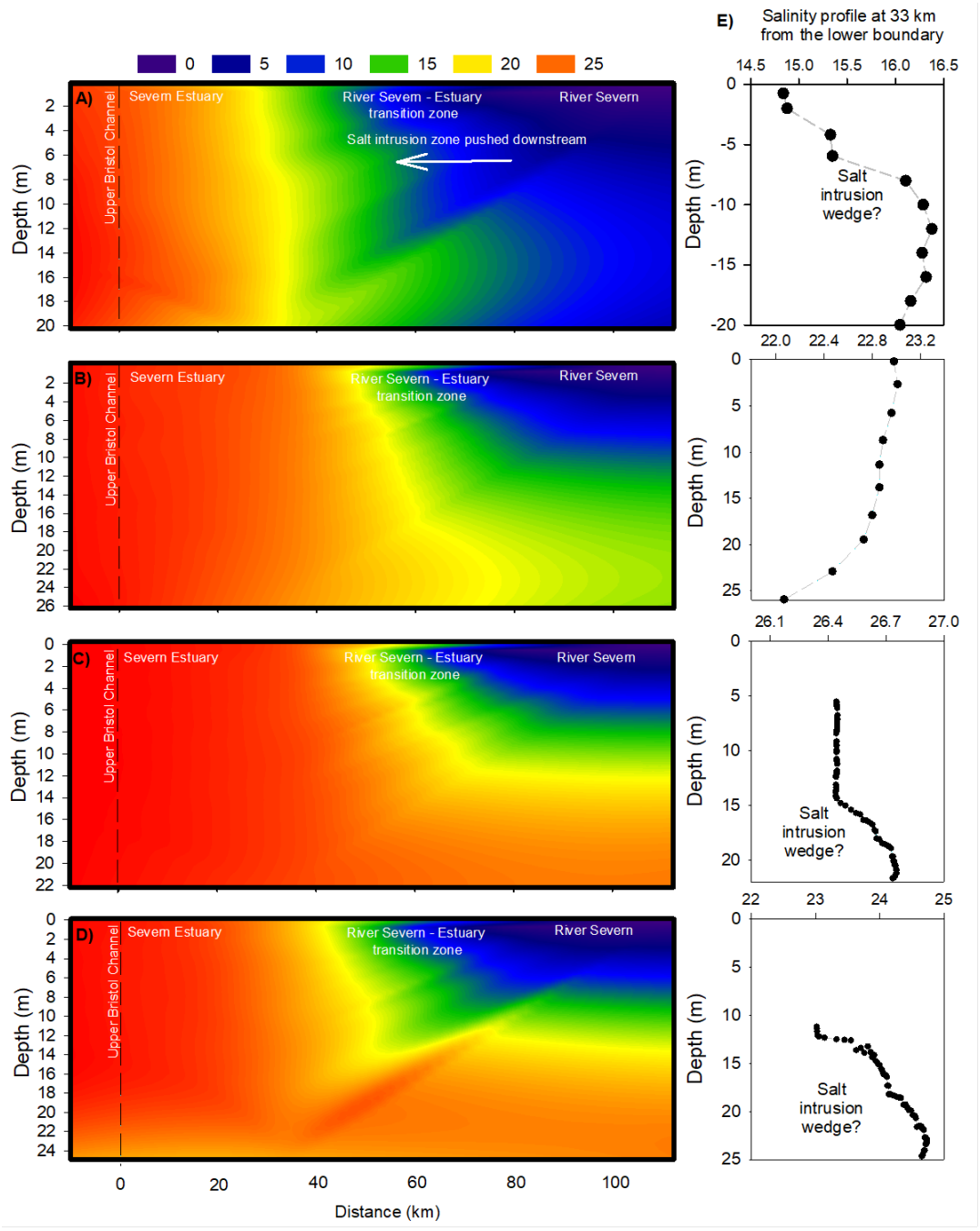

Figure 3.8: Left: Salinity extrapolated between sampled stations along the Severn to show changes in river input between sampled periods (note, higher freshwater further into the estuary in winter). **A)** Winter. **B)** Spring. **C)** Summer. **D)** Autumn. **E:** Salinity depth profile in the upper estuary sampling station (see Chapter Two, Fig. 2.1), to show the salt intrusion wedge each sampled period in 2016.

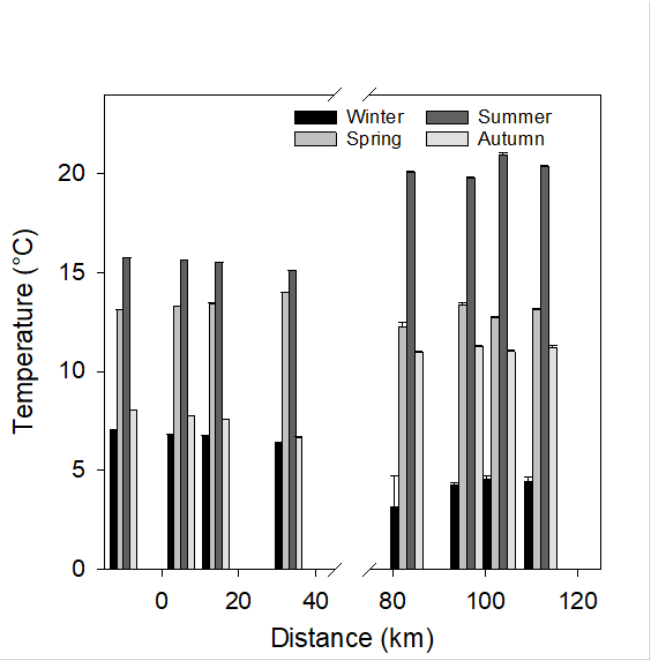

Figure 3.9: Water column temperature along the longitudinal axis of the Severn for sampled periods in 2016. Data reported with 1SE for each station: river (*n=3*), estuary (*n=6*).

Table 3.5: River Severn and Severn Estuary pH values each sampled period in 2016.

Distance (km)	Winter	Spring	Summer	Autumn
112 (River Severn)	6.64 → 6.92	7.34 → 7.80	6.78 → 7.14	6.78 → 6.99
103 (River Severn)	8.18 → 8.31	7.40 → 7.54	7.15 → 7.35	6.82 → 7.04
96 (River Severn)	6.86 → 8.05	7.44 → 7.79	7.25 → 7.40	6.76 → 6.94
83 (River Severn)	7.79 → 8.02	6.67 → 6.73	6.78 → 7.24	7.46 → 7.59
33 (Severn Estuary)	7.64 → 7.83	7.68 → 7.71	6.74 → 7.14	7.56 → 7.67
14 (Severn Estuary)	7.65 → 7.83	7.66 → 7.72	7.20 → 7.31	7.61 → 7.63
5 (Severn Estuary)	7.80 → 7.93	7.66 → 7.72	7.35 → 7.37	7.62 → 7.64
-10 (Bristol Channel)	7.84 → 7.95	7.65 → 7.74	7.40 → 7.52	7.61 → 7.64

3.3.5 Sediment transport

Increased River Severn discharge (Fig. 3.6) was reflected in the amount of suspended particulate matter (SPM), with significantly high (H=17.286, d.f=3, $p<0.001$, *post hoc* analysis $p<0.05$) riverine SPM concentrations measured during the winter sampled period (max. 2.1 g/L), compared to the spring (always below limit of detection), summer (max. 0.01 g/L) and autumn (max. 0.08 g/L). Note, the river SPM concentrations were sampled at low tide. In the turbulent, tidally-dominated Severn Estuary, seasonal changes in river flow rates were less pronounced on the estuarine turbidity, with peak SPM concentrations at each sampled site in the spring (Fig. 3.10). For the sampled periods in 2016, SPM concentrations were on average high in the upper Severn Estuary (Fig. 3.10). In agreement, Environment Agency monitoring SPM data (Agency, 2016) displayed peak SPM concentrations in the upper Severn Estuary, and followed a similar seasonal pattern in 2016: 1.1 g/L (winter), 3.2 g/L (spring), 1.5 g/L (summer), and 1.7 g/L (autumn), lending confidence that our data are directly comparable.

SPM and PBSi relationship in the Severn displayed variability between sampled periods (Fig. 3.10). No clear linear correlation was observed between SPM and PBSi during the winter, but a positive linear correlation was observed in the spring (n=36, r^2=0.52, $p<0.01$), summer (n=36, r^2=0.84, $p<0.001$) and autumn sampled periods (n=36, r^2=0.86, $p<0.001$). Bottom water samples in the Severn Estuary had higher concentrations of SPM and PBSi compared to surface water samples each sampled period in 2016 (Fig. 3.10).

Fine sand dominated the composition of SPM: winter (86%), spring (86%), summer (66%) and autumn (65%) (Fig. 3.11). Corresponding to high discharge rates at the beginning of 2016, a mixture of fine and coarse fractions was observed, whereas towards the second half of 2016, when river discharge rates were reduced (Fig. 5.16), heavier particles likely settled out in the calmer waters: between 50% and 78% of the SPM composition were fine fractions (mud/clays) in the Severn Estuary (Fig. 3.11).

3.3.6 Biochemical mediation of silicon in the Severn

DSi is vital to siliceous photosynthetic diatoms, which uptake DSi, and through biomineralization build their frustules (i.e. BSi). The biomass of these primary productive siliceous organism in the water column and the rate of production could influence the amount of DSi uptake and subsequently the amount of BSi accumulated, a process referred to here as biological mediation of Si.

Water column biomass concentrations (chl *a* in mg/L) was negligible in all sampled periods in the turbid (Fig. 3.10) Severn Estuary and Bristol Channel. The River Severn had relatively higher biomass levels but remained below 0.001 mg/L. Similarly, Environment Agency monitoring chlorophyll *a* data for the Severn (measured following

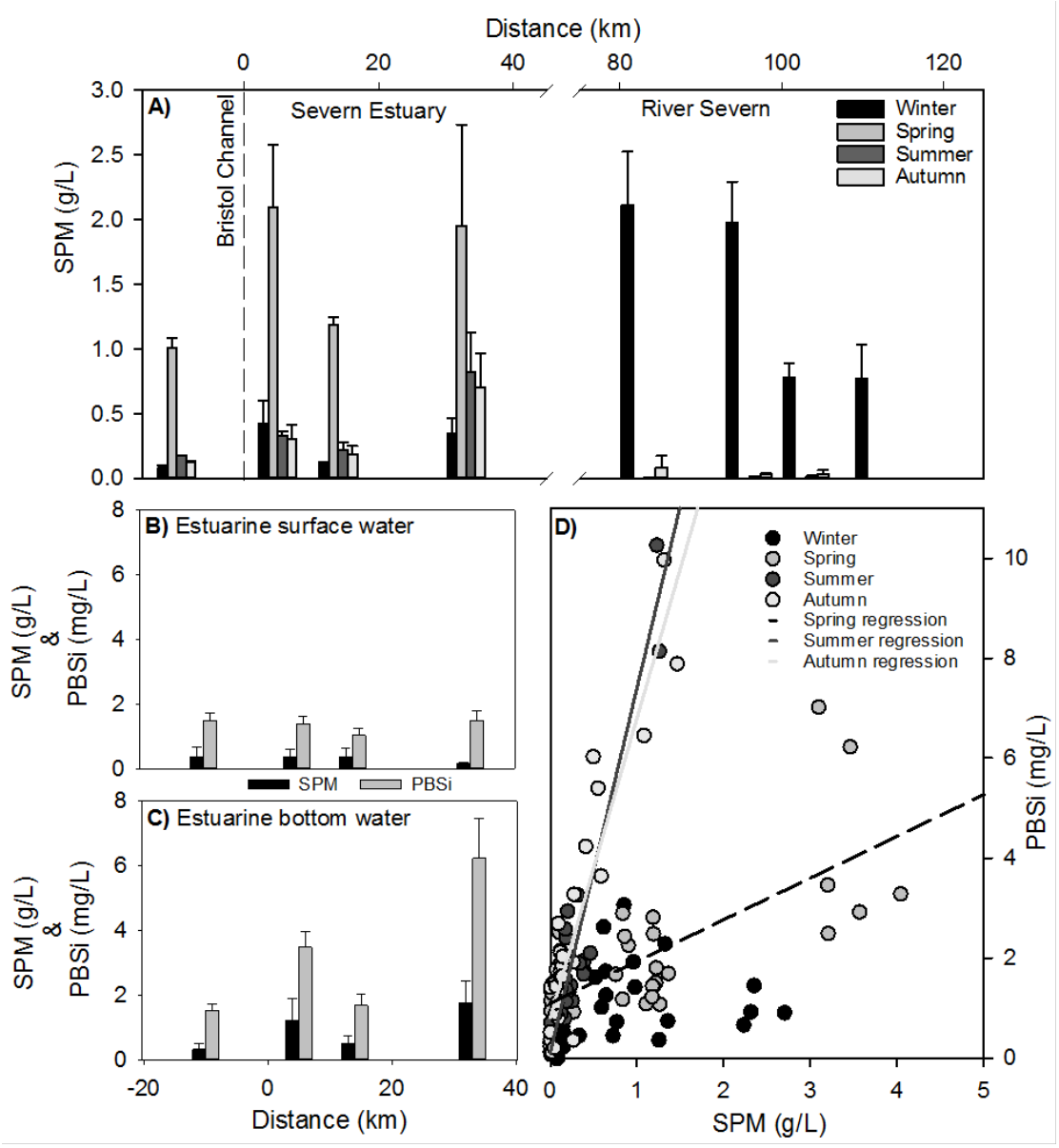

Figure 3.10: Suspended particulate matter (SPM). **A)** SPM concentrations (g/L) in the Severn during sampled period of 2016. Data reported with 1SE for each station: river (n=3), estuary (n=6). **B)** Estuarine surface water (<2 m) year average SPM and pelagic biogenic silica (PBSi) concentrations, presented with 1SE (n=12). **C)** Estuarine bottom water (>15m) average SPM and PBSi concentrations, presented with 1SE (n=12). Note, unit discrepancy: SPM (g/L), PBSi (mg/L). **D)** Linear correlation between PBSi and SPM in the Severn: spring (n=36, r^2=0.52, p<0.01) summer (n=36, r^2=0.84, p<0.001) and autumn (n=36, r^2=0.86, p<0.001).

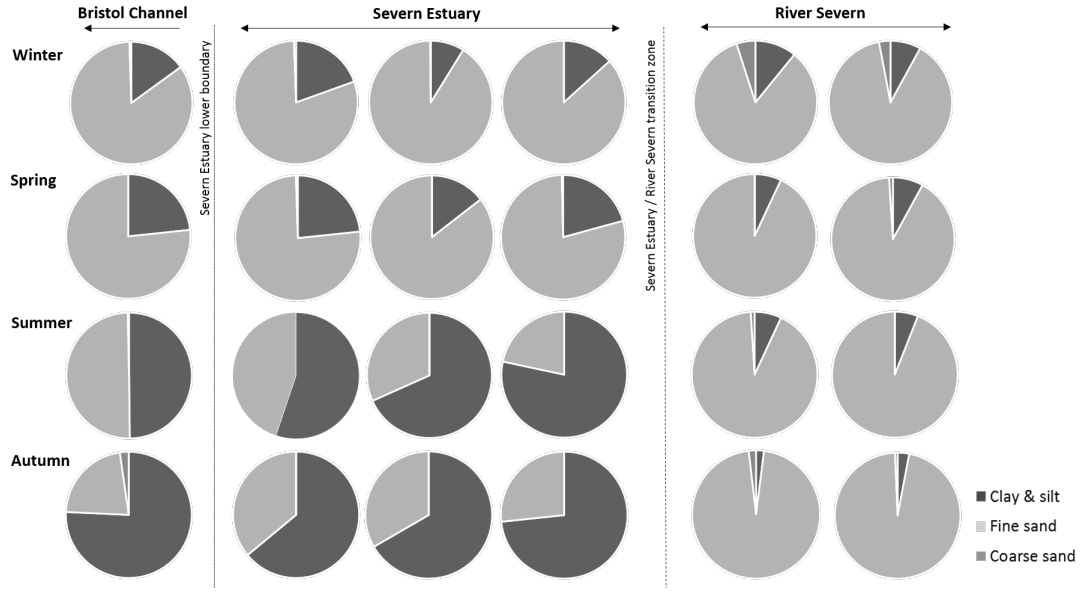

Figure 3.11: Suspended particulate matter composition. Freshwater and tidal zones of the River Severn (right), the upper, mid and lower zones of the Severn Estuary (middle), and Bristol Channel (left).

the acetone extraction methodology), was also low in the Severn (avg. 0.003 mg/L), with relatively higher concentrations in the river compared to the estuary. The high turbidity, which reduced light availability, likely restricted phytoplankton growth, resulting in a lack of chlorophyll fluorescence readings, and low water column primary productivity. Secchi disk depth, an estimate of the transparency of the water, measured when the disk becomes obscure, was low each sampled period in the turbid waters: winter (0.18 m), spring (0.15 m), summer (0.2 m), autumn (0.3 m).

Flow Cytometry technology was applied to analyse the physical characteristics of particles in the water column of the Severn Estuary and Bristol Channel to determine the presence and ratio of centric to pennate diatoms. Note, the Flow Cytometry approach was only carried out on estuarine water samples collected in the summer. The Flow Cytometry approach proved problematic due to the high turbidity, resulting in the samples aggregating, which prevented clear shape definition and clarity between living and non-living matter. However, the total number of particles sampled were relatively higher in the upper estuary (Appendix, Section 3.6.2, Fig. 3.33). The presence of resuspended pennate diatoms was also recorded (Fig. 3.12), along with what appeared to be a lower abundance of centric diatoms in the estuarine waters (*pers. obs.*).

Total Organic Carbon (TOC) concentrations in the River Severn were between the limit of detection and 4.5 mg/L, but lacked significant correlation with PBSi in all seasons (Fig. 3.13). Dissolved oxygen levels in the Severn Estuary during the autumn (note, no data in winter, spring, summer), decreased from 8.4 mg/L in the upper estuary,

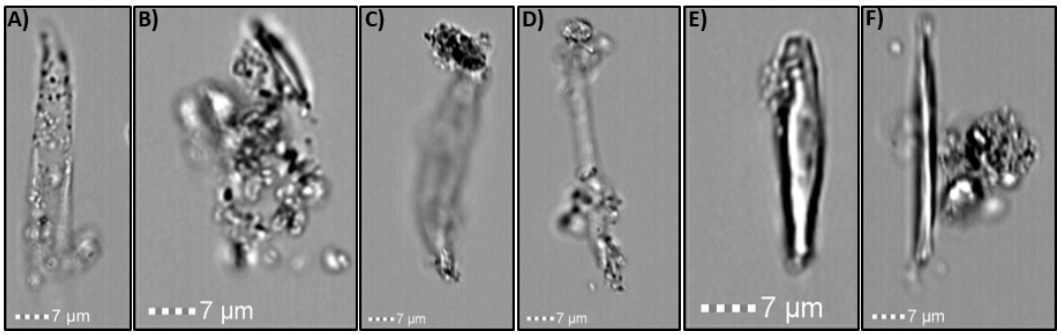

Figure 3.12: Resuspended pennate diatom presence in the Severn Estuary and Bristol Channel. **A-B)** Upper estuary. **C-D)** Middle estuary. **E)** Lower estuary. **F)** Bristol Channel.

to lows of 5.8 mg/L in the outer estuary, and increased to 7.6 mg/L in the Bristol Channel.

Macronutrient concentrations (mg/L) were high in the River Severn compared to the Severn Estuary and Bristol Channel, similar to a decrease in DSi at higher salinity levels (effect of dilution) (Fig. 3.14). Each sampled period, nitrate was the most abundant macronutrient in the River Severn (annual avg. of 4.4 ± 0.7 mg/L) and the Severn Estuary (annual avg. of 1.5 ± 0.3 mg/L). Riverine nitrate concentrations were low in the winter (max. 2.8 mg/L) compared to the spring (max. 6.1 mg/L), summer (max. 4.5 mg/L) and autumn (max. 5.7 mg/L). In the more saline end-member, variation in nitrate concentrations between sampled periods was reduced (Fig. 3.14). Environment Agency monitoring nitrate data along the Severn from 2016 Agency (2016) were in a similar range between 0.6 and 8.2 mg/L, lending confidence that our data are directly comparable. Nitrite and phosphate concentrations were low in the Severn in 2016 (<0.1 mg/L, and <0.6 mg/L, respectively). Ammonium concentrations were below the level of detection (<0.15 mg/L) in the River Severn, and below 0.06 mg/L in the Severn Estuary. Environment Agency monitoring data on nitrite, phosphate and ammonium along the Severn from 2016 Agency (2016) were also of low concentration: nitrite (0.004 to 0.1 mg/L), phosphate (0.05 to 0.4 mg/L), ammonium (0.02 to 0.1 mg/L).

Simple conservative mixing models for nitrate and phosphate revealed variability between sampled periods (Fig. 3.15). Nitrate followed the theoretical conservative dilution line in the spring, and displayed non-conservative behaviour in the winter, summer and autumn. There was likely a removal of nitrate in the estuary during the winter and a supply during the summer and autumn. Phosphate followed the TDL in the spring and summer, and displayed non-conservative behaviour in the winter and autumn. Phosphate was likely removed from the water column in the estuary during the winter and autumn. Note, a steady-state system was assumed in these conservative mixing models, which oversimplifies the system as transient estuarine dynamics are ignored (see Section 3.3.3).

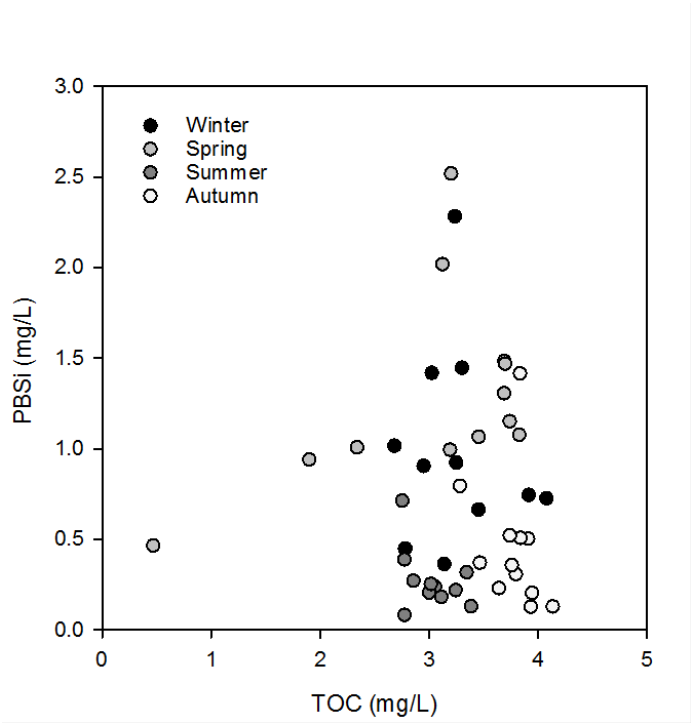

Figure 3.13: Relationship between pelagic biogenic silica (PBSi) and Total Organic Carbon (TOC) in the River Severn. No significant correlations observed.

Si is essential to siliceous organisms, and as a result, the Redfield (1963) nutrient ratio of C:N:P of 106:16:1 was modified and stated to be C:Si:N:P of 106:15:16:1 (Brzezinski, 1985). Each season, the Redfield-Brzezinski nutrient ratios were calculated on a molar basis (mol:mol) to determine nutrient (DSi, nitrate or phosphate) limitation. Note, there are several caveats to using these ratios which effect the ecological stoichiometry in these aquatic environments, including discrepancies between freshwater and saline ratios (Glibert, 2012). Phosphate was potentially limiting in the Severn Estuary in the sampled periods of 2016 (Fig. 3.16). DSi was potentially limiting relative to nitrate during typically biologically productive periods in the river and estuary.

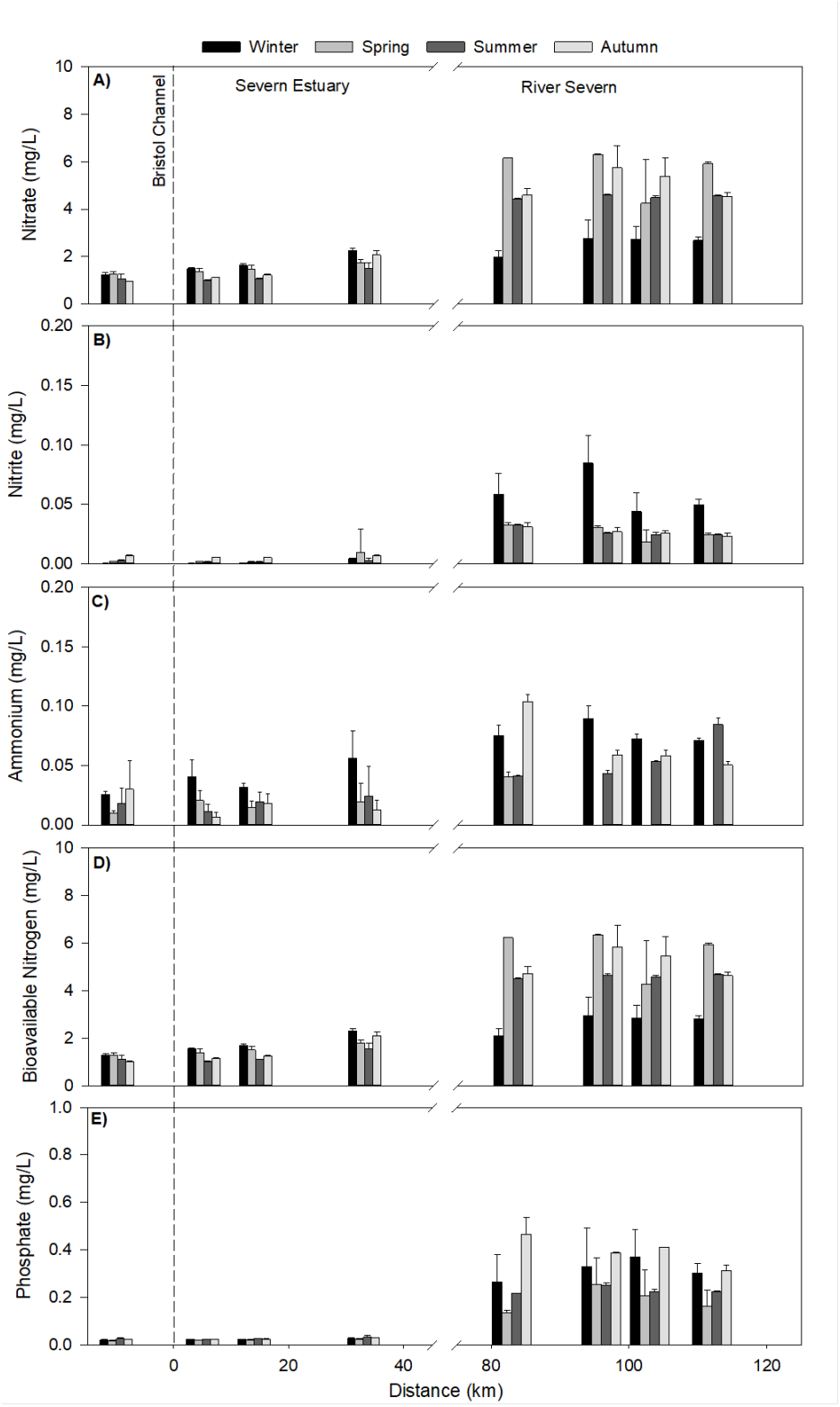

Figure 3.14: Nutrient concentrations in the Severn each sampled period in 2016. **A)** Nitrate (mg/L). **B)** Nitrite (mg/L). **C)** Ammonium (mg/L). **D)** Bioavailable Nitrogen (nitrate + nitrite + ammonium, mg/L). **E)** Phosphate (mg/L). Between 40 and 80 km, River Severn to estuary transition zone (no data available). Lower estuarine boundary defined as 0 km. Data reported with 1SE for each station: river (n=3), estuary (n=6).

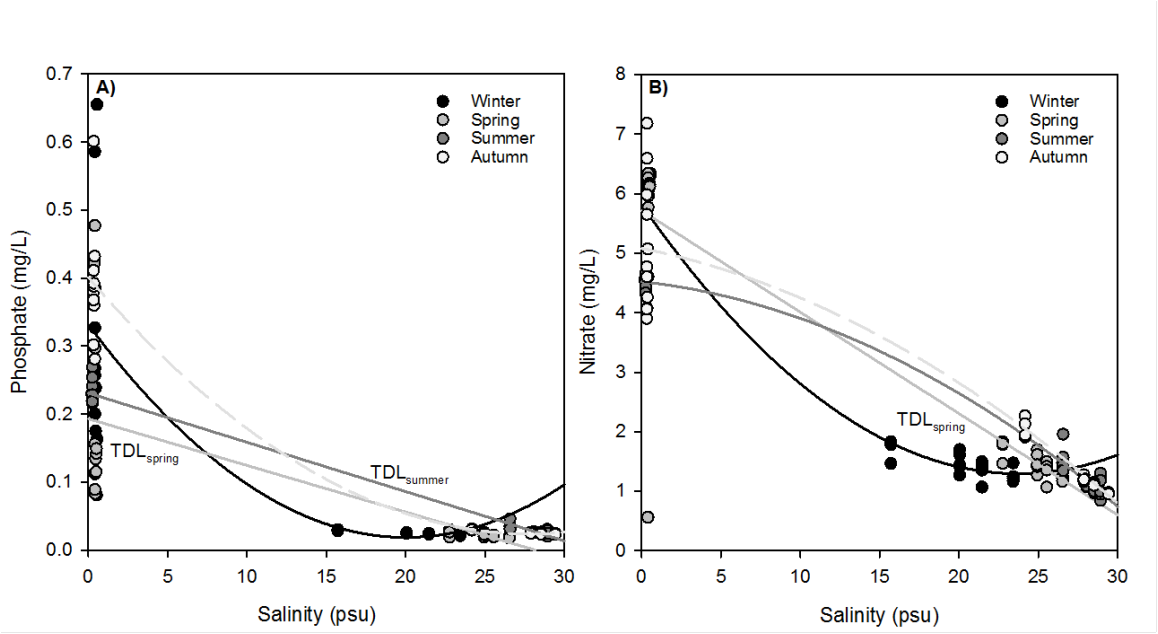

Figure 3.15: Simple conservative mixing plots along the Severn. **A)** Phosphate. **B)** Nitrate.

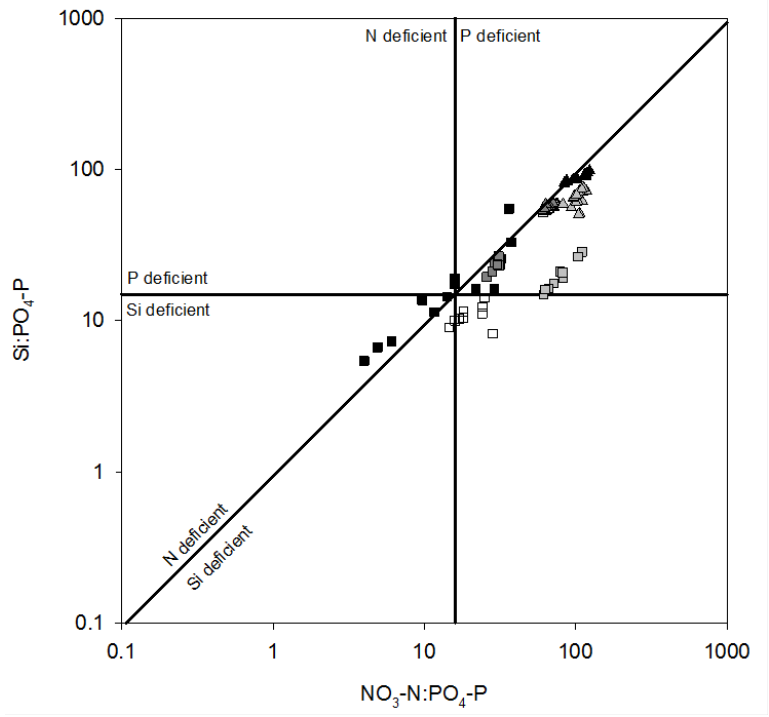

Figure 3.16: Redfield-Brzezinski nutrient ratios in the Severn each sampled period of 2016. River Severn (squares). Severn Estuary (triangles). Sampled period: Winter (black), spring (light grey), summer (dark grey), autumn (white).

3.3.7 Hydro-biogeochemical mediation of silicon in the Severn: a PCA approach

Principal Component Analysis (PCA) for the interconnections between Si and environmental variables in the water column of the Severn was assessed each sampled period. PC1 and PC2 were responsible for the majority of the variance in the winter (71.8%, Fig. 3.17), spring (71.6%, Fig. 3.18), summer (87.2%, Fig. 3.19), and autumn sampled periods (87.7%, Fig. 3.20).

In the spring, summer and autumn, PBSi clustered with SPM, with high loadings, suggesting close association between water column turbidity and PBSi. Similar loadings and clustering of dissolved constituents (PDSi and other macronutrients), suggests they were controlled by a common factor. Each sampled period, salinity and discharge rates displayed similar loadings in PC1 and PC2. The PCA scores were clearly divided between the River Severn and Severn Estuary, except in the winter season, when each separate zone (e.g. upper, mid and lower estuary) clustered individually.

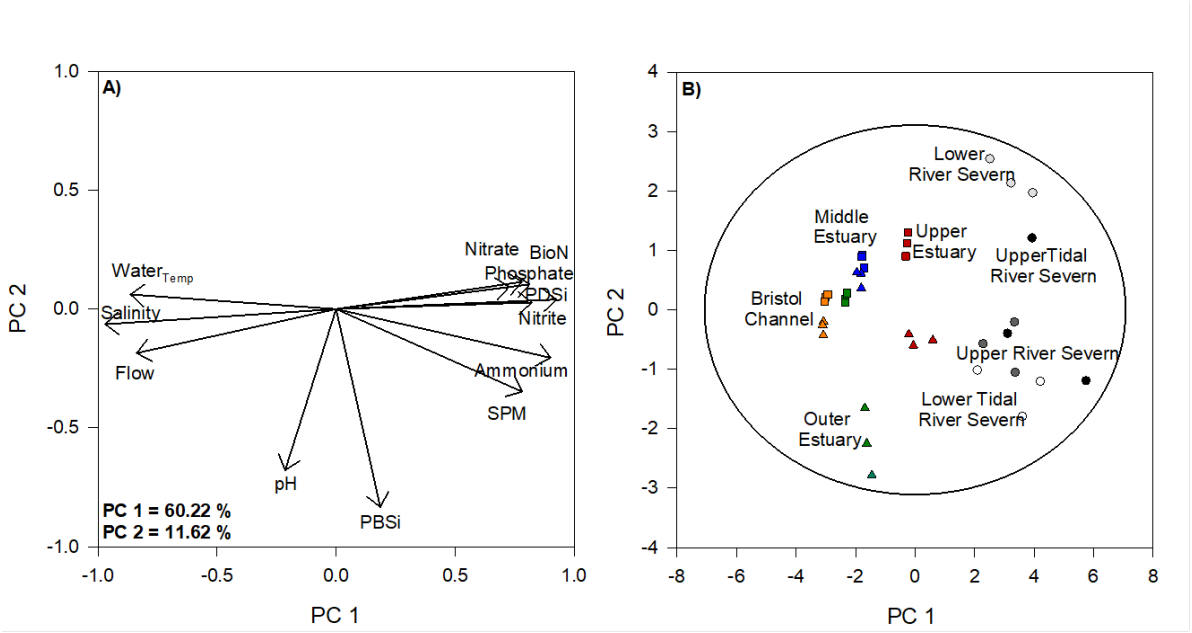

Figure 3.17: Winter sampled period Principal Component Analysis. **A)** PC1 vs PC2 loadings plots. **B)** PC1 vs PC2 score plots with 95% confidence level.

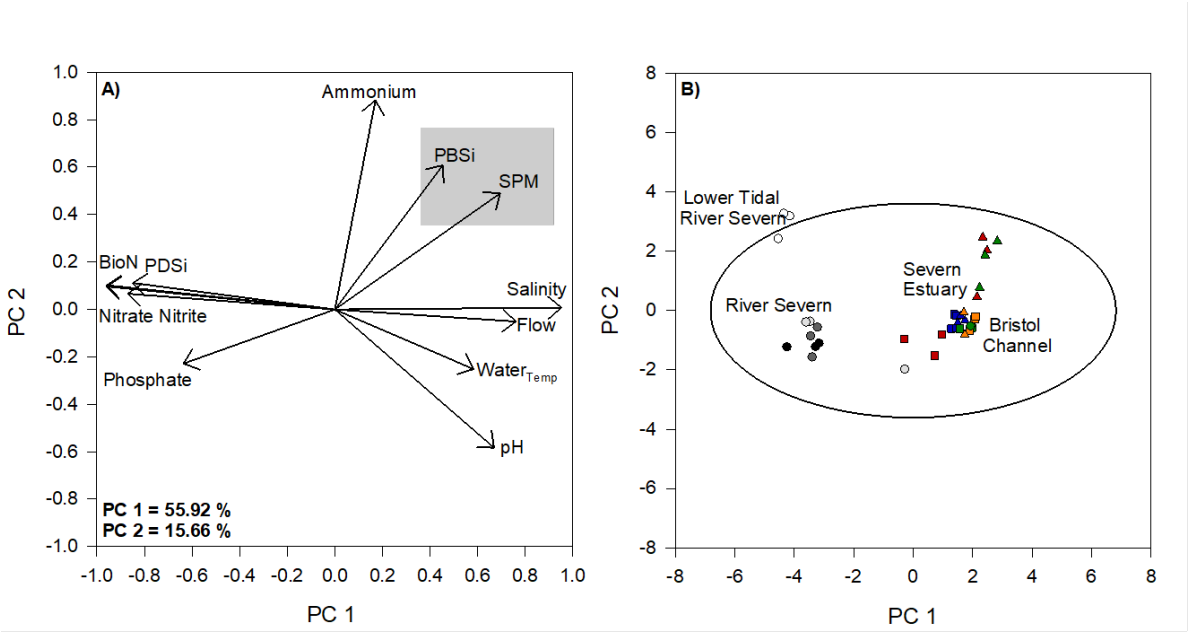

Figure 3.18: Spring sampled period Principal Component Analysis. **A)** PC1 vs PC2 loadings plots. **B)** PC1 vs PC2 score plots with 95% confidence level.

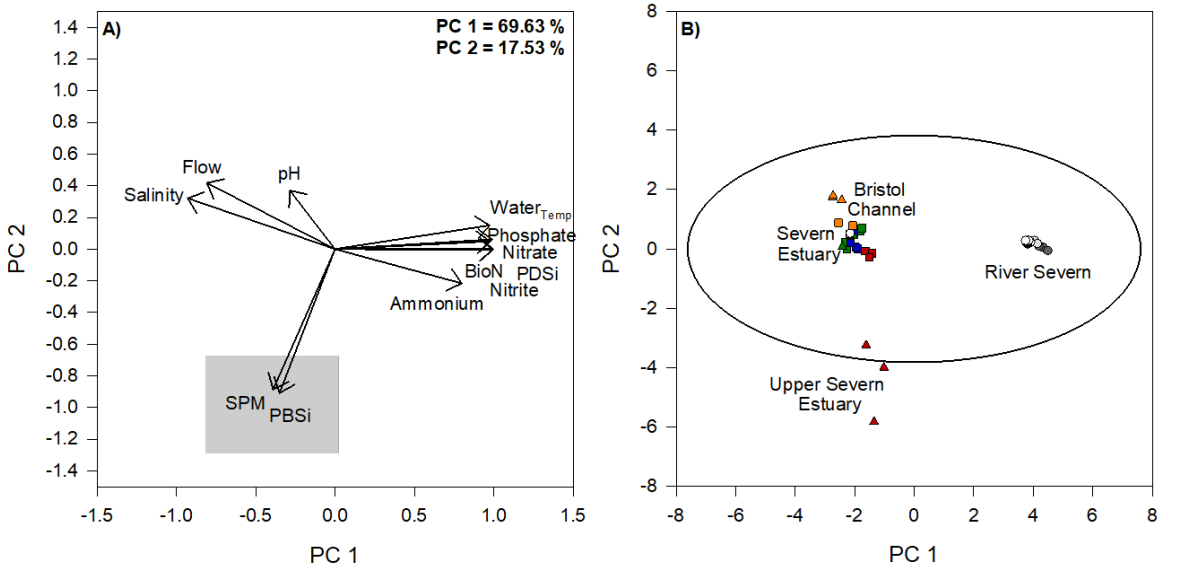

Figure 3.19: Summer sampled period Principal Component Analysis. **A)** PC1 vs PC2 loadings plots. **B)** PC1 vs PC2 score plots with 95% confidence level.

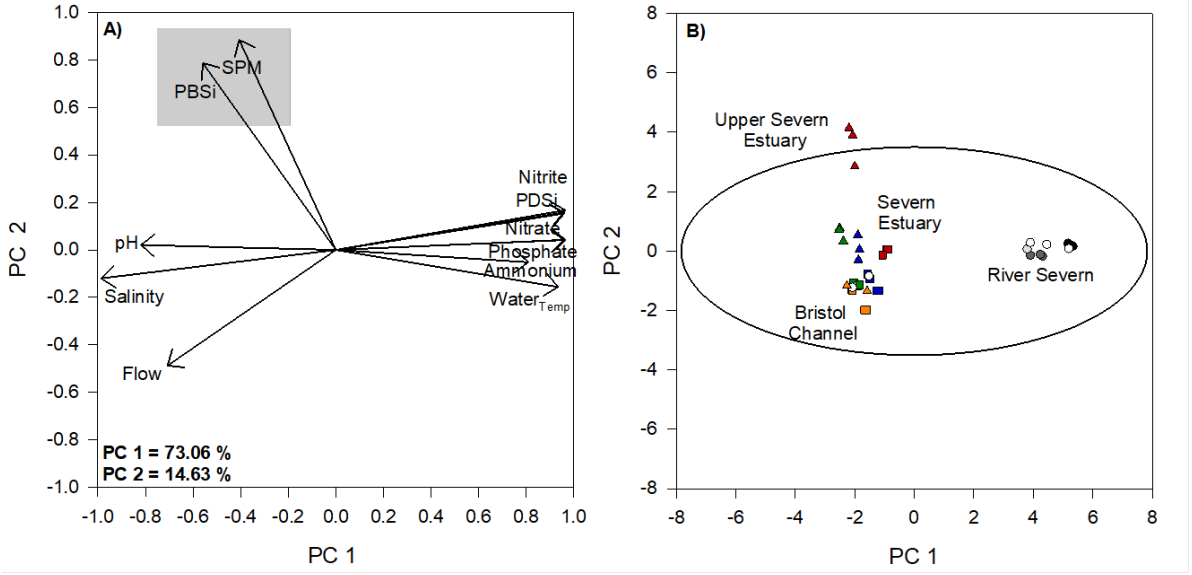

Figure 3.20: Autumn sampled period Principal Component Analysis. **A)** PC1 vs PC2 loadings plots. **B)** PC1 vs PC2 score plots with 95% confidence level.

3.3.8 External source of silicon to the River Severn

3.3.8.1 Groundwater

Groundwater DSi concentrations sampled from boreholes in the south west UK [see Chapter Two Methodology, Fig. 2.1, Agency (2016)] in the catchment area for the Severn Estuary, ranged between 6.71 mg/L and 9.86 mg/L (data only available in May, June and July).

3.3.8.2 Rainwater

Rainwater was collected in the vicinity of the Severn Estuary (at Bristol University), once a month (max. 12 hrs), for 4 months, in 2016. DSi concentrations remained below 0.3 mg/L: January (0.02 mg/L), February (0 mg/L), March (0.2 mg/L) and April (0.3 mg/L).

3.3.8.3 Estuarine tributaries

To ascertain the contribution of tributaries supplying Si to the Severn, three tributaries (River Wye, River Avon and River Usk) and Cardiff Bay (River Taff and Ely) were sampled in the same sampling periods in 2016. These tributaries discharge into the estuary between *ca.* 15 and 45 km from the lower estuarine boundary. Furthermore, to understand the extent of the tidal influence in these tributaries, a sampled transect was carried out from the more saline end-member, within <25 km of the Severn Estuary,

to further upstream, in the freshwater system of each river. To determine how the pelagic ecosystems of these tributaries mediated Si and influenced the export of Si into the estuary, water column biomass (chl *a* and TOC concentrations) were measured, alongside possible environmental factors, which may control the uptake and proportions of available Si. These included the river flow rates, macronutrient limitation, salt and sediment transport, sediment grain size, and water column temperature and pH.

PDSi concentrations in the tributaries (min. 0.2 mg/L, max. 5.7 mg/L) were comparable to PDSi concentrations measured in the River Severn (min. 0.2 mg/L, max. 3.8 mg/L) (Fig. 3.21). Each sampled period, the River Wye PDSi concentrations ranged between 1 and 2.5 mg/L, River Avon between 0.4 and 5.7 mg/L, and the River Usk between 0.2 and 2.1 mg/L (Fig. 3.21). Cardiff Bay waters were within a similar range to these tributaries with PDSi concentrations of 3.5 ± 0.5 mg/L in winter and 2.0 ± 0.3 mg/L in spring (note, no summer and autumn data). PDSi concentrations displayed a significant variation between sampled periods in the tributaries (H=13.66, d.f=3, $p<0.05$). A significant difference was found between the winter and the summer and autumn sampled periods (*post hoc* analysis $p<0.05$), but no difference between the winter and spring sampled periods. Environment Agency monitoring Si data for the Avon at Keynsham in 2016 were in a similar range (between 1.2 to 5.6 mg/L), lending confidence in the tributary data presented in this study.

PBSi concentrations in the tributaries were higher with a wider range (min. 0.0 mg/L, max. 19.4 mg/L, avg. 1.9 ± 0.9 mg/L) compared to PBSi concentrations measured in the River Severn (min. 0.1 mg/L, max. 2.5 mg/L). The River Usk recorded the highest PBSi concentrations of 19.4 mg/L at *ca.* 12 km upstream of the river mouth (Fig. 3.21), with a visible tidal influence (high salinity levels, Fig. 3.21). Cardiff Bay PBSi concentrations were low: winter (0.13 ± 0.1 mg/L) and spring (0.06 ± 0.01 mg/L).

The flux of PDSi and PBSi in the lowest sampled station of the tributaries, within 25 km from the peripheral estuarine mouths, displayed variability between sampled periods, with high Si flux in the winter (max. 449 g DSi/s and 851 g BSi/s) associated with higher river flows (Fig. 3.22), compared to the spring (max. 78 g DSi/s and 77 g BSi/s), summer (max. 106 g DSi/s and 115 g BSi/s), and autumn (max. 32 g DSi/s and 19 g BSi/s) (Table. 3.6). Si flux from Cardiff Bay was not calculated due to the fluctuating outflow from the opening and closing of the locks.

The dissolved form of bioreactive available Si dominated the tributaries in each sampled period in the River Wye and Avon (Table. 3.7). In the River Usk, BSi dominated the proportion of available Si in the winter, associated with a storm that increased river flow rates (Fig. 3.22), and to a lesser extent in the spring and summer sampled periods.

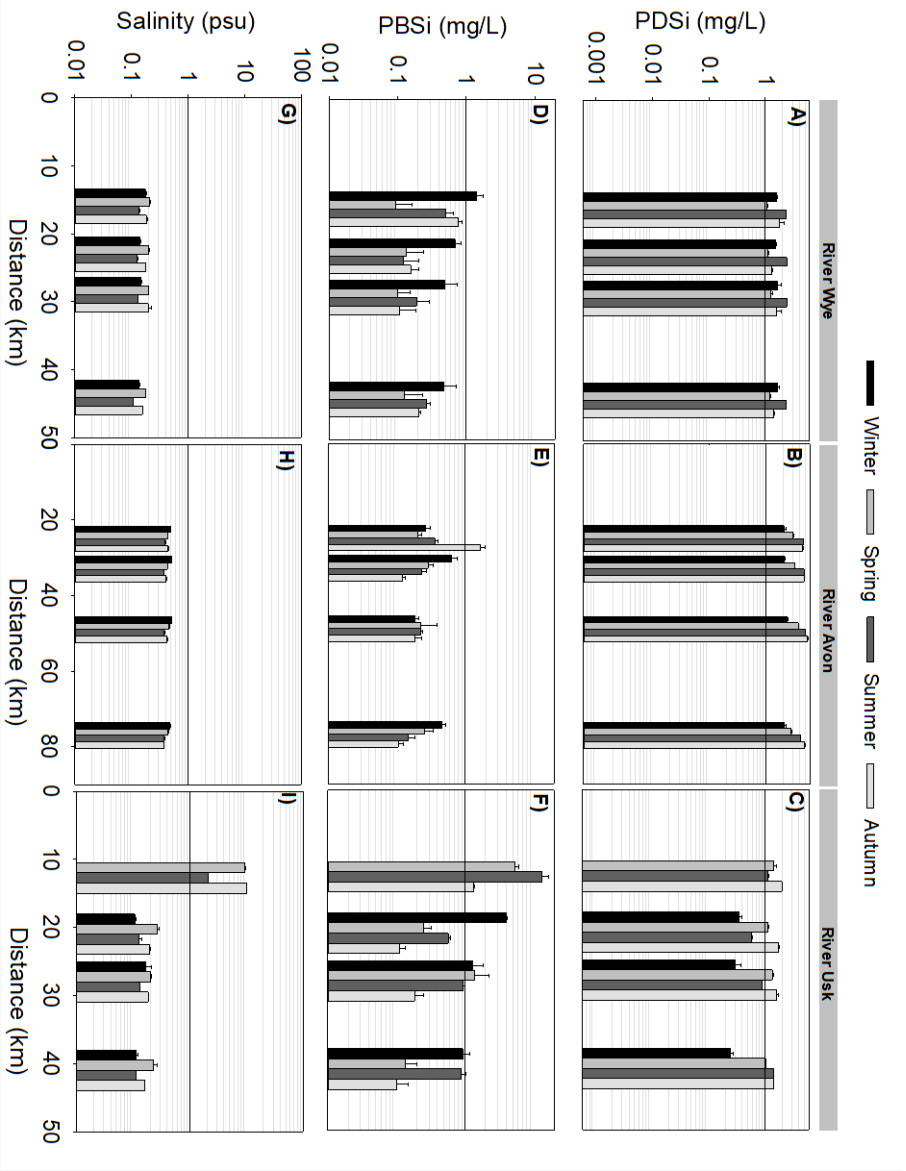

Figure 3.21: PDSi and PBSi concentrations in the Severn Estuary tributaries: River Wye, River Avon and River Usk, each sample period in 2016. **A-C)** Pelagic dissolved silicon (PDSi, mg/L). **D-F)** Pelagic biogenic silica (PBSi, mg/L). PDSi and PBSi plotted on a logarithmic scale. **G-I)** Salinity (psu) plotted on a logarithmic scale. Data presented with 1SE (n=3 at each station). Note, peak salinity at 12 km in River Usk. Note difference in distance on x-axis.

Table 3.6: PDSi and PBSi flux (presented in g/s) from the closest tributary sampling station to the estuary. * storm event. Note unit discrepancy compared to River Severn (kg/s).

Si	Tributary	Winter	Spring	Summer	Autumn
PDSi	Wye	449 ± 76	42 ± 5	106 ± 13	32 ± 7
	Avon	88 ± 13	78 ± 11	23 ± 3	18 ± 1
	Usk	75 ± 23*	16 ± 1	10 ± 4	25 ± 2
PBSi	Wye	401 ± 118	4 ± 3	23 ± 8	14 ± 2
	Avon	11 ± 2	5 ± 1	2 ± 0.3	7 ± 1
	Usk	851 ± 33*	77 ± 10	115 ± 52	19 ± 1

Table 3.7: PDSi and PBSi abundance of total Si (DSi+BSi) in % in the Severn Estuary tributaries: Wye, Avon and Usk.

River	Si	Winter	Spring	Summer	Autumn
Wye	DSi	67%	91%	90%	83%
	BSi	33%	9%	10%	17%
Avon	DSi	85%	93%	95%	90%
	BSi	15%	7%	5%	10%
Usk	DSi	13%	39%	20%	80%
	BSi	87%	61%	80%	20%

River discharge in the tributaries peaked in the winter (January-March) (Fig. 3.22). River flow in the River Wye ranged between 11.9 m^3/s (August) and 432 m^3/s (February). In the Avon, river flow ranged between 4.6 m^3/s (August) and 241 m^3/s (January), and between 2.2 m^3/s (October) and 145 m^3/s (February) in the River Usk (Fig. 3.22). The River Severn catchment size is larger (11,419 km^2) compared to the tributaries: River Wye (4,136 km^2), River Avon (2,800 km^2) and River Usk (1,169 km^2) (Agency, 2016). The larger catchment area results in greater discharge from the Severn compared to the tributaries.

Salinity levels in all three tributaries (note, sampled at low tide), at distances >15 km from the tributaries mouth, were below 0.5 psu, and displayed little variability between sampled periods (Fig. 3.23). Only the River Usk displayed estuarine tidal influences, with salinities reaching highs of 10 psu at *ca.* 12 km upstream. Water temperatures in the tributaries varied between sampled periods, with temperatures as low as 6°C in the winter, and highs of 19°C in the summer. The tributaries lacked spatial variation in water temperatures between sampled stations along each river. Air temperatures followed a similar pattern to water temperatures, with warmer spring and summer sampled periods compared to the autumn (note, no winter data available) (Fig. 3.23). For any given sampled period, the spatial variation in water column pH was negligible, and had a similar range (6-8.5) to the River Severn (Table. 3.8).

Suspended particulate matter (SPM) concentrations (g/L) in the Severn Estuary tributaries fluctuated between sampled periods, with high concentrations during the winter (Fig. 3.24). However, at all sites >15 km from the estuary, SPM concentrations

Table 3.8: River Severn tributaries (Wye, Avon and Usk) pH records each sampled period in 2016.

River	Winter	Spring	Summer	Autumn
Wye	5.48 → 7.43	6.31 → 7.75	6.23 → 7.21	7.04 → 7.97
Avon	7.83 → 8.57	6.15 → 7.40	6.96 → 7.90	6.87 → 7.68
Usk	6.33 → 8.31	6.05 → 8.21	7.11 → 7.63	6.31 → 7.81

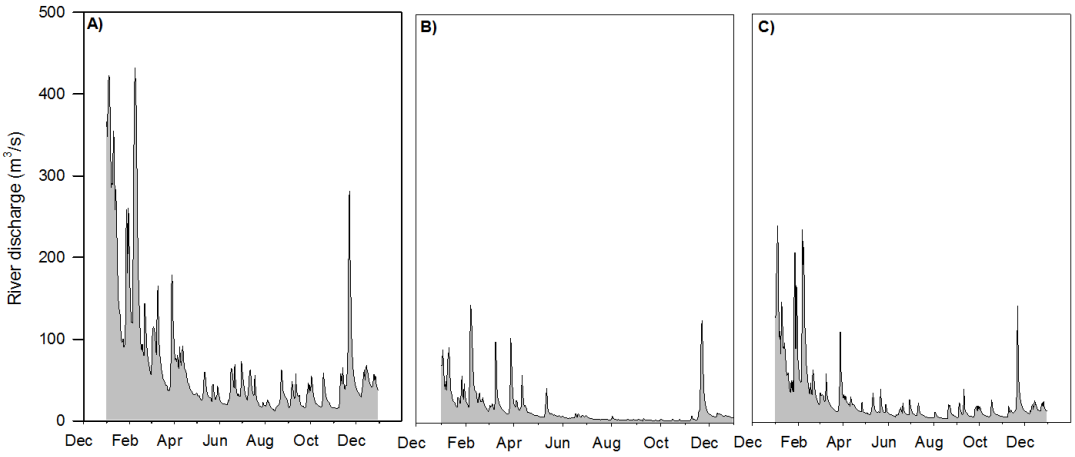

Figure 3.22: River discharge (m^3/s) in the Severn Estuary tributaries. **A)** River Wye. **B)** River Avon. **C)** River Usk. Gauge stations locations: River Wye (*ca.* 30 km from river mouth), River Avon (*ca.* 60 km from river mouth) and River Usk (*ca.* 30 km km from river mouth).

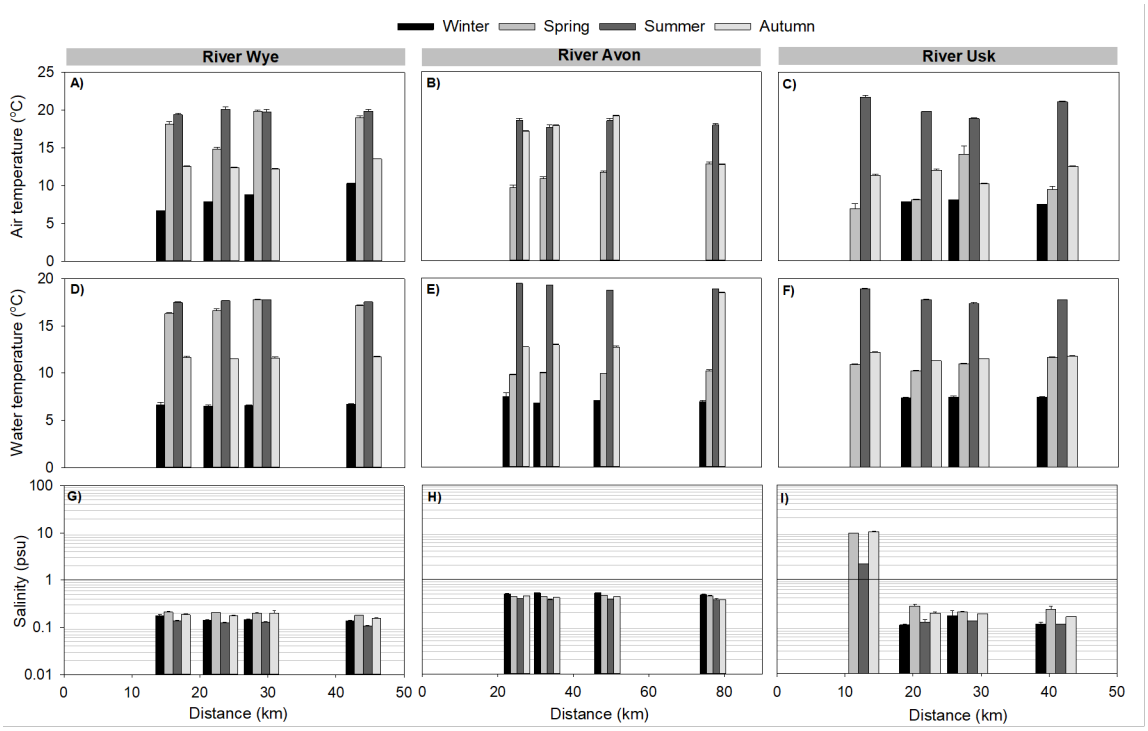

Figure 3.23: Environmental parameters in the Severn Estuary tributaries. **A-C:** Air temperature (°C). **D-F:** Water temperature (°C). **G-I:** Salinity (psu).

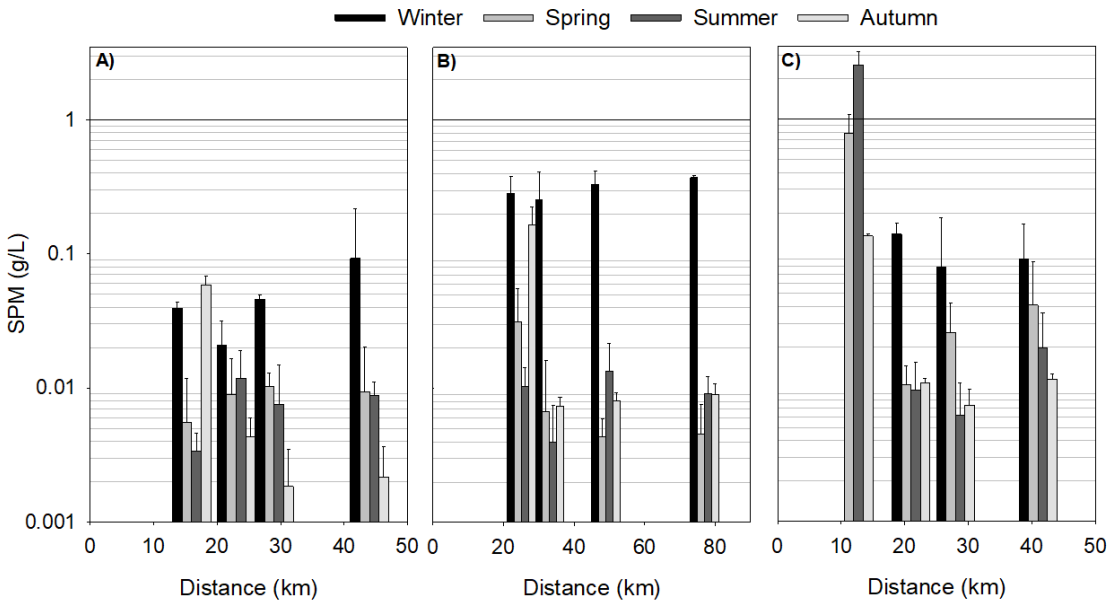

Figure 3.24: Suspended Particulate Matter concentration (g/L) in the Severn Estuary tributaries. **A)** River Wye. **B)** River Avon. **C)** River Usk. Presented with 1 SE (*n=3* at each station).

remained below 0.4 g/L. SPM composition was dominated by fine sands each sampled period in 2016 (Fig. 3.25). At 12 km in the River Usk, SPM peaked at 2.6 g/L during the summer. Cardiff Bay SPM concentrations ranged between 0.05 ± 0.005 g/L (winter) and 0.002 ± 0.0003 g/L (spring). Environment Agency monitoring SPM concentrations displayed similar seasonal variations in the River Avon (note, only data available from the Keynsham station), with relatively higher concentrations in the winter sampling period (0.03 g/L), and lower concentrations during typically dryer seasons: spring (0.013 g/L), summer (0.009 mg/L) and autumn (0.005 mg/L). This lends confidence in the tributary data presented here and in the seasonal trends reported for 2016.

PBSi and SPM had a positive linear correlation in the River Wye and Avon in the autumn (n=12, r^2=0.90, p<0.001, and n=12, r^2=0.70, p<0.05, respectively), and in the River Usk in the spring (n=12, r^2=0.83, p<0.001), summer (n=12, r^2=0.89, p<0.001) and autumn (n=12, r^2=0.96, p<0.001) (Fig. 3.26). No correlation between PBSi and SPM was observed in the tributaries in the winter. However, these correlations were driven by three samples in the lower boundary of these tributaries.

Water column biomass was negligible in each tributary in the sampled periods of 2016 (<0.2 mg/L chl *a*). TOC concentrations in the tributaries peaked during the winter (max. 15 mg/L) compared to the spring (max. 3.7 mg/L), summer (max. 5.3 mg/L) and autumn (max. 3.8 mg/L). TOC concentrations varied significantly between sampled periods (H=53.463, d.f=3, p<0.001), with significantly high TOC concentrations in the winter (*post hoc* analysis p<0.05). No linear correlation was observed between TOC

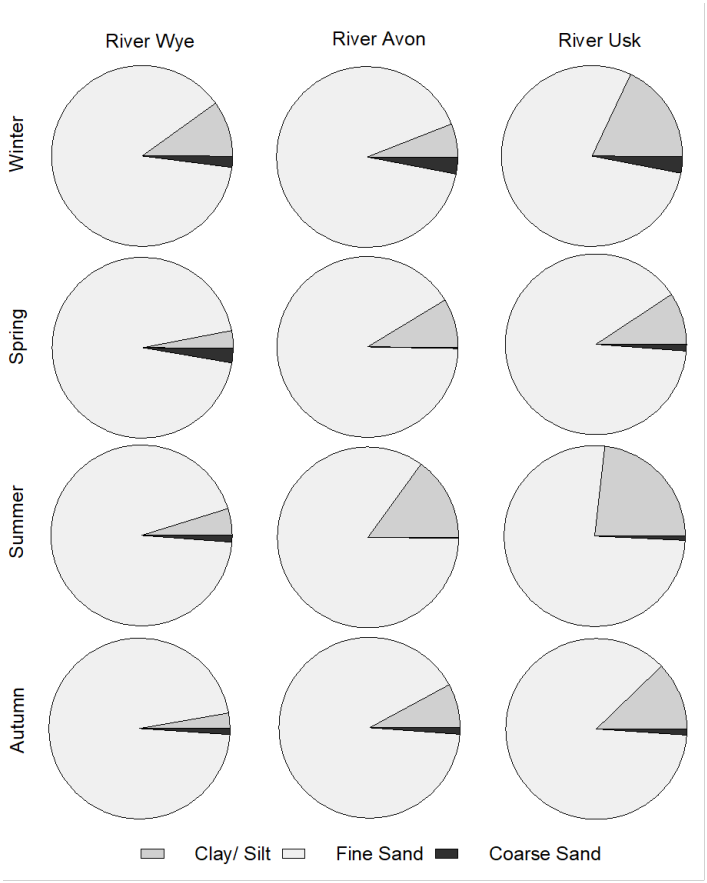

Figure 3.25: Suspended Particulate Matter (SPM) composition in the Severn Estuary tributaries in sampled periods of 2016.

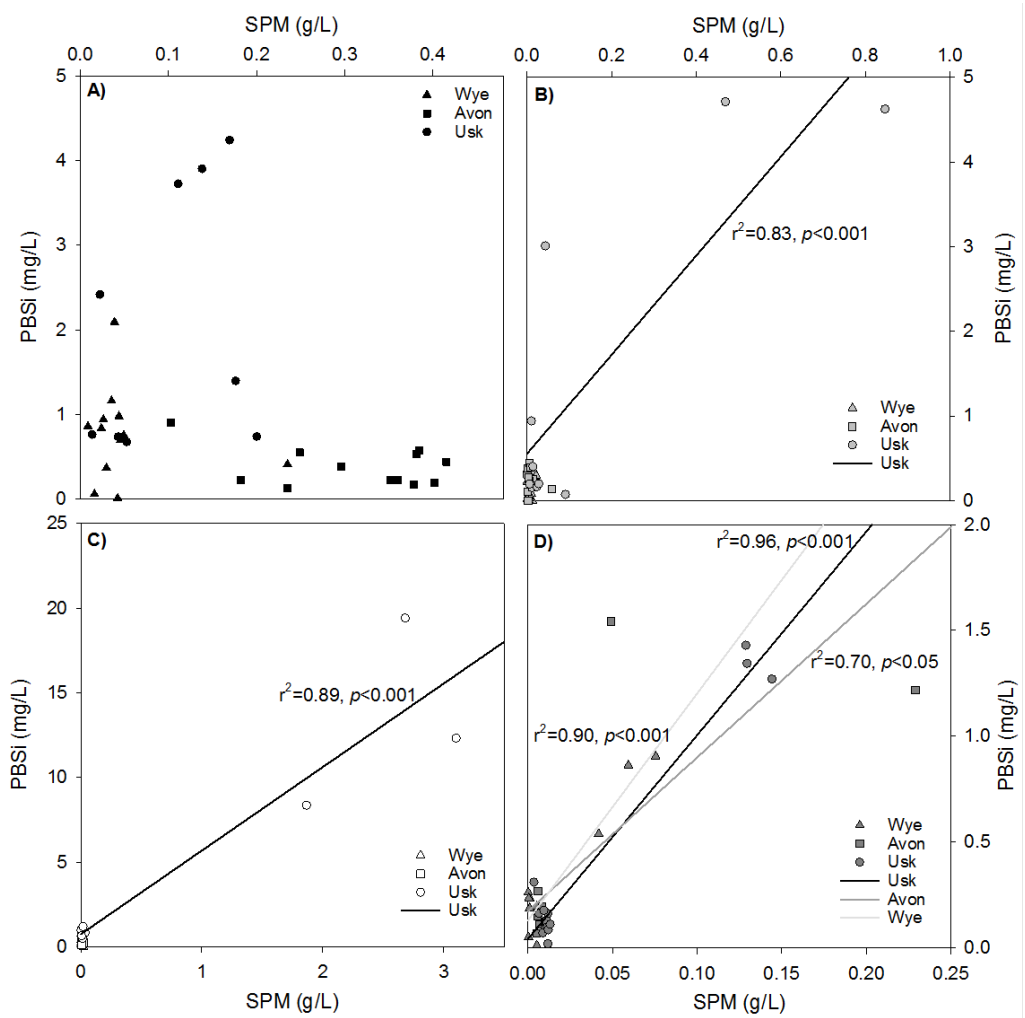

Figure 3.26: Suspended Particulate Matter (SPM) and PBSi relationship in the Severn Estuary tributaries in sampled periods of 2016. **A)** Winter. **B)** Spring. **C)** Summer. **D)** Autumn.

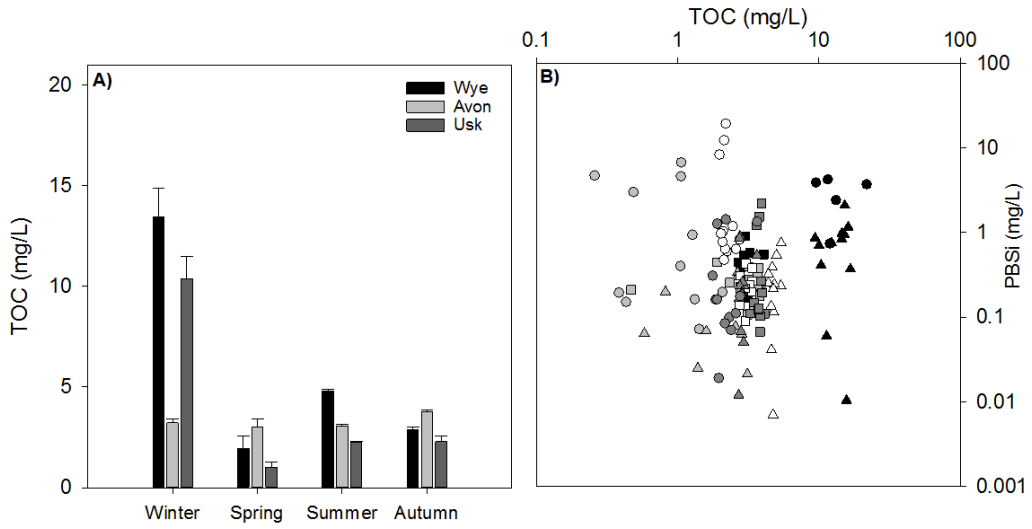

Figure 3.27: A) Total Organic Carbon concentrations (mg/L). Data presented with 1SE (*n=12* per river). **B)** Relationship between TOC and pelagic biogenic silica (PBSi). Data plotted on a logarithmic scale. Triangle: River Wye. Square: River Avon. Circle: River Usk. Winter (black), Spring (light grey), Summer (white), Autumn (dark gray).

and PBSi concentrations (Fig. 3.27).

Nitrate concentrations in the River Avon reached highs of 10 mg/L, compared to the River Wye (<4 mg/L), the River Usk (<2 mg/L) (Fig. 3.28), and Cardiff Bay (<2 mg/L in winter and spring). Environment Agency monitoring nitrate data for the River Avon fluctuated between the seasons, with peak concentrations during the autumn sampling period, in line with the data presented in this study: winter (6.6 mg/L), spring (6.3 mg/L), summer (5.4 mg/L), and autumn (7.2 mg/L). In each season, phosphate concentrations were below the limit of detection (<0.05 mg/L) from the River Avon, Usk and Cardiff Bay (winter and spring), and near the limit from those sampled in the River Wye. Environment Agency monitoring phosphate data for the River Avon was also low (max. 0.4 mg/L, min. 0.03 mg/L) in 2016, lending confidence in the data presented here. All nitrite concentrations were below the limit of detection (<0.15 mg/L) (Fig. 3.28). Environment Agency monitoring nitrite data for the River Avon was also low (< 0.1 mg/L) in 2016. Ammonium concentrations peaked in the urbanised River Avon (max. 0.7 mg/L) (Fig. 3.28). Environment Agency monitoring ammonium data for the River Avon was also in a similar range to the data presented in this study (max. 0.9 mg/L, min. 0.03 mg/L).

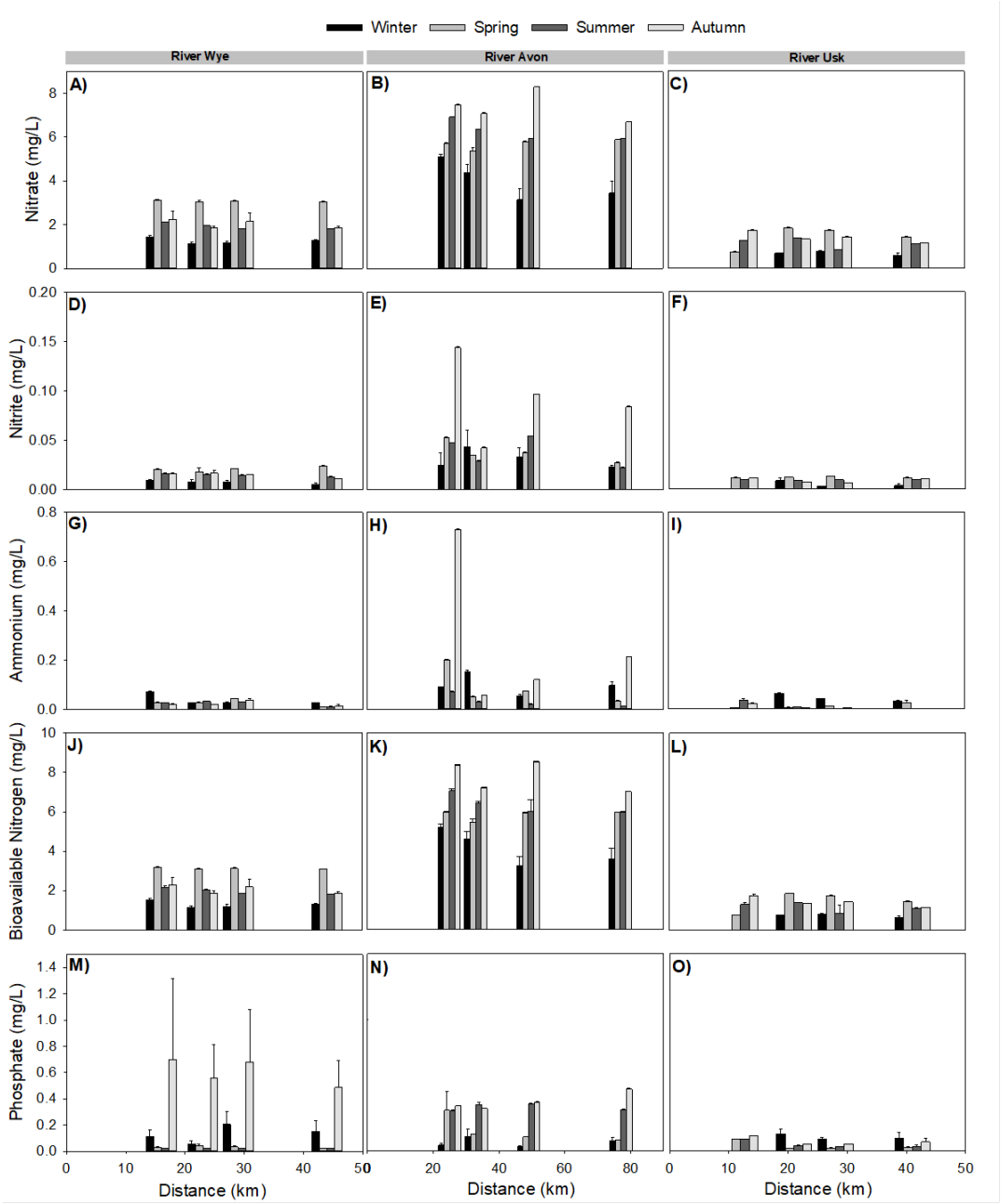

Figure 3.28: Nutrient concentrations in tributary: River Wye, River Avon and River Usk. **A-C)** Nitrate (mg/L). **D-F)** Nitrite (mg/L). **G-I)** Ammonium (mg/L). **J-L)** Bioavailable Nitrogen (nitrate + nitrite + ammonium) (mg/L). **M-O)** Phosphate (mg/L). Data presented with 1 SE (n=3 per station).

3.4 Discussion

River transport is a key source of DSi to the ocean, originating from the temperature dependent weathering of rocks (Derry et al., 2005). Rivers also transport particulate silica (e.g. BSi) in suspension, formed from the production of opal by siliceous organisms (Treguer et al., 1995; Tréguer and De La Rocha, 2013). Large fractions of this riverine DSi can be significantly consumed by estuarine siliceous organisms inhabiting both the pelagic water column and benthic intertidal mudflats, which results in the concomitant increase in estuarine BSi supply to the marine zone (Carbonnel et al., 2009, 2013). Below, the role of the pelagic zone in a hypertidal estuary has in modifying riverine Si inputs to the marine zone is discussed. Estuarine transport and reaction processes that may control the spatial and temporal trends in PDSi and PBSi in the Severn are examined (see Hypothesis One in Chapter One, Section 1.5). Reaction processes include chemical (e.g. dissolution of BSi) and biological reactions (e.g. uptake by photosynthetic diatoms), which depend on environmental conditions (e.g. temperature, light), and hydro-geodynamics (e.g. river discharge rates and sediment transport). Further, the external Si inputs from the estuarine tributaries, groundwater and rainwater are considered.

3.4.1 Hydrodynamic forcings on Si transport

3.4.1.1 Dissolved silicon retention

The hydrodynamics of the Severn Estuary are affected by its geographical location. The northeast-southwest orientation partially protects the estuary from the strong Celtic Sea waves. However, this orientation and geometry channels the westerly winds and funnels the water up the estuary, resulting in high tidal amplitudes at Avonmouth (Neill and Couch, 2011). The low discharge rates in the River Severn compared to the strong tidal current flows in the estuary, associated with the tidal range and the large cross-sectional area (Manning et al., 2010), led to lower Si fluxes in the River Severn and amplified the Si flux in the estuary (Fig. 3.4). Despite the relatively low discharge rates compared to the estuary, no retention of PDSi and PBSi was calculated in the river, with a large flux into the Severn Estuary each season (Table. 3.4). Si retention often exhibits seasonal and spatial variations, for example in the Oder Estuary (Pastuszak et al., 2008), Mississippi (Nelson and Dortch, 1996) and Amazon (Demaster and Pope, 1996). Spatio-temporal variability in Si concentrations can arise as the removal of DSi occurs biologically (Conley and Malone, 1992) or abiotically e.g. reverse weathering, adsorption-desorption on SPM (Chou and Wollast, 2006). Low PDSi retention has also been reported in the temperate tidal Scheldt River (14%, Carbonnel et al., 2013) with an even lower retention (6%) of total Si (DSi+BSi), due to the high export into the Scheldt Estuary. The Scheldt is one of the most studied tidal estuarine systems in the

world, and has a wealth of data and modelling insight, including long-term observations, which provides a perfect foundation for understanding Si transport.

Similar to the River Severn, PDSi was not retained in the Severn Estuary (Table. 3.4). The asymmetrical tidal duration with the ebb flow lasting 2 hrs longer than the flood (Neill and Couch, 2011), combined with the freshwater inputs, whereby a catchment 1/6th the land size of England (Collins and Williams, 1981) induces a flow between boundaries, driving currents out of the estuary, flushed the dissolved constituent out of the estuary into the southwest marine zone. These longitudinal PDSi profiles agree with the classical view of downstream transport and dilution of dissolved constituents, and the association between high estuarine flow rates and less significant Si retentions (Chou et al., 2007). For example, Roubeix (2007) report a low average DSi retention value of 15% for 19 worldwide estuaries. In comparison, the Scheldt Estuary had high DSi retention: 28% (Carbonnel et al., 2013), and 20% (Soetaert et al., 2006), in agreement with the global average estimate of 20% (DeMaster, 1981; Tréguer and De La Rocha, 2013) and 25% for temperate rivers (Treguer et al., 1995). The lack of PDSi retention in the River Severn and Severn Estuary questions the high DSi retention values used in estimates of global Si budgets. Nonetheless, these flux calculations oversimplify the system: assumes a one-directional flow (no lateral component) and does not consider the complex tidal dynamics. Complex mixing processes in the Severn associated with the geometry and hydrodynamics, may be better understood with the application of a numerical model.

3.4.1.2 Effects of dilution on PDSi concentrations

Despite the strong tidal hydrodynamics in the Severn (Manning et al., 2010; Neill and Couch, 2011), temporal fluctuations in Si dynamics were observed between sampled periods (Fig. 3.2). Regardless of the typical dilution effect, relatively high winter PDSi concentrations were measured along the Severn Estuary (Fig. 3.2). These high winter PDSi concentrations were probably associated with high rainfall and discharge rates (Fig. 3.6), transporting larger quantities of PDSi into the system, which shifted the salt intrusion zone downstream (Fig. 3.8). Low salinity levels are not uncommon in the Severn Estuary following high fluvial inputs (Uncles, 1984), but always follow the increasing westward trend to reach peak values of *ca.* 35 psu in the Celtic Sea. High winter PDSi concentrations were also recorded in the Severn Estuary by Morris (1984), and similar concentrations, as well as similar temporal dynamics, have been documented in the Scheldt (Van Der Zee and Chou, 2005; Van Damme et al., 2005; Arndt et al., 2009). High PDSi concentrations are often expected in winter sampled periods, however, for the duration of this study, peak riverine PDSi concentrations were recorded in the summer, despite significantly lower discharge rates (53 m^3/s). In the winter, the rapid, shallow flows over the saturated soils most likely diluted the base-flow

waters enriched in DSi (Chou et al., 2007), and reduced riverine PDSi concentrations compared to those from the summer, consistent with previous studies (e.g. Kennedy, 1971; Schemel and Hager, 1986; Bell, 1994). The relationship between river discharge and PDSi is made complex by the balance between dilution and biological uptake, which prevented a clear relationship in the sampled periods of 2016 (Fig. 3.7). These forcings could also explain the relatively low riverine PDSi concentrations (Table. 3.9) compared to the global riverine average (8.3-13.1 mg/L, Clarke, 1924; Livingstone, 1963; Treguer et al., 1995; Tréguer and De La Rocha, 2013). The PDSi concentrations were however in line with studies from the Mississippi, Danube River in Europe, and the Columbia River, and smaller rivers in the USA. For a summary of global river DSi budgets see Table. 3.9. It is important however, to remember that each system is unique, and no like-for like comparisons can be deduced as a range of factors influence Si dynamics in these transitional environments. This spatio-temporal variability in Si has been shown to be driven by several factors including: a) lithology and continental weathering intensities of silicate-containing minerals, b) variations in land use, for example grassland vs forests (Ronchi, 2014), c) construction of anthropogenic obstructions including locks and dams that perturbate the hydrological cycle [Maavara et al. (2014) and references within], d) riverbed vegetation cover and diatom biological activity, which acts to decrease DSi and accumulate BSi (Conley, 1997), and e) variability in riverine hydro-geology, which influences dilution of dissolved constituents, for example, subsurface flow vs overland flow.

The conservative mixing of PDSi between the freshwater and saline water masses in the winter and spring (Fig. 3.5), was likely a result of dilution by the high discharge rates alongside limited consumption and production rates. As noted before, caution is required when interpreting mixing plots as transient dynamics can also produce these linear correlations (Regnier et al., 1998). Furthermore, macronutrients also displayed a strong interconnectability with PDSi in the PCAs from the winter (Fig. 3.17), spring (Fig. 3.18), summer (Fig. 3.19) and autumn (Fig. 3.20), suggesting complementary factors also controlled the distribution of these dissolved constituents.

3.4.2 Pelagic biological mediation of silicon

3.4.2.1 Low pelagic biomass

Pelagic biological mediation of Si in the Severn and its tributaries was deemed insignificant in the sampled periods of 2016 due to the low phytoplankton biomass levels. The Severn Estuary geometry and tidal dynamics, coupled to the high SPM (Fig. 3.10), likely resulted in light limitation that restricted photosynthesis and phytoplankton development. Further, Maerz et al. (2016) document a close relationship between coastal ecosystem functioning and the transport of SPM. Low pelagic biomass and primary pro-

Table 3.9: River Severn and global river dissolved silicon concentrations. Present study: average DSi concentration of the entire River Severn each sampled period, simplified to the four seasons.

Location	DSi (Mmol/yr)	DSi (mg/L)	DSi (μmol/L)	Study
River Severn (Winter)	610	2.6	89	Present study
River Severn (Spring)	112	1.4	48	Present study
River Severn (Summer)	256	3.4	119	Present study
River Severn (Autumn)	109	2.6	91	Present study
Scheldt River	612			Carbonnel et al. (2013)
Amazon River			138	Conley (1997)
Mississippi River			98	Conley (1997)
Danube River, Europe			55	Conley (1997)
Columbia River			116	Conley (1997)
Congo River, Africa			185	Conley (1997)
Atchafalaya River, USA			113	Conley (1997)
Susquehanna River, USA			52	Conley (1997)
Connecticut River, USA			120	Conley (1997)
Grassland surface flow		avg. 3.5		Thieu et al. (2009)
Arable land surface flow		avg. 3.8		Thieu et al. (2009)
Forests surface flow		3.64		Thieu et al. (2009)
Europe (and Greenland)		5.6		Dürr et al. (2011)
Africa		12.6		Dürr et al. (2011)
N. America		8.0		Dürr et al. (2011)
S. America		9.0		Dürr et al. (2011)
Asia		10.0		Dürr et al. (2011)
Australia		11.8		Dürr et al. (2011)
Average Global River			150	Conley (1997)
Average Global River		8.3		Clarke (1924)
Average Global River		13.1		Livingstone (1963)
Average Global River		10.4		Meybeck (1979)
Average Global River		8.9		Probst (1992)
Average Global River		9.2		Dürr et al. (2011)
Average Global River		9.1		Treguer et al. (1995)
Average Global River		8.8		Meybeck (2003)
Average Global River		9.7		Beusen et al. (2009)

ductivity is common in the turbid Severn Estuary (Joint and Pomroy, 1981; Underwood, 2010), as well as other turbid systems; the tidal Scheldt River and its tributaries (<0.05 chl *a* mg/L, Carbonnel et al., 2009). In the River Severn, the relatively high discharge rates (Fig. 3.6) likely reduced residence times and limited pelagic productivity. Similar limiting conditions were observed for the phytoplankton community in the Rupel basin of the Scheldt (Chou et al., 2007; Arndt et al., 2011) and the Elbe (Geerts et al., 2012). The low pelagic biological activity may have led to reduced riverine PBSi concentrations, and resulted in PDSi dominating the proportion of available Si (Table 3.3).

Compared to the river, higher PBSi concentrations were observed in the marine zone in the Bristol Channel (Fig. 3.3). Coastal BSi inputs were proven significant for the Scheldt (194 Mmol/yr) compared to the riverine input (148 Mmol/yr) (Carbonnel et al., 2013). Coastal Si inputs have also shown to be significant in other estuaries including the Long Island Sound (DeMaster, 1981), Kinsale Estuary (Muylaert and Raine, 1999) and Jiaozhou Bay (Liu et al., 2008). It is unlikely that the peak PBSi in the upper Severn Estuary is exclusively from a coastal origin.

3.4.2.2 Nutrient limitation

Low concentrations of other macronutrients may also have contributed to the low phytoplankton development in the Severn (Fig. 3.14). Redfield-Brzezinski nutrient ratios indicate phosphate limitation in the estuary in the sampled periods of 2016 (Fig. 3.16). Phosphate which is typically limiting in freshwater systems, has increasingly become limiting in saline estuaries due to the direct effect of N-reducing strategies implemented to fight coastal eutrophication (Soetaert et al., 2006). Nonetheless, changes in nutrient ratios would only affect algal growth if more favourable light conditions were reached.

There are several caveats in the Redfield-Brzezinski nutrient ratios used to determine nutrient limitation along the Severn. For example, the elemental composition and cellulous stoichiometry of organic matter can vary widely (Fraga, 2001; Martiny et al., 2013), blurring the link between nutrient supply and demand. Further, the Redfield ratio of C:N:P:Si of 106:16:1:15 varies according to the availability of iron (Fe) (Brzezinski et al., 2003). Several enzymes require Fe for photosynthesis, nitrate assimilation and nitrogen fixation, and thus in low Fe condition, primary production can diminish (Brzezinski et al., 2003). However, in the Severn, Fe is often abundant and unlikely limiting (Morris, 1984). However, compared to marine systems, greater variability around the Redfield ratios have been observed in inland waters, whereby the ratios are often higher in magnitude (Sterner et al., 2008). The Redfield-Brzezinski ratios can also be influenced by species composition, organic matter, temperature, and water residence times (Moreno and Martiny, 2018; Moreno et al., 2018).

As a result of human activity, changes in freshwater and marine ecosystems have been observed (Nixon, 1995), which have resulted in a flux of environmental studies

examining the effects of nutrient supply on ecosystem processes (e.g. Pinckney et al., 2001; Van Der Zee and Chou, 2005; Dodds, 2006). However, compared to the well-studied cycles of nitrogen and phosphorous (Soetaert and Herman, 1995; Conley et al., 1995; Trimmer et al., 1998; Willett et al., 2004; Nixon et al., 2008), the Si cycle remains relatively under-studied. Until recently, Si was not considered at risk of becoming a major limiting nutrient in the coastal zone, however studies in the sub-areas of the Baltic Sea (Sandén et al., 1991; Rahm et al., 1996; Papush, 2011) have shown reduced DSi concentrations. Further estuarine studies have noted non-Redfield ratios (Redfield, 1963), which have resulted in an increase in BSi production and a drawdown of DSi in coastal margins. For example, a decline in diatom abundance due to DSi limitation has been reported in Chinese estuaries (Wang and Kang, 1998; Sun et al., 2002). These studies have raised questions about the possible ecological consequences following Si limitation. This goes beyond the aims of the present study, but the ecological and socio-economic consequences from changes in the nutrient balance in less turbid systems, which have better water quality and light penetration, is an important topic to consider.

3.4.2.3 Bank removal and a supply of terrigenous material

Only during the spring, when PBSi was responsible for 48% of the available riverine Si, pelagic productivity may have increased, potentially signifying a spring bloom, which resulted in the decline in PDSi concentrations (Fig. 3.2) to limiting levels (Fig. 3.16). However, this spring bloom was not recorded in the chlorophyll *a* data. These high PBSi concentrations, which were also observed in the winter, could relate back to the high discharge rates (Fig. 3.6). With low phytoplankton biomass and potentially reduced rates of biosilicification (Thamatrakoln and Hildebrand, 2008), alongside high TOC concentrations (Fig. 3.13), the relatively high riverine PBSi concentrations (Table. 3.2), most likely originated from bank removal, and the transport of plant matter [e.g. phytoliths, microscopic structures formed of Si, see Conley (2002)]. Furthermore, the River Severn and the estuarine tributaries PBSi concentrations were in line with estimated BSi budgets of grasslands (0.35 mg/L), forests (1.01 mg/L) and urbanised areas (2.52 mg/L) (Thieu et al., 2009), a range of habitats observed in the Severn's catchment area. Grasslands and riverbed vegetation cover actively accumulates DSi forming large reservoirs of BSi (Marschner, 1974; Conley, 1997). In addition, high concentrations of SPM (Fig. 3.10), alongside a high suspension of coarse sediment (Fig. 3.11) was measured in the winter, whereby Si content and coarser sediment have been shown to be coupled (Dürr et al., 2011). These PBSi values were in line with other global riverine studies and close to the global river averages published by Conley (1997) (Table. 3.10). For a summary of global river BSi budgets see Table. 3.10.

Mangalaa et al. (2017) report the influence of terrigenous material as a controlling mechanism of Si in the Indian estuaries, with the presence of particulate Si not only

Table 3.10: River Severn and global river biogenic silica concentrations. Present study: average BSi concentration of the entire River Severn each sampled period, simplified to the four seasons.

Location	BSi (Mmol/yr)	BSi (mg/L)	BSi (μmol/L)	Study
River Severn (Winter)	224	0.9	33	Present study
River Severn (Spring)	105	1.3	45	Present study
River Severn (Summer)	20	0.3	9	Present study
River Severn (Autumn)	19	0.5	16	Present study
River Severn (Avergae)	92	0.8	26	Present study
Scheldt River	148			Carbonnel et al. (2013)
Amazon River			74	Conley (1997)
Mississippi River			14	Conley (1997)
Danube River, Europe			18	Conley (1997)
Columbia River			37	Conley (1997)
Congo River, Africa			38	Conley (1997)
Atchafalaya River, USA			25	Conley (1997)
Susquehanna River, USA			23	Conley (1997)
Connecticut River, USA			31	Conley (1997)
Lena River, Russia			8	Conley (1997)
Rhine River, Netherlands			23	Conley (1997)
Average Global River			28	Conley (1997)

originating from diatoms and phytoliths, but also LSi derived from bank erosion. The alkaline extraction time-series plots from the tributaries often (72% of all data) exhibited non-linear - either asymptotic or with outliers - likely due to the low BSi percentage and the limited LSi release during the extraction process, resulting in "noise" above the background levels in the spectrophotometer. Alkaline extraction time-series plots from the estuary on the other hand, showed a simple linear increase in BSi with time ($r^2 > 0.9$), which would suggest all BSi (and potentially ASi, a range of non-crystalline siliceous phases) was released following 1 hr (Fig. 3.29), with the LSi being released in the subsequent hours (DeMaster, 1981). This LSi may have originated from the clay fractions (e.g. illite, kaolinite, usual components of clay in SPM), resuspended from the intertidal mudflats of the estuary, or from the mechanical erosion of sedimentary rocks and bank removal of soils [i.e. silicate minerals and crystals, Dürr et al. (2011)] in the fast-flowing rivers.

3.4.3 Sediment transport

In the Severn Estuary, the hydrodynamics have a major control on the distribution of mobile sediments, up to 70-80% on particles of <1 μm in diameter (Shaw, 1980; Kirby, 2010; Uncles, 2010). Subsequently, the hydrodynamics strongly influence the distribution of the intertidal mudflat. Sediment deposition parallels strong tidal streams with fine cohesive mud fractions settled along the estuarine margins (upper estuary) and sand/gravel and rocky areas (non-cohesive sediment) along the axial region (Kirby and Parker, 1982). The behaviour and distribution of sediment have been explained in detail in complimentary reviews by Kirby (2010) and Manning et al. (2010).

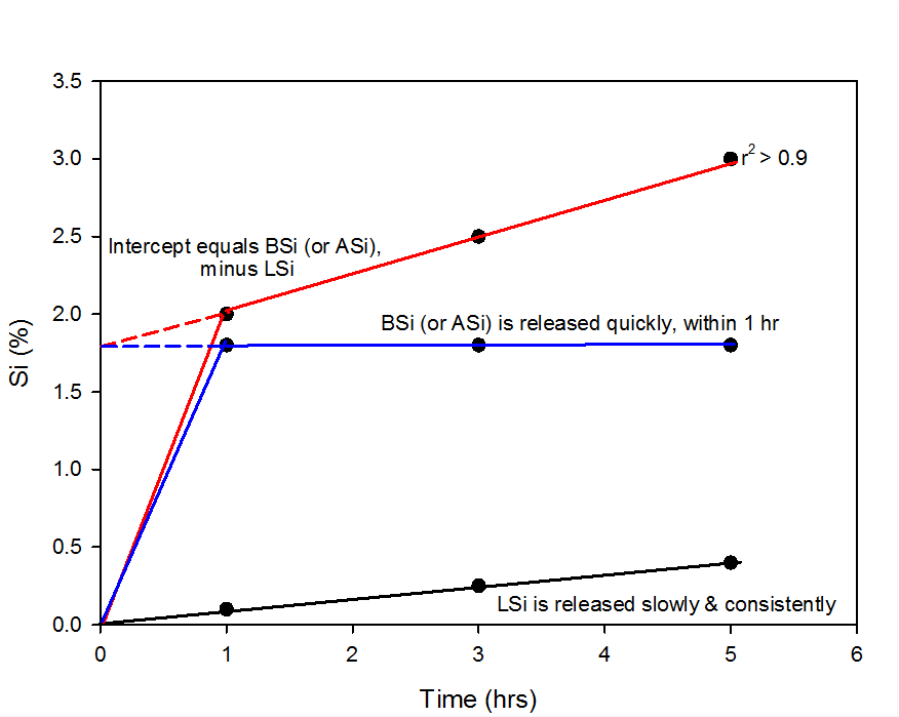

Figure 3.29: Types of silica extraction. Biogenic silica (BSi, in blue) is dissolved quickly (within 1 hr) while Lithogenic silica (LSi, in black) dissolves slowly. BSi + LSi results in a total Si release (red), with the intercept equalling the percentage of BSi (or Amorphous silica, ASi).

SPM concentrations in the Severn Estuary (between 0.03 and 2.1 g/L) were comparable to other temperate estuaries: Humber Estuary (0.27 g/L, Geerts et al., 2012), and Scheldt (0.065 g/L, Chou et al., 2007), but low compared to the maximum SPM concentrations previously measurements in the Estuarine Turbidity Maximum (ETM) zones (0.5-10 g/L). The upper ETM zone, situated near Sharpness (*ca.* 60 km), as previously described by Manning et al. (2010), was likely missed in this 2016 sampling strategy due to accessibility issues between 40 and 80 km. Changes in sediment dynamics in terms of ETM zone over the past 20-30 years cannot be deduced using these observed data.

Low concentrations of SPM (Fig. 3.10) observed on each sampled period in 2016 in the middle of the Severn Estuary (*ca.* 18 km from the lower boundary), may represent the cross-sectional gradient between the English and Welsh coast, where a SPM front runs roughly midway along, and is persistent under both spring/neap tidal regimes and during flood/ebb tides (Kirby and Parker, 1982). During the 2016 study, sampling either side of this front would have altered the longitudinal profile of SPM along the Severn Estuary.

3.4.4 Resuspended benthic biofilms as a source of BSi

3.4.4.1 BSi supply from the intertidal mudflats

Considering the relatively low River Severn PBSi supply (Fig. 3.3), the relatively low tributary PBSi supply (Fig. 3.21), discrepancies between the extraction BSi profiles (Fig. 3.29), the relatively low PBSi concentrations in the marine zone (Table. 3.2), alongside the low pelagic phytoplankton productivity, the relatively high PBSi concentrations in the upper estuary, specifically during the summer and autumn (max. 14.9 mg/L and 10.0 mg/L, respectively), may originate from an alternative source.

PBSi in the upper estuary was unlikely dominated by plant-derived phytoliths, as PBSi concentrations were above the upper estimates for arable land (2.52-5.04 mg/L, Thieu et al., 2009). Due to the strong coupling between SPM and PBSi in these sampled periods (Fig. 3.10), the BSi and sediment may have originated from a relatable source. For example, SPM concentrations, composed of high quantities of mud (a mixture of clay minerals and biological components) in the summer and autumn (Fig. 3.11), displayed a strong positive correlation with PBSi, with 84% of PBSi variability accounted for by SPM in the summer, and 86% in the autumn. In addition, PCA showed clustering of PBSi and SPM during the typically more biologically productive periods (Fig. 3.19 and Fig. 3.20). In the Scheldt Estuary, PBSi was also found to follow SPM dynamics (Chou et al., 2007; Carbonnel et al., 2009). This close coupling between PBSi and SPM is contrary to Admiraal et al. (1990) and Conley (1997), whereby BSi is noted to lack correlation with SPM.

Here, I hypothesise that the estuarine convergence resulted in high tidal current velocities that exceeded the erosion threshold of the intertidal mudflat bed properties. These high flow rates would have led to the resuspension of the cohesive sediment and the associated diatom-dominated biofilms, which have been proposed to exceed the Severn's phytoplankton productivity (Yallop et al., 1994; Underwood, 2010). Subsequently this erosion would lead to the flux of benthic BSi (BBSi) from diatom-dominated biofilm inhabiting the intertidal mudflats into the water column (Welsby et al., 2016). In support, using the Flow Cytometry approach, pennate diatoms were observed in the water column (Fig. 7.19). For an illustrative summary of this hypothesis, see Fig. 3.30.

Uncles (2010) report maximum mean spring tidal (MST) current velocities of 3 m/s in the Severn Estuary, with mean neap tides (MNT) of approximately half the MST velocities. To determine whether the tidal currents were able to erode the biofilms, the bottom shear stress (τ_0 in N/m^2) determined by the quadratic friction law (eq. 3.2) (Arndt et al., 2007) was compared to published critical erosion threshold values of biofilms, $\tau_0$cr: 3.33 to 10.8 N/m^2 at Portishead mudflats, on the south coast of the Severn Estuary (Yallop et al., 2000).

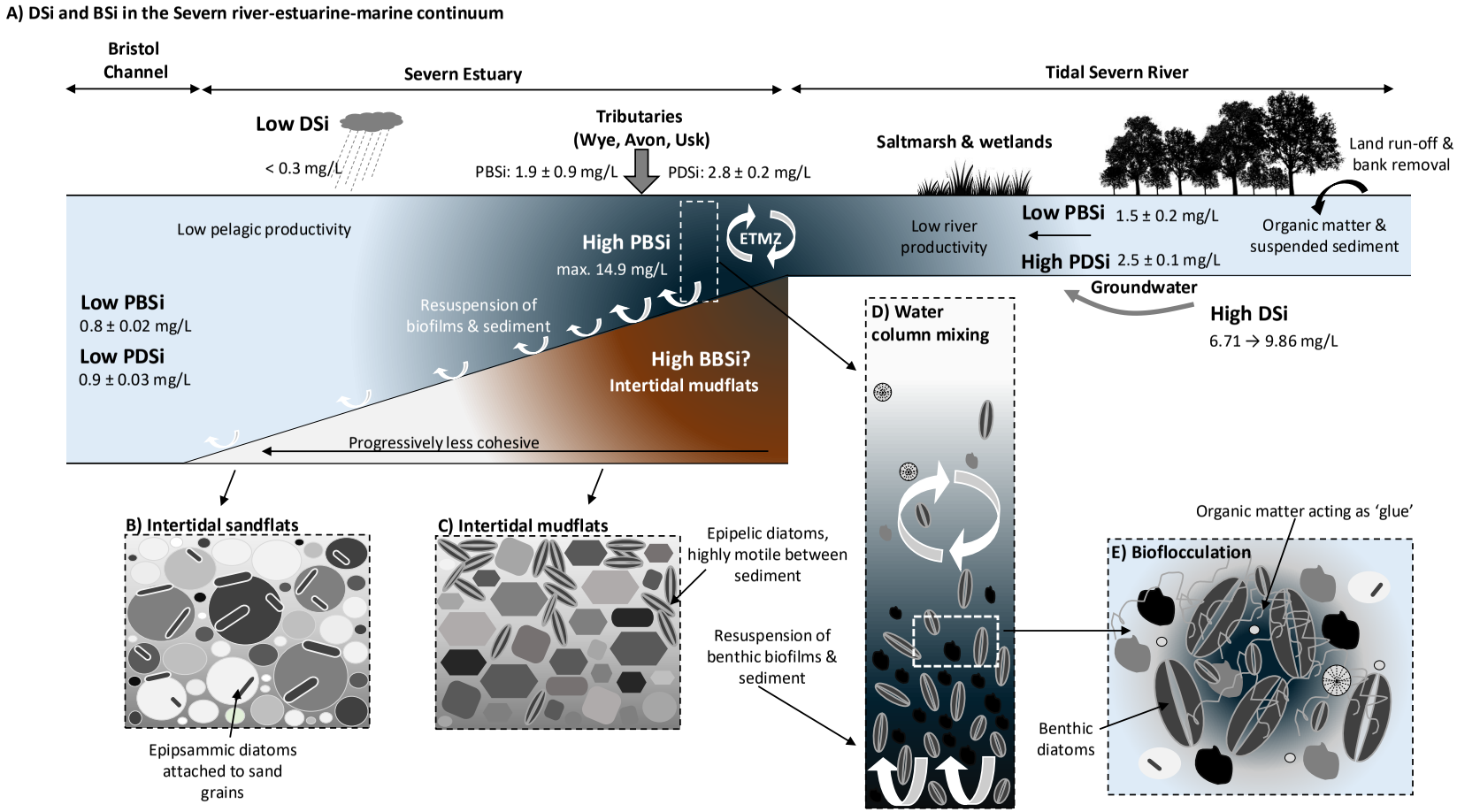

Figure 3.30: Summary of flocculation dynamics and the effect on dissolved silicon (DSi) and particulate (BSi) silica transport in the Severn Estuary. **A)** Flux of PDSi and PBSi from the River Severn and tributaries into the Severn Estuary. **B)** Epipsammic diatoms attached to sand grains. **C)** Epipelic diatoms move freely between sediment grains. **D)** Water column profiles. **E)** Organic matter, sourced from the rivers, land run-off and re-suspended biofilms aid in the bioflocculation of suspended matter. ETM zone: Estuarine Turbidity Maximum zone in the upper estuary.

$$\tau_b = \frac{\rho * g|V|V}{C^2} \tag{3.2}$$

where, ρ is the density of water (1000 kg/m^3), g is the acceleration due to gravity (m/s^2), V is the tidal current velocity in the estuary (m/s), and C is the Chézy coefficient, with typical values of 40 m$^{1/2}$/s for estuaries (Volta et al., 2014).

MST current velocities resulted in a bottoms shear stress of 55.2 N/m^2 >> 3.33−10.8 N/m^2, suggesting the MST currents would have exceeded the erosion threshold of the biofilms. Even the MNT currents, with a bottom shear stress of 13.8 N/m^2 > 3.33−10.8 N/m^2, would have led to some erosion. It was therefore plausible that the erosion of the biofilms led to the transport of SPM and BBSi to the water column. However, the contribution of remobilised BBSi to the pelagic BSi budget remains unknown. Using eq. 3.3, developed from Vollenweider (1968), an estimated flux of benthic DSi and BSi from the Severn's sediment (kg/s) has been calculated using the concentrations of PDSi and PBSi (Fig. 3.31).

$$\frac{d}{dt}(V.Si) = [\frac{d}{dt}(V_i.X_i)] - [\frac{d}{dt}(V_o.X_o)] - Sed(t) \tag{3.3}$$

where, Sed(t) is the time dependent flux per unit area (positive: retention, negative: release), X is either PDSi or PBSi (g/m^3), and V are the input (i) and output (o) water volumes (m^3) between each zone. A zone represents a single sampling location, and it's assumed the location is representative of the whole zone (see Fig. 3.1).

Negative Sed(t) values suggest there was a flux of BDSi (8.51 x10^9 kg/year) and BBSi (1.69 x10^{10} kg/year) out of the Severn's sediment in the sampled periods of 2016 (Fig. 3.31), supporting the hypothesis that the high tidal current velocities eroded the diatom-dominated biofilms on the intertidal mudflats, exporting the benthic Si to the water column. However, these basic calculations have several caveats: i) assumed Si was either released or deposited entirely over the selected area of sediment, ii) neglects any spatial distribution associated with local conditions, iii) assumed all the Si flowing downstream from one zone to another was transported, neglecting tidal dynamics.

3.4.4.2 Bioflocculation

Coupled to the resuspended diatoms is likely a polymer-rich biofilm consisting of macroaggregates of organic material, bacteria, and other microorganisms bound together with, for example, an extracellular polymeric substances (EPS), such as colloidal carbohydrates, an organic bio-stabiliser produced by mud-dwelling organisms (Underwood et al., 1995; Yallop et al., 2000; Tolhurst et al., 2002; Underwood and Paterson, 2003). Here, I further hypothesise the high tidal flow velocities exceed the erosion threshold of these biofilms, despite this biostabilisation. In the turbulent, saline water column of the estuary the dead biofilms rich in organic matter and the SPM may consolidate to form

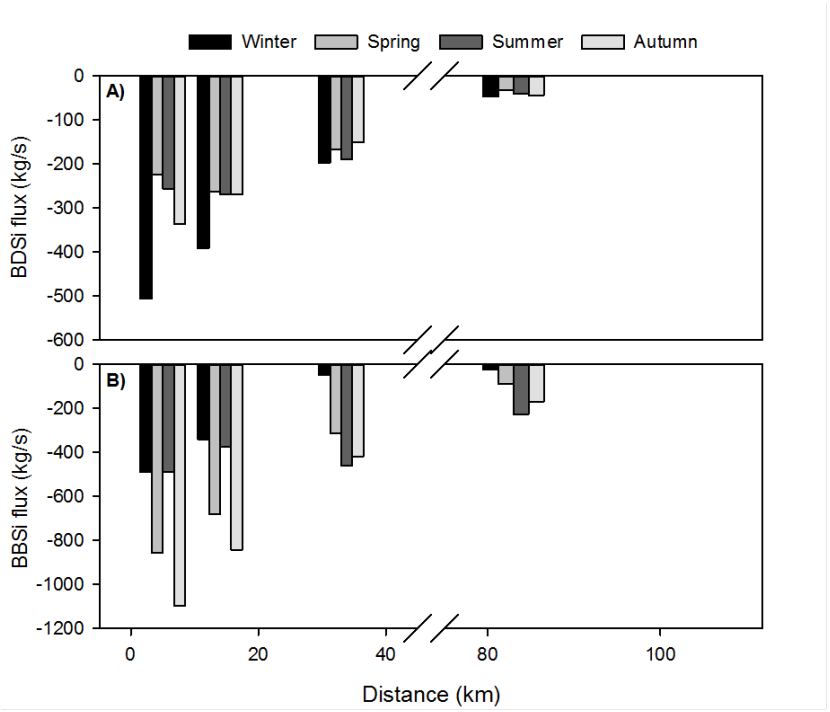

Figure 3.31: Si flux from the River Severn and estuarine sediment. **A)** Benthic dissolved silicon flux (BDSi, kg/s). **B)** Benthic biogenic silica flux (BBSi, kg/s).

one entity, known as 'bioflocculation', a mixture of organic and inorganic (clay/silt, fine sands, gravel) constituents (Perkins et al., 2004a; Manning et al., 2013; Manning and Schoellhamer, 2013). There is growing evidence that algae excretions mediate aggregation, although this would depend on an optimal ratio between the dense SPM and the binding strength ('stickiness') of the algae particles (Fettweis et al., 2014).

Bioflocculation may have been prevalent in the upper estuary, where the mixing zone between the fresh and saline end-members is dominant. Such intense mixing could have resulted in more oxygenated waters shown by the peak in dissolved oxygen levels at this zone (note, only sampled in autumn). The addition of SPM and organic matter (high TOC, Fig. 3.13) from the River Severn and tributaries (Fig. 3.27) could also have aided bioflocculation by contributing towards particle cohesion and raising collision efficiency (Manning and Schoellhamer, 2013). These bioflocs may explain the strong positive relationship observed between SPM and PBSi in the summer and autumn (Fig. 3.10), and the clustering of SPM and PBSi in the PCAs (Fig. 3.19 and Fig. 3.20), as BSi and sediment originate from the intertidal mudflats, and remain as one entity in the water column. The resuspension of carbohydrate-rich suspended matter and the formation of flocs have also been documented in the Ems and Rhine Estuaries [Eisma (1986) and references within]. For a review of factors, including organic matter in aiding flocculation in estuaries, see Eisma (1986) and more recently Manning and Schoellhamer (2013).

3.4.4.3 Vertical distribution of pelagic BSi and SPM

The Severn Estuary water column is well-mixed due to the strong tidal dynamics (Manning et al., 2010), preventing, in any given season, depth variability in water temperature and pH. However, high concentrations of both SPM and PBSi were observed in the bottom waters in the upper estuary, *ca.* 33 km upstream from the lower estuarine boundary (Fig. 3.10). Due to the high degree of resuspension in the estuary, this leads to the formation of lutoclines - distinct vertical zones of variable turbidity (Manning et al., 2010). The mixing and binding of SPM and benthic biofilms potentially increased the floc size (Perkins et al., 2004b,a), which further imbedded minerals during bioflocculation, leading to enhanced sinking velocities (Maerz et al., 2016). This sinking of material would have increased SPM and PBSi concentrations with depth. For example, the fall velocity for suspended particles in the range of >1 to 100 μm, is *ca.* 4000x larger compared to particles of 1 μm (Eisma, 1986). The bioflocculation and settling of sediment and BSi may explain the retention of PBSi in the Severn Estuary each sampled period (Table. 3.4). High retention in the cold winter (50%) and autumn (24%) sampled periods may relate to the accumulation of dead BSi from the previous biologically productive periods. These estimates were in line with retention values from Chesapeake Bay (65%, D'Elia et al., 1983) and the Bay of Brest (48%, Ragueneau et al., 2005).

The effect of slack water could provide an alternative explanation for more concentrated bottom waters. Sampling in the upper estuary occurred towards the end of the flood tide to maximise the distance upstream by the research vessel. During slack water, reduced turbulence may have allowed stationary suspensions to gradually settle as bottom shear stress is reduced. This stationary suspension may have been a combination of the dilute suspensions (typically <1 g/L SPM), which were mixed during the flood tide, and the collapse of the Concentrated Benthic Suspensions (CBS) layer (between 1−10 g/L SPM) (Manning et al., 2010). Alternatively, the depth fluctuation in SPM and PBSi may also represent the salt intrusion wedge (Fig. 3.8), whereby estuarine BSi-rich waters intruded further upstream (but to a lesser extent in the spring, Fig. 3.8), whilst the less dense, BSi-depleted river water flowed downstream at the surface.

3.4.4.4 Benthic biofilm effect in the tributaries

Major sediment sinks occur in the peripheral estuaries, for example, the Avon, Wye and the Usk. The highest PBSi measurement in the entire Severn river-estuary-marine continuum and its tributaries in the sampled periods of 2016 was 19.4 mg/L in the River Usk, 12 km upstream from the peripheral estuarine mouth. The tidal influence from the Severn Estuary was apparent with higher salinity levels at this station (Fig. 3.21). A high percentage of the PBSi could be explained by SPM in the summer (89%) and autumn (96%) (Fig. 3.26), with a greater proportion of mud compared to coarser

material (Fig. 3.25). The composition of the water in this peripheral Usk estuary suggests the influx of estuarine waters, including the pelagic and benthic resuspended BSi coupled to the SPM, increasing the PBSi concentrations in this mixing zone. This influx of estuarine water may also occur in the mouths of the River Avon and Wye, areas which were not accessible at low tide during this study. Alternatively, the benthic biofilms on the muddy banks in the mouths of these tributaries, may have controlled both PBSi and SPM dynamics, similar to the intertidal mudflat biofilms in the Severn Estuary. In agreement, Kirby and Parker (1982) suggested all lower sections of the tributaries into the Severn would be principally muddy.

3.4.5 Alternative sources/sinks of Si

3.4.5.1 Tributaries, groundwater and rainwater Si supply

The true River Severn, the stretch of river past the salt intrusion zone, has been suggested to contribute between 25 and 60% of the freshwater supply into the Severn Estuary (Morris, 1984; Uncles, 1984). Therefore, the tributaries may have influenced Si transport into the Severn Estuary. PDSi concentrations and flux in all three studied tributaries (River Wye, Avon and Usk) and Cardiff Bay (Fig. 3.21), were within a similar range to the River Severn (Fig. 3.2 and Fig. 3.4), and could have acted as a source of DSi and macronutrients (Fig. 3.28) in the upper estuary, resulting in the non-conservative behaviour of these dissolved constituents (Fig. 3.5 and Fig. 3.15). Similarly, tributaries of the Scheldt supplied high concentrations of DSi into the Scheldt Estuary (Carbonnel et al., 2013). In addition, PBSi concentrations in the River Severn and tributaries were similar, and with the peak PBSi of 19.4 mg/L in the River Usk most likely attributed to estuarine BSi influx (see above), the estuarine tributaries were likely a less significant source of BSi compared to the intertidal mudflats.

Chemical weathering of silicate material in sediment and rocks releases DSi, along with other solutes, which are then acquired by groundwater. There is growing evidence suggesting groundwater pathways transport nutrients through permeable sediments and aquifers to the land-ocean boundary (Georg et al., 2009; Statham, 2012; Pradeep et al., 2016), and has been attributed to enriching nutrient levels in coastal environments (Rutkowski et al., 1999), and influencing benthic ecosystems (Jahnke et al., 2003). For example, Sospedra et al. (2018), concluded groundwater DSi supply accounted for 59% of the Gulf of Valencia coastal DSi budget. Groundwater DSi concentrations in the vicinity of the Severn were between 6 and 10 mg/L in the sampled periods of 2016, and could easily have contributed as a source of DSi to the Severn's system, although to which extent remains unknown. DSi in groundwater is related to the bedrock geology: DSi concentrations were high in groundwater from Old Red Sandstone, predominately formed of quartz, compared to Carboniferous Limestone. Rainwater, on the other hand,

which measured <0.3 mg/L of DSi, most likely only influenced PDSi transport indirectly through surface land run-off and high discharge rates.

3.4.5.2 Abiological processes

Adsorption of DSi onto aluminium oxide surfaces on clay minerals, such as those suspended and deposited on the intertidal mudflats, may have influenced DSi transport in the Severn. This adsorption, and removal of DSi, would have had greater influence during the summer and autumn when the mineral phase was predominantly silts and clays (Fig. 3.11). For example, Weiss et al. (2015) report high adsorption of DSi onto clays consisting of illite, kaolinite and chlorite. A high SPM adsorption capacity would be needed to reduce PDSi concentrations, for example, in SPM concentrations of *ca.* 1 g/L, as observed in the Gironde Estuary (Abril et al., 1999). Therefore, in the Severn, when SPM concentrations exceeded 1 g/L (Fig. 3.10), and illite dominated the clay fraction (Morris, 1984), adsorption onto clays may have contributed, in concert with hydrodynamics, to the decline in PDSi along the estuary.

The formation of secondary authigenic aluminosilicate minerals (known as reverse weathering) may also impact estuarine particulate silica concentrations (Mackenzie and Garrels, 1966a,b). These weathering processes have been documented in deltaic depocenters (Mackenzie and Garrels, 1966a,b; Wollast and De Broeu, 1971; Michalopoulos and Aller, 1995), such as the Amazon (Michalopoulos et al., 2000). Further, Presti and Michalopoulos (2008), suggest reverse weathering in non-tropical deltaic systems as a silica sink could be more important than previously thought; 20-25% of all riverine input of silicon to the ocean according to Holland (2005). However, the hypertidal Severn is incomparable in many ways to these deltaic systems, and the rapid, frequent resuspension rates (Manning et al., 2010), likely prevent rapid diagenesis. However, reverse weathering is a process that is not currently fully understood, and without further research the effect of this reaction on BSi transport in estuaries such as the Severn remains unresolved.

Both fresh and saline natural waters are often unsaturated with respect to DSi, with the direction of equilibrium favouring the dissolution of Si. The BSi structure of diatom tests may dissolve following deposition under specific conditions, such as relatively high pH and temperature, and the removal of the external organic protective layer by bacterial degradation (Cooper, 1953; Iler, 1955). In the estuary, pH had little to no spatial fluctuation during the winter, summer and autumn sampled periods (Fig. 3.9), suggesting with no significant increase, pH had little influence on BSi dissolution during these periods. However, in the spring, pH increased from 6.7 to 7.7. Loucaide et al. (2008) compared dissolution rates of different forms of BSi and found that the rates doubled as pH was increased from 6.3 to 8.1. BSi dissolution rates may have increased during the spring, resulting in the adverse low upper estuarine PBSi concentrations (Fig.

3.3). Further, in contrast to the other seasons, water column temperature peaked in the upper estuary in the spring, potentially affecting the dissolution kinetics and solubility of BSi (see Appendix, Section 3.6.1, Fig. 3.32). High dissolution rates in the saline, alkaline marine zone, could also explain the low PBSi concentrations in the Bristol Channel compared to the Severn Estuary, although a reduced input of BBSi would be more pertinent.

3.5 Conclusions

The transport of PDSi and PBSi in the water column of the Severn, from the freshwater zone to the saline limit of the Severn Estuary was investigated for different periods in 2016. For the first time, a time-series dataset of PDSi and PBSi concentrations in the Severn has been produced, which has improved our knowledge of the pelagic Si cycle in hypertidal estuaries. These findings highlight the importance of documenting the way in which an estuary modifies Si along its path to the ocean, prior to incorporating the riverine Si flux into global Si budgets such as the ones presented by Treguer et al. (1995), Ragueneau et al. (2000), and Tréguer and De La Rocha (2013).

The biological mediation of Si in the water column of the River Severn, Severn Estuary, and its tributaries was low regardless of variability between sampled periods, agreeing with the hypothesis stated in Chapter One (see Section 1.5). Strong fluvial and tidal hydrodynamics drove dissolved components (PDSi and macronutrients) and prevented any retention of PDSi in the tidal system. Further, a combination of high turbidity, potential nutrient limitation, and reduced residence times prevented phytoplankton growth. Sediment dynamics were strongly coupled to BSi in the summer and autumn periods. With relatively low PBSi export from the River Severn, and relatively low marine PBSi concentrations in the Bristol Channel, I hypothesised that the resuspended intertidal benthic diatom-dominated biofilms (Underwood, 2010), which have been proposed to have fast turn-over rates of BSi (Welsby et al., 2016), increased the accumulation of BSi in the water column during biologically productive periods. Through bioflocculation, this enhanced the retention of PBSi in the estuary.

In the following chapter, the benthic DSi and BSi budgets on the intertidal mudflats, along with the biological and abiological processes influencing these Si budgets, are examined. In addition, the complex mixing of PDSi and PBSi along the length of the Severn, will be further explored in this thesis using Si isotopes (Chapter Six), and a more in-depth computational model (Chapter Severn) that encompasses the Severn's geometry, hydrodynamics (river discharge, tide cycle), salt and sediment transport, and both the pelagic and benthic Si systems.

3.6 Appendix

3.6.1 Water column temperatures

Water column temperatures lacked stratification in the Severn Estuary and Bristol Channel (Fig. 3.32).

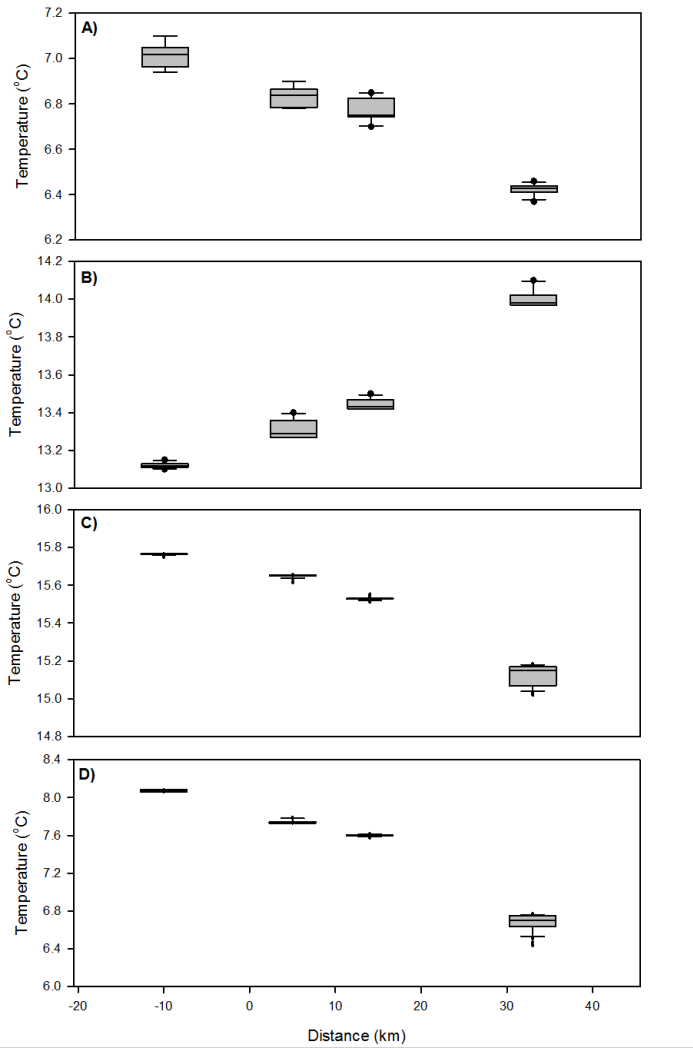

Figure 3.32: Water column temperature (°C) variability at each sampled station along the Severn Estuary. **A)** Winter. **B)** Spring. **C)** Summer. **D)** Autumn.

3.6.2 Biological mediation of silicon: Flow Cytometry analysis

Flow Cytometry, a laser-based, biophysical technology was employed to count the abundance of suspended particles in the water column along with their size and shape, to determine the ratio of pennate to centric diatoms in the Severn Estuary. In theory, this Flow Cytometry approach should have been ideal for samples with a low concentration, however due to the high turbidity, the samples aggregated, preventing clear definition of the particles (Fig. 3.33). Because of this complication, only summer samples were analysed. There is a requirement to test different methods to reduce the coagulation of particles, including the use of a variety of surfactants to disperse the particles for longer periods. However, despite this obstacle, the number of particles sampled in each run, proved valuable in terms of the distribution and abundance of SPM along the Severn. For example, corresponding to the high turbidity (Fig. 3.10) in the upper estuarine bottom waters during the summer, a high abundance of particulates were measured using the Flow Cytometry technique (Fig. 3.33).

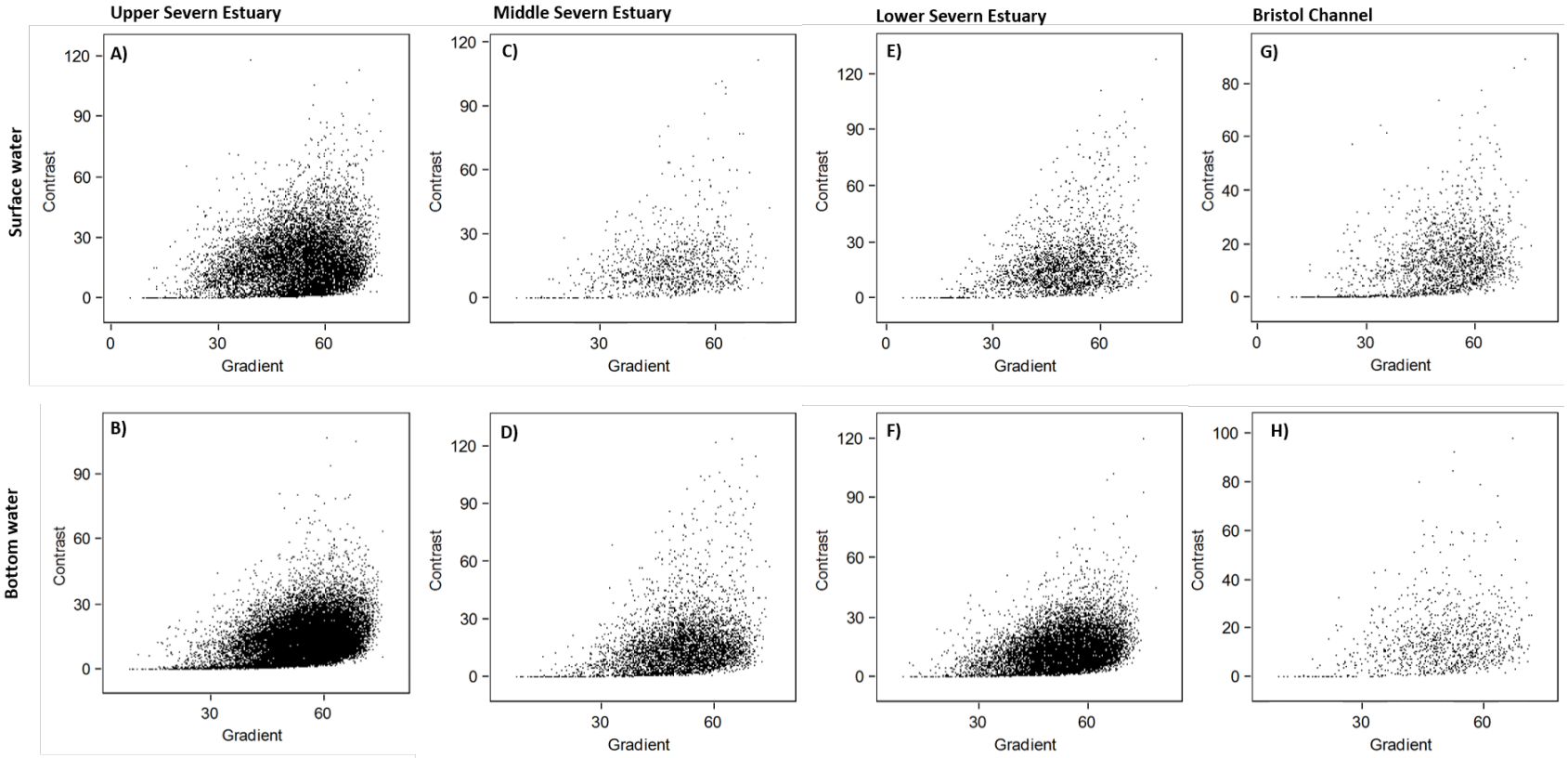

Figure 3.33: Flow Cytometry output of gradient vs contrast illustrating the poor sharpness of quality of the samples from the Severn Estuary in the summer of 2016. Note, a high abundance of particles in the upper Severn Estuary. **A-B)** Upper Severn Estuary. **C-D)** Middle Severn Estuary. **E-F)** Lower Severn Estuary. **G-H)** Bristol Channel. Top: surface water samples. Bottom: Bottom water samples.

Chapter 4

Benthic biofilm silicon cycling in the Severn Estuary intertidal mudflats

4.1 Introduction

Rivers can form estuaries at the land-ocean interface, which can either be marine or river-dominated, or an intermediate between the two (Volta et al., 2014). In estuaries, the convergence of riverine freshwater and the saline marine end-member leads to enhanced hydrological and biogeochemical processes, which can alter the export of sediment, salt, species, and nutrients between these two zones. Most importantly for siliceous dependant organisms, estuaries can influence the cycling of dissolved and particulate silica (Arndt and Regnier, 2007; Arndt et al., 2007; Chou et al., 2007; Arndt et al., 2009; Carbonnel et al., 2009; Laruelle et al., 2009a,b; Papush, 2011; Carbonnel et al., 2013; Volta et al., 2014, 2016). In the previous chapter, this study outlined multiple factors influencing pelagic dissolved silicon (PDSi) and biogenic silica (PBSi) in the River Severn, its estuary and tributaries. Fluvial and tidal hydrodynamics were shown to drive the dissolved nutrient components, including PDSi, whereas sediment transport exhibited an important coupling to PBSi. The investigation found that due to the high turbidity, phytoplankton biomass and productivity were low, indicating the biological mediation of Si was also low in the sampled periods of 2016. Despite this low pelagic productivity, PBSi concentrations were elevated in the upper estuary. The study hypothesised that a proportion of the PBSi may have originated from the resuspended microphytobenthos (MPB) biofilms inhabiting the sediment-water interface (SWI) on the intertidal mudflats.

In hypertidal estuaries, the large tidal range results in expansive areas of exposed intertidal mudflats. Intertidal MPB biofilms in temperate regions, such as those along

the Severn Estuary, are dominated by epipelic, photosynthetic diatoms, although other groups of diatoms, for example epipsammic and tychoplankton, and other phototrophs such as cyanobacteria and euglenoids are present (Yallop et al., 1994; Underwood, 2010). Despite being compressed into a thin biofilm only a few millimetres thick (Perkins et al., 2003), these MPB communities have high rates of primary productivity, which can often exceed that of phytoplankton in the overlying turbid water column (Underwood, 2010). This pattern between benthic and pelagic ecosystems has been previously recorded in meso and macro-tidal, fine sediment-dominated estuaries where turbidity limits phytoplankton growth (Radford, 1994; Heip et al., 1995; Kocum et al., 2002). Previous research suggests these diatom-dominated biofilms (Underwood, 2010) have the potential to significantly influence benthic dissolved silicon (BDSi) concentrations and the percentage of benthic biogenic silica (BBSi) (Welsby et al., 2016). Further, the strong hydrodynamics in the estuary results in high resuspension rates of the mudflats (Manning et al., 2010), creating a potential export of Si from the benthic system into the water column.

The primary aim of this chapter is to determine the BDSi and BBSi budgets of the MPB biofilms inhabiting four intertidal mudflats of the Severn Estuary. This in turn, may show if this benthic system could be a source of the relatively high BSi concentrations measured in the water column during sampled periods of 2016. Further, this chapter explores the multiple benthic factors that could influence the uptake of BDSi and the subsequent build-up of BBSi over spatio-temporal scales. Within this secondary aim, the specific objectives are to:

- Determine the benthic biofilm biomass and the photosynthetic rate of the diatoms, and discuss the potential impact they have on the assimilation of DSi to BSi.
- Determine *in situ* how diatoms adapt to the harsh mudflat environments, for example through behavioural photoprotection and/or photophysiological photoprotective mechanisms.
- Determine how environmental forcings (e.g. light intensity, temperature, sediment composition and macronutrient concentrations) influence diatom ability to biologically mediate Si.

4.2 Methodology

To assess the BDSi and BBSi mudflat budgets, four intertidal mudflat sites were sampled during daytime low tide periods, during the same sampled periods in 2016. The mudflats ranged from the upper Estuary (Severn Beach = Site 1), to the mid-estuary on the English coastline (Portishead = Site 2) and on the Welsh coastline (Newport Wetlands = Site 3), towards the outer Estuary (Sand Bay = Site 4). For a detailed outline of the field methodology, refer to Chapter Two (Section 2.1).

4.2.1 Sediment analyses

The surficial 5 mm biofilms were extracted and analysed for BBSi content, chl content, and sediment grain size. Chl pigment contents were measured following the acetone extraction protocol buffered with $MgCO_3$ (Mackereth et al., 1978). Cell counts of pennate and centric diatoms, cyanobacteria and euglenoids were estimated using a Sedgewick Rafter Counting Cell under a light microscope (Olympus CH). Dried surface algal biofilms were measured for BBSi following the weak alkaline extraction method of marine sediments, adapted from DeMaster (1981). BBSi is presented as a percentage of dried Si mass (g/g). For a detailed outline of these procedures see Chapter Two (Section 2.2).

From three randomly selected stations at each site, mudflat sediment compositions were analysed using the grain size weight (g) of each size fractions separated using sampling sieves (<63 μm, 63-106 μm, 106-212 μm, 212-250 μm, 250-300 μm and >300 μm), and presented as a percentage of the total mass.

4.2.2 Mudflat water analyses: nutrients and Total Organic Carbon

Air and mudflat water temperatures (°C) were recorded at each station using a hand-held digital thermometer. Mudflat water (a mixture of surface and pore fluid) was sampled (50 mL), with the supernatant decanted and filtered through PALL Acrodisc PF 32 mm syringe filters with 0.8/0.2 μm pore space supor membranes for the concentrations of BDSi, Total Organic Carbon (TOC), phosphate, nitrate, nitrite and ammonium. Aliquots of all filtered samples of the mudflat water were diluted with Milli-Q H_2O for BDSi concentrations (mg/L) following the Heteropoly Blue method (Strickland and Parsons, 1972). Nitrate (NO_3-N), nitrite (NO_2-N), phosphate (PO_4-P) and ammonium (NH_4-N) concentrations were measured using cuvette test following the designated LCK methods. TOC concentrations (mg/L of C) were measured using the Non-Purgeable Organic Carbon (NPOC) technique at the School of Geographical Sciences, University of Bristol. For a detailed outline of these methodologies, refer to Chapter Two (Section 2.2).

4.2.3 Chlorophyll fluorescence

Variable chlorophyll fluorescence of undisturbed diatom-dominated biofilms was logged at each station using a Water Pulse Amplitude Modulation (PAM) fluorometer (Walz, Effeltrich, Germany). For a detailed explanation of this setup, see Chapter Two (Section 2.1.2.2). At each station, ambient irradiance (μmol photons/m^2/s) was measured using the Mini Quantum Sensor attached to the Walz PAM fluorometer.

Rapid Light Curves (RLCs) were used to show the relationship between nine different actinic irradiance levels of a duration of 20s and the relative Electron Transport Rate (rETR: *rel. units*). RLCs were used to determine the rETR, the maximum relative ETR ($rETR_{max}$: *rel. units*); light saturation coefficient i.e. the PAR value at which light saturation begins (E_K: μmol photons/m^2/s), and the light use coefficient for PSII i.e. the initial slop of the RLC (α). These fluorescent parameters were derived from the curve fitting of the model of Eilers and Peeters (1988), using R studio software (RStudio Team, 2015). Also presented here are the minimum operational PSII chl fluorescence yields in actinic light ($F^{'}$), the maximum PSII chl fluorescence yields in actinic light ($F^{'}_{m}$), the regulated Y(NPQ) and the non-regulated energy dissipation Y(NO), the maximum quantum efficiency of PSII photochemistry [Y(PSII)], and F_v/F_m i.e. an indicator of photosystem stress. For a detailed explanation of these photosynthetic parameters see Chapter One (Section 1.3.4), and for their formulation see Chapter Two (Section 2.1.2.2).

4.2.4 Biogenic silica dissolution rates

BSi dissolution in the intertidal mudflat sediments was investigated using sediment sampled during different periods in 2016. Surficial biofilms were dried at 85°C, and crushed, with 1 g of sediment placed into 25 mL clean centrifuge tubes, and vortex mixed with DI water. Samples were subject to different environmental conditions:

- Samples were left in daylight at room temperature (20°C).
- Samples were left in the dark at room temperature (20°C).
- Samples were left in the dark at below 4°C.

Sub-samples were taken each month, filtered, and measured for Si concentrations (mg/L) using the Heteropoly Blue Method described above. After a year, samples were dried and measured for BSi content following the above weak alkaline extraction procedure. Using the time elapsed between each measurement (s), the DSi concentrations (mg/L) were first corrected for the dilution in 15 mL DI water (DSi in mg), and then the flux of Si was calculated (mg/s) and converted to kg/s. These fluxes were then scaled-up to determine the dissolution flux from the mudflats, using published intertidal mudflat area estimates (SEP, 2009), and for the entire estuarine area: 55,684 ha (Potts and Swaby, 1993), and the SAC area of 73,714 ha (JNCC, 2018).

4.3 Results

4.3.1 Benthic silicon budgets

4.3.1.1 BDSi and BBSi variability between sampled periods

BDSi concentrations at all four mudflat sites averaged 10.9 ± 1.5 mg/L during the winter, and were high compared to the spring (1.1 ± 0.3 mg/L), summer (1.0 ± 0.4 mg/L) and autumn (1.2 ± 0.4 mg/L) sampled periods (Fig. 4.1). A significant difference was found between the winter and spring (H=9.78, d.f=3, $p<0.001$; *post hoc* analysis $p<0.001$), between the winter and summer (*post hoc* analysis, $p<0.001$), and between the winter and autumn sampled periods (*post hoc* analysis, $p<0.001$).

BBSi was high in the spring (0.74 ± 0.03%) and summer (0.76 ± 0.05%) compared to the winter (0.59 ± 0.04%) and autumn (0.69 ± 0.04%) sampled periods (Fig. 4.1). A significant difference was found between the winter and spring (H=9.78, d.f=3, $p<0.05$; *post hoc* analysis $p<0.01$), and between the winter and summer (*post hoc* analysis, $p<0.05$). No significant difference was found between the winter and autumn sampled periods.

4.3.1.2 BDSi and BBSi spatial variability among sampled mudflats

Mudflat water BDSi concentrations in the winter peaked at Site 1 (H=24.36, d.f=3, $p<0.001$) in the upper Severn Estuary. At each consecutive site towards the outer estuary, BDSi concentrations decreased (Fig. 4.1). This pattern among the sampled sites was not observed in the spring, summer and autumn sampled periods. The percentage of BBSi sampled in the winter, resembled an opposite trend to BDSi (Fig. 4.1). Peak BBSi content was observed at Site 2 and 3 in both spring and summer sampled periods (Fig. 4.1).

The coefficient of variation (CV), a measure of the relative variability of Si between sampled sites (spatial) each sampled period (temporal), was high for BDSi (137%) compared to BBSi (47%) for the 2016 data set. Considering only spatial variability in BDSi, CV was high in the summer (85%) and autumn (71%) (Table. 4.1). BBSi spatial variability was low in the spring (34%), suggesting similar BBSi content (%) between sampled mudflats. Considering only temporal variability in BDSi concentrations at each site, CV was high (>114%), whereas CV of BBSi was low, between 37% and 49% (Table. 4.1).

4.3.1.3 BDSi and BBSi small-scale heterogeneity

On individual intertidal mudflats, BDSi concentrations and BBSi (Fig. 4.2) percentages varied across the 100 m sampled profile (*n=15*), representing the extreme heterogeneity

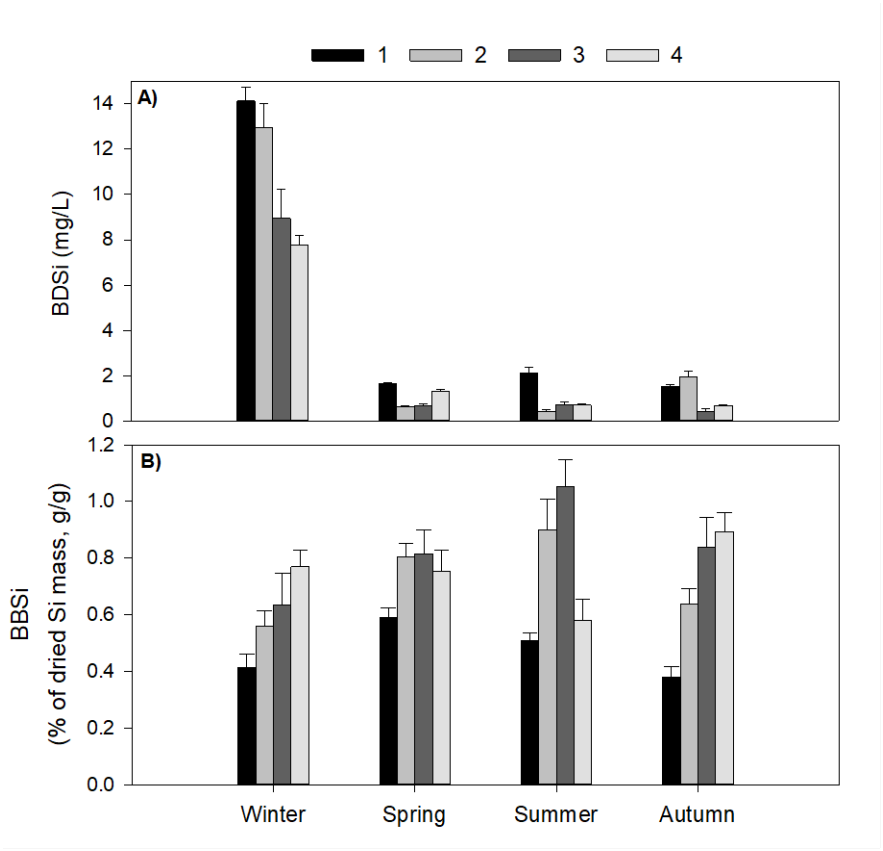

Figure 4.1: A) Benthic dissolved silicon concentrations (BDSi, mg/L) from the Severn Estuary intertidal mudflat water. **B)** Benthic biogenic silica (BBSi, % of dried Si mass, g/g). Sites: Severn Beach (1), Portishead (2), Newport Wetlands (3), Sand Bay (4). Presented with 1SE (*n=15* stations).

Table 4.1: Coefficient of variation (the standard deviation as a percentage of the mean) of mudflat water BDSi concentrations and biofilm BBSi percentage over spatio-temporal scales.

	Season	**Site 1**	**Site 2**	**Site 3**	**Site 4**	**All**
BDSi	Winter	17	32	56	21	**40**
	Spring	16	47	68	19	**51**
	Summer	45	69	48	27	**85**
	Autumn	19	43	128	22	**71**
	All	**114**	**141**	**163**	**119**	
BBSi	Winter	46	38	69	28	**51**
	Spring	22	22	40	37	**34**
	Summer	22	47	35	50	**51**
	Autumn	35	34	49	30	**49**
	All	**37**	**41**	**49**	**38**	

observed on small spatial scales in these environments. Large ranges in BDSi concentrations were observed at Site 2 and 3 during the winter and autumn sampled periods (Fig. 4.2). A narrow range in BDSi concentrations were observed in the spring at all sampled stations. BBSi heterogeneity was high at Site 3 (winter and spring) and Site 2 and 3 (summer), but overall low compared to BDSi (Fig. 4.2).

4.3.1.4 Silicon released by the dissolution of mudflat sediment: a preliminary experimental study

Si dissolution rates (regardless of the sampled period or experimental controls), varied between each measurement on a monthly rota Fig. 4.3). Si could be present as BSi, LSi and/or ASi, but the more reactive Si (i.e. surface adsorbed Si, BSi and/or other amorphous phases) are most likely dissolving. A larger build-up of DSi was present in the sediment sampled during the winter periods (Fig. 4.3), associated with peak dissolution rates (Table. 4.2). Spatial variability in Si dissolution was more pronounced in the winter sediment: Site 1 and 3 had higher DSi concentrations compared to Sites 2 and 4 (Fig. 4.4).

Based on the experiment dissolution rates, the overall supply of DSi from the dissolution of particulate silica, regardless of the environmental conditions associated with changes in temperature and light, was <0.001 kg/s (see Table. 4.2). But, when the estuarine area was considered, and scaled-up for a year, dissolution resulted in a maximum of *ca.* 43,000 kg DSi/year (note, under dark/warm conditions). Under dark and cold conditions, the sediment from each sampled period had low dissolution rates (Table. 4.2), which resulted in low concentrations of DSi in the sub-samples (Fig. 4.4). Under warmer conditions, regardless of light availability, Si dissolution rates increased (Table. 4.2).

On average, after a year exposed to the specific environmental conditions, BSi (%) decreased (Fig. 4.5). Note, discrepancies in this trend was likely associated with the comparison between the average BSi values representing the conditions of 15 stations on the mudflats, and the single sample collected for the dissolution experiment.

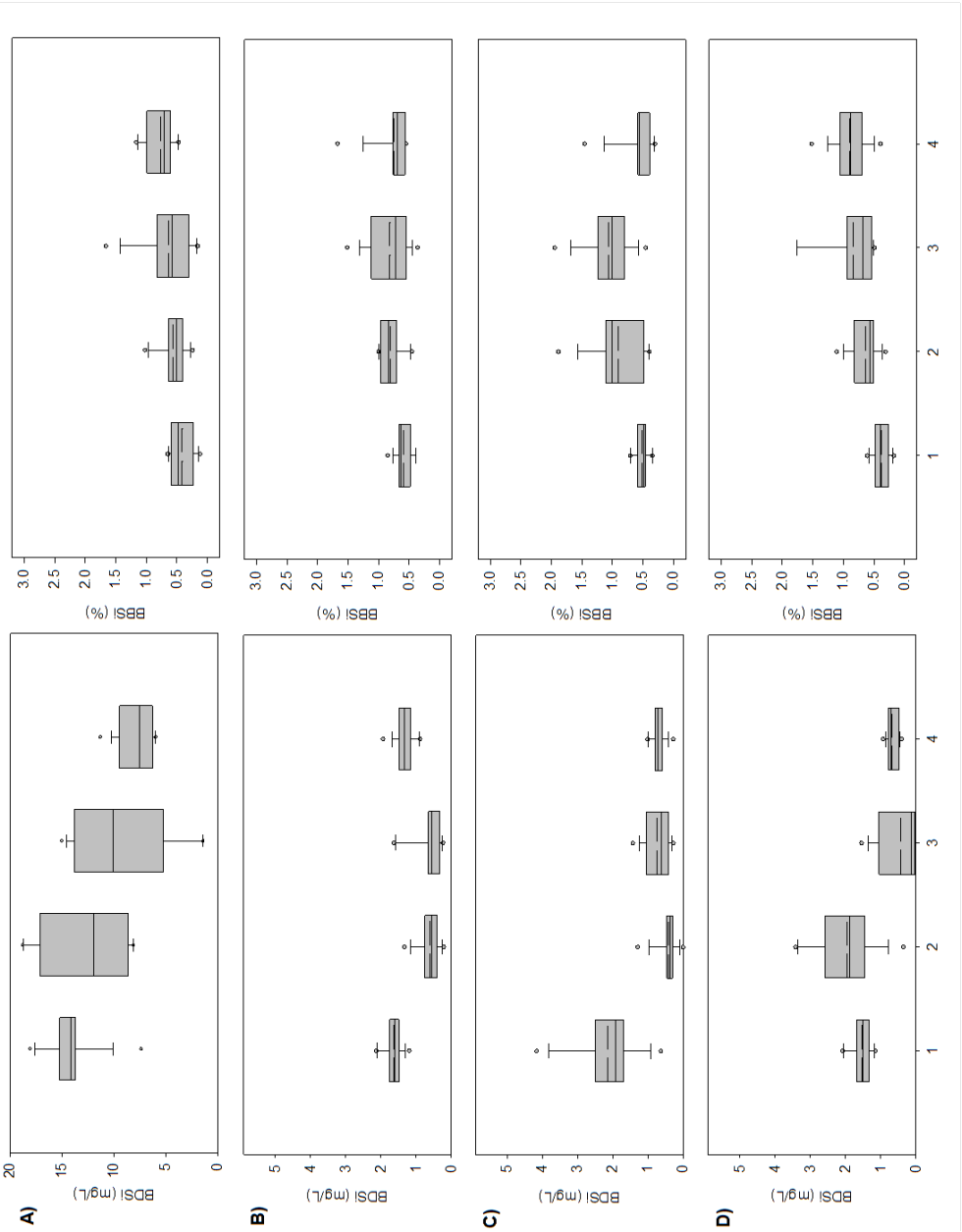

Figure 4.2: Left: Dissolved silicon concentrations (mg/L). Right: Biogenic silica (BBSi, % of dried Si mass, g/g). **A)** Winter. **B)** Spring. **C)** Summer. **D)** Autumn. Sites: Severn Beach (1), Portishead (2), Newport Wetlands (3), Sand Bay (4).

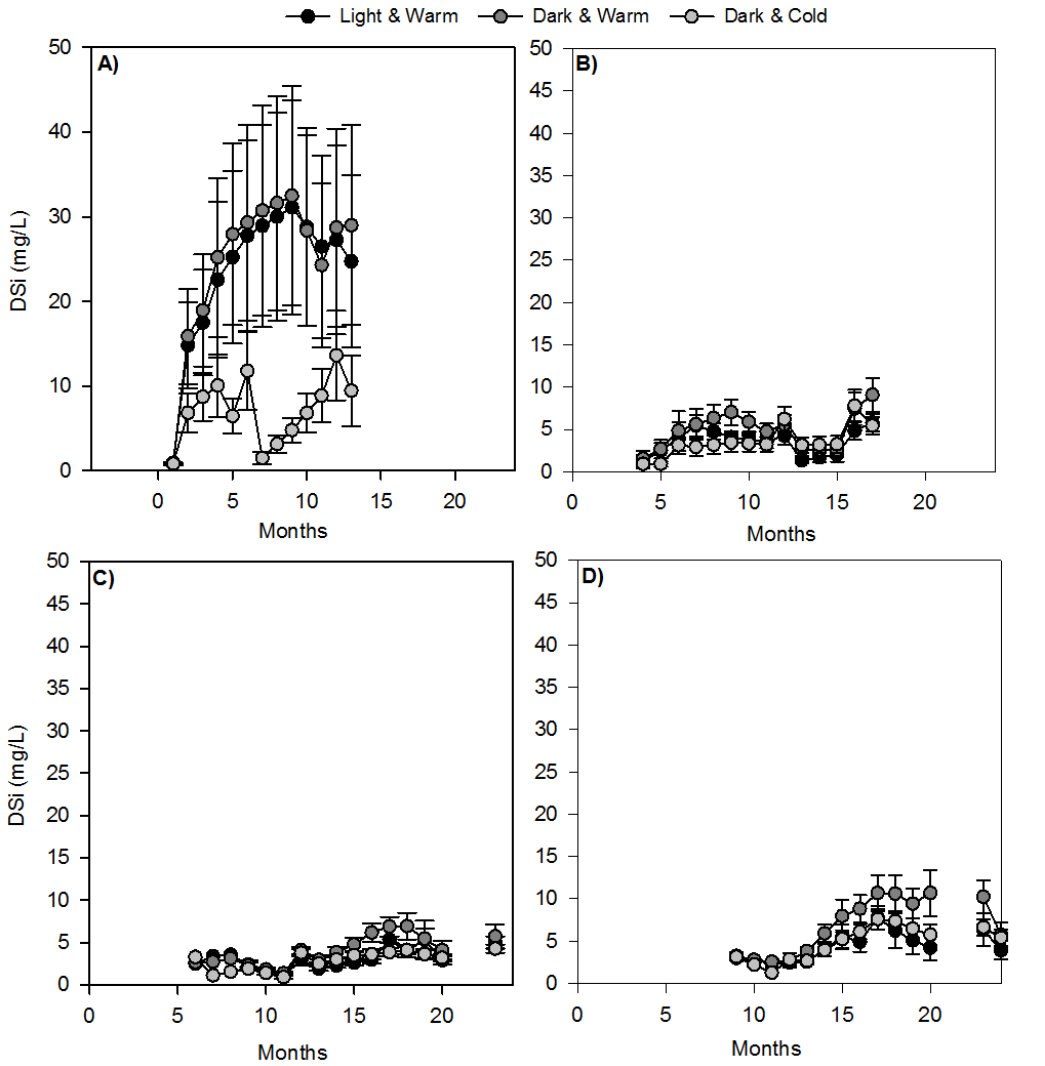

Figure 4.3: Average DSi concentrations (mg/L) in sub-samples taken each month from sediment samples exposed to each environmental condition. Sediment sampled from each period: **A)** Winter. **B)** Spring. **C)** Summer. **D)** Autumn. Note, dissolution experiment began after each sampled period. 1st Month = February 2016. Presented with 1SE (n=4).

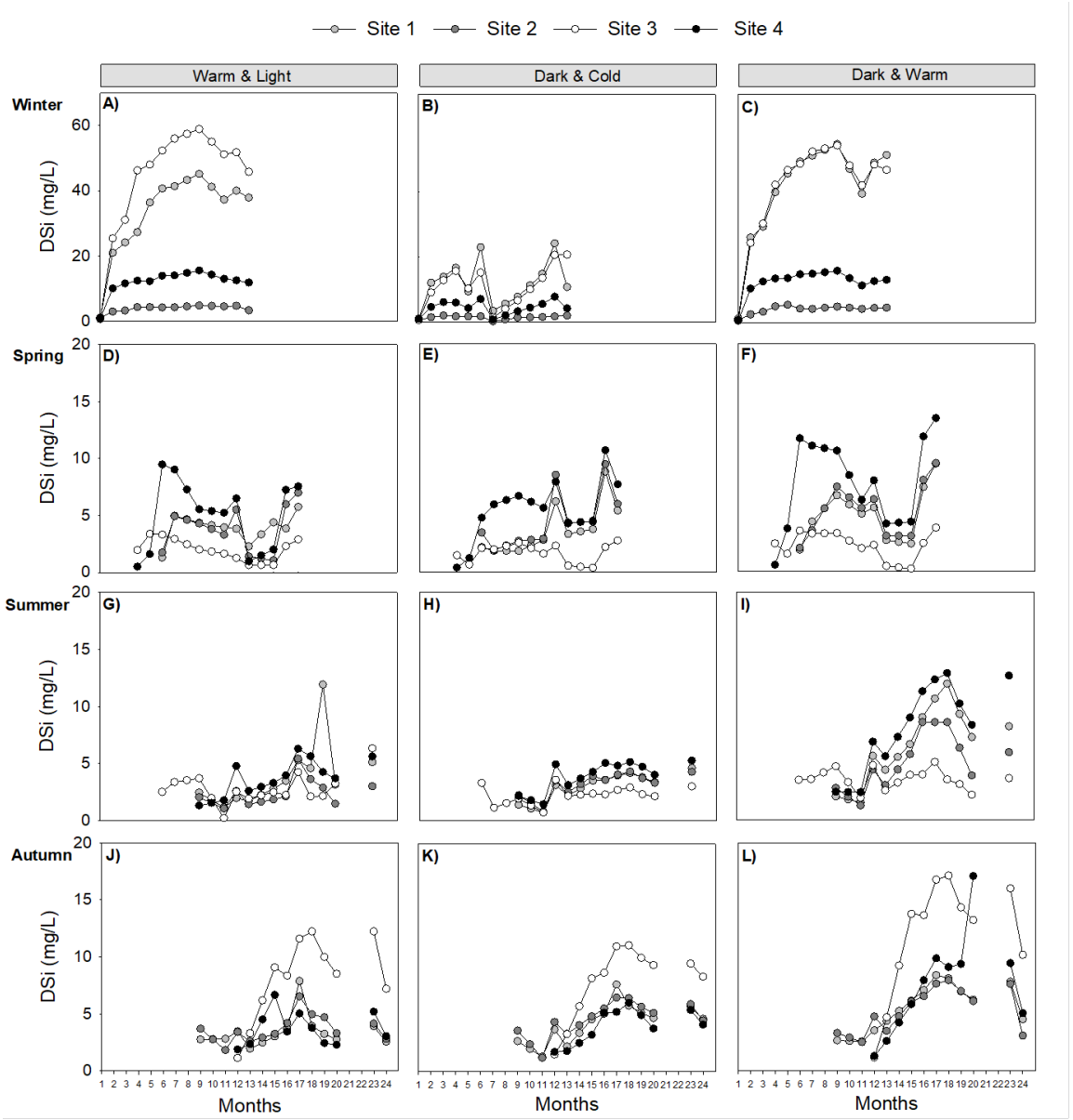

Figure 4.4: DSi concentrations (mg/L) in sub-samples taken each month from each mudflat site. Left: warm & light. Centre: Dark & cold. Right: Dark & warm. **A-C)** Winter. **D-F)** Spring. **G-I)** Summer. **J-L)** Autumn. Site 1 (light grey), Site 2 (dark grey), Site 3 (white) and Site 4 (black). Dissolution experiment began after each sampled period. 1st Month = February 2016. Note different y-axis scale, and no sample replication.

Table 4.2: Average Si dissolution rates (kg/s and kg/year) from the Severn Estuary mudflat sediment (*n=4*) sampled each period and placed under different environmental conditions. Data scaled-up for the intertidal mudflats and estuarine area. Positive values (dissolution), negative values (e.g. adsorption). Presented with 1 SE (*n=4*).

	Light & Warm	**Dark & Warm**	**Dark & Cold**
Winter (kg/s)	1.11 ± 0.48 x10^{-3}	1.32 ± 0.55 x10^{-3}	0.39 ± 0.20 x10^{-3}
Spring (kg/s)	0.20 ± 0.05 x10^{-3}	0.33 ± 0.10 x10^{-3}	0.15 ± 0.05 x10^{-3}
Summer (kg/s)	-0.20 ± 0.01 x10^{-3}	-0.09 ± 0.01 x10^{-3}	-0.10 ± 0.01 x10^{-3}
Autumn (kg/s)	-0.23 ± 0.03 x10^{-3}	-0.31 ± 0.02 x10^{-3}	-0.17 ± 0.02 x10^{-3}
Avg. in kg/s **(a)**	0.24 x10^{-3}	0.31 x10^{-3}	0.06 x10^{-3}
Avg. in kg/s **(b)**	0.82 x10^{-3}	1.04 x10^{-3}	0.31 x10^{-3}
Avg. in kg/s **(c)**	1.08 x10^{-3}	1.37 x10^{-3}	0.41 x10^{-3}
Avg. in kg/year **(a)**	7,659	9,867	2,028
Avg. in kg/year **(b)**	25,843	32,748	9,814
Avg. in kg/year **(c)**	34,210	43,351	12,991

(a) Used an intertidal area of 20,300 ha (SEP, 2009).

(b) Used the estuarine area of 55,684 ha (Potts and Swaby, 1993).

(c) Used the SAC estuarine area of 73,714 ha (JNCC, 2018).

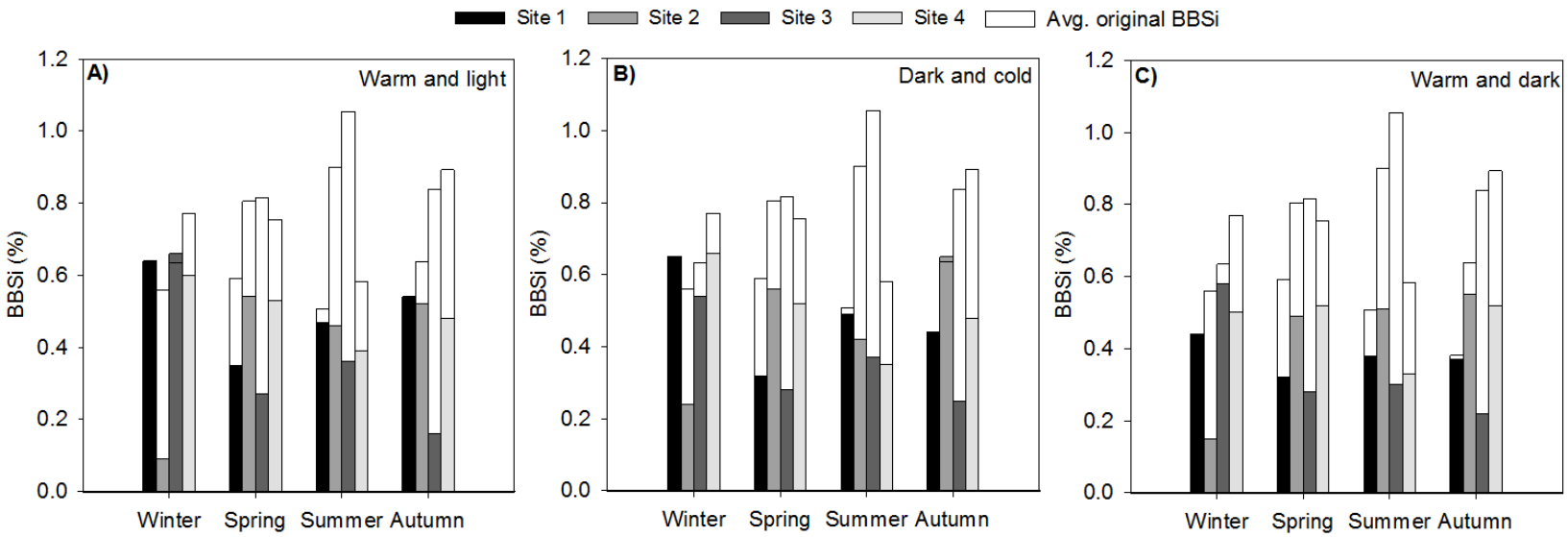

Figure 4.5: Benthic biogenic silica (BBSi) percentage (% of dried Si mass, g/g) in the surface sediment at the end of the experiment (1 year, note no replications). Environmental conditions: **A)** Warm & light. **B)** Dark & cold. **C)** Warm & dark. Clear boxes: original average (*n=15*) mudflat BBSi content.

4.3.2 Benthic microphytobenthos biofilm biomass

Chl *a* content increased between sampling periods in 2016 (Fig. 4.6). Low chl *a* content was measured during the winter (30.6 ± 5.0 μg/g *dw. sed.*), and increased during the spring (35.7 ± 3.9 μg/g *dw. sed.*) and summer (55.1 ± 6.9 μg/g *dw. sed.*) to significantly higher levels during the autumn (116.8 ± 16.2 μg/g *dw. sed.*). There was a significant difference in chl *a* between winter and the other sampled periods in 2016 (H=55.82, d.f=3, $p<0.05$; *post hoc* analysis $p<0.01$), but no difference between the spring and summer sampled periods. No linear correlation was calculated between chl *a* and BBSi in the sampled periods of 2016. Peak chl *a* content was recorded at Site 3 in the autumn (max. station value of 445.0 μg/g *dw. sed.*), and remained below 40.9 μg/g *dw. sed.* for each sampled period at Site 1.

Chl *b* contents (a proxy for the presence of green algae) were relatively low during the winter (11.3 ± 1.6 μg/g *dw. sed.*), spring (21.2 ± 8.9 μg/g *dw. sed.*), and autumn (50.3 ± 7.1 μg/g *dw. sed.*) compared to the summer (187.4 ± 48.6 μg/g *dw. sed.*) sampled periods (Fig. 4.6). A significant difference was found between the summer and the other sampled periods (H=70.12, d.f=3, $p<0.001$, *post hoc* analysis $p<0.05$). Notably at Site 3, chl *b* content averaged 690 ± 125 μg/g *dw. sed.* (Fig. 4.6).

Chl *c* data (a proxy for the presence of diatoms) were considered defective with some data recording 0 μg/g *dw. sed.* content despite visible diatom abundance. The low chl *c* content was likely related to the difficulties associated with extracting chl *c* using standard extraction methods (*pers. comm.* with Prof Marian Yallop). In addition, two potential issues in the extraction of chl pigments are identified: even though the samples were corrected for the water content, the pigments may not have been efficiently extracted due to the wet sediment which may have decreased the strength of the extraction by the solvent, and despite adding $MgCO_3$ to prevent the degradation of chl *a* to phaeophytin, there may have been a percentage of degraded pigments in the samples to begin with.

A significantly difference was found in TOC concentrations between the sampled sites (H=25.08, d.f=3, $p<0.001$, *post hoc* analysis $p<0.001$), with high concentrations of TOC recorded in the mudflat water at Site 3 during the winter sampled period (max. 28.1 mg/L) (Fig. 4.7). No linear correlation was found between TOC and BBSi in the sampled periods of 2016 (Fig. 4.8).

Benthic biofilms during the spring and summer sampled periods were exposed to high air and water temperatures (Fig. 4.10), and prolonged photoperiods (Fig. 4.9) of higher light levels (Fig. 4.10). Significantly higher air (H=167.51, d.f=3, $p<0.001$, *post hoc* analysis $p<0.001$) and water temperatures (H=112.64, d.f=3, $p<0.001$, *post hoc* analysis $p<0.001$) were measured during the summer compared to the other sampled periods in 2016 (Fig. 4.10). The total number of sunshine hours were on average higher in the spring (177 hrs) and summer (154 hrs), compared to the winter (65 hrs) and

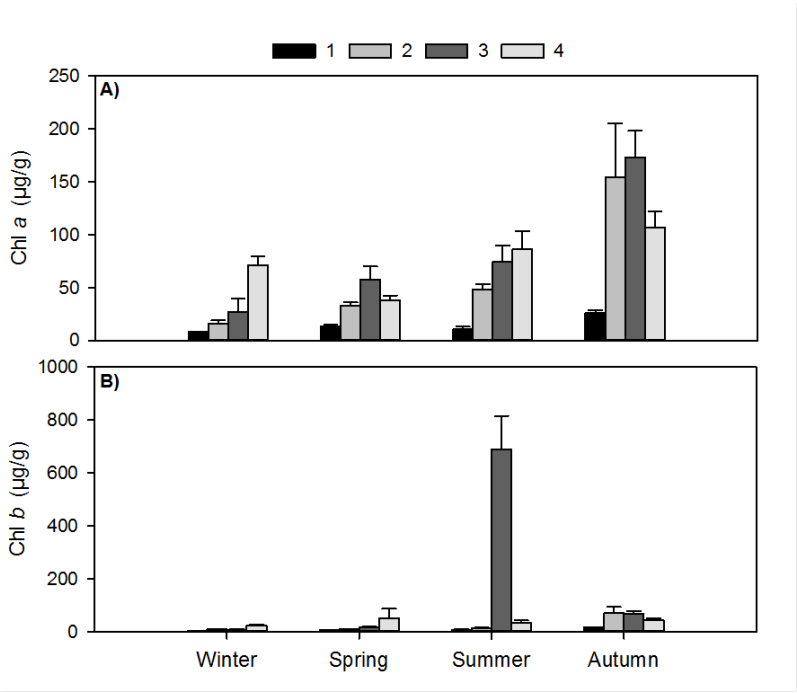

Figure 4.6: Chlorophyll content (μg/g *dw. sed.*) in the Severn Estuary intertidal mudflats benthic microphytobenthos biofilms sampled during different periods in 2016. Sites: Severn Beach (1), Portishead (2), Newport Wetlands (3), Sand Bay (4). Presented with 1SE (*n=15* stations). Note, chl *c* data considered defective, and therefore not presented.

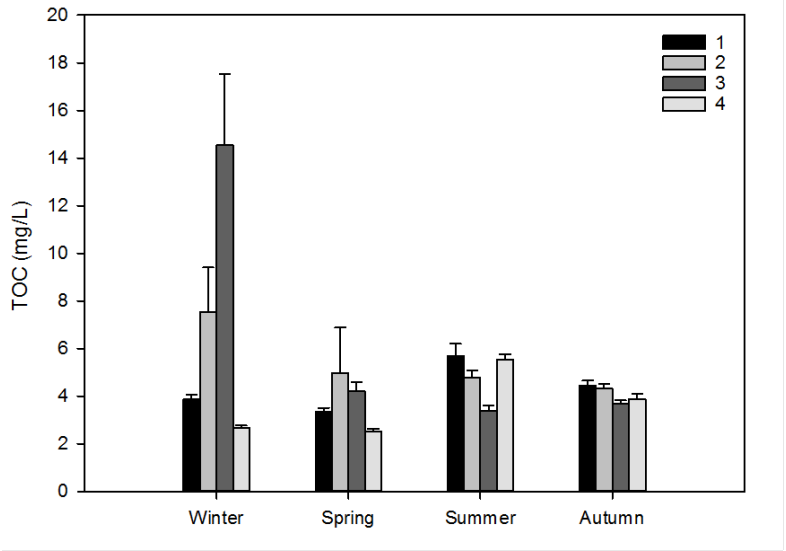

Figure 4.7: Total Organic Carbon concentrations (mg/L) in the Severn Estuary intertidal mudflat water in 2016. Sites: Severn Beach (1), Portishead (2), Newport Wetlands (3), Sand Bay (4). Presented with 1SE (*n=15* stations).

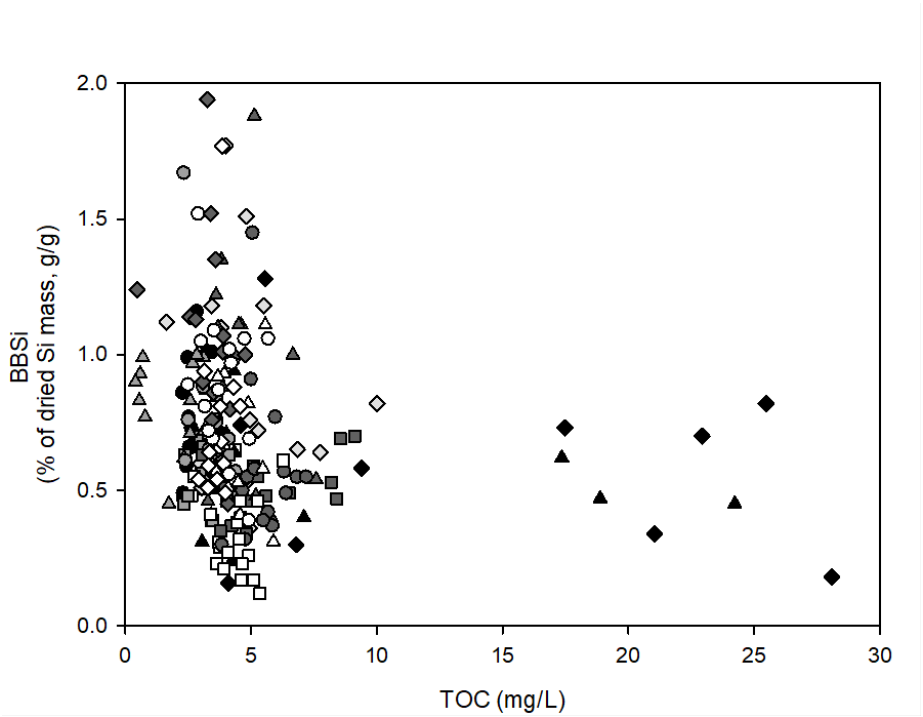

Figure 4.8: Relationship between Total Organic Carbon concentrations (mg/L) and the percentage of BBSi (% of dried Si mass, g/g). Winter (black), spring (grey), summer (dark grey), autumn (white). Site 1 (square), Site 2 (triangle), Site 3 (diamond), Site 4 (circle).

autumn (84 hrs) sampled periods (Fig. 4.9). Irradiance levels at the time of sampling (between *ca.* 11:00 hrs and 16:00 hrs), were high (>1253 μmol photons/m^2/s) during the summer, and low (<150 μmol photons/m^2/s) during the autumn, alongside less sunshine hours (Fig.4.9). Note, only Site 3 in the winter had recorded light levels (135 μmol photons/m^2/s).

Water content in the mudflats lacked significant variability between sampled periods: winter (41 $\pm$ 0.02 %), spring (53 $\pm$ 0.02 %), summer (43 $\pm$ 0.02 %), and autumn (45 $\pm$ 0.02 %) (Fig. 4.10). Over an emersion period, the exposed sediment can experience desiccation, causing a loss of water and an increase in bulk density, which can result in lower chl content when expressed per unit mass (Perkins et al., 2003). Chl content was corrected for the water content at the time sampled to account for this, however the expected change in dewatering between the different sampled periods (e.g. summer vs winter) could not be accounted for without a large study measuring dewatering rates to account for changes in bulk density on each day sampled. Despite this, with the samples collected during mid-emersion periods, and because there was no significant difference in water content between sampled periods, it is possible to assume the dewatering rates were similar.

Pennate diatoms dominated the MPB biofilm assemblage on the intertidal mudflat during 2016 (Fig. 4.11). Peak pennate cell count was found at Site 4 in the autumn

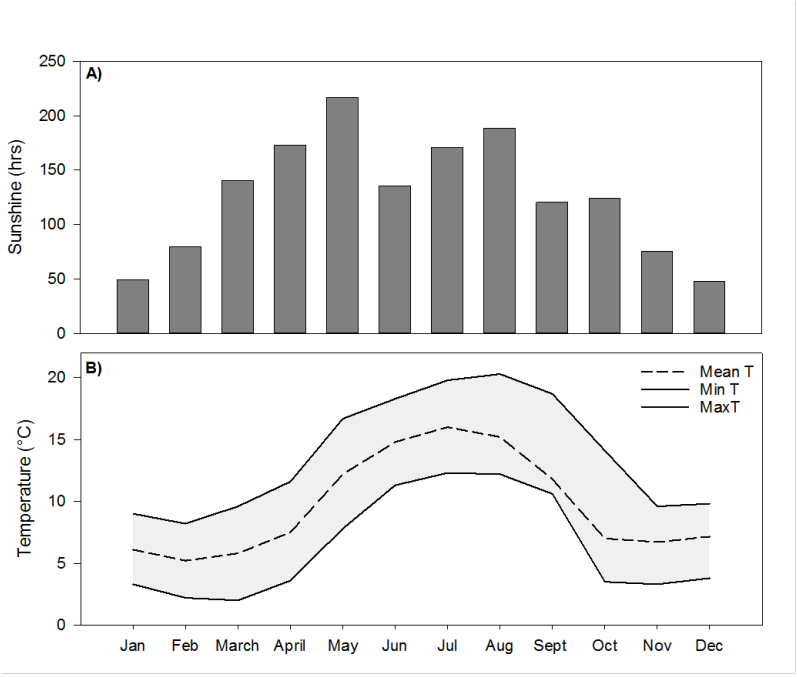

Figure 4.9: Meteorological conditions in the Severn Estuary in 2016. **A)** Number of hours of sunshine each season. **B)** Mean, minimum and maximum air temperatures (°C) each season. Data from MetOffice (2016).

sampled periods (*ca.* 4,071,400 cells per gram of sediment), followed by Site 4 in the spring sampled periods (*ca.* 3,915,000 cells per gram of sediment). Centric diatoms only reached highs of *ca.* 180,000 cells per gram of sediment in the spring sampled periods (Fig. 4.11). Cyanobacteria estimated abundance peaked during the spring sampled periods at Site 4 (*ca.* 705,000 cells per gram of sediment) (Fig. 4.11). Euglenoids estimated abundance peaked during the autumn sampled periods at Site 4 (*ca.* 607,100 cells per gram of sediment) (Fig. 4.11).

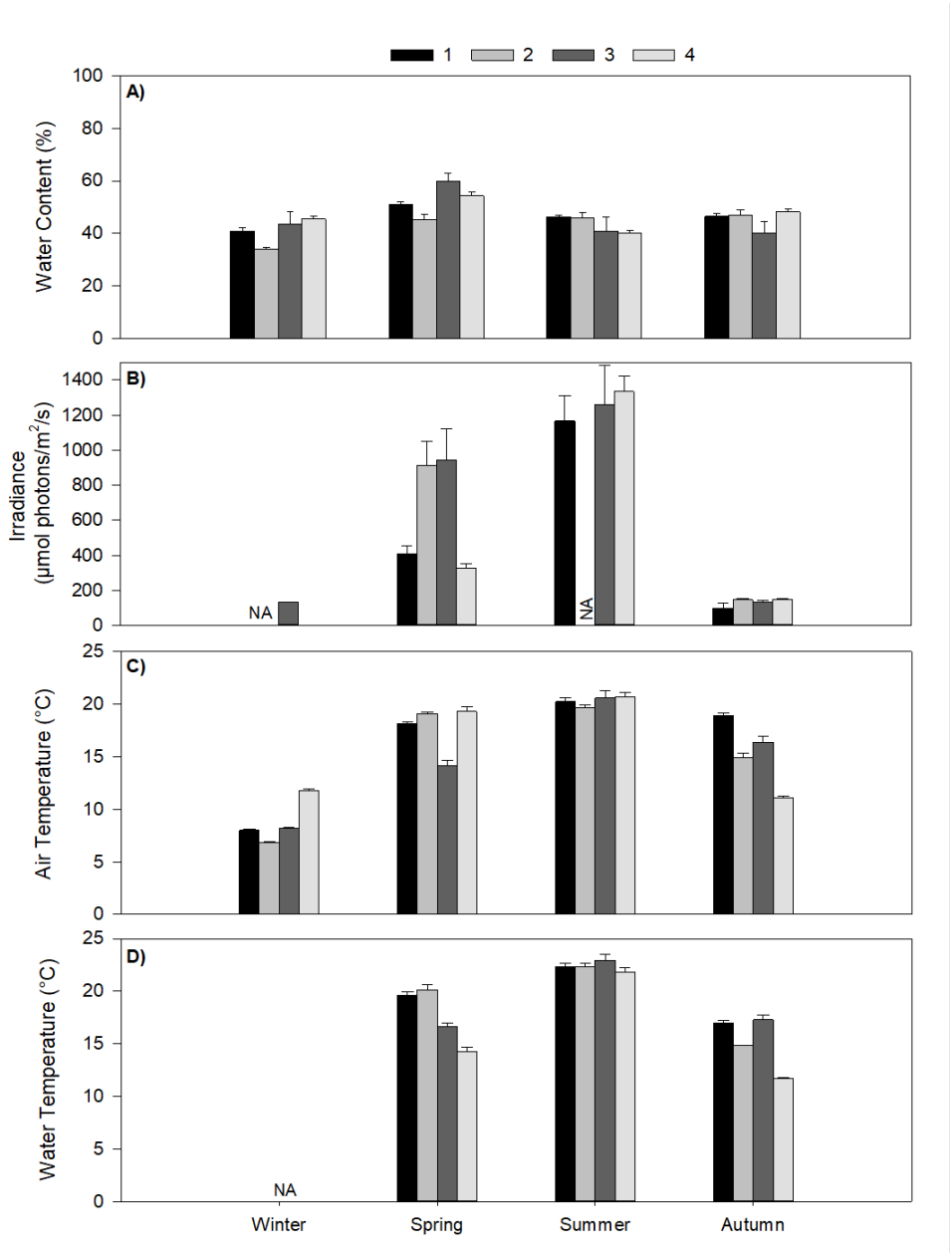

Figure 4.10: Environmental conditions on the Severn Estuary intertidal mudflats. **A)** Water content (%). **B)** Irradiance (μmol photons/m^2/s). **C)** Air temperature (°C). **D)** Water temperature (°C). Sites: Severn Beach (1), Portishead (2), Newport Wetlands (3), Sand Bay (4). Presented with 1SE (*n=15* stations).

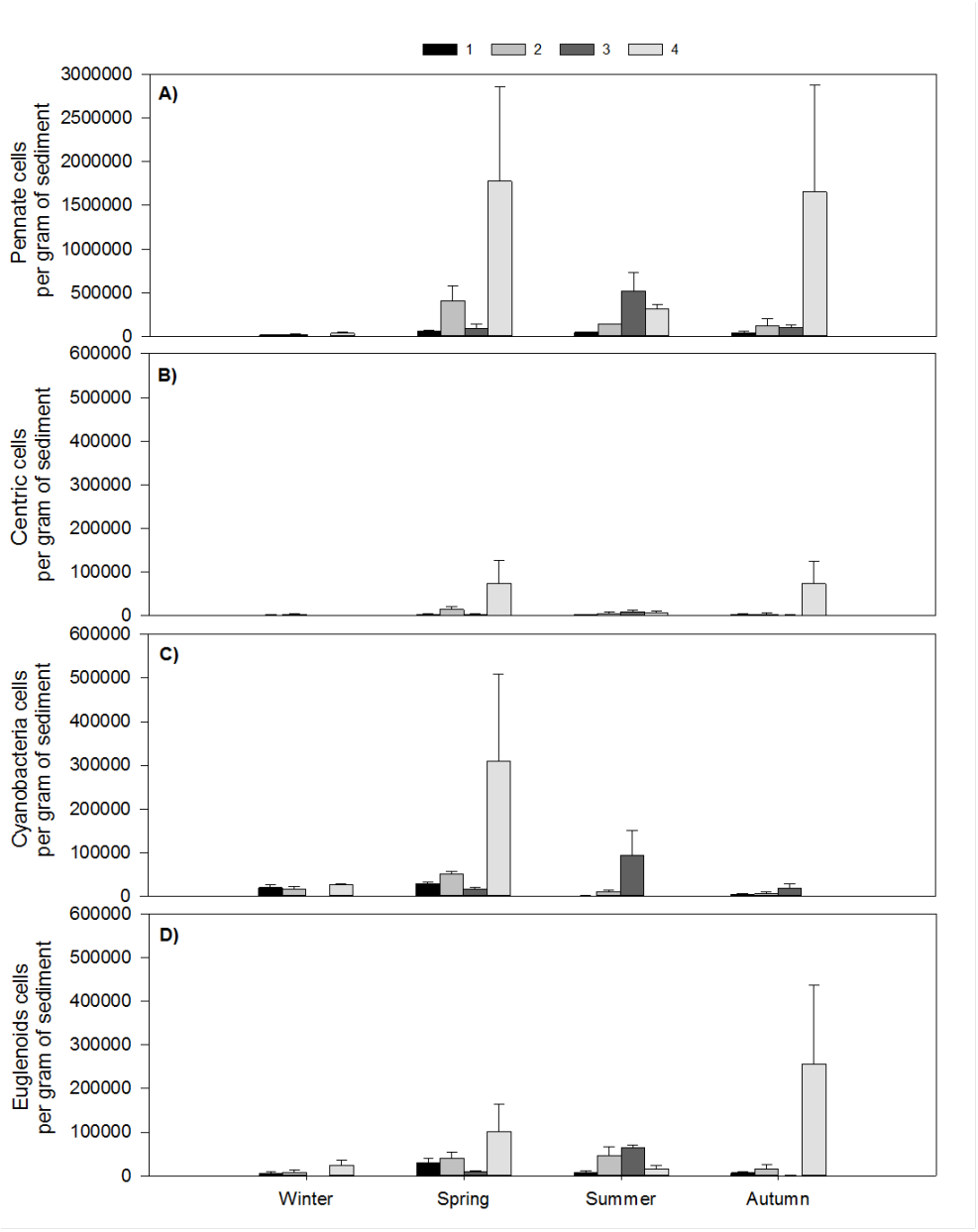

Figure 4.11: Species abundance in the microphytobenthos assemblage on the intertidal mudflats of the Severn Estuary during sampled periods in 2016. **A)** Pennate diatom cells per gram of sediment. **B)** Centric diatom cells per gram of sediment. **C)** Cyanobacteria cells per gram of sediment. **D)** Euglenoids cells per gram of sediment. Note difference in y-axis scale. Sites: Severn Beach (1), Portishead (2), Newport Wetlands (3), Sand Bay (4). Presented with 1SE (*n=15* stations).

4.3.3 Chlorophyll fluorescence analysis: a proxy of benthic algal primary productivity

4.3.3.1 Rapid Light Curves

RLCs (Fig. 4.12), an average of all the RLCs produced at each mudflat (*n=15*), at each sampled period, showed good replication (i.e. small standard error), suggesting the biofilms behaved, on average, uniformly despite expected small-scale heterogeneity (note, a few stations RLCs were outliers, see Appendix, Section 4.6). On average, the RLCs produced from the winter and autumn sampled periods saturated (Fig. 4.12). The $rETR_{max}$ averaged 126 ± 7 *rel. units* in the winter and 142 ± 28 *rel. units* in the autumn sampled periods (Fig. 4.13). Two scenarios were observed in the RLCs produced during the spring sampled periods: at Site 1 and 2 the RLCs failed to saturate on average, whilst at Sites 3 and 4 the RLCs saturated (Fig. 4.12). The $rETR_{max}$ at Site 1 and 2 averaged 329 ± 97 *rel. units*, whilst the $rETR_{max}$ at Site 3 and 4 averaged 142 ± 13 *rel. units* (Fig. 4.13). In the summer sampled periods, all RLCs failed to saturate (Fig. 4.12). RLCs with increasing irradiance levels that did not saturate, overestimated the calculation of $rETR_{max}$ (avg. of 389 ± 21 *rel. units* in summer) and E_K (Fig. 4.13). The lack of RLC saturation was likely associated with cell downward movement in response to increasing irradiance (Perkins et al., 2010a). Consequently, Y(PSII) in PSII photochemistry, which has been used to estimate the rETR through PSII, were erroneous. Thus, $rETR_{max}$ and E_K values are presented in clear bars in Fig. 4.13.

During the sampled periods of 2016, α displayed no spatial variation among the sampled sites or sampled periods, but ranged between 0.20 and 0.32 (Fig. 4.13). Without including the erroneous E_K values (spring at Site 1 and 2, and all sites in the summer), peak E_K was measured in the winter sampled period at Site 4 (1168 ± 210 μmol photons/m^2/s).

4.3.3.2 Photophysiological and behavioural photoprotection

In the sampled periods in 2016, with increasing PAR levels, the minimum fluorescence yield (F') increased (Fig. 4.14). At low light the maximum fluorescence yield (F'_m) increased in the winter and autumn, but at the beginning of the RLCs, declined in the spring and summer sampled periods. Each sampled period, at high light levels, F'_m decreased (Fig. 4.14). A decline in fluorescence yield is indicative of behavioural down-regulation through cell motility away from high irradiance levels and/or NPQ induction. In the winter and autumn sampled periods, $F'_{m\ max}$ was reached towards the beginning of the RLC (Fig. 4.14), whereas in the spring and summer sampled periods, $F'_{m\ max}$ occurred towards higher actinic light levels (Fig. 4.14).

The maximum quantum efficiency of PSII photochemistry, F_v/F_m ratios were between 0.58 and 0.70 (Table. 4.3).

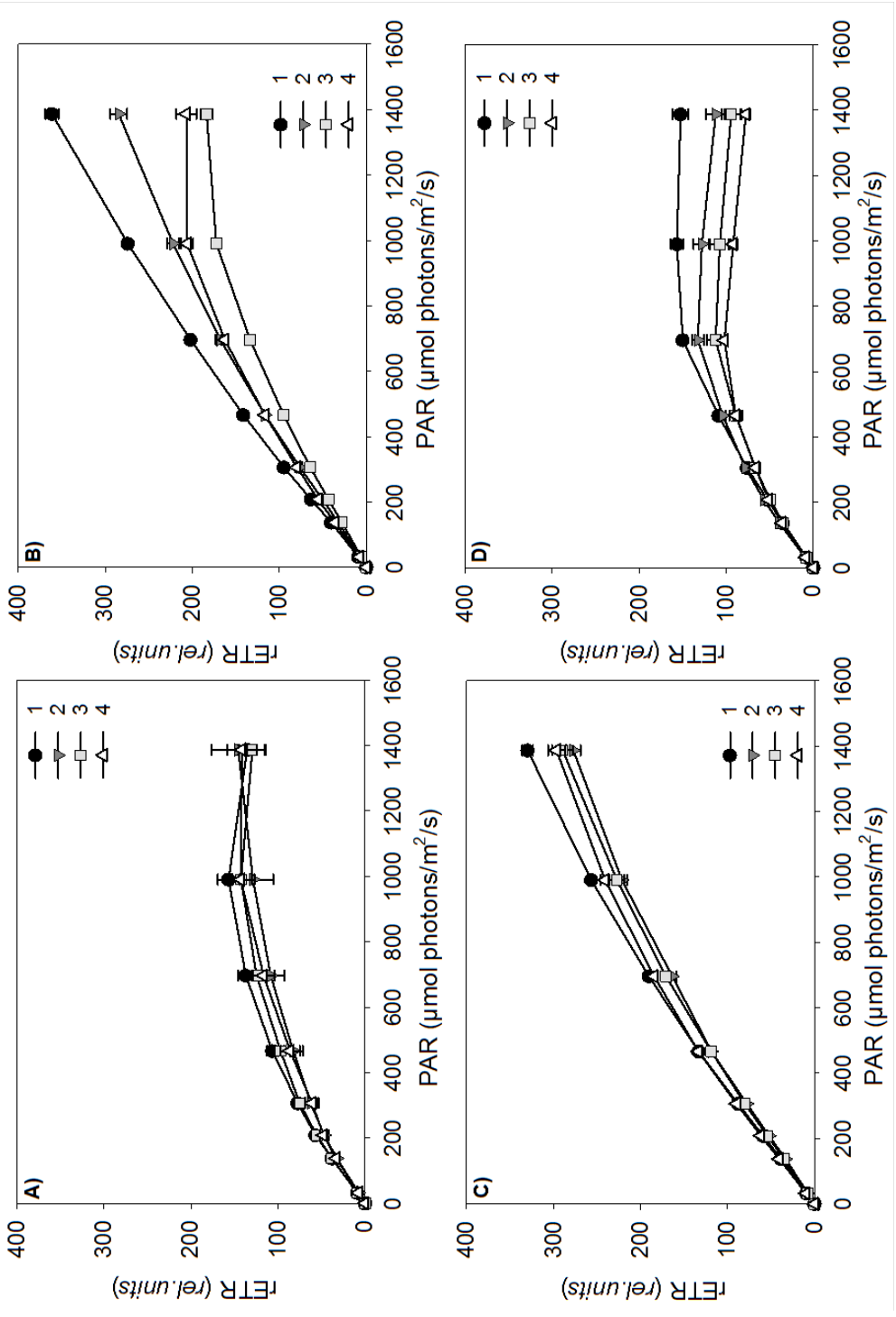

Figure 4.12: Rapid Light Curves. **A)** Winter. **B)** Spring. **C)** Summer. **D)** Autumn. Sites: Severn Beach (1), Portishead (2), Newport Wetlands (3), Sand Bay (4). Presented are the average and 1SE of 15 RLCs from each mudflat, from each sampled period.

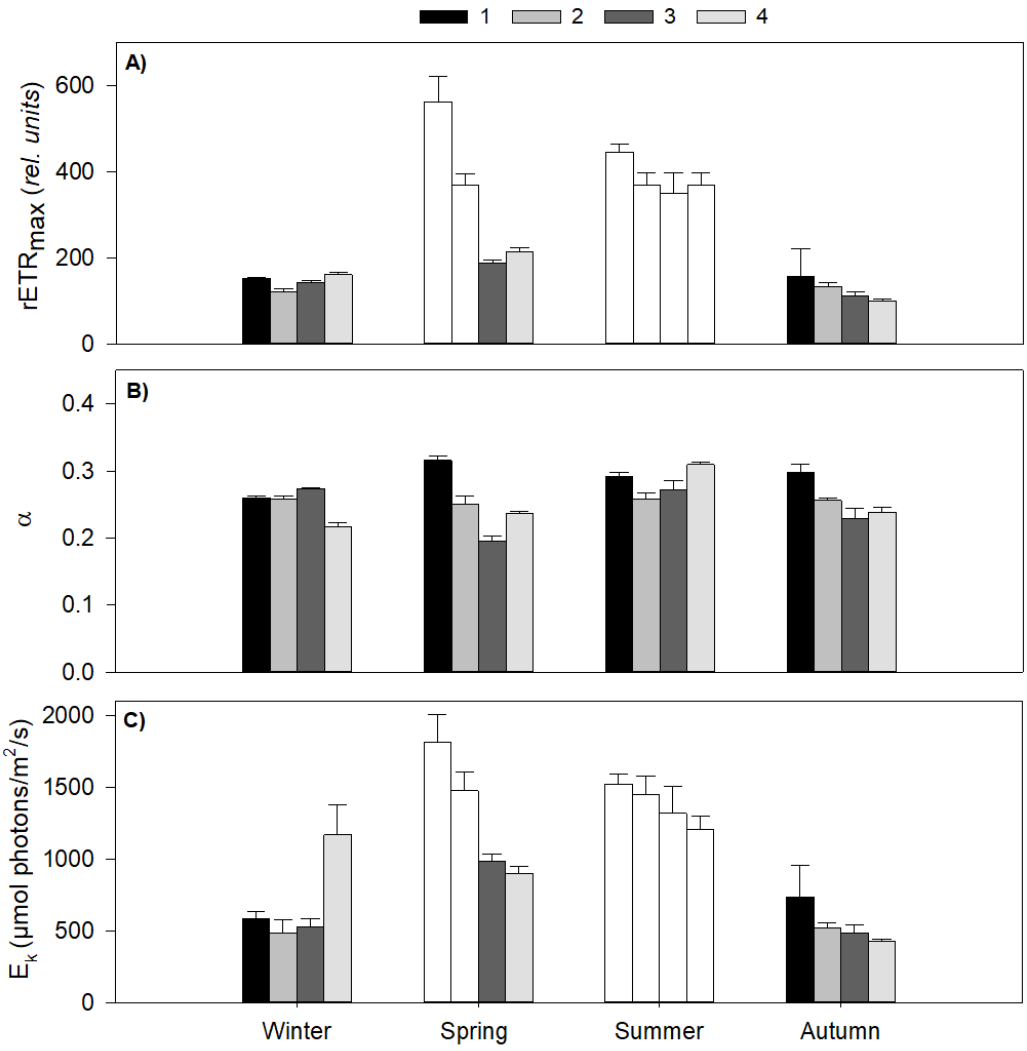

Figure 4.13: **A)** Relative Maximum Electron Transport Rate, $rETR_{max}$ (*rel. units*). **B)** Light use coefficient for photosystem II, α. **C)** Light saturation coefficient, E_K (μmol photons/m^2/s). Clear boxes: overestimated $rETR_{max}$ and E_K. Sites: Severn Beach (1), Portishead (2), Newport Wetlands (3), Sand Bay (4). $rETR_{max}$ and α reported with 1SE of all stations (n=15). Propagated standard error where $E_K = \alpha/rETR_{max}$.

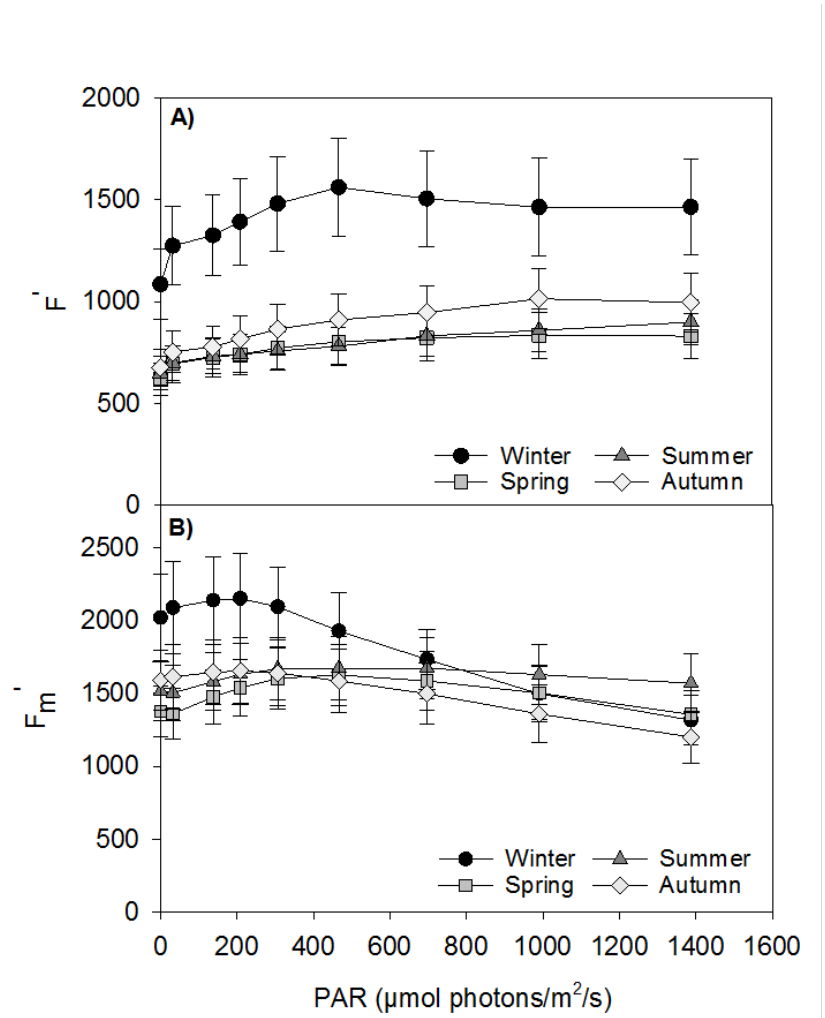

Figure 4.14: Minimum chlorophyll fluorescence, F' **(A)**, and maximum chlorophyll fluorescence, F'_m **(B)** with increasing Photosynthetic Active Radiation (PAR). Data reported with 1SE of 15 stations sampled on each mudflats (n=60).

Table 4.3: Maximum quantum efficiency of PSII photochemistry (F_v/F_m), presented with 1SE of 15 stations.

	Winter	**Spring**	**Summer**	**Autumn**
Site 1	0.68 ± 0.02	0.68 ± 0.02	0.66 ± 0.04	0.58 ± 0.01
Site 2	0.62 ± 0.06	0.58 ± 0.02	0.61 ± 0.02	0.66 ± 0.01
Site 3	0.64 ± 0.01	0.59 ± 0.02	0.59 ± 0.02	0.61 ± 0.03
Site 4	0.65 ± 0.05	0.70 ± 0.02	0.68 ± 0.02	0.63 ± 0.01

In the sampled periods of 2016, average values of Y(NPQ) remained below Y(NO) (Fig. 4.15). In the winter and autumn sampled periods, with increasing exposure to higher actinic light levels (>400 μmol photons/m^2/s) over the RLC, Y(NPQ) increased (Fig. 4.15). There was greater NPQ induction [Y(NPQ)] in the winter and autumn (max. average of 0.36 ± 0.05 *rel. units*) compared to the spring and summer (max. average of 0.12 ± 0.02 *rel. units*) (Fig. 4.15). With increasing PAR, Y(PSII) decreased, with a greater decrease in the winter and autumn compared to the spring and summer sampled periods (Fig. 4.15). In the spring and summer sampled periods, Y(PSII) initially declined at the beginning of the RLC (Fig. 4.15), associated with a drop in F'_m (Fig. 4.14).

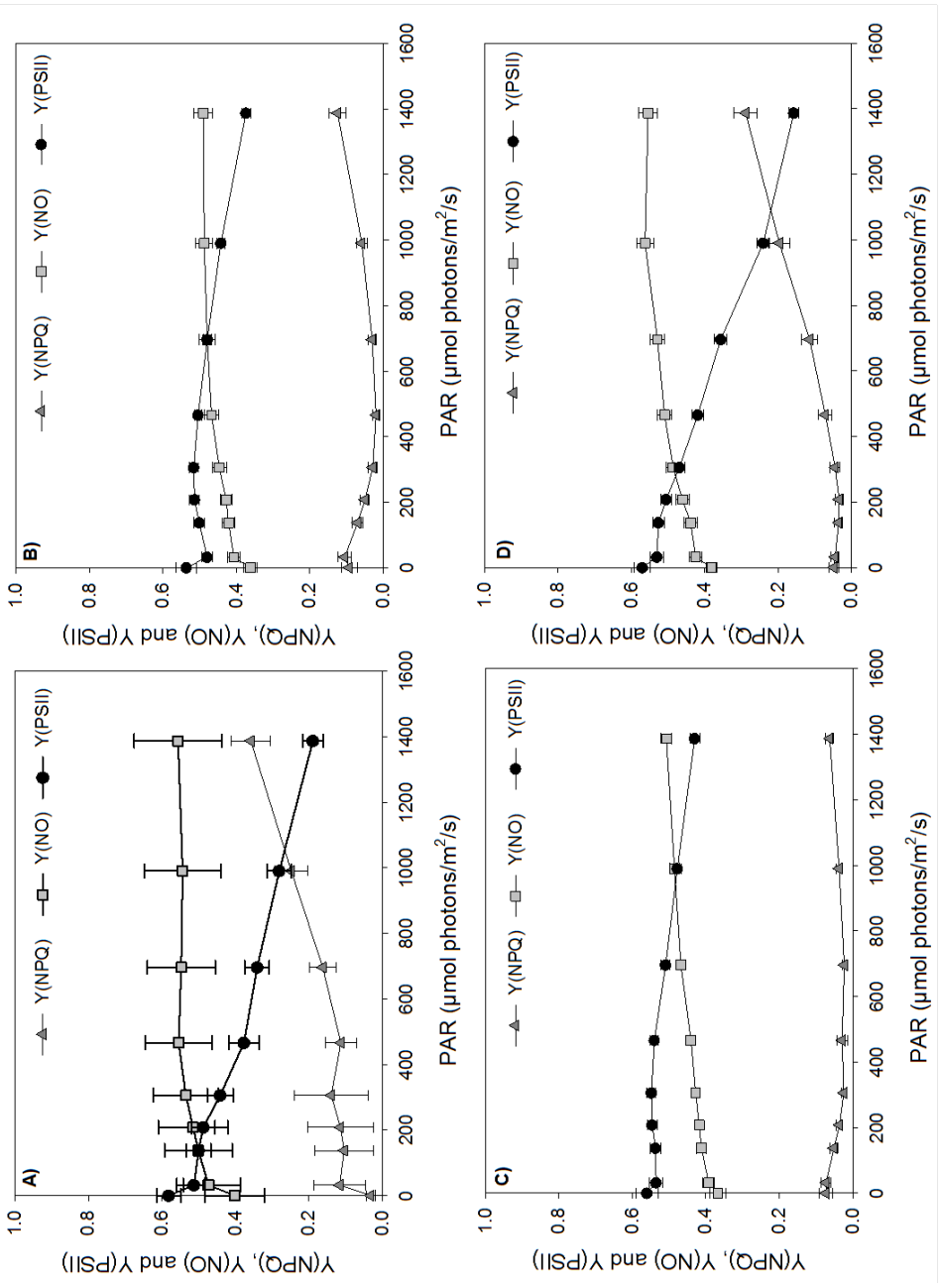

Figure 4.15: Photophysiological forms of down-regulation. Y(NPQ): regulated non-photochemical quenching (*rel. units*). Y(NO): non-regulated heat dissipation (*rel. units*). Y(PSII): fraction of energy that's photochemically converted in PSII. **A)** Winter. **B)** Spring. **C)** Summer. **D)** Autumn. Average values reported with 1SE of four sampled mudflats each sampled period (n=*60*).

4.3.4 Mudflat sediment characteristics

Sediment grain size of <63 μm dominated the intertidal mudflats of the Severn Estuary in the sampled periods of 2016, but fluctuated between sampled periods, with higher average abundances of fine fractions (<63 μm) during the winter (74%), and autumn (85%) compared to the spring (69%) and summer (54%) (Fig. 4.16). Sediment porosity lacked significant variance between sampled periods: winter (0.60 ± 0.02), spring (0.77 ± 0.02), summer (0.64 ± 0.02), and autumn (0.67 ± 0.02).

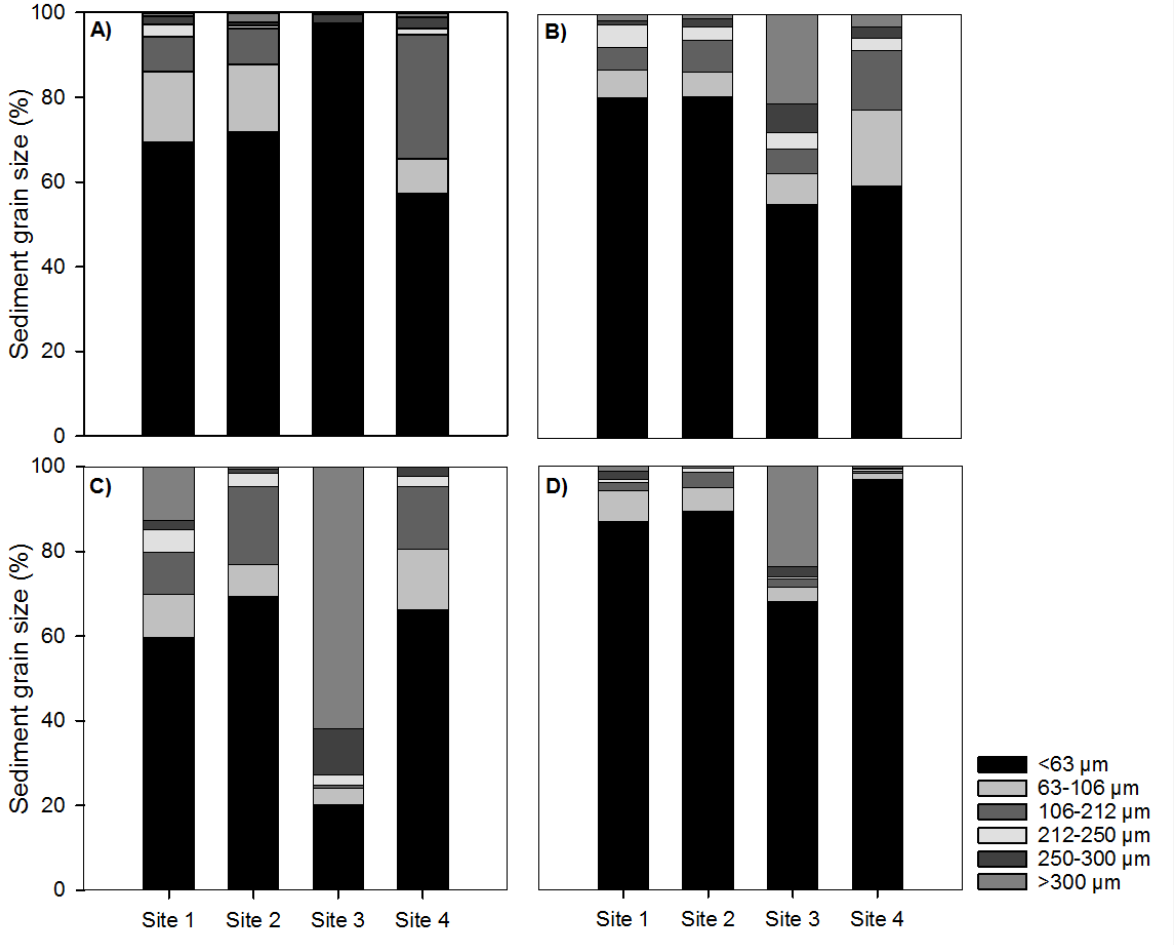

Figure 4.16: Sediment grain size (%) of the intertidal mudflats. **A)** Winter. **B)** Spring. **C)** Summer. **D)** Autumn. Sites: Severn Beach (1), Portishead (2), Newport Wetlands (3), Sand Bay (4).

4.3.5 Nutrient availability

Macronutrient availability in the intertidal mudflat water was assessed as an external factor which may limit the biological mediation of Si. Nitrate concentrations were <1

mg/L, and below the limit of detection (0.23 mg/L) at Site 3 and 4 during the autumn sampled periods (Fig. 4.17). Except for Site 1 in the winter and spring, nitrite concentrations were below the limit of detection (0.015 mg/L). Ammonium concentrations were below the limit of detection in each sampled period of 2016 (0.2 mg/L) (Fig. 4.17). Bioavailable N (i.e. nitrate, nitrite and ammonium) was dominated by the relatively higher concentrations of nitrate compared to nitrite and ammonium (Fig. 4.17). Phosphate concentrations were below 0.3 mg/L (Fig. 4.17).

The modified Redfield-Brzezinski nutrient ratio C:Si:N:P of 106:15:16:1 (Brzezinski, 1985), was calculated on a molar basis (mol:mol) to determine nutrient limitation on the mudflats. Each sampled period in 2016, nitrate was potentially more limiting relative to phosphate and DSi (Fig. 4.18). Under warmer conditions, diatoms were potentially limited by DSi relative to phosphate (Fig. 4.18). A few stations each period displayed phosphate limitation relative to nitrate and DSi. There are several caveats to using these ratios, which were previously discussed in Chapter Three (Section 3.4.6).

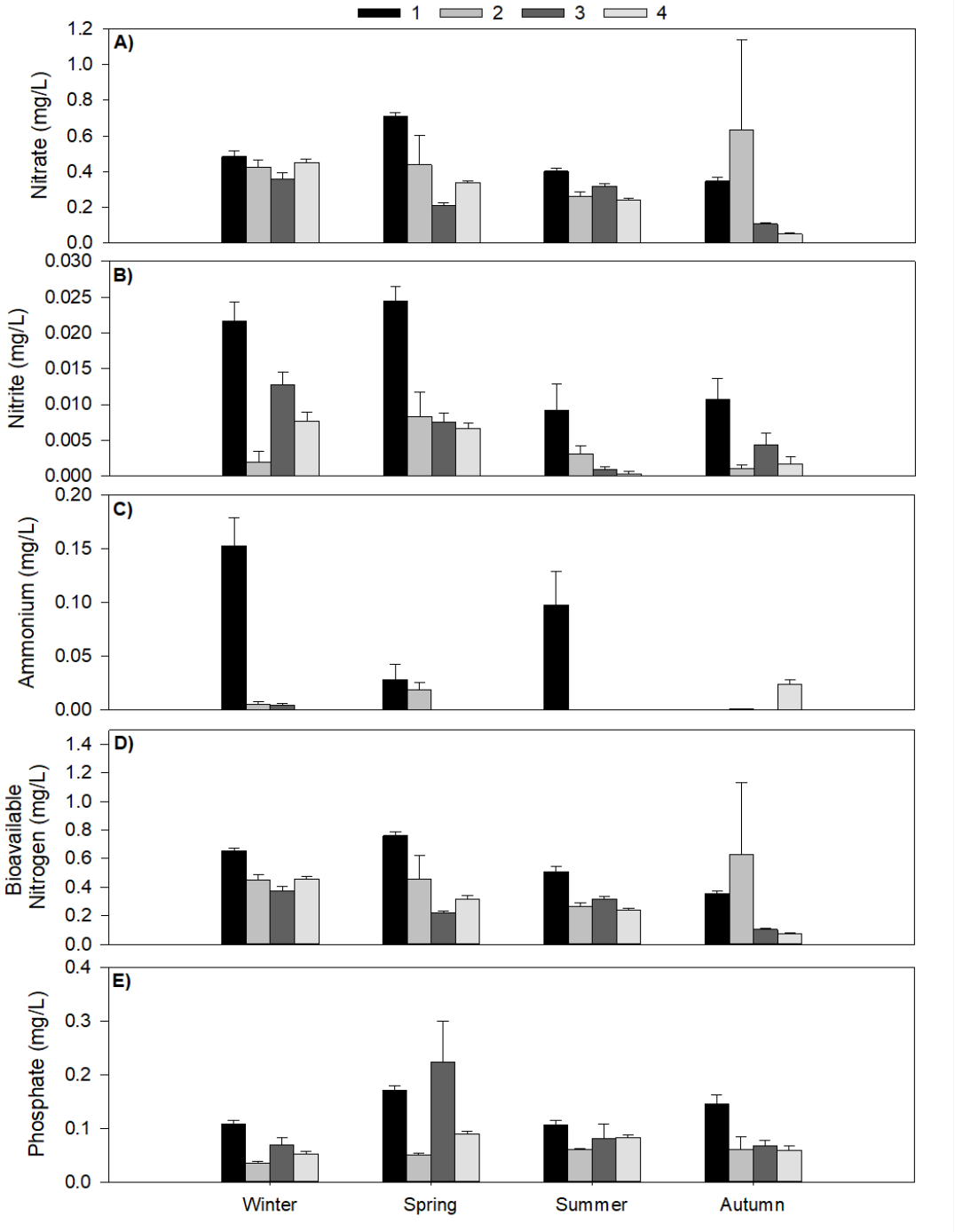

Figure 4.17: Nutrient concentrations in the Severn Estuary intertidal mudflat water each sampled period in 2016. **A)** Nitrate (mg/L). **B)** Nitrite (mg/L). **C)** Ammonium (m/L). **D)** Bioavailable Nitrogen (mg/L). **E)** Phosphate (mg/L). Sites: Severn Beach (1), Portishead (2), Newport Wetlands (3), Sand Bay (4). Data presented with 1SE (*n=15* stations).

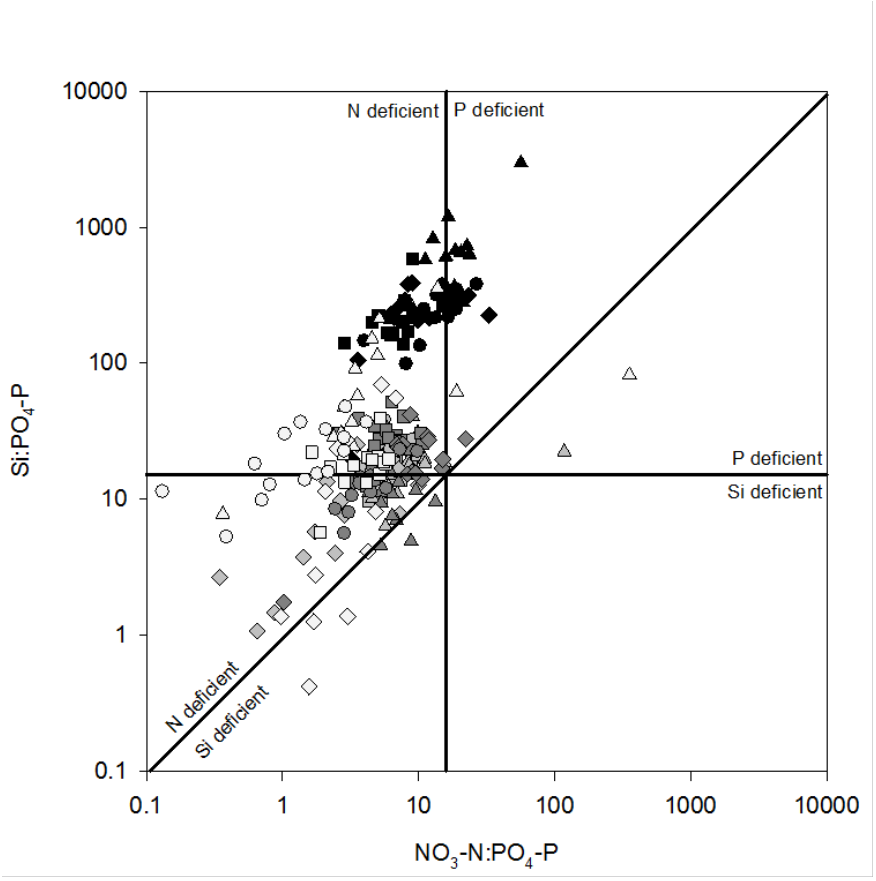

Figure 4.18: Redfield-Brzezinski nutrient ratio in the mudflat water. Winter (black), spring (grey), summer (dark grey), autumn (light grey). Site 1 (square), Site 2 (triangle), Site 3 (diamond), Site 4 (circle).

4.3.6 External controls on the benthic biological mediation of Si: a PCA approach

Principal component analysis (PCA) was carried out for each sampled period in 2016 to assess the interconnections between biogeochemical variables and Si on the intertidal mudflats of the Severn Estuary. PC1 and PC2 contributed to a less than half of the total variability, attributed to the complex environment on intertidal mudflats: 46.2% (winter), 45.4% (spring), 45.4% (summer), 38.0% (autumn).

BDSi and BBSi showed different loadings in PC1 in the winter (Fig. 4.19), spring (Fig. 4.20), summer (Fig. 4.21) and autumn (Fig. 4.22). A Pearsons correlation test of independence was calculated to determine whether BBSi was independent of BDSi. A negative, weak linear interaction was found each period, whereby an increase in BBSi led to a drawdown of BDSi, however the correlations lacked significance.

BBSi and MPB biomass (chl *a*) clustered in the PCAs. In the winter, BBSi and air temperature clustered in PC1 and PC2 (Fig. 4.19), but lacked any significant linear correlation. In the winter and autumn, MPB biomass (chl *a*) and green algae (chl *b*) clustered (Fig. 4.19 & 4.22). Further, light and chl pigments (*a* and *b*) clustered in the autumn. In the summer, chl *b* content and BBSi clustered (Fig. 4.21). In PC1 of the spring, summer and autumn sampled periods, primary productivity proxies ($rETR_{max}$, α, and E_K) had different loadings to biofilm biomass and BBSi.

BDSi and chlorophyll pigments displayed different loadings in PC1 in all PCAs, suggesting the uptake of DSi was associated with an increase in biomass, however no significant linear relationships were observed. Further, in all PCAs, biomass and BBSi showed different loadings to macronutrients.

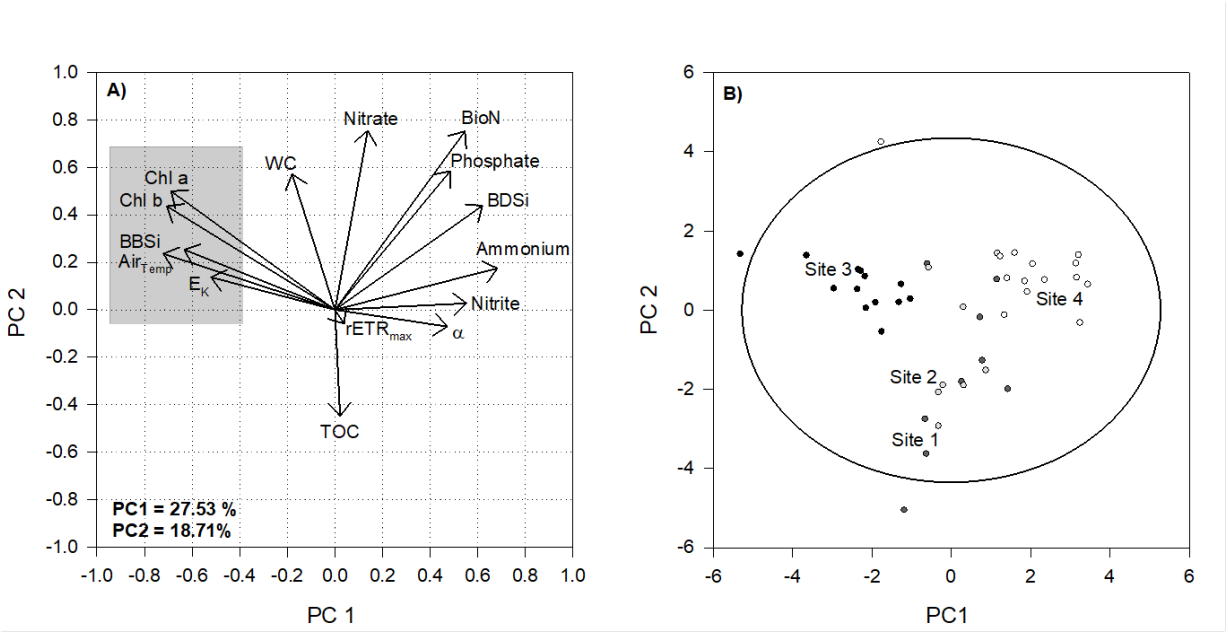

Figure 4.19: Winter Principal Component Analysis. **A)** PC1 vs PC2 loading plots. **B)** PC1 vs PC2 score plot with the 95% confidence level.

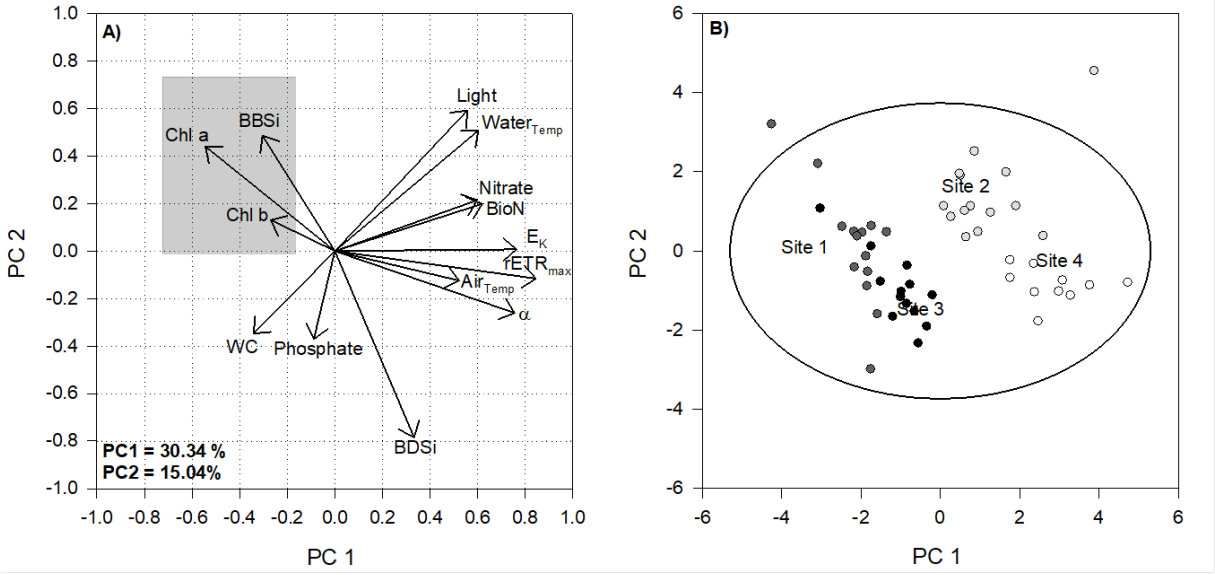

Figure 4.20: Spring Principal Component Analysis. **A)** PC1 vs PC2 loading plots. **B)** PC1 vs PC2 score plot with the 95% confidence level.

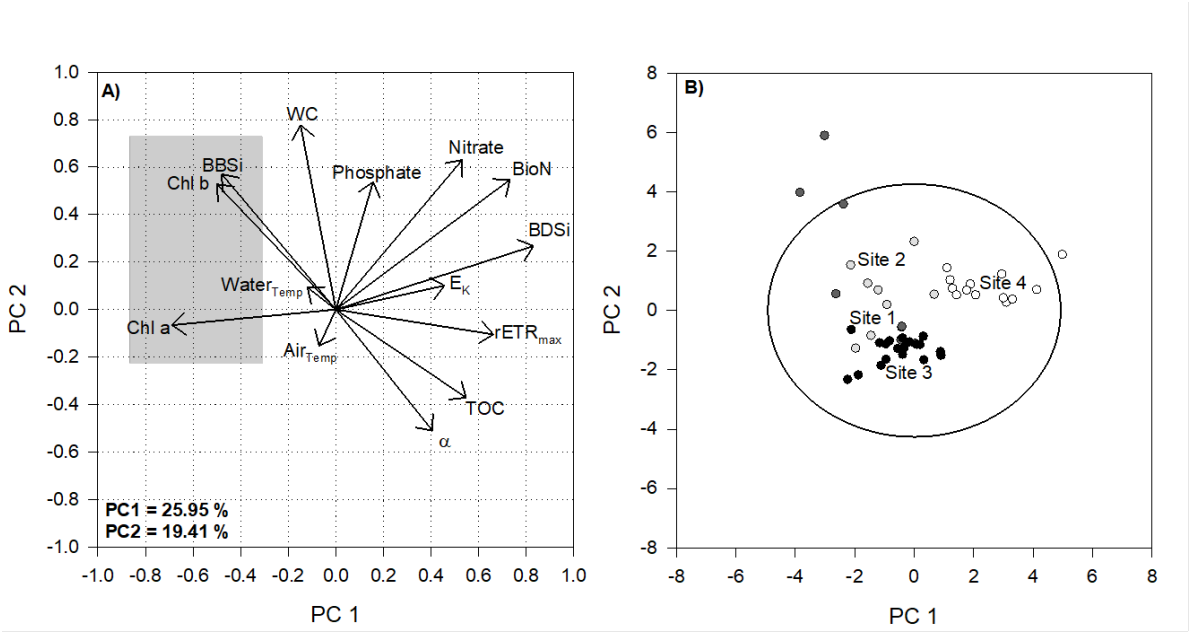

Figure 4.21: Summer Principal Component Analysis. **A)** PC1 vs PC2 loading plots. **B)** PC1 vs PC2 score plot with the 95% confidence level.

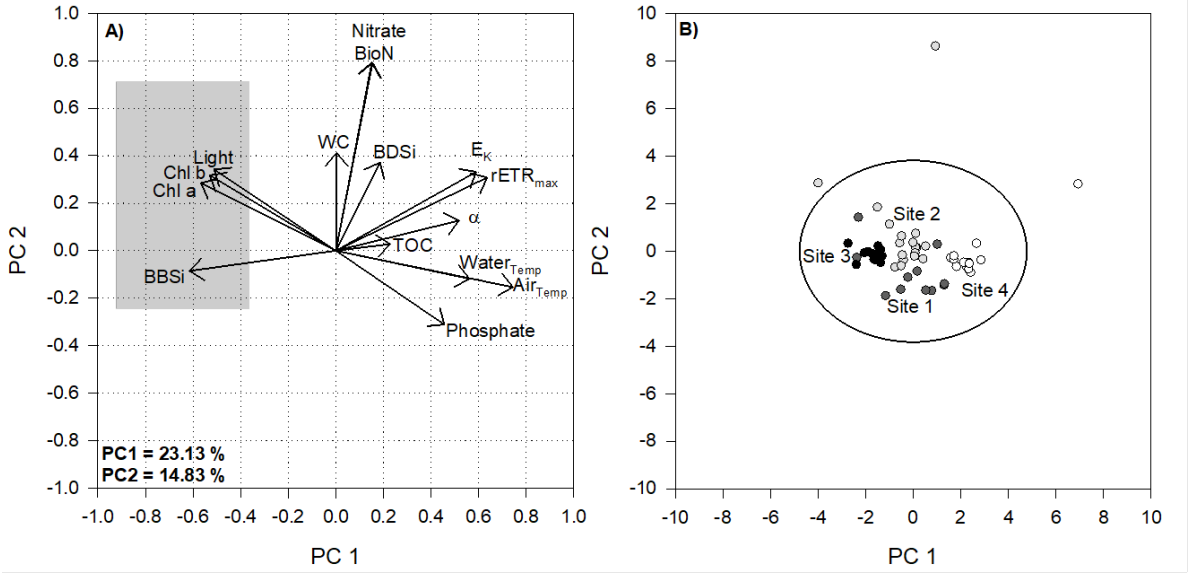

Figure 4.22: Autumn Principal Component Analysis. **A)** PC1 vs PC2 loading plots. **B)** PC1 vs PC2 score plot with the 95% confidence level.

4.4 Discussion

To understand the contribution of the benthic Si export to the pelagic Si budgets of the Severn Estuary, the benthic DSi (BDSi) and benthic BSi (BBSi) budgets on the intertidal mudflats were assessed. I hypothesised that the diatom-dominated biofilms on the intertidal mudflats had high rates of primary productivity, resulting in large biofilm biomass and the uptake of DSi and accumulation of BBSi (see Hypothesis Two in Chapter One, Section 1.5). To interpret the oscillations in these BDSi and BBSi budgets, it was important to look at the combined impact of multiple consumption/production processes, with an emphasis on the benthic biological mediation of Si, alongside environmental forcings. The following discussion aims to decipher the contribution of these forcings in mediating BDSi and BBSi.

4.4.1 Intertidal mudflat Si budgets

Mudflat DSi and BSi studies (see Table. 4.4) are relatively rare compared to the pelagic estuarine system. In the Severn Estuary, mudflat water BDSi concentrations (Fig. 4.1) were high during the cold winter sampled periods, and low during the warmer periods (Fig. 4.10), similar to Welsby et al. (2016). Despite this variability between sampled periods, the percentage of BBSi on average were low (<1%), but slightly elevated compared to the percentage of BBSi measured from the same mudflats in 2014 (see Table. 4.4). Chou and Wollast (2006) also report low (between 0.05% and 1.5%) BBSi percentages on the intertidal mudflats of the Scheldt, further supported by Arndt and Regnier (2007) and Arndt et al. (2007). The percentage of BBSi in mudflat biofilms are often low due to the dynamic nature of hypertidal and macrotidal estuaries. Strong hydro-geomorphological processes enhance the resuspension of the sediments and the associated biofilms, increasing the water column turbidity, and preventing the build-up of BBSi at the SWI. Despite the low percentage, if there is a continuous supply of BSi on each immersion period, there may be an accumulation of these remobilised biofilms and the associated BBSi in the water column. However, the contribution of remobilised BBSi to the pelagic BSi budget remains unknown and will be investigated in detail in the following chapter.

Spatio-temporal changes in the heterogeneous distributions of BDSi concentrations and the percentage of BBSi in the mudflat biofilms (Fig. 4.1) could have been influenced by several processes, including:

Biological mediation of Si

During periods of biological activity, the development of the diatom biofilms likely resulted in the uptake of DSi, which reduced mudflat water BDSi concentrations, and

Table 4.4: Benthic dissolved (BDSi) concentrations and percentage of biogenic silica (BBSi) in coastal systems.

Estuary	DSi (mg/L)	DSi (μmol/L)	BSi % of dried Si mass, g/g	Paper
Severn average (Winter)	10.9 ± 1.5	379 ± 20.0	0.59 ± 0.04	Present study
Severn average (Spring)	1.1 ± 0.3	36.8 ± 2.4	0.74 ± 0.03	Present study
Severn average (Summer)	1.0 ± 0.4	34.7 ± 3.8	0.76 ± 0.05	Present study
Severn average (Autumn)	1.2 ± 0.4	39.9 ± 3.6	0.69 ± 0.04	Present study
Severn max. (Winter)	18.8	650.5	1.66	Present study
Severn max. (Spring)	2.1	73.7	1.67	Present study
Severn max. (Summer)	4.2	144.2	1.94	Present study
Severn max. (Autumn)	3.4	118.3	1.77	Present study
Severn (summer)	2.9 ± 0.5		0.6	Welsby et al. (2016)
Severn (winter)	22.6 ± 1.0		0.5	Welsby et al. (2016)
Oder			5.16	Pastuszak et al. (2008)
Jiaozhou Bay			1.8	Liu et al. (2008)
Daguhe			1	Liu (2005)
Scheldt			0.05-1.5	Chou and Wollast (2006)
Nakdong (Korea)		140-170		Leynaert et al. (2011)
Scheldt marshes	4.1-6.4			Struyf et al. (2005a,b)
Argentine Basin		97.7		Holstein and Hensen (2010)

through enhanced rates of biomineralization, increased the potential for BBSi accumulation at the SWI. In agreement, BBSi and chl *a* content clustered in the PCA's during the winter (Fig. 4.19), spring (Fig. 4.20), summer (Fig. 4.21) and autumn (Fig. 4.22). Uniform growth of the biofilms could have led to homogeneous conditions in the percentage of BBSi, with CV as low as 34% in the spring (Table. 4.1). The biological mediation of Si is discussed in detail in the next section.

Trapping of enriched riverine PDSi in the mudflat water during emersion periods

In the upper Severn Estuary at Site 1, the strong hydrodynamic forcings (Allen, 1990; Jonas and Millward, 2010; Manning et al., 2010), whereby the combination of high flow rates and resuspension can directly and indirectly (by increasing BSi dissolution by providing Si-depleted waters) enhance diffusive transport during submersion (Raimonet et al., 2013), may have caused the enriched PDSi water column and BDSi mudflat water to mix. Upon emersion, these mixed DSi signatures may have become trapped in the pore spaces between the newly deposited sediment grains. Similarly, during submersion periods in less energetic areas of the estuary, and areas of PDSi depleted waters, the concentration gradient between the SWI and the water column could favour the diffusive flux of DSi from the sediment, reducing the mudflat water BDSi concentrations. In coastal regions, the DSi concentration of mudflat water is generally higher than that in the overlaying water column (Leynaert et al., 2011). In agreement, water BDSi concentrations on the mudflats were high in the winter sampled periods compared to the River Severn and Severn Estuary PDSi concentrations (see Chapter Three, Section 3.3.1).

Regeneration of DSi in the sediment from the dissolution of silica

A source of DSi in coastal areas is the progressive dissolution of the accumulated frustules (Iler, 1979). For example, during the winter sampled period, the stored BSi (formed during biologically productive periods) was likely temporarily preserved at the SWI (see dissolution experiment, Table. 4.2). According to Iler (1979), the dissolution rate can decrease by a factor of >10 when there's a temperature drop below 20°C. Once the temperatures increased on the mudflats (note higher dissolution rates under warm/dark and warm/light conditions, connected to thermodynamics of solubility, Fig. 4.3), the siliceous skeletal material dissolved. The dissolution of BSi is quite rapid relative to the dissolution of mineral crystalline forms (e.g. LSi), which can be considered inert for ecological purposes (Yamada and D'Elia, 1984). With increased Si dissolution rates (Table. 4.2), the percentage of BBSi in the biofilms would have decreased, whilst BDSi concentrations consequently increased (Fig. 4.5). These dissolution rates resemble culture measurements by Roubeix et al. (2008) originating from the Scheldt Tidal River

sediment. This dissolution of BSi over a year, considering all environmental conditions (i.e. cold vs warm; dark vs light), resulted in an average conversion of 6,500 ± 2,300 kg DSi/year. Scaled-up for the entire estuarine area, this resulted in a conversion of 22,800 ± 6,800 kg DSi/year (55,684 ha: Potts and Swaby, 1993) and 30,200 ± 9,000 kg/DSi/year (SAC area of 73,714 ha: JNCC, 2018) (see Table. 4.2). The dissolution rates could also have reflected adsorption or precipitation processes, decreasing the DSi concentrations (Fig. 4.3).

Note, despite homogenising the sediment prior to sub-sampling, this was an uncontrolled experiment, and ambient conditions in the laboratory may have influenced the samples that were not refrigerated. The samples that were refrigerated, likely experienced changes in dissolution associated with bacterial reactions (Longphuirt et al., 2009b). Further, the incorporation of aluminium in the BSi matrix (Van Cappellen et al., 2002) can also lower the Si dissolution rates, reducing the BDSi concentrations in the mudflat water. Aluminium concentrations were not measured in the present study, but high levels have been reported in a mosaic distribution in the muds of the Severn Estuary (Hamilton, 1979; Little and Smith, 1994). This was a preliminary experimental study, which has shown abiological processes such as Si dissolution and adsorption, could be taking place on the intertidal mudflats. A more sophisticated, controlled experiment is required to further investigate the role of dissolution/adsorption on the Si budgets of intertidal mudflats.

Remineralization

The non-monotonic increase in Si release during the laboratory dissolution experiment (Fig. 4.3), regardless of the environmental conditions, represents the dynamic exchange of Si between aqueous and solid phases, for example, Si adsorption or chemical reactions (such as reverse weathering) (Frings et al., 2016). Reverse weathering is a 'back-reaction' that recombines DSi and alkali metal cations, in the formation of secondary authigenic aluminosilicate minerals (i.e. clay) (Isson and Planavsky, 2018). Reverse weathering would reduce the concentrations of BDSi, and through the method to determine BSi (DeMaster, 1981), could increase the percentage of particulate Si, but in the form of ASi and LSi (see Chapter Three, Section 3.4.2.4).

The presence of benthic fauna enhancing DSi diffusion and BSi dissolution

Hydrobia snails which were abundant at Site 4 (*pers. obs.*), may have enhanced the transport and flushing of BDSi out of the sediment through bioirrigation, as previously described by Aller (1980a,b). Seasonal variation in the community structure of benthic bioturbating fauna may further explain the temporal induced variability in BDSi concentrations between the sampled periods in 2016. Bioturbation through increased

oxygenation of the sediment (Waldbusser et al., 2004) can also increase the degradation of organic matter, and in turn, BSi dissolution, increasing the flux of DSi from the sediment.

Deposition of BSi

Spatial variation in the estuarine energy can lead to greater deposition and burial rates in sheltered environments. Centric diatoms deposited on the intertidal mudflats likely settled depending on the energy difference associated with local tidal dynamics. Furthermore, pennate diatoms eroded into the water column can live, and deposit elsewhere, subsequently transporting the BSi around the estuary.

The combination of the above processes likely drove the high spatial heterogeneity in BDSi between the sampled mudflats, with CV reaching highs of 85% (Table. 4.1). CV values of BDSi are often high, for example, CV of 59% in the Elorn and Aulne Estuaries of the Bay of Brest (Raimonet et al., 2013) and 40% in the Indian River Estuary in Florida (Montgomery et al., 1979). These high CV values reflect the large heterogeneity of water properties on intertidal mudflats, highlighting the uncertainties that stem from upscaling these values to global scales. BBSi on the other hand only reached highs of 51% and was more spatially homogeneous compared to BDSi.

It is important to note, that only four intertidal mudflats could be sampled in 2016 due to time commitments (i.e. sampling the Severn Estuary water column, tributaries and processing of samples), leaving large gaps between sampling events. In addition, only one mudflat on the Welsh coast could be sampled due to accessibility issues. Accessibility issues are often reported as a problem in studies on the Severn Estuary (Underwood, 2010), with previous published systematic surveys only on the English coastline, and with no studies carried out upstream towards Sharpness. This relatively low spatial coverage has left gaps in our understanding of the benthic Si cycle on these intertidal mudflats, which place limitations on our interpretation of the ecological and ecosystem functioning, along with associated errors in upscaling.

4.4.2 Benthic biological mediation of silicon on the intertidal mudflats

Biological mediation of Si by the diatom-dominated biofilms on the intertidal mudflats of the Severn Estuary was investigated to determine the effects of biological activity on the concentrations of BDSi and biofilm percentage of BBSi. This biological mediation was tested through the variability in MPB biomass, and diatom electron transport rate (a proxy for primary productivity) between the sampled periods in 2016 and the mudflats. These are discussed in detail below.

4.4.2.1 Microphytobenthos biomass

Spatio-temporal variation between sampled sites and periods in 2016

Average MPB biofilm biomass (chl *a* content) increased between sampling periods during 2016 to reach significantly high values of 116.8 μg/g *dw. sed.* in the autumn (Fig. 4.6). Compared to published data from systematic surveys of the same mudflats between 1990 and 1991 (Underwood and Paterson, 1993; Yallop et al., 1994), the MPB biomass was higher in 2016 (Table. 4.5). However, it would be presumptuous to conclude MPB biomass had increased over the past *ca.* 30 years. For example, high spatial biofilm heterogeneity and targeting extensive biofilms in the 2014 (Welsby et al., 2016) and 2016 sampling schemes may have induced bias. Further, inconsistency between the chl extraction method (acetone vs methanol) may have led to discrepancy between the measured biomass levels. Note, the similarity between the chl *a* contents presented here and previous measurements (Table. 4.5) in the Severn Estuary, may suggest the acetone extraction was relatively successful at least for chl *a*. There is also evidence of high temporal variability in the MPB biomass levels in these mudflats (Table. 4.5), a common characteristic of estuarine intertidal MPB assemblages (Underwood, 2010). This temporal variability is not exclusive to periods over months or years but has been shown to fluctuate daily. For example, Underwood and Paterson (1993) report changes in biofilm chl *a* content over an eight-day sampling period in the upper estuary (Aust) of *ca.* 60 μg/g *dw. sed.*, attributing the variation to changes in sediment deposition. Alternatively, some estuaries may not experience any temporal variability, for example the Tagus Estuary, Portugal (Brotas et al., 1995; Cabrita and Brotas, 2000). However, the Tagus Estuary only has a tidal range of 2.6 m, leading to less erosion-deposition controls.

MPB biomass also displayed spatial variability among the sampled mudflat sites. Chl *a* content was relatively low, varying between 1.9 and 41 μg/g *dw. sed.* each sampled period in the upper estuary (Site 1) (Fig. 4.6). Underwood (2010) also report relatively lower chl *a* values in the upper estuary (Aust). High tidal energy and regular resuspension likely prevented the establishment of dense MPB biofilms, and subsequently, would have reduced the accumulation of BBSi at Site 1, which recorded minimum values each sampled period (Fig. 4.1). Low biomass content could also be explained by changes in the MPB assemblage due to changes in nutrient supply. Relatively high ammonium concentrations were recorded in the sampled periods of 2016 (Fig. 4.17), which reflect the close proximity of human settlement to Site 1 (Severn Beach). Further, sediment composition could have influenced the chl *a* content, with high coarse sediment at Site 4 (Sand Bay) (Fig. 4.6). Underwood (2010) report low MPB biomass content (<1.0 μg/g *dw. sed.*) in the mudflats near Hinkley Point in the Bristol Channel, and attributed these low biomass levels to a high proportion of fine sands.

Table 4.5: A summary of the average benthic biomass (chl *a* content) in the Severn Estuary for all sampled periods. Note, sourced literature chl *a* content ranges from different tide heights.

Location	Chl a	Unit	Year	Source
Aust	12.9-20.7 (*n=24*)	μg/g dw. sed.	1990-1	Underwood (2010)
Aust	7.6-19.9 (*n=63*)	μg/g dw. sed.	May 1991 - September 1992	Yallop et al. (1994)
Severn Beach	14.4 $\pm$ 1.4 (*n=59*)	μg/g dw. sed.	2016	Present study
Severn Beach	11.1 $\pm$ 1.2 (*n=12*)	mg/g dw. sed.	summer 2014	Welsby et al. (2016)
Severn Beach	24.5 $\pm$ 3.2 (*n=12*)	mg/g dw. sed.	winter 2014	Welsby et al. (2016)
Portishead	63.1 $\pm$ 14.3 (*n=60*)	μg/g dw. sed.	2016	Present study
Portishead	11.3 $\pm$ 2.1 (*n=12*)	mg/g dw. sed.	summer 2014	Welsby et al. (2016)
Portishead	19.2 $\pm$ 1.6 (*n=12*)	mg/g dw. sed.	winter 2014	Welsby et al. (2016)
Portishead	12.1-20.8 (*n=62*)	μg/g dw. sed.	May 1991 - September 1992	Yallop et al. (1994)
Portishead	13.1-174.8 (*n=51*)	μg/g dw. sed.	1999	Yallop et al. (2000)
Portishead	5.9-59.7 (*n=35*)	μg/g dw. sed.	March 1991 - February 1992	Underwood and Paterson (1993)
Newport Wetlands	83.3 $\pm$ 10.9 (*n=60*)	μg/g dw. sed.	2016	Present study
Newport Wetlands	17.3 $\pm$ 1.7 (*n=12*)	mg/g dw. sed.	summer 2014	Welsby et al. (2016)
Newport Wetlands	26.6 $\pm$ 3.2 (*n=12*)	mg/g dw. sed.	winter 2014	Welsby et al. (2016)
Sand Bay	75.7 $\pm$ 14.3 (*n=60*)	μg/g dw. sed.	2016	present study
Sand Bay	9.9-31.8	μg/g dw. sed.	March 1991 - February 1992	Underwood (2010)

Presence of non-siliceous organisms

Changes in the MPB biofilm assemblage, whereby non-siliceous organisms outcompete epipelic pennate diatoms, may have consequences on the benthic biofilm's ability to biologically mediate Si. BBSi and TOC concentrations from the intertidal mudflats lacked correlations (Fig. 4.8), suggesting the organic matter measured in the sampled periods of 2016 was not of a siliceous origin. An increase in cyanobacteria and euglenoids abundance (Fig. 4.11), suggest there were changes in the MPB community, as organisms responded to more favourable species-specific growth conditions (Fig. 4.10). Cyanobacteria, euglenoids and green algae have previously been documented in the Severn's intertidal mudflat MPB assemblages (Yallop et al., 1994; Underwood, 2010).

Chl *b* pigment content, a proxy for the presence of green algae, was present in each sampled period of 2016, with significantly high contents in the summer at Site 3, on the mudflats adjacent to Newport Wetland and Saltmarsh. Peak chl *b* content was accompanied by high TOC concentrations (Fig. 4.7), most likely associated with high levels of peat (*pers. obs.*). Further, runoff from the wetlands and saltmarshes could have transported organic matter to the mudflats. In addition, Welsby et al. (2016) report peak bulk biomass and high BBSi percentages at this location in 2014, attributing the biofilm growth to terrestrial nutrient inputs, along with the supply of detrital BSi, e.g. phytoliths (Conley, 2002), which are enriched in wetlands and saltmarsh environments (Norris and Hackney, 1999; Struyf et al., 2005a,b). These terrestrial Si inputs may also explain high percentages of BBSi at Site 3 in the summer sampled periods of 2016 (Fig. 4.1), and the clustering of BBSi and chl *b* pigments (Fig. 4.21). In addition, unfavourable growth conditions may have hindered diatom growth at Site 3. For example, peak water content (75%) and large sediment grain size (Fig. 4.16) would have reduced sediment stability, impeding the establishment of a diatom-dominated biofilm, and promoting the abundance of cyanobacteria and euglenoids (Underwood, 2010). The poorly sorted sediment may have further reduced BDSi concentrations (Raimonet et al., 2013), as observed in the Scheldt Estuary (Rebreanu, 2009), which may have become limiting (Fig. 4.18). Studies (Busby and Lewin, 1967; Davis, 1976; Doering et al., 1989; Sigmon and Cahoon, 1997) suggest diatoms do not have the ability to store silica intracellularly, and require immediate DSi availability prior to cell division.

4.4.2.2 Diatom photosynthesis

The biological mediation of Si by the benthic diatoms has also been evaluated based on the diatom's electron transport rate, a proxy for primary productivity. Further, analyses of the photoprotective mechanism carried out by diatoms, in terms of both behavioural (cell movement) and physiological (NPQ) down-regulation, has provided a depiction of the diatom's activities in these biofilms. The potential impact of these

photoprotective mechanisms on the diatoms ability to survive the harsh conditions of the intertidal mudflats, and consequently on the ability of the diatoms to assimilate DSi to BSi are discussed below.

Presence of photoprotective mechanisms aiding diatom photosynthetic rates

The optimum irradiance levels to maximise $rETR_{max}$ for the Severn Estuary diatom biofilms sampled in different periods of 2016, was likely reached during the winter and autumn sampled periods, as well as the spring sampled periods at Site 3 and 4, where the RLCs saturated (Fig. 4.12). The saturation of 80% and 100% of the winter and autumn RLCs (Fig. 4.12) could have been associated with photoprotective mechanisms. For example, at irradiance levels >400 μmol photons/m^2/s, F' declined (Fig. 4.14), whilst Y(NPQ) increased (Fig. 4.15), indicating diatoms began to regulate these higher irradiance levels by inducing NPQ and/or vertically moving to lower irradiance levels in the sediment. The latter, which is known to occur during light curves, can hamper the validity of RLCs and the associated physiological parameters (Serôdio et al., 2006). However, the Y(PSII) values were sensible (i.e. indicate healthy cells and align with expected values in literature) (see Fig. 4.13), leading to the saturation of the RLCs (Fig. 4.12) and feasible estimates of rETR and thus $rETR_{max}$, which indicates NPQ induction occurred (Fig. 4.15), or either there was reduced vertical cell movement, and/or a change in the species community. NPQ induction could have resulted in the quenching of Y(NO) and Y(PSII) (Fig. 4.15). However, Y(NPQ) was less than Y(NO) (Fig. 4.15) throughout the RLCs, and the maximum ratio between the regulated NPQ and the non-regulated energy dissipation [Y(NPQ)/Y(NO)] remained below 1, where, Y(PSII) + Y(NPQ) + Y(NO) is always unity (Klughammer and Schreiber, 2008). Therefore, regulated NPQ induction occurred, but Y(NPQ) was not enough to cause a decrease in Y(NO).

In comparison, vertical cell movement could have prevented 78% and 100% of the spring (Site 1 and 2) and summer RLCs (respectively) from reaching saturation, and overestimated the rETR (Fig. 4.12) and $rETR_{max}$ (Fig. 4.13) values, as reported in Perkins et al. (2010a). Overestimation of rETR in sediments due to cell movement and changes in species community at the sediment surface during the RLC (i.e. 'deep layer fluorescence'), have been reported extensively (Kromkamp et al., 1998; Serôdio, 2004; Jesus et al., 2006; Cartaxana and Serôdio, 2008; Mouget et al., 2008; Perkins et al., 2010a,b). This overestimation can be in the orders of 60% according to Forster and Kromkamp (2004). In the spring (Site 1 and 2) and summer RLCs, at low PAR, Y(PSII) initially increased, potentially associated with NPQ reversal and/or cell movement. Physiologically, increasing irradiance is highly unlikely to induce NPQ reversal and hence this supports the hypothesis that diatoms performed behavioural down-regulation through vertical cell movement into the sediment and into a lower light field

to prevent photoinhibition (Fig. 4.10). At higher PAR levels, Y(PSII) decreased, but at a lower rate than the Y(PSII) values measured from the winter and autumn sampled periods (Fig. 4.15). Further, Y(NPQ) remained below Y(NO) throughout the RLC and displayed little increase at higher actinic light levels (Fig. 4.15), suggesting diatoms preferentially used cell movement rather than inducing regulated NPQ during these RLCs.

In summary, the RLCs that didn't saturate indicate vertical cell movements, and during these periods of cell movement, there was less down-regulation via the induction of NPQ. Similar scenarios were reported in Perkins et al. (2010a), where cell movement was energetically more favourable than physiological down-regulation (NPQ), indicating regulated NPQ is a secondary response to light with cell vertical movement the driving function to optimise photosynthetic rate when cell movement is possible, in agreement with Serôdio (2004), Cartaxana et al. (2011), Serôdio et al. (2012) and Laviale et al. (2015). However, to truly disentangle whether diatoms were inducing NPQ or vertically moving in the sediment during these sampled periods, further research is required. For example, using motility inhibitors such as Latrunculin A (Lat A) (Cartaxana et al., 2008), which does not have adverse effects on the photosynthetic activity by inducing the xanthophyll cycle, could tease out whether the diatoms induced NPQ or vertically moved into deeper sediment layers. Nevertheless, considering the maximum rETR from the saturated RLCs (Fig. 4.13), along with the diatoms ability to optimise photosynthesis through combined down-regulation mechanisms, these likely contributed to the diatoms success and the formation of biomass-rich MPB biofilms (Fig. 4.6). Subsequently these highly productive biofilms would have increased the biofilms potential to assimilate DSi to BSi. For example, Saburova and Polikarpov (2003) study indicates that biofilm bulk biomass has the potential to assimilate DSi. Further, Sigmon and Cahoon (1997) suggest fluxes of DSi were controlled by daily fluctuations in photosynthetic activity. However, whether migration processes directly influence DSi uptake dynamics and the accumulations of BBSi, remains unknown (Longphuirt et al., 2009a).

Environmental factors influencing diatom photosynthetic rates

The preference to induce NPQ or vertically move to deeper sediment may have originated from species-specific adverse conditions. Possible factors that could have influenced diatom photoprotection and photosynthetic rates, including temperature, irradiance, and species, are discussed below.

Temperature

Cold weather can reduce diatom metabolic activity at the SWI, leading to lower cell movement. Previous studies have linked reduced cell movement to lower temperatures (Round and Palmer, 1966; Cohn et al., 2003; Du et al., 2010, 2012; Welsby et al., 2016).

For example, Serôdio et al. (2005a) on MPB biofilms from Ria de Aveiro, Portugal, report seasonal changes in NPQ operation as a factor of temperature, with more NPQ induction in November compared to the biofilms sampled in July. Anning et al. (2001) also report the xanthophyll pool size in diatoms increases in response to lower growth temperatures. Further, at relatively high temperatures that result in sediment desiccation, vertical movement is likely to be restricted (Laviale et al., 2015). Vieira et al. (2013), investigating how temperature and irradiance affect ETR by fitting the model of Blanchard et al. (1997), estimate an optimum temperature of between 34 and 35°C. Air and water temperature on the intertidal mudflats were significantly higher in the summer sampled periods in 2016, with air temperatures having increased from an average of 8.7 ± 0.4°C in the winter to 20.3 ± 0.6°C in the summer (Fig. 4.10). With more RLCs saturating in the winter and autumn sampled periods (Fig. 4.12), and a lack of saturation in the warmer summer sampled periods (Fig. 4.12) associated with vertical cell movement (Fig. 4.15), temperature may have been a contributing factor in determine the balance between photophysiological and behavioural forms of down-regulation, with diatoms preferentially inducing NPQ when acclimated to lower temperatures, when cell movement is reduced.

Irradiance

Irradiance can fluctuate greatly over an emersion period and can impact directly on the photosynthetic rates and forms of photoprotection. For example, Chevalier et al. (2010) note a higher $rETR_{max}$ measured in the afternoon compared to the morning. In this study, the chlorophyll fluorescence measurements were sampled between *ca.* 11:00 hrs and 16:00 hrs, and the spatio-temporal variability in the photosynthetic parameters (Fig. 4.12, 4.13, 4.14, 4.15) could be attributed to the diurnal cycle (light and tidal cycles) (**?**Kromkamp et al., 1998; Serôdio et al., 2006). All sampling periods coincided with spring tidal cycles. However, the mudflats in the summer could have been exposed to more harsh conditions over these long emersion periods (higher irradiance levels and sunshine hours), potentially contributing to the diatom preference for cell movement.

High irradiance levels have been associated with behavioural forms of photoprotection (Kromkamp et al., 1998; Serôdio et al., 2006; Cartaxana and Serôdio, 2008; Perkins et al., 2010a; Laviale et al., 2015; Cartaxana et al., 2016). Serôdio et al. (2012) on temperate mudflat sediments studied *ex situ*, report epipelic communities were able to withstand high irradiance levels of up to 1200 μmol/m^2/s for 3 hours. This high irradiance is similar to the average irradiance level of 1253 μmol/m^2/s recorded in the summer sampled periods (Fig. 4.10), suggesting with higher PAR values the RLCs would have saturated (Fig. 4.12), if cells motility was reduced. These diatom communities, which lacked RLC saturation (Fig. 4.12), may not have been acclimated to high light (overestimated E_K) but low light, and had a higher efficiency of limiting irradiance (high α).

Diatom communities which resulted in saturated RLCs were similarly acclimated to low light levels (low E_K) associated with lower irradiance levels (Fig. 4.10) and less sunshine hours (Fig. 4.9), and were also able to maximise electron transport with NPQ and/or cell movement maintaining a relatively high α (Fig. 4.13).

Changes in species composition

The diatom community sampled in different periods of 2016 was assessed based simply on the abundance (cell count) of pennate (and centric) diatoms, alongside the abundance of euglenoids and cyanobacteria (Fig. 4.11). Note, no discrimination was made for living or dead cells. The MPB biofilms community changed between the sampled periods (Fig. 4.11), however, the high epipelic pennate abundance on the mudflats, regardless of the time of year sampled, would suggest these biofilms were diatom-dominated, in agreement with Underwood (2010). Further, Oppenheim (1988) and Oppenheim (1991) report the presence of 65 diatom taxa on these intertidal mudflats. Nevertheless, changes in the diatom community and genera could have influenced the photophysiological parameters (Underwood et al., 2005; Serôdio et al., 2012; Laviale et al., 2015; Barnett et al., 2015).

Spatio-temporal variability in sediment composition can drive changes in the biofilm communities from epipelic diatoms in cohesive sediment to epipsammic communities of less motile diatoms in sandy substrata, where cell migration is absent (Jesus et al., 2009) and NPQ capacity is high (Barnett et al., 2015; Blommaert et al., 2018). In support of this theory, Site 3 and 4 RLCs during the spring sampled periods saturated (Fig. 4.12). These sites were characterised by sandy substrata (Fig. 4.16), indicating the presence of less mobile diatoms, favouring regulated NPQ.

Changes in species composition could also have been responsible for the abnormally high chl *a* contents measured in the autumn sampled periods (Fig. 4.6). This autumnal peak in biomass was unexpected due to the less favourable environmental growth conditions, including lower air and water temperatures, reduced number of sunshine hours of significantly low irradiance levels (Fig. 4.10), and significantly low nutrient levels (Fig. 4.17). With all four sampled mudflats showing a peak in chl *a* content, a common factor, irrespective of spatial differences associated with the site conditions, was likely influencing these short-term changes. Most likely, a change in species composition occurred, in favour of cold-acclimated species, associated with seasonal changes in salinity, irradiance levels, temperature, water content and sediment organic matter, as previously described by Underwood (2010). Further, during the winter and autumn sampled periods, chl *a* and chl *b* clustered in the PCA (Fig. 4.19 & 4.22), indicating an increase in the presence of green algae (Fig. 4.6). Species-specific responses to changes in other environmental conditions (e.g. temperature, irradiance levels) could also have accounted for the balance between behaviour and physiological forms of down-regulations, as previously reported

by Paterson (1986), Hay et al. (1993), and Underwood et al. (2005). The combination of these environmental pressures along with changes in the species community, may have been responsible for low photochemical efficiency in the dark-adapted state (F_v/F_m) (Table. 4.3).

Delving into the taxonomy and community structure of the MPB biofilms in detail was not possible in the present study, but further research should build on the works of e.g. Jesus et al. (2006), Salleh and McMinn (2011), and Vieira et al. (2013) to investigate the role of environmental parameters on diatom photosynthetic activity and the balance between behavioural and physiological forms of down-regulation.

4.5 Conclusions

Benthic biofilm dissolved silicon concentrations (BDSi) and benthic biogenic silica (BBSi) on the intertidal mudflats of the Severn, were evaluated for sampled periods in 2016. BBSi content was low but in-line with previous estimates in the Severn, and compared well to other estuarine systems. The percentage of biofilm BBSi was low during the cold winter sampled periods, which contributed to significantly high BDSi concentrations. The spatio-temporal distribution of BDSi and BBSi on the mudflats were coupled to several factors, including: biological mediation by the diatom biofilms (MPB biomass and diatom photosynthetic rate); hydro-geodynamics (deposition, burial and resuspension); abiological processes (Si dissolution and reverse weathering); and bioturbation by the benthic fauna aiding the dissolution of BSi and the diffusive flux of DSi.

Biofilm bulk biomass levels were high but conformed with previous studies on these mudflats. Despite the high abundance of diatoms, the mudflats adjacent to wetlands and saltmarshes were also associated with non-siliceous organisms such as green algae. Chlorophyll fluorescence technique has been applied directly to the biofilms, bringing a new dataset to the current literature on photosynthetic rates in *in-situ* biofilms, which is essential as variations in environmental factors can greatly modify the behaviour and functioning of diatoms. The epipelic diatom-dominated biofilms were shown to have high productivity ($rETR_{max}$ of up to 223 *rel. units* in autumn). Diatoms were shown to induce both behavioural and photophysiological forms of down-regulation to mitigate adverse conditions such as temperature and irradiance. These photoprotective mechanisms likely allowed the diatoms to maximise photosynthetic efficiency, and through high rates of photosynthesis, maximised BDSi uptake and biomineralization, aiding the accumulation of BBSi. The productive diatoms, which are highly adapted to the harsh conditions on the mudflats, would have had high turn-over rates between immersion periods, increasing the potential to establish BBSi in a short period of time. This agrees with the hypothesis stated in Chapter One (see Section 1.5). Upon immersion, the newly formed biofilms and BBSi, may have been transported into the water column during resuspension by the fast-flowing tidal currents. The BBSi on the intertidal mudflats may have thus contributed to the pelagic BSi budget. However, prior to the incoming of the tide, many diatoms often migrate down into the sediment to prevent becoming resuspended. Whether these diatoms are eroded and contribute to the pelagic BSi budget, remains unquantified. Further, the effects of biostabilization on the resuspension of BBSi is unknown. This will be further explored in the following chapter.

4.6 Appendix

4.6.1 Rapid Light Curves

Individual Rapid Light Curves (RLCs) produced on each mudflat in the winter (Fig. 4.23), spring (Fig. 4.24), summer (Fig. 4.25) and autumn (Fig. 4.26) sampled periods, displayed spatial variability.

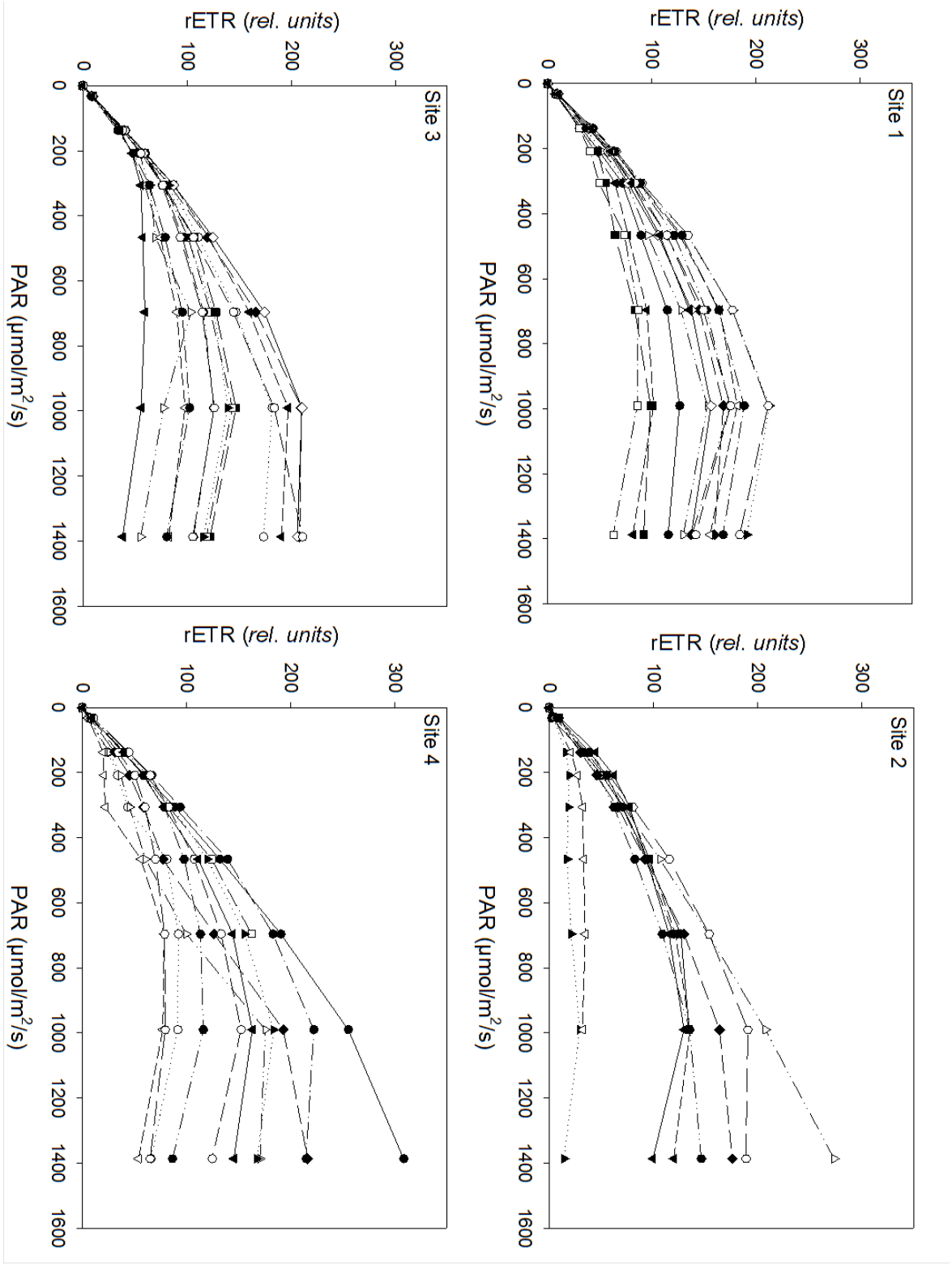

Figure 4.23: Winter Rapid Light Curves.

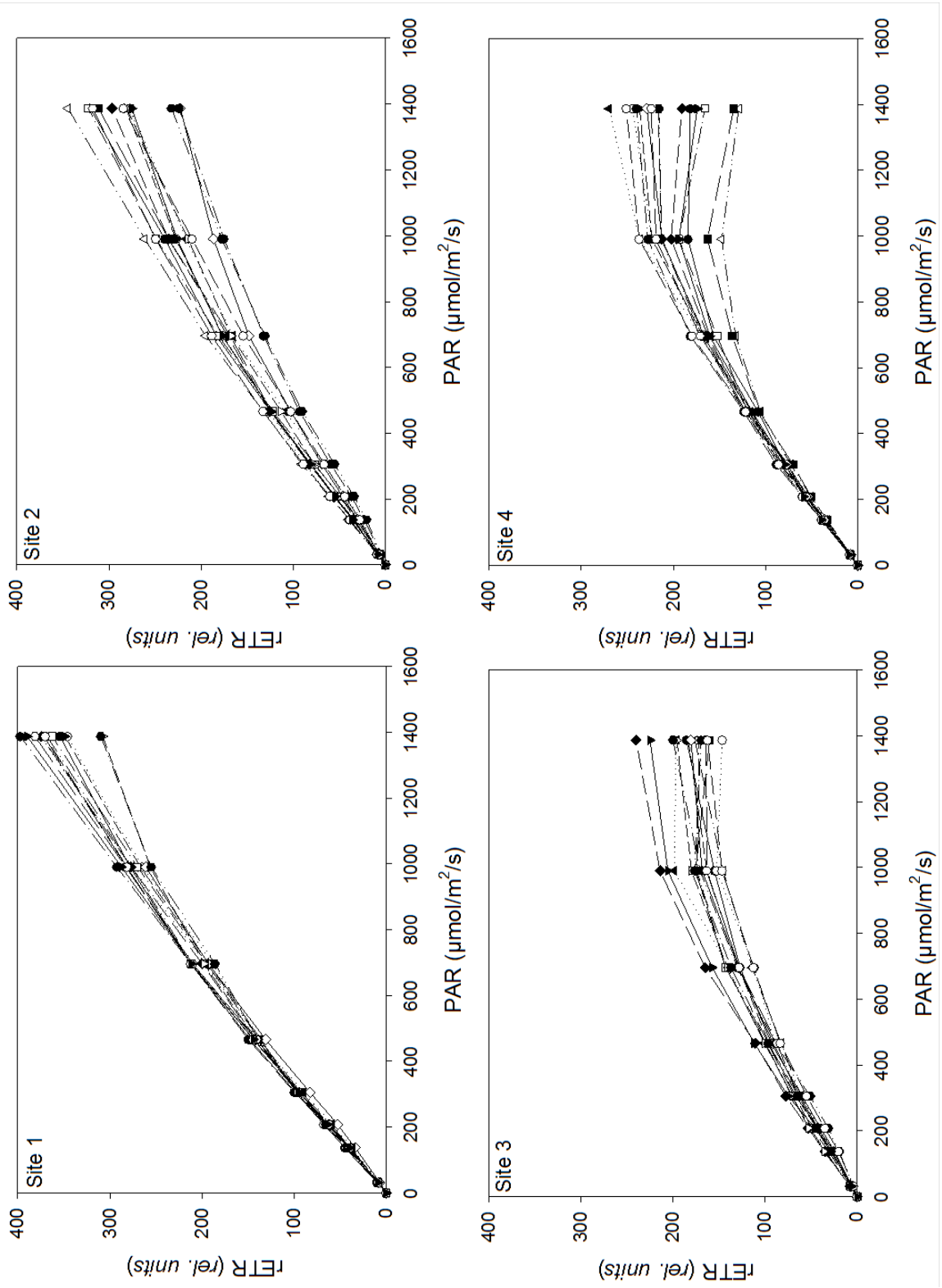

Figure 4.24: Spring Rapid Light Curves.

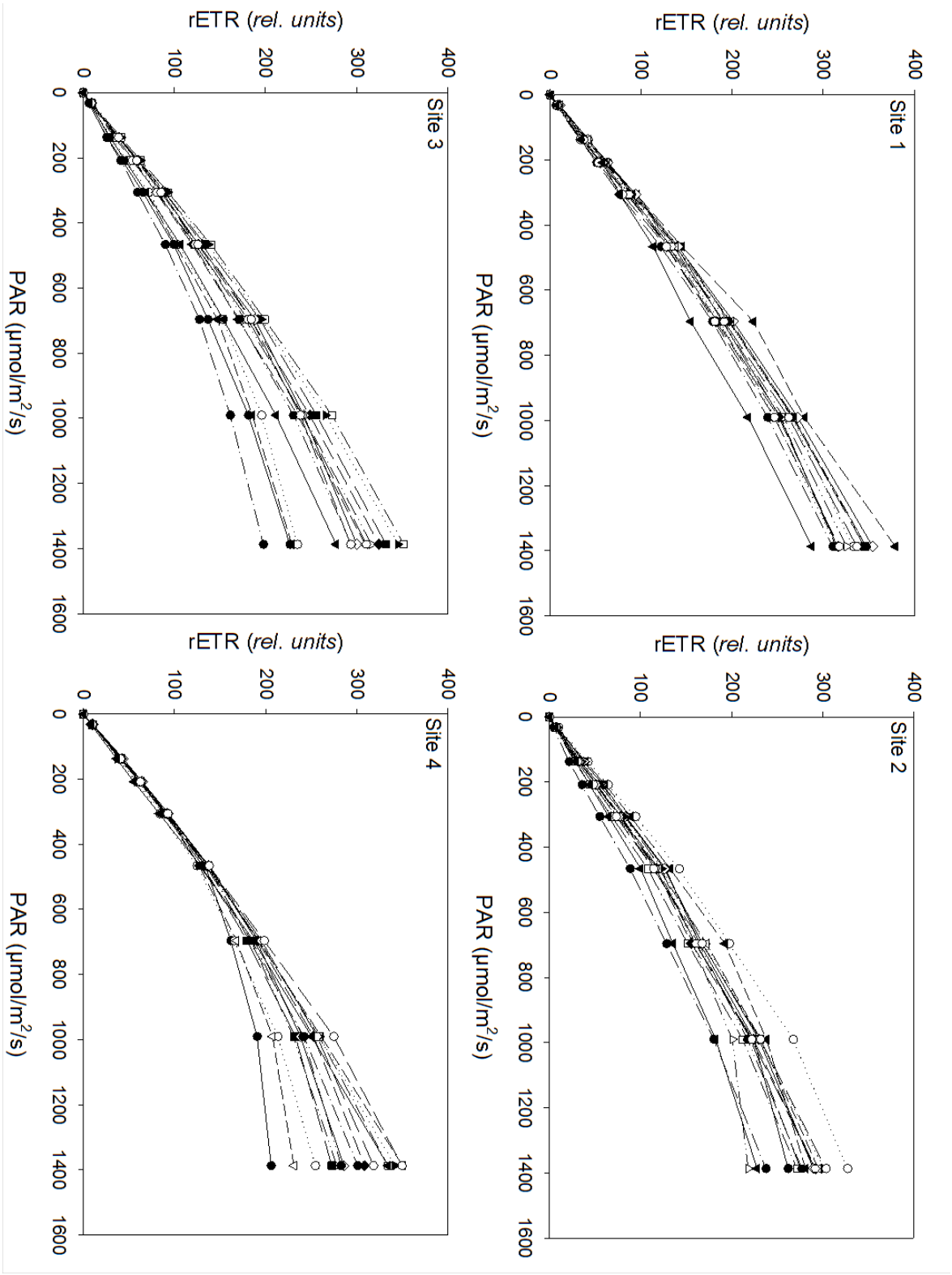

Figure 4.25: Summer Rapid Light Curves.

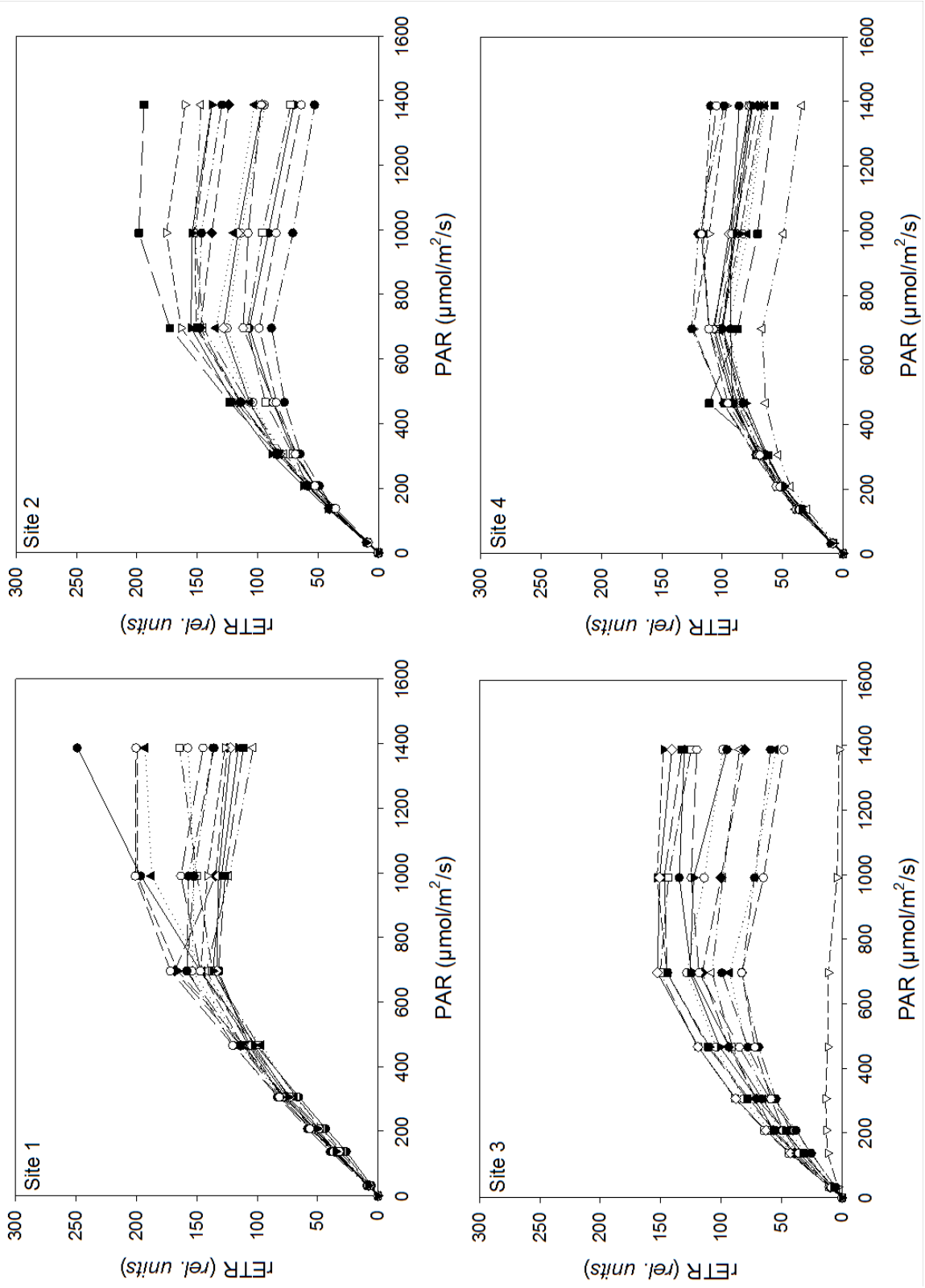

Figure 4.26: Autumn Rapid Light Curves.

Chapter 5

Benthic intertidal mudflat silicon supply: a biostabilization study

5.1 Introduction

The microphytobenthos (MPB), an assemblage of benthic microalgae and bacteria (e.g. pennate diatoms, euglenophytes, green algae, cyanobacteria, heterotrophic protists and heterotrophic bacteria) inhabiting the sediment-water interface (SWI), have high rates of biogeochemical cycling (Arndt and Regnier, 2007), and play a vital role in mediating nutrient flux between the benthic and pelagic system. For example, benthic pore fluids are often enriched in dissolved silicon (BDSi) and other macronutrients, which drive strong gradients and conditions for diffusive flux from the sediment into the water column when submerged (Leynaert et al., 2011). Ragueneau et al. (2002) in the Bay of Brest in France, demonstrated the importance of this benthic DSi flux in supporting pelagic phytoplankton during biologically productive periods when riverine DSi supply was low. However, multiple inter-connecting forces control this flux of DSi. For example, the uptake by diatom-dominated MPB biofilms at the SWI (Sigmon and Cahoon, 1997; Bartoli et al., 2003), and the formation of burrows by benthic fauna, which enhance DSi flux through bioirrigation (Aller, 1980a,b; Raimonet et al., 2013). These MPB biofilms further act as a barrier, reducing the flux of DSi and other nutrients from the sediment (MacIntyre et al., 2004). Previously in this study, the changes in DSi concentrations along the estuarine gradient, in both the pelagic and benthic realms, has been partially attributed to the diffusive flux of BDSi from the intertidal mudflats. To my knowledge, the diffusive flux of BDSi at the SWI of the intertidal mudflats of the Severn Estuary, is yet to be explored. Whether this diffusive flux is comparable to the amount of pore fluid BDSi resuspended upon erosion of the mudflats, is also unknown.

Microbial metabolism results in the secretion of various long chain molecules, collectively called extracellular polymeric substances (EPS) (Underwood et al., 1995). These

secretions can form polysaccharides and glycoprotein-rich mucilage, an organic-rich network surrounding sediment and detrital particles (Yallop et al., 2000). This self-assembled, interconnected biofilm at the SWI increases sediment particle cohesion and impedes erosion (Underwood and Smith, 1998; Tolhurst et al., 2002). This process has been defined as 'biostabilization', and has been well documented in intertidal environments (Underwood and Paterson, 1993; Paterson, 1994; Tolhurst et al., 1999; Blanchard et al., 2000; Decho, 2000; Yallop et al., 2000). The biological polymeric substances not only aid in sediment stability (reduces the removal of biofilms by tidal action), but also supports diatom motility in order to avoid photodamaging irradiance levels (Mouget et al., 2008), and performs a variety of other functions including protection against desiccation, extremes in pH and salinity, and increases the MPB resistance against pollutants/toxins (Decho, 1990). An explanation of sediment biostabilization is given in Chapter One (Section 1.3.3), and references within. The extent to which sediment biostabilization by diatom-dominated biofilms influences the mudflat the concentrations of BDSi and the percentage of biofilm BBSi, remains to be resolved.

Biofilms in tidal-dominated estuaries experience frequent periods of resuspension during immersion, for example, 20-40% resuspension rates in the Ems Estuary (De Jonge and Van Beuselom, 1992), which enhances floc formation and turbidity in the water column. Measurements on the benthic diatoms on the intertidal mudflats of the Severn Estuary [Chapter Four, and the publication by Welsby et al. (2016)], report highly productive and biomass-rich biofilms, which had the potential to accumulate benthic biogenic silica (BBSi). Despite these high rates of productivity, upon immersion, the high tidal current velocities (Uncles, 2010) could erode the biofilms (see Chapter Three, Section 3.4.4). The erosion of the mudflats supplies sediment and potentially BBSi to the pelagic zone, preventing the significant build-up of BBSi at the SWI of these mudflats. Reported in Chapter Three (Section 3.4.4), the bottom shear stress (spring tide: 55.2 N/m^2, neap tide: 13.8 N/m^2), determined by the quadratic friction law (Arndt et al., 2007), exceeded, especially under spring tide conditions, previous erosion thresholds estimates on these mudflats [e.g. 3.33-10.8 N/m^2 in Yallop et al. (2000)]. It was hypothesised that this benthic Si export was a source to the relatively high PBSi concentrations in the estuarine water column during the summer and autumn sampled periods of 2016, due to the strong correlation between SPM and PBSi, and the lack of riverine PBSi inputs. Further, the resuspension of the polymer-rich matrix accompanying the benthic diatoms was suggested to have resulted in bioflocculation, and the accumulation of both SPM and BSi in the upper estuarine bottom waters. The erosion, deposition (during low bed shear stress conditions) and flocculation of sediment in the Severn Estuary, have been explained in detail in complimentary reviews by Kirby (2010) and Manning et al. (2010). The concentration of BBSi and BDSi supplied to the water column through the erosion of the MPB biofilms, is unknown. As a result, this

chapter has the following aims:

- Determine the erosion rates of BDSi and BBSi.
- Determine the diffusive flux of BDSi from the SWI to the overlying water.
- Determine sediment stability and the impact of biostabilization on the budgets of BDSi and BBSi.

5.2 Methodology

5.2.1 Pilot study

Sampling was carried out on four intertidal mudflats of the Severn Estuary, UK: Site 1, Severn Beach (51°57′N, 2°67′W), Site 2, Portishead (51°49′N, 2°77′W), Site 3, Newport Wetlands (51°53′N, 2°95′W), and Site 4, Sand Bay (51°38N, 2°97′W). For continuity, the same mudflats that were sampled in 2016 were sampled for this study. In August 2017, a pilot study was carried out. Up to 10 stations were sampled on each mudflat. Surface water BDSi concentrations (mg/L) were measured, alongside the percentage of biofilm BBSi. This procedure followed the fieldwork sampling methodology described in Chapter Two (Section 2.1.2). Sediment grain size, water temperature and conductivity were also measured at each station. Further, a Cohesive Strength Meter (CSM) was used to determine the equivalent horizontal bed shear stress (τ_0 in N/m^2) and the shear velocity (U*). For the results of this pilot study, see this chapter's Appendix (Section 5.6). In September 2018, this pilot study was built-upon, with five stations surveyed using a random-sampling scheme to target areas of extensive biofilms at each of the four mudflats noted above. This experiment is described in detail below.

5.2.2 BBSi content

MPB biofilm mini-cores with a diameter of 2.54 cm were taken at each station for the surficial 5 mm biofilm. Samples were dried at 85°C for 24 hrs to determine the percentage loss of mass upon drying. The dried biofilms were crushed, weighed (∼0.05 g), and measured for BBSi content following the weak alkaline extraction method of marine sediment, adapted from DeMaster (1981). This procedure is described in detail in Chapter Two (Section 2.2.2). BBSi is presented as a percentage of dried Si mass (g/g).

5.2.3 BDSi and BBSi depth profiles

Sediment cores with an inner diameter of 5 cm, were extracted, and subsampled every cm up to 20 cm's deep. Sediment cores were taken immediately after the tide had receded in order to sample the overlaying surface water for the diffusion calculations (Section 5.2.4), and to imitate the expected conditions during periods of immersion. Surface water was immediately sampled, and filtered through PALL Acrodisc PF 32 mm syringe filters with 0.8/0.2 μm supor membranes. Sediment slices (1 cm thick) were placed into 50 mL centrifuge tubes, stored in a cool box and centrifuged on return to the laboratory. The supernatant was decanted and filtered. BDSi concentrations in the pore fluids were measured using the Heteropoly Blue method described in Chapter Two (Section 2.2.3), and presented here in mg/L.

A randomly selected core from each mudflat site was dried at 85°C for 24 hrs, crushed, and sub-sampled (∼0.05 g) for BBSi variability with depth. BBSi (% g/g dried Si mass) was measured as described in detail in Chapter Two (Section 2.2.2).

5.2.4 Quantifying BDSi diffusive flux

BDSi flux ($BDSi_{flux}$) across the SWI from each sediment core, was calculated using Fick's First Law of diffusion under steady-state conditions (eq. 5.1), defined as the diffusion of DSi along a concentration gradient, from the enriched pore fluids around sediment grains, to the overlaying PDSi depleted water column.

$$BDSi_{flux} = -\phi * D_{sed} * \frac{dC}{dx} \tag{5.1}$$

where, ϕ is the sediment porosity, the relative pores space between sediment grains, and was determined following the ratio between the mass of the dry and wet sediment (eq. 5.2) (Hensen et al., 2006). D_{sed} is the diffusion coefficient of DSi in the sediment, which involves the diffusion coefficient of the water (D_{water}) corrected for tortuosity (θ), which is commonly used to describe the more realistic non-linear diffusive path in a porous medium (eq. 5.3) (Boudreau, 1996). dC/dx is the DSi concentration gradient with depth. Quantifying the correct gradient has a major impact on DSi flux. Here, multiple gradients (dC/dx) have been considered, and the sum of all fluxes, yields the minimal estimated value of the total DSi diffusive flux from each sediment core. This methodology has followed the approach of Schulz and Zabel (2006).

$$\phi = \frac{\text{mass of wet sediment (g)} - \text{mass of dry sediment (g)}}{\text{mass of wet sediment (g)}} \times \frac{\rho_s}{\rho_w} \tag{5.2}$$

where, ρ_s is the wet bulk density (assumed to be 1.5 for unconsolidated, water-logged sediment), and ρ_w is the density of water (assumed to be about that of seawater, 1.02).

$$\theta^2 = 1 - ln(\phi^2) \tag{5.3}$$

Rebreanu et al. (2008) report varying D_{water} with changing temperatures and salinity. For the mudflats of the Severn Estuary, based on the temperature (T in °C) and a salinity of 36 as opposed to 0, two values for D_{water} were used: when T was nearer to 20°C, D_{water} was 0.91 ± 0.04 x10^{-10} m^2/s, and when T was nearer to 15°C, D_{water} was 0.80 ± 0.01 x10^{-10} m^2/s. D_{sed} (m^2/s) was estimated following (eq. 5.4) (Hensen et al., 2006).

$$D_{sed} = \frac{D_{water}}{\theta^2} \tag{5.4}$$

The average BDSi diffusive flux (mg/m^2/year) from all stations (n=20) was then scaled-up against the surface area of the Severn Estuary intertidal mudflats: 20,300 ha

(SEP, 2009); 18,898 ha for a spring tide and 9,881 ha for a neap tide (Pethick et al., 2009). There are several estimates of the area of the intertidal mudflats, attributed to the position of the lower estuarine limit. Here, this has been set between Lavernock Point and south of Weston-Super-Mare, in line with the Cardiff-Weston barrage proposal. To account for the diffusion of silicon from the intertidal mudflats during immersion periods, the benthic diffusive flux was halved. The average BDSi diffusive flux was also scaled-up against the surface area of the estuary: 55,684 ha (Potts and Swaby, 1993), and the SAC area of 73,714 ha (JNCC, 2018). This calculation was carried out to determine the overall benthic flux of DSi (kg/year) from both the mudflats and the estuarine sediment. The benthic flux of DSi is presented with propagated standard error, assuming a 10% error in the estuarine and mudflat areas.

5.2.5 Sediment stability

To determine the sediment stability *in situ*, a portable CSM device was deployed at each station. The CSM is described in detail in Tolhurst et al. (1999), and has been widely used to determine the relative stability of estuarine intertidal sediments (Tolhurst et al., 2000; Defew et al., 2002; Tolhurst et al., 2006, 2008). The device consists of a 29 mm diameter water-filled chamber (sensor head), which was vertically pushed into the sediment. A jet of water was released and directed towards the SWI, disrupting the sediment. A series of tests with increasing increments of water pressure was performed according to the Mud 7 program: jet fired for 1 s, test started at 0.3 Psi, with increasing increments of 0.3 Psi per test (every 30 seconds) up to 12 Psi.

The equivalent horizontal bed shear stress (τ_0 in N/m^2) was calculated (eq. 5.5) using the eroding jet pressure (kPa), following the calibration in Tolhurst et al. (1999). The equivalent horizontal bed shear stress, i.e. the stress applied to the particle, was converted into shear velocity (U*), i.e. the velocity of the water flowing above the particle, following eq. 5.6 (Tolhurst et al., 1999), using τ_0 and water density (1000 kg/m^3). The critical erosion threshold was defined as the pressure step at which the light transmission across the test chamber dropped below 90% (Tolhurst et al., 1999). The critical erosion threshold ($\tau_{0\ \text{critical}}$) is the moment when the horizontal bed shear stress overcomes the restrictive force (e.g. friction), i.e. the threshold for particle entrainment. Once $\tau_{0\ \text{critical}}$ exerted by the moving fluid over the bed is exceeded, sediment erosion will occur. Below $\tau_{0\ \text{critical}}$, little erosion will occur.

$$\tau_0 \mathrm{Cr} = \mathrm{Y}_0 + \mathrm{A1} * [1 - \exp(\frac{-\mathrm{x}}{\mathrm{t1}})] + A2 * [1 - \exp(\frac{-\mathrm{x}}{\mathrm{t2}})] \tag{5.5}$$

where, Y_0 is zero, x is the eroding pressure (kPa), A1 (67), A2 (-195), t1 (310) and t2 (1623) are constants.

$$U^* = (\frac{\tau_0}{\rho})^{0.5} \quad (5.6)$$

At the end of each CSM measurement (i.e. after 12 Psi was reached), the bulk resuspended matrix in the test chamber was sampled and placed into 50 mL centrifuge tubes, with 5 mL subsampled and filtered for BDSi concentrations (mg/L). The remaining matrix of a known volume (mL) was centrifuged, decanted, and dried at 85°C for 24 hrs to determine the concentration of suspended particulate matter (SPM). A sub-sample (∼0.05 g) of the dried sediment was measured for resuspended BBSi concentrations (mg/L), following the method described in Chapter Two (Section 2.2.2).

Alongside each CSM measurement, sediment cores (2.54 cm diameter, 1 cm deep) were collected for sediment grain analysis. The sediment grain size of each fraction was weighed (g): <63 μm, 63-125 μm, 125-250 μm >300 μm, and is presented here as a percentage of the total mass (g). Also, at each station, surface water temperature (°C) and salinity levels were measured using an Extech EC170 digital handheld temperature and salinity meter.

5.2.6 Resuspension of BDSi and BBSi

Using the time (s) elapsed between the start of the CSM measurements and the point at which $\tau_{0\ \text{critical}}$ was reached, along with the volume of the bulk resuspended matrix (mL) in the sensor head chamber, and the concentration of BDSi, BBSi and SPM, the total flux of Si and sediment expressed per unit area (sensor head diameter = 29 mm) was calculated (mg/m^2/s). This flux was calculated for each individual station and averaged for each site. These fluxes were then scaled-up to determine the erosion flux of Si and sediment (kg/s) from the mudflats, following the above method, using published intertidal area estimates (SEP, 2009; Pethick et al., 2009), and presented with their propagated standard error (see Section 5.2.4).

5.2.7 Surf zone PBSi, PDSi and SPM concentrations

The surf zone was sampled (1 L x 3 replicas) for PDSi, PBSi and SPM concentrations (mg/L). Sub-samples (5 mL) were filtered for PDSi concentrations, measured following the above protocol. Sub-samples (50 mL) were centrifuged, decanted, and dried at 85°C for 24 hrs to determine the concentration of SPM. The dried sediment (∼0.05 g) was measured for PBSi concentrations. The surf zone was not measured at Site 4 due to the local dangers associated with the long distance between the foreshore and the sea.

5.2.8 Carbohydrate and chlorophyll *a* concentrations

The surficial biofilms from the intertidal mudflat were measured for both total and colloidal carbohydrate concentrations. Carbohydrates were measured following the phenol-sulfuric acid assay (Dubois et al., 1956), which measures the total carbohydrate concentration of the sediment, including any extracellular, intracellular and particle-bound material (Underwood et al., 1995). Sediment samples from each station were weighed (g), freeze-dried overnight at -20°C, transferred to a desiccator, before obtaining freeze-dried mass. For the extraction of colloidal-S carbohydrates, 4 mL of saline 25‰ was added to each sediment subsample (with a dry mass between 50-100 mg). Samples were vortexed (10 seconds) and left in a water bath at 20°C for 20 minutes. Samples were re-vortexed and then centrifuged for 15 minutes at 3,620 *g*. The extracted colloidal-S carbohydrate fraction (liquid phase) contains both polymeric and non-polymeric material. For both the total and colloidal-S fractions, to each known mass of sample, 1 mL distilled H_2O was added, followed by 0.5 mL of 5% aqueous phenol (w/v) and immediately by 2.5 mL of concentrated sulfuric acid (H_2SO_4), the latter two delivered using dispensers to standardize delivery times. Samples were immediately vortexed twice for 5 seconds each time. The absorbance was measured against a reagent blank at 485 nm, on a spectrophotometer (Biochrom, WPA Biowave II, Cambridge, UK). The glucose equivalent concentration was calculated against a glucose standard curve with concentrations ranging from 20 -150 μg, made up fresh on the day of measurements. The total and colloidal-S carbohydrate concentrations are presented as glucose equivalents in μg/g freeze-dry mass sediment.

Chlorophyll *a* pigment concentrations (μg/g *dw. sed.*) were determined following a modified protocol from Staats et al. (2001). Samples were freeze-dried, subsampled (100 mg), with 2.0 mL of N,N-dimethylformamide (DMF) added for the pigment extraction. Samples were incubated for 4 hours in the dark, centrifuged for 10 minutes at 4,000 rpm with the absorbance measured at 665 nm and 750 nm in a 1 cm quartz glass cuvette, on a spectrophotometer (Biochrom, WPA Biowave II, Cambridge, UK). Samples were acidified to a final concentration of 3 mM HCl (Axler and Owen, 1994) to measure the breakdown pigments of chlorophyll. Chl *a* concentrations were calculated following De Winder et al. (1999).

All carbohydrate and chl *a* pigment analyses were carried out by Prof. Marian Yallop at the University of Bristol.

5.3 Results

5.3.1 Surface BBSi content and BDSi concentrations

BBSi content displayed significant spatial variation among the sampled sites (H=14.48, d.f=3, $p<0.05$). The percentage of BBSi at Site 1 in the upper reaches of the estuary were significantly lower (0.27 ± 0.03%, *post hoc* analysis $p<0.05$) compared to the other sampled sites. Relatively higher BBSi content was measured at both Site 2 (1.00 ± 0.08%) and Site 3 (0.98 ± 0.17%) (Fig. 5.1). However, Site 3, commonly known as Newport Wetlands, has an adjoining saltmarsh, which due to the sea-wall defence cannot migrate inland, and is increasingly being encroached by the mudflats. Two of the mudflat stations were sampled next to saltmarsh 'clumps'. Studies in saltmarsh sediment have shown large accumulations of phytoliths (the silica component in plants) (Norris and Hackney, 1999; Conley, 2002), which, here could also have caused the high BBSi content. By removing these two stations, the average BBSi percentage is reduced to 0.70 ± 0.01%.

BDSi concentrations in the surface water displayed significant spatial variation among sampled sites (H=16.36, d.f=3, $p<0.001$). Relatively high BDSi concentrations were observed at Site 1 (2.1 ± 0.1 mg/L) and Site 4 (2.0 ± 0.2 mg/L) (Fig. 5.1), alongside lower percentages of BBSi (Fig. 5.1). No significant difference in BDSi concentrations was found between Site 1 and Site 4, but a significant difference in BDSi concentrations was found between Site 1 and Sites 2 and 3 (*post hoc* analysis $p<0.05$), and between Site 4 and Sites 2 and 3 (*post hoc* analysis $p<0.05$). Lower BDSi concentrations were measured at Site 2 (0.6 ± 0.1 mg/L) and Site 3 (1.1 ± 0.1 mg/L), both of which recorded relatively high percentages of BBSi. Considering all data, a significant negative linear correlation was observed between BDSi and BBSi (n=20, r^2=0.57, $p<0.05$).

5.3.2 BDSi and BBSi depth profiles

The concentration of BDSi in the pore fluids at each sampled site, despite small fluctuations, displayed a (pseudo)asymptotic profile (Fig. 5.2), with BDSi concentrations ranging between 0.37 and 2.29 mg/L in the upper 1 cm and 2.38 to 7.88 mg/L at 20 cm deep. At Sites 1, 3 and 4, BDSi concentrations in the overlaying surface water were relatively high compared to the concentrations at 1 cm deep. At Site 2, the formations of channels meant the flowing runoff was confined to these areas, allowing pools of water to become isolated on the mudflat crests. Sampling these pools resulted in the more commonly expected low DSi concentrations in the overlaying surface water, which were absent at Sites 1, 3 and 4.

The percentage of BBSi in the depth profiles from selected cores, generally displayed an inverse relationship to the asymptotic curve of BDSi (Fig. 5.3). The BBSi depth profiles were associated with high fluctuations at each sampled depth, which represented the "true" variability at each station, as opposed to sampling errors (see Fig. 5.3, small

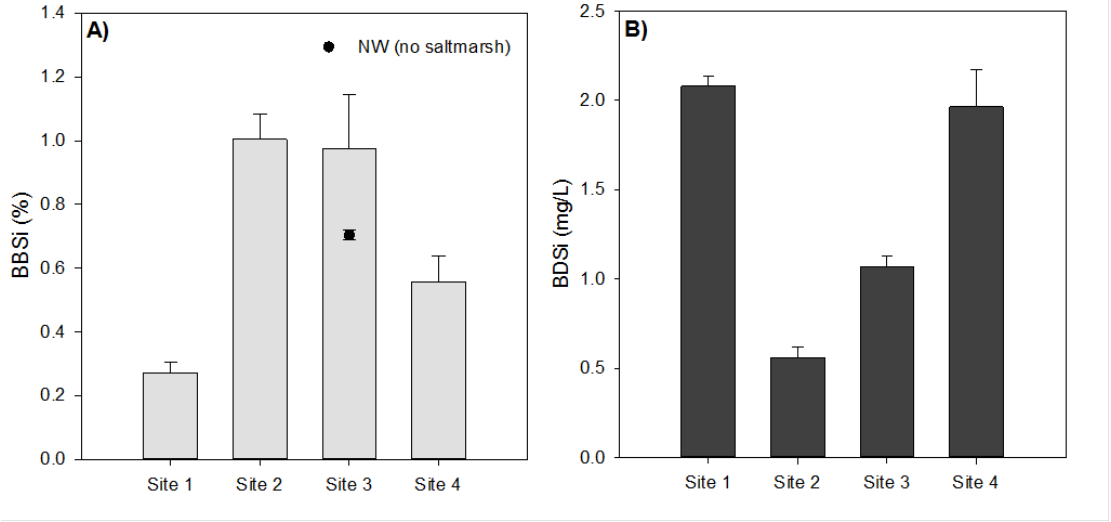

Figure 5.1: A) Average microphytobenthic biofilm biogenic silica content (% of dried Si mass, g/g) in the Severn Estuary in September 2018. **B)** Average benthic dissolved silicon concentrations (mg/L) in the overlaying surface water (note: different to pore fluid). Presented with 1SE of 5 stations.

error bars representing 1SE of three replicas at 1 cm, 10 cm and 20 cm deep). The percentage of BBSi for all stations sampled, ranged between 0.27% and 0.45% at 1 cm, and between 0.23% and 0.43% at 20 cm deep.

5.3.3 BDSi diffusive flux into the overlaying water column

The theoretical BDSi diffusive fluxes across the SWI from each sediment core were calculated from the sum of different concentration gradients following the approach of Schulz and Zabel (2006), using Fick's First Law (see Section 5.2.4). A summary of each sediment core and the selected gradients can found in Fig. 5.4. The equation has previously been scrutinised for its sensitivity to the porosity value. Porosity was measured to be between 0.68 and 0.92 (Table. 5.1), and these values are in-line with the typically values of 0.8 (Hensen et al., 2006). The overall diffusive flux of BDSi was greatest at Site 2, with 928 mg/m^2/year BDSi diffusing into the surface water from the porefluids. Similarly, Site 3 had a high diffusive flux of BDSi (235 mg/m^2/year), whereas Site 1 and Site 4, had low BDSi diffusion flux (30 and 23 mg/m^2/year, respectively). Considering an intertidal mudflat area of 23,000 ha (SEP, 2009), the BDSi diffusive flux was estimated to be 61,500 $\pm$ 29,000 kg/year. Using the spring and neap intertidal areas (18,898 ha and 9,881 ha, respectively), landward of the Cardiff-Weston Barrage 'line' as presented in Pethick et al. (2009), the diffusive flux ranged between 57,500 $\pm$

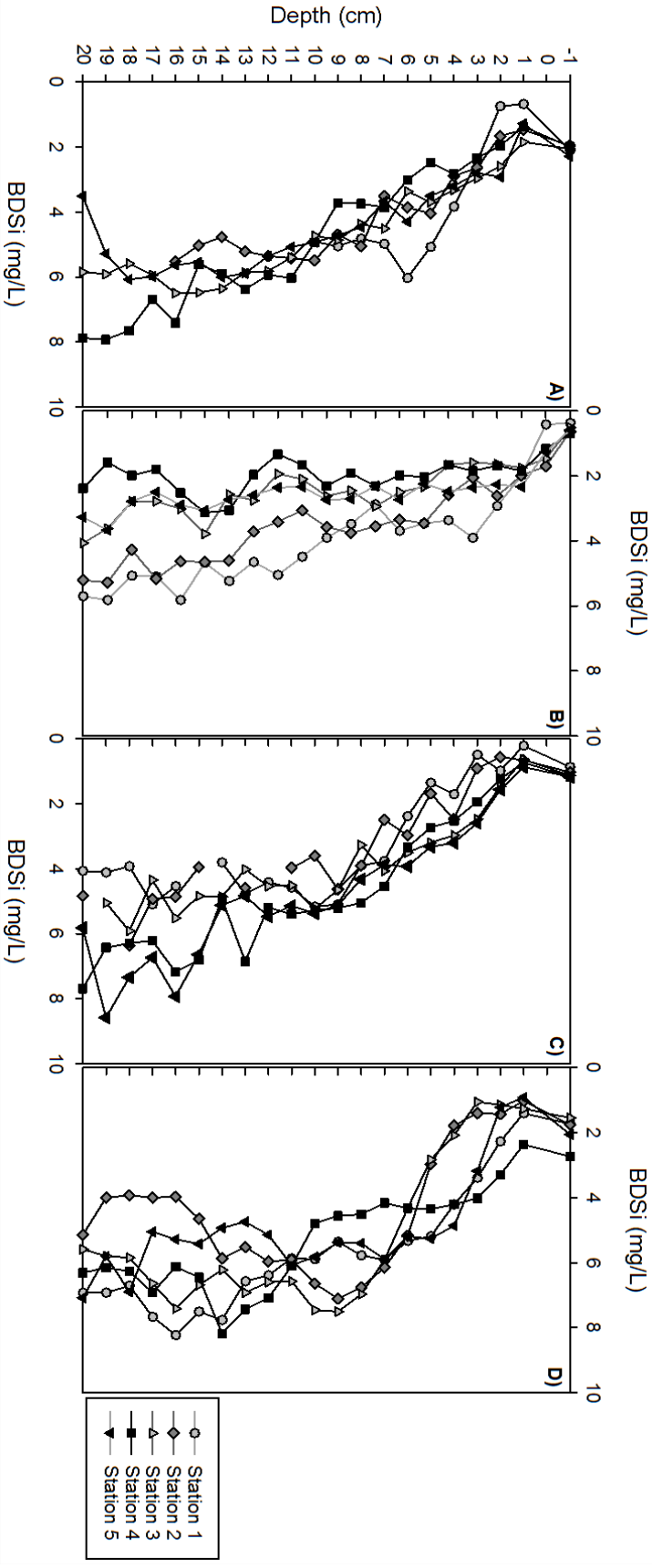

Figure 5.2: Depth profiles of benthic dissolved silicon concentrations (mg/L) in the mudflat pore fluids. **A)** Site 1. **B)** Site 2. **C)** Site 3. **D)** Site 4. Note, plots with missing data points are areas where there was insufficient water to extract for DSi measurements.

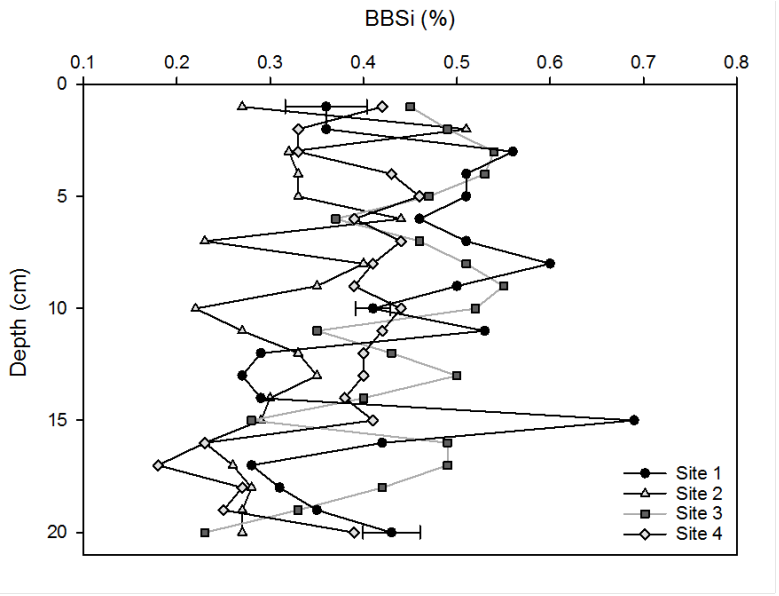

Figure 5.3: Depth profile of the sediment biogenic silica content (% of dried Si mass, g/g). Site 1: station 4 presented with 1SE of three replicas at 1 cm, 10 cm and 20 cm deep. Site 2: station 2. Site 3: station 3. Site 4: station 3.

27,000 kg/year (spring) and 30,000 ± 15,000 kg/year (neap). With two high tides a day, and with a similar length of time when the mudflats are exposed and submerged, these mudflat BDSi diffusive flux estimates can be halved. A summary of these different diffusive flux estimates can be found in Table. 5.1. The diffusive flux of BDSi would not only be confined to the intertidal mudflats upon immersion but would be widespread throughout the estuary. With an estuarine area of 55.684 ha (Potts and Swaby, 1993), this would result in an estimated BDSi flux of 169,500 ± 79,500 kg/year. Considering the even larger SAC estuarine area of 73,714 ha (JNCC, 2018), this would result in an estimated BDSi flux of 224,000 ± 105,000 kg/year. Note, these calculations based on the estuarine area do not consider the effects of the tide.

5.3.4 Sediment stability

The critical erosion threshold ($\tau_{0\ \text{critical}}$), the point at which the sediment particles could be entrained, displayed significant spatial variability (H=9.509, d.f=3, $p<0.05$) among the sampled sites. The $\tau_{0\ \text{critical}}$ was significantly higher at Site 2 (4.2 ± 0.5 N/m^2) indicative of high sediment stability (Fig. 5.5), but remained between 2.1 ± 1.2 and 2.3 ± 0.8 N/m^2 at Site 3 and 4, respectively. The $\tau_{0\ \text{critical}}$ was significantly lower at Site 1 (0.5 ± 0.1 N/m^2, *post hoc* analysis $p<0.05$). The shear velocity (U*), which is directly comparable to the erosion threshold (Tolhurst et al., 1999), and thereby displayed the same pattern (Fig. 5.5), was also high at Site 2 (6.5 ± 0.4 cm/s). The $\tau_{0\ \text{critical}}$ and U* had a positive linear relationship with BBSi and an inverse relationship with BDSi

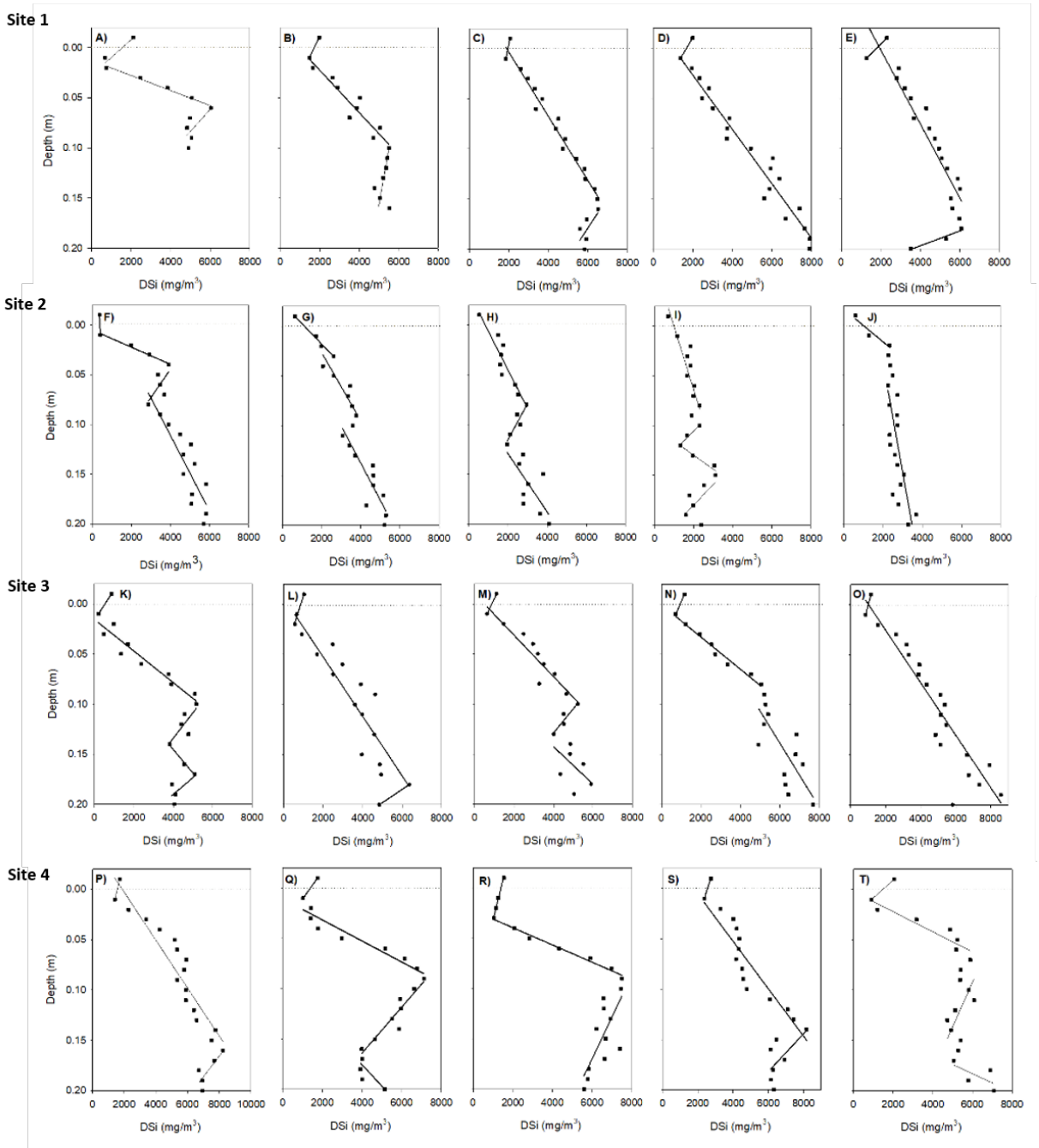

Figure 5.4: Individual site station depth (m) profiles of the sediment porefluid benthic dissolved silicon (mg/m^3), with multiple gradients (dC/dx) considered to calculate the diffusive flux of DSi from the sediment to the surface water. Data presented following Schulz and Zabel (2006). **A-E)** Site 1 stations. **F-J)** Site 2 stations. **K-O)** Site 3 stations. **P-T)** Site 4 stations. Dotted line: sediment-water-interface.

Table 5.1: Benthic dissolved silicon (BDSi) diffusive flux across the sediment-water interface estimated using Fick's First Law of diffusion for four intertidal mudflats sampled in the Severn Estuary in September 2018. * assuming diffusive flux only during immersion periods.

Site	Porosity (ϕ)	D_{water} (m^2/s)	D_{sed} (m^2/s)	BDSi diffusive flux (J) ($mg/m^2/year$)
1	0.76	9.1 x10^{-10}	7.3 x10^{-10}	-30
2	0.82	8.0 x10^{-10}	6.7 x10^{-10}	-928
3	0.92	9.1 x10^{-10}	8.4 x10^{-10}	-235
4	0.68	8.0 x10^{-10}	6.0 x10^{-11}	-23
a) Intertidal mudflats				
				61,500 ± 29,000 kg/year
*				31,000 ± 14,500 kg/year
b) Intertidal mudflats(spring)				
				57,500 ± 27,000 kg/year
*				28,500 ± 13,500 kg/year
c) Intertidal mudflats (neap)				
				30,000 ± 14,000 kg/year
*				15,000 ± 7,000 kg/year
d) Estuary				
				169,500 ± 79,500 kg/year
e) Estuary				
				224,000 ± 105,000 kg/year

(a) Used an intertidal area of 20,300 ha (SEP, 2009).

(b) Used an intertidal area of 18,898 ha (Pethick et al., 2009).

(c) Used an intertidal area of 9,881 ha (Pethick et al., 2009).

(d) Used an estuarine area of 55,684 ha (Potts and Swaby, 1993).

(e) Used a SAC estuarine area of 73,714 ha (JNCC, 2018).

(Fig. 5.6), but none of the relationships were statistically significant.

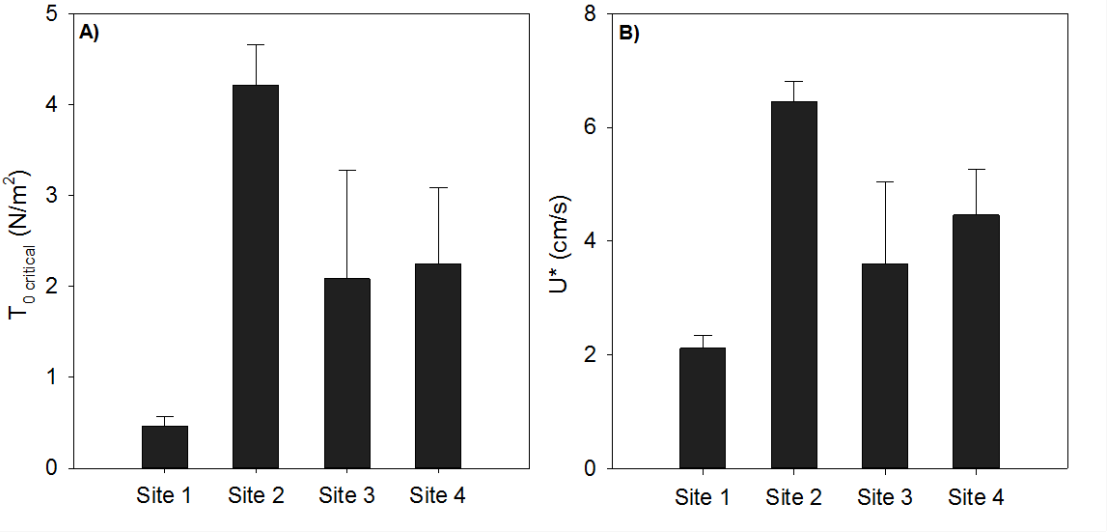

Figure 5.5: A) Average critical erosion threshold ($\tau_{0\ \text{critical}}$ in N/m^2) from the intertidal mudflat sediments of the Severn Estuary in September 2018. **B)** Average shear velocity (U* in cm/s). Presented with 1SE of 5 stations.

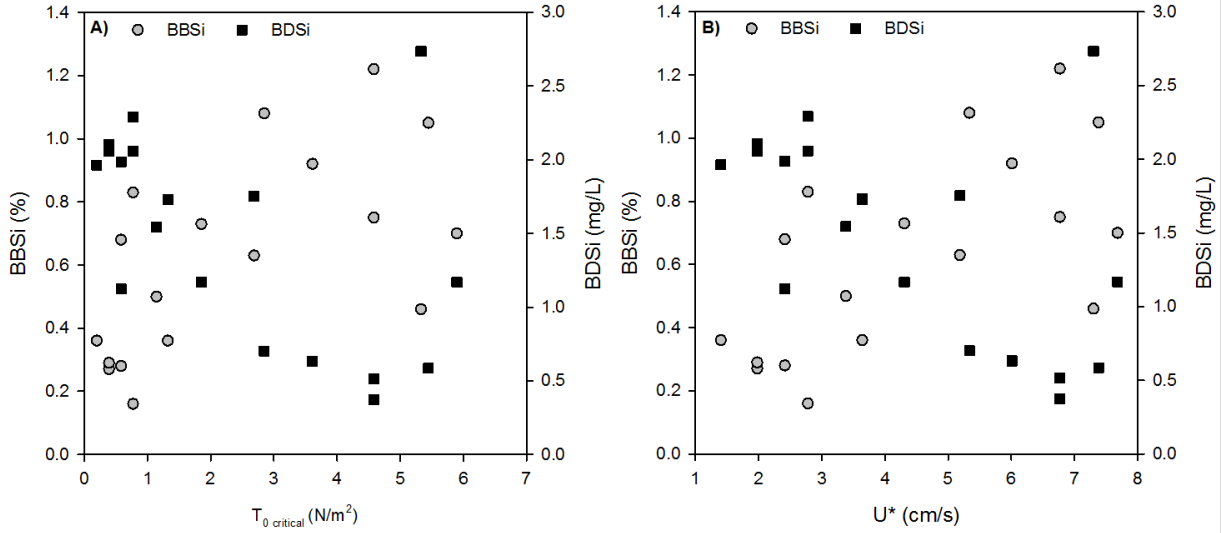

Figure 5.6: A) $\tau_{0\ \text{critical}}$ vs BBSi content and BDSi concentrations. **B)** U* vs BBSi content and BDSi concentrations.

The average CSM erosion profiles from the intertidal mudflats followed the characteristic decreasing loss in transmission across the sensor head chamber with increasing pressure (Fig. 5.7). At Site 1, the displacement of loose surface material and the de-

tachment of small flocs from the surface was followed quickly by complete bed failure (steep gradient) (Fig. 5.7). At sites 2, 3 and 4, the biofilms were more stable, with more gradual rates of erosion, compared to Site 1. There was significant spatial variability (large error bars) in the erosion profiles between each station on each of the mudflats (n=5), especially at Site 3 (Fig. 5.7).

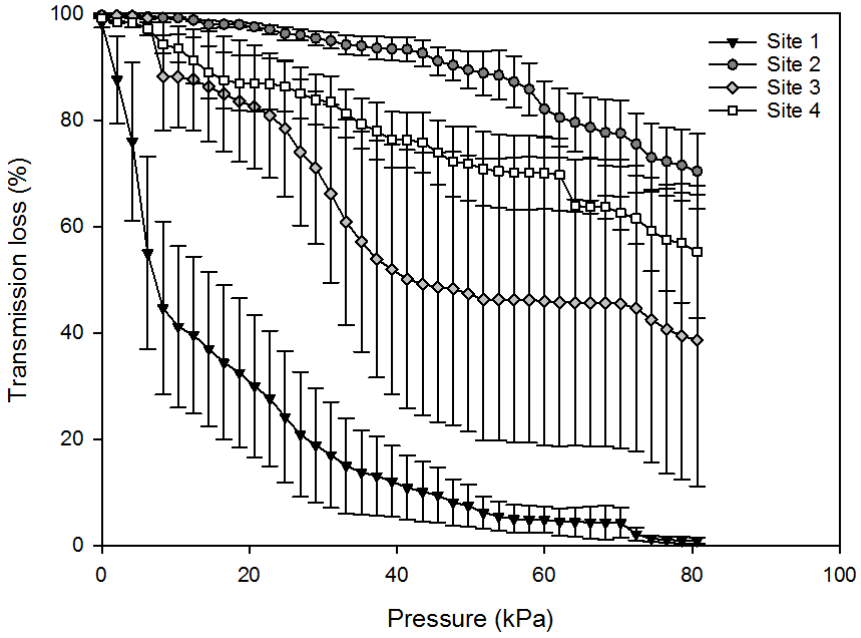

Figure 5.7: Average erosion profiles from the four sampled intertidal mudflats in the Severn Estuary in September 2018. Presented with 1SE of 5 stations.

5.3.5 Resuspended BDSi and BBSi

Following the erosion of the biofilms by the CSM, the bulk resuspended sediment matrix in the sensor head chamber was sampled and measured for eroded BDSi, BBSi and sediment (now SPM) concentrations (Fig. 5.8). BDSi concentrations displayed significant spatial variability between sampled sites (H=17.58, d.f=3, p<0.001, *post hoc* analysis p<0.05), with peak concentrations of 2.0 mg/L at Site 1 (Fig. 5.8). At all sampled sites, higher concentrations of BBSi was eroded compared to BDSi (Fig. 5.8). BBSi concentrations in the resuspended matrix lacked spatial variability between sites, but peaked at 91.4 mg/L at Site 3. Note, the average resuspended BBSi concentrations of the first two stations sampled near saltmarsh 'clumps', was relatively low (54.6 ± 5.6 mg/L) compared to the average of the 'true' mudflats at this site (84.8 ± 6.4 mg/L) (Fig. 5.8). SPM concentrations lacked significant spatial variation between the mudflats

but reached highs of 21.2 ± 6.6 g/L at Site 1 and lows of 6.9 ± 2.1 g/L at Site 2 (Fig. 5.8). The resuspended SPM and BBSi concentrations in the CSM sensor head chamber, at individual sites, showed significant correlations (except Site 2), suggesting the flux of BBSi and sediment were coupled (Table. 5.2).

Table 5.2: Pearson's correlation coefficient between SPM and BBSi in the resuspended matrix in the CSM sensor head chamber (*n=5* at each site). Values of r significance at: * $p<0.05$; ** $p<0.01$.

	SPM
BBSi (Site 1)	0.979 **
BBSi (Site 2)	0.846
BBSi (Site 3)	0.951 *
BBSi (Site 4)	0.899 *

The average erosion rate of BDSi from the sampled intertidal mudflats (*n=20*) of the Severn Estuary was 0.3 ± 0.1 mg/m^2/s, equalling 9.6 ± 2.5 kg BDSi/m^2/year (Table. 5.3). BBSi erosion rate was high compared to BDSi, with an average rate of 19 ± 6 mg/m^2/s, equalling 600 ± 200 kg BBSi /m^2/year (Table. 5.3). The average SPM erosion rate from the measured mudflats was high compared to both BDSi and BBSi at 5,800 ± 1,600 mg/m^2/s, equalling 183,600 ± 51,500 kg SPM/m^2/year (Table. 5.3).

Using a total intertidal mudflat area of 20,300 ha (SEP, 2009), the erosion flux of BDSi was estimated to be *ca.* 9.7 x10^8 ± 2.7 x10^8 kg/year (Table 5.3). BBSi erosion flux was comparably high at *ca.* 6.1 x10^{10} ± 1.9 x10^{10} kg/year. A total of *ca.* 1.9 x10^{13} ± 5.6 x10^{12} kg/year of sediment was estimated to have eroded from the intertidal mudflats (Table. 5.3). These estimates using the intertidal area of 20,300 ha are comparable to the erosion estimates presented in Table 5.3, using the spring intertidal area presented in Pethick et al. (2009), but high compared to the estimates using a neap intertidal area.

5.3.6 Surf zone silicon and sediment concentrations

BDSi concentrations in the surf zone of the intertidal mudflats of the Severn Estuary displayed significant spatial variability between the sampled mudflats (F=19.42, d.f=1,7, $p<0.01$). Site 1 had significantly higher BDSi concentrations (2.0 ± 0.02 mg/L) compared to sites 2 and 3 (0.8 ± 0.01 mg/L, 0.8 ± 0.06 mg/L, respectively, *post hoc* analysis $p<0.5$) (Fig. 5.9). Note, no surf water was sampled at Site 4 due to the natural dangers of the site.

BBSi concentrations in the surf zone displayed significant spatial variability (F=11.5, d.f=1,7, $p<0.01$). Site 3 had significantly higher BBSi concentrations (11.8 ± 1.8 mg/L) compared to sites 1 and 2 (4.4 ± 1.2 mg/L, 4.8 ± 0.3 mg/L, respectively, *post hoc* analysis $p<0.5$) (Fig. 5.9). SPM concentrations lacked spatial variability between sampled

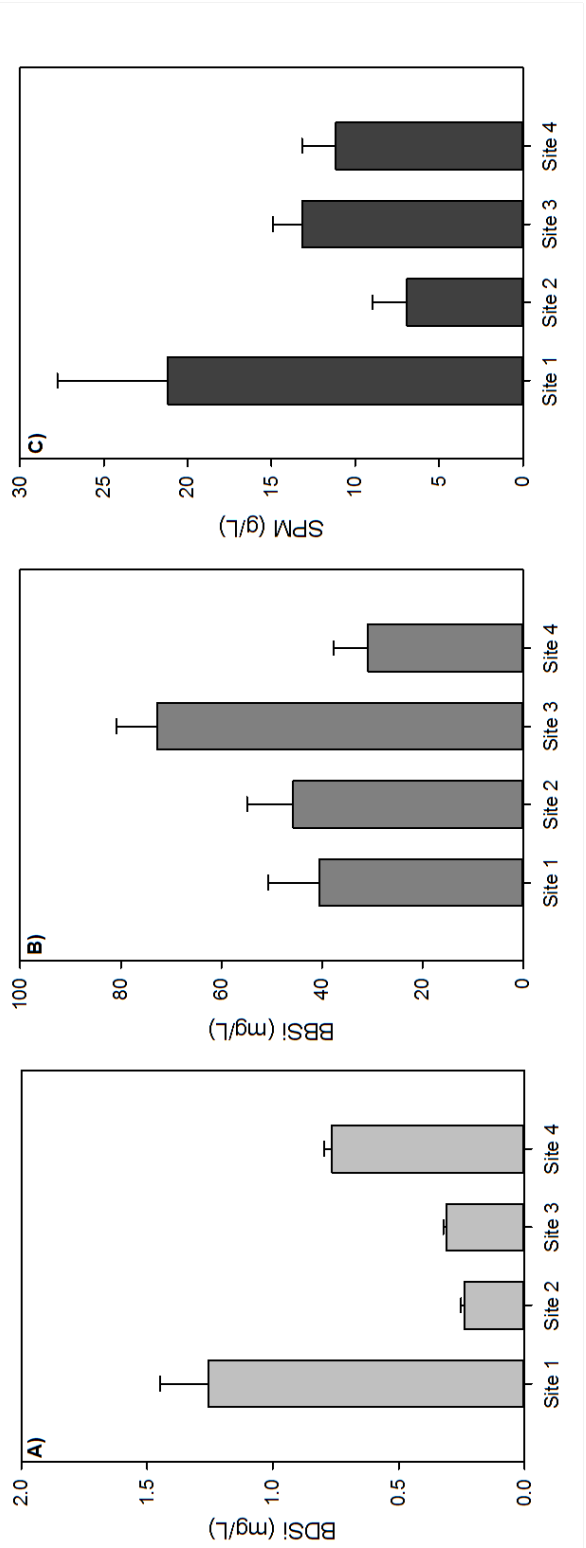

Figure 5.8: Silicon and sediment concentrations in the eroded matrix from the mudflats of the Severn Estuary in September 2018. **A)** Benthic dissolved silicon (mg/L). **B)** Benthic biogenic silica (mg/L). **C)** Suspended Particulate Matter (g/L). Note unit discrepancy between sediment and silicon concentrations. Presented with 1SE of 5 stations.

Table 5.3: BDSi and BBSi and sediment erosion flux from the intertidal mudflats of the Severn Estuary in September 2018.

Site	Unit	$BDSi_{erosion\ flux}$	$BBSi_{erosion\ flux}$	$Sediment_{erosion\ flux}$
1	$mg/m^2/s$	0.8 ± 0.07	26 ± 6.1	13,300 ± 3,700
2	$mg/m^2/s$	0.02 ± 0.002	3 ± 0.6	500 ± 130
3	$mg/m^2/s$	0.2 ± 0.10	41 ± 20	7,200 ± 3,400
4	$mg/m^2/s$	0.2 ± 0.05	7 ± 2.3	2,600 ± 900
Average	$mg/m^2/s$	0.3 ± 0.1	19 ± 5.6	5,800 ± 1,600
	$kg/m^2/year$	9.6 ± 2.5	600 ± 200	183,600 ± 51,500
a)	kg/year	$9.7\ x10^8 \pm 2.7\ x10^8$	$6.1\ x10^{10} \pm 1.9\ x10^{10}$	$1.9\ x10^{13} \pm 5.6\ x10^{12}$
b)	kg/year	$9.1\ x10^8 \pm 2.5\ x10^8$	$5.7\ x10^{10} \pm 1.8\ x10^{10}$	$1.7\ x10^{13} \pm 5.2\ x10^{12}$
c)	kg/year	$4.7\ x10^8 \pm 1.3\ x10^8$	$3.0\ x10^{10} \pm 9.2\ x10^9$	$9.1\ x10^{12} \pm 2.7\ x10^{12}$

(a) Used an intertidal area of 20,300 ha (SEP, 2009).

(b) Used an intertidal area of 18,898 ha (Pethick et al., 2009).

(c) Used an intertidal area of 9,881 ha (Pethick et al., 2009).

mudflats (Fig. 5.9). SPM concentrations were similar between Site 1 (1.9 ± 1.0 g/L) and Site 3 (1.8 ± 0.03 g/L), and low at Site 2 (0.6 ± 0.01 g/L), but had high standard error at Site 1. Note, the surf zone at sites 1 and 2, located in the upper estuary, were dominated by lateral tidal flows, whereas the surf zone at Site 3 was sheltered. The surf zone SPM and BBSi concentrations (all data) showed significant positive linear correlation ($n=9$, $r^2=0.75$, $p<0.05$), suggesting the flux of BBSi and sediment remained coupled in the surf zone.

5.3.7 Biostabilization

Total carbohydrate concentrations ranged between 7.3 and 19.2 mg/g (Fig. 5.10), but displayed no significant spatial variation between the sampled sites. Colloidal-S carbohydrate concentrations ranged between 0.08 and 5.1 mg/g (Fig. 5.10), and also did not display any significant spatial variation, despite the relatively low colloidal-S carbohydrate concentrations recorded at Site 1 (minimum of 0.09 mg/g).

Chl *a* content was highly heterogeneous between sampled stations, with an exception at Site 1 (Fig. 5.11). Chl *a* content ranged between 4.8 and 266.5 μg/g *dw. sed.* in September 2018. Relatively high chl *a* content was measured in the stations sampled near saltmarsh 'clumps' at Site 3: 266.5 and 126.7 μg/g *dw. sed.*. Chl *a* content displayed significant spatial variation between the sampled sites (H=11.16, d.f=3, $p<0.01$). A significant difference was found between Site 1 and Site 3 (*post hoc* analysis $p<0.01$).

For the entire dataset, no significant relationship was found between chl *a* and total and colloidal-S carbohydrates (Fig. 5.12). However, with the outlier removed (see Fig. 5.12), chl *a* displayed a significant linear relationship with total carbohydrates ($n=19$, $r^2=0.53$, $p<0.05$), and colloidal-S carbohydrate concentrations ($n=16$, $r^2=0.72$,

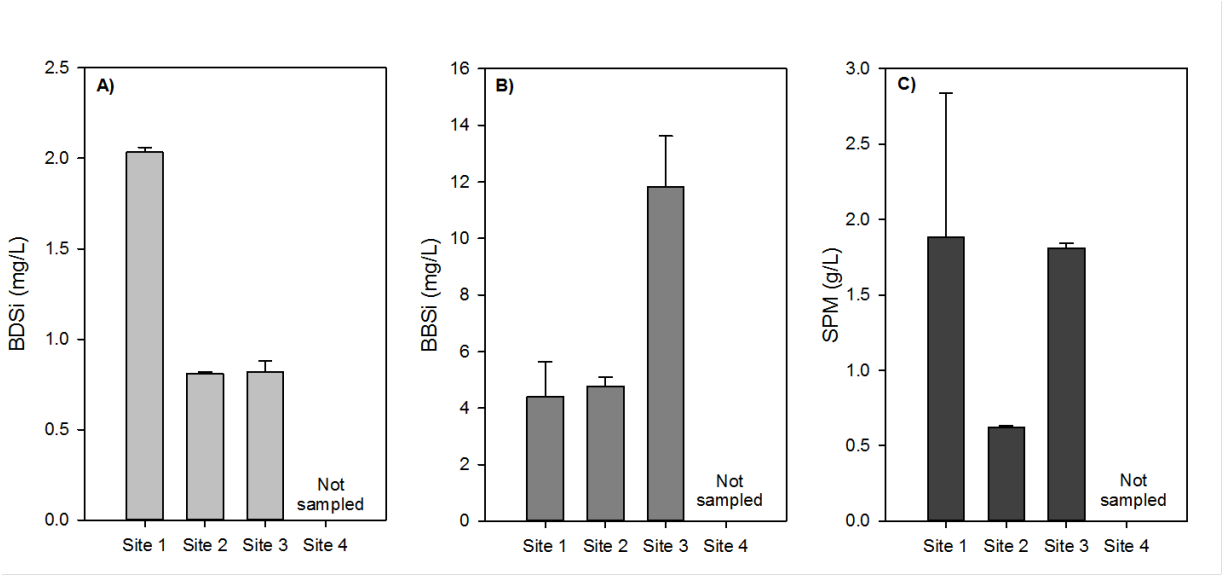

Figure 5.9: Silicon and sediment concentrations in the surf zone of three of the sampled mudflats in the Severn Estuary in September 2018. **A)** Benthic dissolved silicon (mg/L). **B)** Biogenic silica (mg/L). **C)** Suspended Particular Matter (g/L). Note unit discrepancy between silicon and sediment concentrations. Presented with 1SE of 3 replicas.

$p<0.05$). For the entire dataset, no significant relationship was found between chl *a* or carbohydrates with $\tau_{0\ \text{critical}}$ (even with the outlier removed) (Fig. 5.13). Considering individual sites, a positive linear correlation was observed at sites 2 and 3 between colloidal-S and $\tau_{0\ \text{critical}}$, but lacked any statistical significance.

A significant linear relationship was found between biofilm BBSi content and chl *a* content ($n=20$, $r^2=0.54$, $p<0.01$, Fig. 5.14), but no significant relationship was found between BBSi and the total and colloidal-S carbohydrate concentrations. A downwards trend in surface water BDSi concentrations with increasing biomass was observed but lacked any statistical significance (even with the outlier removed) (Fig. 5.14).

5.3.8 Environmental conditions

Desiccation of sediment during emersion periods, and the resulting de-watering and compaction of the sediment particles, plays a key role in biostabilization (Perkins et al., 2003). Water content lacked significant spatial variation between the sampled mudflats: 51.5 ± 2.7% (Site 1), 55.6 ± 1.2% (Site 2), 62.3 ± 1.6% (Site 3), 46.3 ± 1.5% (Site 4) (Fig. 5.15). No relationships were observed between water content and surface water BDSi concentrations, nor with the percentage of biofilm BBSi, or chl *a* and carbohydrate concentrations.

Surface salinity levels were significantly different between sites ($F=68.7$, d.f=1,18, $p<0.001$), and remained above 25 at each mudflat (Fig. 5.15), indicating a strong influence by the marine saline water on the pore fluids. A significant difference was

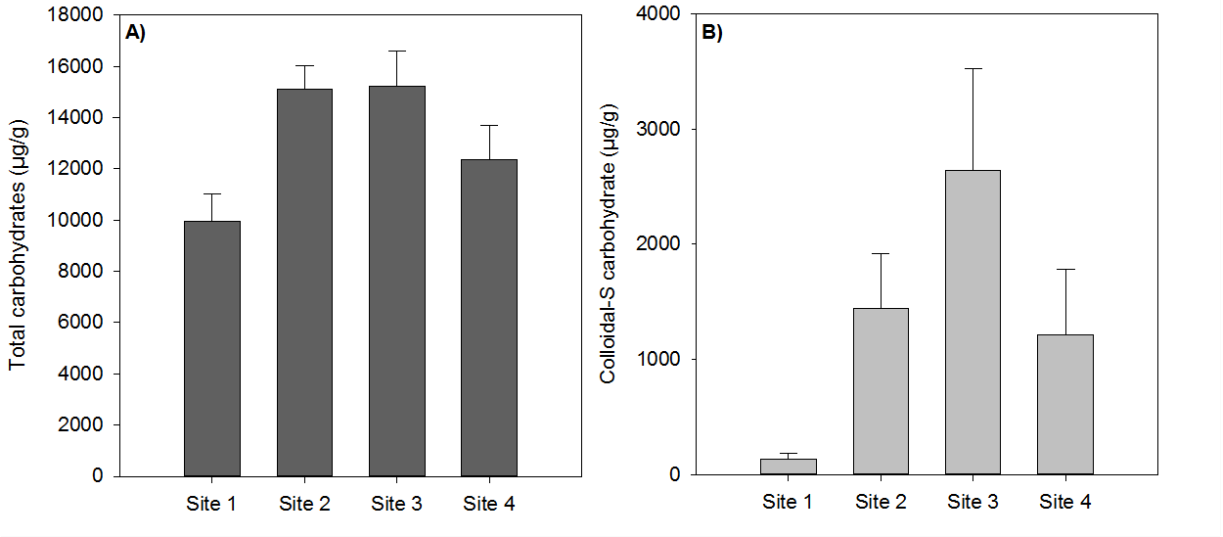

Figure 5.10: Total carbohydrate **(A)** and colloidal-S carbohydrate **(B)** concentrations (μg/g) from the intertidal mudflat on the Severn Estuary in September 2018. Presented with 1SE of 5 stations except at Site 1 where only 2 stations had data.

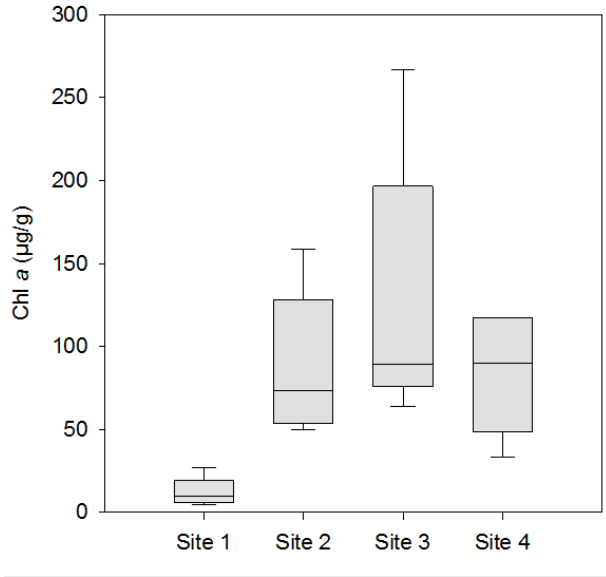

Figure 5.11: Chlorophyll *a* content (μg/g *dw. sed.*) from the intertidal mudflat on the Severn Estuary in September 2018.

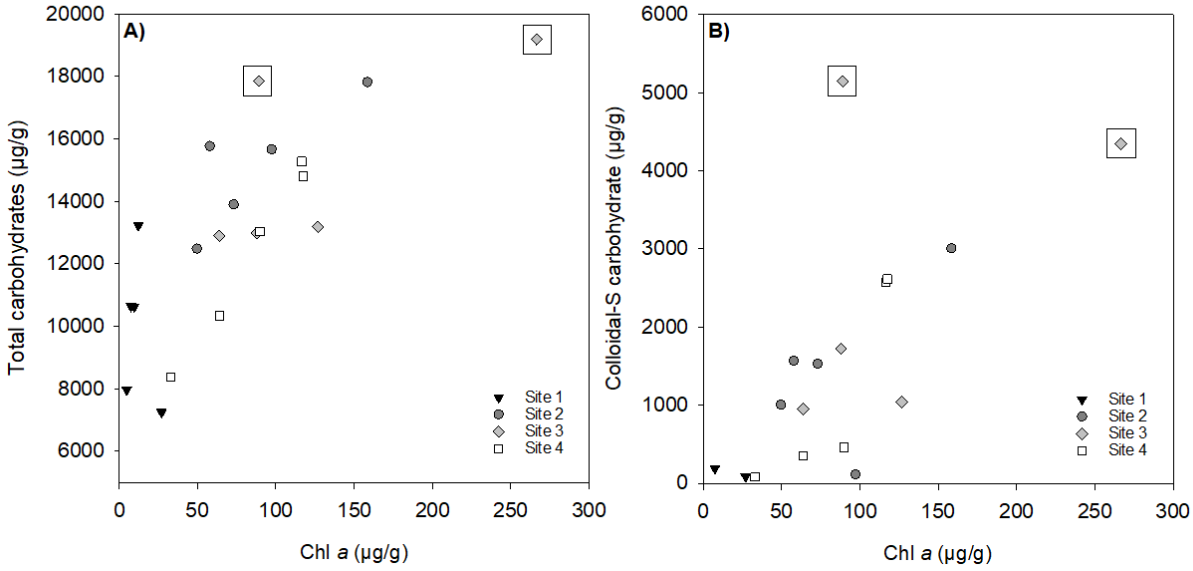

Figure 5.12: Chlorophyll *a* content relationship with total **(A)** and colloidal-S carbohydrate **(B)** concentrations. With the removal of the outliers (boxes: two samples taken near the saltmarsh at Site 3) (>250 μg/g chl *a*, and >5000 μg/g colloidal-S carbohydrate concentrations), a positive linear relationship was found (**A:** *n=19*, r^2=0.53, p<0.05. **B:** *n=16*, r^2=0.72, p<0.05.

found between Site 1 and 4 (*post hoc* analysis p<0.5), whilst no significant difference was found between Site 2 and 3. Surface water temperatures were significantly different between mudflats (F=19.79, d.f=1,18, p<0.001), ranging between 14.9 and 19.4°C (Fig. 5.15). Surface water temperature at Site 4 was significantly low (*post hoc* analysis p<0.5) compared to the other sampled mudflats. No significant relationship was found between chl *a* or the carbohydrate concentrations with these environmental factors (salinity and temperature).

Fine sediment (clay/silt) dominated the intertidal mudflats of the Severn Estuary in September 2018 (Fig. 5.16), with over 92% of the sediment at sites 1, 2 and 3 with a grain size of <63 μm. Site 4, commonly known as Sand Bay, had a high abundance of coarse sediment (>250 μm). No significant relationship was found between chl *a* or the carbohydrate concentrations and the different sediment grain sizes.

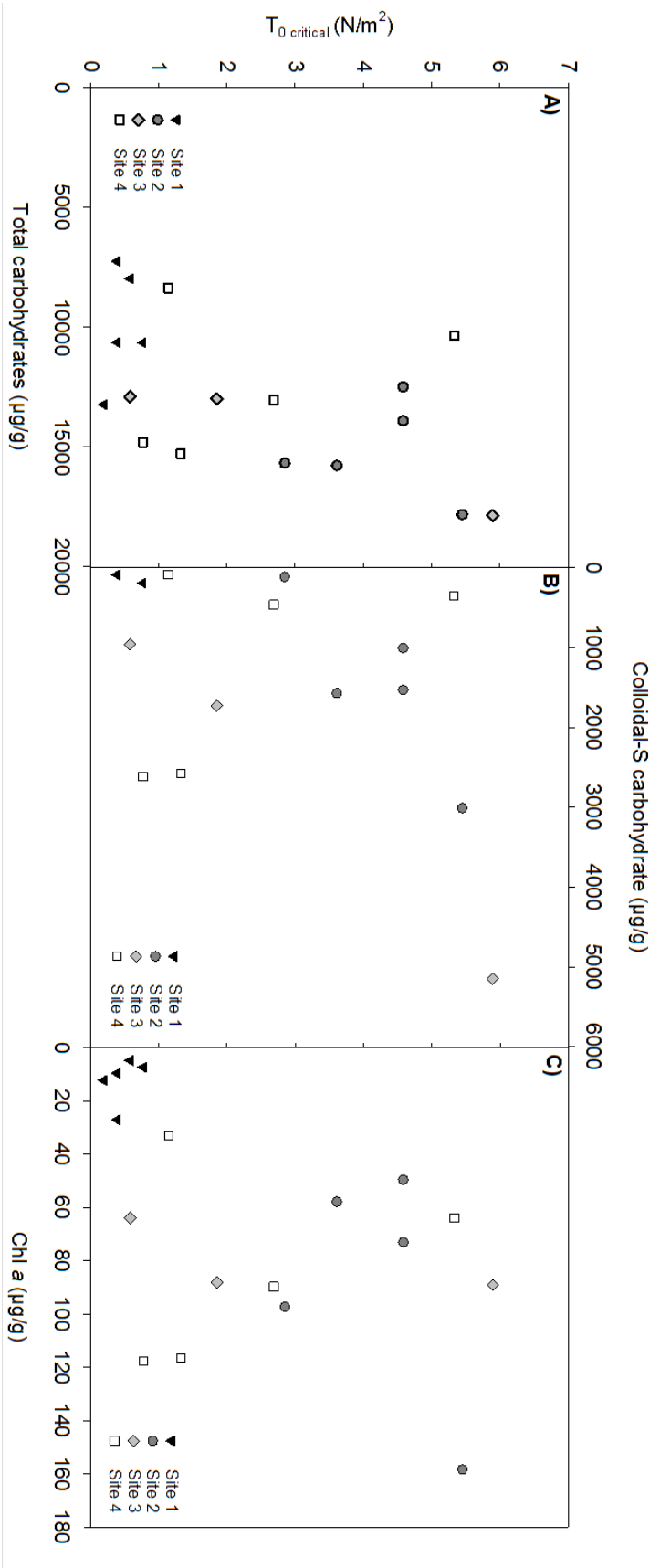

Figure 5.13: Sediment stability ($\tau_{0\ \mathrm{critical}}$) relationship with chlorophyll *a* content, and total and colloidal-S carbohydrate concentrations.

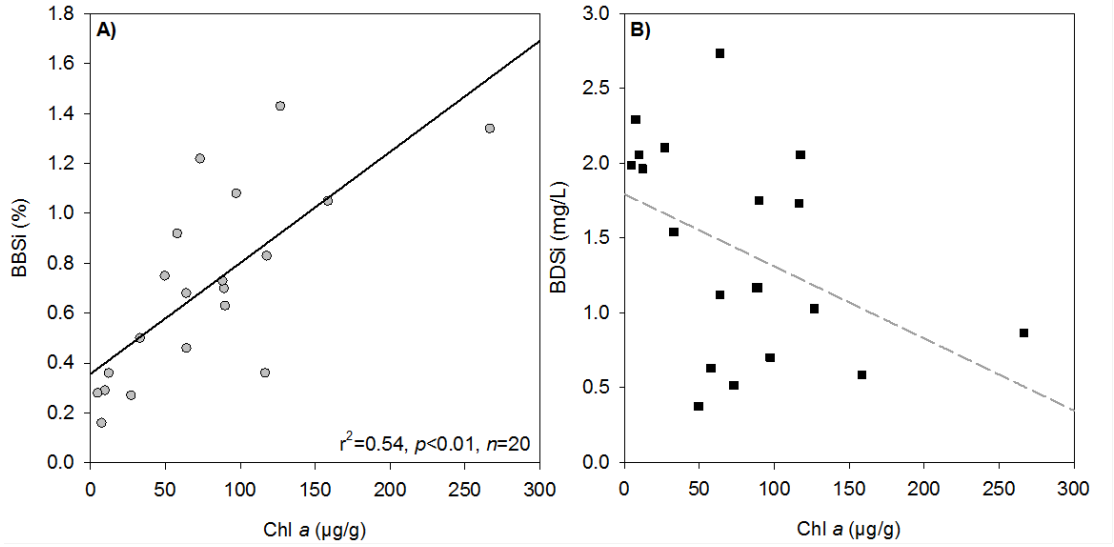

Figure 5.14: Benthic biogenic silica (% of dried Si mass, g/g) **(A)** and dissolved silicon (mg/L) **(B)** relationship with chl *a* content (*µ*g/g *dw. sed.*). No linear relationship between BDSi and chl *a* content, even with the removal of an outlier.

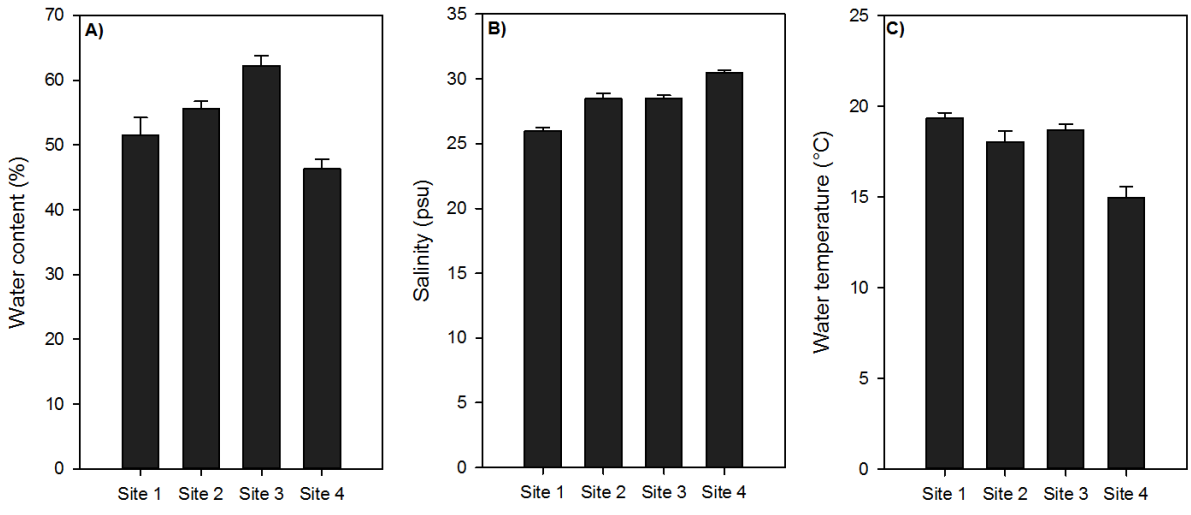

Figure 5.15: Environmental parameters measured on the intertidal mudflats of the Severn Estuary in September 2018. **A)** Water content (%). **B)** Salinity (psu). **C)** Water temperature (°C). Presented with 1SE of 5 stations.

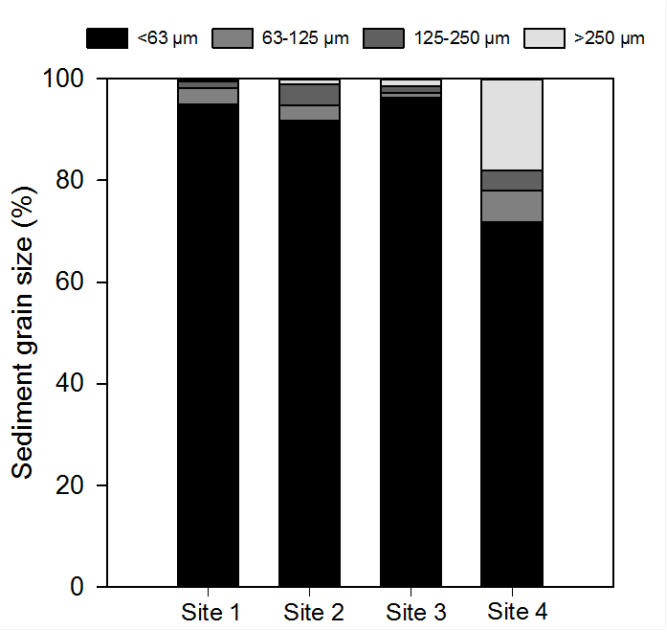

Figure 5.16: Sediment grain size (%) at each sampled mudflat on the Severn Estuary in September 2018. Average of 5 stations.

5.3.9 External controls on Si budgets: a PCA approach

A principal component analysis was carried out to assess the interconnections between the multiple environmental factors aiding sediment stability and whether these influenced the erosion of Si from the intertidal mudflats. PC1 and PC2 contributed to 59.2% of the variability in the data, whilst PC3 was responsible for a further 13.3% of the variability (Fig. 5.17).

In PC1 and PC2, BBSi, Chl *a*, total and colloidal-S carbohydrate concentrations, and $\tau_{0\ \text{critical}}$ clustered (Fig. 5.17). BBSi, an additional proxy indicating the presence of diatoms, appeared to control the sediment stability through the production of biostabilizing secretions. In addition, Chl *a* clustered with BBSi in PC3 (Fig. 5.17), suggesting with more diatoms (BBSi), biofilm biomass and sediment stability increased. With higher biomass, Si uptake by diatoms would lead to a reduction in surface DSi concentrations, which in PC1, displayed opposite loadings to both BBSi and chl *a*. The eroded BBSi sampled from the CSM chamber clustered with fine grain sediment ($<$ 63 μm) in PC1 and PC2, indicating the transport of the benthic diatoms along with the smaller grains, which have previously displayed strong linear correlations once resuspended (Table. 5.2). Similarly, the eroded DSi concentrations clustered with the surface BDSi concentrations in PC1 and PC3.

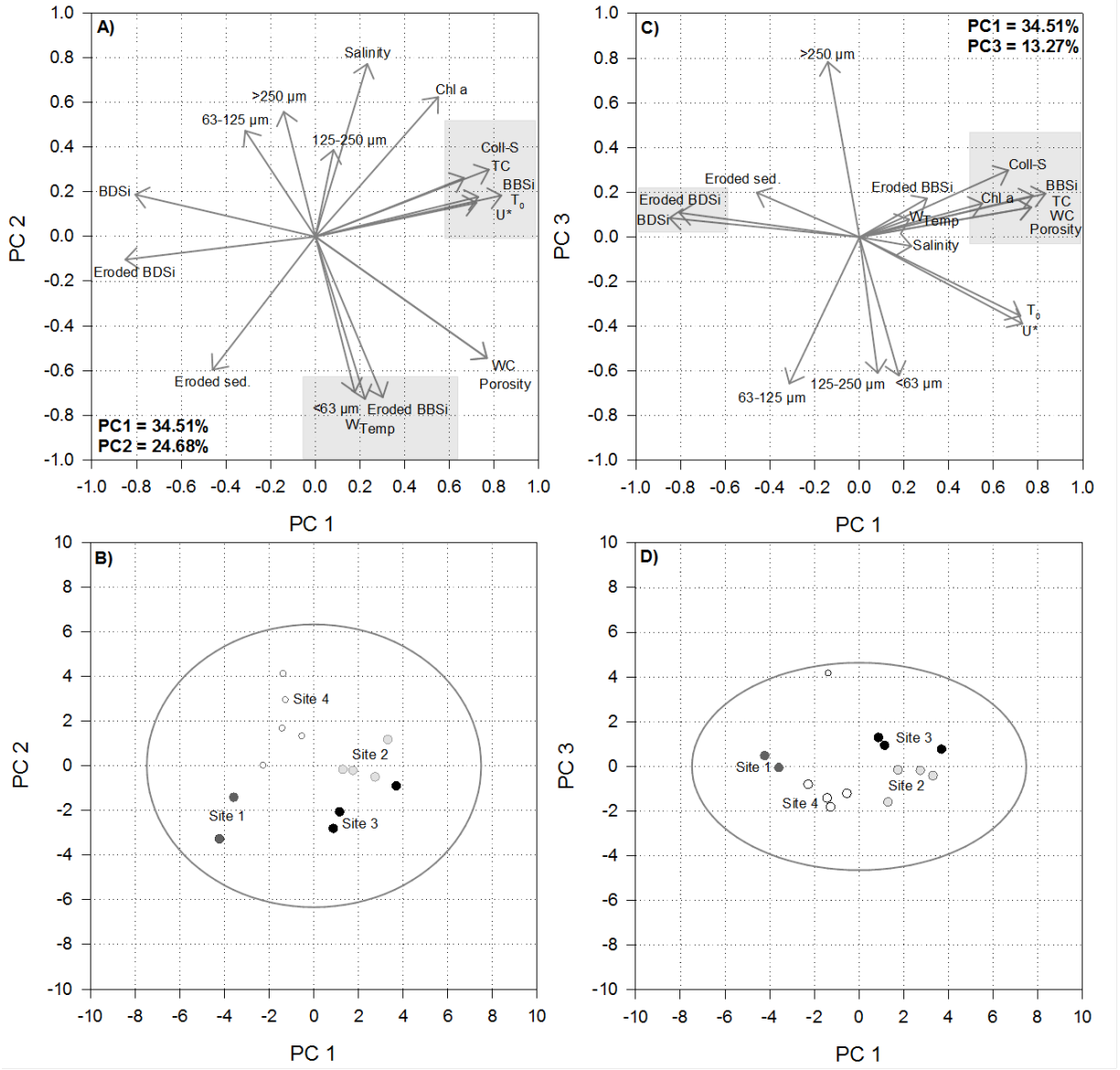

Figure 5.17: External controls on Si budgets: Principal Component Analysis, September 2018. **A)** PC1 vs PC2 loading plot. **B)** PC1 vs PC2 score plot. **C)** PC1 vs PC3 loading plot. **D)** PC1 vs PC3 score plot. Plotted: Eroded BBSi, Eroded BDSi, Eroded sediment, WC = water content, W_{Temp} = water temperature, salinity, porosity, BDSi = surface dissolved silicon concentrations, BBSi = benthic biogenic silica content, chl a = chlorophyll a, Coll-S = colloidal-S carbohydrate concentrations, TC = Total carbohydrates, τ_0 = critical erosion threshold, U* = shear velocity, and the sediment grain size fractions: <63 μm, 63-125 μm, 125-250 μm, >250 μm.

5.4 Discussion

The sediment benthic flux of Si to the water column is a key component in the benthic-pelagic coupling of estuarine ecosystems (Leynaert et al., 2011). The diffusive DSi flux from the intertidal sediment can sustain MPB development at the SWI, and through bottom-up control, can support coastal pelagic phytoplankton production (Longphuirt et al., 2009b). This benthic DSi flux significantly contributes to the success of siliceous organisms in estuaries when riverine DSi supply is low (Ragueneau et al., 2002; Fouillaron et al., 2007). As previously described in Chapters Three and Four, the MPB can also be an additional source of BBSi to the water column. To determine this contribution of Si from the intertidal mudflats to the water column of the Severn Estuary, the erosion of surface BDSi and BBSi, and the diffusive flux of DSi across the SWI, have been calculated. The multiple forcings controlling these benthic Si fluxes are discussed below. Most importantly, the effect of sediment biostabilization by the formation of diatom-dominated biofilms on the export of Si is examined (see Hypothesis Three - objective one, Chapter One, Section 1.5).

5.4.1 BDSi concentrations and percentage of biofilm BBSi

The percentage of BBSi on the Severn Estuary intertidal mudflats in the summer of 2018, were relatively low (<1.4%) (Fig. 5.1), but concur with the 2016 study (see Chapter Four, Section 4.3.1.1), the 2017 pilot study (see this chapter's Appendix, Section 5.6), and published estuarine studies (Chou and Wollast, 2006; Liu et al., 2008; Welsby et al., 2016). The reasoning behind the relatively low percentage values is commonly attributed to the strong hydrodynamics in estuarine systems, which prevents the accumulation of BSi on the intertidal mudflats. BDSi concentrations also conform with previous concentrations measured in the summers of 2014 (Welsby et al., 2016), seasonal sampled periods in 2016 (see Chapter Four, Section 4.3.1.1), and the summer of 2017 (see this chapter's Appendix, Section 5.6) (Fig. 5.18). A synthesis of all the BBSi and BDSi budgets measured since 2014 (see Fig. 5.18) reflects the high spatio-temporal variation in Si commonly reported in these dynamics environments (Ragueneau et al., 2002; Longphuirt et al., 2009b; Leynaert et al., 2011; Raimonet et al., 2013; Welsby et al., 2016). The multiple production/consumption processes and reactions which modify the Si budgets and contribute to their heterogenous spatial distribution on intertidal mudflats, have been discussed in Chapter Four, and remain applicable to the Si budgets presented here. Primarily, the strong negative correlation between BDSi and BBSi and the opposite loading in the PCAs (Fig. 5.17), suggests Si biological uptake through the assimilation of DSi to BSi, significantly decreased BDSi concentrations, and accumulated BBSi in the sampled period of 2018.

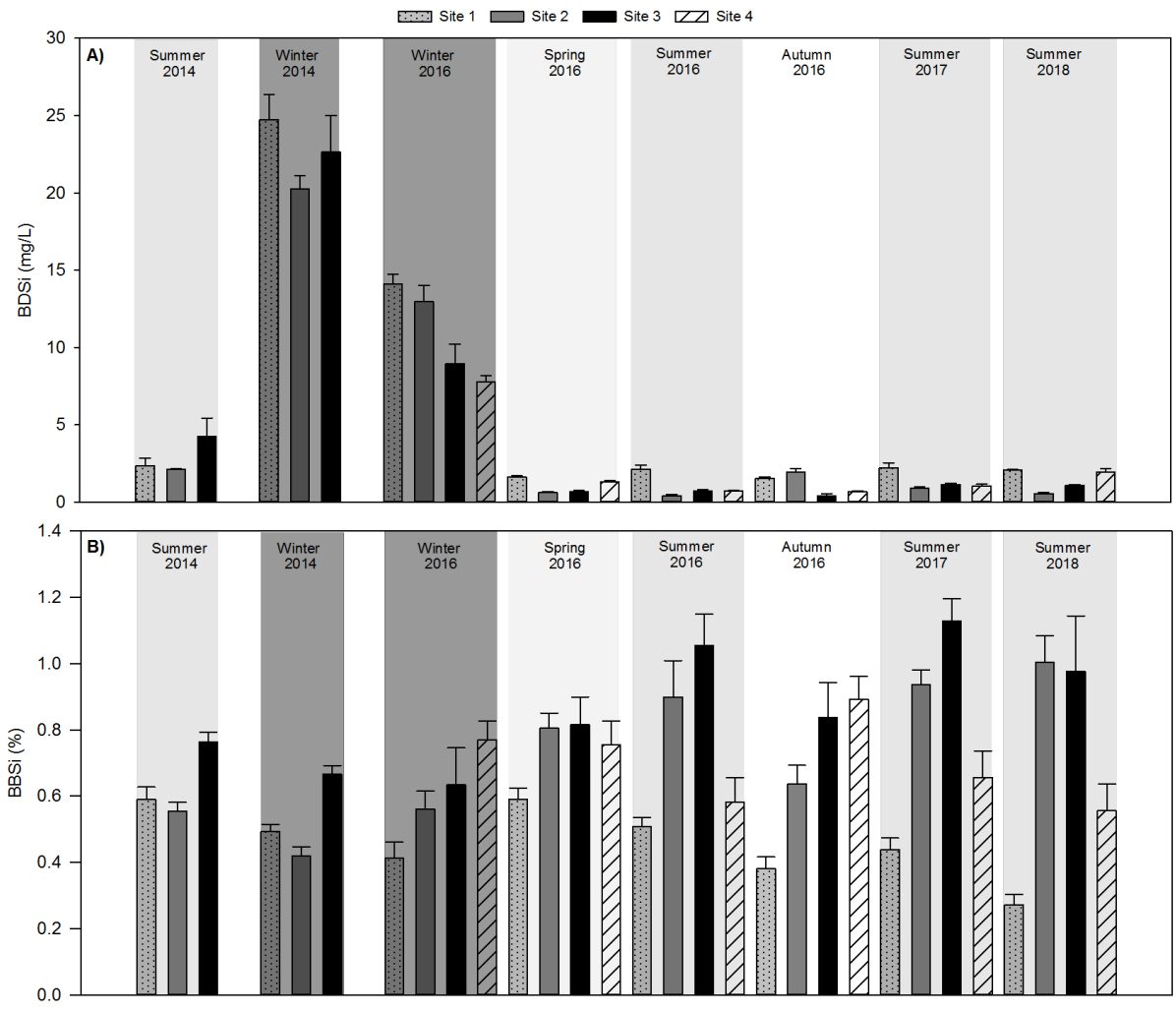

Figure 5.18: Summary of mudflat Si budgets **A)** Benthic Dissolved silicon (BDSi, mg/L). **B)** Benthic Biogenic silica (BBSi, % of dried Si mass, g/g). Presented with 1SE of the number of sampled stations: 2014 (*n=12*), 2016 (*n=15*), 2017 (*n=10*), 2018 (*n=5*).

5.4.2 Impacts of biostabilization on BDSi and BBSi budgets

The $\tau_{0\ \text{critical}}$ at Site 1 was significantly low compared to the other sampled mudflat sites (0.5 ± 0.1 N/m^2, Fig. 5.5). Low sediment stability was likely driven by significantly lower biomass levels (avg. 12.2 ± 3.9 μg/g, Fig. 5.11) and recently deposited sediment. The high bottom shear stress formed by the fast-flowing tidal currents in this area may have restricted biofilm formation. In addition, the CSM erosion profile at Site 1 displayed a sharp drop in transmission across the sensor head chamber with increasing pressure (Fig. 5.7), indicative of complete bed failure. A similar CSM erosion profile was also observed in the pilot study in 2017 (see this chapter's Appendix, Section 5.6). The chl *a* values were also lower when compared to the 2016 measurements at this mudflat (see Chapter Four, Section 4.3.2). In addition, no colloidal-S carbohydrates were measured in 60% of the samples at this site (Fig. 5.10), which may have reduced the biostabilization properties of the biofilms. The low MPB biomass could have reduced Si assimilation, leading to high surface BDSi concentrations (Fig. 5.1), and the inverse relationship between chl *a* and BDSi (Fig. 5.14). DSi uptake by diatoms at the sediment surface and at depth has been discussed in Leynaert et al. (2011), and references within, but the direct link between DSi uptake and MPB populations still requires significant research. Low MPB biomass may have lowered the potential for biostabilization, leading to high rates of BBSi erosion and low percentages of BBSi (<0.36%, Fig. 5.1). The subsequent enriched surface and pore fluid BDSi concentrations, which would have resulted in higher diffusive flux and a higher concentration of eroded DSi, could have contributed to the significantly high PDSi concentrations in the surf zone in the upper estuary (Fig. 5.9). These surf zone concentrations (avg. 2.0 ± 0.02 mg/L, Fig. 5.9) were similar to PDSi concentrations measured in the upper estuary in 2016 (between 1.2 and 3.2 mg/L, see Chapter Three, Section 3.3.1).

Compared to Site 1, the more sheltered Site 2 and 3, indicated the presence of sediment biostabilization. A significant relationship was observed between chl *a* and carbohydrate (total and colloidal-S) concentrations (Fig. 5.12) following the removal of an outlier. Several studies document this relationship between chl *a* and colloidal-S carbohydrate concentrations (Underwood and Paterson, 1993; Underwood et al., 1995; Sutherland et al., 1998; Blanchard et al., 2000; Yallop et al., 2000). Colloidal-S carbohydrates consist of both polymeric and non-polymeric material. Underwood et al. (1995) report that only 20-25% of the secreted colloidal carbohydrates is polymeric, e.g. colloidal-EPS, the polymeric substance released by diatoms as a by-product of photosynthesis. Despite the likely hood of high quantities of non-polymeric material, a strong linear correlation was observed (Fig. 5.12), which would suggest the growth of the biofilms aided sediment stability, a processes referred to as biostabilization. However, no significant relationship was found between the erosion threshold of the sediment and the colloidal-S carbohydrate concentration (Fig. 5.13). Perkins et al. (2004a) note that

a high concentration of colloidal carbohydrates was required to reach a high erosion threshold.

Increased MPB biomass reduced BDSi concentrations (Fig. 5.14), and alongside increased biostabilization (Fig. 5.10), led to significantly higher erosion thresholds (Fig. 5.5), and potentially higher percentages of BBSi. In support, the CSM erosion parameters clustered with BBSi in the PCA (Fig. 5.17). Further, chl *a* displayed a strong linear correlation with BBSi content (Fig. 5.14). At Site 3, the sampled stations near the saltmarsh 'clumps' had high chl *a* values (266.5 and 126.7 μg/g *dw. sed*), which, given to the likely high abundance of phytoliths, drove high percentages of BBSi.

Site 4 on the other hand, commonly known as Sand Bay, had low MPB biomass and colloidal-S carbohydrate concentrations, possibly attributed to the high abundance of coarser material (Fig. 5.16). Further, sand grains are often colonised by epipsammic diatoms, which have little movement, and potentially have less bound carbohydrates (*pers. comm.* with Prof Marian Yallop). Therefore, among the sampled sites, there was high spatial variability in biostabilization, driven by changes in MPB biomass and carbohydrate (total and colloidal-S) concentrations, associated with environmental conditions (e.g. sediment composition, erosion and deposition processes). In the absence of any species counts, this study cannot rule out the possibility of changes in the species community (e.g. other algae, euglenoids, cyanobacteria), which could have influenced the chl *a* content and the concentrations of total and colloidal-S carbohydrates. However, visually these biofilms appeared to be diatom-dominated (golden brown in colour, *pers. obs.*). Further research could look into, for example, chl *b* pigments to determine the presence of green algae, and investigate the effect of their presence on sediment stability.

5.4.3 Benthic supply of BDSi and BBSi to the Severn Estuary water column

5.4.3.1 Erosion of BBSi and BDSi from the mudflats

Despite the spatial variability in biostabilization, the erosion thresholds of all the measured MPB biofilms in September 2018 (Fig. 5.5) were below the calculated values (using the quadratic friction law, see Chapter Three, Section 3.4.4.1) needed to resist erosion by the estuarine bottom currents. For example, peak $\tau_{0\ \text{critical}}$ of 4.2 N/m^2 was less than the bottom shear stress calculated for the spring tide (55.2 N/m^2) and neap tide (13.8 N/m^2). The erosion thresholds presented here (max. of 5.9 N/m^2) are in-line with published values from Site 2 [0.4−10.8 N/m^2, Yallop et al. (2000)]. Further, the shear velocity (U*) was below 8 cm/s in September 2018, and significantly below the mean spring and neap tidal current velocities (Uncles, 2010). Therefore, based on these calculations, the MPB biofilms sampled in September 2018 and in the pilot study in

August 2017, would likely have been eroded, transporting the associated BBSi into the water column. This erosion supports the second hypothesis stated in Chapter Three (Section 3.4.4), whereby the high tidal flows exceed the erosion threshold of the biofilms despite the presence of the MPB aiding sediment biostabilization.

The bulk resuspended BBSi concentrations in the sensor head chamber of the CSM were considerably higher (e.g. 91.4 mg/L at Site 3, Fig. 5.8) compared to the PBSi concentrations in the surf zone (e.g. 11.8 mg/L at Site 3, Fig. 5.9). The combination of the estuarine geometry and hydrodynamics likely immediately dispersed the eroded biofilms. Further, with high deposition rates (Manning et al., 2010) coupled to the export of BSi out of the estuary (e.g. into the Bristol channel, or tidal currents transporting BSi up the estuary and into the tributaries peripheral estuaries), this may have led to the lower values of PBSi concentrations measured in the water column. A considerable intertidal mudflat BBSi erosion flux of 5.7 x10^{10} kg/year (spring tide) and 3.0 x10^{10} kg/year (neap tide) was calculated (Table 5.3). These erosion fluxes were within a magnitude of error compared to the calculated BBSi flux in Chapter Three (Section 3.4.4): Sed(t) = 1.69 x10^{10} kg/year, which was calculated from the PBSi loads assuming a downward transport of Si along the Severn. Note, the BBSi flux estimated in Chapter Three was based on PBSi concentrations sampled on a neap cycle. Despite the assumptions in these two calculations and the temporal variation between the sampled years, they output similar large BBSi erosion estimates, which further supports the hypothesis that the intertidal mudflats are a source of BSi.

Here, the erosion flux of BDSi is described by the processes of advection, defined as the transport of DSi responding to a pressure gradient or a force, which along with diffusion (see Section 5.4.3.2), can result in the export of DSi from the sediment (Corey and Auvermann, 2003). For example, during the flood tide, the turbulence and advection generated by the tidal currents disturbs the pore fluids as the MPB biofilms are eroded, which then leads to the mixing of BDSi-rich pore fluid with the overlying bottom water. Compared to BBSi, a relatively small concentration of BDSi was eroded (avg. 1.3 $\pm$ 0.2 mg/L at Site 1, Fig. 5.8). DSi erosion rates calculated from this September 2018 study were low (Table. 5.3) compared to the DSi flux (Sed[t] = 8.51 x10^{9} kg/year) estimated in Chapter Three (Section 3.4.4). The BDSi erosion flux reported in this chapter was estimated based on the intertidal mudflat area (SEP, 2009; Pethick et al., 2009), whereas the higher estimate using Vollenweider (1968) considered the entire estuarine volume (see Chapter Three, Section 3.4.4).

Accompanying the high BBSi erosion, a significant export of sediment was calculated in September 2018 (max. 37.7 g/L at Site 1, note unit discrepancy). At each mudflat site, BBSi and SPM concentrations in the CSM sensor head chamber correlated (Table. 5.2), suggesting that once the erosion thresholds of the biofilms were overcome, the diatom cells and the accompanying biofilm and sediment were resuspended. The

PCA also showed similar variance in the fine sediment fractions (< 63 μm) and the eroded BBSi data (Fig. 5.17). The possibility of bioflocculation in the upper estuary (the focal point of intense estuarine mixing) was previously discussed in Chapter Three (Section 3.4.4.2). The strong correlation between SPM and BBSi concentrations in the resuspended matrix (Table. 5.2) and in the surf zone (see Section 5.3.6), supports the presence of bioflocculation in this high energy zone (Manning et al., 2010). Further research should analyse these floc mixtures *in-situ*, to help understand the natural transport of this benthic matrix and the associated Si.

As expected, the SPM erosion rates were high compared to those of BBSi and BDSi, with up to 1.9 x10^{13} kg SPM/year exported from the intertidal mudflats. These sediment erosion rates are vastly overestimated compared to previous estimates in the Severn, for example, 2.4-4.0 x10^{9} kg/yr for the entire fine sediment supplied from the mudflats, rivers, cliffs etc. (Kirby, 2010). In addition, Allen (1990) suggests a total of 1.16 x10^{13} kg of sediment in the Severn Estuary (including the water column, mudflats and saltmarshes). This discrepancy could be attributed to the simplicity of the erosion equation used here, which assumes, i) the average erosion rate is the same for the entire intertidal area, and ii) the tidal currents in all locations on the mudflats results in erosion (i.e. τ_b greater than $\tau_{0\ \mathrm{critical}}$). Further, this discrepancy also implies that the BBSi and BDSi erosion estimates are also overestimated. Clearly, the erosion of the mudflats is a complex process, which is dependent upon multiple competing processes, including the stage in the tidal cycle, river discharge rates, local characteristics (exposed vs sheltered), and sediment composition. Further, there is a continuous recycling of SPM through the erosion and deposition of sediment, which can aid in the formation of cohesive sediment beds on the intertidal mudflats. These processes have been discussed in commentary reviews by Kirby (2010), Manning et al. (2010), Uncles (2010), and published papers within. These complex sediment processes could be better captured using numerical models, for example those previously applied to the Severn in Owen (1980), Uncles (1984), Wolf (1987), Xia et al. (2010a), and Xia et al. (2010b).

5.4.3.2 BDSi diffusive flux from the intertidal sediment

During immersion periods, the pore fluids of the subsurface of intertidal mudflats are substantially enriched in DSi primarily due to the dissolution of accumulated diatoms (Sigmon and Cahoon, 1997). These enriched pore fluids forms strong concentration gradients across the SWI that creates favourable conditions for the diffusive fluxes of DSi into the overlaying water column (Leynaert et al., 2011). In September 2018, depth profiles up to 20 cm deep at all sampled stations (Fig. 5.2), displayed the (pseudo)asymptotic profile often reported in intertidal sediments (Leynaert et al., 2011). To account for the varying changes in BDSi concentrations with depth, several gradients (dC/dx) were considered and summed (Fig. 5.4) in order to estimate the flux of BDSi from the sediment into

the overlaying pelagic water. Negative flux values were reported between 1 cm deep and the surface water at Site 1, 3 and 4, possibly linked to processes such as mixing, advection (rejuvenation of DSi-rich surface water by land-runoff), and biological uptake by benthic diatoms in the SWI. Sigmon and Cahoon (1997) also report negative flux values (i.e. lower DSi concentrations in the sediment), and attributed this to reduced dissolution rates and higher MPB growth.

The overall diffusive flux was greatest at Site 2 and Site 3, and low at Site 1 and Site 4 (Table. 5.1). This spatial variation can be explained by several physical, chemical and biological processes which can alter the overall flux of BDSi and other nutrients from the sediment into the water column. These include turbulence (tidal current velocities), bioturbation, temperature, deposition rates, groundwater and surface water flow, sediment composition and porosity, which all occur over different spatial-temporal scales (Callender and Hammond, 1982; Sigmon and Cahoon, 1997; Srithongouthai et al., 2003). These processes could also have influenced the BBSi depth profile. In comparison to the asymptotic BDSi profiles, BBSi displayed the common inverse relationship, and fluctuated significantly between each 1 cm increment increase in depth. BBSi also remained high at a depth of 20 cm's, indicating burial of BBSi (Fig. 5.3). The balance between Si assimilation and remineralization rates could have impacted these Si depth profiles, including biological uptake, adsorption, desorption, reverse weathering and regeneration of DSi from the dissolution of silica. Some of the abiological processes are explored in the following chapter, through an analysis of Si isotopes.

The BDSi diffusive flux from the sampled intertidal mudflats averaged (-)9.7x10^{-6} $\pm$ 6.2x10^{-6} mg/m^2/s, equivalent to 0.001 mmol/m^2/hr. This diffusive flux is considerably low when compared to other coastal environments (Aller and Benninger, 1981; Nixon, 1981; D'Elia et al., 1983; Yamada and D'Elia, 1984). For example, Leynaert et al. (2011) report diffusive fluxes of 0.8 to 1.5 mmol/m^2/hr for the Nakdong Estuary in Korea. Even when scaled-up for the area of the intertidal mudflats [20,300 ha, SEP (2009)], this resulted in only a diffusive flux of 62,000 kg/yr (Table. 5.1), which is considerably less that the BDSi flux supplied when the biofilms and associated DSi-rich porefluids are eroded (9.7x10^8 $\pm$ 2.7x10^8 kg/year, Table. 5.3). Leynaert et al. (2011) studied the difference between advective (i.e. bulk movement of the biofilm and porefluid due to tidal currents increasing turbulence at the SWI) and diffusive DSi flux, and concluded advective flux to be responsible for most of the DSi transfer from the sediment to the overlaying bottom waters during the first few minutes of immersion (400 times higher) compared to the diffusive flux occurring throughout the rest of the tidal cycle. Notably, they report this sudden exchange cannot be captured by benthic chambers or permanently flooded cores. Benthic chambers and DSi profiles have been used for such *in-situ* experiments, however there is a disagreement whether they produce similar or different diffusive flux estimates (Ragueneau et al., 2000). It is possible that the

fluxes calculated in this study were underestimated due to the simple design of the DSi profiles, however the surface water DSi concentrations (Fig. 5.1) concur with the samples measured in the surf zone (Fig. 5.9). The benthic chambers are also advantageous as they consider processes such as bioturbation, which can increase/decrease DSi diffusive flux (Ragueneau et al., 2000).

5.5 Conclusion

The flux of benthic DSi and BSi from the intertidal mudflats into the water column of the Severn Estuary, was investigated in September 2018. The percentage of biofilm BBSi and BDSi concentrations on the intertidal mudflats compared well to measurements taken in 2017, 2016 and 2014 on the same mudflats, and are in line with other estuarine systems.

A direct relationship was observed between MPB biomass and carbohydrate (total colloidal-S) concentrations, indicative of sediment biostabilization. Further, with significant correlations between MPB biomass and BBSi content, the growth of the biofilms was seen to be coupled to an increase in BBSi accumulation at the sediment surface. Therefore, despite the lack of correlation between $\tau_{0\ \text{critical}}$ and Si, through increased biomass, biostabilization has been shown to positively impact BBSi accumulation. Due to the high spatial heterogeneity in biofilm formation, biostabilization varied greatly between sites, with Site 1 in the upper estuary associated with low sediment stability and a low percentage of biofilm BBSi, compared to more sheltered sites (Site 2 and 3). However, despite the MPB biofilm biostabilization, the erosion thresholds were under the required level to prevent erosion of the biofilms due to the fast-flowing tidal currents creating intense mixing and resuspension in the hypertidal estuary. High estimated values of eroded DSi and BSi concentrations compared well to estimates calculated in Chapter Three (Section 3.4.4), despite large assumption in their calculations (e.g. assumes biofilms are present across the entire mudflat, and erosion is always greater than biostabilization). In addition, the diffusive flux of BDSi from the sediment into the surface water was less than the flux associated with the advective transport (i.e. erosion) of the DSi-rich porefluid expected upon immersion.

The resuspension of the mudflat sediment was closely coupled to the erosion of the BBSi. This relationship further supports the theory of bioflocculation in the water column, whereby sediment and the associated biofilm (BBSi) remain one-entity in the water column. The processes of bioflocculation requires further research, preferably *in-situ*, to better understand the impact and implications of this coupling on the transport of BSi.

In conclusion, this experiment has shown that the mudflats could be a contributing supply of BBSi and BDSi to the water column of the Severn Estuary, or at least the surf zone of the mudflats, in agreement with Hypothesis Three stated in Chapter One (Section 1.5). The following chapter uses silicon isotopes as an alternative technique to explore this export of Si, and aims to further interpret the multiple consumption/production processes mediating Si on the mudflats.

5.6 Appendix

In August 2017, a pilot study was carried out on the intertidal mudflats of the Severn Estuary, prior to the full-scale research project conducted in September 2018. This 2017 study found a trend between increased sediment stability ($\tau_{0\ \text{critical}}$) and higher percentage of biofilm BBSi, with lower mudflat water (a mixture of surface and pore fluid) BDSi concentrations (Fig. 5.19 & Fig. 5.20).

The erosion profiles followed the characteristic decreasing loss in transmission across the sensor head chamber with increasing pressure, with a complete loss of bed failure (steep gradient) at Site 1 and Site 4 (Fig. 5.20). The biofilms at Site 2 and 3, in the middle of the Severn Estuary were more stable, with a more gradual rate of erosion up until *ca.* 60 kPa, followed by bed failure. There was high spatial variability (large error bars) in the erosion profiles at Site 4.

Fine sediment (clay/silt) was only responsible for between 40 and 53% of the total sediment grain size, indicative of less cohesive sediments. In addition, the water content of the mudflats varied between 46% and 68%, possibly attributed to the large grain size increasing sediment porosity. Salinity averaged in the range of 17 to 23, representing a more terrestrial (riverine/groundwater) influence on the mudflat water as opposed to a tidal, saline influence.

This pilot study highlighted a connection between Si and sediment stability, but further research was required to link the benthic and pelagic systems, for example through sediment erosion and diffusion processes.

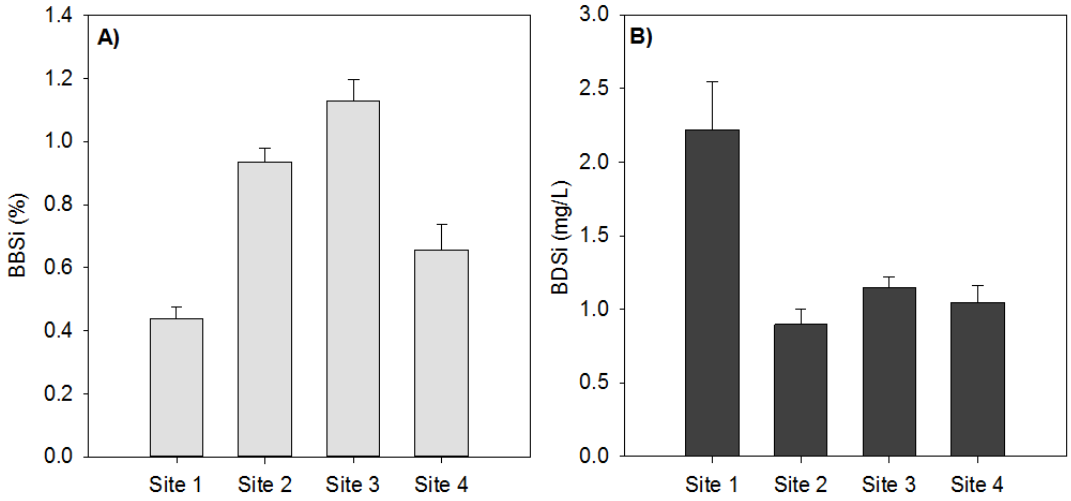

Figure 5.19: A) Average microphytobenthic biofilm biogenic silica (BBSi, % of dried Si mass, g/g) in the Severn Estuary in August 2017. **B)** Average benthic dissolved silicon concentrations (mg/L). Presented with 1SE, *n=10* at each Site).

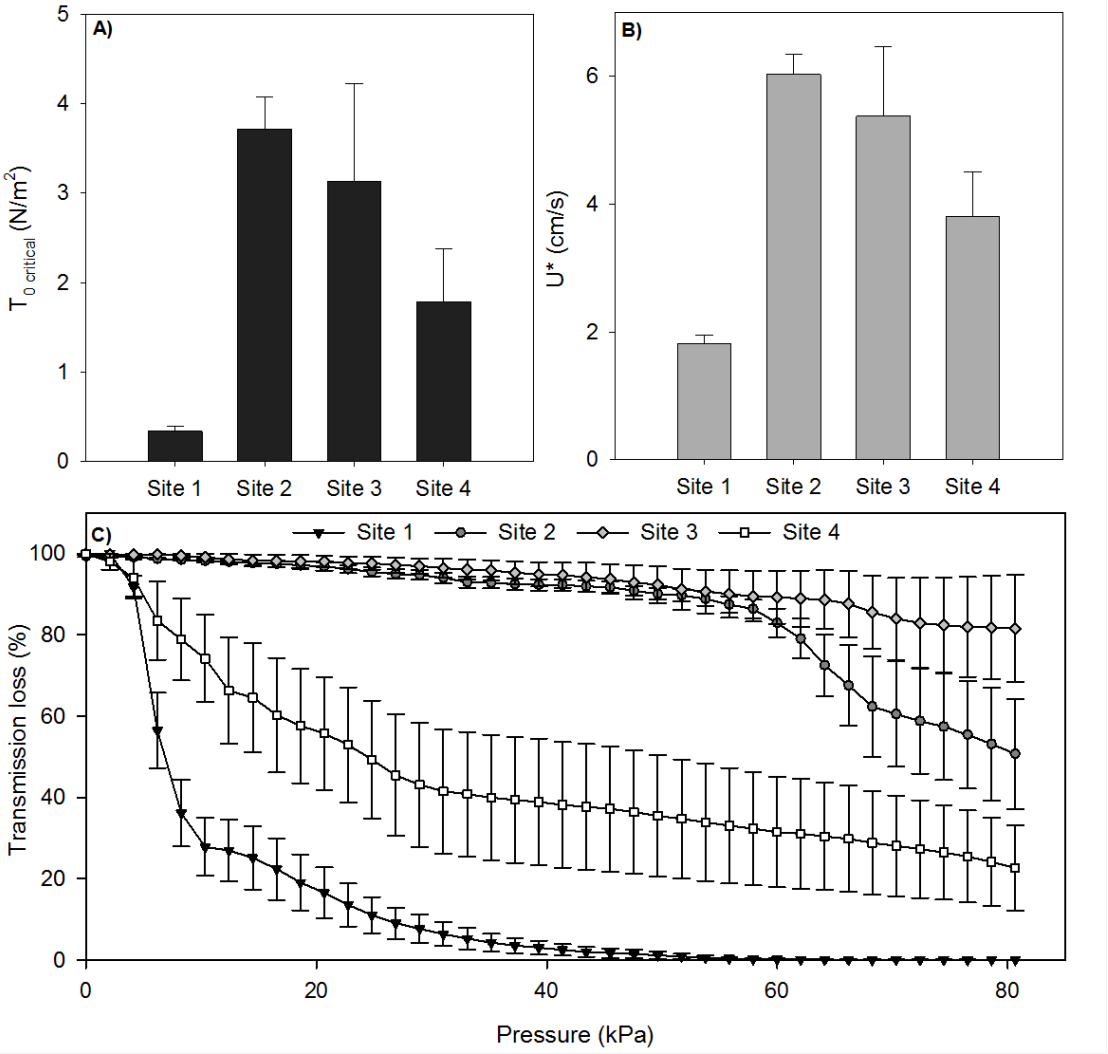

Figure 5.20: A) Average critical erosion threshold (τ_0 in N/m^2) from the intertidal mudflat sediments of the Severn Estuary in August 2017. **B)** Average shear velocity (U* in cm/s). **C)** Average erosion profiles of each station. Presented with 1SE, *n=10* at each Site.

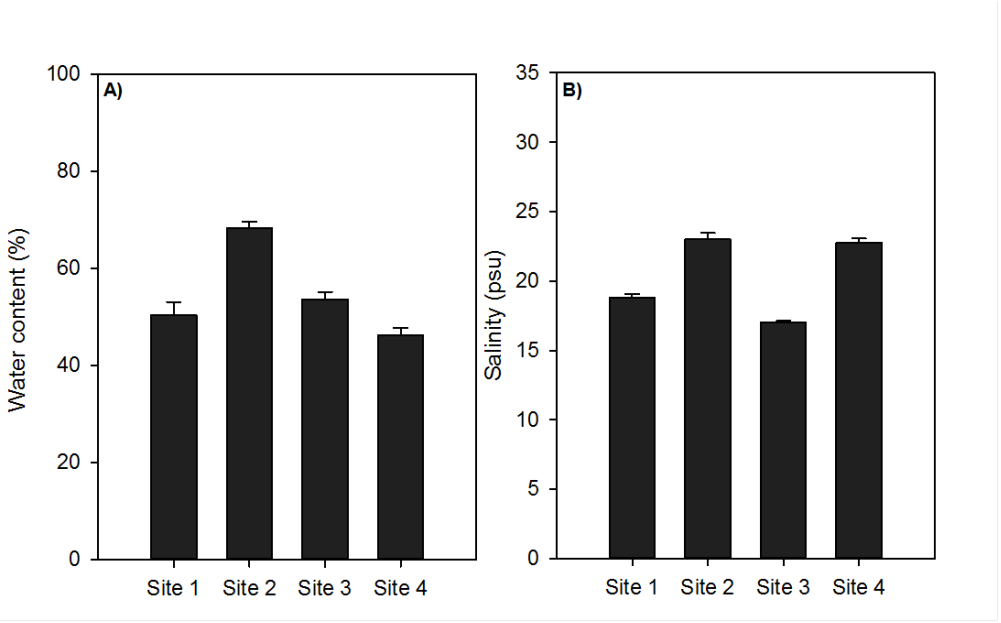

Figure 5.21: Environmental parameters measured on the intertidal mudflats of the Severn Estuary in August 2017. **A)** Water content (%). **B)** Salinity (psu). Presented with 1SE, *n=10* at each Site.

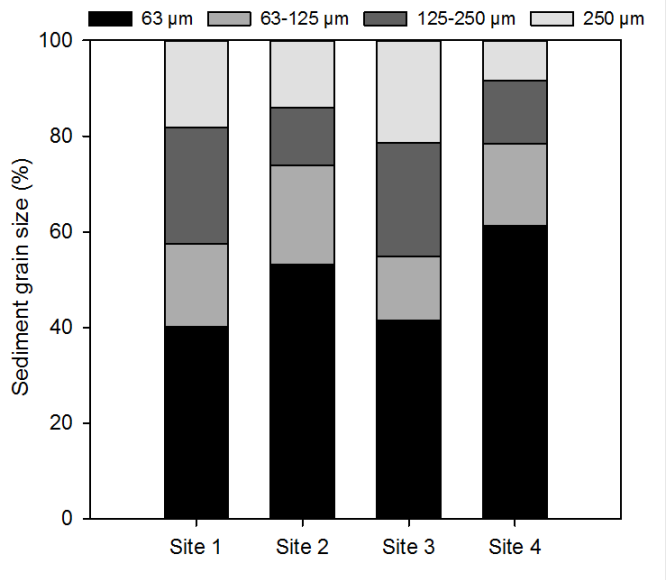

Figure 5.22: Sediment grain size (%) at each sampled mudflat on the Severn Estuary in August 2017. Average of 10 stations.

Chapter 6

Silicon isotopes in the Severn Estuary

6.1 Introduction

Silicon (Si), the second most abundant element in the Earth's crust, is a key component of biogeochemical cycles (Opfergelt and Delmelle, 2012). Photosynthetic siliceous organisms require dissolved silicon (DSi), and through their life-cycle, indirectly play a major role in the oceanic carbon cycle, and subsequently on Earth's climate system (Tréguer et al., 2018). Between 70-85% of the DSi entering the ocean is supplied in rivers and groundwater (Treguer et al., 1995). The turbid Severn Estuary, in the southwest UK, has been used as a case study to investigate the role a hypertidal estuary has on influencing the supply of riverine DSi to a coastal zone. Further, the supply of particulate Si, in the form of biogenic silica (BSi), has been investigated to determine the siliceous productivity and uptake of DSi in this coastal system.

The hypertidal regime forms extensive intertidal mudflats, which are inhabited by siliceous diatom-dominated biofilms (Underwood, 2010). This study has previously shown that for the sampled periods in 2016, the high concentrations of suspended particulate matter (SPM) in the water column of the Severn Estuary, limited phytoplankton growth and productivity, which could not exclusively account for the relatively high BSi concentrations (see Chapter Three). The pelagic BSi (PBSi) dynamics mirrored the seasonal cycles of benthic diatoms on the intertidal mudflats, which were shown to have high rates of productivity with the potential to biologically mediate Si, through enhanced rates of DSi uptake and accumulation of benthic BSi (BBSi) (see Chapter Four). The fast-flowing tidal currents associated with high bottom shear stress, likely exceeded the erosion threshold of the biofilms, despite the high levels of biostabilization, and resulted in high resuspension rates of the mudflat sediment, biofilm and subsequently BBSi (see Chapter Five). The high erosion rate prevented the build-up of BBSi on the mudflats.

However, the benthic diatoms, especially during the typically productive periods, had fast turnover rates, which likely led to a continuous supply of BBSi to the water column.

Stable Si isotopes (^{28}Si, ^{29}Si and ^{30}Si) are an exciting new approach to research the complex biological and abiological controls on riverine DSi supply. Si isotopes have recently gained momentum as tools for investigating the marine system, but few have applied them in the study of estuarine Si cycling. The purpose of this contribution is to further investigate the relationship between the benthic intertidal and pelagic Si systems in the Severn Estuary. Si isotopes from the water column of the River Severn and Severn Estuary from the summer and autumn sampled periods of 2016, alongside Si isotopes from the mudflat waters (a mixture of surface and pore fluid), have been measured to shed more light on the apparent close coupling between the benthic and pelagic systems during these periods (see Chapter Three).

Within this framework, the specific aims of this chapter are to:

- Give an overview of δ^{30}Si of DSi values, hereafter $\delta^{30}Si_{DSi}$, in rivers and estuaries.
- Measure the first $\delta^{30}Si_{DSi}$ values from the Severn's pelagic and benthic systems.
- Determine the biological and abiological processes influencing the isotopic signatures in the pelagic and benthic systems of the Severn.

6.1.1 Silicon isotope fractionation

Isotopes of an element in their atomic nucleus have the same number of protons and electrons, but a different number of neutrons, which results in different masses. Compared to the radiogenic isotopes, which spontaneously convert to other nuclei, stable isotopes don't decay over time. There are three stable isotopes of Si which occur naturally: ^{28}Si, ^{29}Si and ^{30}Si, which have a relative abundance of *ca.* 92.2%, 4.7% and 3.1%, respectively. The atomic masses are 27.97693, 28.97649 and 29.97377, respectively (Frings et al., 2016).

Isotopic fractionation is the variation in the isotopic abundance between two components, which can be described by two types of mass-dependent fractionation laws: equilibrium and kinetic. Equilibrium fractionation is defined as the partial separation of isotopes due to the difference in atomic masses between two or more substances in chemical equilibrium. Kinetic fractionation is the result of a unidirectional chemical reaction and/or transport between two components that separate the stable isotopes from each other by their mass. Both forms of fractionation generally favour the preferential transfer of the lighter isotope leaving the heavier isotope in the initial component. Most low-temperature processes that occur in the oceanic-continental Si cycle lead to the fractionation of Si isotopes, including, a) the removal of DSi during the dissolution of primary silicates, b) during the formation of secondary silicate minerals (clays)

(Michalopoulos and Aller, 2004), c) through the adsorption of Si onto iron oxide (Opfergelt et al., 2009), and d) during the biological formation and abiological dissolution of biogenic silica (BSi) (e.g. diatom frustules and sponges), and higher plants. During these chemical and biological processes, Si isotopes are fractionated, with the light isotope of Si (^{28}Si) preferentially incorporated into the precipitated phases, leaving the surrounding residual aqueous medium isotopically heavy (^{29}Si & ^{30}Si) (De La Rocha et al., 2000). Therefore, this fractionation offers a great potential as a tracer of Si cycling in aquatic environments.

Si stable isotope variations are presented here in delta notation as δ^{30}Si. The delta notation is the deviation in part per thousand of a given ratio, for example, ^{30}Si/^{28}Si, against the ratio of a standard reference material: international Si standard Quartz RM8546 (NBS-28), distributed by the National Institute of Standards (NIST). The Si isotopic value of a sample was calculated (eq. 6.1) and presented here in ‰ to be consistent with the International Union of Pure and Applied Chemistry (IUPAC) nomenclature:

$$\delta^{x}\mathrm{Si}(‰) = \left(\frac{\left(\frac{^{x}\mathrm{Si}}{^{28}\mathrm{Si}}\right)_{\mathrm{SMP}}}{\left(\frac{^{x}\mathrm{Si}}{^{28}\mathrm{Si}}\right)_{\mathrm{STD}}} - 1 \right) * 1000 \tag{6.1}$$

where, x corresponds to ^{29}Si or ^{30}Si, SMP is the sample, and STD is the standard Quartz RM8546 (NBS-28).

6.1.2 δ^{30}Si in rivers and estuaries

The elevated $\delta^{30}\mathrm{Si}_{\mathrm{DSi}}$ in the hydrosphere compared to silicate rocks reflect the above isotopic fractionation (Fontorbe et al., 2013). Whereas the $\delta^{30}\mathrm{Si}_{\mathrm{DSi}}$ of seawater reflects the balance between the riverine and groundwater DSi supply (generally between 0.0 and +3.4 ‰) and DSi supplied by deep sea hydrothermal vents (generally -0.3 ‰), in conjunction with other precipitation reactions, including the biomineralization of BSi (Fontorbe et al., 2013).

Isotope fractionation in diatoms was recently suggested to be species dependent, with a fractionation factor (ϵ) on average of -1.2 ± 0.5 ‰ reported in marine diatoms (Sutton et al., 2013) and -1.1 ‰ reported in freshwater diatoms (Alleman et al., 2005). Other silicifying organisms, for example benthic filter-feeding sponges that uptake DSi for skeletal growth, show a wide range in the apparent fractionation factor from -1 to -5 ‰ (Wille et al., 2010; Hendry et al., 2011; Hendry and Robinson, 2012), which varies according to the ambient DSi concentration, and can differ between different types of sponge spicules (Hendry et al., 2015). Further, radiolarians, a marine protist zooplankton group, have a higher average fractionation factor of *ca.* -1.5 ‰ compared

to diatoms (Fontorbe et al., 2016).

To date, many studies have measured riverine $\delta^{30}Si_{DSi}$ (De La Rocha et al., 2000; Alleman et al., 2005; Georg et al., 2006, 2007, 2009; Cardinal et al., 2010; Engström et al., 2010; Ding et al., 2011; Hughes et al., 2012; Delvaux et al., 2013; Hughes et al., 2013; Fontorbe et al., 2013), with *ca.* 557 $\delta^{30}Si$ values measured. River $\delta^{30}Si_{DSi}$ values range from -0.14 to +4.66 ‰, and have a mean of +1.28 ‰ with a standard deviation of 0.68 ‰ (Frings et al., 2016). In comparison, marine $\delta^{30}Si_{DSi}$ values range between +0.4 and +3.1 ‰ (Opfergelt and Delmelle, 2012). One of the key issues in estimating global $\delta^{30}Si_{DSi}$ values, is that they are extrapolated from riverine values, which are often sourced at considerable distances upstream from their mouths. Therefore, these estimates don't include important variations induced by the complex estuarine dynamics. Further, there is little knowledge as to what extent estuarine processes modify $\delta^{30}Si$ before the reactive Si reaches the oceans, which makes distinguishing whether the $\delta^{30}Si$ change is due to coastal/ocean mixing or estuarine processes difficult.

Temperate riverine and estuarine $\delta^{30}Si_{DSi}$ values vary depending on, a) discharge rates, whereby an increase in river flow will decrease $\delta^{30}Si$ values through reduced biological uptake, and b) the longitudinal length of a river, whereby $\delta^{30}Si$ values will increase further downstream as a result of slower water flow increasing water residence time (Frings et al., 2016). Further, the Si isotopic value can vary over spatial and temporal scales due to, a) mixing of base flow and superficial runoff (Georg et al., 2006), b) by the biomineralization of BSi by silicifiers, for example diatoms and phytoliths (Ding et al., 2004; Hughes et al., 2013), c) by the dissolution of BSi (Demarest et al., 2009) and d) the reverse weathering of BSi (Delstanche et al., 2009). These processes can imprint on the Si cycle in rivers/estuaries and have the potential to influence their Si isotope budget (Frings et al., 2016). The estuarine filter encompasses several biological and abiological processes that have the potential to influence DSi and BSi, together with their isotopic signatures. For instance, if the estuary is highly productive, DSi will be removed and stored. For example, in the Amazon River, diatom blooms can consume up to 50% of riverine DSi (DeMaster, 2002), and 100% in the Scheldt (Chou and Wollast, 2006). Unlike these phytoplankton productive systems, the benthic intertidal system in the Severn Estuary, which exhibits several biological and abiological processes, (as discussed in previous chapters), is likely to be key in influencing the Severn's isotopic Si budget.

6.2 Methodology

6.2.1 Fieldwork and laboratory work

The Severn Estuary was surveyed during sampled periods in the summer and autumn seasons of 2016. A transect from the upper freshwater zone of the River Severn, down to the inner Bristol Channel was surveyed. Water column samples were taken at four stations in the river, three in the estuary, and one in the Bristol Channel. No continuous transect was possible in the Severn due to accessibility issues (see Chapter Three, Section 3.4.6). In the estuary, water column samples were collected at two depths, one <2 m deep to represent the estuarine surface waters, and one >15 m deep to represent the deep estuarine waters, referred to here as the bottom water. For a detailed field methodology see Chapter Two (Section 2.1).

Water column samples were measured for pelagic DSi concentrations and pelagic BSi concentrations. PBSi was measured following the weak alkaline extraction method of marine sediments using the filtered sediment, adapted from DeMaster (1981). Freshwater PDSi and all PBSi concentrations were measured following the standard Heteropoly Blue method (Strickland and Parsons, 1972) on a Hach Lange DR3900 spectrophotometer. Filtered saline samples were measured for PDSi at Plymouth Marine Laboratory on a SEAL analytical AAIII segmented flow colorimetric auto-analyser. For a detailed outline of the above procedures see Chapter Two (Section 2.2).

6.2.2 Silicon isotopes

Filtered river, estuarine and mudflat water samples were analysed for their Si isotope value (δ^{30}Si). Note: no Si isotope data has been produced for the winter and spring sampled periods. Saline water samples were prepared following the MAGnesium Induced Co-precipitation (MAGIC) method of Karl and Tien (1992) with modifications by Reynolds et al. (2006), commonly used by Souza et al. (2012) and Grasse et al. (2013). The pH of all samples was tested before co-precipitation. Alkaline samples (pH>7.4) were acidified with 0.1% v/v HCl and left for 24 hrs to re-equilibrate. 1.2% v/v 1 M NaOH was added and left for 48 hrs for brucite precipitation. Samples were centrifuged (3000 rpm for 3 min), and the supernatant was transferred, and 1% v/v 1 M NaOH was added to the supernatant and left 48 hrs to extract any residual Si. The two precipitates were mixed with 0.001 M NaOH solution prior to a final separation by centrifugation. This was repeated three times. The precipitate was then dissolved by adding 6 M HCl, prior to column chromatography using the cation exchange resin, adapted from Georg et al. (2006).

A total of 1.8 mL of BioRad resin (AG50W-X12, 200-400 mesh in H^+ form) was precleaned, and rinsed with one distilled in-house HCl acid (3 M, 6 M and concentrated HCl) and Milli-Q H_2O, before the samples and standards (NBS and LMG08) were

Table 6.1: An example of silicon separation procedure for cation exchange chromatography.

Separation stage	Solution matrix	Volume
Rinse	Milli-Q H_2O	full reservoir
Cleaning	3 M HCl	10 mL
Cleaning	6 M HCl	10 mL
Cleaning	10 M HCl	10 mL
Cleaning	6 M HCl	5 mL
Cleaning	3 M HCl	5 mL
Rinse	Milli-Q H_2O	10 mL
Sample or standard	LMG08	433 μL
Elution	Milli-Q H_2O	3.2 mL

passed through the columns (see Table 6.1). This procedure was carried out, whereby the more concentrated acid was gradually added, to avoid air bubbles associated with the fast expansion of the resin. The samples and standards were purified though the BioRad resin to separate the positively charged cations such as Na^+, Mg^{2+} and Fe^{2+} from the solution without retaining Si. The uncharged silicic acid, in equilibrium with trihydrogen orthosilicate (H_3SiO_4) between pH values of 2 and 8, was passed through the column. The volume of each sample added to the columns was determined in order to produce a concentration of 7.2 μg of Si and a total volume (with the Milli-Q H_2O elute) of 3.6 mL, with a final 2 ppm Si solution. Samples and standards were stored in pre-cleaned LDPE 8 mL bottles, and analysed the following day.

6.2.2.1 Processing of isotope data

On the day of isotope analyses, samples were treated with 50 μL of Mg to obtain a 1:1 voltage intensity ratio between ^{24}Mg and ^{28}Si (Cardinal et al., 2003), and acidified with 30 μL of 0.1 M H_2SO_4 and 50 μL of 1 M HCl to remove any matrix effects on the solution from, for example, riverine sulphate and chloride (Hughes et al., 2011).

The determination of Si isotopes (^{28}Si, ^{29}Si, ^{30}Si) was performed on a Thermo Scientific Neptune Plus High Resolution multicollector inductively coupled plasma mass spectrometer (MC-ICP-MS) at the Bristol Isotope Group laboratories, University of Bristol. Prior to sample measurements, a purified Si solution was used to tune the mass spectrometer to reach the expected intensity, and correct for mass-independent fractionation. To compensate for machine drift, Si and Mg isotope peak centering was performed each session. To avoid interferences, for example from molecular ions with a similar mass-to-charge ratio, all measurements were made on the low mass side of the peaks (i.e. shoulder).

Table 6.2: Standard-sample bracketing protocol.

Blank
Standard (NBS)
Standard (LMG08) or sample
Standard (NBS)
Blank

6.2.2.2 Post processing of isotope data

Raw measurements were a) blank corrected, and b) corrected for instrument mass bias which effects fractionation using a standard-sample bracketing protocol and Mg isotopes (^{24}Mg, ^{25}Mg, ^{26}Mg) (Cardinal et al., 2003).

a) Blank correction on the isotopes (^{28}Si, ^{29}Si, ^{30}Si, ^{24}Mg, ^{25}Mg, and ^{26}Mg) of the samples and the bracketing standards was applied by taking the intensity average of two bracketing blanks corresponding to each peak. For example, following eq. 6.2:

$$\mathrm{X_{corrected}} = \mathrm{X_{raw}} - \mathrm{mean(X_{blank})} \tag{6.2}$$

where X is the selected isotope (e.g. ^{28}Si, ^{29}Si, ^{30}Si, ^{24}Mg, ^{25}Mg, or ^{26}Mg).

The standard-sample bracketing protocol allows the cancellation of the mass-bias since both the standard and sample are equally affected for similar standard and sample intensity (Table. 6.2).

b) Mg isotopes, which have a similar mass to Si and has three isotopes, are expected to behave in a similar manner with respect to mass bias in the plasma mass spectrometer. Mg was added to use Mg isotopes (Inorganic Venture 1484 Mg Standard) to correct for mass bias effect in the plasma-spectrometer interface during Si isotope measurements (Zambardi and Poitrasson, 2011). Mg was added to the samples and the standards to give a concentration of 0.1 ‰. Si isotope ratios were corrected with a Mg isotope fractionation factor ($\epsilon_{\ \mathrm{Mg}}$), which was calculated from the result of the ^{25}Mg/^{24}Mg and ^{26}Mg/^{24}Mg ratio following the exponential mass bias law (eq. 6.3), and then applied to the measured Si isotope ratio (^{29}Si/^{28}Si and ^{30}Si/^{28}Si) (eq. 6.4).

$$\varepsilon_{\mathrm{Mg}} = \ln\left(\frac{\left(\frac{^{26}\mathrm{Mg}}{^{24}\mathrm{Mg}}\right)_{\mathrm{true}}}{\left(\frac{^{26}\mathrm{Mg}}{^{24}\mathrm{Mg}}\right)_{\mathrm{measured}}}\right) / \ln\left(\frac{\mathrm{mass}^{26}\mathrm{Mg}}{\mathrm{mass}^{24}\mathrm{Mg}}\right) \tag{6.3}$$

$$\left(\frac{^{30}\mathrm{Si}}{^{28}\mathrm{Si}}\right)_{\mathrm{true}} = \left(\frac{^{30}\mathrm{Si}}{^{28}\mathrm{Si}}\right)_{\mathrm{measured}} * \left(\frac{\mathrm{mass}^{30}\mathrm{Si}}{\mathrm{mass}^{28}\mathrm{Si}}\right)^{f} \tag{6.4}$$

The δ^{30}Si was then calculated using the internally normalised ^{29}Si/^{28}Si and ^{30}Si/^{28}Si sample ratios (A) with the internally-normalised ^{29}Si/^{28}Si and ^{30}Si/^{28}Si bracketing-standard ratio (B) (eq. 6.5):

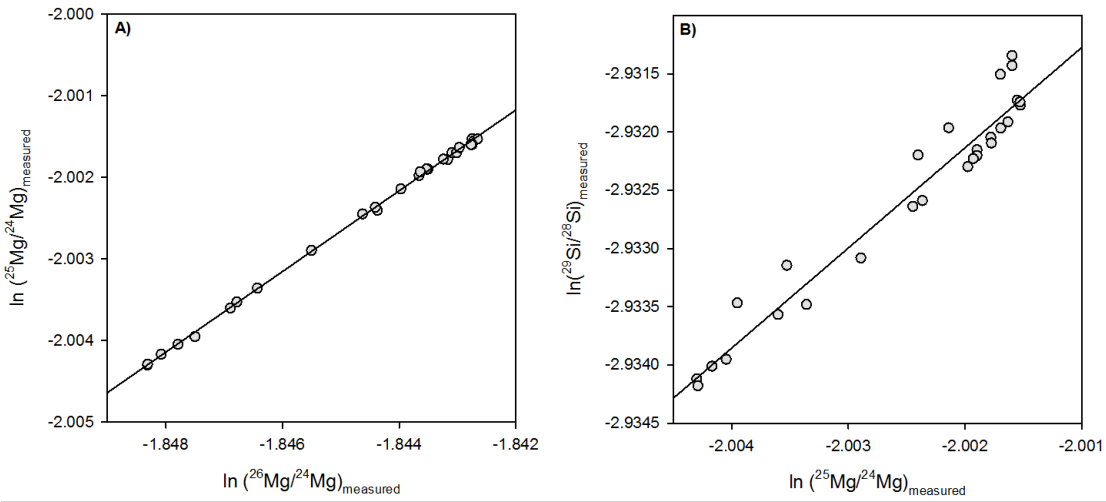

Figure 6.1: MC-ICP-MS measured ratios of **A)** ln(^{25}Mg/^{24}Mg) vs ln(^{26}Mg/^{24}Mg) which follows the predictable linear relationship of y=0.4952x-1.089, r^2=0.999, **B)** ln(^{29}Si/^{28}Si) vs ln(^{25}Mg/^{24}Mg) (y=0.8599x-1.211, r^2=0.944) on 1st June 2017.

$$\delta^{30}\mathrm{Si} = \frac{\left(\frac{^{30}\mathrm{Si}}{^{28}\mathrm{Si}}\right)_{\mathrm{A}}}{\left(\frac{^{30}\mathrm{Si}}{^{28}\mathrm{Si}}\right)_{\mathrm{B}}} - 1 \tag{6.5}$$

Differences in instrumental conditions result in changes in the absolute value of Si and Mg isotopic ratios (Cardinal et al., 2003). Thus calculations are only based on ln(^{29}Si/^{28}Si)$_{\mathrm{measure}}$ and ln(^{25}Mg/^{24}Mg)$_{\mathrm{measure}}$ obtained within the same analysis run, for example Fig. 6.1. Large Mg-corrections suggests Mg and Si are behaving dissimilarly, and either the above outlined correction procedures didn't work or there was a large mass-bias, for example, effect of organic matter (Hughes et al., 2011).

The long-term external reproducibility of the measurements was assessed using sponge standard LMG08 (Hendry et al., 2011), with values measured at: δ^{29}Si = -1.71 ± 0.07 ‰, n=17, and δ^{30}Si = -3.47 ± 0.06 ‰, n=17. These values compared well to reported mean values (Hendry et al., 2011) of: δ^{29}Si = -1.72 ± 0.08 ‰, and δ^{30}Si = -3.37 ± 0.17 ‰.

A three-isotope plot (Fig. 6.2) showed that some estuarine and mudflat samples had mass-independent fractionation. These samples were not included in this study. Samples included in the study have δ^{29}Si and δ^{30}Si values that fall along the expected mass-dependent fractionation line, with δ^{30}Si: $\delta^{29}\mathrm{Si} = 0.512\delta^{30}\mathrm{Si} + 0.04$, r^2=0.997, n=42 (Fig. 6.2), which follows the mass-dependent equilibrium fractionation array for Si of $\delta^{29}\mathrm{Si} = 0.5178\delta^{30}\mathrm{Si}$, r^2=0.96 (Georg et al., 2006).

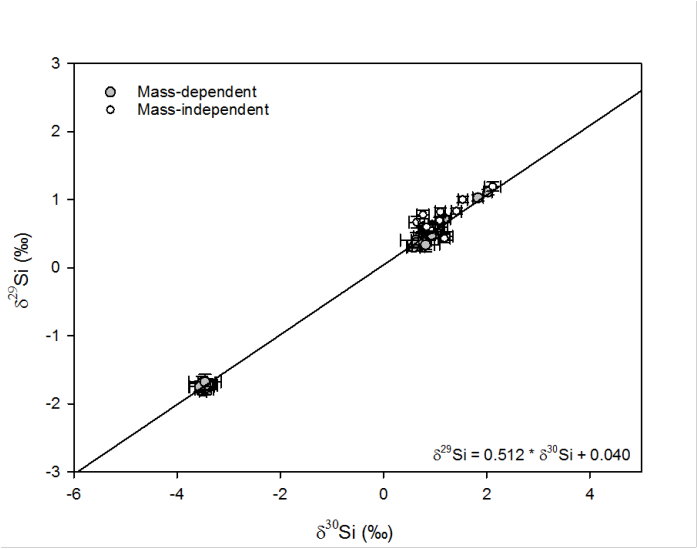

Figure 6.2: Mass-dependence fractionation between δ^{29}Si and δ^{30}Si of all pelagic and benthic samples and LMG standards (grey). Mass-independent fractionation (white) - samples rejected in this study. Error bars are 2SD internal error. Mass dependent fractionation $\delta^{29}\text{Si} = 0.512\ \delta^{30}\text{Si}+0.04$ (n=42, r^2=0.997).

6.2.3 $\delta^{30}Si$ mass balance

Mass balance of Si isotopes has been described in terms of a simple box model following eq. 6.6, to provide information on the Si sources and processes within the Severn Estuary. Mass balances have previously been applied to several systems and for a range of elements (Boyle et al., 1974; Martin and Meybeck, 1979; Bowes and House, 2001; Raymond and Bauer, 2001; Fripiat et al., 2011). Mass balances are useful applications to analyse the physical system and are revolved around the conservation of mass. The freshwater zone of the River Severn was used to illustrate the riverine isotopic inputs, and the outer estuary δ^{30}Si average values were used to illustrate the estuarine isotopic export from the system, alongside the pelagic DSi concentrations (in Mmol/yr). The difference between the upper and lower systems, i.e. the residual DSi load and its isotopic signature, were calculated for the summer and autumn sampled periods of 2016. This calculated external Si isotopic input into the Severn was then compared to the measured benthic isotope value in the mudflat water to see if the benthic flux of Si was transported into the water column.

$$\delta^{30}\text{Si} = \left(\frac{\text{DSi}_{\text{river}}}{\text{DSi}_{\text{estuary}}}\right) * \delta^{30}\text{Si}_{\text{river}} + \left(\frac{\text{DSi}_{\text{benthic}}}{\text{DSi}_{\text{estuary}}}\right) * \delta^{30}\text{Si}_{\text{benthic}} \tag{6.6}$$

6.3 Results

Presented here are the first $\delta^{30}Si_{DSi}$ values from the River Severn, estuary and intertidal mudflats. Silicon isotopes have been used to understand the importance of the benthic-pelagic coupling in mediating Si during the summer and autumn sampled periods. Several factors such as high organic matter and salinity greatly impacted these Si isotope measurements, with several samples displaying mass-independent fractionation. These samples have not been considered in the following section. Despite this now limited dataset, some findings are valuable to the overall research of Si cycling in the Severn.

6.3.1 $\delta^{30}Si$ evolution along the Severn

Pelagic $\delta^{30}Si_{PDSi}$ in the Severn continuum during the summer ranged between +0.61 and +1.04 ‰ (avg. 0.86 ± 0.06 ‰), and between +0.64 and +1.05 ‰ (avg. 0.87 ± 0.06 ‰) in the autumn (Fig. 6.3), with a LMG 2SD of 0.19. $\delta^{30}Si_{PDSi}$ during the summer and autumn displayed distinctive differences between the freshwater and saline systems of the Severn (Fig. 6.4). River Severn $\delta^{30}Si_{PDSi}$ averaged +0.77 ± 0.06 ‰ (summer) and +0.75 ± 0.05 ‰ (autumn). The Severn Estuary averaged higher $\delta^{30}Si_{PDSi}$ of +0.97 ± 0.06 ‰ (summer) and +1.0 ± 0.03 ‰ (autumn). Between 40 and 80 km, considered here as the river-estuary transition zone, $\delta^{30}Si_{PDSi}$ appeared to increase in the summer and autumn sampled periods, corresponding to a rise in PBSi concentrations (Fig. 6.3). Heavier isotopic estuarine waters were associated with low PDSi concentrations (Fig. 6.4). $\delta^{30}Si_{PDSi}$ displayed a similar exponential relationship with PBSi and SPM (Fig. 6.4). Note, there is no Si data for this zone, and trends between the river and estuary should be considered with caution. To this end, Environment Agency monitoring PDSi and SPM data from 2016 (Agency, 2016) has been used to help interpret the dynamics in the transition zone between the River Severn and Severn Estuary (Fig. 6.3). PDSi from the present study and the Environment Agency monitoring data followed a similar trend, lending confidence that our data are directly comparable. Further, the PDSi concentrations agree with Jonas and Millward (2010): River Severn silicate concentrations were > 3 mg/L, and Bristol Channel silicate concentrations were *ca.* 1 mg/L. Despite the expected large temporal variability in SPM concentrations, which is highly dependent on the tidal dynamics, SPM concentrations showed relatively good association between the SPM data presented in this study and the Environment Agency monitoring data (Fig. 6.3). Further, SPM concentrations resemble a similar pattern to Jonas and Millward (2010), with peak SPM concentrations (max. *ca.* 1.8 g/L) near the river-estuary transition zone, lending confidence in the data presented here. However, caution must be applied to these comparisons due to the large temporal variation.

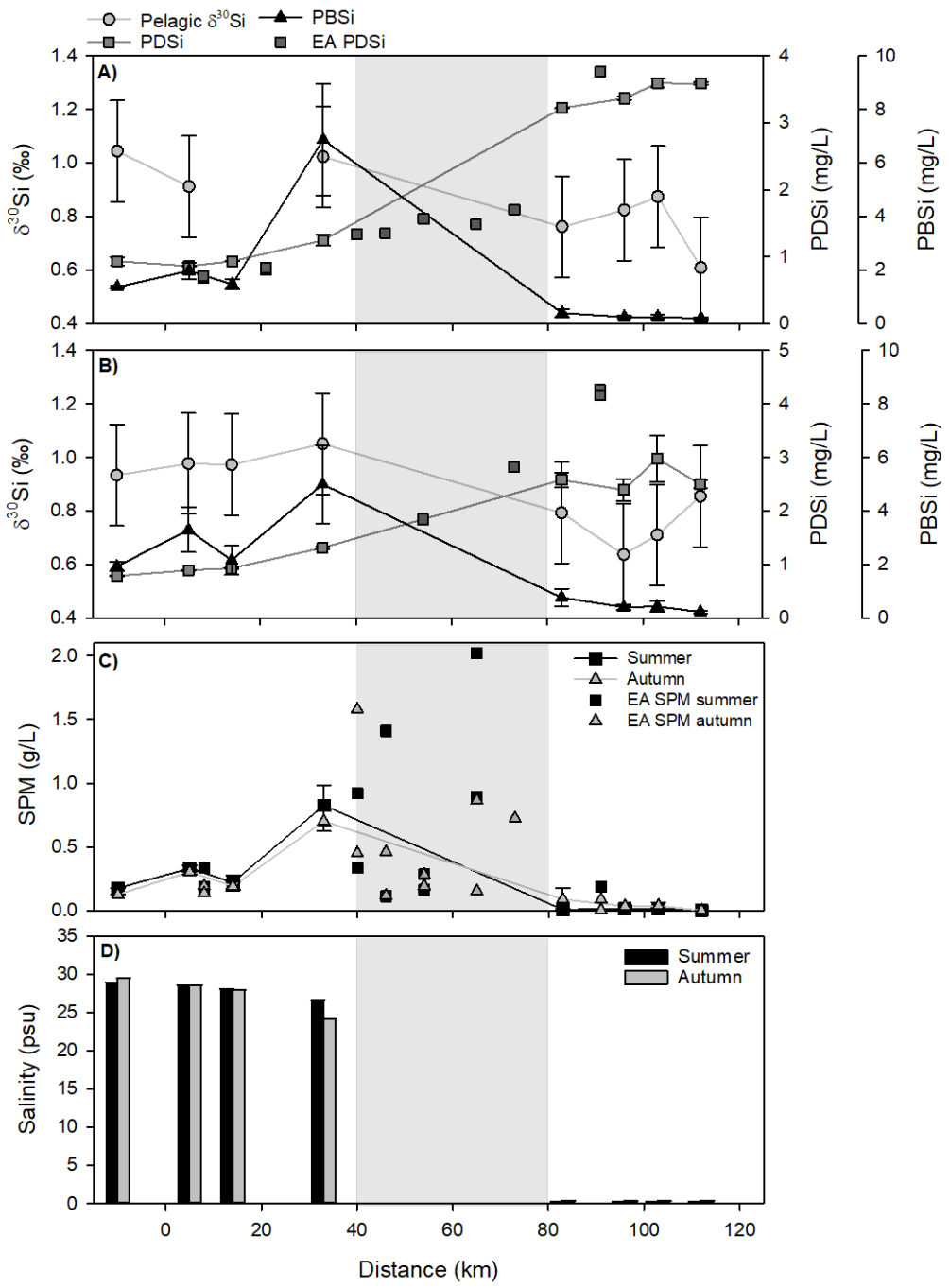

Figure 6.3: Silicon isotope evolution in the River Severn-estuary-marine zone. **A)** Summer δ^{30}Si. **B)** Autumn δ^{30}Si. δ^{30}Si presented with a LMG 2SD of 0.19. PDSi concentrations (mg/L) (grey squares) and PBSi concentrations (mg/L) (black triangles) presented with 1SE (n=6 per station). Pelagic δ^{30}Si (grey circle) presented with 2SD of long-term reproducibility. **C)** SPM concentrations (mg/L) presented with 1SE (n=6 per station). **D)** Salinity (psu), presented with 1SE (n=6 per station). Environment Agency data presented to fill in the transition zone where no data was collected in the present study (Agency, 2016).

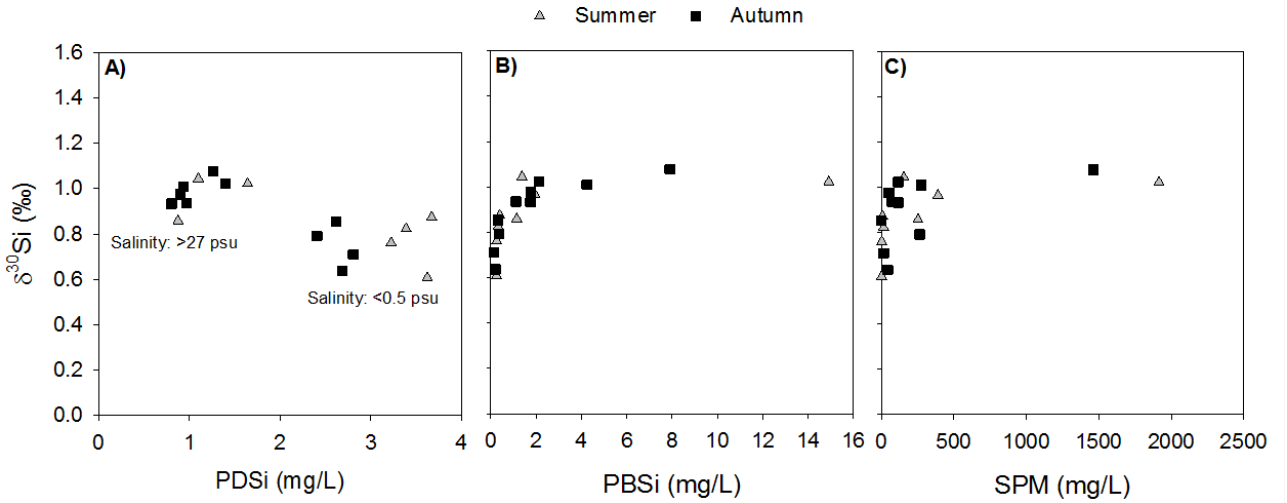

Figure 6.4: δ^{30}Si relationship with PDSi, PBSi and SPM in the River Severn and its estuary in the summer (*n=8*) and autumn (*n=10*). **A)** δ^{30}Si vs PDSi concentrations. **B)** δ^{30}Si vs PBSi concentrations. **C)** δ^{30}Si vs SPM concentrations.

6.3.2 $\delta^{30}Si$ mixing models

Simple mixing models of DSi and $\delta^{30}Si_{PDSi}$ against salinity in the summer and autumn (Fig. 6.5), deviated from the theoretical conservative dilution line (TDL), suggesting non-conservative behaviour between the freshwater zone and the saline limit of the Severn Estuary. For a detailed discussion of mixing model limitations, refer to Chapter Three (Section 3.3.3).

6.3.3 Si and $\delta^{30}Si$ water column distribution in the Severn

Water samples in the Severn Estuary were sampled at the surface (<2 m deep) and at depths (>15 m deep), and analysed for water column variation in PDSi, PBSi and $\delta^{30}Si_{PDSi}$ (Fig. 6.6).

Surface summer $\delta^{30}Si_{PDSi}$ ranged between +0.86 & +1.04 ‰, whilst bottom water samples ranged between +0.97 & +1.02 ‰. Autumn surface water samples had a smaller range between +0.93 & +1.02 ‰, whilst bottom water samples ranged between +1.01 & +1.08 ‰. Note, due to mass-independent issues, only 50% of the summer samples, and 75% of the autumn samples, were considered in this depth comparison.

In the Severn Estuary surface and bottom water PDSi concentrations and $\delta^{30}Si_{PDSi}$ (for locations with both surface and bottom water values) were similar, suggesting the estuary was well mixed for dissolved constituents (Fig. 6.6). In contrast to the dissolved constituents, PBSi and SPM concentrations displayed clear differences between the surface and bottom water in the upper Severn Estuary in both sampled periods (Fig. 6.6) (see Chapter Three, Section 3.4.4.3, for a detailed explanation).

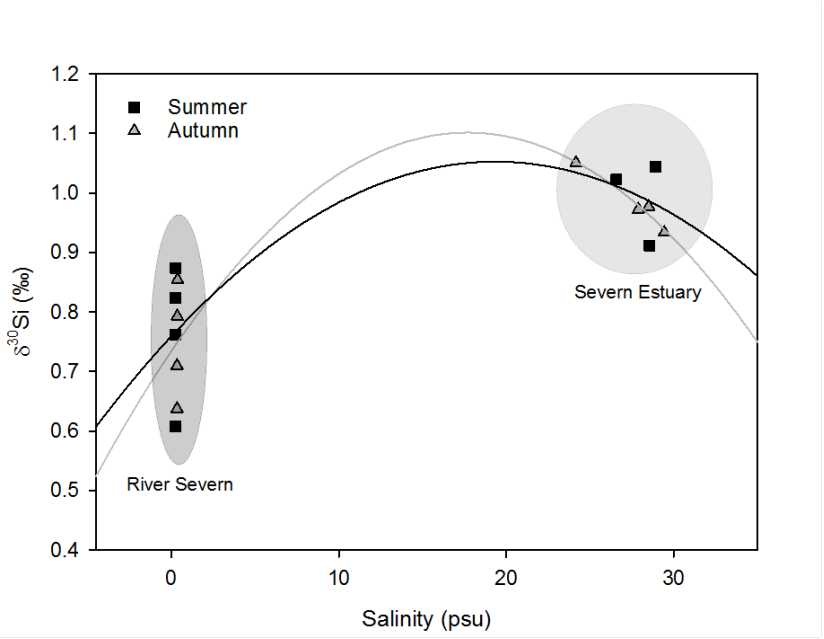

Figure 6.5: δ^{30}Si values vs salinity, with non-conservative mixing lines.

6.3.4 Severn's $\delta^{30}Si$ budget

Mass balance of PDSi and $\delta^{30}Si_{PDSi}$ was used to determine the flux of Si from the River Severn to the outer Severn Estuary, in the summer and autumn sampled periods of 2016.

In the summer, low riverine inputs of PDSi (266 Mmol/yr), with isotopically light waters (+0.61 ‰), discharged into the Severn Estuary (Fig. 6.7). A greater flux of PDSi was calculated in the outer estuary (180,399 Mmol/yr), with isotopically heavier waters (+0.91 ‰) (Fig. 6.7). The difference between the freshwater and saline end-members, amounted to a large calculated external input of DSi (180,132 Mmol/yr) into the Severn Estuary, which had an isotopically calculated heavy signature (+0.91 ‰) (Fig. 6.7).

In the autumn, a similar mass balance was produced, although PDSi riverine flux was reduced (104 Mmol/yr) and had a heavier isotopic signature (+0.85 ‰) (Fig. 6.7). Further, the estuarine output flux of PDSi was higher (233,264 Mmol/yr), with a heavier isotopic signature (+0.98 ‰). The difference between the freshwater and saline end-members in the autumn, amounted to an external calculated flux of 233,160 Mmol/yr, with a calculated heavier isotopic signal (+0.98 ‰) (Fig. 6.7).

6.3.5 $\delta^{30}Si$ in the intertidal mudflats of the Severn

The mass-balance calculations for DSi and δ^{30}Si (Fig. 6.7) suggests there was an input of DSi with an isotopically heavy signature entering the Severn Estuary during the summer and autumn sampled periods of 2016. The external flux of DSi and the source of heavier isotopes may have originated from the intertidal mudflats of the Severn Estuary. To

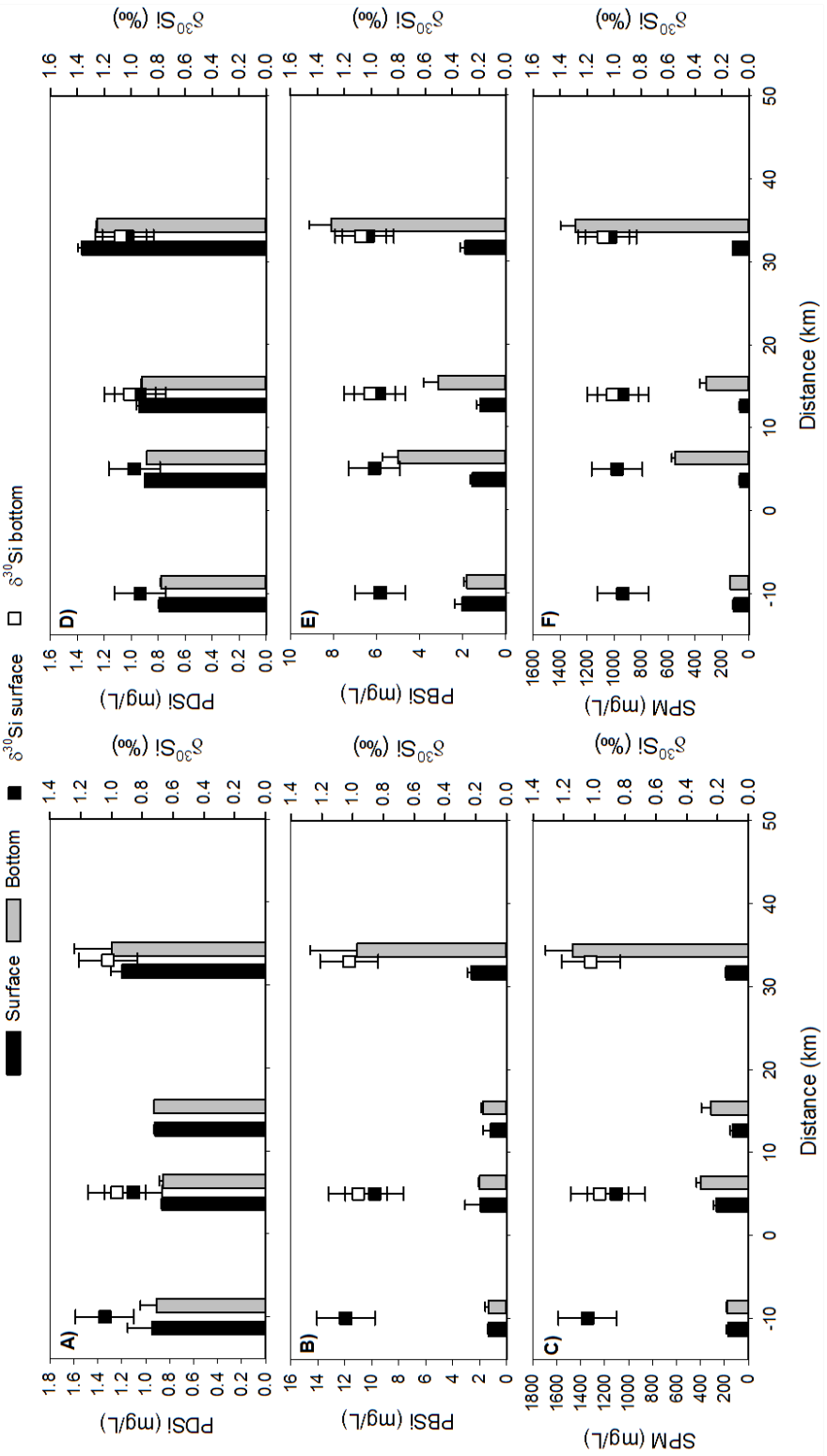

Figure 6.6: $\delta^{30}Si_{PDSi}$ and PDSi, PBSi and SPM concentrations (mg/L) in the surface (black) and bottom (light grey) waters of the Severn Estuary (0 to 40 km) and Bristol Channel (< 0 km). **A-C)** Summer. **D-F)** Autumn. Si and SPM data presented with 1SE of (n=3 per station). δ^{30}Si presented with a LMG 2SD of 0.19.

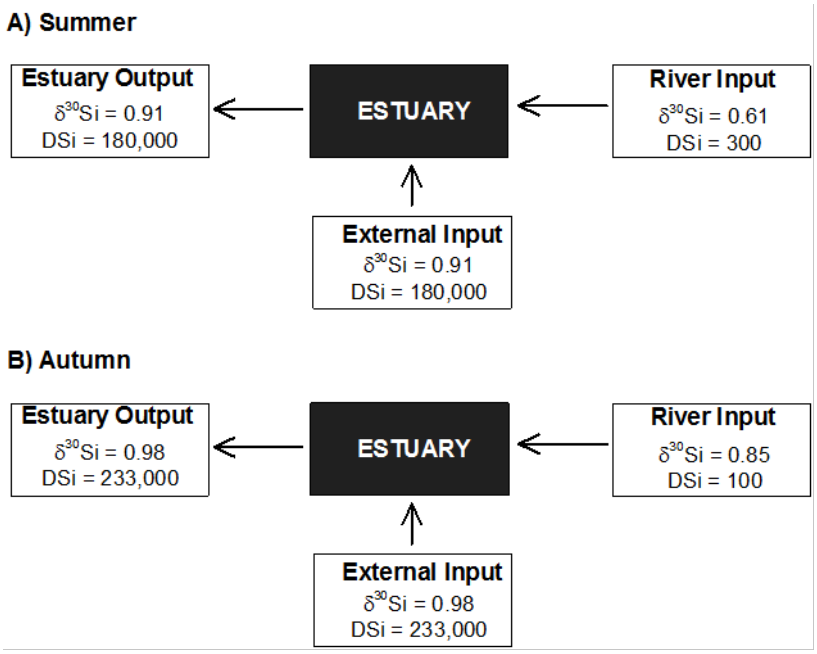

Figure 6.7: PDSi in Mmol/yr and δ^{30}Si (‰) budgets, with calculated external Si supply and isotopic value. **A)** Summer. **B)** Autumn.

determine whether this was the case, the mudflat water was assessed for its isotopic value. Studies on the Si isotopic signature of mudflats have only recently begun, with very few methodologies established to handle the adverse conditions, for example, high organic matter content, which can have high impacts on mass-independent fractionation and interference. Mass-independent fractionation occurred in most of the mudflat water samples, with only 38% (n=8) of samples showing mass-dependent fractionation. Of this limited dataset, the mudflat water δ^{30}Si values in the summer and autumn were heavy (see Table. 6.3).

Table 6.3: Benthic intertidal mudflat δ^{30}Si values. Presented with 2SD of long-term reproducibility.

Season	Site	δ^{30}Si (‰)
Summer	Site 1	1.83 ± 0.19
	Site 2	*
	Site 3	*
	Site 4	2.03 ± 0.19
Autumn	Site 1	1.19 ± 0.19
	Site 2	*
	Site 3	*
	Site 4	*

* Mass-independent samples = rejected.

6.4 Discussion

Si isotopes have been used as a tracer of weathering (Georg et al., 2007; Opfergelt et al., 2008) and diatom production (De La Rocha et al., 1998) in riverine locations worldwide, including; the Amazon (Hughes et al., 2013), the Nile (Cockerton et al., 2013), the Ganges (Fontorbe et al., 2013; Frings et al., 2015), Icelandic rivers (Georg et al., 2007), and the Yangtze River, China (Ding et al., 2004). Only a few studies have applied Si isotopes to estuaries, for example, the Scheldt Estuary (Delvaux et al., 2013) and the Changjiang Estuary (Zhang et al., 2015). Therefore, knowledge of the extent estuaries alter the isotopic Si signature prior to reaching the oceans, is poorly constrained. Below, the Si isotope signatures of the River Severn and estuary are discussed, alongside the mudflat water isotopic Si budgets (see Hypothesis Three - objective two, Chapter One, Section 1.5).

6.4.1 Silicon isotopes in rivers

The Severn's $\delta^{30}Si_{PDSi}$ values were all positive (Fig. 6.3), suggesting the formation of secondary silica products, for example, in the form of BSi, amorphous Si (ASi), or clay formations. These positive values agree with the common consensus that, following chemical isotopic fractionation processes, $\delta^{30}Si$ values measured in rivers and soils are more positive compared to the average $\delta^{30}Si$ of silicate rock (-0.3 to +0.3 ‰) (Ziegler et al., 2005; Basile-Doelsch, 2006; Georg et al., 2006; Cardinal et al., 2010; Opfergelt and Delmelle, 2012; Frings et al., 2016). Only one repeat measurement from the river had mass-independent fractionation which provided a complete dataset to compare the isotopic budgets of the summer and autumn sampled periods in the river. Possible explanations as to why mass-independent fractionation was more prevalent in the estuarine water column and the mudflat water samples, are discussed later.

The River Severn $\delta^{30}Si_{PDSi}$ values were low (avg. 0.77 ± 0.06 ‰ in summer and 0.75 ± 0.05 ‰ in autumn, Fig. 6.3) compared to the Severn Estuary (avg. 0.97 ‰ in summer and 1.0 ‰ in autumn). However, the $\delta^{30}Si_{PDSi}$ of the River Severn were within the range reported for 557 rivers (-0.14 ‰ to +4.66 ‰), but below the mean of +1.28 ± 0.68 ‰, potentially reflecting the spatio-temporal variability in rivers which often has a high variance of 0.5 to 1.0 ‰ (Frings et al., 2016). Deviation towards the lower end of the isotopic range (Table. 6.4), potentially resulted from the dissolution of clays, along with the dissolution of phytoliths, diatom and sponges. For example, forests occupy the catchment of the Severn and are often associated with isotopically light waters (the presence of humic acid favours clay dissolution), whereas towards the Severn Estuary, agricultural lands dominate, potentially contributing to the isotopically heavier waters. Similar land use controls were reported by Delvaux et al. (2013) in the Scheldt. Hughes et al. (2012) report isotopic signatures from the Tana River, Kenya that were affected

by the climate, a factor of soil drainage and weathering. Alternatively, the low riverine $\delta^{30}Si_{PDSi}$ values could have been driven by high inputs of isotopically light groundwater [*ca.* -1.5 to +0.5 ‰, Opfergelt and Delmelle (2012)]. The effect of groundwater can't be excluded in the present study, especially with DSi rich groundwaters recorded in the catchment area of the Severn (see Chapter Three, Section 3.4.5.1).

$\delta^{30}Si_{PDSi}$ in the River Severn lacked variability between the sampled periods in the summer and autumn of 2016, likely as a result of low discharge rates and biological uptake. Generally $\delta^{30}Si_{PDSi}$ decreases with higher discharge rates (Georg et al., 2006), however flow rates in these periods were similar (difference of <25 m^3/s) along with the amount of rainfall (summer: 80 mm; autumn: 100 mm). With relatively low flow rates, increased water residence times would usually promote phytoplankton development and biological activity, resulting in variability in $\delta^{30}Si_{PDSi}$ between sampled periods that is superimposed on a constant abiological $\delta^{30}Si$ value (Opfergelt and Delmelle, 2012). However, low water column biomass levels in both these periods suggests pelagic biological activity had little impact on $\delta^{30}Si_{PDSi}$.

6.4.2 Silicon isotopes in estuaries

Estuarine $\delta^{30}Si_{PDSi}$ of between +0.91 and +1.05 ‰ were towards the lower range of reported values in previous estuarine studies (Table. 6.4). However, Delvaux et al. (2013) also report similar isotopic values in the Scheldt Estuary (mean +0.95 ‰). These relatively low isotopic signatures go against the consensus that estuarine estimates need to be revised towards heavier $\delta^{30}Si_{DSi}$ values (Hughes et al., 2010). The Severn's estuarine isotopic values were in fact near the global signature estimate of continental Si supply (*ca.* +0.9 ‰) reported by Hughes et al. (2010).

The commonly expected increase in $\delta^{30}Si_{PDSi}$ downstream coupled to a decrease in PDSi concentrations (Fig. 6.3) was somewhat evident in the limited summer and autumn datasets when the entire system was considered, similar to other coastal environments. For example, Cockerton et al. (2013) report a progressive downstream enrichment of $\delta^{30}Si_{PDSi}$ in the Nile, coupled to a decline in DSi concentrations, attributed to the cumulative Si uptake by Si-accumulating aquatic organisms. Weiss et al. (2015) also report a similar downstream enrichment of $\delta^{30}Si_{PDSi}$ in the Elbe, Germany. Further, Delvaux et al. (2013) report isotopic enrichment along the Scheldt Estuary during the winter, which couldn't be explained by diatom activity (low chl *a* concentrations), but was attributed to abiological processes set by land-use and lithology, and simple conservative mixing with tributaries.

The deviation from the TDL between $\delta^{30}Si_{PDSi}$ and salinity (Fig. 6.5) indicated a supply of heavy $\delta^{30}Si$ into the Severn Estuary. As noted above, and hypothesised in previous chapters, the benthic biofilm system on the intertidal mudflats may have contributed as a supply of heavy $\delta^{30}Si$. However, this non-conservative trend is not

Table 6.4: δ^{30}Si global budgets.

Location/type	δ^{30}Si (‰)	Study
River Severn (summer)	+0.61 → +0.87	Present study
River Severn (autumn)	+0.64 → +0.85	Present study
Severn Estuary (summer)	+0.91 → +1.02	Present study
Severn Estuary (autumn)	+0.93 → +1.05	Present study
Bristol Channel (summer)	+1.04	Present study
Bristol Channel (autumn)	+0.93	Present study
Soil and pore fluid (*n=172*)	∼ -2.0 → ∼ +2.2	*Estimated values from Fig. 4 in Frings et al. (2016)
Groundwater (*n=44*)	∼ -1.5 → ∼ +2.0	*
River water (*n=557*)	-0.14 → +4.66	*
Lake water (*n=64*)	∼ +0.5 → ∼ +2.6	*
Seawater (*n=636*)	+0.4 → +3.1	Opfergelt and Delmelle (2012)
North Atlantic	+1.4	De La Rocha et al. (2000)
North Pacific	+0.8	De La Rocha et al. (2000)
Southern Ocean (sponge)	+1.3 → +1.8	Hendry et al. (2010)
Secondary minerals (*n=112*)	∼ +-3.0 → ∼ +2.5	*
Diatom BSi (*n=197*)	∼ -1.0 → ∼ +3.0	*
Sponge BSi (*n=95*)	∼ -5.8 → ∼ +1.0	*
Phytoliths (*n=124*)	∼ -1.8 → ∼ +6.0	*
Sedimentary BSi (*n=969*)	∼ -4.2 → ∼ +3.0	*
Pore fluid from Peruvian margin	+1.1 → +1.9	Ehlert et al. (2016)
Continental supply	+0.9	Hughes et al. (2010)
Forest floor leachates	∼ -1.38 → ∼ -2.05	Cornelis et al. (2010)
Yangtze Estuary, China	+0.7 → +3.4	Ding et al. (2004)
Nile Estuary (dry season)	+1.54 → +4.66	Cockerton et al. (2013)
Nile Estuary (wet season)	+0.48 → +3.45	Cockerton et al. (2013)
Changjiang Estuary (dry season)	+1.48 → +2.35	Zhang et al. (2015)
Changjiang Estuary (wet season)	+1.54 → +1.95	Zhang et al. (2015)
Ganges River, Himalaya	+0.49 → +2.17	*
Switzerland (40 rivers)	avg. 0.84	Georg et al. (2006)
Scheldt Estuary	+0.9 → 1.7	Hughes et al. (2010)
Lake Baikal, Siberia inflow	+0.90 → 1.77	Panizzo et al. (2017)
Selenga Delta	avg. +1.52	Panizzo et al. (2017)
Congo River wetlands	+0.02	Cardinal et al. (2010)

always observed in other riverine/estuarine systems, perhaps due to the lack of a benthic-dominated system. For example, Hughes et al. (2012) in the Tana River, conclude that DSi followed conservative mixing along the salinity gradient (no Si isotope fractionation). In comparison, Engström et al. (2010) in the Lena River, Siberia, suggests that DSi was consistently removed along the salinity gradient, however δ^{30}Si decreased, likely due to mixing with isotopically light water masses. Discrepancies of δ^{30}Si and Si transport between these systems, highlight the unique characteristics of each of these transition zones, and the particular control they enforce on Si cycling. Thus, δ^{30}Si is a useful proxy, alongside DSi and BSi concentrations, to distinguish between the controls on Si, and acts as an accessory parameter to evaluate the global Si budgets.

6.4.3 Intertidal mudflats: a potential source of heavy δ^{30}Si

Phytoplankton productivity was minimal throughout 2016 (see Chapter Three, Section 3.3.6), suggesting the relatively heavier isotopic signatures in the estuary compared to the river, were unlikely caused by fractionation through siliceous phytoplankton DSi uptake. Alternatively, the benthic diatom-dominated biofilms, sampled at four intertidal mudflats, were highly photosynthetically productive, had the potential to accumulate BBSi (see Chapter Four). Here, I hypothesise that the fractionation resulting from the uptake of DSi by the benthic diatoms, which preferentially incorporated δ^{28}Si, led to more isotopically heavy residual mudflat water, with values reaching highs of >2.0 ‰. These $\delta^{30}Si$ values, to my knowledge, are some of the first Si isotope data from intertidal sediments, and are high compared to other sediment settings, for example, Western Antarctic Peninsula marine sediments where $\delta^{30}Si$ values were <1.41 ‰(Cassarino, 2018), but comparable to published values from the Peruvian upwelling margin (+1.1 to +1.9 ‰, Ehlert et al., 2016), and average soil and pore fluid values, between +2.0 and +2.2 ‰, presented in Frings et al. (2016).

Due to the hypertidal nature of the estuary, the mudflat water and the associated sediment may have been resuspended upon immersion and mixed in the high-energy system, transporting the heavy δ^{30}Si mudflat water signature into the water column (Fig. 6.8). This benthic input may have accounted for the isotopically heavy external supply in the isotope mass-balance (Fig. 6.7). The calculated mass-balance external supply of DSi presented in this chapter of 180,000 Mmol/yr (summer) and 233,000 Mmol/yr (autumn) (see Fig. 6.7), compares well to the BDSi erosion rates from the September 2018 study (see Chapter Five, Section 5.3.5) when considering the entire estuarine area of 185,200 Mmol/yr (55,684 ha, SEP, 2009) and 245,110 Mmol/yr (73,714 ha, JNCC, 2018). It is possible that the intertidal mudflats were a source of BDSi alongside BBSi, through the erosion and mixing between pelagic and benthic fluids. Further, several estuarine and benthic water analyses required large Mg isotope corrections and had large mass-independent fractionation, compared to the riverine water analyses.

Despite the potential supply of δ^{30}Si from the mudflats, the complex morphology of the estuary may complicate this signal. For example, alongside the intertidal mudflats, the Severn Estuary is surrounded by wetlands and saltmarshes, which may exhibit low isotopic values, reducing the supply of δ^{30}Si into the water column. For example, due to considerable clay dissolution, Cardinal et al. (2010) report on the Congo wetlands low Si isotopic signatures (*ca.* +0.02 ‰). Further, the presence of saltmarshes may have influenced the isotopic signatures. For example, δ^{30}Si values measured at Site 3 on the intertidal mudflats, which laid opposite to a wetland and saltmarsh, required large Mg isotope corrections, and had large mass-independent fractionation, indicative of strong mass bias within the plasma mass spectrometer. Such mass bias is likely matrix-related and is possibly due to high organic carbon content associated with these types of land cover. In addition, the dissolution of clays under the action of organic matter may have influenced the isotopic signatures, similar to reports by Cardinal et al. (2010). A similar explanation can be used for the mass-independent fractionation in samples from Site 2 and 4, which also have adjacent saltmarshes. In comparison at Site 1, where samples had mass-dependent fractionation, the mudflat has no wetlands or saltmarshes in the vicinity. Even though the effect of land cover and land use on isotopic signatures in the estuary is out of the scope of the present study, this limited isotopic data shows that isotopes may constitute a useful proxy to trace anthropogenic modifications. These processes which potentially effected the isotopic budget of the Severn are compiled in Fig. 6.9.

6.4.3.1 Origin of heavy silicon isotopes

Whether the heavy isotopic signatures originated from biological fractionation (i.e. benthic diatom growth) or clay formation (abiological processes) is discussed below.

The isotopic fractionation during biological uptake leads to a BSi lighter compared to DSi with a constant fractionation factor (ϵ). To investigate which fractionation processes increased the Si isotopic ratios along the Severn (i.e. biological uptake or clay formation), the constant fractionation factor (ϵ) was calculated following Sutton et al. (2013), for two simple models - assuming an open (eq. 7.7) and closed (eq. 7.8) system. All mass-dependent samples were used in these calculations (*n=16*). De La Rocha et al. (1997) following a laboratory culture study on three different diatom species showed that this ϵ was equivalent to -1.1 ‰. However, a culture study by Sutton et al. (2013) report species-specific variations, leading to high variability in ϵ from -0.54 ‰ to -2.09 ‰, although these variations were observed in cultures of marine polar diatom species. To date, there are no estimates of ϵ from benthic diatoms.

The open system model considered a continuous supply of DSi into the Severn. The evolution of $\delta^{30}Si_{PDSi}$ from the initial $\delta^{30}Si_{PDSi}$ entering the system is defined in the model as a linear relationship. The initial DSi concentration is the peak value entering

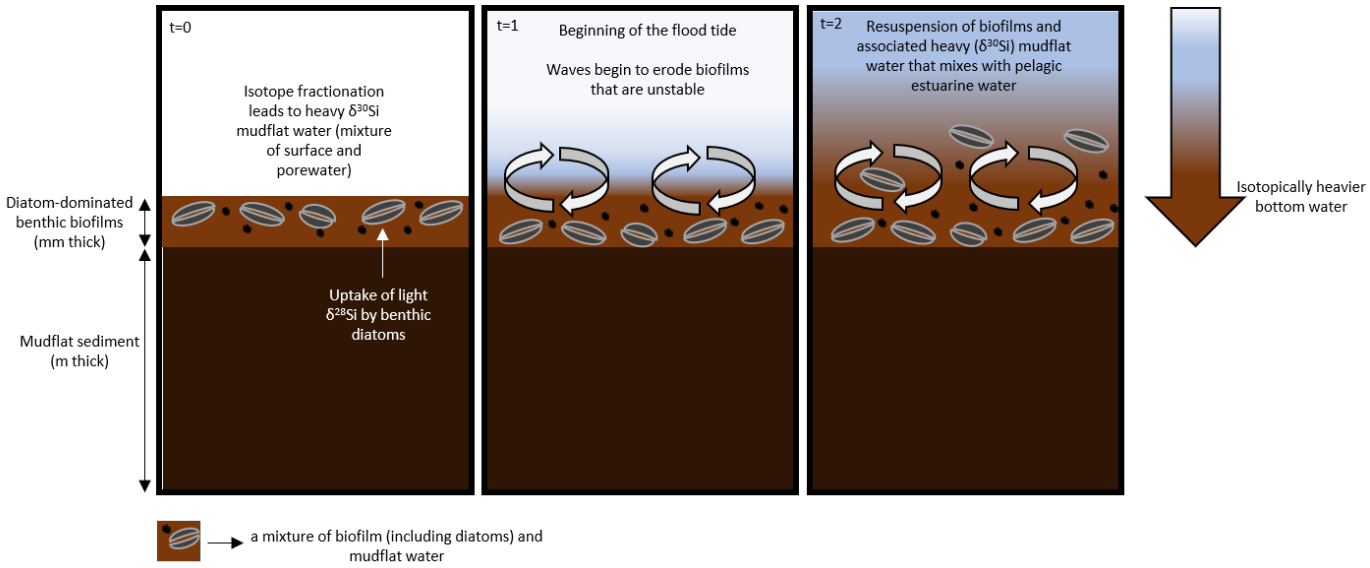

Figure 6.8: Origin of heavy δ^{30}Si in the Severn. Benthic diatom biofilms preferentially uptake ^{28}Si, enriching the residual mudflat water in ^{30}Si during emersion periods (t=0). Upon immersion (t=1), diatom biofilms (BBSi) along with the mudflat sediment and heavy δ^{30}Si BDSi in the mudflat water (a mixture of surface and pore fluids) are resuspended and transported into the water column, leading to an overall heavier isotopic signature in the water column (t=2).

the system, whilst the end value is the minimum DSi concentration in the system. The initial $\delta^{30}Si_{PDSi}$ is assumed here as the minimum Si isotope value in the system. Using this open model configuration, the ϵ can be estimated by the gradient of $\delta^{30}Si_{PDSi}$ vs the fraction of DSi remaining in the system, defined as f:

$$\delta^{30}Si_{PDSi} = \delta^{30}Si_{PDSi(initial)} - \epsilon\,(1 - f) \tag{6.7}$$

Alternatively, the closed system model considers a single supply event of DSi, which is then isolated from its source. The evolution of $\delta^{30}Si_{PDSi}$ is expressed by the initial $\delta^{30}Si_{PDSi}$ with a fractionation factor (ϵ) multiplied by the natural log of f, following Rayleigh distillation curves (De La Rocha et al., 1997). In this closed model configuration, the ϵ can be estimated by the gradient of $\delta^{30}Si_{PDSi}$ vs the natural log of DSi:

$$\delta^{30}Si_{PDSi} = \delta^{30}Si_{PDSi(initial)} - \epsilon ln f \tag{6.8}$$

The ϵ for the Severn is presented in two ways: as an average calculated from each ϵ datapoint along the Severn, and secondly from the gradient of $\delta^{30}Si_{PDSi}$ vs DSi/initial DSi (open system) and vs ln(DSi) (closed system) (see Table. 6.5).

The fractionation factor (ϵ) from the gradient was greater than the average value for both open and closed scenarios in the summer and autumn (Table. 6.5). The gradient was a clear line between two clusters: the riverine samples and the estuarine samples. There was a downstream trend in the ϵ, but with the same number of datapoints in the

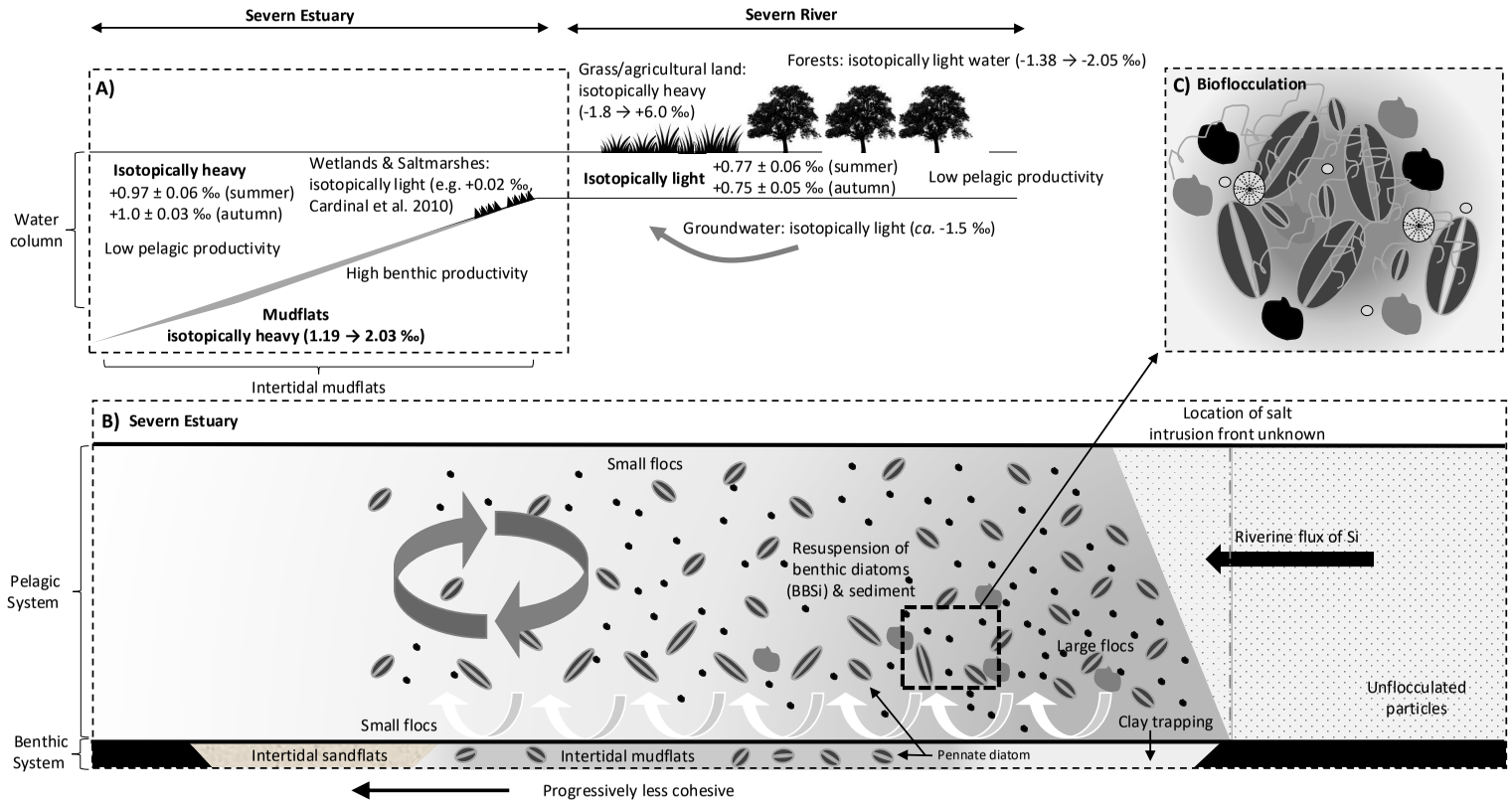

Figure 6.9: Silicon isotope signatures in the Severn's river-estuary-marine continuum. **A)** Land use/type and biological productivity effect on Si isotope budgets in the River Severn and Estuary. **B)** Benthic algal biofilm productivity - export of BBSi and δ^{30}Si from the intertidal mudflats into the water column of the Severn Estuary. **C)** Close-up of the possible bioflocculation of resuspended benthic biofilms (pennate diatoms) and sediment taking place in the water column.

Table 6.5: Fractionation factor (ϵ) in the River Severn-estuary-marine continuum. ϵ (average) calculated from each datapoint along the Severn. ϵ (gradient) is the gradient from the relationship between $\delta^{30}Si_{PDSi}$ vs DSi/initial DSi (open system) and vs ln(DSi) (closed system).

Type	ϵ **(average)**	ϵ **(gradient)**	**Study**
Ferrihydrite	-1.04 ‰		Delstanche et al. (2009)
Geothite	-1.56 ‰		Delstanche et al. (2009)
Allophane	-2 ‰		Ziegler et al. (2005)
Weathering of basalt	-1.53 ‰		Georg et al. (2007)
Soil	-1 → -3 ‰		Ziegler et al. (2005); Georg et al. (2006, 2009)
Water-marine diatoms	-1.1 → -1.5 ‰		De La Rocha et al. (1997); Fripiat et al. (2011)
Summer (closed)	-1.37 ‰	-3.33 ‰	Present study
Summer (open)	-1.22 ‰	-1.96 ‰	Present study
Autumn (closed)	-0.43 ‰	-2.80 ‰	Present study
Autumn (open)	-0.60 ‰	-1.76 ‰	Present study

river and estuary, there was no bias towards a particular system.

Considering both an open and closed system, the average ϵ values from the summer (-1.22 to -1.96‰) were near the isotopic ϵ of water-marine diatoms, which have previously been repeatedly measured to be between -1.1 and -1.5 ‰ (De La Rocha et al., 1997; Fripiat et al., 2011). These isotopic ϵ values suggest that during the summer, biological activity dominated isotopic fractionation rather than clay formations. In the autumn, considering both open and closed systems, the ϵ values had a wider range (-0.43 to -1.76 ‰), potentially signalling a form of biological productivity, but not necessarily only diatoms, e.g. phytoliths, or a higher background level of clay formation (Table. 6.5). The gradient calculation under both open and closed system scenario for each season, gave high ϵ values (-3.33 and -2.8 ‰), which could reflect this background clay formation signal alongside biological activity in these seasons. For example, studies by Ziegler et al. (2005) and Opfergelt et al. (2008) show that with increased soil weathering, the crystalline clay formation becomes more isotopically negative (^{28}Si) whilst producing an isotopically heavy soil solution. The ϵ were close to reported values for allophane, a precursor to kaolinite formation (Ziegler et al., 2005; Fontorbe et al., 2013). Studies in the Congo region show kaolinitic clay neoformations was a key mechanism behind the high δ^{30}Si riverine end-member due to the high abundance (58%) of kaolinite clay minerals in the soil clay fraction (Alexandre et al., 1997) and 80% abundance in the suspended clays (Jouanneau et al., 1990). Kaolinite has been documented to account for *ca.* 10.8% of the clay mineral assemblage in the Severn (Allen, 1991), and could have influenced these isotopic signatures. However, clay reactions are unlikely present in less cohesive sediment. For example, towards the Bristol Channel at Site 4, Sand Bay, there is an abundance of quartz, a stable mineral which does not undergo clay mineral reactions. Georg et al. (2006) proposed aluminium concentrations and the Si/Al ratio could be used as a tracer of secondary phase formations. Bayon et al. (2018) report high Al/Si ratios associated with higher rates of secondary weathering in tropical rivers (e.g. Amazon, Mississippi, Nile and Yangtze), which were coupled to isotopically light clay fractions. Reverse weathering is promoted in these tropical regions, for example, a study by White and Blum (1995) show weathering rates as a linear function of precipitation and an exponential function of temperature. However, the climate of the Severn is temperate, and there is generally less secondary weathering in this type of drainage basin. Further, this closed system scenario is unlikely representative of the hypertidal Severn, whereas a constant riverine recharge of DSi is expected, which is best represented by the open system scenario.

6.5 Conclusions

For the first time, silicon isotopes were measured in the pelagic and benthic systems of the Severn. Despite the limited dataset, this new technique has widened our perception of this complex transition zone and has shed light on the importance of often overlooked processes, including the benthic ecosystem, in influencing Si transport in the Severn.

Silicon isotopes were shown to be driven by both biological and abiological processes, which led to complex isotopic signatures, which with the current dataset can only be speculative. In the river, the Si isotopes represented a combination of different land-use: forests associated with isotopically light waters through the dissolution of clays, which, towards the estuary, transitioned into agricultural land (rich in phytoliths), associated with isotopically heavy water. Coupled to these land-use changes, groundwater, enriched in DSi, may have influenced the isotopically light riverine waters, which were towards the lower range of global river Si isotopic budgets. In the estuary, morphology may also have had a dominant control on the isotopic signatures, with saltmarshes and wetlands driving isotopically light signatures, and biological/abiological processes on the intertidal mudflats driving isotopically heavy waters. The biological signal was superimposed on the abiological signal (clay formation), which was more pronounced in the summer compared to the autumn sampled periods. The ϵ values in the summer were comparable to estimates from marine diatoms, but the low ϵ values from the autumn suggest biological activity by other siliceous organisms (a change in the community), when the diatoms were likely suppressed (see Chapter Four, Section 4.4.2.2). Although the silicon isotopes have provided a more detailed, accession to Si cycling in the Severn, the limited isotope data set prevented any further analysis of the origin of the heavy δ^{30}Si values.

Due to the hypertidal regime of the Severn, upon immersion, the isotopically heavy mudflat water was likely resuspended, and mixed with the isotopically lighter riverine waters, which pushed the estuarine Si isotopic signatures to more positive values compared to the river. This supply of organic matter to the estuarine water column may have contributed to the mass-independent fractionation measured in these samples. Due to the strong tidal forcings, alongside dispersion, diffusion and advection transport processes, the resuspended BDSi and $\delta^{30}Si_{PDSi}$ were likely transported along the Severn in the direction of the dominant flow. Whereas, the resuspended sediment and BBSi, which were possibly coupled through bioflocculation, leading to a higher mass, accumulated in the upper estuarine bottom waters.

The Si isotopes have further enforced the hypothesis that both BBSi and BDSi is supplied to the water column from the intertidal mudflats. These findings have again shown the importance of understanding the effect estuaries have on influencing Si export to the marine zone. The isotope box model presented in this chapter is a useful tool to

give an approximation of the mechanisms taking place and controlling Si supply to the estuary, however it grossly simplifies the system. The use of a more complex, reactive transport models will be explored in the following chapter.

Chapter 7

Biogeochemical cycling of silicon in the Severn Estuary: a 1D reaction-transport modelling approach

7.1 Introduction

Tidal estuaries situated at the interface between the continent and the marine zone play an important role in transporting and modulating riverine nutrients and sediments to the ocean (Dürr et al., 2011). For siliceous phytoplankton inhabiting the water column in coastal environments, terrestrial silicon (Si) supply is vital. Biogeochemical processes in the water column and at the estuarine floor modify land-derived inputs of Si, present as dissolved silicon (DSi) and as particulates, along with other macronutrients, through a wide array of mechanism, including the biological uptake and incorporation into biomineralized structures. For example, photosynthetic diatoms uptake DSi, an inorganic macronutrient, and biomineralize to form their frustules from biogenic silica (BSi). Furthermore, processes such as silica dissolution, deposition and burial in sediments, and remobilization through the erosion of sediments, modify these variable fractions of riverine Si along the dynamic estuarine gradient. These modifications are forced by a complex interplay between the estuarine geometry, geology, hydrology, and pelagic and benthic biogeochemical processes, which are modulated by several forcing mechanism, including tidal dynamics, riverine discharge rates, light availability and temperature (Volta et al., 2014). These modifications result in strong spatial gradients in nutrients, salinity and sediment from the tidally dominated estuarine mouth to the freshwater dominated riverine reaches upstream. Further, temporal variability is pronounced in these estuarine systems, from hours to months, as a response to fluctuating

tidal forcings, and seasonal riverine discharge. As a result, the quantitative significance of estuaries as a modulator of nutrient flux, primarily Si, remains poorly constrained. Observations which provide instantaneous and localised information, similar to the data presented in previous chapters, limits our understanding of the spatio-temporal variability in estuaries.

Reactive-transport models (RTMs) are a powerful tool to disentangle and help quantify these complex estuarine processes, and have been used here, in conjunction with field observations, to help better understand Si transport in the hypertidal Severn Estuary, UK. For example, in addition to gaining a more rounded view on the seasonal transport of Si, the application of a RTM should prove useful in revealing the changes in Si transport in the river-estuary transition zone (40-80 km), where no observations were possible (see Chapter Three, Section 3.4.6). RTMs have been applied to several of Earth's systems (Lin et al., 2007; Baklouti et al., 2011), and several specific estuarine systems, for example, Chesapeake Bay (Cerco et al., 2010), St. Lawrence Estuary (Lefort et al., 2012) and the Scheldt Estuary (Vanderborght et al., 2007; Arndt and Regnier, 2007; Arndt et al., 2007, 2009). This study has applied a modified version of the one-dimensional general RTM called the Carbon-Generic Estuary Model (C-GEM) (Volta et al., 2014), to simulate the Severn's estuarine environment, in particular, Si transport.

Individual estuarine systems have high internal heterogeneity, which can make it difficult to quantify the net Si balance. In C-GEM, estuarine physics has provided a framework to address the large-scale biogeochemical processes (Volta et al., 2014), whereby assertive features of Si transport along the estuary have been constrained using estuarine geometry and hydrodynamics (Savenije, 1994, 2006, 2012). C-GEM takes advantage of the mutual dependency between geometry (data is easily constrainable and available) and estuarine hydrodynamics/transport. The latter requires more observations to validate/calibrate. The model is created on the premise that the hydrodynamic transport exerts a first-order control on estuarine biogeochemical dynamics (Alpine and Cloern, 1992; Friedrichs and Hofmann, 2001; Arndt et al., 2007), maximising the advantage of the inter-dependency between estuarine geometry and hydrodynamics in alluvial estuaries. It is therefore critical that the estuarine hydrodynamics are modelled accurately. Despite the geometric simplification, C-GEM can provide a more accurate description of estuarine hydrodynamics, along with nutrient, sediment and salt transport over different spatial and temporal scales (Volta et al., 2014, 2016), compared to simple box models, which are still widely used (Vollenweider, 1968; Laruelle et al., 2009b). Further, compared to 2D and 3D models, less data is required to constrain and parametrize C-GEM, making the model computationally efficient. Here, the application of a modified version of C-GEM will build upon our current understanding of the complex estuarine mixing in the Severn, which has been documented in previous chapters.

C-GEM includes a generic pelagic biogeochemical reaction network, which here, has been customized to include both dissolved and particulate forms of Si. The importance of the benthic algal biofilm system on the intertidal mudflat of the Severn on Si transport in the estuary has been discussed in detail throughout this thesis. To account for this, the biogeochemical network has been coupled to a Si-driven benthic biofilm component, focused on the growth-death and suspension-deposition cycles of benthic diatoms. For this study, C-GEM will be referred to as: Silicon-Generic Estuary Model (Si-GEM). Built on this framework, this chapter has the following specific aims:

- Adapt C-GEM to represent the geometry of the Severn.
- Adapt C-GEM to capture the hydrodynamics of the Severn.
- Adapt C-GEM to capture the transport of salinity and sediment in the Severn.
- Adapt the biogeochemical reaction network of C-GEM to include the Si cycle and couple to a benthic biofilm component (referred to here as Si-GEM).
- Address the sensitivity of the newly coupled benthic-pelagic model, and explore the variability in Si cycling to forcing mechanism.
- Model the Si transport along the Severn over seasonal scales.

7.2 Model description

The Si-GEM contains several components, which include; the estuarine geometry (depth and width), hydrodynamics (river discharge and tidal constituents), transport schemes, and a biogeochemical reaction network. Additionally, the biogeochemistry network, which here has been extensively customised for the Si cycle, has been coupled to a benthic biofilm component. A concept of Si-GEM can be seen in Fig. 7.1, and each component is described in detail in this section.

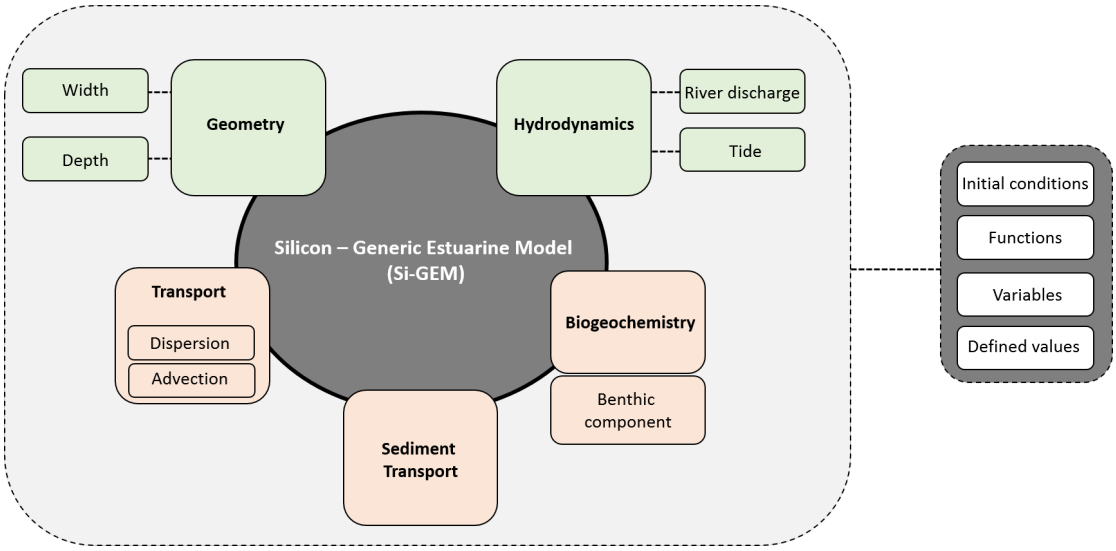

Figure 7.1: Silicon-Generic Estuarine Model components: geometry, hydrodynamics, transport schemes and biogeochemistry, accompanied by the initial conditions, variables, defined values and functions. Model run initially begins with the model components highlighted in green. When time > warmup period (i.e. a spin-up to make sure the model output is not influenced by the initial conditions), the transport of sediment and nutrients are initiated (components in light red).

7.2.1 Geometry

Alluvial estuaries display a wide range of shapes, from funnelled-shaped estuaries such as the tidally dominated Severn, to Ria's (drowned river valley by rising sea levels), Fjords (deep, U-shaped basin), Deltas, and prismatic estuaries that have a fluvial dominance (Savenije, 1994). Despite the variability in estuarine shape, under tidally averaged conditions, these estuaries share a common distinctive geometry that are compatible with estuarine idealized representations; the width ($\overline{B}$) can be described by an exponential decrease as a function of distance (x) from the lower estuarine boundary to the upper system boundary (eq. 7.1) (Savenije, 1994, 2006, 2012; Volta et al., 2014, 2016).

$$\overline{B} = B_0 \times \exp(-\frac{x}{b}) \tag{7.1}$$

where, B_0 is the cross-section width at the estuarine mouth (x=0), b is the width convergence length. The width convergence length is defined as the distance over which the estuarine width reduces to 37%(e^{-1}) of the width at the lower estuarine boundary (Savenije, 1994, 2012).

The idealised depth (H), i.e. the mean longitudinal variation in estuarine depth, was calculated (eq. 7.2) following Savenije (1994):

$$H = \frac{A_0}{B_0} \times \exp(-\frac{x(a-b)}{ab}) \tag{7.2}$$

where, A_0 is the cross-section area at the estuarine mouth (x=0), a is the convergence length, i.e. the distance from when x=0, to the point at which the tangent intersects the x-axis.

The estuarine length was obtained through Google Earth using the distance measure tool. The convergence length can be found in Uncles (1981). The upper and lower boundary H and $\overline{B}$ were determined using ArcGIS as described in Chapter Three. The geometry parameters are summarised in Table.7.1, and are presented visually in Fig. 7.2.

Tide and river discharge are two dominant drivers of estuarine shape, that are used to classify alluvial estuaries. The Severn Estuary has been classified according to:

a) the dimensionless hydrodynamic Canter-Cremers number (N) (eq. 7.3), defined as the ratio between the river flow volume referred to as the bankfull discharge, Q_b [the maximum river discharge in m^3/s that has the best ability to shape an estuary, see Savenije (2012)], and the saline water volume flowing into an estuary during a tidal period (T), with 12.4 h for a semidiurnal tide (Pond and Pickard, 1983). This ratio is governed by the tidal prism, the volume of water between mean high tide and mean low tide, expressed by the relationship: $P = H_T * A_S$, where H_T is the average tidal range taken as 11.5 m at Avonmouth, and A_S is the Severn's basin surface area from the lower boundary to the upper boundary, taken as 55,684 ha from Potts and Swaby (1993). River Severn Q_b, taken as 120 m^3/s can be found in Couperthwaite (1997).

$$N = \frac{Q_b * T}{P} \tag{7.3}$$

b) the dimensionless Estuarine Shape Number (S) (eq. 7.4), defined as the ratio between the convergence length (a) and the tidally averaged depth at the estuarine lower boundary (H_0).

$$S = \frac{a}{H_0} \tag{7.4}$$

The Severn Estuary, characterised by a short-convergence length, is classified as a funnel-shaped system (Fig. 7.3). The geometry of the Severn vs the idealised geometry

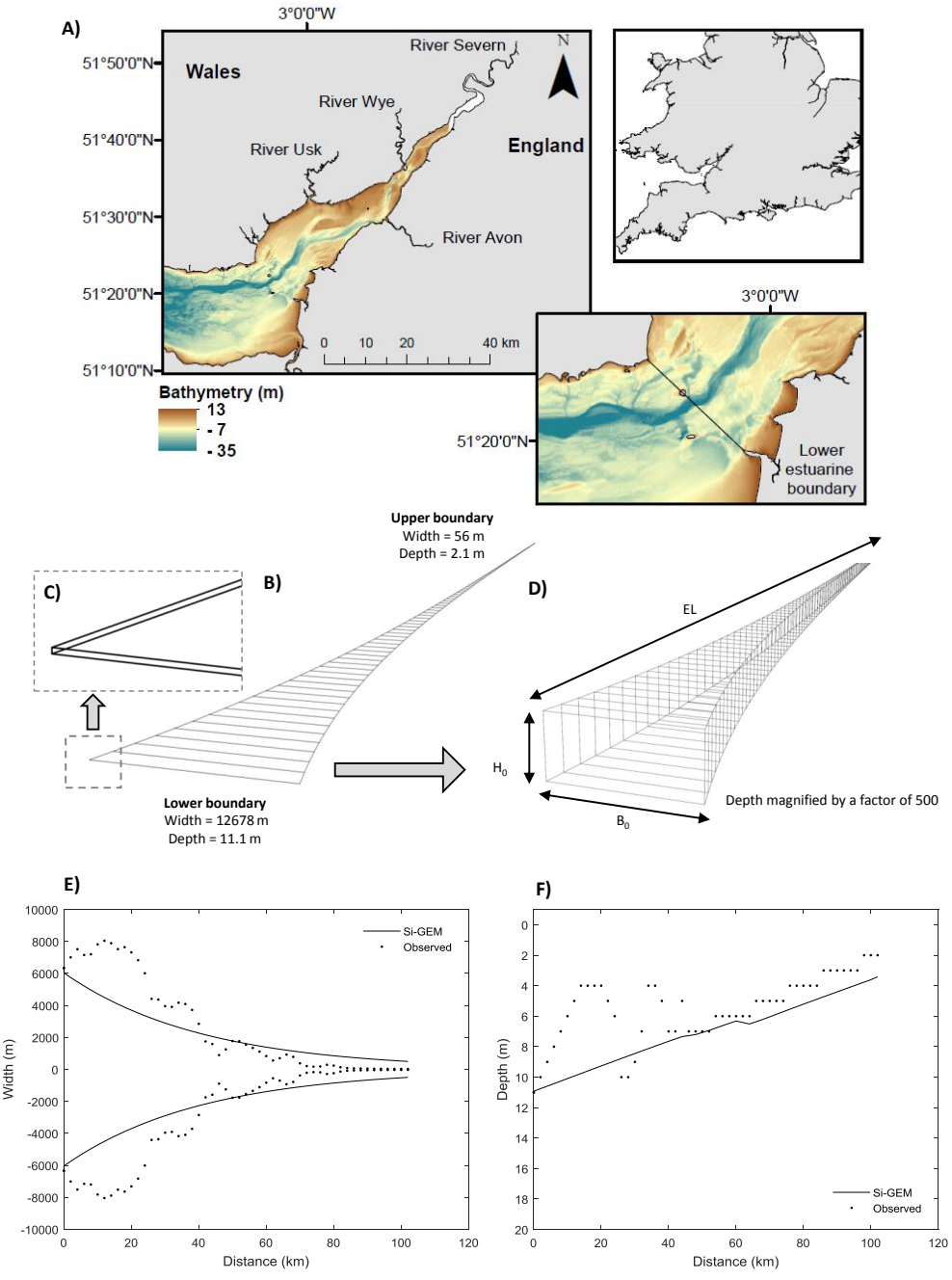

Figure 7.2: Geometry of the Severn Estuary. **A)** Bathymetry of the Severn Estuary and the location of the lower estuarine boundary. **B)** Si-GEMs geometry setup to scale. **C)** Estuarine width larger than the estuarine depth. **D)** Magnified view of the estuarine depth: visual description of the 1D setup with a grid size of 2005 m. **E)** Comparison between observed width (m) and simulated width. **F)** Comparison between observed depth (m) and simulated depth.

Table 7.1: Physical parameters.

Name	Description	Value
Qb	Bankfull river discharge (m^3/s)	120
H_0	Depth at the lower estuarine boundary (m)	11.1
B_0	Width at the lower estuarine boundary (m)	12,678
H_L	Depth at the upper boundary (m)	2.1
B_L	Width at the upper boundary (m)	56
EL	Estuarine length (m)	102,255
LC	Convergence Length (m)	41,000
DELXI	Grid width (m)	2005

(Fig. 7.2) displays the typical feature of a funnel-shaped estuary: large width and deep water in the lower boundary, followed by a convergence width, and shallowing of the water depth. Funnelled-shaped estuaries are typically characterised by a short width convergence length, and have rapidly converging banks in an upstream direction, with a low freshwater river input, and tidal energy equally spread along the estuarine longitudinal axis, resulting in a dome shaped salt intrusion wedge; characteristics expected in the Severn. The Severn Estuary has a shorter convergence length (41 km) compared to the Scheldt (56 km) (Uncles, 1981). Small N (<0.01) and S values (<8000) are distinctive of tidally dominated funnelled-shaped estuaries (Volta et al., 2014). A new formula to estimate N has been proposed by Gisen et al. (2015), however using this calculation, N is very similar for the Severn and Scheldt, which would not be expected due to the Severn's hyper-tidal characteristics (Table. 7.1). Further, bulk river discharge in the Scheldt was high compared to the Severn, emphasising the dominance of the tidal influence in the hyper-tidal Severn, supporting the calculations of Savenije (1994) (Table. 7.2). The relationship between geometry (S) and hydrodynamics (N) in the Severn have been summarised (see Fig. 7.3).

Table 7.2: N and S values of the Severn and Scheldt Estuaries.

Classification	Severn	Scheldt
N	0.001[1]	0.019[1]
N	0.014[2]	0.010[2]
S	3.4	2.6

[1] Savenije (1994). [2] Gisen et al. (2015).

7.2.2 Hydrodynamics

Estuarine hydrodynamics in slowly converging estuaries are fundamentally driven by the freshwater influx from the river and the tidal inflow from the marine zone. Estuaries are subject to tidal forcings, where at the lower estuarine boundary the tidal variations produce a tidal wave which propagates up the funnelled estuary. The geometry of the estuary and the river discharge distorts this progressive wave, increasing the tidal

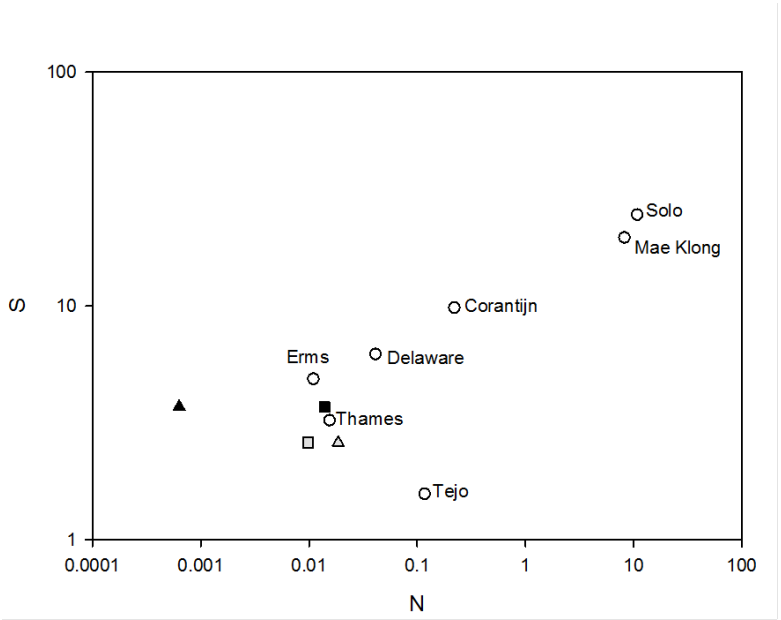

Figure 7.3: Relationship between the hydrodynamic Canter-Cremers number (N) (hydrodynamics), and Estuarine Shape Number (S) (geometry) for selected funnel-shaped type (Severn, Scheldt), mixed types (Corantijn), prismatic type (Solo, Mae Klong), and alluvial (Tejo) estuaries, calculated following Savenije (1994). The Severn Estuary (black) and Scheldt Estuary (grey). N values are shown following Savenije (1994) (triangles) and Gisen et al. (2015)(squares) calculations.

amplitude, a factor of the energy gained through channel convergence and energy loss due to channel bed friction. When bed friction becomes more pronounced, this reduces the tidal amplitude of the wave.

In the Severn, a well-mixed estuary, whereby H is smaller than $\bar{\mathrm{B}}$ (Fig. 7.2), the hydrodynamics can be described by a one-dimensional barotropic, cross-sectional integrated mass and momentum conservation equations for an estuary with varying geometry (Nihoul and Ronday, 1976; Regnier et al., 1998; Regnier and Steefel, 1999). The coupled partial differential equations (eq. 7.5; eq. 7.6) are solved by specifying the elevation $\xi(\mathrm{t})$ at the lower estuarine boundary, and the river discharge $\mathrm{Q_r}$ at the upper estuarine boundary. Average seasonal discharge data was used: winter (261 $\mathrm{m^3/s}$), spring (94 $\mathrm{m^3/s}$), summer (47 $\mathrm{m^3/s}$), and autumn (73 $\mathrm{m^3/s}$). River Severn flow rates were obtained from a gauge station at Haw Bridge in Tirley (see Chapter Two for monitoring station locations) (Agency, 2016).

$$\mathrm{r_s}\frac{\partial \mathrm{A}}{\partial \mathrm{t}} + \frac{\partial \mathrm{Q}}{\partial \mathrm{x}} = 0 \tag{7.5}$$

$$\frac{\partial \mathrm{U}}{\partial \mathrm{t}} + U\frac{\partial \mathrm{U}}{\partial \mathrm{x}} = -\mathrm{g}\frac{\partial \xi}{\partial \mathrm{x}} - \mathrm{g}\frac{\mathrm{U}|\mathrm{U}|}{\mathrm{C}^2\mathrm{H}'} \tag{7.6}$$

where:

r_s = Cross-sectional storage ratio ($r_s = B_s/\bar{B} = 1.2$).

B_s = Storage width (m).

A = Cross-sectional area ($A = H \,.\, \bar{B}$) (m^2).

t = Time (s).

Q = Cross-sectional discharge ($Q = A \,.\, U$) (m^3/s).

U = Flow velocity (m^2/s).

x = Distance along the longitudinal axis (m).

C = Chézy coefficient ($m^{1/2}/m$).

H = Water depth ($H = h + \xi$).

The storage width ratio (r_s), i.e. lateral flow, is always larger than unity, and when $\bar{B}$ is > H, $r_s > 1$. In systems with large intertidal mudflats the ratio can be significant, but in all practical cases $r_s < 1.2$. The friction exerted by the estuarine bed on the moving water has been described by means of a bed roughness with a Chézy coefficient (C, $m^{1/2}/m$), following Manning-Strickler (Savenije, 2012). The Chézy coefficient is dependent upon the bottom material (channel roughness coefficient, n) and H (Volta et al., 2014). Different Chézy values were tested (simulated tidal amplitude vs observed tidal amplitudes) and applied to all season's simulations. Observed tidal amplitudes can be found in Admiralty Tide Tables (Office, 2016). For grid cells <40 km from x=0, Chézy coefficient was defined at 70 $m^{1/2}/m$, between *ca.* 40 km and *ca.* 60 km, Chézy coefficient was defined at 20 $m^{1/2}/m$, and for distances >60 km, Chézy coefficient was defined at 5 $m^{1/2}/m$. This significantly low value was set to create high bed friction in the river, to dampen down the tidal force in the upper boundary, and was likely a contributing factor to the small step in the depth profile at 60 km (Fig. 7.2).

In the Severn Estuary, the principle lunar semi-diurnal M_2 tide is the largest tidal constituent (for elevation and currents under average conditions, every 12.4 hrs) (Uncles, 2010; Neill and Couch, 2011; Liang et al., 2014). Due to the strong tidal dynamics in the Severn, several of the tidal constituents that contribute to the tide were implemented (Evans and Pugh, 1981), following eq. 7.7, and simply added together. The N_2 component, occurring every other spring/neap cycle causing the tidal amplitude to be more/less pronounced than before, caused problems in the spring-neap tidal range, resulting in four low and high tides a day. To circumvent this problem, the N_2 tide was excluded. The tidal constituent's tidal amplitude, phase and speed are summarised in Table. 7.3.

$$h(t) = R\cos(wt - \phi) \tag{7.7}$$

where:

Table 7.3: Tidal constituents used in Si-GEM. *N_2 tide removed.

Tidal constituent	Amplitude	Speed (°/hr)	Phase (°)
M_2	3.901	28.984	189.9
S_2	1.379	30.0	246.2
N_2*	0.738	28.440	174.0
K_1	0.068	15.041	134.0
O_1	0.088	13.943	0.7
MM	0.083	0.544	202.1
MSF	0.077	1.016	41.0
Q_1	0.033	13.399	340.6
M_1	0.013	14.497	203.4
J_1	0.016	15.585	210.4
OO_1	0.023	16.139	222.2
MU_2	0.358	27.968	250.1
L_2	0.307	29.528	165.3
$2SM_2$	0.095	31.016	66.2
MO_3	0.011	42.927	214.2
M_3	0.044	43.476	192.0
MK_3	0.013	44.025	224.6
MN_4	0.064	57.424	8.5
M4	0.166	57.968	30.1
SN_4	0.032	58.440	167.9
MS_4	0.073	58.984	42.3
$2MN_6$	0.024	86.408	177.1
M6	0.032	86.952	205.8
MSN_6	0.026	87.424	235.5
$2MS_6$	0.048	87.968	274.0
$2SM_6$	0.020	88.984	317.5

h(t) is the height of the partial tide for time t.

R is the constituent amplitude (m).

wt is the speed (°/hr).

ϕ is the phase (°).

7.2.3 Transport

Using the cross-sectional discharge and area (Qr & A) provided in the hydrodynamic model, the one-dimensional, tidally-resolved, advection-dispersion equation for a constituent with a concentration, C (x,t) (Pritchard, 1958), was used to describe the coupling of mass transport and chemical reactions (eq. 7.8).

$$\frac{\partial \mathrm{C}}{\partial \mathrm{t}} + \frac{\mathrm{Qr}}{\mathrm{A}} \frac{\partial \mathrm{C}}{\partial \mathrm{x}} = (\mathrm{AD} \frac{\partial \mathrm{D}}{\partial \mathrm{x}}) + \mathrm{P} \tag{7.8}$$

where:

A = Cross-sectional area.

Qr = Cross-sectional discharge.

P = Sum of all production and consumption processes rates for the solute C.

D = Effective dispersion coefficient (m^2/s).

x = Distance along the longitudinal axis (m).

To describe the mixing of the freshwater and saline water in the Severn, the effective dispersion coefficient (D) (m^2/s), which accounts for the dispersion mechanisms associated with sub-grid-scale processes was used (Volta et al., 2014). This empirical, predictive relationship is used to quantify dispersion in a system for which there is no salinity data available. However, the equation can over and underpredict the salt intrusion. D is generally maximum near the saline limit and becomes virtually zero in freshwater, near the tail of the saline intrusion zone where $\bar{B}$ becomes narrower. For the Severn, due to the lack of salinity data between 40-80 km, this dispersion equation was used. However, the observed salinity data was used to find the best agreement between the simulated and observed values. The effective dispersion at the estuarine lower boundary (D_0) can be quantified following the relationship between water depth and N (Volta et al., 2014). However for the Severn, a dispersion coefficient of 315 m^2/s was incorporated into the dispersion formula following published research on dispersion in the estuary (Uncles, 1982). D varies along an estuarine gradient and can be described by Van der Burgh's equation (eq. 7.9), considering bankfull river discharge (Q_b) and A. The Van der Burgh's coefficient (K) is a shape factor (eq. 7.10), that can be constrained from estuarine geometry, and has a range of $0<K<1$ (Savenije, 1994, 2012).

$$\frac{\partial D}{\partial x} = -K\frac{Q_b}{A} \tag{7.9}$$

where:

D = Effective dispersion coefficient (m^2/s).

K = Van der Burgh coefficient.

Q_b = Bankfull river discharge (m^3/s).

A = Cross-sectional area.

$$K = 4.32 * \frac{H_0^{0.36}}{B_0^{0.21} * b^{0.14}} \tag{7.10}$$

where:

K = Van der Burgh coefficient.

H_0 = Tidally averaged depth at the lower estuarine boundary (m).

B_0 = Width at the lower boundary (m).

b = Width convergence length (m).

For a detailed explanation of these formulations see Volta et al. (2014) and references within.

7.2.4 Suspended Particulate Matter

In turbid estuaries such as the Severn, the simulation of the suspended particulate matter (SPM) was required for the prediction of light availability for photosynthetic pelagic organisms in the water column. Local erosion of estuarine beds or the deposition of SPM, along with the local hydrodynamics conditions, all control the SPM concentration. SPM is subject to advective and dispersive transport in estuaries (Arndt and Regnier, 2007). The one-dimensional, tidally resolved, advection-dispersion equation for SPM, follows a similar equation to that used for solutes (C) (eq. 7.8), but with the addition of erosion (R_{ero}) and deposition (R_{dep}) rates. A detailed explanation of this SPM advection-dispersion equation and the mathematical formulation of R_{ero} and R_{dep} can be found in Arndt and Regnier (2007), Volta et al. (2014), Volta et al. (2016) and their supplementary information. This formulation is simplified, although is commonly used as it captures the main features of SPM distributions, which is required to constrain gross primary productivity (GPP). For a summary of the sediment parameter used in Si-GEM and the origin of their values, see Table. 7.4.

Table 7.4: Sediment parameters.

Name	Description	Value
g	Acceleration due to gravity (m/s^2)	9.81
ρ_w	Density of pure water (kg/m^3)	1000
w^s	SPM settling velocity (m/s)	3.4 x10^{-3} (1)
E^0_{cr}	Critical shear stress for erosion in the estuary (N/m^2)	2.3 (3)
D^0_{cr}	Critical shear stress for deposition in the estuary (N/m^2)	0.1 (2)
E^1_{cr}	Critical shear stress for erosion in the river (N/m^2)	0.5 (3)
D^1_{cr}	Critical shear stress for deposition in the river (N/m^2)	0.1 (2)
E_0	Erosion coefficient in the estuary ($kg/m^2/s$)	3.5 x10^{-6} (4)
E_1	Erosion coefficient in the river ($kg/m^2/s$)	6.0 x10^{-5} (4)

1. Manning et al. (2010). **2.** Gao et al. (2011). **3.** Severn Estuary erosion study in 2018: lower boundary at Site 4, upper boundary at Site 1. Assumed river shear stress for erosion was similar to conditions at Site 1 in the upper estuary. **4.** Volta et al. (2014).

7.2.5 Biogeochemistry: benthic-pelagic coupled network

7.2.5.1 Description of C-GEM's original pelagic network

In C-GEM, the production and consumption process rates for a solute (C) in the water column of the estuary was referred to as the biogeochemistry reaction network. This included the following state variables: pelagic dissolved silicon (PDSi); phytoplankton diatoms (DIA); nitrate; ammonium; phosphate; Total Organic Carbon (TOC); and oxygen. This biogeochemical reaction network was comprised of: Si consumption; GPP (a factor of light availability, nutrient limitation, and the rate of photosynthesis); net primary productivity (NPP); phytoplankton mortality; net ecosystem metabolism (NEM) - a biogeochemical indicator of estuarine trophic status defined as the difference between NPP and total heterotrophic degradation (aerobic degradation and denitrification) (see Volta et al. (2014) and references within); aerobic degradation; denitrification; nitrification; and air-water gas exchange for oxygen and carbon dioxide. For a detailed description of aerobic degradation, denitrification, and nitrification see (Regnier and Steefel, 1999; Vanderborght et al., 2002, 2007; Arndt et al., 2009).

In estuaries, the interplay between light and nutrient availability and flushing rates (control the residence time of diatoms in the water column), all influence NPP (Cloern et al., 2014). NPP rates determine the relative extent as to which DSi and macronutrients (N and P) are consumed. GPP dynamics were calculated in C-GEM using the maximum specific photosynthetic rate (P^{B}_{max}) (Volta et al., 2014). This setup involved a vertical resolution of the photic depth and considered an exponential decrease of light intensity with depth. This depth profile depends on the extinction coefficient, a function of the SPM concentration, calculated by the SPM model component. The difference between GPP and autotrophic algal respiration was used to calculate NPP, which is divided into a maintenance term [i.e. population of diatoms, see Vanderborght et al. (2002)] and a biosynthesis term i.e. growth, see Langdon (1993), along with excretion rates (Lancelot et al., 2000). The availability of ammonium triggered the switch between ammonium and nitrate utilization pathways for photosynthesis, with the consumption of N and P described according to the stoichiometric Redfield ratios (Redfield, 1963). Nutrient dependency for phytoplankton growth was assessed using macronutrient concentrations through a succession of Michaelis-Menten terms, along with their corresponding half-saturation constants (Arndt et al., 2009). In diatom-dominated estuaries, DSi is often limiting (Arndt et al., 2007). The spatial and temporal changes of PDSi in the estuarine water column relates to the transport processes (advection and dispersion, as described previously), and Si consumption, which is related to NPP by the Si:C ratio of 0.12 (Brzezinski, 1985).

For Si-GEM, the P^{B}_{max} was determined following the temperature-dependence equation according to the sigmoidal relationship for a hypothetical river-coastal zone follow-

ing Volta et al. (2016) and Gamier et al. (1995):

$$P^{B}_{max}(T) = P^{B}_{max}, L * \exp[-((T-13)^2/21^2)] \quad (7.11)$$

Where, P^{B}_{max},L is the optimum growth rate for freshwater diatoms [0.06/hour, where P/B ≈ growth rate, Ahlgren (1987)], the optimum temperature is 13°C, and the temperature range is 21°C (Billen and Garnier, 1997). T is the average water column temperatures (°C) from each season in 2016 (see Chapter Three, Section 3.3.4). A sensitivity test is carried out to determine the variability of P^{B}_{max} on diatom concentrations, and the limitations of this formula is discussed in detail (see Section 7.3.3.4).

Diatom mortality rate (0.02/day, Laruelle et al., 2009a), which integrate the effects of cell lysis and grazing by higher trophic levels, was used to calculate diatom mortality using the temperature-dependent equation used on the Scheldt Estuary [Volta et al. (2016), and references within].

The pelagic reaction processes (P) dynamics and their mathematical formulation are described in detail in Volta et al. (2014) and supplementary material. Further detailed descriptions can be found in the works of Vanderborght et al. (2007) and Arndt et al. (2009). For a detailed description of the GPP formulation see Arndt et al. (2007).

7.2.5.2 Coupling a benthic biofilm network to Si-GEM

To account for the intense element recycling at the sediment water interface (SWI) in the Severn Estuary, a benthic-pelagic exchange was required in Si-GEM. The C-GEM pelagic biogeochemistry network was expanded in this modified version to also include: pelagic biogenic silica (PBSi); benthic dissolved silicon (BDSi); benthic biogenic silica (BBSi); benthic living diatoms (bDIA); and suspended benthic living diatoms (sbDIA). The pelagic data for the state variables collected in 2016 (see Chapter Three) was used for the biogeochemical boundary conditions. Benthic state variables, which are calculated by the model, were initialised assuming concentrations of approximately zero (1 x10^{-20} mmol/m^3) at t=0. This benthic-pelagic model setup is described in in detail below and summarised in Fig. 7.4.

BSi was added into the pelagic regime, whereby phytoplankton death (assuming diatoms were abundant) contributed to the PBSi pool, using the Si:C ratio of 0.12 (Brzezinski, 1985). With low chl *a* concentrations in the sampled periods of 2016, the contribution of pelagic diatoms to the PBSi pool was minimal. The dissolution of PBSi, using the dissolution rate constant from Arndt and Regnier (2007), would increase the PDSi pool, while the consumption of PDSi by the living phytoplankton would decrease the PDSi pool.

The benthic biofilm component was implemented via the growth - resuspension - deposition and mortality cycles of benthic diatoms, calculated as a non-transient com-

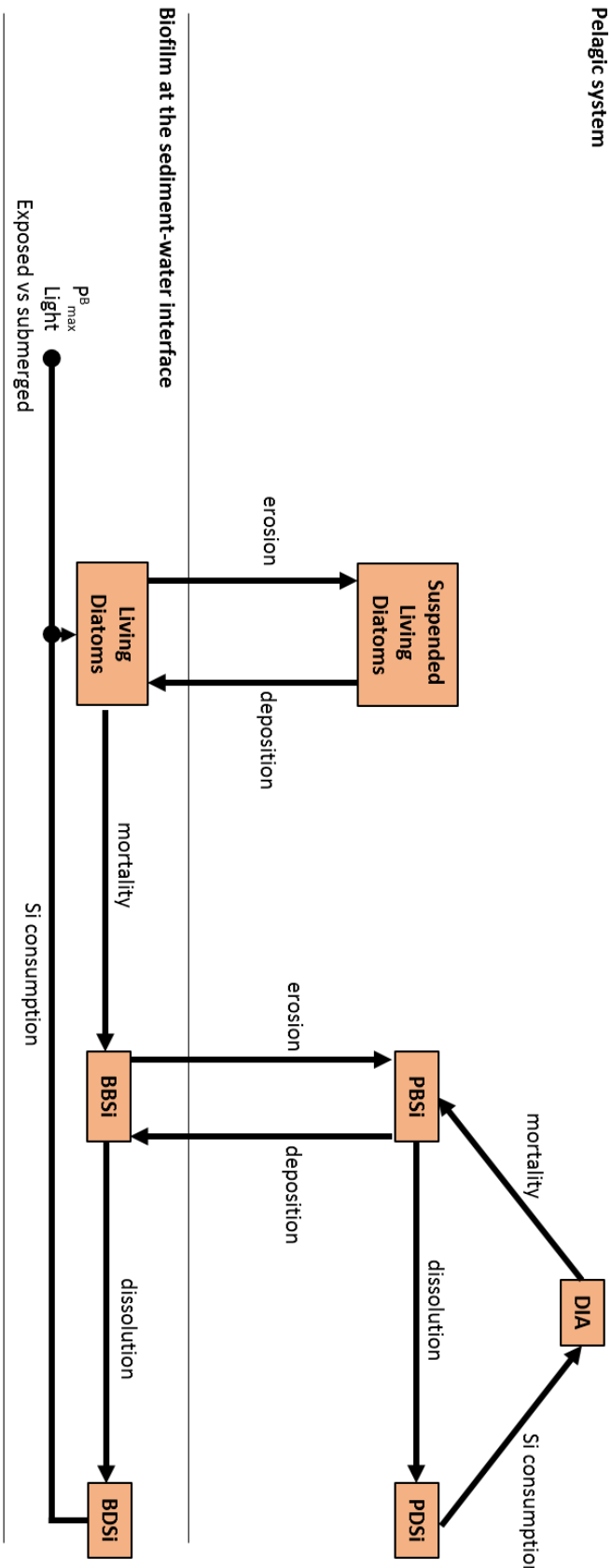

Figure 7.4: Conceptual scheme of the coupled Si benthic-pelagic model implemented in Si-GEM.

ponent existing at the SWI. In recognition of the immersion and emersion cycles of the mudflats, a conditional clause was added: if $H/\overline{B}$ was below 0, the mudflats would be exposed (i.e. no tidal effect). A second condition clause was added, whereby diatoms (bDIA) could only grow during daylight (I0), based on the light regime of the pelagic model, i.e. photoperiod corrected for cloud cover (Brock, 1981; Billen et al., 1994; Volta et al., 2014). Diatom growth was a factor of the benthic maximum specific photosynthetic rate (P^B_{max}) and benthic nutrient limitation (bnlim). Benthic P^B_{max} was calculated following the above protocol. Benthic nutrient limitation was calculated using the same formulation as for the pelagic (i.e. DIA) constituents (Volta et al., 2014), but observed BDSi and macronutrient concentrations from the mudflats sampled in 2016 were applied (see Chapter Four). Primary production was assumed to be carried out by diatoms due to their abundance in the Severn (Underwood, 2010), with Si being the main nutrient to limit production. These formulas are explored in more detail later.

The living diatoms were subject to erosion-deposition processes. A condition clause was added; if the erosion rates were above 0 the diatoms would be transported into the water column, forming the suspended diatom pool, sbDIA. Similarly, if the deposition rates were above 0, the sbDIA would settle out of the water column. Because of the close correlation between SPM and BBSi (an alternative proxy for diatoms), and the high probability of bioflocculation (see Chapter Three and Five), the same settling velocity was applied to both the sediment and the diatoms (Manning et al., 2010). The death of diatoms at the SWI was governed by the benthic diatom mortality, calculated following the above protocol for pelagic diatoms, but was not limited to the tidal cycles. The dead diatoms fuelled the BBSi pool (using the Si:C ratio of 0.12: Brzezinski, 1985). Therefore, the death and erosion of the diatoms would lead to lower benthic living diatom concentrations (mmol C/m^3), whilst the growth and deposition of living diatoms, would lead to higher concentrations.

The BBSi pool was also subject to erosion-deposition processes, similar to the living benthic diatoms; once resuspended, the BBSi would add to the PBSi pool. Alternatively, if deposition occurred, the PBSi could settle onto the mudflats (using the same settling velocities applied to the sbDIA), increasing the BBSi pool. To limit the exponential growth of the BBSi pool, the dissolution of silica was again implemented using the dissolution rate constant from Arndt and Regnier (2007). The dissolution of BBSi would add to the BDSi pool, which is again mediated by benthic diatom consumption (i.e. uptake of BDSi). This benthic consumption of DSi was calculated following the pelagic formulation (Volta et al., 2014). A final conditional clause was added, whereby no benthic input was added to the PBSi pool after 80 km upstream, i.e. in the 'true' river where no mudflats are present. In order to compare the simulated PBSi concentrations with the observed data collected in 2016 (see Chapter Three, Section 3.3.1), the Si component of the sbDIA was simply added to the PBSi concentrations (i.e. externally

in MATLAB).

7.2.6 Numerical solution

Non-linear partial differential equations were solved by a finite difference scheme on a regular grid following a similar approach by Regnier et al. (1997), Regnier and Steefel (1999) and Vanderborght et al. (2002). A grid size of 2005 m and a time step of 150 s were kept constant along the longitudinal axis of the Severn. The spatial resolution can be reduced for smaller lengthen estuaries to ensure a minimum of 20 grid points within the computational domain. Similarly, the temporal resolution can be easily modified.

7.2.7 Model-data comparison

A warm-up period of 1 year was applied to each seasonal simulation (winter and spring = 91 days, summer and autumn = 92 days). The 1-year warmup period was ran in order to spin-up the hydrodynamics and transport routines, prior to the initiation of the biogeochemical and sediment network. For example, the hydrodynamics have been validated by comparing observed and simulated tidal amplitude profiles, and the transport model has been validated by comparing simulated longitudinal salinity profiles with the observed data.

The performance of the one-dimensional RTM using idealised geometries has been evaluated for several estuarine systems of different classifications (Volta et al., 2016). The C-GEM version has shown to successfully reproduce the extent of the estuarine salt intrusion (Volta et al., 2014, 2016). Further, the biogeochemistry network of C-GEM has been approved using different estuaries. For example, simulations on the funnelled-shaped Scheldt Estuary in Belgium and the Netherlands, and the Elbe Estuary in Germany, alongside six European estuaries discharging into the North Sea, have been validated using model-model and model-data comparisons (Volta et al., 2014, 2016). This analysis has been pursued here by evaluating the Severn's Si-GEM simulations output of solutes (C) and SPM using model-data comparison from observed measurements in 2016.

7.3 Results and Discussion

7.3.1 Hydrodynamics

7.3.1.1 Tidal amplitude

The simulated tidal amplitude longitudinal profile (Fig. 7.5) follows the characteristic features of a converging channel (Savenije, 1994, 2012). This channel convergence results in the amplification of the spring and neap tidal waves, which peak *ca.* 40 km from the lower estuarine boundary, a few km northeast of Avonmouth (Fig. 7.5). The simulated spring tidal amplitude reached highs of 6.2 m, resulting in a tidal range of over 12.4 m. The neap tidal amplitude reached highs of 3.2 m, with a tidal range of 6.4 m, in agreement with previous research (Uncles, 2010; Xia et al., 2010a; Kirby, 2010).

In the lower estuary, the strong tidal dynamics overpower the river influence, whereby the deeper water, associated with lower bottom friction levels, contributes to the high tidal amplitudes (Fig. 7.5). As the spring and neap tidal waves move upstream, the influence of the river energy progressively increases, and through increased bottom friction (Chézy coefficient = 5.0 $m^{1/2}/m$), the tidal amplitude is dampened. In the upper river, the model slightly overestimates the tidal amplitude during a spring tide, and underestimates the tidal amplitude during a neap cycle. Similar discrepancies were reported in Volta et al. (2014), and were attributed to seasonal variations in river discharge, along with the use of an idealised estuarine shape. These limitations also hold true for the tidal amplitude simulations presented here for the Severn.

During the model set-up stage, this study attempted to include a more accurate depiction of the Severn's geometry (i.e. width and depth). By interpolating between known width ($\overline{B}$) and depth (H) values along the Severn (observed data), the width and depth from each grid cell was defined. This method of using the observed data was carried out to form the most accurate representation of the Severn's undulating width and depth. To account for these sharp changes in the geometry (see Fig. 7.2), which could reduce the effectiveness of the model, a moving average was applied (i.e. a smooth profile), and a constant $\overline{B}$ value was given for the first 20 km. Even with these changes, the geometry and daily flow rates negatively impacted the hydrodynamics, likely due to the formation of embayments and troughs that trapped water. Trapping, which arises from the irregularity of estuarine banks, for example mudflats and 'dead ends', often results in a phase difference between the main estuary flow and the tidal flat; slack can occur at high tide on the mudflat whilst the water still flows upstream. This latter process can result in density differences as the mudflats discharges freshwater into the flood flow, which can impact on the transport of solutes (Savenije, 1994). Further, this study attempted to include daily flow data (Fig. 7.6). However, during periods of low rainfall and subsequently low river discharge (min. of 21.7 m in 2016, Fig. 7.6), the

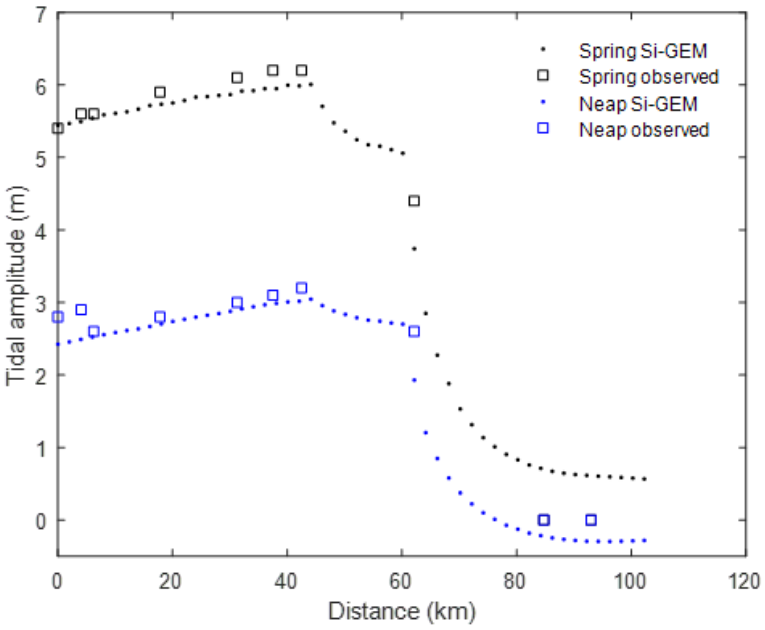

Figure 7.5: Comparison between simulated (Si-GEM) spring and neap tidal amplitudes using a constant freshwater discharge, $Q_r = 118$ m^3/s, and observed tidal amplitudes: Admiralty Tide Charts, Office (2016).

tidal dynamics were significant compared to the bottom friction produced by these low riverine flows, which resulted in high tidal amplitudes (over 6 m) in the upper reaches of the river. Therefore, the idealised geometry and a constant flow rate for each season were considered the most accurate for the Severn's hydrodynamics. Ideally, a 2D or even 3D numerical model (e.g. see Falconer et al. (2009) and references within) with a curvilinear computational mesh (to better represent the coastline, and concentrate grid points on important areas), which can also capture more of the complex tidal hydrodynamics (e.g. turbulent mixing, residual currents over mudflats, mixing of ebb and flood channels) would be beneficial. However, 2D or 3D models are computationally expensive, and would require a comprehensive observational dataset. The latter is a key issue in modelling nutrient transport in estuarine systems, which are often, in such systems as the Severn, data-scarce.

7.3.1.2 Salinity transport

The balance between upstream dispersion and downstream advection controls the longitudinal profile of salinity (Savenije, 2006, 2012). The dispersion coefficient revealed the common dome-shaped profile typical of funnel-shaped estuaries (Savenije, 2006, 2012; Volta et al., 2016), from 315.0 m^2/s at the estuarine mouth to 0 at *ca.* 60 km (Fig. 7.7). This dispersion setup best suited the observed salinity data, and thus the simulated salinity profile (Fig. 7.8). The salt intrusion wedge observed between *ca.* 40 and 70 km

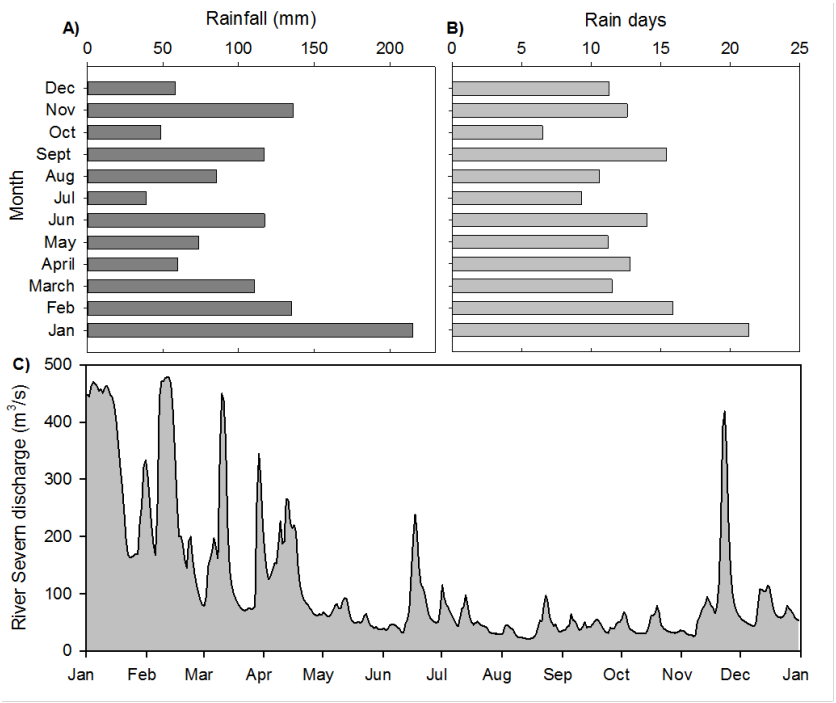

Figure 7.6: A) Rainfall in the Severn's catchment area (mm). **B)** Number of rain days. **C)** River Severn discharge (m^3/s) in 2016. Data from Agency (2016) and MetOffice (2016).

has the common sharp interface; saltwater is entrained as the freshwater River Severn flows at the surface. In reality, shear stress and turbulent mixing would cause a downward force on the saltwater wedge, which would be counterbalanced by the upwards movement driven by the density difference. However, the model overestimates the salt intrusion profile compared to the observed data (Fig. 7.8), although each season, the observed data was measured on a neap cycle when salinity levels are reduced compared to a spring cycle. Furthermore, the low resolution of salinity data makes the model-data comparison difficult to interpret. Therefore, Environment Agency monitoring data from 2016 (Agency, 2016) has been used for a higher resolution (Fig. 7.8). The Si-GEM appears to capture the salinity transport in the Severn Estuary, and highlights the importance of using representative salinity values for the individual seasonal simulations. For example, salinity data collected during the winter monitoring season are relatively low due to the higher freshwater discharge from the River Severn.

The temporal change in salinity at different distances along the Severn show that the model was in a steady-state after a warmup of 1 year (Fig. 7.9). These temporal plots, especially at 60 km, show the influence of the river discharge on the tidal evolution of salinity, causing variability between *ca.* 3 to 15 psu. In comparison at the lower boundary (0 km) and 10 km upstream, the tidal influence is dominant, with little variability in the salinity levels. Once in the upper freshwater riverine system, the tidal dynamics had no influence on the salinity levels (Fig. 7.9).

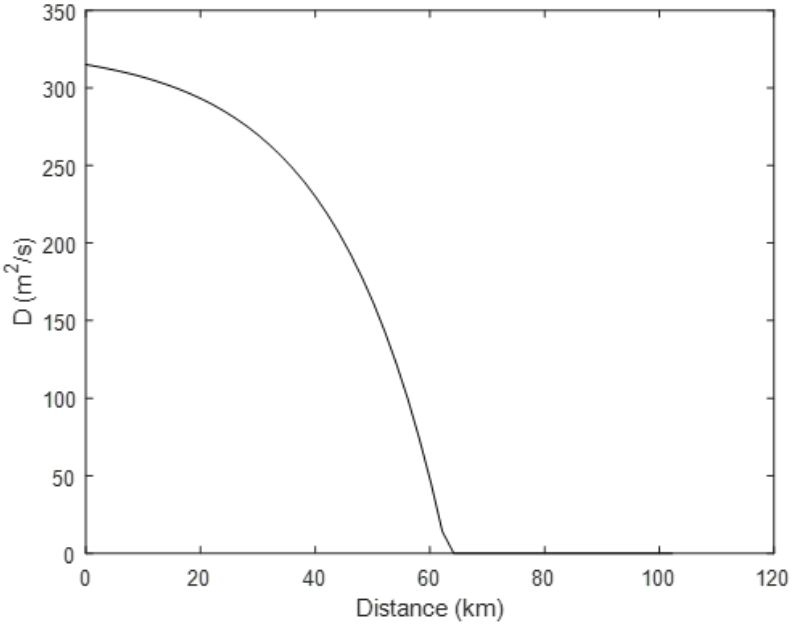

Figure 7.7: Longitudinal dispersion coefficient, set at 315.0 m^2/s at the lower estuarine boundary, and modelled using a river bankfull discharge of 118 m^3/s.

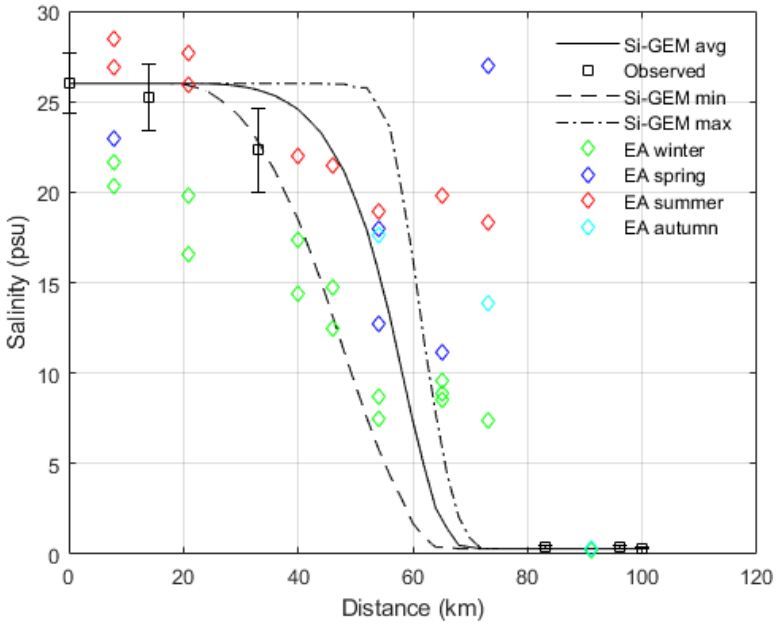

Figure 7.8: Longitudinal profile of salinity along the Severn. Comparison between observed and simulated salinity levels (average of all data collected in 2016), modelled using an annual river flow of 118 m^3/s. Presented with the mean (-), maximum (-.-) and minimum (–) simulated salinity levels. Environment Agency data for each season in 2016 presented: winter (green), spring (blue), summer (red), autumn (light blue).

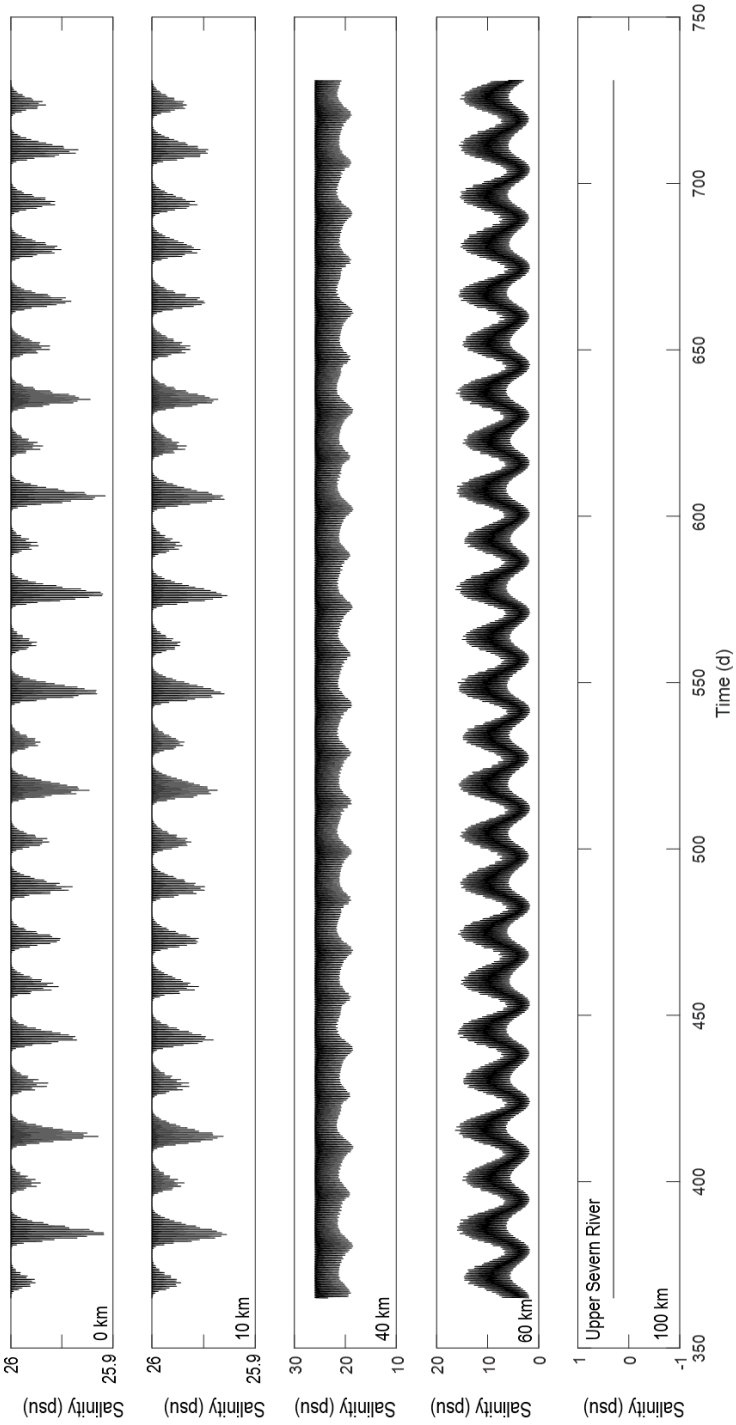

Figure 7.9: Tidal salinity variation over a year at specific locations along the Severn.

7.3.2 Sediment transport

The SPM concentrations along the Severn, despite having a high sensitivity to changes in the physical forcing conditions (Volta et al., 2014), displayed a similar trend along the longitudinal axis of the estuary each simulated season in 2016 (Fig. 7.10). The SPM concentrations in the lower estuary, where the tidal regime is almost exclusively accountable for the mechanical energy in this area, showed very little temporal variability, with concentrations below 2 g/L. Approximately *ca.* 60 km upstream of the lower estuarine boundary, where the channel converges, causing a rise in the tidal amplitude (Fig. 7.5), a peak in SPM concentrations was simulated each season (Fig. 7.10). This area is known as the upper Estuarine Turbidity Maximum zone (ETM), which resides near Sharpness, *ca.* 57 km from the lower estuarine boundary (Manning et al., 2010). This ETM zone forms as a direct result of the energy produced by the intensification of the tidal amplitude, coupled with the availability of erodible sediment on the intertidal mudflats and the riverine sediment influx. For example, the tidal amplitudes still reached highs of 4.4 m (spring) and 2.6 m (neap) at *ca.* 60 km (Fig. 7.5). As the influx of sediment encounters the saltwater, flocculation occurs, which is further enhanced by the presence of organic matter (see Chapter Three and Five). The simulated peak SPM concentrations (*ca.* between 0.3 and 6.5 g/L) were in the range reported by Manning et al. (2010) for this zone (between 0.5 and 10 g/L). Uncles et al. (2002) note up to 50 g/L can be reached in the ETM zone during spring tides, when tidal-currents are flood-dominated, driving sediments upstream. Compared to the erosion study carried out in September 2018, when resuspended sediment concentrations in the near-bed suspension reached highs of 21.2 g/L (see Chapter Five, Section 5.3.5), these simulated estimates are expectedly low. Near-bed SPM concentrations are often significantly high, sometimes leading to fluid-mud layers on neap tides in less energetic regions of the estuary (Kirby, 2010). However, these simulated SPM concentrations compared well to the surf zone SPM concentrations (< 2 g/L, see Chapter Five, Section 5.3.6), which would have been more susceptible to dispersion-advection processes, despite the temporal difference between the sampled years.

The peak in SPM concentrations at *ca.* 60 km corresponds to the peak in the erosion rates (Fig. 7.11), where the bottom shear stress is greater than the critical shear stress for erosion, i.e. erosion threshold of the sediment. This erosion appears to be focused around 60 km, where the convergence of the estuary and the transition into the tidal river is pronounced, resulting in strong horizontal and vertical mixing (Uncles, 2010). The peak SPM concentrations recorded at *ca.* 33 km from the lower boundary could represent the beginning of this ETM zone (e.g. see the spring simulation, Fig. 7.10). This Si-GEM setup therefore captures the Severn's upper ETM zone, which was not visible in the observed data due to the sampling constraints. Further, Environment Agency monitoring SPM data (g/L) further support the seasonal Si-GEM simulations

(Fig. 7.10). In addition, the Severn's SPM profile presented in Jonas and Millward (2010) follows a similar profile to the Si-GEM seasonal simulations (Fig. 7.10), lending confidence in the model output and the observed data collected in 2016.

The more gradual drop in SPM concentrations seaward of the ETM zone is likely a combination of reduced erosion rates and higher deposition rates (Fig. 7.11). The overall high deposition rates compared to the simulated erosion rates, is consistent with the formation of the intertidal mudflats; sediment settles when flow velocities are reduced.

Once upstream of 60 km, corresponding to the increase in bottom friction, the riverine influence increased. This increase in friction dampened the strong tidal dynamics (Fig. 7.5), and along with a smaller area of intertidal mudflats (i.e. a reduced supply of sediment), the SPM concentrations decreased. In the winter simulation, the so called 'balance-point' was obvious at *ca.* 80 km, whereby the fluvial flux and the tidal energy (which moving upstream is progressively dampened by friction) are balanced, and are of low magnitude (Volta et al., 2014). The reduced energy results in low SPM concentrations (Fig. 7.10). The dampening of the tidal energy on the SPM concentrations can also be seen in the SPM time series plots, for example, the temporal variability in SPM concentrations at specific distances along the Severn produced using the winter setup (Fig. 7.12). Further, these time series plots show SPM concentrations to be higher on spring tides compared to neap cycles (Fig. 7.12). Less energetic neap tides (slower tidal currents) are often associated with lower SPM concentrations and have less influence on the SPM regime further upstream compared to the spring tides (Manning et al., 2010). Arndt and Regnier (2007) on the Scheldt, also show that the variation in SPM over tidal timescales is more pronounced in the lower estuary compared to the tidal river.

In the River Severn, the SPM concentrations displayed temporal variability, with peak SPM concentrations in the winter simulated period (Fig. 7.10), associated with higher rainfall/discharge increasing bank removal (Fig. 7.6). In this riverine zone (>80 km), energy dissipation is controlled by the riverine flux. Surprisingly, this SPM regime in the upper river was captured well by Si-GEM, with the simulated concentrations resembling the observed concentrations. Volta et al. (2014) note that these steady-state simulations don't necessarily capture the true nature of sediment transport, for example, small changes in the physical forcings can impact greatly on local SPM concentrations, resulting in large local fluctuations. However, here, these SPM profiles and the close agreement with the observed data [and the Environment Agency 2016 data, Agency (2016)] has been very informative, especially between 40 and 80 km where sampling was not possible.

Note, due to the 1D RTM setup, these simulated SPM profiles do not show SPM variability with depth. Therefore, the high concentrations of SPM in the bottom waters reported in Chapter Three (Section 3.3.5), associated with the concentrated benthic suspension and settling following flocculation, could not be simulated. Instead, the

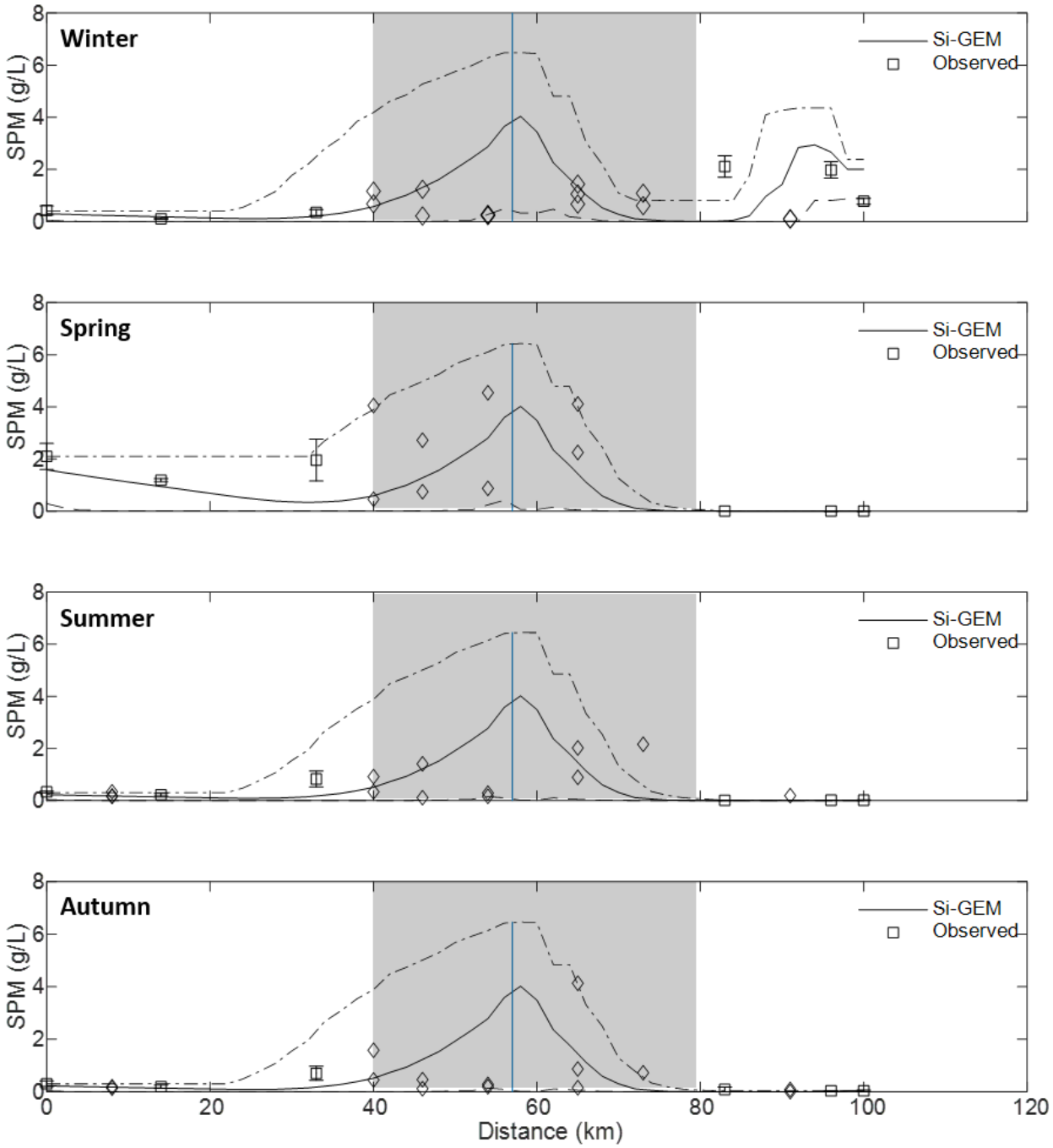

Figure 7.10: Longitudinal profile of suspended particulate matter (SPM) in g/L along the Severn, each simulated season in 2016. Peak SPM at *ca.* 60 km near the documented Estuarine Turbidity Maximum (ETM) zone. Grey area: river-estuary transition zone not sampled in this study. Environment Agency SPM data presented (diamonds) Agency (2016).

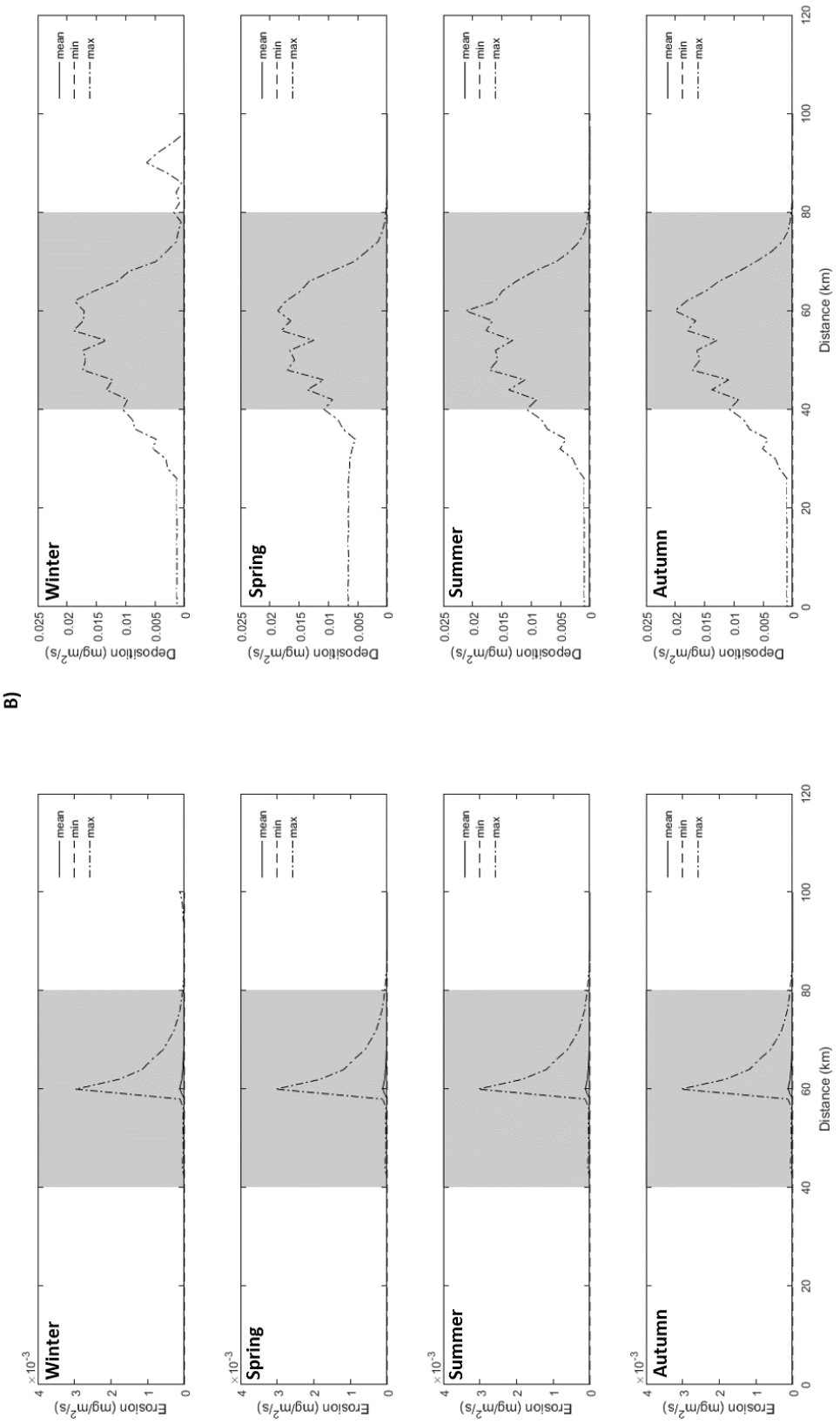

Figure 7.11: Sediment erosion **(A)** and deposition **(B)** rates (mg/m^2/s) each simulated season in 2016. Maximum (- - -) and mean (-) rates shown, minimum rates are 0 mg/m^2/s. Grey area: river-estuary transition zone not sampled in this study.

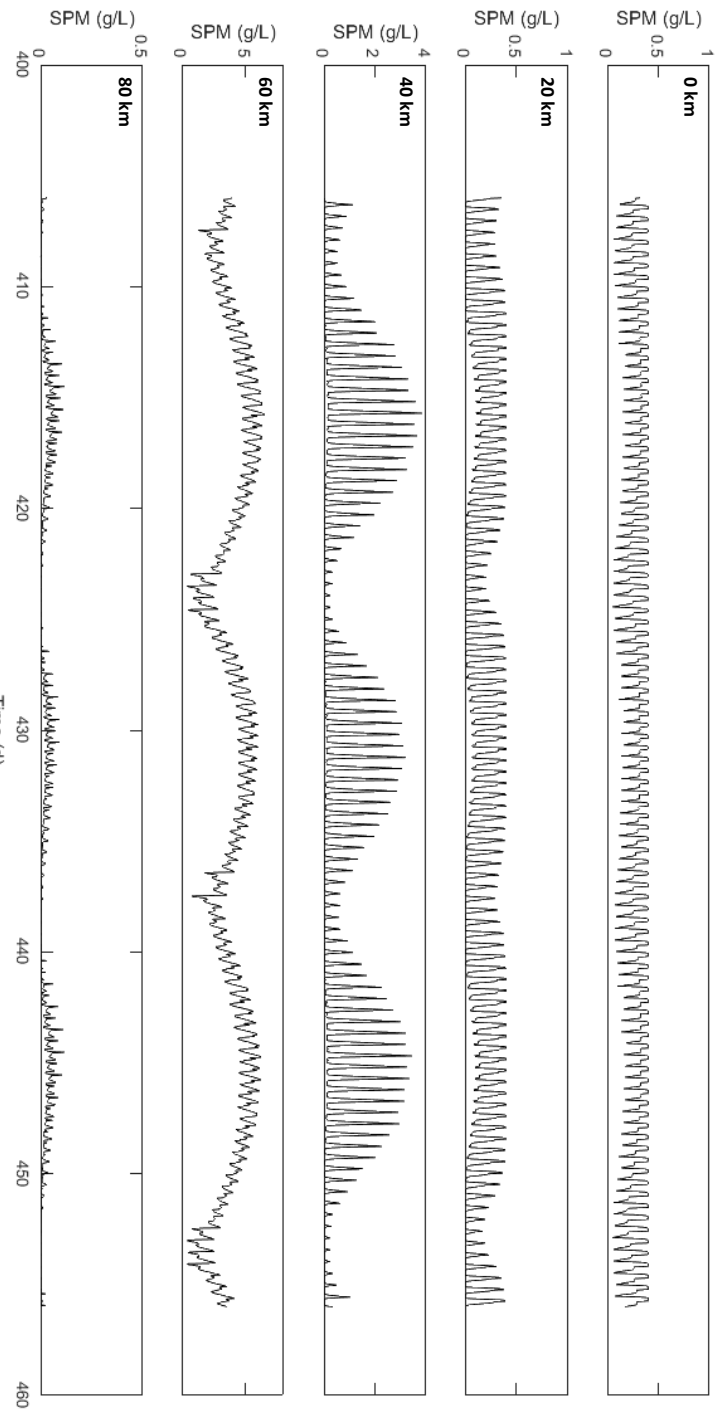

Figure 7.12: Temporal evolution of simulated winter suspended particular matter concentrations (g/L) along the Severn.

observed SPM concentrations plotted against the simulated SPM, is the average of the surface and bottom water SPM concentrations.

7.3.3 Biogeochemistry: coupled benthic-pelagic model

7.3.3.1 Benthic biogenic silica flux

To test the sensitivity of the benthic-pelagic coupled model to the amount of BBSi eroded (i.e. the contribution of dead benthic diatoms) to the pelagic BSi pool, several model simulations were tested. These tests included a range from 80% to 50% of the eroded BBSi material, with the remaining BBSi 'removed' from the benthic BSi pool, through processes not defined in the current model setup e.g. burial (see this chapter's Appendix, Section 7.5). The 'best-fit' between the simulated total PBSi (a sum of both living and dead PBSi) and the observed PBSi concentrations, in the winter, spring and autumn simulations were found assuming 60% of the BBSi was eroded. In comparison, for the best fit summer simulations, 70% of the BBSi was eroded. The high removal rates (>30%) suggests two possible conditions; either external processes such as burial were occurring (and at high rates), reducing the BBSi content at the SWI, or the model overestimates the growth and subsequently death of the benthic diatoms, requiring high removal rates of BBSi. Burial of BBSi is plausible; in Chapter Five (Section 5.3.3), despite the depth profile of BBSi fluctuating at each subsequent increase in depth (every 1 cm), the BBSi content at the SWI and at 20 cm deep were similar.

Using the above 'best-fit' seasonal model setups for BBSi erosion, the BBSi concentrations displayed both seasonal and spatial variability (Fig. 7.14). BBSi concentrations increased along the longitudinal axis of the estuary, similar to the spatial variability in BBSi (% of dried Si mass, g/g) observed among the sampled mudflat sites in 2016 (see Chapter Four, Section 4.3.1.1). BBSi concentrations were similar in the winter, spring and autumn simulations (<400 mmol Si/m^3), and were comparably high in the summer simulation when BBSi concentrations reached >1500 mmol Si/m^3 at *ca.* 60 km upstream of the lower estuarine boundary (associated with less removal e.g. burial). Here, in the river-estuary transition zone, BBSi concentrations peaked each season, possibly a combination of, 1) a large surface area of exposed intertidal mudflats, increasing the overall benthic diatom biomass, which upon death, increased the BBSi pool, and 2) high erosion-deposition rates increasing the contribution of eroded BBSi to the PBSi pool, and subsequently the settling of this PBSi, augmenting the BBSi pool. Compared to the eroded BBSi concentrations from the sediment stability study undertaken in September 2018 (min: 500 mmol Si/m^3 and max: 3,100 mmol Si/m^3, see Chapter Five, Section 5.3.5), these simulated BBSi concentrations could arguably be plausible. Nonetheless, the large annual variability in BBSi, which was summarised in Fig. 5.18 in Chapter Five (Section 5.4.1), is likely to play a large factor between these sampled periods. With a

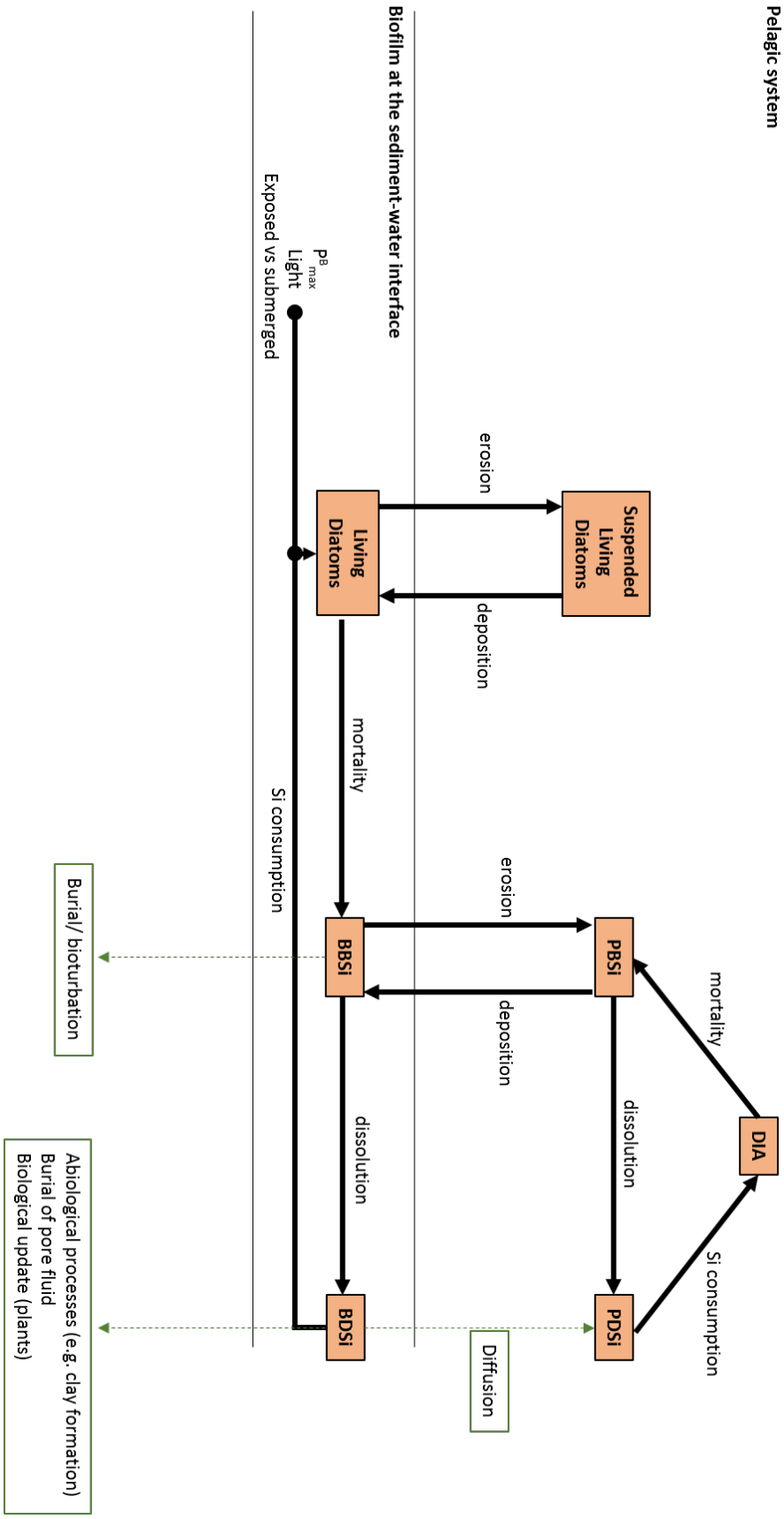

Figure 7.13: Conceptual scheme of the coupled Si benthic-pelagic model with processes that could also mediate BBSi and BDSi at the sediment-water interface (boxes). Burial/bioturbation considered as a single 'removal' term of BBSi in Si-GEM.

peak in BBSi and SPM concentrations at *ca.* 60 km, the model findings indicate that sampling within this river-estuary transition zone would be beneficial to increase the confidence in these model evaluations. This model output is an example of how model findings can re-inform future sampling strategies (Bradley et al., 2015).

7.3.3.2 Total pelagic biogenic silica concentrations

Considering the low chl *a* concentrations measured in the water column of the Severn (<0.001 mg/L, see Chapter Three, Section 3.3.6), the growth and subsequent death of pelagic diatoms contributed to a small amount of the total PBSi pool. With little pelagic diatom growth in the estuary, the riverine influx of BSi would likely be removed overtime through deposition of BSi onto the intertidal mudflats or through dissolution. Therefore, the BBSi contribution to the total PBSi concentrations in the water column, a function of benthic diatom growth/death subject to erosion-deposition cycles, was predominately the source of BSi each simulated season in 2016 (Fig. 7.14), supporting the hypothesis that the benthic diatoms are a source of BSi to the water column. This erosion and flux of BBSi from the mudflats, could also explain the low percentage of BBSi measured on the mudflats in 2016 (see Chapter Four, Section 4.3.1.1). However, Si-GEM did not include the Si inputs through tributaries.

Longitudinal steady-state profiles of PBSi, show a relatively good agreement with the measured data each season in 2016 (Fig. 7.15). Furthermore, the simulated PBSi concentrations were in-line with the surf zone PBSi concentrations sampled in September 2018 (min: 95 mmol Si/m^3, max: 532 mmol Si/m^3), but low compared to PBSi concentrations in the near-bed suspensions (see Chapter Five, Section 5.3.5). The range between the simulated minimum and maximum PBSi concentrations highlights the variability in the BBSi supply. For example, the minimum PBSi concentrations represents periods when minimal BBSi is supplied into the system; when there is no erosion and/or when there is no/little diatom growth (e.g. at night). However, with these model-data comparisons it's important to note that the observed data only represent snap-shots in time.

Within a well-mixed estuary, cross-sectional differences can arise, for example between the channel and the intertidal mudflats, which could impact the PBSi concentrations. These are less important for pelagic dynamics due to the strong vertical and horizontal mixing, but for the benthic biofilm system at the SWI of the mudflats, along with their high spatial heterogeneity, single-point data are not representative of the entire mudflat cross-section. Furthermore, local changes in sediment composition from sandflats to mudflats, and the associated changes in species community (Underwood, 2010), and subsequently BBSi production, is not reflected in this simple 1D biofilm model component.

The erosion and deposition cycles of BBSi was coupled to the SPM regime, and

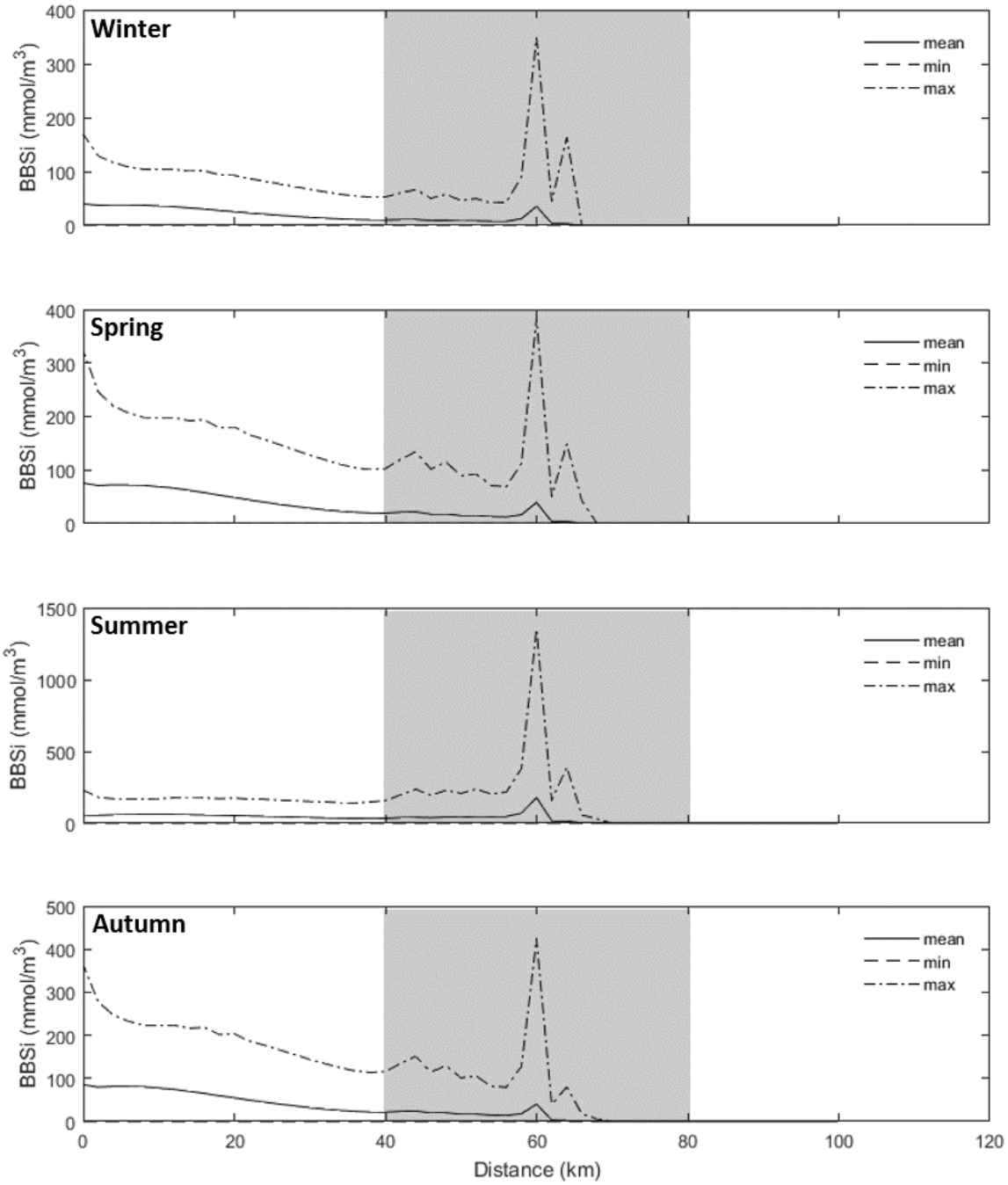

Figure 7.14: Simulated benthic biogenic silica (BBSi) concentrations (mmol Si/m^3) each season in 2016. Grey area: river-estuary transition zone not sampled in this study.

therefore it was no surprise that the BSi export peaked in the ETM zone, similar to the SPM concentrations (Fig. 7.10). The good agreement between the model-derived PBSi concentrations and the measured values, however, does suggest that the conditions in the model setup were appropriate. For example, the same settling velocity for SPM and the suspended BSi was used, further supporting the hypothesis stated in Chapter Three (Section 3.4.4.2) regarding bioflocculation; diatoms settle at a similar rate to the 'heavier' suspended sediment because they are one entity.

Temporal change in the total PBSi concentrations was also noted over the tidal cycles, for example in the winter simulation (Fig. 7.16). The PBSi profiles in the lower estuarine boundary displayed little variation over the spring-neap cycles. Whereas, in the upper estuary large fluctuations in PBSi concentrations were simulated (Fig. 7.16). Extensive intertidal mudflats are exposed between 40 and 60 km; the difference in the area exposed during a spring tide compared to a neap tide resulting in different amounts of BBSi export. A large quantity of BSi is therefore transported on a spring cycles compared to a neap, which agrees with the consensus that more sediment (and therefore more biofilms and buried BBSi) are eroded and transported when there is more energy in the system (Allen, 1990; Manning et al., 2010; Kirby, 2010). The daily fluctuation in the supply of BBSi was also evident, with low or zero PBSi concentrations associated with periods when the mudflats were exposed, and erosion was zero.

7.3.3.3 Pelagic dissolved silicon concentrations

In this model simulation, only the biogeochemical processes of phytoplankton consumption and PBSi dissolution influenced PDSi concentrations. The dissolution of silica, a factor of the dissolution rate constant (Arndt and Regnier, 2007), leads to the concomitant rise in PDSi concentrations. During periods with a high flux of BBSi increasing the PBSi concentrations, the increased dissolution of silica led to higher PDSi concentrations (Fig. 7.17). The model simulation of PDSi agreed relatively well to the observed data, with the common decreasing trend in DSi towards the marine zone (Fig. 7.17), and were similar to the PDSi profiles simulated in the Scheldt (Arndt et al., 2009, 2011; Volta et al., 2014). Further, the PDSi simulations agree relatively well to the Environment Agency monitoring PDSi data from 2016 (Agency, 2016) (Fig. 7.17), lending confidence in the model simulations and the data collected in 2016. In addition, the decreasing profile from the River Severn to the Bristol Channel is comparable to the silicate profile of the Severn presented in Jonas and Millward (2010) for the years 2004 and 2005.

A large component of the PDSi profile was likely governed by estuarine hydrodynamics transporting PDSi from the river along the longitudinal axis of the Severn. This strong control by the hydrodynamics on PDSi transport is also evident in the temporal evolution of PDSi along different sections of the Severn (see Fig. 7.18); high riverine PDSi concentrations at 60 km fluctuated significantly between spring/neap cycles, whilst

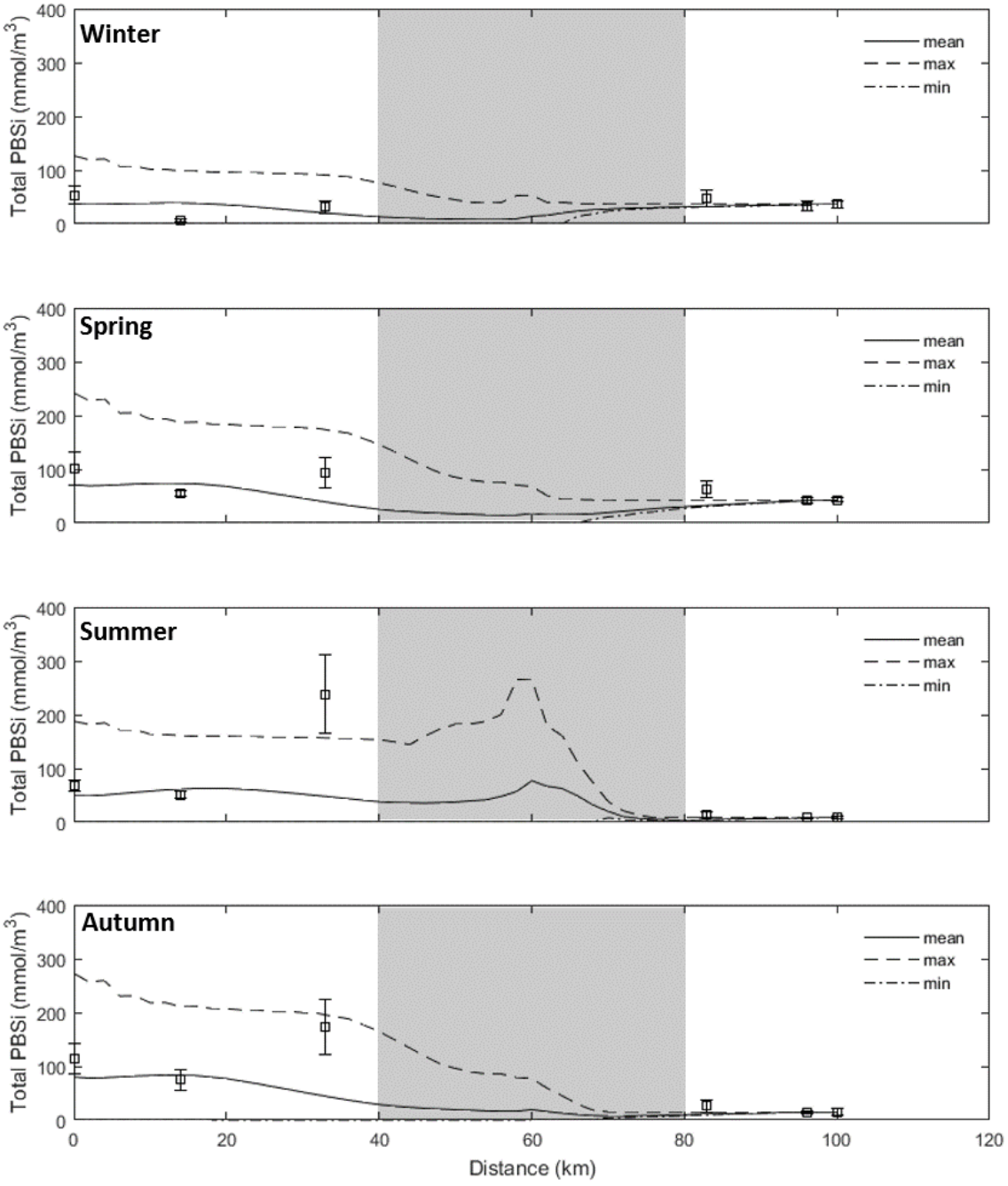

Figure 7.15: Total pelagic biogenic silica (PBSi) concentrations (mmol Si/m^3) each season in 2016. Grey area: river-estuary transition zone not sampled in this study.

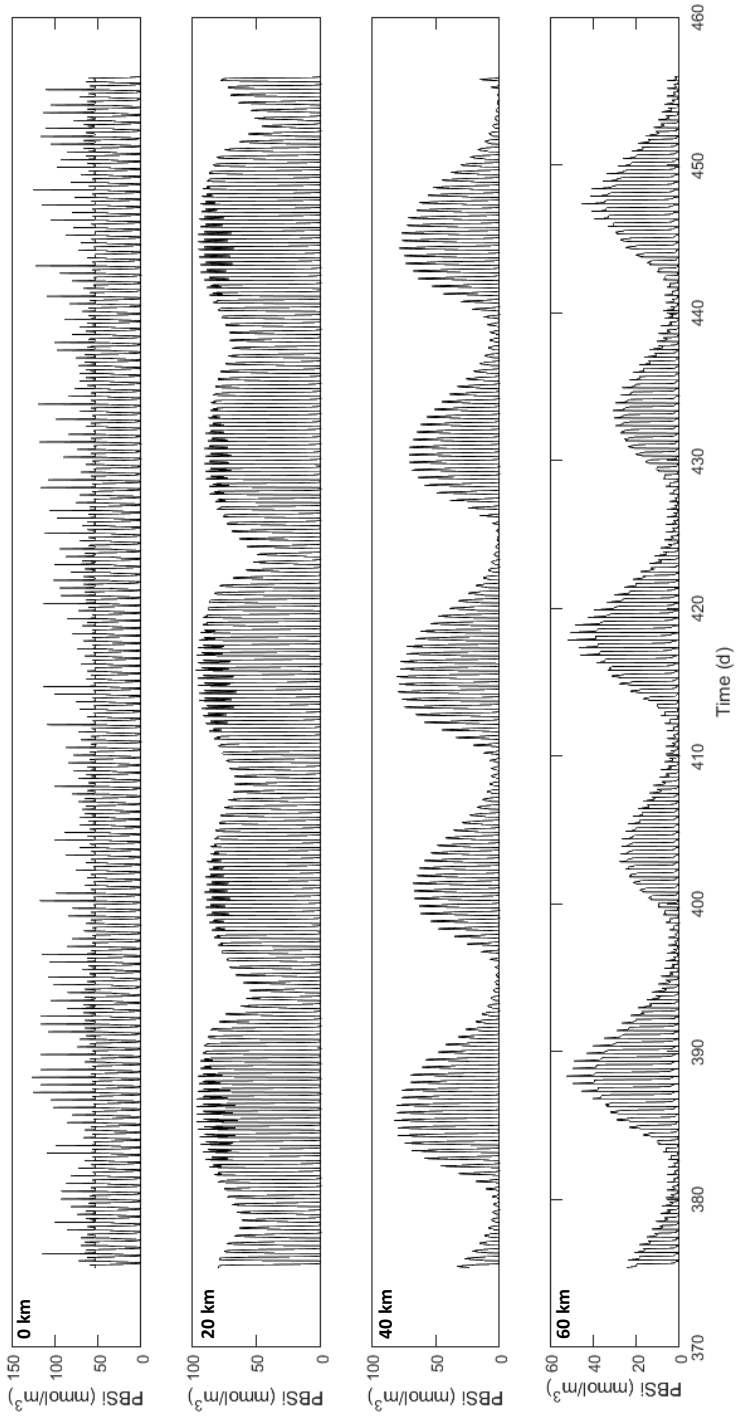

Figure 7.16: Temporal evolution of simulated total pelagic biogenic silica (PBSi) concentrations (mmol Si/m^3) along the Severn in the winter of 2016.

at 0 to 20 km, little variation in PDSi occurred over the tidal cycle. The diffusion of BDSi (a factor of benthic diatom consumption and BBSi dissolution), supplementing the PDSi pool, was not interconnected in the current model setup. Furthermore, external processes such as abiological reactions (e.g. adsorption of DSi onto clay particles, see Chapter Three and Six), and the burial of DSi-rich pore fluids, which would decrease BDSi concentrations, were not considered (see Fig. 7.13). In addition, the DSi input via the tributaries (e.g. Wye, Usk and Avon) was not considered.

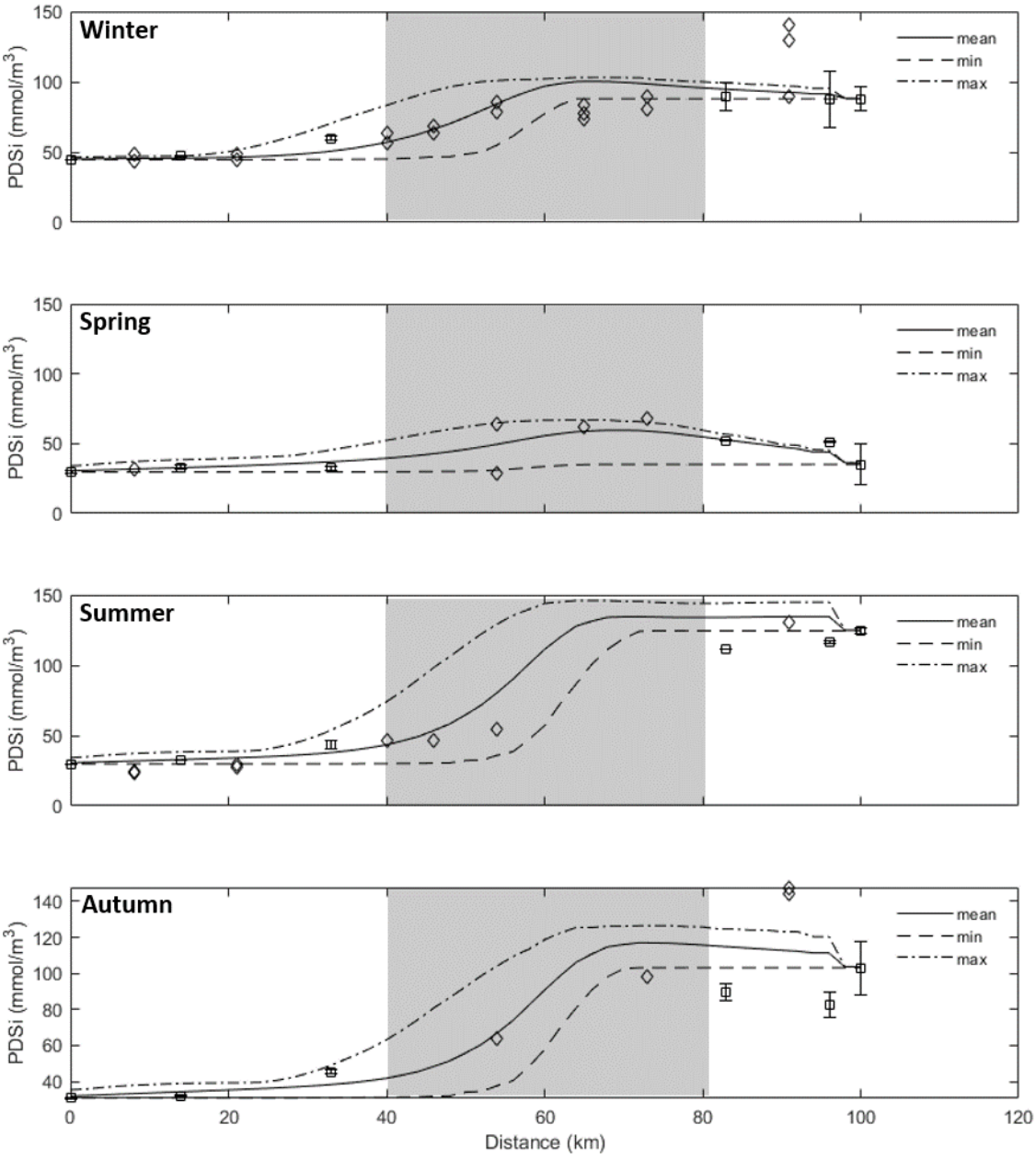

Figure 7.17: Total pelagic dissolved silicon (PDSi) concentrations (mmol Si/m^3) each season in 2016. Grey area: river-estuary transition zone not sampled in this study. Environment Agency monitoring DSi data Agency (2016) presented (diamonds).

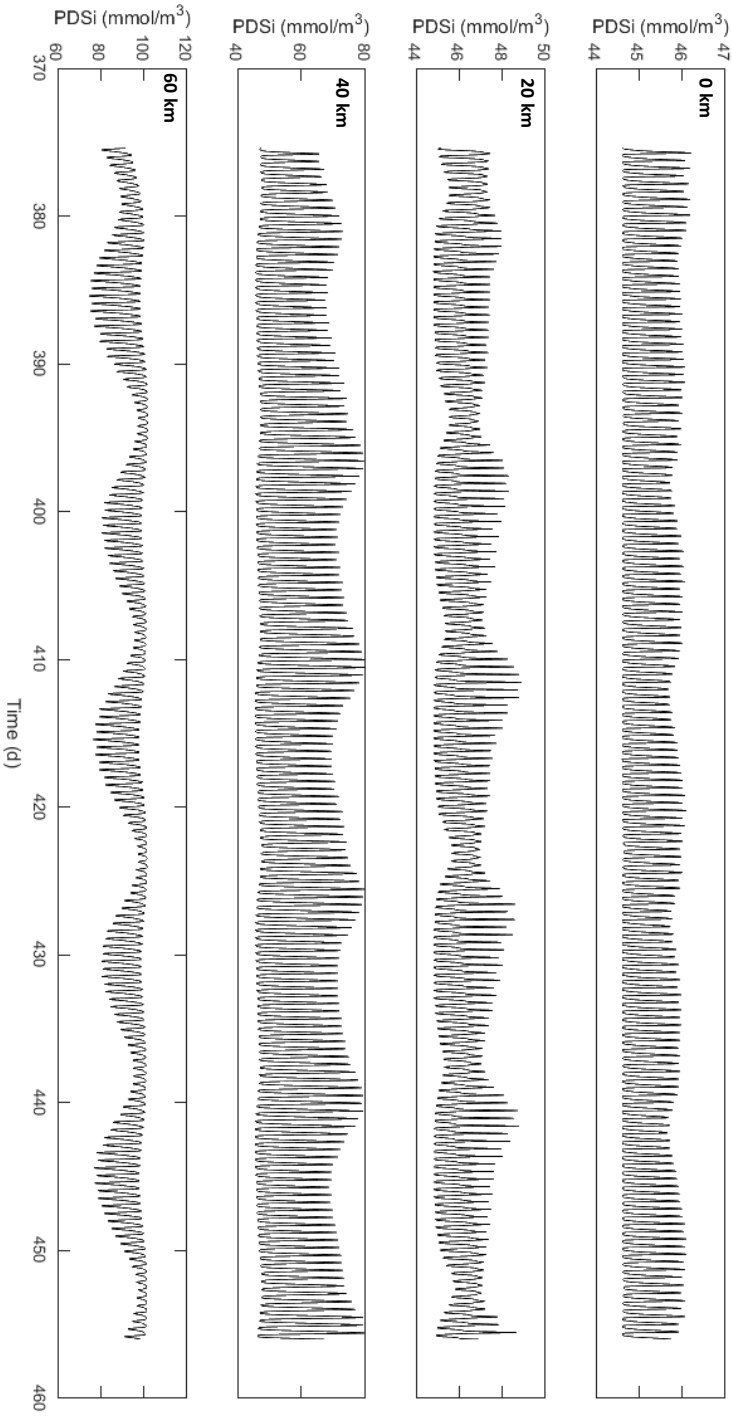

Figure 7.18: Temporal evolution of simulated total pelagic dissolved silicon (PDSi) concentrations (mmol Si/m^3) along the Severn in the winter of 2016.

7.3.3.4 Benthic diatom growth

Compared to the simulated BBSi concentrations (i.e. the dead benthic diatoms), the simulated living fraction of benthic diatoms at the SWI was relatively low each season in 2016 (<20 mmol C/m^3, Fig. 7.19). Consequently, the suspended living diatom fraction was also low (<4 mmol C/m^3, Fig. 7.20), and contributed to a small proportion of the total PBSi concentrations (Fig. 7.15). The rate of supply to the BBSi pool, a function of diatom death and deposition (through the erosion-deposition cycle), was greater than the rate of removal (e.g. dissolution of silica). Therefore, despite the low diatom biomass, the accumulation of BBSi overtime led to the discrepancy between the living biomass and the BBSi content (i.e. the dead benthic diatoms). Therefore, these simulations suggest there is more dead-BBSi compared to living-BBSi on the intertidal mudflats.

To evaluate the model, the simulated benthic diatom concentrations are compared to the observed diatom concentrations, estimated using the chl *a* content from the intertidal mudflats sampled in 2016 (see Chapter Four, Section 4.3.2). The diatom concentrations were estimated using: 1) the sediment bulk density estimated using the water content (for example, sediment with a water content of 77% had a sediment bulk density of *ca.* 23%), 2) by assuming the biofilms were 1000 μm thick (1% of 1 m^3 of sediment, Perkins et al., 2003), and 3) by assuming a C to chl *a* ratio of 50 g C/g chl *a*) (Arndt et al., 2007). The simulated benthic diatom concentrations were grossly underestimated compared to these 'observed' diatom concentrations (Fig. 7.19). However, the measured chl *a* content represent only thick biofilms and did not consider the 'patchy' nature of these biofilms (Orvain et al., 2003). Thus, when considering the entire intertidal mudflat area (including areas where no biofilms are present), the overall diatom concentration would be significantly lower. Furthermore, several assumptions are made in the calculation of the benthic diatoms from the chl *a* content, including in the estimate of the sediment bulk density. For example, over an emersion period, the desiccation of the sediments leads to dewatering and compaction, which reduces water content and increases sediment bulk density (Perkins et al., 2003). Therefore, sediment bulk density can vary greatly with depth, which is often not considered in these large-scale models. For example, the sediment density of sand (2650 kg/m^3) is often used in benthic-pelagic coupled models (Arndt and Regnier, 2007).

Several factors were implemented to limit diatom growth, including, a) exposed vs submerged mudflats; b) day vs night; c) nutrient limitation; d) P^B_{max} [Volta et al. (2014) and references within]; e) mortality rates, and f) erosion-deposition dynamics. A few of these processes are discussed in-detail below:

Nutrient limitation

The benthic macronutrient concentrations, which could limit benthic diatom growth,

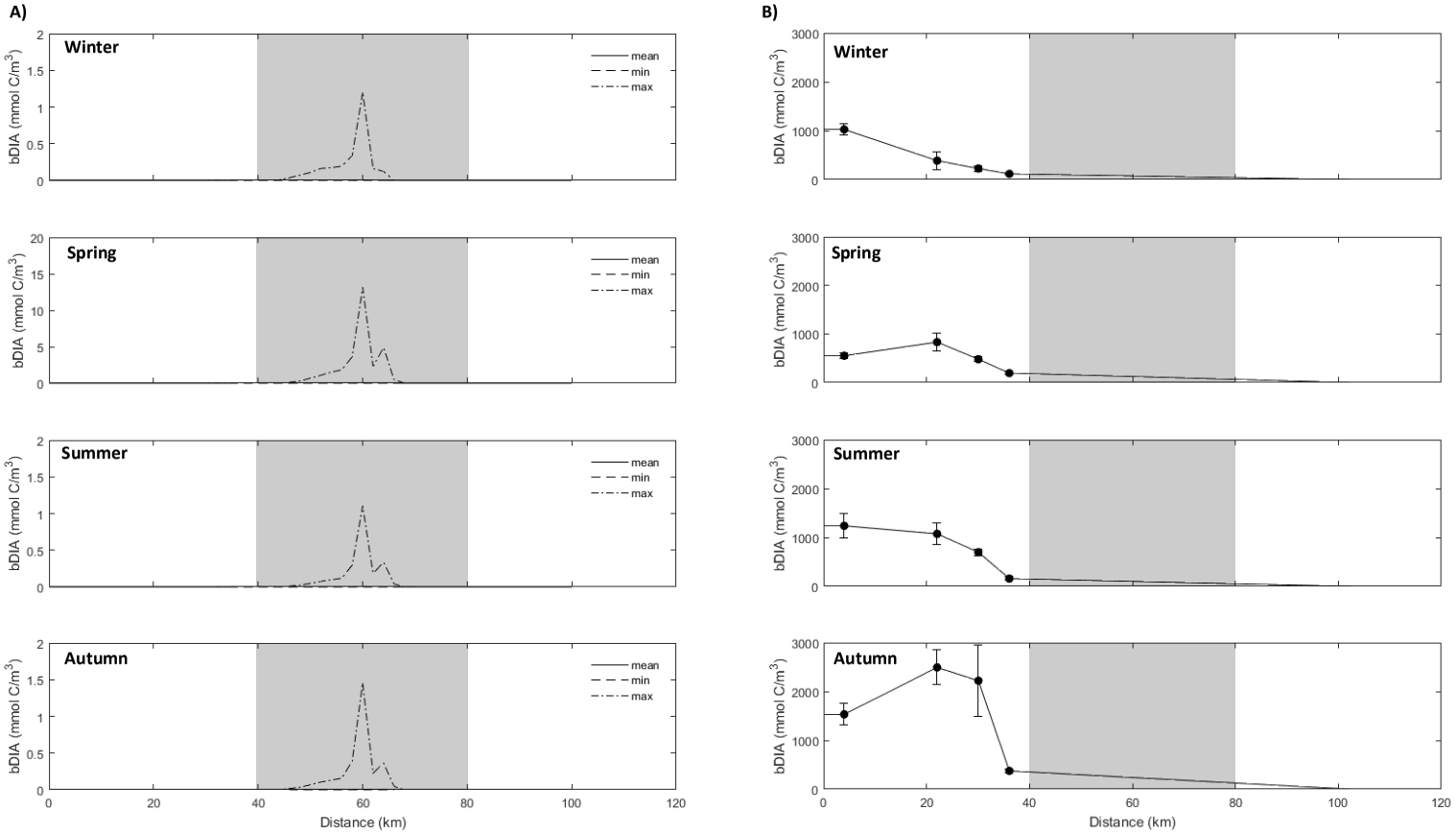

Figure 7.19: A) Simulated benthic diatom concentrations (mmol C/m^3) each season in 2016. **B)** Estimated benthic diatom concentrations (mmol C/m^3) from measured biofilm chlorophyll *a* content, presented with SE of n=15 stations. Grey area: river-estuary transition zone not sampled in this study.

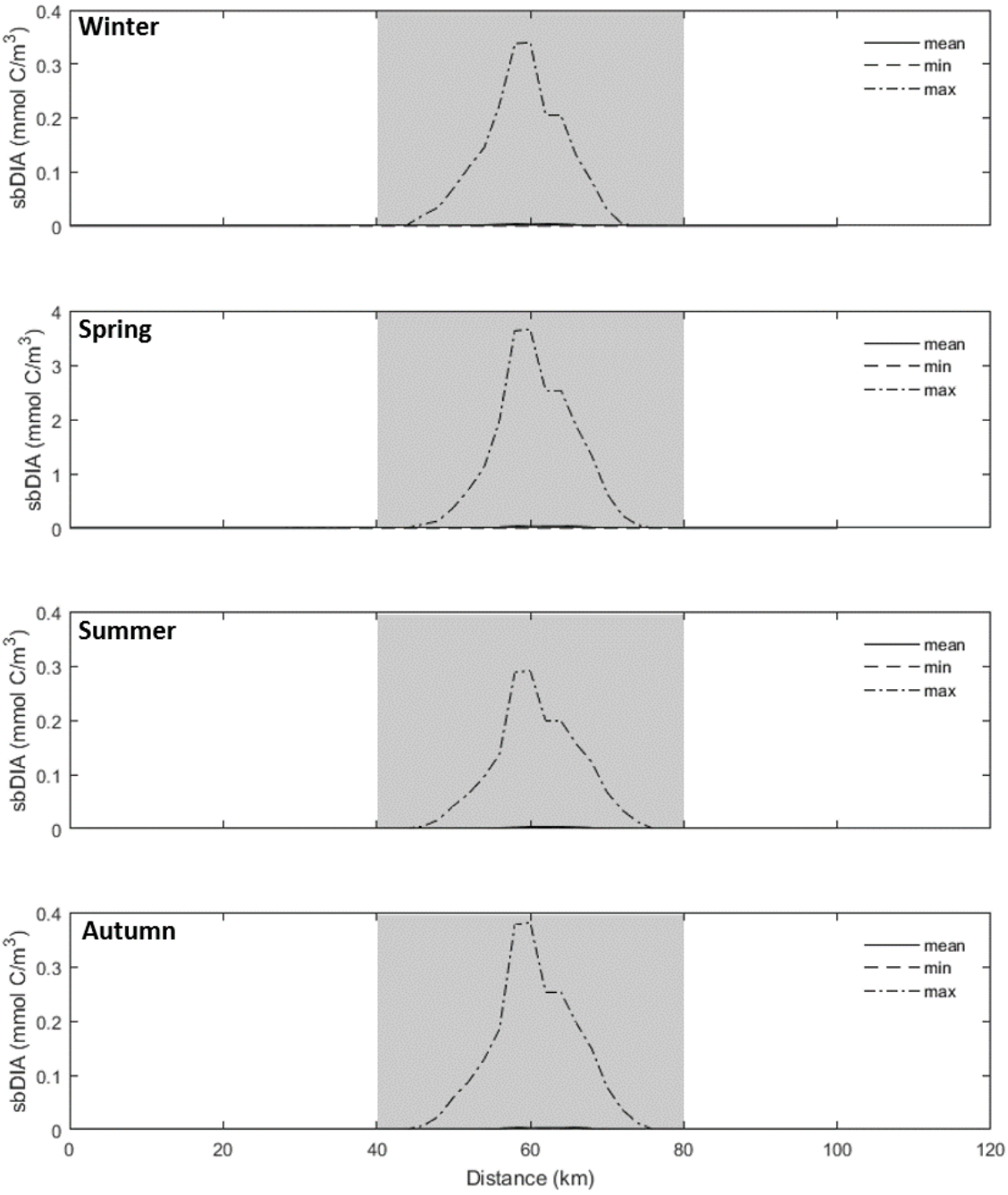

Figure 7.20: Suspended living diatom concentrations (mmol C/m^3) each season in 2016. Grey area: river-estuary transition zone not sampled in this study.

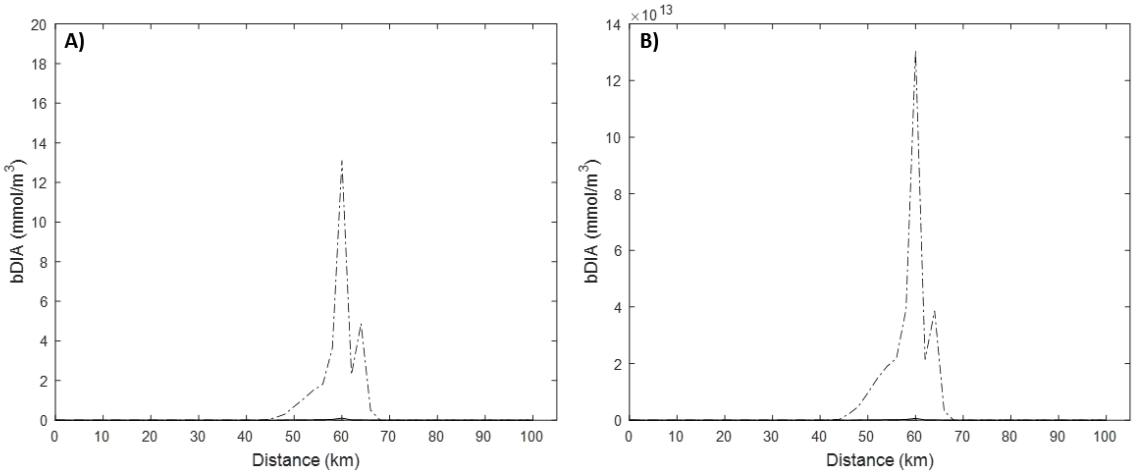

Figure 7.21: A) Benthic diatom concentrations limited by nutrients. **B)** Benthic diatom concentrations not limited by nutrients. Note, different scale on the y-axis.

were considered following Volta et al. (2014), using a succession of Michaelis-Menten terms (Gamier et al., 1995). The assumption of using Michaelis-Menten terms may not be valid for benthic systems. For example, Leynaert et al. (2009) show DSi uptake kinetics follow the Michaelis-Menten hyperbolic saturation equation at low concentrations, but at higher concentrations (>100 μmol/L), other secondary uptake systems are apparent. This goes beyond the present study, although highlights the limited research on nutrient uptake by benthic diatoms. If nutrients are not limiting, benthic diatoms grow exponentially (e.g. see Fig. 7.21), and exceed the observed benthic diatom concentrations estimated from the measured chl *a* content data. This output implies, at least for this model setup, nutrient limitation is required to prevent the growth of diatoms exceeding the rates of removal (e.g. mortality/erosion). However, this could also indicate another external process that might limit diatom growth, which is not captured by the model, e.g. desiccation.

Rate of photosynthesis ($\mathbf{P^B_{max}}$)

The temperature-dependent maximum rate of photosynthesis (P^B_{max}), using the formula for a hypothetical river-coastal zone in (Gamier et al., 1995), displays a sigmoidal relationship (Fig. 7.22), whereby P_{max} increases exponentially with temperature until an optimum temperature is reached, followed by a decline in P_{max}. The model of Blanchard et al. (1997) also follows a similar profile, but suggests a higher optimum temperature is reached (between 25 to 30°C). It's possible that the P^B_{max} equation of Gamier et al. (1995) could underestimate the growth of the diatoms by having an optimum temperature of only 13°C (Billen and Garnier, 1997). This formula considered only freshwater diatoms (Billen and Garnier, 1997). In the estuary, where conditions are more saline, other diatom species are likely present and may follow different growth

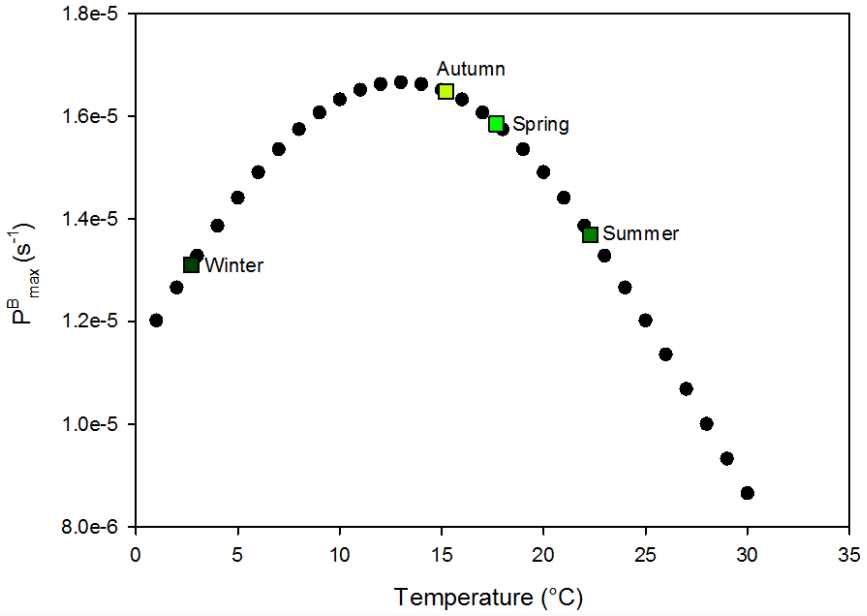

Figure 7.22: P^B_{max} from 1 to 30°C, following Gamier et al. (1995) equation for freshwater diatoms. Billen and Garnier (1997): optimum temperature of 13°C and a temperature range of 21°C). Squares: benthic diatoms P^B_{max} values used in the Si-GEM simulations.

conditions. For example, using the formulation for seawater diatoms, P^B_{max} was low and resulted in a low diatom concentration (Fig. 7.23). Alternatively, considering Billen and Garnier (1997) conditions for freshwater chlorophyll (algal biomass), the simulated diatom concentrations were high (up to 7 x10^5 mmol C/m^3). In addition to these caveats, the temperatures of the mudflat water can vary greatly over spatio-temporal scales (see Chapter Four, Section 4.3.2). Underwood (2001) report temperatures on a mudflats can fluctuate significantly during an emersion period (2-3°C), and even as high as 20°C during a day. Furthermore, the temperature of the surficial few mm is expected to be significantly higher than the temperature measured from the pore fluids within the sediment. The P^B_{max} values used here (1.31 x10^{-5} to 1.65 x10^{-5} s^{-1}), calculated using the average pore fluid temperatures, are however comparable to other estuarine studies [1.07 x10^{-6} to 6.90 x10^{-5} s^{-1}, see Volta et al. (2016)]. Nevertheless, the Si-GEM is highly sensitive to even small changes in P^B_{max}. For example, using the outlying minimum and maximum temperatures from all spring measurements, the change in P^B_{max} had a significant impact on the growth of the benthic diatoms (see Fig. 7.24). This is not an estuarine-specific issues, for example published P^B_{max} values for the Scheldt Estuary also vary significantly: 7.16 x10^{-41} s^{-1} (Gypens et al., 2013); 1.23 x10^{-5} s^{-1} (Arndt et al., 2011); 2.76 x10^{-5} s^{-1} (Gypens et al., 2013); 2.80 x10^{-5} s^{-1} (Gypens et al., 2013); 6.90 x10^{-5} s^{-1} (Gypens et al., 2013).

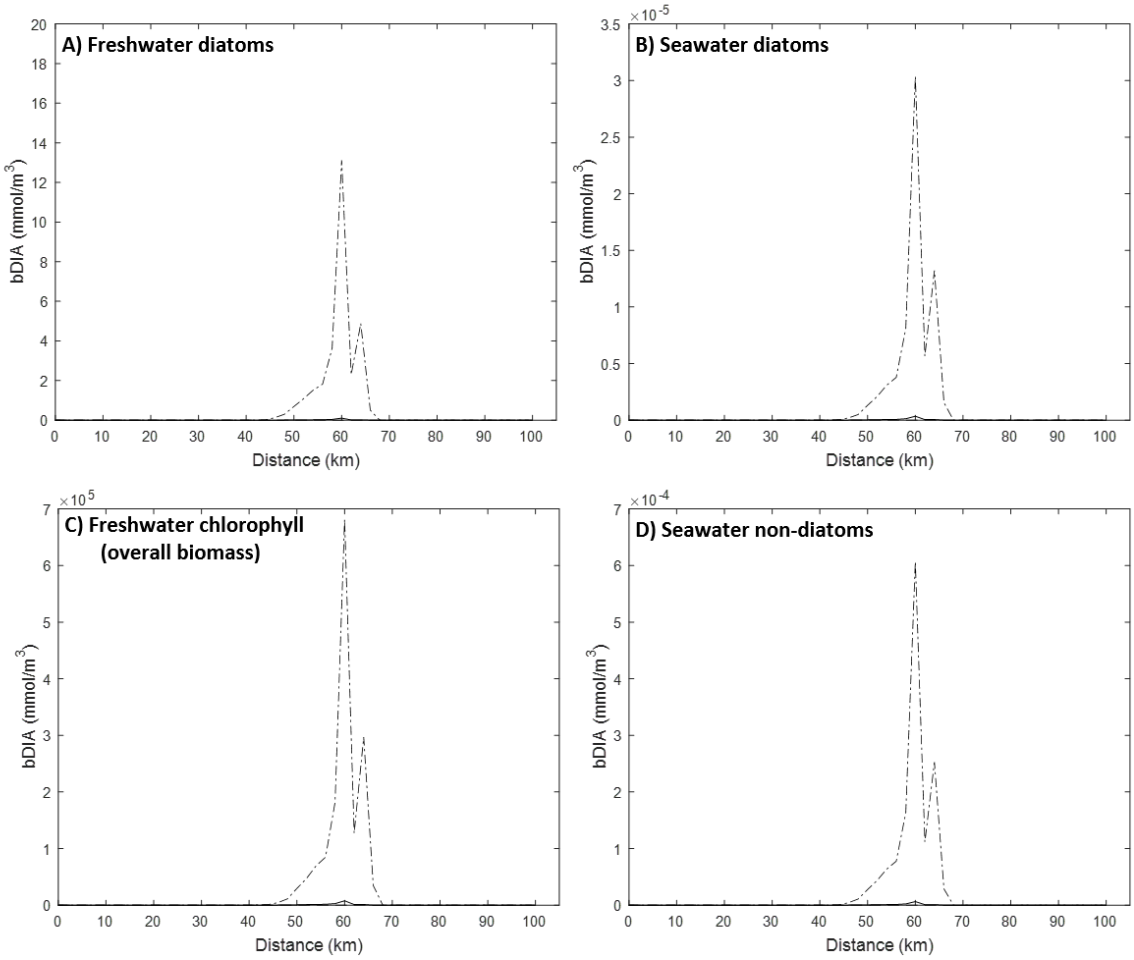

Figure 7.23: Spring Si-GEM simulation of benthic diatom concentrations (mmol C/m^3) with different P^B_{max} values calculated using different growth rates, optimum temperatures and temperature ranges (Billen and Garnier, 1997). **A)** Freshwater diatoms. **B)** Seawater diatoms. **C)** Freshwater chlorophyll (assumed overall biomass). **D)** Seawater non-diatoms. Note, different scale on the y-axis.

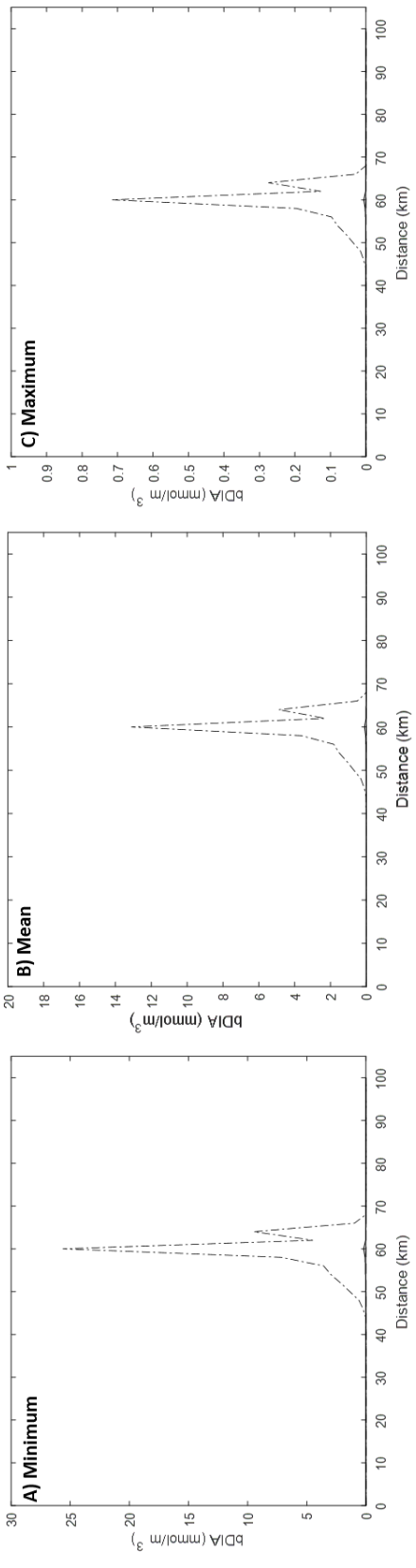

Figure 7.24: Spring Si-GEM simulations with different P^{B}_{max} values. **A)** P^{B}_{max} calculated using the minimum pore fluid temperature of 12.1 °C. **B)** P^{B}_{max} calculated using the mean pore fluid temperature of 17.7 °C. **C)** P^{B}_{max} calculated using the maximum pore fluid temperature of 24.4 °C.

Benthic mortality

The temperature-dependent diatom mortality was calculated using the mortality rate of 0.02/day (Laruelle et al., 2009a). Here, we assume the formulation for phytoplankton (Volta et al., 2016) is suitable for benthic diatoms; benthic mortality rates ranged between 2.79 x10^{-7} and 1.10 x10^{-6} s^{-1}, which are within the estimates for phytoplankton in temperate estuaries (2.35 x10^{-7} and 2.35 x10^{-5} s^{-1}, see Volta et al. (2016) and references within). Benthic mortality was considered to occur at any time and was not restricted to the emersion-immersion cycles of the biofilms. With a constraint on diatom mortality (i.e. limited to immersion periods only), the benthic diatom concentrations increased further (see Fig. 7.25), but remained below the observed diatom concentrations estimated using the chl *a* contents (see Fig. 7.19). Furthermore, several formulations for mortality are provided in Volta et al. (2016). Using the formulation following Gamier et al. (1995), with similar conditions for P^{B}_{max}, benthic mortality was reduced, increasing the benthic diatom concentrations (Fig. 7.25). Compared to nutrient limitation and P^{B}_{max}, diatom mortality appeared to have less control on diatom growth, and subsequently on BBSi accumulation.

7.3.3.5 Si-GEM application to the Severn: future use and prospects

Si-GEM presented here has been useful in deciphering the transport of PBSi along the Severn's system, and has shed light on the possible Si dynamics in the transition zone (40-80 km), which otherwise would remain unknown. Furthermore, the model simulated a peak in estuarine turbidity at *ca.* 60 km from the lower estuarine boundary, in conjunction with previous research on turbidity in the Severn. The conjoined peak in the simulated SPM and BSi concentrations in this transition zone, has presented an important area, which requires more research. These findings should now inform future sampling strategies, in order to target this area (40-80 km), when investigating sediment and nutrient transport in the Severn.

The model showed higher deposition rates compared to erosion, backed by the presence of intertidal mudflats. Over longer periods, to what extent changes in these erosion and deposition rates will have on these intertidal mudflats, is unclear. For example, Kirby (2010) suggests a predicted loss of these mudflats with an up-shore retreat of 4 to 10 m/yr associated with sea-level rise. With the additional effects of coastal squeeze, e.g. at Newport Wetlands due to the sea defence structure preventing landward migration, this could have dire consequences for the Severn's mudflat and saltmarsh habitats, including the future of the benthic diatom biofilms.

The benthic biofilm supply of BBSi has been shown computationally to influence the PBSi concentrations in the simulated periods of 2016, agreeing with the hypothesis set forward in previous chapters. However, Si-GEM (an adaption of C-GEM), both

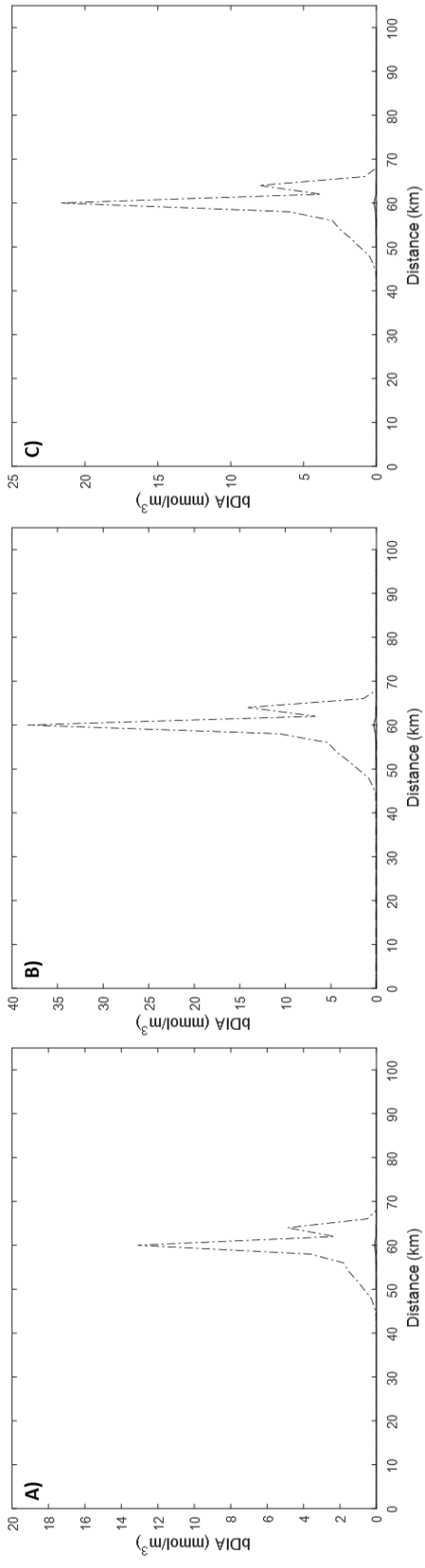

Figure 7.25: Spring Si-GEM simulations with different diatom mortality rates. **A)** Using the temperature-dependent formulation for the Scheldt Estuary (Volta et al., 2014). **B)** Using the temperature-dependent formulation for the Scheldt Estuary (Volta et al., 2014) with benthic diatom death limited to immersion periods. **C)** Using the temperature-dependent formulation following Gamier et al. (1995).

are largely simplified representations of estuarine systems, and therefore, have several limitations. In terms of the benthic-pelagic Si model, one of the key issues lies in the calculation of benthic diatom growth (i.e. P^{B}_{max} and benthic nutrient limitation), which requires further research to improve our confidence in these values. Habit mapping of the benthic biofilms to gain a better understanding of their distribution, would also help predict a more accurate export of diatoms, and thus BBSi (e.g. Launeau et al., 2018). Furthermore, this benthic-pelagic coupling does not consider a benthic sediment component directly, whereby processes such as burial and bioturbation could modify the benthic BBSi pool. The sediment model, for example, published by Arndt and Regnier (2007) could be applied, to explore such benthic processes.

7.4 Conclusion

Previous chapters have presented the possibility that the intertidal mudflats, inhabited by diatom-dominated biofilms, are a source of BSi to the estuarine water column. This has been shown following ecological surveys of the Severn Estuary, its tributaries and intertidal mudflats during selected periods of 2016. Despite sampling every season, and from different locations within the estuary, the temporal and spatial data-resolution was relatively poor. Here, a 1D RTM was applied to the Severn to help disentangle the multiple processes governing DSi and BSi transport, from the freshwater end-member to the outer Severn Estuary, in order to capture the spatio-temporal changes in more detail. The recently developed, computationally efficient C-GEM platform, which reduces data requirements, was applied to the Severn. This version was further modified to represent the Severn system, and includes a benthic-pelagic coupled Si component, and is referred to here, as the Silicon-Generic Estuarine Model.

Si-GEMs simulations have shown that the erosion of BBSi from the SWI to the water column, contributes to the PBSi pool, which otherwise would be low due to the low phytoplankton growth in the water column and the relatively low riverine supply of BSi. Furthermore, the model has shed light on the transport of Si and sediment in the river-estuary transition zone, an area which could not be sampled. For example, the simulations identified the upper ETM zone, which has been documented in several sediment transport publications on the Severn. Therefore, these findings can be used to inform future sampling procedures, especially those focused on silicon and sediment transport.

Despite these achievements, the model is still in development. The model was limited in several areas, most importantly in the calculation of the benthic diatoms, and the findings should be treated with caution. The study also made several assumptions regarding the removal of BBSi from the biofilm, e.g. through burial. Given the importance of benthic BSi in the Severn Estuary, it would be desirable to include a spatially resolved representation of, at least, the benthic intertidal mudflat environment, to account for the high spatial heterogeneity in biofilm growth and erosion/deposition (i.e. sediment stability). Ideally a 3D representation would best represent the Si cycle in the Severn. However, a 3D model would have a high (and possibly prohibitive) computational cost, and the data requirement for the model set-up, parametrization, calibration and validation would be exponentially high. A 1D model, such as this Si-GEM, but with a 2D representation of the benthic environment, that captures the complex erosion/deposition processes on the tidal flats, would be optimal. To achieve this modelling approach, further research is required in the following areas:

- Sample the river-estuary transition zone (40-80 km) to better constrain the model. With a larger data set, transient simulations could be compiled.

- Undertake habit mapping to determine the degree of biofilm spatial heterogeneity across the intertidal mudflats to better constrain the export of BBSi from the intertidal mudflats.
- Improve the current formulation for the benthic diatom concentrations, for example, by sampling more accurate temperature data to improve the outcome of the P^{B}_{max} equation.
- Couple a benthic sediment system to the benthic biofilm to consider processes not considered directly in this Si-GEM version, e.g. burial, bioturbation - see the sediment component of Arndt and Regnier (2007) benthic-pelagic coupled model.

7.5 Appendix

7.5.1 BBSi contribution to PBSi

To determine a reasonable export of BBSi from the intertidal mudflats to the PBSi pool in the estuarine water column, several tests assuming different export concentrations were conducted. This was achieved by implementing a removal term, whereby BBSi would be lost from the system, e.g. through sediment processes such as burial, which are not currently implemented Si-GEM. Each seasonal model was compiled for four different setups', including:

80% BBSi eroded, with the remaining 20% BBSi lost to the system.

70% BBSi eroded, with the remaining 30% BBSi lost to the system.

60% BBSi eroded, with the remaining 40% BBSi lost to the system.

50% BBSi eroded, with the remaining 50% BBSi lost to the system.

The 'best fit' profile of PBSi was considered for each season, and used to further explore the living diatom pool:

Winter: 60% BBSi eroded (Fig. 7.26).

Spring: 60% BBSi eroded (Fig. 7.27).

Summer: 70% BBSi eroded (Fig. 7.28).

Autumn: 60% BBSi eroded (Fig. 7.29).

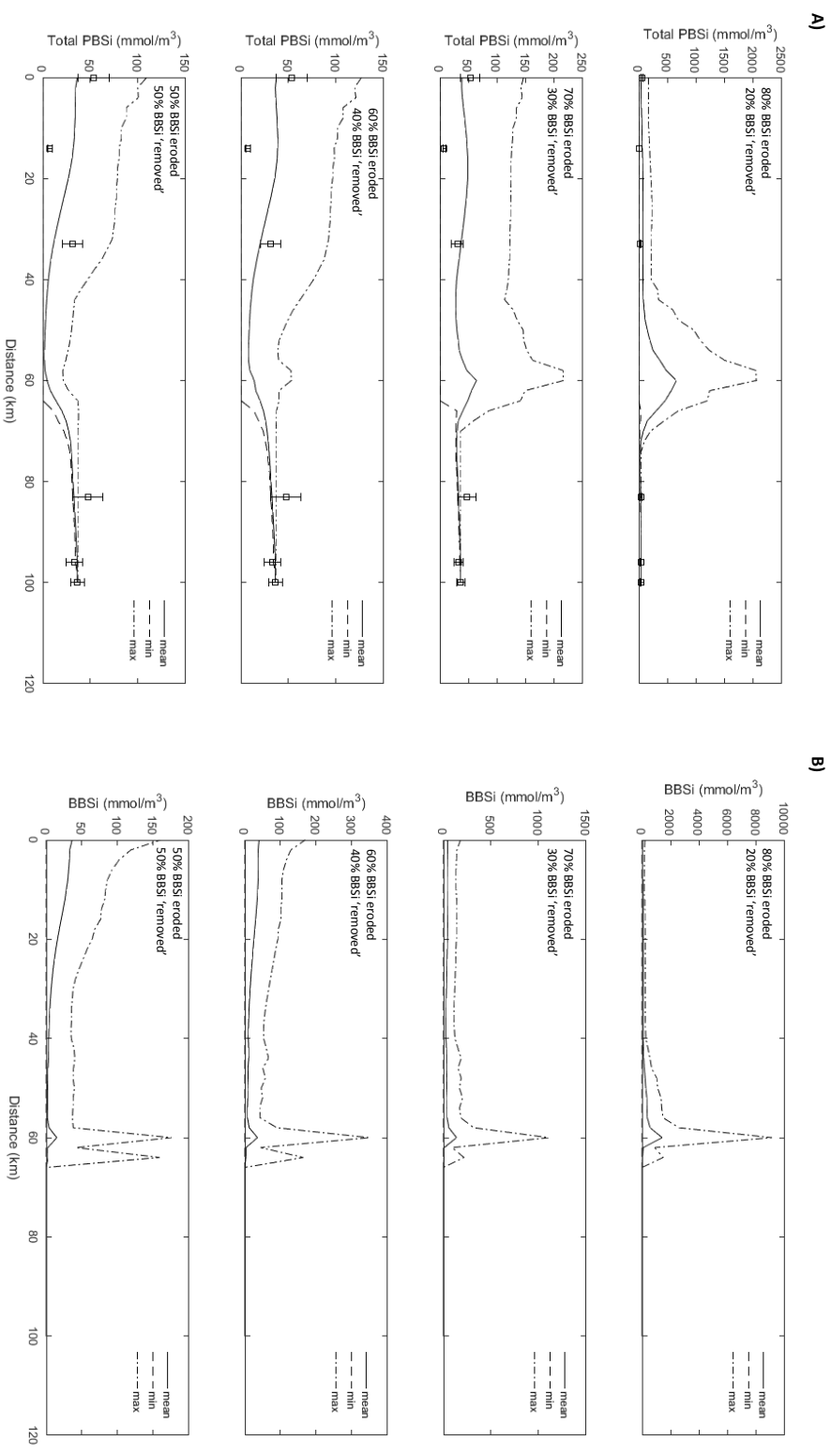

Figure 7.26: Winter simulations. **A)** Total pelagic biogenic silica concentrations (mmol Si/m^3). **B)** Benthic biogenic silica concentrations (mmol Si/m^3).

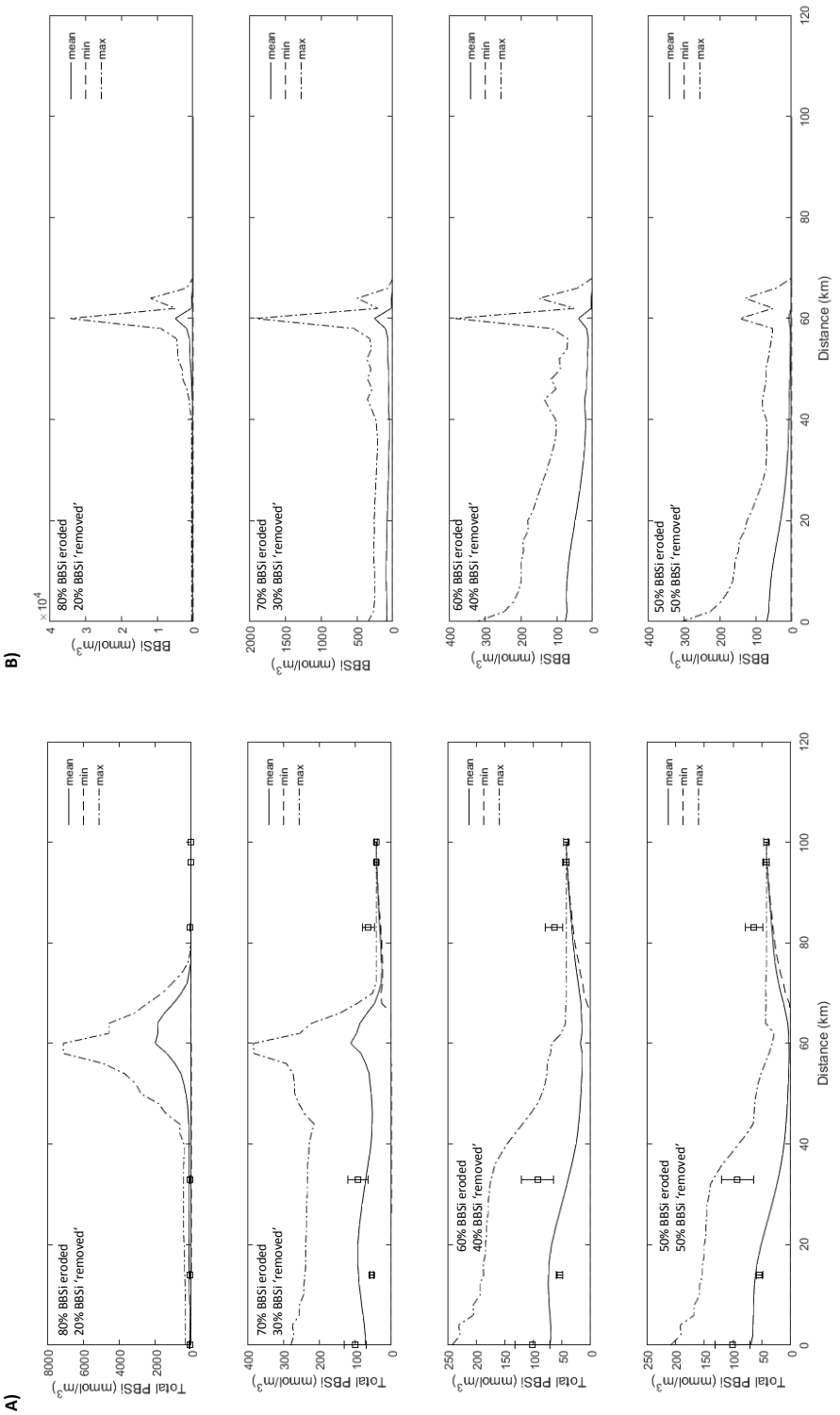

Figure 7.27: Spring simulations. **A)** Total pelagic biogenic silica concentrations (mmol Si/m^3). **B)** Benthic biogenic silica concentrations (mmol Si/m^3).

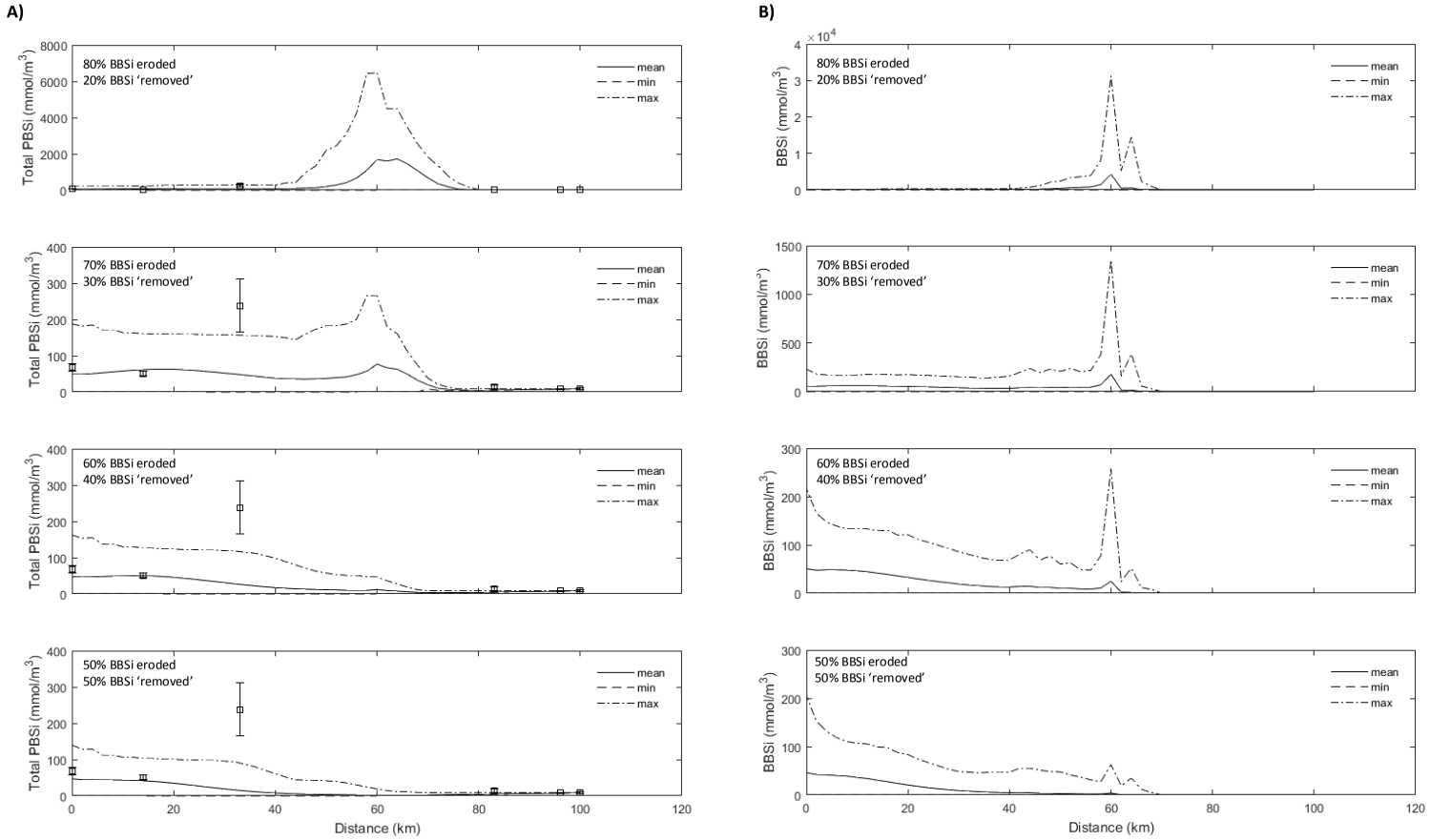

Figure 7.28: Summer simulations. **A)** Total pelagic biogenic silica concentrations (mmol Si/m^3). **B)** Benthic biogenic silica concentrations (mmol Si/m^3).

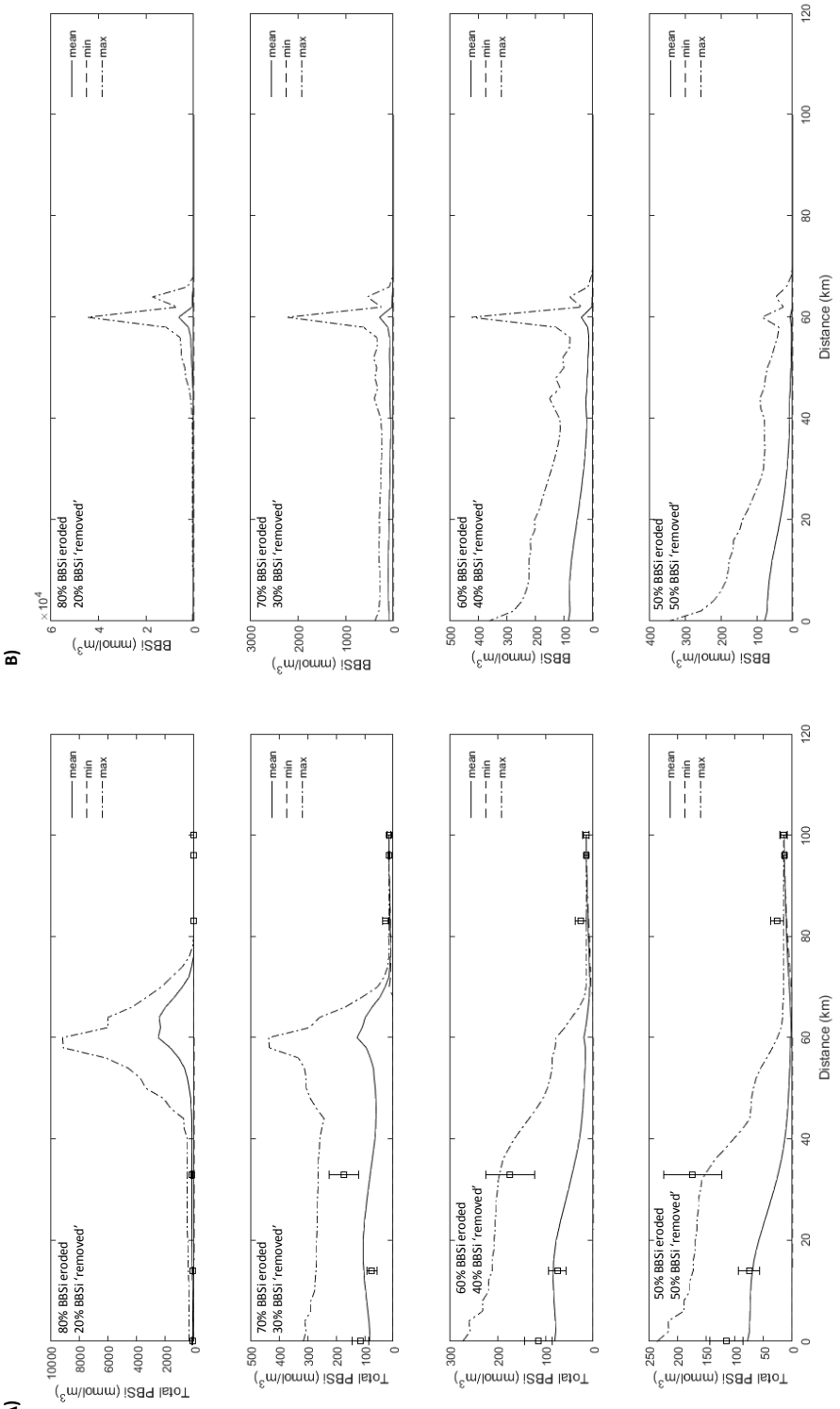

Figure 7.29: Autumn simulations. **A)** Total pelagic biogenic silica concentrations (mmol Si/m^3). **B)** Benthic biogenic silica concentrations (mmol Si/m^3).

Chapter 8

Synthesis and application of research presented in the thesis

Silicon (Si), the second-most-abundant element in the Earth's crust (Conley et al., 2006), is a key nutrient in the hydrosphere, required for growth of siliceous organisms, for example photosynthetic diatoms. Compared to the well-studied biogeochemical cycles of nitrogen and phosphorus, only since the late twentieth century has the importance of the Si cycle become paramount. Most importantly, constructed world ocean Si budgets have shown a tight coupling between the oceanic Si cycle (growth of siliceous organisms) and the draw down and sequestration of atmospheric carbon dioxide in the deep ocean, forming an important process in the climate cycle (Pondaven et al., 2000). Si, a product of weathering of the Earth's crust, can be transported to the ocean via four distinctive pathways. These include: the discharge of dissolved silicon (DSi) by rivers and groundwater into estuaries and the coastal zone; the riverine transport of particulate silica, in the form of Biogenic silica (BSi), Lithogenic silica (LSi) and Amorphous silica (ASi), along with the supply of silica through the deposition of dust onto the ocean surface, both of which can dissolve and become an external source of DSi; dissolution of terrigenous silicates in sediment in continental margins; and the release of DSi at hydrothermal vents (Tréguer and De La Rocha, 2013).

Only recently have studies focused in-depth on the Si cycle in coastal zones, an area which is highly sensitive to human activity, such as the construction of dams, tidal barrages and flood defence structures. These barriers can decrease the supply of DSi and particulate silica to the marine zone. Estuaries, which form the transition zone between the terrestrial riverine Si supply and the ocean, have the potential to biogeochemically modify this Si export. Processes such as reverse weathering and phytoplankton production in estuarine and deltaic settings have gained considerable attention over the past few decades. However, a potentially equally important but often neglected process, is the influence of benthic-pelagic coupling in estuaries on DSi consumption and BSi production.

Here, the Severn Estuary, southwest UK has been used as a case study to shed more light on this process. The hypertidal regime in the Severn Estuary forms large intertidal mudflats, home to diatom-dominated microphytobenthos (MPB) biofilms (Underwood, 2010), which have been shown to be biologically productive (Welsby et al., 2016). This thesis investigated the role of several consumption and production process in mediating DSi and BSi transport from the River Severn to the marine zone in the Bristol Channel. Within this framework, the study investigated how these benthic diatom-dominated biofilms mediated Si, and whether upon resuspension, they were an additional source of BSi to the estuarine pelagic zone, and in a similar manner, a supply of Si to the southwest marine zone. This was achieved by several ecological surveys, using a wide range of techniques, including;

- Pelagic surveys, sampling the water column of the Severn River, Estuary and Bristol Channel, along with the Severn's tributaries (River Wye, Avon, Usk and Cardiff Bay). Measured DSi, BSi and nutrient concentrations, and water column salinity levels, temperature and turbidity.
- Benthic surveys of the intertidal mudflats of the Severn Estuary. Investigated the mudflat water dissolved silicon concentrations and percentage of benthic biogenic silica in the biofilms, and the environmental factor influencing the mediation of Si, including diatom electron transport rate (a proxy for primary productivity measured using chlorophyll fluorescence), and sediment stability (measured using a Cohesive Strength Meter, CSM).
- Application of silicon isotopes as a powerful tool to constrain the different biological/abiological processes controlling the benthic and pelagic DSi and BSi budgets. To my knowledge, these are the first silicon isotope measurements to have been conducted in the Severn System.
- Adaption and used of a 1D reactive transport model coupled to a benthic biofilm component, called the Silicon Generic Estuarine Model (Si-GEM), to explore the complex estuarine system and its control on DSi and BSi transport.

The following section summarises the key findings of this research, which are subsequently put into context for considering the future of the Severn Estuary in terms of climate change, and renewable energy developments.

8.1 Summary of the key findings

Initially, the pelagic processes influencing DSi consumption and BSi production in the Severn's water column were investigated during sampled periods of 2016. It was hypothesised and confirmed, that the pelagic productivity in the turbid Severn Estuary

was relatively low, reducing the importance of the pelagic biological mediation of Si (see Chapter Three). In the River Severn, the relatively low phytoplankton production, contributed to isotopically light waters relative to the mean $\delta^{30}Si_{DSi}$ values of 557 rivers (Frings et al., 2016), in both the summer and autumn sampled periods. The study suggested a combination of high turbidity (light limitation), low nutrient concentrations, and low residence times, restricted the growth of large phytoplankton communities. This low phytoplankton production has been observed previously in the Severn Estuary (Joint and Pomroy, 1981; Underwood, 2010) and other tidal-dominated estuarine systems, for example, the Scheldt (Carbonnel et al., 2009).

Strong fluvial flow and tidal hydrodynamics were shown to be key drivers influencing the transport and biological consumption of dissolved constituents, including DSi, nitrate, nitrite, ammonium and phosphate. The longitudinal profile of these nutrients followed the classical view of downstream transport and dilution in estuaries, resulting in relatively low concentrations in the saline regions of the Bristol Channel. Further, DSi and other nutrient data presented here concours with Environment Agency monitoring data collected in 2016 (Agency, 2016). The 1D RTM simulations for different sampled periods in 2016, also exhibited this decreasing trend in PDSi concentrations, empathising the dominant control of estuarine hydrodynamics on PDSi transport. Despite other estuarine systems retaining DSi (global average of 20%: DeMaster, 1981; Tréguer and De La Rocha, 2013), the strong river flow and the hypertidal regime in the Severn Estuary prevented any significant DSi retention.

The contribution of the Severn's groundwater and tributary Si supply was also considered. The DSi concentrations measured from boreholes in the catchment area of the Severn in 2016, were found to have high DSi concentrations (6-10 mg/L). The groundwater could also have supplied isotopically light waters into the River Severn. To what degree this groundwater DSi supply fuelled and controlled the Severn's DSi and isotopic budget remains unknown, but this advocates the need for further research into this nutrient pathway, and the influence it may have on coastal ecosystems.

The riverine input of DSi and BSi in the tributaries (Usk, Wye, Avon and Cardiff Bay) were similar to those from the River Severn, and could have contributed to the overall Si budget of the Severn. In the peripheral estuaries of the Severn's tributaries, the intertwined estuarine and fluvial processes created a dynamic environment, which resulted, for example, in high BSi concentrations in the lower tidal River Usk. This BSi could have been sourced from further upstream (but BSi concentrations were low), or either originated from the benthic diatoms on the muddy banks of the river, or was brought in from the estuary on the flood tide. PBSi concentrations in the upper estuary peaked in the summer (max. 14.8 mg/L) and autumn sampled periods (max. 10.0 mg/L), and were characterised by isotopically heavy waters. In this study, it was hypothesised that the high tidal current velocities exceeded the erosion thresholds of

the diatom-dominated biofilms, resulting in the transport of benthic diatoms (and thus benthic BSi) into the water column. Using the quadratic friction law (Arndt et al., 2007), the bottom shear stress of the estuarine tidal currents (Uncles, 2010) were found to be in excess of published erosion thresholds of the biofilms (Yallop et al., 2000). The study further hypothesised, that associated with these benthic diatoms was a polymer-rich biofilm, which once resuspended in the saline waters, may have mixed with the riverine and mudflat supply of cohesive sediment, forming one entity, a process defined as bioflocculation. These bioflocs can explain the significant linear correlation found between the SPM and BSi concentrations in the water column during the summer and autumn sampled periods.

To determine whether these hypotheses were correct, first the study had to quantify the budgets of benthic DSi (BDSi) and BSi (BBSi) on the intertidal mudflats of the Severn Estuary, which in turn, showed whether the biofilms could have been a source of Si to the pelagic systems. Secondly, biological DSi consumption and BSi production processes controlling these benthic Si budgets were outlined in Chapter Four (Section 4.3.2). Similar to other estuarine systems, the percentage of BBSi was low, associated with the strong hydrodynamics, preventing the accumulation of BBSi at the sediment-water interface (SWI). Nevertheless, it was hypothesised and confirmed that the diatom-dominated biofilms had high productivity (relative electron rates of *ca.* 155 $\pm$ 13 *rel. units*), driven by their adaption to these harsh environments, for example, their photoprotective mechanisms (non-photochemical quenching and vertical cell movement). These adaptations likely aided the growth of biomass-rich biofilms, and during the biologically productive periods, led to a greater consumption of BDSi and accumulation of BBSi. MPB growth was also supported by the isotopically heavy mudflat water (a mixture of surface and pore fluid) sampled in the summer and autumn periods, whereby biological and abiological processes, e.g. diatom growth and clay formations, removed $\delta^{30}Si_{DSi}$ from the mudflat water. Evidence presented in this study, supports the conclusion put forward in Welsby et al. (2016); the biofilms had fast turn-over rates, increasing the accumulation of BBSi between immersion periods.

To quantify the possible export of BBSi from the intertidal mudflats into the water column, the erosion rates of the biofilms, along with their biostabilization properties, were investigated in this study (see Chapter Five). Measurements included sediment biostabilization (chl *a* content and carbohydrate concentrations), sediment stability (erosion thresholds measured using a CSM), and the eroded concentrations of BSi and DSi in the CSM erosion chamber. Despite the heterogeneous nature of biostabilization across the sampled mudflats, the erosion thresholds of the biofilms were below the shear stress from the fast-flowing tidal currents, leading to the resuspension of the coupled sediment-polymer-diatom matrix, with high concentrations of resuspended BBSi (max. 91.4 mg/L). The resuspended sediment and BBSi remained tightly coupled in

the near-bed suspension (fluid-mud layer) and in the surf zones, again supporting the hypothesis of bioflocculation. Upon immersion, the isotopically heavy mudflat water would also have mixed with the isotopically light riverine waters, contributing to the progressive heavier downstream signal. Compared to the riverine samples, silicon isotope analyses of mudflat samples, and some of the estuarine water column samples, were mass-independent, likely due to strong mass bias within the plasma mass spectrometer, resulting from the high organic matter content present on the intertidal mudflats.

The three presented estimates of eroded BSi flux from the intertidal mudflats (see Chapter Five) were in overall good agreement with one another (Fig. 8.1), with peak BBSi flux occurring during a spring tidal cycle. The intertidal mudflats were also found to be a source of DSi, through advection (transport of DSi as the pore fluids were disturbed) and diffusion from the SWI upon immersion. These estimates however, assumed the erosion of the biofilms was occurring across the entire intertidal area, discounting the patchy nature of the biofilms, and were likely overestimating the BBSi export into the water column. This was also an issue in the Si-GEM applied in this thesis, which due to the simple setup of this 1D model, could not capture the high spatial heterogeneity of the biofilms, and overestimated the BBSi flux. Therefore, the model is still in development, and requires a 2D representation of the benthic system, and a high-resolution observational data to better constrain the complex benthic processes.

Si-GEM showed that the maximum erosion (and deposition) rates occurred in the river-estuarine transition zone between 40-80 km upstream of the outer estuarine boundary, a function of estuarine convergence and tidal/fluvial dynamics. Despite this transition zone being inaccessible during this sampling study, the model simulated an Estuarine Turbidity Maximum zone in this area. The quantity of SPM simulated by the model, and its location along the Severn's longitudinal axis, corroborated with previous research on sediment transport in the estuary (Manning et al., 2010; Uncles, 2010), including the Environment Agency monitoring data from the Severn in 2016 (Agency, 2016). Similarly, BSi peaked in the ETM zone, associated with estuarine convergence accumulating all the BSi sourced from multiple areas including the River Severn, tributaries and most importantly the benthic biofilms on the intertidal mudflats. Regardless of Si-GEM's assumptions and limitations, the model highlighted the importance of the area (40-80 km) in terms of sediment and Si cycling, and should be used to inform future fieldwork excursions in this zone.

Alongside the benthic biological mediation of Si, several abiological processes could have influenced Si concentrations and $\delta^{30}Si_{DSi}$. These include, but are not limited to:

- Remineralization, e.g. reverse weathering, the transformation of silica into clay minerals, which by recombining DSi, can reduced DSi concentrations in the estuary, and subsequently increase particulate silica content in the form of ASi and LSi.

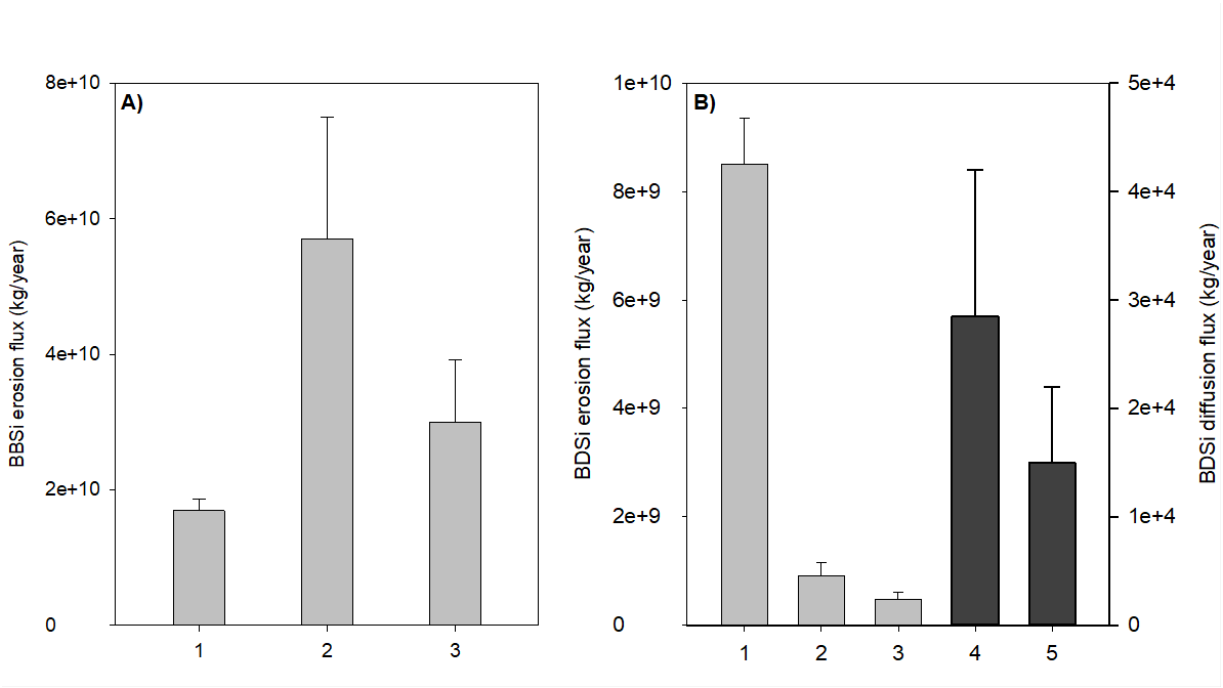

Figure 8.1: Summary of benthic biogenic silica (BBSi) and benthic dissolved silicon (BDSi) flux from the intertidal mudflats. **A)** BBSi erosion estimated using a modified version of Vollenweider (1968) mass balance calculation for a neap cycle (1), and using the resuspended BBSi concentrations in the CSM erosion chamber following Pethick et al. (2009) estimate for a spring (2) and neap (3) intertidal mudflat area. **B)** BDSi advection through the mixing of pore water and estuarine water using a modified version of Vollenweider (1968) mass balance calculation for a neap cycle (1), and using the resuspended BDSi concentrations in the CSM erosion chamber following (Pethick et al., 2009) estimate for a spring (2) and neap (3) intertidal mudflat area, and assuming only diffusion during immersion. BDSi diffusive flux from the mudflats (dark grey bars) following Pethick et al. (2009) estimate for a spring (4) and neap (5) area. Presented with propagated SE of the flux and a 10% error in the area (see Chapter Three, Section 3.4.4.1, and Chapter Five, Section 5.3.5). Note, different axis scales.

- Dissolution of BSi and regeneration of DSi following deposition under specific conditions (factor of saturation state, pH, temperature), which on the mudflats, could have been enhanced by bioturbating organisms.
- Dissolution of clays, diatoms, phytoliths etc. resulting in $\delta^{30}Si_{DSi}$ isotopically-light waters.
- Adsorption-desorption of DSi onto aluminium oxide surfaces of clay minerals, which would have removed/supplied DSi into the system.

Despite the high BSi contribution from the intertidal mudflats, the annual estuarine flux of PBSi from the Severn Estuary only amounted to a small percentage (0.2%) of the global particulate riverine silica supply to the ocean of 147 ± 44 Tmol/yr (Dürr et al., 2011). However, this global budget was calculated considering all forms of particulate silica (BSi+LSi+ASi). When compared to the global riverine BSi supply of 1.1 ± 0.2 Tmol/yr in Conley (1997), surprisingly the estuary accounted for 27% of this budget. Similarly, considering only the riverine supply of PDSi which averaged 0.0003 Tmol/yr, this accounted for a small percentage (0.004%) of the global DSi riverine inputs (6.2 ± 1.8 Tmol/yr, Tréguer and De La Rocha, 2013). In comparison, the Severn Estuary with an average PDSi input of 0.14 Tmol/yr, supplied a larger percentage (2.2%) of the total DSi supply into the ocean. These calculations highlight a key issue: the consumption and production of Si by the benthic ecosystem in estuarine systems are significant, on a global scale, and must be included in Si budget mass balance estimates. This research shows that under-sampling of estuaries, leaves changes in the DSi and BSi budgets goes unnoticed. Global estimates of riverine Si budgets have been invaluable in understanding the Si cycle, and have allowed results from separate systems, for example from the terrestrial and marine realms, to be placed into a wider context. However, there is a requirement to expand these studies on Si transport to include both the pelagic and benthic ecosystems in temperate and tropical estuarine systems, in order to reduce the large uncertainties in these continental Si supply estimates.

To conclude, biological and abiological processes on the Severn Estuary intertidal mudflats have been shown to modify the BBSi and BDSi budgets, together with the isotopic signatures of the mudflat water. Upon immersion, these benthic fractions and isotopic signatures can be transported into the water column. Once in the pelagic realm, the BSi likely undergoes a series of erosion-deposition events, and can be removed from the system through burial/dissolution (retention), or can be transport out of the estuary on the ebb tide. Considering a large fraction of BSi is exported from the mudflats, and unlike DSi, could be transport further afield (DSi would likely be used up in more productive, less turbid areas of the Severn), the BSi could dissolve and replenish the Bristol Channel and even the Celtic Sea, with DSi ready to be consumed by phytoplankton, the latter supporting several important fisheries (Cefas, 2005). The link between estuarine

biogeochemical cycling and important natural resources, highlights the socio-economic importance of these intertidal mudflats, which for many decades have been mistaken as "predominately barren" or "evolving towards a barren system" (Pethick et al., 2009). Future research should investigate the transport of the estuarine-sourced BSi to these productive areas, through continued field campaigns and modelling efforts.

8.2 Prospects of the Severn's benthic diatoms

The UK is estimated to have half of all European's wave and tidal resources (Hinson, 2018). With the third highest tidal range in the world, the Severn Estuary has been at the centre of renewable energy developments. Tidal energy is often divided into tidal streams (i.e. extracting energy from tidal currents similar to wind turbines), and tidal range (i.e. through the construction of a barrage or lagoon when the reservoir water flushes through turbines to generate energy). The tidal barrage schemes have re-emerged in recent years as the pressures from climate change and the need to find renewable energy increases; the UK is also under pressure to meet EU renewable energy targets and produce 20% of its total energy from such resources by 2020 (Xia et al., 2010a). The most prominent tidal barrage, usually referred to as the Cardiff-Weston scheme, lies between Lavernock Point and Brean Down in Somerset. There have been other barrage proposal including the 'Shoots' Barrage and the 'Outer' Barrage in the Bristol Channel. Despite having the potential to generate substantial, consistent electrical output, and with the added benefit of reducing coastal flood risks, the possible environmental impacts make the schemes controversial, and the environmental benefits are often disputable (Pethick et al., 2009). Much of the environmental emphasis has been focussed on migratory waterfowl, sea grass (*Zostera* beds), and the extent of saltmarshes and intertidal mudflats. In the case of the latter, several environmental concerns have been outlined, often centred around impacts to feeding grounds (Burton et al., 2001). Except for a review on phytoplankton and MPB productivity by Underwood (2010) and the possibility of MPB biofilm reference in grey literature, to my knowledge, no direct reference has been made to the benthic diatoms and their prospects post-barrage, in the formal Environmental Impact Assessments (EIA). Below, four possible impacts on the benthic biofilms are outlined with respect to the construction of a Cardiff-Weston scheme.

1. **Considerable reduction (76%) in the extent of the intertidal mudflats (Pethick et al., 2009).** Under the Cardiff-Weston scheme, higher mean water levels would be reached in the impounded area, resulting in a significant loss of the lower shore intertidal habitats, and with a lower spring tidal range, the loss of upper intertidal areas (Underwood, 2010). The reduction in viable intertidal mudflats would inevitably reduce the potential area for these heterogeneous biofilms to

colonise. In turn, a reduction in a suitable habitat, would lower MPB biomass, and subsequently reduce BBSi production. Underwood (2010) noted that the barrage would reduce annual MPB production by 77%. Arguably, new mudflats could form in a post-barrage scenario. Underwood (2010) suggests that the export of sand further upstream by the tides would be reduced, converting sand-rich intertidal areas to more clay-rich areas, promoting the growth of MPB biofilms.

These mudflats are also under pressure from Climate Change and coastal squeeze. Considering the sampled mudflats, for example at Site 2 and 3, the sea defence at these sites, limits the mudflats migration inland. With the predicted increase in sea levels rise (e.g. 1-1.2 m in the Severn by 2100, Xia et al., 2011), the prospects for the retention of these biofilms, regardless of the pressures from the tidal power industry, are poor.

2. **Duration of exposure is likely to be reduced.** It is expected that the water in the impounded estuary would be held for several hours to let a sufficient head of water to form. It is possible with a shorter emersion period, the amount of benthic diatom growth could be limited, and thus the production of BBSi would be reduced.

3. **Increased water quality.** Kirby and Shaw (2005) suggest a reduction in SPM by 85%, caused by a lower tidal range and reduced tidal-wind induced mixing (i.e. less sediment remobilization), and settling of sediment in deeper water. This reduced turbidity is expected to increase water column biological productivity, followed by increased biomass and species diversity within benthic assemblages. Pethick et al. (2009) note this will "replace the existing assemblage of restricted species diversity". Less turbidity is often considered a benefit of these renewable schemes, however, considering the MPB biofilms are currently diatom-dominated, with increased competition and changes in sedimentation, erosion and light regimes, whether their dominance would remain is unproven. Similarly, Underwood (2010) reported a change in species composition of MPB in a post-barrage scenario, which could influence the functioning of the MPB in terms of Si export.

4. **Effects of winnowing.** Pethick et al. (2009) suggests coarser sediment is expected in a post-barrage scenario, a result of winnowing (loss of fine sediments). Winnowing has occurred in the Eastern Scheldt, a possible post-barrage analogue for the Severn (Pethick et al., 2009). It was concluded, from investigations on erosion (see Chapter Five, Section 5.4.2), the low chl *a* content at Site 4 (Sand Bay) was attributed to the high abundance of coarse sediment. Therefore, a change in sediment composition could impact the biomass of diatoms, and result in a change in the species assemblage, for example from epipelic to epipsammic di-

atoms. In addition, with changes in sediment erosion and deposition rates, along with the effect of storm events (higher river flow rates) exposing harder, more consolidated material, there will likely be less suitable colonisation substrata for the more motile diatoms. With potentially reduced benthic diatom biomass, and less tidal energy for erosion, the export of BBSi from the mudflats would likely also be reduced. Whether the increased water column biological production of BSi would compensate for the loss in BBSi production is unchartered territory.

Several of the points outlined above are speculative but enforce the need to further understand the benthic diatoms and their impact on the estuarine Si cycle, along with the impact they may have further afield (e.g. fisheries). This research is essential during the EIA stages of these large, industrial projects. In 2010, the Cardiff-Weston scheme was deemed financially unviable, with other low carbon options more favourable. However, the unpopularity of this scheme did not hinder the tidal power industry. Over recent years there has been a greater awareness of tidal lagoons, with many thinking (but not universally) they are more economical, technically feasible and more environmentally-friendly (Hinson, 2018). Tidal Lagoon Power (TLP) were hoping to construct a 'pathfinder' Tidal Lagoon in Swansea Bay, with the hope this would lead to other lagoons in the UK: Cardiff, Newport, Colwyn Bay, West Cumbria and Bridgewater Bay. Many of the environmental concerns outlined above for the Barrage scheme hold true for these tidal lagoons, including a loss of intertidal habitats. To the best of my knowledge, no direct reference has been given to the benthic diatoms in any of the tidal lagoon environmental assessments, similar to the Barrage Schemes. On the 25th of June 2018, the government also deemed the Tidal Lagoon project financial unviable and would not enter a contract with TLP.

Despite the failure of making these tidal power schemes a reality, it is highly likely that more tidal projects will be proposed for the Severn in the future. However, the benthic diatom biofilms should be considered in future EIAs due to their importance as a food source, in sediment stability and aiding saltmarsh development, but also, as described in detail in this study, as an important factor in the Severn's Si cycle. Research undertaken for this PhD has increased the data coverage of benthic MPB distribution and production, and has helped to understand the transport of Si and nutrients along the Severn and its tributaries. This is the first in-depth study of Si transport in the Severn, and several of the key findings presented here lays a foundation for further research. Suggested areas for future development include:

- Investigate the transport of BSi (fluvial and benthic sourced) from the Severn Estuary into the Bristol Channel and further afield into the Celtic Sea.
- Create high-resolution habitat maps of the benthic biofilms in the Severn Estuary.

- Investigate the future impacts of climate change (sea level rise) and flooding on the MPB biofilms.
- Target field campaigns to difficult-to-reach areas of the estuary, and produce a high-resolution dataset to improve modelling outputs.

Bibliography

Abril, G., Etcheber, H., Le Hir, P., Bassoullet, P., Boutier, B., and Frankignoulle, M. (1999). Oxic/anoxic oscillations and organic carbon mineralization in an estuarine maximum turbidity zone (The Gironde, France). *Limnology and Oceanography*, 44(5):1304–1315.

Admiraal, W., Breugem, P., Jacobs, D., and Van Steveninck, E. D. R. (1990). Fixation of dissolved silicate and sedimentation of biogenic silicate in the lower river Rhine during diatom blooms. *Biogeochemistry*, 9(2):175–185.

Agency, E. (2016). Hydrology data.

Ahlgren, G. (1987). Temperature functions in biology and their application to algal growth constants. *Oikos*, pages 177–190.

Alexandre, A., Meunier, J.-D., Colin, F., and Koud, J.-M. (1997). Plant impact on the biogeochemical cycle of silicon and related weathering processes. *Geochimica et Cosmochimica Acta*, 61(3):677–682.

Alleman, L. Y., Cardinal, D., Cocquyt, C., Plisnier, P.-D., Descy, J.-P., Kimirei, I., Sinyinza, D., and André, L. (2005). Silicon isotopic fractionation in Lake Tanganyika and its main tributaries. *Journal of Great Lakes Research*, 31(4):509–519.

Allen, J. (1990). The Severn Estuary in southwest Britain: its retreat under marine transgression, and fine-sediment regime. *Sedimentary Geology*, 66(1-2):13–28.

Allen, J. (1991). Fine sediment and its sources, Severn Estuary and inner Bristol Channel, southwest Britain. *Sedimentary geology*, 75(1-2):57–65.

Allen, J. R. L. and Rae, J. (1987). Late Flandrian shoreline oscillations in the Severn Estuary: a geomorphological and stratigraphical reconnaissance. *Philosophical Transactions of the Royal Society of London. B, Biological Sciences*, 315(1171):185–230.

Aller, R. and Benninger, L. (1981). Spatial and temporal patterns of dissolved ammonium, manganese, and silica fluxes from bottom sediments of Long Island Sound, USA. *JMR-MR-213;(United States)*, 39(2).

Aller, R. C. (1980a). Quantifying solute distributions in the bioturbated zone of marine sediments by defining an average microenvironment. *Geochimica et Cosmochimica Acta*, 44(12):1955–1965.

Aller, R. C. (1980b). Relationships of tube-dwelling benthos with sediment and overlying water chemistry. *Marine benthic dynamics*, pages 285–308.

Alpine, A. E. and Cloern, J. E. (1992). Trophic interactions and direct physical effects control phytoplankton biomass and production in an estuary. *Limnology and Oceanography*, 37(5):946–955.

Anning, T., Harris, G., and Geider, R. J. (2001). Thermal acclimation in the marine diatom Chaetoceros calcitrans (Bacillariophyceae). *European Journal of Phycology*, 36(3):233–241.

Archer, A. W. (2013). World's highest tides: Hypertidal coastal systems in North America, South America and Europe. *Sedimentary Geology*, 284:1–25.

Arndt, S., Lacroix, G., Gypens, N., Regnier, P., and Lancelot, C. (2011). Nutrient dynamics and phytoplankton development along an estuary–coastal zone continuum: a model study. *Journal of Marine Systems*, 84(3-4):49–66.

Arndt, S. and Regnier, P. (2007). A model for the benthic-pelagic coupling of silica in estuarine ecosystems: sensitivity analysis and system scale simulation. *Biogeosciences Discussions*, 4(2):747–796.

Arndt, S., Regnier, P., and Vanderborght, J.-P. (2009). Seasonally-resolved nutrient export fluxes and filtering capacities in a macrotidal estuary. *Journal of Marine Systems*, 78(1):42–58.

Arndt, S., Vanderborght, J.-P., and Regnier, P. (2007). Diatom growth response to physical forcing in a macrotidal estuary: Coupling hydrodynamics, sediment transport, and biogeochemistry. *Journal of Geophysical Research: Oceans*, 112(C5).

Axler, R. P. and Owen, C. J. (1994). Measuring chlorophyll and phaeophytin: whom should you believe? *Lake and Reservoir Management*, 8(2):143–151.

Azam, F., Hemmingsen, B. B., and Volcani, B. E. (1974). Role of silicon in diatom metabolism. *Archives of microbiology*, 97(1):103–114.

Baklouti, M., Chevalier, C., Bouvy, M., Corbin, D., Pagano, M., Troussellier, M., and Arfi, R. (2011). A study of plankton dynamics under osmotic stress in the Senegal River Estuary, West Africa, using a 3D mechanistic model. *Ecological modelling*, 222(15):2704–2721.

Barao, L., Vandevenne, F., Clymans, W., Frings, P., Ragueneau, O., Meire, P., Conley, D. J., and Struyf, E. (2015). Alkaline-extractable silicon from land to ocean: A challenge for biogenic silicon determination. *Limnology and Oceanography: Methods*, 13(7):329–344.

Barnett, A., Méléder, V., Blommaert, L., Lepetit, B., Gaudin, P., Vyverman, W., Sabbe, K., Dupuy, C., and Lavaud, J. (2015). Growth form defines physiological photoprotective capacity in intertidal benthic diatoms. *The ISME journal*, 9(1):32.

Bartoli, M., Nizzoli, D., and Viaroli, P. (2003). Microphytobenthos activity and fluxes at the sediment-water interface: interactions and spatial variability. *Aquatic Ecology*, 37(4):341–349.

Basile-Doelsch, I. (2006). Si stable isotopes in the Earth's surface: A review. *Journal of Geochemical Exploration*, 88(1-3):252–256.

Bayon, G., Delvigne, C., Ponzevera, E., Borges, A., Darchambeau, F., De Deckker, P., Lambert, T., Monin, L., Toucanne, S., and André, L. (2018). The silicon isotopic composition of fine-grained river sediments and its relation to climate and lithology. *Geochimica et Cosmochimica Acta*, 229:147–161.

Beer, S., Björk, M., and Beardall, J. (2014). *Photosynthesis in the marine environment*. John Wiley & Sons.

Bell, R. G. (1994). Behaviour of dissolved silica, and estuarine/coastal mixing and exchange processes at Tairua Harbour, New Zealand. *New Zealand Journal of Marine and Freshwater Research*, 28(1):55–68.

Bellinger, B., Abdullahi, A., Gretz, M., and Underwood, G. (2005). Biofilm polymers: relationship between carbohydrate biopolymers from estuarine mudflats and unialgal cultures of benthic diatoms. *Aquatic Microbial Ecology*, 38(2):169–180.

Beusen, A., Bouwman, A., Dürr, H., Dekkers, A., and Hartmann, J. (2009). Global patterns of dissolved silica export to the coastal zone: Results from a spatially explicit global model. *Global Biogeochemical Cycles*, 23(4).

Bilger, W. and Björkman, O. (1990). Role of the xanthophyll cycle in photoprotection elucidated by measurements of light-induced absorbance changes, fluorescence and photosynthesis in leaves of Hedera canariensis. *Photosynthesis research*, 25(3):173–185.

Billen, G. and Garnier, J. (1997). The Phison River plume: coastal eutrophication in response to changes in land use and water management in the watershed. *Aquatic microbial ecology*, 13(1):3–17.

Billen, G., Garnier, J., and Hanset, P. (1994). Modelling phytoplankton development in whole drainage networks: the RIVERSTRAHLER model applied to the Seine river system. In *Phytoplankton in Turbid Environments: Rivers and Shallow Lakes*, pages 119–137. Springer.

Blanchard, G., Paterson, D., Stal, L., Richard, P., Galois, R., Huet, V., Kelly, J., Honeywill, C., De Brouwer, J., Dyer, K., et al. (2000). The effect of geomorphological structures on potential biostabilisation by microphytobenthos on intertidal mudflats. *Continental Shelf Research*, 20(10-11):1243–1256.

Blanchard, G. F., Guarini, J.-M., Gros, P., and Richard, P. (1997). Seasonal effect on the relationship between the photosynthetic capacity of intertidal microphytobenthos and temperature. *Journal of Phycology*, 33(5):723–728.

Blommaert, L., Lavaud, J., Vyverman, W., and Sabbe, K. (2018). Behavioural versus physiological photoprotection in epipelic and epipsammic benthic diatoms. *European journal of phycology*, 53(2):146–155.

Boudreau, B. P. (1996). The diffusive tortuosity of fine-grained unlithified sediments. *Geochimica et Cosmochimica Acta*, 60(16):3139–3142.

Bowes, M. and House, W. (2001). Phosphorus and dissolved silicon dynamics in the River Swale catchment, UK: a mass-balance approach. *Hydrological Processes*, 15(2):261–280.

Boyle, E., Collier, R., Dengler, A., Edmond, J., Ng, A., and Stallard, R. (1974). On the chemical mass-balance in estuaries. *Geochimica et cosmochimica acta*, 38(11):1719–1728.

Bradley, J., Anesio, A., Singarayer, J. S., Heath, M., and Arndt, S. (2015). SHIMMER (1.0): a novel mathematical model for microbial and biogeochemical dynamics in glacier forefield ecosystems. *Geoscientific Model Development Discussions*, 8(8):6143–6216.

Brewer, P. and Riley, J. (1965). The automatic determination of nitrate in sea water. In *Deep Sea Research and Oceanographic Abstracts*, volume 12, pages 765–772. Elsevier.

Brewin, R. J., de Mora, L., Jackson, T., Brewin, T. G., and Shutler, J. (2016). Correction: On the Potential of Surfers to Monitor Environmental Indicators in the Coastal Zone. *PloS one*, 11(9):e0162591.

Brock, T. D. (1981). Calculating solar radiation for ecological studies. *Ecological modelling*, 14(1-2):1–19.

Brotas, V., Cabrita, T., Portugal, A., Serôdio, J., and Catarino, F. (1995). Spatio-temporal distribution of the microphytobenthic biomass in intertidal flats of Tagus Estuary (Portugal). In *Space Partition within Aquatic Ecosystems*, pages 93–104. Springer.

Brzezinski, M. A. (1985). The Si: C: N ratio of marine diatoms: interspecific variability and the effect of some environmental variables. *Journal of Phycology*, 21(3):347–357.

Brzezinski, M. A., Dickson, M.-L., Nelson, D. M., and Sambrotto, R. (2003). Ratios of Si, C and N uptake by microplankton in the Southern Ocean. *Deep Sea Research Part II: Topical Studies in Oceanography*, 50(3-4):619–633.

Burton, N., Armitage, M., Raven, M., Rehfisch, M., and Clark, N. (2001). The Effect of the Cardiff Bay Barrage on Waterbird Populations 11. Distribution and Movement Studies August 1999-May 2000. *BTO Research Report*.

Busby, W. F. and Lewin, J. (1967). Silicate uptake and silica shell formation by synchronously dividing cells of the diatom Navicula pelliculosa. *Journal of Phycology*, 3(3):127–131.

Cabrita, M. T. and Brotas, V. (2000). Seasonal variation in denitrification and dissolved nitrogen fluxes in intertidal sediments of the Tagus estuary, Portugal. *Marine Ecology Progress Series*, 202:51–65.

Callender, E. and Hammond, D. E. (1982). Nutrient exchange across the sediment-water interface in the Potomac River estuary. *Estuarine, Coastal and Shelf Science*, 15(4):395–413.

Carbonnel, V., Lionard, M., Muylaert, K., and Chou, L. (2009). Dynamics of dissolved and biogenic silica in the freshwater reaches of a macrotidal estuary (The Scheldt, Belgium). *Biogeochemistry*, 96(1-3):49–72.

Carbonnel, V., Vanderborght, J.-P., Lionard, M., and Chou, L. (2013). Diatoms, silicic acid and biogenic silica dynamics along the salinity gradient of the Scheldt estuary (Belgium/The Netherlands). *Biogeochemistry*, 113(1-3):657–682.

Cardinal, D., Alleman, L. Y., de Jong, J., Ziegler, K., and André, L. (2003). Isotopic composition of silicon measured by multicollector plasma source mass spectrometry in dry plasma mode. *Journal of Analytical Atomic Spectrometry*, 18(3):213–218.

Cardinal, D., Gaillardet, J., Hughes, H., Opfergelt, S., and André, L. (2010). Contrasting silicon isotope signatures in rivers from the Congo Basin and the specific behaviour of organic-rich waters. *Geophysical Research Letters*, 37(12).

Carey, J. and Fulweiler, R. (2014). Salt marsh tidal exchange increases residence time of silica in estuaries. *Limnology and Oceanography*, 59(4):1203–1212.

Cartaxana, P., Brotas, V., and Serôdio, J. (2008). Effects of two motility inhibitors on the photosynthetic activity of the diatoms Cylindrotheca closterium and Pleurosigma angulatum. *Diatom Research*, 23(1):65–74.

Cartaxana, P., Cruz, S., Gameiro, C., and Kühl, M. (2016). Regulation of intertidal microphytobenthos photosynthesis over a diel emersion period is strongly affected by diatom migration patterns. *Frontiers in microbiology*, 7:872.

Cartaxana, P., Ruivo, M., Hubas, C., Davidson, I., Serôdio, J., and Jesus, B. (2011). Physiological versus behavioral photoprotection in intertidal epipelic and epipsammic benthic diatom communities. *Journal of Experimental Marine Biology and Ecology*, 405(1-2):120–127.

Cartaxana, P. and Serôdio, J. (2008). Inhibiting diatom motility: a new tool for the study of the photophysiology of intertidal microphytobenthic biofilms. *Limnology and Oceanography: Methods*, 6(9):466–476.

Cary, L., Alexandre, A., Meunier, J.-D., Boeglin, J.-L., and Braun, J.-J. (2005). Contribution of phytoliths to the suspended load of biogenic silica in the Nyong basin rivers (Cameroon). *Biogeochemistry*, 74(1):101–114.

Cassarino, L., Hendry, K. R., Meredith, M. P., Venables, H. J., and Christina, L. (2017). Silicon isotope and silicic acid uptake in surface waters of Marguerite Bay, West Antarctic Peninsula. *Deep Sea Research Part II: Topical Studies in Oceanography*, 139:143–150.

Cassarino, L. A. (2018). *From micro to macro: silicon isotope fractionation during biogenic opal formation*. PhD thesis, University of Bristol.

Cefas (2005). Fisheries and marine ecology of the Celtic Sea.

Cerco, C. F., Tillman, D., and Hagy, J. D. (2010). Coupling and comparing a spatially- and temporally-detailed eutrophication model with an ecosystem network model: an initial application to Chesapeake Bay. *Environmental Modelling & Software*, 25(4):562–572.

Chevalier, E. M., Gévaert, F., and Créach, A. (2010). In situ photosynthetic activity and xanthophylls cycle development of undisturbed microphytobenthos in an intertidal mudflat. *Journal of Experimental Marine Biology and Ecology*, 385(1-2):44–49.

Chou, L., Carbonnel, V., Vanderborght, J. P., Roevros, N., Tsagaris, M., Zeeder, V. C., Leonard, M., Muylaert, K., Dasseville, R., Viverman, W., et al. (2007). Silica retention

in the Scheldt continuum and its impact on coastal eutrophication (SISCO). *Final report EV/17. Belgian Science Policy: Brussel, Belgium. 95 pp.*

Chou, L. and Wollast, R. (2006). Estuarine silicon dynamics. *The Silicon Cycle: Human Perturbations and Impacts on Aquatic Systems, edited by: Ittekkot, D., Unger, C., Humborg, C., and Tac An, N., Vol. Scope*, 66:93–120.

Clarke, F. W. (1924). The data of geochemistry. *US Geol. Survey*, 770:941.

Cloern, J. E., Foster, S., and Kleckner, A. (2014). Phytoplankton primary production in the world's estuarine-coastal ecosystems. *Biogeosciences*, 11(9):2477–2501.

Cockerton, H., Street-Perrott, F., Leng, M., Barker, P., Horstwood, M., and Pashley, V. (2013). Stable-isotope (H, O, and Si) evidence for seasonal variations in hydrology and Si cycling from modern waters in the Nile Basin: implications for interpreting the Quaternary record. *Quaternary Science Reviews*, 66:4–21.

Coelho, H., Vieira, S., and Serôdio, J. (2009). Effects of desiccation on the photosynthetic activity of intertidal microphytobenthos biofilms as studied by optical methods. *Journal of Experimental Marine Biology and Ecology*, 381(2):98–104.

Cohn, S. A., Farrell, J. F., Munro, J. D., Ragland, R. L., Weitzell Jr, R. E., and Wibisono, B. L. (2003). The effect of temperature and mixed species composition on diatom motility and adhesion. *Diatom Research*, 18(2):225–243.

Collins, N. and Williams, R. (1981). Zooplankton of the Bristol Channel and Severn Estuary. The distribution of four copepods in relation to salinity. *Marine Biology*, 64(3):273–283.

Conley, D. J. (1997). Riverine contribution of biogenic silica to the oceanic silica budget. *Limnology and Oceanography*, 42(4):774–777.

Conley, D. J. (2002). Terrestrial ecosystems and the global biogeochemical silica cycle. *Global Biogeochemical Cycles*, 16(4):68–1.

Conley, D. J., Frings, P. J., Fontorbe, G., Clymans, W., Stadmark, J., Hendry, K. R., Marron, A. O., and De La Rocha, C. L. (2017). Biosilicification drives a decline of dissolved Si in the oceans through geologic time. *Frontiers in Marine Science*, 4:397.

Conley, D. J. and Malone, T. C. (1992). Annual cycle of dissolved silicate in chesapeake bay: implications for the production and fate of phytoplankton biomass. *Marine ecology progress series. Oldendorf*, 81(2):121–128.

Conley, D. J., Smith, W. M., Cornwell, J. C., and Fisher, T. R. (1995). Transformation of particle-bound phosphorus at the land-sea interface. *Estuarine, Coastal and Shelf Science*, 40(2):161–176.

Conley, D. J., Sommer, M., Meunier, J., Kaczorek, D., and Saccone, L. (2006). Silicon in the terrestrial biogeosphere. In *The Silicon Cycle: Human Perturbations and Impacts on Aquatic Systems*, volume 66, pages 13–28. Island Press.

Consalvey, M., Paterson, D. M., and Underwood, G. J. (2004). The ups and downs of life in a benthic biofilm: migration of benthic diatoms. *Diatom Research*, 19(2):181–202.

Consalvey, M., Perkins, R. G., Paterson, D. M., and Underwood, G. J. (2005). PAM fluorescence: a beginners guide for benthic diatomists. *Diatom Research*, 20(1):1–22.

Cooper, R. (1953). The role of lichens in soil formation and plant succession. *Ecology*, 34(4):805–807.

Corey, A. and Auvermann, B. (2003). Transport by advection and diffusion revisited. *Vadose Zone Journal*, 2(4):655–663.

Cornelis, J.-T., Delvaux, B., Cardinal, D., André, L., Ranger, J., and Opfergelt, S. (2010). Tracing mechanisms controlling the release of dissolved silicon in forest soil solutions using Si isotopes and Ge/Si ratios. *Geochimica et Cosmochimica Acta*, 74(14):3913–3924.

Couperthwaite, J. S. (1997). *Downstream change in channel hydraulics along the River Severn, UK*. PhD thesis, University of Birmingham.

Dale, A. W. and Prego, R. (2002). Physico-biogeochemical controls on benthic pelagic coupling of nutrient fluxes and recycling in a coastal upwelling system. *Marine Ecology Progress Series*, 235:15–28.

Davis, C. O. (1976). Continuous culture of marine diatoms under silicate limitation. Effect of light intensity on growth and nutrient uptake of Skeletonema Costatum. *Journal of phycology*, 12(3):291–300.

De Deckere, E., Tolhurst, T., and De Brouwer, J. (2001). Destabilization of cohesive intertidal sediments by infauna. *Estuarine, Coastal and Shelf Science*, 53(5):665–669.

De Jonge, V. and Van Beuselom, J. (1992). Contribution of resuspended microphytobenthos to total phytoplankton in the Ems estuary and its possible role for grazers. *Netherlands Journal of Sea Research*, 30:91–105.

De La Rocha, C., Brzezinski, M. A., DeNiro, M., and Shemesh, A. (1998). Silicon-isotope composition of diatoms as an indicator of past oceanic change. *Nature*, 395(6703):680.

De La Rocha, C., Brzezinski, M. A., and DeNiro, M. J. (1997). Fractionation of silicon isotopes by marine diatoms during biogenic silica formation. *Geochimica et Cosmochimica Acta*, 61(23):5051–5056.

De La Rocha, C., Brzezinski, M. A., and DeNiro, M. J. (2000). A first look at the distribution of the stable isotopes of silicon in natural waters. *Geochimica et Cosmochimica Acta*, 64(14):2467–2477.

De Winder, B., Staats, N., Stal, L., and Paterson, D. (1999). Carbohydrate secretion by phototrophic communities in tidal sediments. *Journal of Sea Research*, 42(2):131–146.

Decho, A. W. (1990). Microbial exopolymer secretions in ocean environments: their role (s) in food webs and marine processes. *Oceanogr Mar Biol*, 28(737153):9–16.

Decho, A. W. (2000). Microbial biofilms in intertidal systems: an overview. *Continental shelf research*, 20(10-11):1257–1273.

Defew, E. C., Tolhurst, T. J., and Paterson, D. M. (2002). Site-specific features influence sediment stability of intertidal flats. *Hydrology and Earth System Sciences Discussions*, 6(6):971–982.

D'Elia, C. F., Nelson, D. M., and Boynton, W. R. (1983). Chesapeake Bay nutrient and plankton dynamics: III. The annual cycle of dissolved silicon. *Geochimica et Cosmochimica Acta*, 47(11):1945–1955.

Delstanche, S., Opfergelt, S., Cardinal, D., Elsass, F., André, L., and Delvaux, B. (2009). Silicon isotopic fractionation during adsorption of aqueous monosilicic acid onto iron oxide. *Geochimica et Cosmochimica Acta*, 73(4):923–934.

Delvaux, C., Cardinal, D., Carbonnel, V., Chou, L., Hughes, H., and André, L. (2013). Controls on riverine δ30Si signatures in a temperate watershed under high anthropogenic pressure (Scheldt Belgium). *Journal of marine systems*, 128:40–51.

Demarest, M. S., Brzezinski, M. A., and Beucher, C. P. (2009). Fractionation of silicon isotopes during biogenic silica dissolution. *Geochimica et Cosmochimica Acta*, 73(19):5572–5583.

DeMaster, D. J. (1981). The supply and accumulation of silica in the marine environment. *Geochimica et Cosmochimica acta*, 45(10):1715–1732.

DeMaster, D. J. (2002). The accumulation and cycling of biogenic silica in the Southern Ocean: revisiting the marine silica budget. *Deep Sea Research Part II: Topical Studies in Oceanography*, 49(16):3155–3167.

DeMaster, D. J., Knapp, G. B., and Nittrouer, C. A. (1983). Biological uptake and accumulation of silica on the Amazon continental shelf. *Geochimica et Cosmochimica Acta*, 47(10):1713–1723.

Demaster, D. J. and Pope, R. H. (1996). Nutrient dynamics in Amazon shelf waters: results from AMASSEDS. *Continental Shelf Research*, 16(3):263–289.

Derry, L. A., Kurtz, A. C., Ziegler, K., and Chadwick, O. A. (2005). Biological control of terrestrial silica cycling and export fluxes to watersheds. *Nature*, 433(7027):728.

Ding, T., Gao, J., Tian, S., Wang, H., and Li, M. (2011). Silicon isotopic composition of dissolved silicon and suspended particulate matter in the Yellow River, China, with implications for the global silicon cycle. *Geochimica et Cosmochimica Acta*, 75(21):6672–6689.

Ding, T., Wan, D., Wang, C., and Zhang, F. (2004). Silicon isotope compositions of dissolved silicon and suspended matter in the Yangtze River, China. *Geochimica et Cosmochimica Acta*, 68(2):205–216.

Dodds, W. K. (2006). Nutrients and the dead zone: the link between nutrient ratios and dissolved oxygen in the northern Gulf of Mexico. *Frontiers in Ecology and the Environment*, 4(4):211–217.

Doering, P., Oviatt, C., Beatty, L., Banzon, V., Rice, R., Kelly, S., Sullivan, B., and Frithsen, J. (1989). Structure and function in a model coastal ecosystem: Silicon, the benthos and eutrophication. *Marine ecology progress series. Oldendorf*, 52(3):287–299.

Du, G. Y., Li, W. T., Li, H., and Chung, I. K. (2012). Migratory responses of benthic diatoms to light and temperature monitored by chlorophyll fluorescence. *Journal of Plant Biology*, 55(2):159–164.

Du, G. Y., Oak, J.-H., Li, H., and Chung, I.-K. (2010). Effect of light and sediment grain size on the vertical migration of benthic diatoms. *Algae*, 25(3):133–140.

Dubois, M., Gilles, K. A., Hamilton, J. K., Rebers, P. t., and Smith, F. (1956). Colorimetric method for determination of sugars and related substances. *Analytical chemistry*, 28(3):350–356.

Dugdale, R. C. and Wilkerson, F. P. (1998). Silicate regulation of new production in the equatorial Pacific upwelling. *Nature*, 391(6664):270.

Duquesne, S., Newton, L. C., Giusti, L., Marriott, S. B., Stärk, H.-J., and Bird, D. J. (2006). Evidence for declining levels of heavy-metals in the Severn Estuary and Bristol Channel, UK and their spatial distribution in sediments. *Environmental Pollution*, 143(2):187–196.

Dürr, H., Meybeck, M., Hartmann, J., Laruelle, G., and Roubeix, V. (2011). Global spatial distribution of natural riverine silica inputs to the coastal zone. *Biogeosciences*, 8(3):597–620.

Dyer, K. R. (1973). *Estuaries: a physical introduction.*

Ehlert, C., Doering, K., Wallmann, K., Scholz, F., Sommer, S., Grasse, P., Geilert, S., and Frank, M. (2016). Stable silicon isotope signatures of marine pore waters–Biogenic opal dissolution versus authigenic clay mineral formation. *Geochimica et Cosmochimica Acta*, 191:102–117.

Eilers, P. and Peeters, J. (1988). A model for the relationship between light intensity and the rate of photosynthesis in phytoplankton. *Ecological modelling*, 42(3-4):199–215.

Eisma, D. (1986). Flocculation and de-flocculation of suspended matter in estuaries. *Netherlands Journal of Sea Research*, 20(2-3):183–199.

Engström, E., Rodushkin, I., Ingri, J., Baxter, D. C., Ecke, F., Österlund, H., and Öhlander, B. (2010). Temporal isotopic variations of dissolved silicon in a pristine boreal river. *Chemical Geology*, 271(3-4):142–152.

Evans, J. and Pugh, D. T. (1981). An analysis of a year of sea-level data at Flat Holm, Severn Estuary.

Ezequiel, J., Laviale, M., Frankenbach, S., Cartaxana, P., and Serôdio, J. (2015). Photoacclimation state determines the photobehaviour of motile microalgae: the case of a benthic diatom. *Journal of experimental marine biology and ecology*, 468:11–20.

Falconer, R. A., Xia, J., Lin, B., and Ahmadian, R. (2009). The Severn Barrage and other tidal energy options: Hydrodynamic and power output modeling. *Science in China Series E: Technological Sciences*, 52(11):3413–3424.

Fettweis, M., Baeye, M., Van der Zande, D., Van den Eynde, D., and Lee, B. J. (2014). Seasonality of floc strength in the southern North Sea. *Journal of Geophysical Research: Oceans*, 119(3):1911–1926.

Fong, S. and Heaps, N. S. (1978). Note on quarter wave tidal resonance in the Bristol Channel.

Fontorbe, G., Christina, L., Chapman, H. J., and Bickle, M. J. (2013). The silicon isotopic composition of the Ganges and its tributaries. *Earth and Planetary Science Letters*, 381:21–30.

Fontorbe, G., Frings, P. J., Christina, L., Hendry, K. R., Carstensen, J., and Conley, D. J. (2017). Enrichment of dissolved silica in the deep equatorial Pacific during the Eocene-Oligocene. *Paleoceanography*, 32(8):848–863.

Fontorbe, G., Frings, P. J., Christina, L., Hendry, K. R., and Conley, D. J. (2016). A silicon depleted North Atlantic since the Palaeogene: Evidence from sponge and radiolarian silicon isotopes. *Earth and Planetary Science Letters*, 453:67–77.

Forster, R. M. and Kromkamp, J. C. (2004). Modelling the effects of chlorophyll fluorescence from subsurface layers on photosynthetic efficiency measurements in microphytobenthic algae. *Marine Ecology Progress Series*, 284:9–22.

Fouillaron, P., Claquin, P., L'Helguen, S., Huonnic, P., Martin-Jézéquel, V., Masson, A., Longphuirt, S. N., Pondaven, P., Thouzeau, G., and Leynaert, A. (2007). Response of a phytoplankton community to increased nutrient inputs: a mesocosm experiment in the Bay of Brest (France). *Journal of Experimental Marine Biology and Ecology*, 351(1-2):188–198.

Fraga, F. (2001). Phytoplanktonic biomass synthesis: application to deviations from Redfield stoichiometry. *Scientia Marina*, 65(S2):153–169.

Friedrichs, M. A. and Hofmann, E. E. (2001). Physical control of biological processes in the central equatorial Pacific Ocean. *Deep Sea Research Part I: Oceanographic Research Papers*, 48(4):1023–1069.

Frings, P. J., Clymans, W., Fontorbe, G., Christina, L., and Conley, D. J. (2016). The continental Si cycle and its impact on the ocean Si isotope budget. *Chemical Geology*, 425:12–36.

Frings, P. J., Clymans, W., Fontorbe, G., Gray, W., Chakrapani, G. J., Conley, D. J., and De La Rocha, C. (2015). Silicate weathering in the Ganges alluvial plain. *Earth and Planetary Science Letters*, 427:136–148.

Frings, P. J., Clymans, W., Jeppesen, E., Lauridsen, T. L., Struyf, E., and Conley, D. J. (2014). Lack of steady-state in the global biogeochemical Si cycle: emerging evidence from lake Si sequestration. *Biogeochemistry*, 117(2-3):255–277.

Fripiat, F., Cavagna, A.-J., Dehairs, F., Speich, S., André, L., and Cardinal, D. (2011). Silicon pool dynamics and biogenic silica export in the Southern Ocean inferred from Si-isotopes. *Ocean science*, 7(5):533–547.

Gamier, J., Billen, G., and Coste, M. (1995). Seasonal succession of diatoms and Chlorophyceae in the drainage network of the Seine River: Observation and modeling. *Limnology and Oceanography*, 40(4):750–765.

Gao, G., Falconer, R. A., and Lin, B. (2011). Numerical modelling sediment-bacteria interaction processes in the Severn Estuary. *Journal of Water Resource and Protection*, 3(01):22.

Geerts, L., Maris, T., Meire, P., Wolfstein, K., Manson, S., Saathoff, S., Soetaert, K., Cox, T., and Meire, A. (2012). An interestuarine comparison for ecology in TIDE.

Genty, B., Briantais, J.-M., and Baker, N. R. (1989). The relationship between the quantum yield of photosynthetic electron transport and quenching of chlorophyll fluorescence. *Biochimica et Biophysica Acta (BBA)-General Subjects*, 990(1):87–92.

Georg, R., Reynolds, B. C., Frank, M., and Halliday, A. N. (2006). Mechanisms controlling the silicon isotopic compositions of river waters. *Earth and Planetary Science Letters*, 249(3-4):290–306.

Georg, R., West, A., Basu, A., and Halliday, A. (2009). Silicon fluxes and isotope composition of direct groundwater discharge into the Bay of Bengal and the effect on the global ocean silicon isotope budget. *Earth and Planetary Science Letters*, 283(1-4):67–74.

Georg, R. B., Reynolds, B. C., West, A. J., Burton, K. W., and Halliday, A. N. (2007). Silicon isotope variations accompanying basalt weathering in Iceland. *Earth and Planetary Science Letters*, 261(3-4):476–490.

Gisen, J., Savenije, H., and Nijzink, R. (2015). Revised predictive equations for salt intrusion modelling in estuaries. *Hydrology and Earth System Sciences*, 19(6):2791–2803.

Glibert, P. M. (2012). Ecological stoichiometry and its implications for aquatic ecosystem sustainability. *Current Opinion in Environmental Sustainability*, 4(3):272–277.

GOV. (2006). Landscape Character Assessments for the following Study Areas: The Severn Vale; Upper Thames Valley; Vale of Moreton; Vale of Evesham Fringe. In *Gloucestershire Landscape Character Assessment*.

Grachev, M., Denikina, N., Belikov, S., Likhoshvai, E., Usol'Tseva, M., Tikhonova, I., Adel'Shin, R., Kler, S., and Shcherbakova, T. (2002). Elements of the active center of silicon transporters in diatoms. *Molecular Biology*, 36(4):534–536.

Grasse, P., Ehlert, C., and Frank, M. (2013). The influence of water mass mixing on the dissolved Si isotope composition in the Eastern Equatorial Pacific. *Earth and Planetary Science Letters*, 380:60–71.

Grasshoff, K. (1976). Determination of nitrate and nitrite. *Methods of Seawater Analysis. Verlag Chemie, Weinheim, New York*.

Grouneva, I., Gollan, P. J., Kangasjärvi, S., Suorsa, M., Tikkanen, M., and Aro, E.-M. (2013). Phylogenetic viewpoints on regulation of light harvesting and electron transport in eukaryotic photosynthetic organisms. *Planta*, 237(2):399–412.

Grouneva, I., Jakob, T., Wilhelm, C., and Goss, R. (2009). The regulation of xanthophyll cycle activity and of non-photochemical fluorescence quenching by two alternative

electron flows in the diatoms Phaeodactylum tricornutum and Cyclotella meneghiniana. *Biochimica et Biophysica Acta (BBA)-Bioenergetics*, 1787(7):929–938.

Gypens, N., Delhez, E., Vanhoutte-Brunier, A., Burton, S., Thieu, V., Passy, P., Liu, Y., Callens, J., Rousseau, V., and Lancelot, C. (2013). Modelling phytoplankton succession and nutrient transfer along the Scheldt estuary (Belgium, The Netherlands). *Journal of marine systems*, 128:89–105.

Hamilton, D. (1979). The high energy, sand and mud regime of the Severn Estuary, SW Britain. In *Tidal Power and Estuary Management*, volume 30, pages 162–172. Scientechnica Bristol.

Hawkings, J. R., Wadham, J. L., Benning, L. G., Hendry, K. R., Tranter, M., Tedstone, A., Nienow, P., and Raiswell, R. (2017). Ice sheets as a missing source of silica to the polar oceans. *Nature communications*, 8:14198.

Hay, S. I., Maitland, T. C., and Paterson, D. M. (1993). The speed of diatom migration through natural and artificial substrata. *Diatom Research*, 8(2):371–384.

Heip, C., Goosen, N., Herman, P., Kromkamp, J., Middelburg, J., and Soetaert, K. (1995). Production and consumption of biological particles in temperate tidal estuaries. *Oceanography and Marine Biology: an annual review*, 33:1–149.

Hendry, K., Swann, G. E., Leng, M. J., Sloane, H. J., Goodwin, C., Berman, J., and Maldonado, M. (2015). Silica stable isotopes and silicification in a carnivorous sponge Asbestopluma sp. *Biogeosciences*, 12(11):3489–3498.

Hendry, K. R. and Brzezinski, M. A. (2014). Using silicon isotopes to understand the role of the Southern Ocean in modern and ancient biogeochemistry and climate. *Quaternary Science Reviews*, 89:13–26.

Hendry, K. R., Georg, R. B., Rickaby, R. E., Robinson, L. F., and Halliday, A. N. (2010). Deep ocean nutrients during the Last Glacial Maximum deduced from sponge silicon isotopic compositions. *Earth and Planetary Science Letters*, 292(3-4):290–300.

Hendry, K. R., Leng, M. J., Robinson, L. F., Sloane, H. J., Blusztjan, J., Rickaby, R. E., Georg, R. B., and Halliday, A. N. (2011). Silicon isotopes in Antarctic sponges: an interlaboratory comparison. *Antarctic Science*, 23(1):34–42.

Hendry, K. R. and Robinson, L. F. (2012). The relationship between silicon isotope fractionation in sponges and silicic acid concentration: Modern and core-top studies of biogenic opal. *Geochimica et Cosmochimica Acta*, 81:1–12.

Hensen, C., Zabel, M., and Schulz, H. N. (2006). Benthic cycling of oxygen, nitrogen and phosphorus. In *Marine Geochemistry*, pages 207–240. Springer.

Herlory, O., Richard, P., and Blanchard, G. F. (2007). Methodology of light response curves: application of chlorophyll fluorescence to microphytobenthic biofilms. *Marine Biology*, 153(1):91–101.

Hinson, S. (2018). Tidal lagoons. *House of Commons Library*, (7940).

Holland, H. D. (2005). Sea level, sediments and the composition of seawater. *American Journal of Science*, 305(3):220–239.

Holstein, J. M. and Hensen, C. (2010). Microbial mediation of benthic biogenic silica dissolution. *Geo-Marine Letters*, 30(5):477–492.

Hopkins, J. (1966). The role of water in the behaviour of an estuarine mud-flat diatom. *Journal of the Marine Biological Association of the United Kingdom*, 46(3):617–626.

Hopkins, J. T. (1963). A study of the diatoms of the Ouse Estuary, Sussex. The movement of the mud-flat diatoms in response to some chemical and physical changes. *Journal of the Marine Biological Association of the United Kingdom*, 43(3):653–663.

Hopkins, J. T. (1965). Some light-induced changes in behaviour and cytology of an estuarine mud-flat diatom. *Light as an ecological factor*, pages 336–358.

Hughes, H., Bouillon, S., André, L., and Cardinal, D. (2012). The effects of weathering variability and anthropogenic pressures upon silicon cycling in an intertropical watershed (Tana River, Kenya). *Chemical geology*, 308:18–25.

Hughes, H., Bouillon, S., Rousseau, V., André, L., and Cardinal, D. (2010). A first look at silicon isotopes in two contrasting estuaries. In *Geophysical Research Abstracts*, number EGU2010-4999-1.

Hughes, H., Sondag, F., Santos, R., André, L., and Cardinal, D. (2013). The riverine silicon isotope composition of the Amazon Basin. *Geochimica et Cosmochimica Acta*, 121:637–651.

Hughes, H. J., Delvigne, C., Korntheuer, M., de Jong, J., André, L., and Cardinal, D. (2011). Controlling the mass bias introduced by anionic and organic matrices in silicon isotopic measurements by MC-ICP-MS. *Journal of analytical atomic spectrometry*, 26(9):1892–1896.

Hydes, D., Aoyama, M., Aminot, A., Bakker, K., Becker, S., Coverly, S., Daniel, A., Dickson, A., Grosso, O., Kerouel, R., et al. (2010). Determination of Dissolved Nutrients (N, P, SI) in Seawater With High Precision and Inter-Comparability Using Gas-Segmented Continuous Flow Analysers.

Iler, K. R. (1979). The chemistry of silica. *Solubility, Polymerization, Colloid and Surface Properties and Biochemistry of Silica*.

Iler, R. K. (1955). *The colloid chemistry of silica and silicates*, volume 80. LWW.

Isson, T. T. and Planavsky, N. J. (2018). Reverse weathering as a long-term stabilizer of marine pH and planetary climate. *Nature*, 560(7719):471.

Jacobs, S., Struyf, E., Maris, T., and Meire, P. (2008). Spatiotemporal aspects of silica buffering in restored tidal marshes. *Estuarine, Coastal and Shelf Science*, 80(1):42–52.

Jahnke, R., Alexander, C., and Kostka, J. (2003). Advective pore water input of nutrients to the Satilla River Estuary, Georgia, USA. *Estuarine, Coastal and Shelf Science*, 56(3-4):641–653.

Jesus, B., Brotas, V., Ribeiro, L., Mendes, C., Cartaxana, P., and Paterson, D. (2009). Adaptations of microphytobenthos assemblages to sediment type and tidal position. *Continental Shelf Research*, 29(13):1624–1634.

Jesus, B., Perkins, R., Consalvey, M., Brotas, V., and Paterson, D. (2006). Effects of vertical migrations by benthic microalgae on fluorescence measurements of photophysiology. *Marine Ecology Progress Series*, 315:55–66.

JNCC (2018). Severn Estuary.

Joint, I. and Pomroy, A. (1981). Primary production in a turbid estuary. *Estuarine, Coastal and Shelf Science*, 13(3):303–316.

Jonas, P. and Millward, G. (2010). Metals and nutrients in the Severn Estuary and Bristol Channel: Contemporary inputs and distributions. *Marine Pollution Bulletin*, 61(1-3):52–67.

Jouanneau, J.-M., Lapaquellerie, Y., Latouche, C., and Tastet, J. (1990). Résultats préliminaires de la campagne Oubangui-Congo de novembre 1988. Microgranulométrie, minéralogie, analyses chimiques des matières en suspension/Preliminary results of the Oubangui-Congo cruise (November 1988). Microgranulometry, mineralogy, chemical analysis of suspended matter. *Sciences Géologiques, bulletins et mémoires*, 43(1):3–14.

Juneau, P., Barnett, A., Méléder, V., Dupuy, C., and Lavaud, J. (2015). Combined effect of high light and high salinity on the regulation of photosynthesis in three diatom species belonging to the main growth forms of intertidal flat inhabiting microphytobenthos. *Journal of experimental marine biology and ecology*, 463:95–104.

Karl, D. M. and Tien, G. (1992). MAGIC: A sensitive and precise method for measuring dissolved phosphorus in aquatic environments. *Limnology and Oceanography*, 37(1):105–116.

Kennedy, V. (1971). Silica variation in stream water with time and discharge. *Nonequilibrium systems in natural water chemistry*, pages 94–130.

Kim, G., Ryu, J.-W., Yang, H.-S., and Yun, S.-T. (2005). Submarine groundwater discharge (SGD) into the Yellow Sea revealed by 228Ra and 226Ra isotopes: Implications for global silicate fluxes. *Earth and Planetary Science Letters*, 237(1-2):156–166.

Kirby, R. (2010). Distribution, transport and exchanges of fine sediment, with tidal power implications: Severn Estuary, UK. *Marine pollution bulletin*, 61(1-3):21–36.

Kirby, R. and Parker, W. (1982). A suspended sediment front in the Severn Estuary. *Nature*, 295(5848):396.

Kirby, R. and Shaw, T. (2005). Severn barrage, UK environmental reappraisal. In *Proceedings of the Institution of Civil Engineers-Engineering Sustainability*, volume 158, pages 31–39. Thomas Telford Ltd.

Kirkwood, D. (1989). *Simultaneous determination of selected nutrients in sea water*. International Council for the Exploration of the Sea (ICES).

Klughammer, C. and Schreiber, U. (2008). Complementary PS II quantum yields calculated from simple fluorescence parameters measured by PAM fluorometry and the Saturation Pulse method. *PAM application notes*, 1(2):201–247.

Kocum, E., Underwood, G. J., and Nedwell, D. B. (2002). Simultaneous measurement of phytoplanktonic primary production, nutrient and light availability along a turbid, eutrophic UK east coast estuary (the Colne Estuary). *Marine ecology progress series*, 231:1–12.

Kromkamp, J., Barranguet, C., and Peene, J. (1998). Determination of microphytobenthos PSII quantum efficiency and photosynthetic activity by means of variable chlorophyll fluorescence. *Marine Ecology Progress Series*, 162:45–55.

Kuczynska, P., Jemiola-Rzeminska, M., and Strzalka, K. (2015). Photosynthetic pigments in diatoms. *Marine drugs*, 13(9):5847–5881.

Lancelot, C., Hannon, E., Becquevort, S., Veth, C., and De Baar, H. J. (2000). Modeling phytoplankton blooms and carbon export production in the Southern Ocean: dominant controls by light and iron in the Atlantic sector in Austral spring 1992. *Deep Sea Research Part I: Oceanographic Research Papers*, 47(9):1621–1662.

Langdon, C. (1993). The significance of respiration in production measurements based on oxygen. In *ICES Mar. Sci. Symp*, volume 197, pages 69–78.

Langston, W., Pope, N., Jonas, P., Nikitic, C., Field, M., Dowell, B., Shillabeer, N., Swarbrick, R., and Brown, A. (2010a). Contaminants in fine sediments and their consequences for biota of the Severn Estuary. *Marine Pollution Bulletin*, 61(1-3):68–82.

Langston, W. J., Jonas, P. J. C., and Millward, G. E. (2010b). The Severn Estuary and Bristol Channel: a 25 year critical review. *Marine pollution bulletin*, 61(1):1.

Laruelle, G. G. (2009). *Quantifying nutrient cycling and retention in coastal waters at the global scale. Geologica Ultraiectina (312)*. PhD thesis, Departement Aardwetenschappen.

Laruelle, G. G., Roubeix, V., Sferratore, A., Brodherr, B., Ciuffa, D., Conley, D. J., Dürr, H. H., Garnier, J., Lancelot, C., Le Thi Phuong, Q., et al. (2009a). Anthropogenic perturbations of the silicon cycle at the global scale: Key role of the land-ocean transition. *Global biogeochemical cycles*, 23(4).

Laruelle, G. G., Roubeix, V., Sferratore, A., Brodherr, B., Ciuffa, D., Conley, D. J., Dürr, H. H., Garnier, J., Lancelot, C., Le Thi Phuong, Q., et al. (2009b). The global biogeochemical cycle of silicon: role of the land-ocean transition and response to anthropogenic perturbation. *Global Biogeochem. Cy*, 23.

Launeau, P., Méléder, V., Verpoorter, C., Barillé, L., Kazemipour-Ricci, F., Giraud, M., Jesus, B., and Le Menn, E. (2018). Microphytobenthos biomass and diversity mapping at different spatial scales with a hyperspectral optical model. *Remote Sensing*, 10(5):716.

Lavaud, J. (2007). Fast regulation of photosynthesis in diatoms: mechanisms, evolution and ecophysiology. *Functional Plant Science and Biotechonology*, 1:267–287.

Lavaud, J. and Goss, R. (2014). The peculiar features of non-photochemical fluorescence quenching in diatoms and brown algae. In *Non-photochemical quenching and energy dissipation in plants, algae and cyanobacteria*, pages 421–443. Springer.

Lavaud, J. and Kroth, P. G. (2006). In diatoms, the transthylakoid proton gradient regulates the photoprotective non-photochemical fluorescence quenching beyond its control on the xanthophyll cycle. *Plant and Cell Physiology*, 47(7):1010–1016.

Lavaud, J. and Lepetit, B. (2013). An explanation for the inter-species variability of the photoprotective non-photochemical chlorophyll fluorescence quenching in diatoms. *Biochimica et Biophysica Acta (BBA)-Bioenergetics*, 1827(3):294–302.

Lavaud, J., Rousseau, B., Van Gorkom, H. J., and Etienne, A.-L. (2002). Influence of the diadinoxanthin pool size on photoprotection in the marine planktonic diatom Phaeodactylum tricornutum. *Plant Physiology*, 129(3):1398–1406.

Laviale, M., Barnett, A., Ezequiel, J., Lepetit, B., Frankenbach, S., Méléder, V., Serôdio, J., and Lavaud, J. (2015). Response of intertidal benthic microalgal biofilms to a coupled light–temperature stress: evidence for latitudinal adaptation along the Atlantic coast of Southern Europe. *Environmental microbiology*, 17(10):3662–3677.

Lefort, S., Gratton, Y., Mucci, A., Dadou, I., and Gilbert, D. (2012). Hypoxia in the Lower St. Lawrence Estuary: How physics controls spatial patterns. *Journal of Geophysical Research: Oceans*, 117(C7).

Leynaert, A., Longphuirt, S. N., An, S., Lim, J.-H., Claquin, P., Grall, J., Kwon, B. O., and Koh, C. H. (2011). Tidal variability in benthic silicic acid fluxes and microphytobenthos uptake in intertidal sediment. *Estuarine, Coastal and Shelf Science*, 95(1):59–66.

Leynaert, A., Longphuirt, S. N., Claquin, P., Chauvaud, L., and Ragueneau, O. (2009). No limit? The multiphasic uptake of silicic acid by benthic diatoms. *Limnology and Oceanography*, 54(2):571–576.

Liang, D., Xia, J., Falconer, R. A., and Zhang, J. (2014). Study on tidal resonance in Severn Estuary and Bristol Channel. *Coastal engineering journal*, 56(01):1450002.

Lin, J., Xie, L., Pietrafesa, L. J., Ramus, J. S., and Paerl, H. W. (2007). Water quality gradients across Albemarle-Pamlico estuarine system: seasonal variations and model applications. *Journal of Coastal Research*, pages 213–229.

Little, D. and Smith, J. (1994). Appraisal of contaminants in sediments of the Inner Bristol Channel and Severn Estuary. *Biological Journal of the Linnean Society*, 51(1-2):55–69.

Liu, S. M., Ye, X. W., Zhang, J., Zhang, G. S., and Wu, Y. (2008). The silicon balance in Jiaozhou Bay, North China. *Journal of Marine Systems*, 74(1-2):639–648.

Liu, W.-C. (2005). Water column light attenuation estimation to simulate phytoplankton population in tidal estuary. *Environmental geology*, 49(2):280–292.

Livingstone, D. A. (1963). *Chemical composition of rivers and lakes*. US Government Printing Office.

Longphuirt, S. N., Lim, J.-H., Leynaert, A., Claquin, P., Choy, E.-J., Kang, C.-K., and An, S. (2009a). Dissolved inorganic nitrogen uptake by intertidal microphytobenthos:

nutrient concentrations, light availability and migration. *Marine Ecology Progress Series*, 379:33–44.

Longphuirt, S. N., Ragueneau, O., Chauvaud, L., Martin, S., Jean, F., Thouzeau, G., and Leynaert, A. (2009b). Diurnal heterogeneity in silicic acid fluxes in shallow coastal sites: causes and implications. *Estuarine, Coastal and Shelf Science*, 82(3):495–502.

Loucaide, S., Van Cappelle, P., and Behrends, T. (2008). Dissolution of biogenic silica from land to ocean: role of salinity and pH. *Limnology and Oceanography*, 53(4):1614–1621.

Maavara, T., Dürr, H. H., and Van Cappellen, P. (2014). Worldwide retention of nutrient silicon by river damming: From sparse data set to global estimate. *Global Biogeochemical Cycles*, 28(8):842–855.

MacIntyre, H. L., Lomas, M. W., Cornwell, J., Suggett, D. J., Gobler, C. J., Koch, E. W., and Kana, T. M. (2004). Mediation of benthic–pelagic coupling by microphytobenthos: an energy-and material-based model for initiation of blooms of Aureococcus anophagefferens. *Harmful Algae*, 3(4):403–437.

Mackenzie, F. T. and Garrels, R. M. (1966a). Chemical mass balance between rivers and oceans. *American Journal of Science*, 264(7):507–525.

Mackenzie, F. T. and Garrels, R. M. (1966b). Silica-bicarbonate balance in the ocean and early diagenesis. *Journal of Sedimentary Research*, 36(4):1075–1084.

Mackereth, F., Heron, J., and Talling, J. (1978). Water analysis of freshwater. *Biol. Ass. Publ*, 36:120.

Maerz, J., Hofmeister, R., Lee, E. M., Gräwe, U., Riethmüller, R., and Wirtz, K. W. (2016). Maximum sinking velocities of suspended particulate matter in a coastal transition zone. *Biogeosciences*, 13(17):4863–4876.

Malhotra, S. and Zanoni, A. (1970). Chloride interference in nitrate nitrogen determination. *Journal-American Water Works Association*, 62(9):568–571.

Mangalaa, K., Cardinal, D., Brajard, J., Rao, D., Sarma, N., Djouraev, I., Chiranjeevulu, G., Murty, K. N., and Sarma, V. (2017). Silicon cycle in Indian estuaries and its control by biogeochemical and anthropogenic processes. *Continental Shelf Research*, 148:64–88.

Mann, D. G. and Vanormelingen, P. (2013). An inordinate fondness? The number, distributions, and origins of diatom species. *Journal of eukaryotic microbiology*, 60(4):414–420.

Manning, A., Langston, W., and Jonas, P. (2010). A review of sediment dynamics in the Severn Estuary: influence of flocculation. *Marine Pollution Bulletin*, 61(1-3):37–51.

Manning, A. and Schoellhamer, D. (2013). Factors controlling floc settling velocity along a longitudinal estuarine transect. *Marine Geology*, 345:266–280.

Manning, A. J., Spearman, J. R., Whitehouse, R. J., Pidduck, E. L., Baugh, J. V., and Spencer, K. L. (2013). Flocculation dynamics of mud: sand mixed suspensions. In *Sediment transport processes and their modelling applications*. IntechOpen.

Mantoura, R. and Woodward, E. (1983). Optimization of the indophenol blue method for the automated determination of ammonia in estuarine waters. *Estuarine, Coastal and Shelf Science*, 17(2):219–224.

Marschner, H. (1974). Mechanisms of regulation of mineral nutrition in higher plants. *Bull R Soc NZ*.

Martin, J.-M. and Meybeck, M. (1979). Elemental mass-balance of material carried by major world rivers. *Marine chemistry*, 7(3):173–206.

Martin-Jézéquel, V., Hildebrand, M., and Brzezinski, M. A. (2000). Silicon metabolism in diatoms: implications for growth. *Journal of phycology*, 36(5):821–840.

Martiny, A. C., Pham, C. T., Primeau, F. W., Vrugt, J. A., Moore, J. K., Levin, S. A., and Lomas, M. W. (2013). Strong latitudinal patterns in the elemental ratios of marine plankton and organic matter. *Nature Geoscience*, 6(4):279.

MetOffice (2016). Historical Station Observations.

Meybeck, M. (1979). Concentrations des eaux fluviales en elements majeuis et apports en solution awx oceans. *Rev. Geol. Dyn. Geogr. Phys.*, 21:215–246.

Meybeck, M. (1987). Global chemical weathering of surficial rocks estimated from river dissolved loads. *American journal of science*, 287(5):401–428.

Meybeck, M. (1988). How to establish and use world budgets of riverine materials. In *Physical and chemical weathering in geochemical cycles*, pages 247–272. Springer.

Meybeck, M. (2003). Global occurrence of major elements in rivers. *Treatise on geochemistry*, 5(605):05164–1.

Meyer-Reil, L.-A. (1994). Microbial life in sedimentary biofilms-the challenge to microbial ecologists. *Marine ecology progress series. Oldendorf*, 112(3):303–311.

Michalopoulos, P. and Aller, R. C. (1995). Rapid clay mineral formation in Amazon delta sediments: reverse weathering and oceanic elemental cycles. *Science*, 270(5236):614–617.

Michalopoulos, P. and Aller, R. C. (2004). Early diagenesis of biogenic silica in the Amazon delta: alteration, authigenic clay formation, and storage. *Geochimica et Cosmochimica Acta*, 68(5):1061–1085.

Michalopoulos, P., Aller, R. C., and Reeder, R. J. (2000). Conversion of diatoms to clays during early diagenesis in tropical, continental shelf muds. *Geology*, 28(12):1095–1098.

Montgomery, J. R., Zimmermann, C. F., and Price, M. T. (1979). The collection, analysis and variation of nutrients in estuarine pore water. *Estuarine and Coastal Marine Science*, 9(2):203–214.

Moreno, A. R., Hagstrom, G. I., Primeau, F. W., Levin, S. A., and Martiny, A. C. (2018). Marine phytoplankton stoichiometry mediates nonlinear interactions between nutrient supply, temperature, and atmospheric CO2. *Biogeosciences (Online)*, 15(9).

Moreno, A. R. and Martiny, A. C. (2018). Ecological stoichiometry of ocean plankton. *Annual review of marine science*, 10:43–69.

Morris, A. (1984). The chemistry of the Severn Estuary and the Bristol Channel. *Marine pollution bulletin*, 15(2):57–61.

Morris, A., Howland, R., Woodward, E., Bale, A., and Mantoura, R. (1985). Nitrite and ammonia in the Tamar Estuary. *Netherlands Journal of Sea Research*, 19(3-4):217–222.

Mouget, J.-L., Perkins, R., Consalvey, M., and Lefebvre, S. (2008). Migration or photoacclimation to prevent high irradiance and UV-B damage in marine microphytobenthic communities. *Aquatic Microbial Ecology*, 52(3):223–232.

Muylaert, K. and Raine, R. (1999). Import, mortality and accumulation of coastal phytoplankton in a partially mixed estuary (Kinsale harbour, Ireland). *Hydrobiologia*, 412:53–65.

Neill, S. P. and Couch, S. J. (2011). Impact of Tidal Energy Converter (TEC) array operation on sediment dynamics. In *Proceedings of the 9th European Wave and Tidal Energy Conference*.

Nelson, D. M. and Dortch, Q. (1996). Silicic acid depletion and silicon limitation in the plume of the Mississippi River: evidence from kinetic studies in spring and summer. *Marine Ecology Progress Series*, 136:163–178.

Nelson, D. M., Goering, J. J., Kilham, S. S., and Guillard, R. R. (1976). Kinetics of silicic acid uptake and rates of silica dissolution in the marine diatom Thalassiosira Pseudonana. *Journal of Phycology*, 12(2):246–252.

Nihoul, J. and Ronday, F. (1976). Modèles destuaires partiellement stratifiés. *Projet Mer*, 10:71–98.

Nixon, S. W. (1981). Remineralization and nutrient cycling in coastal marine ecosystems. In *Estuaries and nutrients*, pages 111–138. Springer.

Nixon, S. W. (1995). Coastal marine eutrophication: a definition, social causes, and future concerns. *Ophelia*, 41(1):199–219.

Nixon, S. W., Buckley, B. A., Granger, S. L., Harris, L. A., Oczkowski, A. J., Fulweiler, R. W., and Cole, L. W. (2008). Nitrogen and phosphorus inputs to Narragansett Bay: past, present, and future. In *Science for ecosystem-based management*, pages 101–175. Springer.

Norris, A. and Hackney, C. (1999). Silica content of a mesohaline tidal marsh in North Carolina. *Estuarine, Coastal and Shelf Science*, 49(4):597–605.

Office, U. H. (2016). *ADMIRALTY Tide Tables: United Kingdom and Ireland - Including European Channel Ports*, volume 1 of *NP201*.

Opfergelt, S., de Bournonville, G., Cardinal, D., André, L., Delstanche, S., and Delvaux, B. (2009). Impact of soil weathering degree on silicon isotopic fractionation during adsorption onto iron oxides in basaltic ash soils, cameroon. *Geochimica et Cosmochimica Acta*, 73(24):7226–7240.

Opfergelt, S. and Delmelle, P. (2012). Silicon isotopes and continental weathering processes: Assessing controls on Si transfer to the ocean. *Comptes Rendus Geoscience*, 344(11-12):723–738.

Opfergelt, S., Delvaux, B., André, L., and Cardinal, D. (2008). Plant silicon isotopic signature might reflect soil weathering degree. *Biogeochemistry*, 91(2-3):163–175.

Oppenheim, D. (1988). The distribution of epipelic diatoms along an intertidal shore in relation to principal physical gradients. *Botanica Marina*, 31(1):65–72.

Oppenheim, D. R. (1991). Seasonal changes in epipelic diatoms along an intertidal shore, Berrow Flats, Somerset. *Journal of the Marine Biological Association of the United Kingdom*, 71(3):579–596.

Orvain, F., Galois, R., Barnard, C., Sylvestre, A., Blanchard, G., and Sauriau, P.-G. (2003). Carbohydrate production in relation to microphytobenthic biofilm development: an integrated approach in a tidal mesocosm. *Microbial ecology*, 45(3):237–251.

Orvain, F., Sauriau, P.-G., Sygut, A., Joassard, L., and Le Hir, P. (2004). Interacting effects of Hydrobia ulvae bioturbation and microphytobenthos on the erodibility of mudflat sediments. *Marine ecology progress series*, 278:205–223.

Owen, A. (1980). A three-dimensional model of the Bristol Channel. *Journal of Physical Oceanography*, 10(8):1290–1302.

Panizzo, V., Swann, G. E., Mackay, A. W., Vologina, E., Alleman, L., André, L., Pashley, V., and Horstwood, M. S. (2017). Constraining modern-day silicon cycling in Lake Baikal. *Global Biogeochemical Cycles*, 31(3):556–574.

Papush, L. (2011). *Silicon cycling in the Baltic Sea: Trends and budget of dissolved silica*. PhD thesis, Linköping University Electronic Press.

Pastuszak, M., Conley, D. J., Humborg, C., Witek, Z., and Sitek, S. (2008). Silicon dynamics in the Oder estuary, Baltic Sea. *Journal of Marine Systems*, 3(73):250–262.

Paterson, D. (1994). Biological mediation of sediment erodibility: ecology and physical dynamics. *Cohesive sediments*.

Paterson, D. M. (1986). The migratory behaviour of diatom assemblages in a laboratory tidal micro-ecosystem examined by low temperature scanning electron microscopy. *Diatom Research*, 1(2):227–239.

Paterson, D. M. (1989). Short-term changes in the erodibility of intertidal cohesive sediments related to the migratory behavior of epipelic diatoms. *Limnology and Oceanography*, 34(1):223–234.

Peltier, W., Shennan, I., Drummond, R., and Horton, B. (2002). On the postglacial isostatic adjustment of the British Isles and the shallow viscoelastic structure of the Earth. *Geophysical Journal International*, 148(3):443–475.

Perkins, R., Honeywill, C., Consalvey, M., Austin, H., Tolhurst, T., and Paterson, D. (2003). Changes in microphytobenthic chlorophyll a and EPS resulting from sediment compaction due to de-watering: opposing patterns in concentration and content. *Continental Shelf Research*, 23(6):575–586.

Perkins, R., Underwood, G., Brotas, V., Jesus, B., Ribeiro, L., and Snow, G. (2001). In situ microphytobenthic primary production during low tide emersion in the Tagus estuary, Portugal: production rates, carbon partitioning and vertical migration. *Mar Ecol Prog Ser*, 223:101–112.

Perkins, R., Williamson, C., Lavaud, J., Mouget, J.-L., and Campbell, D. (2018). Time-dependent upregulation of electron transport with concomitant induction of regulated excitation dissipation in Haslea diatoms. *Photosynthesis research*, 137(3):377–388.

Perkins, R. G., Kromkamp, J. C., Serôdio, J., Lavaud, J., Jesus, B., Mouget, J.-L., Lefebvre, S., and Forster, R. M. (2010a). The application of variable chlorophyll

fluorescence to microphytobenthic biofilms. In *Chlorophyll a fluorescence in aquatic sciences: methods and applications*, pages 237–275. Springer.

Perkins, R. G., Lavaud, J., Serôdio, J., Mouget, J.-L., Cartaxana, P., Rosa, P., Barillé, L., Brotas, V., and Jesus, B. M. (2010b). Vertical cell movement is a primary response of intertidal benthic biofilms to increasing light dose. *Marine Ecology Progress Series*, 416:93–103.

Perkins, R. G., Paterson, D. M., Sun, H., Watson, J., and Player, M. A. (2004a). Extracellular polymeric substances: quantification and use in erosion experiments. *Continental Shelf Research*, 24(15):1623–1635.

Perkins, R. G., Sun, H., Watson, J., Player, M. A., Gust, G., and Paterson, D. M. (2004b). In-line laser holography and video analysis of eroded floc from engineered and estuarine sediments. *Environmental science & technology*, 38(17):4640–4648.

Pethick, J. S., Morris, R. K., and Evans, D. H. (2009). Nature conservation implications of a Severn tidal barrage–A preliminary assessment of geomorphological change. *Journal for Nature Conservation*, 17(4):183–198.

Pinckney, J. L., Paerl, H. W., Tester, P., and Richardson, T. L. (2001). The role of nutrient loading and eutrophication in estuarine ecology. *Environmental health perspectives*, 109(suppl 5):699–706.

Pond, S. and Pickard, G. (1983). Introductory dynamical oceanography. Butterwotrh Heinemann.

Pondaven, P., Ragueneau, O., Treguer, P., Hauvespre, A., Dezileau, L., and Reyss, J. L. (2000). Resolving the opal paradox in the Southern Ocean. *Nature*, 405(6783):168.

Potts, G. W. and Swaby, S. E. (1993). *Review of the status of estuarine fishes*. Marine Biological Association.

Powers, S. M., Bruulsema, T. W., Burt, T. P., Chan, N. I., Elser, J. J., Haygarth, P. M., Howden, N. J., Jarvie, H. P., Lyu, Y., Peterson, H. M., et al. (2016). Long-term accumulation and transport of anthropogenic phosphorus in three river basins. *Nature Geoscience*, 9(5):353.

Pradeep, K., Nepolian, M., Anandhan, P., Kaviyarasan, R., Prasanna, M. V., Chidambaram, S., et al. (2016). A study on variation in dissolved silica concentration in groundwater of hard rock aquifers in Southeast coast of India. In *IOP Conference Series: Materials Science and Engineering*, volume 121, page 012008. IOP Publishing.

Presti, M. and Michalopoulos, P. (2008). Estimating the contribution of the authigenic mineral component to the long-term reactive silica accumulation on the western shelf of the Mississippi River Delta. *Continental Shelf Research*, 28(6):823–838.

Pritchard, D. W. (1958). The equations of mass continuity and salt continuity in estuaries. *Journal of Marine Research*, 17:412–423.

Probst, J.-L. (1992). *Géochimie et hydrologie de l'érosion continentale. Mécanismes, bilan global actuel et fluctuations au cours des 500 derniers millions d'années*, volume 94. Persée-Portail des revues scientifiques en SHS.

Radford, P. (1994). Pre-and post-barrage scenarios of the relative productivity of benthic and pelagic subsystems of the Bristol Channel and Severn estuary. *Biological journal of the Linnean Society*, 51(1-2):5–16.

Ragueneau, O., Chauvaud, L., Leynaert, A., Thouzeau, G., Paulet, Y.-M., Bonnet, S., Lorrain, A., Grall, J., Corvaisier, R., Le Hir, M., et al. (2002). Direct evidence of a biologically active coastal silicate pump: ecological implications. *Limnology and Oceanography*, 47(6):1849–1854.

Ragueneau, O., Chauvaud, L., Moriceau, B., Leynaert, A., Thouzeau, G., Donval, A., Le Loch, F., and Jean, F. (2005). Biodeposition by an invasive suspension feeder impacts the biogeochemical cycle of Si in a coastal ecosystem (Bay of Brest, France). *Biogeochemistry*, 75(1):19–41.

Ragueneau, O. and Tréguer, P. (1994). Determination of biogenic silica in coastal waters: applicability and limits of the alkaline digestion method. *Marine Chemistry*, 45(1-2):43–51.

Ragueneau, O., Tréguer, P., Leynaert, A., Anderson, R., Brzezinski, M., DeMaster, D., Dugdale, R., Dymond, J., Fischer, G., Francois, R., et al. (2000). A review of the si cycle in the modern ocean: recent progress and missing gaps in the application of biogenic opal as a paleoproductivity proxy. *Global and Planetary Change*, 26(4):317–365.

Rahm, L., Conley, D., Sandén, P., Wulff, F., and Stålnacke, P. (1996). Time series analysis of nutrient inputs to the Baltic Sea and changing DSi: DIN ratios. *Marine ecology progress series*, 130:221–228.

Rahman, S., Tamborski, J. J., Charette, M. A., and Cochran, J. K. (2019). Dissolved silica in the subterranean estuary and the impact of submarine groundwater discharge on the global marine silica budget. *Marine Chemistry*, 208:29–42.

Raimonet, M., Ragueneau, O., Andrieux-Loyer, F., Philippon, X., Kérouel, R., Le Goff, M., and Mémery, L. (2013). Spatio-temporal variability in benthic silica cycling in two macrotidal estuaries: causes and consequences for local to global studies. *Estuarine, Coastal and Shelf Science*, 119:31–43.

Raymond, P. A. and Bauer, J. E. (2001). Use of 14C and 13C natural abundances for evaluating riverine, estuarine, and coastal DOC and POC sources and cycling: a review and synthesis. *Organic Geochemistry*, 32(4):469–485.

Rebreanu, L. (2009). Study of the Si biogeochemical cycle in the sediments of the Scheldt continuum, Belgium/The Netherlands.

Rebreanu, L., Vanderborght, J.-P., and Chou, L. (2008). The diffusion coefficient of dissolved silica revisited. *Marine chemistry*, 112(3-4):230–233.

Redfield, A. C. (1963). The influence of organisms on the composition of seawater. *The sea*, 2:26–77.

Regnier, P., Arndt, S., Goossens, N., Volta, C., Laruelle, G. G., Lauerwald, R., and Hartmann, J. (2013a). Modelling estuarine biogeochemical dynamics: from the local to the global scale. *Aquatic geochemistry*, 19(5-6):591–626.

Regnier, P., Friedlingstein, P., Ciais, P., Mackenzie, F. T., Gruber, N., Janssens, I. A., Laruelle, G. G., Lauerwald, R., Luyssaert, S., Andersson, A. J., et al. (2013b). Anthropogenic perturbation of the carbon fluxes from land to ocean. *Nature geoscience*, 6(8):597.

Regnier, P., Mouchet, A., Wollast, R., and Ronday, F. (1998). A discussion of methods for estimating residual fluxes in strong tidal estuaries. *Continental Shelf Research*, 18(13):1543–1571.

Regnier, P. and Steefel, C. I. (1999). A high resolution estimate of the inorganic nitrogen flux from the Scheldt estuary to the coastal North Sea during a nitrogen-limited algal bloom, spring 1995. *Geochimica et Cosmochimica Acta*, 63(9):1359–1374.

Regnier, P., Wollast, R., and Steefel, C. (1997). Long-term fluxes of reactive species in macrotidal estuaries: Estimates from a fully transient, multicomponent reaction-transport model. *Marine Chemistry*, 58(1-2):127–145.

Reynolds, B. C., Frank, M., and Halliday, A. N. (2006). Silicon isotope fractionation during nutrient utilization in the North Pacific. *Earth and Planetary Science Letters*, 244(1-2):431–443.

Rijstenbil, J. (2005). UV-and salinity-induced oxidative effects in the marine diatom Cylindrotheca closterium during simulated emersion. *Marine biology*, 147(5):1063–1073.

Robinson, G. W. (1922). Note on the mechanical analysis of humus soils. *The Journal of Agricultural Science*, 12(3):287–291.

Ronchi, B. (2014). *Controlling factors of dissolved Silicon in upstream catchments with different land uses*. University Press.

Roubeix, V. (2007). *Transformations biogochimiques et transfert du silicium dans la zone de transition fleuve-mer: le rle des diatomes planctoniques*. PhD thesis, Universite Libre de Bruxelles, Belgium.

Roubeix, V., Rousseau, V., and Lancelot, C. (2008). Diatom succession and silicon removal from freshwater in estuarine mixing zones: From experiment to modelling. *Estuarine, Coastal and Shelf Science*, 78(1):14–26.

Round, F. (1979). A diatom assemblage living below the surface of intertidal sand flats. *Marine Biology*, 54(3):219–223.

Round, F. and Palmer, J. (1966). Persistent, vertical-migration rhythms in benthic microflora: Field and laboratory studies on diatoms from the banks of the River Avon. *Journal of the Marine Biological Association of the United Kingdom*, 46(1):191–214.

Rowbotham, F. (1983). *The Severn Bore*. David & Charles Publishers.

RStudio Team (2015). *RStudio: Integrated Development Environment for R*. RStudio, Inc., Boston, MA.

Rutkowski, C. M., Burnett, W. C., Iverson, R. L., and Chanton, J. P. (1999). The effect of groundwater seepage on nutrient delivery and seagrass distribution in the northeastern Gulf of Mexico. *Estuaries*, 22(4):1033–1040.

Saburova, M. A. and Polikarpov, I. G. (2003). Diatom activity within soft sediments: behavioural and physiological processes. *Marine Ecology Progress Series*, 251:115–126.

Saccone, L., Conley, D. J., Koning, E., Sauer, D., Sommer, M., Kaczorek, D., Blecker, S. W., and Kelly, E. F. (2007). Assessing the extraction and quantification of amorphous silica in soils of forest and grassland ecosystems. *European Journal of Soil Science*, 58(6):1446–1459.

Salleh, S. and McMinn, A. (2011). The effects of temperature on the photosynthetic parameters and recovery of two temperate benthic microalgae, Amphora cf. Coffeaeformis and Cocconeis cf. Sublittoralis (Bacillariophyceae). *Journal of phycology*, 47(6):1413–1424.

Sandén, P., Rahm, L., and Wulff, F. (1991). Non-parametric trend test of Baltic Sea data. *Environmetrics*, 2(3):263–278.

Savenije, H. (2012). Salinity and Tides in Alluvial Estuaries (2nd completely revised edition).

Savenije, H. H. (2006). *Salinity and tides in alluvial estuaries*. Elsevier.

Savenije, H. H. G. (1994). Rapid assessment technique for salt intrusion in alluvial estuaries.

Schemel, L. E. and Hager, S. W. (1986). Chemical variability in the Sacramento River and in northern San Francisco Bay. *Estuaries*, 9(4):270–283.

Schulz, H. and Zabel, M. (2006). *Marine Geochemistry*. Springer, Berlin, Heidelberg.

SEP (2009). The Severn Estuary European Marine Site. *Natural Resources Wales*, pages 1–175.

SEP (2018). Severn Estuary Gateway.

Serôdio, J. (2004). Analysis of variable chlorophyll fluorescence in microphytobenthos assemblages: implications of the use of depth-integrated measurements. *Aquatic Microbial Ecology*, 36(2):137–152.

Serôdio, J., Cruz, S., Vieira, S., and Brotas, V. (2005a). Non-photochemical quenching of chlorophyll fluorescence and operation of the xanthophyll cycle in estuarine microphytobenthos. *Journal of Experimental Marine Biology and Ecology*, 326(2):157–169.

Serôdio, J., Ezequiel, J., Barnett, A., Mouget, J.-L., Méléder, V., Laviale, M., and Lavaud, J. (2012). Efficiency of photoprotection in microphytobenthos: role of vertical migration and the xanthophyll cycle against photoinhibition. *Aquatic Microbial Ecology*, 67(2):161–175.

Serôdio, J. and Lavaud, J. (2011). A model for describing the light response of the nonphotochemical quenching of chlorophyll fluorescence. *Photosynthesis research*, 108(1):61–76.

Serodio, J., Vieira, S., and Cruz, S. (2008). Photosynthetic activity, photoprotection and photoinhibition in intertidal microphytobenthos as studied in situ using variable chlorophyll fluorescence. *Continental Shelf Research*, 28(10-11):1363–1375.

Serôdio, J., Vieira, S., Cruz, S., and Barroso, F. (2005b). Short-term variability in the photosynthetic activity of microphytobenthos as detected by measuring rapid light curves using variable fluorescence. *Marine Biology*, 146(5):903–914.

Serôdio, J., Vieira, S., Cruz, S., and Coelho, H. (2006). Rapid light-response curves of chlorophyll fluorescence in microalgae: relationship to steady-state light curves and non-photochemical quenching in benthic diatom-dominated assemblages. *Photosynthesis research*, 90(1):29–43.

Shaw, T. (1980). Environmental appraisal of tidal power stations: with particular reference to the Severn barrage.

Sherbakova, T., Masyukova, Y. A., Safonova, T., Petrova, D., Vereshagin, A., Minaeva, T., Adelshin, R., Triboy, T., Stonik, I., Aizdaitcher, N., et al. (2005). Conserved motif CMLD in silicic acid transport proteins of diatoms. *Molecular Biology*, 39(2):269–280.

Sigmon, D. and Cahoon, L. B. (1997). Comparative effects of benthic microalgae and phytoplankton on dissolved silica fluxes. *Aquatic Microbial Ecology*, 13(3):275–284.

Smith, D. J. and Underwood, G. J. (1998). Exopolymer production by intertidal epipelic diatoms. *Limnology and Oceanography*, 43(7):1578–1591.

Soetaert, K. and Herman, P. M. (1995). Nitrogen dynamics in the Westerschelde estuary (SW Netherlands) estimated by means of the ecosystem model MOSES. *Hydrobiologia*, 311(1-3):225–246.

Soetaert, K., Middelburg, J. J., Heip, C., Meire, P., Van Damme, S., and Maris, T. (2006). Long-term change in dissolved inorganic nutrients in the heterotrophic Scheldt estuary (Belgium, The Netherlands). *Limnology and Oceanography*, 51(1part2):409–423.

Sospedra, J., Niencheski, L. F. H., Falco, S., Andrade, C. F., Attisano, K. K., and Rodilla, M. (2018). Identifying the main sources of silicate in coastal waters of the Southern Gulf of Valencia (Western Mediterranean Sea). *Oceanologia*, 60(1):52–64.

Souza, G. F., Reynolds, B. C., Rickli, J., Frank, M., Saito, M. A., Gerringa, L. J., and Bourdon, B. (2012). Southern Ocean control of silicon stable isotope distribution in the deep Atlantic Ocean. *Global biogeochemical cycles*, 26(2).

Srithongouthai, S., Sonoyama, Y.-I., Tada, K., and Montani, S. (2003). The influence of environmental variability on silicate exchange rates between sediment and water in a shallow-water coastal ecosystem, the Seto Inland Sea, Japan. *Marine pollution bulletin*, 47(1-6):10–17.

Staats, N., de Deckere, E. M., de Winder, B., and Stal, L. J. (2001). Spatial patterns of benthic diatoms, carbohydrates and mud on a tidal flat in the Ems-Dollard estuary. *Hydrobiologia*, 448(1-3):107–115.

Stal, L. and De Brouwer, J. (2003). Biofilm formation by benthic diatoms and their influence on the stabilization of intertidal mudflats. *Berichte-Forschungszentrum Terramare*, 12:109–111.

Statham, P. J. (2012). Nutrients in estuaries: an overview and the potential impacts of climate change. *Science of the total environment*, 434:213–227.

Sterner, R. W., Andersen, T., Elser, J. J., Hessen, D. O., Hood, J. M., McCauley, E., and Urabe, J. (2008). Scale-dependent carbon: nitrogen: phosphorus seston stoichiometry in marine and freshwaters. *Limnology and Oceanography*, 53(3):1169–1180.

Strickland, J. D. and Parsons, T. R. (1972). A practical handbook of seawater analysis.

Struyf, E. and Conley, D. J. (2009). Silica: an essential nutrient in wetland biogeochemistry. *Frontiers in Ecology and the Environment*, 7(2):88–94.

Struyf, E., Mörth, C.-M., Humborg, C., and Conley, D. J. (2010). An enormous amorphous silica stock in boreal wetlands. *Journal of Geophysical Research: Biogeosciences*, 115(G4).

Struyf, E., Van Damme, S., Gribsholt, B., and Meire, P. (2005a). Freshwater marshes as dissolved silica recyclers in an estuarine environment (Schelde estuary, Belgium). *Hydrobiologia*, 540(1-3):69–77.

Struyf, E., Van Damme, S., Gribsholt, B., Middelburg, J. J., and Meire, P. (2005b). Biogenic silica in tidal freshwater marsh sediments and vegetation (Schelde estuary, Belgium). *Marine Ecology Progress Series*, 303:51–60.

Sun, J., Liu, D., Yang, S., Guo, J., and Qian, S. (2002). The preliminary study on phytoplankton community structure in the central Bohai Sea and the Bohai Strait and its adjacent area. *Oceanologia et Limnologia Sinica*, 33(5):461–471.

Sutherland, T., Amos, C., and Grant, J. (1998). The effect of buoyant biofilms on the erodibility of sublittoral sediments of a temperate microtidal estuary. *Limnology and Oceanography*, 43(2):225–235.

Sutton, J. N., Varela, D. E., Brzezinski, M. A., and Beucher, C. P. (2013). Species-dependent silicon isotope fractionation by marine diatoms. *Geochimica et Cosmochimica Acta*, 104:300–309.

Thamatrakoln, K. and Hildebrand, M. (2008). Silicon uptake in diatoms revisited: a model for saturable and nonsaturable uptake kinetics and the role of silicon transporters. *Plant physiology*, 146(3):1397–1407.

Thamatrakoln, K. and Kustka, A. B. (2009). When to say when: can excessive drinking explain silicon uptake in diatoms? *BioEssays*, 31(3):322–327.

Thieu, V., Billen, G., and Garnier, J. (2009). Nutrient transfer in three contrasting NW European watersheds: the Seine, Somme, and Scheldt Rivers. A comparative application of the Seneque/Riverstrahler model. *Water research*, 43(6):1740–1754.

Thornton, D. C., Dong, L. F., Underwood, G. J., and Nedwell, D. B. (2002). Factors affecting microphytobenthic biomass, species composition and production in the Colne Estuary (UK). *Aquatic Microbial Ecology*, 27(3):285–300.

Tolhurst, T., Black, K., Paterson, D., Mitchener, H., Termaat, G., and Shayler, S. (2000). A comparison and measurement standardisation of four in situ devices for determining the erosion shear stress of intertidal sediments. *Continental Shelf Research*, 20(10-11):1397–1418.

Tolhurst, T., Black, K., Shayler, S., Mather, S., Black, I., Baker, K., and Paterson, D. (1999). Measuring the in situ erosion shear stress of intertidal sediments with the Cohesive Strength Meter (CSM). *Estuarine, Coastal and Shelf Science*, 49(2):281–294.

Tolhurst, T., Consalvey, M., and Paterson, D. (2008). Changes in cohesive sediment properties associated with the growth of a diatom biofilm. *Hydrobiologia*, 596(1):225–239.

Tolhurst, T., Defew, E., De Brouwer, J., Wolfstein, K., Stal, L., and Paterson, D. (2006). Small-scale temporal and spatial variability in the erosion threshold and properties of cohesive intertidal sediments. *Continental Shelf Research*, 26(3):351–362.

Tolhurst, T., Gust, G., and Paterson, D. (2002). The influence of an extracellular polymeric substance (EPS) on cohesive sediment stability. In *Proceedings in Marine Science*, volume 5, pages 409–425. Elsevier.

Tréguer, P., Bowler, C., Moriceau, B., Dutkiewicz, S., Gehlen, M., Aumont, O., Bittner, L., Dugdale, R., Finkel, Z., Iudicone, D., et al. (2018). Influence of diatom diversity on the ocean biological carbon pump. *Nature Geoscience*, 11(1):27.

Treguer, P., Nelson, D. M., Van Bennekom, A. J., DeMaster, D. J., Leynaert, A., and Queguiner, B. (1995). The silica balance in the world ocean: a reestimate. *Science*, 268(5209):375–379.

Tréguer, P. J. and De La Rocha, C. L. (2013). The world ocean silica cycle. *Annual review of marine science*, 5:477–501.

Trimmer, M., Nedwell, D., Sivyer, D., and Malcolm, S. (1998). Nitrogen fluxes through the lower estuary of the river Great Ouse, England: the role of the bottom sediments. *Marine Ecology Progress Series*, 163:109–124.

Turner, R. E., Rabalais, N. N., Dortch, Q., et al. (2003). Future aquatic nutrient limitations. *Marine Pollution Bulletin*, 46(8):1032–1034.

Ubertini, M., Lefebvre, S., Rakotomalala, C., and Orvain, F. (2015). Impact of sediment grain-size and biofilm age on epipelic microphytobenthos resuspension. *Journal of experimental marine biology and ecology*, 467:52–64.

Uncles, R. (1981). A note on tidal asymmetry in the Severn estuary. *Estuarine, Coastal and Shelf Science*, 13(4):419–432.

Uncles, R. (1982). Residual currents in the Severn estuary and their effects on dispersion. *Oceanologica Acta*, (4).

Uncles, R. (1984). Hydrodynamics of the Bristol channel. *Marine Pollution Bulletin*, (2).

Uncles, R. (2010). Physical properties and processes in the Bristol Channel and Severn Estuary. *Marine Pollution Bulletin*, 61(1-3):5–20.

Uncles, R., Stephens, J., and Smith, R. (2002). The dependence of estuarine turbidity on tidal intrusion length, tidal range and residence time. *Continental Shelf Research*, 22(11-13):1835–1856.

Underwood, G. (2001). *Microphytobenthos*, volume 6. Encyclopedia of Ocean Sciences.

Underwood, G., Paterson, D., and Parkes, R. (1995). The measurement of microbial carbohydrate exopolymers from intertidal sediments. *Limnology and Oceanography*, 40(7):1243–1253.

Underwood, G., Perkins, R., Consalvey, M., Hanlon, A., Oxborough, K., Baker, N., and Paterson, D. (2005). Patterns in microphytobenthic primary productivity: Species-specific variation in migratory rhythms and photosynthetic efficiency in mixed-species biofilms. *Limnology and Oceanography*, 50(3):755–767.

Underwood, G. and Smith, D. (1998). Predicting epipelic diatom exopolymer concentrations in intertidal sediments from sediment chlorophyll a. *Microbial Ecology*, 35(2):116–125.

Underwood, G. J. (2010). Microphytobenthos and phytoplankton in the Severn estuary, UK: present situation and possible consequences of a tidal energy barrage. *Marine Pollution Bulletin*, 61(1-3):83–91.

Underwood, G. J. and Paterson, D. M. (2003). The importance of extracellular carbohydrate productionby marine epipelic diatoms. *Advances in botanical research*, 40:183–240.

Underwood, G. J. C. and Paterson, D. M. (1993). Seasonal changes in diatom biomass, sediment stability and biogenic stabilization in the Severn Estuary. *Journal of the Marine Biological Association of the United Kingdom*, 73(4):871–887.

Van Cappellen, P., Dixit, S., and van Beusekom, J. (2002). Biogenic silica dissolution in the oceans: Reconciling experimental and field-based dissolution rates. *Global Biogeochemical Cycles*, 16(4):23–1.

Van Damme, S., Struyf, E., Maris, T., Ysebaert, T., Dehairs, F., Tackx, M., Heip, C., and Meire, P. (2005). Spatial and temporal patterns of water quality along the estuarine salinity gradient of the Scheldt estuary (Belgium and The Netherlands): results of an integrated monitoring approach. *Hydrobiologia*, 540(1-3):29–45.

Van Der Zee, C. and Chou, L. (2005). Seasonal cycling of phosphorus in the Southern Bight of the North Sea. *Biogeosciences*, 2(1):27–42.

Vandenbruwaene, W., Plancke, Y., Verwaest, T., and Mostaert, F. (2013). Interestuarine comparison: hydrogeomorphology: hydro-and geomorphodynamics of the TIDE estuaries Scheldt, Elbe, Weser and Humber. *WL Rapporten*.

Vanderborght, J.-P., Folmer, I. M., Aguilera, D. R., Uhrenholdt, T., and Regnier, P. (2007). Reactive-transport modelling of C, N, and O2 in a river–estuarine–coastal zone system: application to the Scheldt estuary. *Marine chemistry*, 106(1-2):92–110.

Vanderborght, J.-P., Wollast, R., Loijens, M., and Regnier, P. (2002). Application of a transport-reaction model to the estimation of biogas fluxes in the Scheldt Estuary. *Biogeochemistry*, 59(1-2):207–237.

Vieira, S., Ribeiro, L., da Silva, J. M., and Cartaxana, P. (2013). Effects of short-term changes in sediment temperature on the photosynthesis of two intertidal microphytobenthos communities. *Estuarine, Coastal and Shelf Science*, 119:112–118.

Vilmin, L., Flipo, N., Escoffier, N., and Groleau, A. (2018). Estimation of the water quality of a large urbanized river as defined by the European WFD: what is the optimal sampling frequency? *Environmental Science and Pollution Research*, 25(24):23485–23501.

Vollenweider, R. (1968). Scientific fundamentals of the eutrophication of lakes and flowing waters, with particular reference to phosphorus and nitrogen as factors in eutrophication. *Organ. Econ. Coop. Devel. Tech. Rep. OAS/CSI/68.27*.

Volta, C., Arndt, S., Savenije, H. H., Laruelle, G. G., and Regnier, P. (2014). C-GEM (v 1.0): a new, cost-efficient biogeochemical model for estuaries and its application to a funnel-shaped system. *Geoscientific Model Development*, 7(4):1271–1295.

Volta, C., Laruelle, G. G., Arndt, S., and Regnier, P. (2016). Linking biogeochemistry to hydro-geometrical variability in tidal estuaries: a generic modeling approach. *Hydrology and earth system sciences*, 20(3):991–1030.

Vrieling, E. G., Sun, Q., Tian, M., Kooyman, P. J., Gieskes, W. W. C., van Santen, R. A., and Sommerdijk, N. A. J. M. (2007). Salinity-dependent diatom biosilicification implies an important role of external ionic strength. *Proceedings of the National Academy of Sciences*, 104(25):10441–10446.

Waldbusser, G. G., Marinelli, R. L., Whitlatch, R. B., and Visscher, P. T. (2004). The effects of infaunal biodiversity on biogeochemistry of coastal marine sediments. *Limnology and Oceanography*, 49(5):1482–1492.

Wang, J. and Kang, Y. (1998). Study on population dynamics of phytoplankton in the Bohai Sea. *Marine fisheries research*, 19(1):43–52.

Waring, J., Underwood, G. J., and Baker, N. R. (2006). Impact of elevated UV-B radiation on photosynthetic electron transport, primary productivity and carbon allocation in estuarine epipelic diatoms. *Plant, cell & environment*, 29(4):521–534.

Weiss, A., De La Rocha, C., Amann, T., and Hartmann, J. (2015). Silicon isotope composition of dissolved silica in surface waters of the Elbe Estuary and its tidal marshes. *Biogeochemistry*, 124(1-3):61–79.

Welsby, H., Hendry, K., and Perkins, R. (2016). The role of benthic biofilm production in the mediation of silicon cycling in the Severn Estuary, UK. *Estuarine, Coastal and Shelf Science*, 176:124–134.

West, A. J., Galy, A., and Bickle, M. (2005). Tectonic and climatic controls on silicate weathering. *Earth and Planetary Science Letters*, 235(1-2):211–228.

White, A. F. and Blum, A. E. (1995). Effects of climate on chemical weathering in watersheds. *Geochimica et Cosmochimica Acta*, 59(9):1729–1747.

Wille, M., Sutton, J., Ellwood, M. J., Sambridge, M., Maher, W., Eggins, S., and Kelly, M. (2010). Silicon isotopic fractionation in marine sponges: A new model for understanding silicon isotopic variations in sponges. *Earth and Planetary Science Letters*, 292(3-4):281–289.

Willett, V., Reynolds, B., Stevens, P., Ormerod, S., and Jones, D. (2004). Dissolved organic nitrogen regulation in freshwaters. *Journal of Environmental Quality*, 33(1):201–209.

Wolf, J. (1987). A 3-D model of the Severn Estuary. In *Elsevier oceanography series*, volume 45, pages 609–624. Elsevier.

Wollast, R. and De Broeu, F. (1971). Study of the behavior of dissolved silica in the estuary of the Scheldt. *Geochimica et Cosmochimica Acta*, 35(6):613–620.

Xia, J., Falconer, R., Lin, B., and Tan, G. (2011). Estimation of future coastal flood risk in the Severn Estuary due to a barrage. *Journal of Flood Risk Management*, 4(3):247–259.

Xia, J., Falconer, R. A., and Lin, B. (2010a). Hydrodynamic impact of a tidal barrage in the Severn Estuary, UK. *Renewable energy*, 35(7):1455–1468.

Xia, J., Falconer, R. A., and Lin, B. (2010b). Impact of different tidal renewable energy projects on the hydrodynamic processes in the Severn Estuary, UK. *Ocean Modelling*, 32(1-2):86–104.

Yallop, M., Paterson, D., and Wellsbury, P. (2000). Interrelationships between rates of microbial production, exopolymer production, microbial biomass, and sediment stability in biofilms of intertidal sediments. *Microbial ecology*, 39(2):116–127.

Yallop, M. L., de Winder, B., Paterson, D. M., and Stal, L. J. (1994). Comparative structure, primary production and biogenic stabilization of cohesive and non-cohesive marine sediments inhabited by microphytobenthos. *Estuarine, Coastal and Shelf Science*, 39(6):565–582.

Yamada, S. S. and D'Elia, C. F. (1984). Silicic acid regeneration from estuarine sediment cores. *Marine ecology progress series. Oldendorf*, 18(1):113–118.

Zambardi, T. and Poitrasson, F. (2011). Precise determination of silicon isotopes in silicate rock reference materials by MC-ICP-MS. *Geostandards and Geoanalytical Research*, 35(1):89–99.

Zhang, A., Zhang, J., Hu, J., Zhang, R., and Zhang, G. (2015). Silicon isotopic chemistry in the Changjiang Estuary and coastal regions: Impacts of physical and biogeochemical processes on the transport of riverine dissolved silica. *Journal of Geophysical Research: Oceans*, 120(10):6943–6957.

Zhang, J., Zhang, G., and Liu, S. (2005). Dissolved silicate in coastal marine rainwaters: comparison between the Yellow Sea and the East China Sea on the impact and po-

tential link with primary production. *Journal of Geophysical Research: Atmospheres*, 110(D16).

Ziegler, K., Chadwick, O. A., Brzezinski, M. A., and Kelly, E. F. (2005). Natural variations of δ30Si ratios during progressive basalt weathering, Hawaiian Islands. *Geochimica et Cosmochimica Acta*, 69(19):4597–4610.

Zurzolo, C. and Bowler, C. (2001). Exploring bioinorganic pattern formation in diatoms. a story of polarized trafficking. *Plant Physiology*, 127(4):1339–1345.